A 3D architectural rendering of a city with various building heights and shapes. The top surfaces of the buildings are covered with satellite or aerial imagery, showing green spaces, roads, and urban structures. The background is a light, neutral color.

FICUP
An International Conference on Urban Physics
B. Beckers, T. Pico, S. Jimenez (Eds.)
Quito - Galápagos, Ecuador, 26 - 30 September 2016

FICUP 2016

First International Conference on Urban Physics

Proceedings

- Massive 3D models and physical data
- Local observations and remote sensing
- Environmental physics and urban climate
 - Renewable energies and sustainable urban planning
 - Finite element and other simulation methods

ICUP No.01**September 2016 Quito - Galápagos**

FICUP First International Conference on Urban Physics

President of the Pontifical Catholic University of Ecuador

PhD. Fernando Ponce León S.J.

Vice - President of the Pontifical Catholic University of Ecuador

Dr. Fernando Barredo S.J.

General Academic Director - PUCE

Dr. Graciela Monesterolo Lencioni

Research Director - PUCE

PhD. Rommel Montúfar

Dean of the School of Architecture, Design and Arts - PUCE

Msc. MPhil. Arch. Sylvia Jiménez

FICUP 2016 Organization

Msc. Arch. Tannya Pico

Arch. Jairo Acuña Paz y Miño

Layout & Cover Design

M. Des. Guillermo Sánchez B

Scientific Committee

Chairman: Benoit Beckers (Université de Pau et des Pays de l'Adour, France)

Daniel Aliaga (Purdue University, USA)

Pierre Alliez (Inria Sophia Antipolis – Méditerranée, France)

Viorel Badescu (Candida Oancea Institute, Polytechnic University of Bucharest and Romanian Academy, Romania)

Pierre Beckers (Université de Liège, Belgium)

Gonzalo Besuievsky (Universitat de Girona, Spain)

Philippe Blanc (Mines ParisTech, France)

Bert Blocken (Eindhoven University of Technology, the Netherlands and Leuven University, Belgium)

Emmanuel Bozonnet (Université de La Rochelle, France)

Piotr Bretkopf (Université de Technologie de Compiègne, France)

Wouter Buytaert (Imperial College London, London, UK)

Guedi Capeluto (Technion - Israel Institute of Technology, Israel)

Alberto Cardona (Universidad Nacional del Litoral, Santa Fe, Argentina)

Alain Clappier (Université de Strasbourg, France)

Raphaël Compagnon (Haute Ecole d'Ingénierie et d'architecture de Fribourg, Switzerland)

Philippe R B Devloo (Universidade Estadual de Campinas – FEC, Brazil)

Eduardo Fernández (Universidad de la República, Montevideo, Uruguay)

Gérard Hégron (IFSTTAR, France)

Adnan Ibrahimbegovic (Université de Technologie de Compiègne, France)

Jérôme Kämpf (Ecole Polytechnique Fédérale de Lausanne, Switzerland)

Vincent Lemort (Université de Liège, Belgium)

John Mardaljevic (Loughborough University, UK)

Alberto Martilli (Ciemat, Madrid, Spain)

Valéry Masson (Centre National de Recherches Météorologiques, Toulouse, France)

Edward Ng (Chinese University of Hong Kong, China)

Gustavo Patow (Universitat de Girona, Spain)

Marius Paulescu (West University of Timisoara, Rumania)

Claude Puech (INRIA Chile, Chile)

Luis Quiroz (Universidad de Concepción, Chile)

Alain Rassineux (Université de Technologie de Compiègne, France)

François Sillion (INRIA, France)

James Voogt (University of Western Ontario, Canada)

Benoit Beckers, Tannya Pico & Sylvia Jiménez Editors

ISBN (electronic)

978-9942-951-53-3

Architecture, FADA, PUCE

Av.12 de Octubre 1076 y Patria

Quito, Ecuador

Telephone: (593) 02 299 17 00

**Representative of the United Nations
Development Programme (UNDP) in Ecuador**

Mr. Diego Zorrilla

**Responsible of the Environment
and Energy Area**

Mr. Gabriel Jaramillo

**Technical Officer of the Environment
and Energy Area**

Mr. Merijn de Smet

Communications Officer

Mr. José Martino

Communications Assistant

Mr. Paola Brito Ayala

Published by:

UNDP Ecuador

United Nations Development Programme

Av. Amazonas 2889 y la Granja

Quito, Ecuador

Telephone: (593) 02 246 03 30

The analysis and recommendations of this report do not necessarily reflect the views of the United Nations Development Programme, its Executive Board or the United Nations Member States.

Acknowledgement

The completion of this undertaking could not have been possible without the collaboration of the United Nations Development Programme, Consejo de Gobierno del Régimen Especial de Galápagos, Maestría en Arquitectura y Sostenibilidad - FADA, Université de Technologie de Compiègne, Université de Pau et des Pays de l'Adour and the Charles Darwin Foundation.

We owe a special word of gratitude to María Antonieta Sanchez, María Francisca Tapia and Jairo Acuña for their early encouragement and commitment with this project. We are grateful to all the members of the staff who have worked with us through the development of this international conference.

Their contribution is sincerely appreciated and gratefully acknowledged.

*Benoit Beckers, Tannya Pico & Sylvia Jiménez,
FICUP 2016*

First International Conference on Urban Physics (FICUP)

INDEX

Forewords of Diego Zorrilla, Representative of the United Nations Development Programme (UNDP) in Ecuador.....	ii
Forewords of S. J. Fernando Ponce León, Rector of the Pontifical Catholic University of Ecuador.....	iii
Scientific Committee.....	iv
Introduction:	
Why Urban Physics and Why in Ecuador? by PhD Benoit Beckers.....	ix
Sparse Matrix Solution for Computing Urban Radiation Exchange, José Pedro Aguerre, Eduardo Fernández, Gonzalo Besuvievsky, and Benoit Beckers	1
Historical Urban Landscape as a Descriptive Feature for Risk Assessment: the ‘Quebradas’ of Quito, Sheika M. Aragundi, Alexandra P. Mena, and Jenny J. Zamora	14
Fast And Accurate View Factor Generation, Benoit Beckers and Pierre Beckers	22
Skyline-control Based LoD Generation for Solar Analysis in 3D Cities, Gonzalo Besuievsky, Benoit Beckers, and Gustavo Patow.....	32
Towards Reduced-Order Modeling Of Complex Phenomena In Urban Physics, Piotr Breitkopf, Pierre Villon.....	45
Energy Strategies towards a Fully Sustainable Galapagos Archipelago, Pedro Calle, Siebe Broersma	51
An Electrifying Change: The Need To Introduce Electric Vehicles In Ecuador, And Its Potential Impact On The Energy Sector, Davis, M.J.M.....	62
From Theory to Practice: Building Physics in Urban Design, John Martin Evans and Silvia de Schiller.....	72
A study of solar access in Bogotá: the Las Nieves neighborhood, R. Franco, P. Bright, J Benitez, and B. Beckers.....	96

Environmental Quality At District Scale: A Transdisciplinary Approach Within The EUREQUA Project , Gauvreau B., Guillaume G., Can A., Gaudio N., Lebras J., Lemonsu A., Masson V., Carissimo B., Richard I. and Haouès-Jouve S.....	122
Climate Comparision In The Urban Areas Of The Oyambaro And Quito Valleys , Jiménez R., Sylvia; Van Sluys, Christine	135
Multiphysic Design of a Street Section , Catherine Knopf-Lenoir, David Muñoz, Raphaël Nahon, Benoit Beckers	147
Plenary Session : Urban Climate, Human behavior & Energy consumption: from LCZ mapping to simulation and urban planning (the MAPUCE project) , V. Masson, J. Hidalgo, A. Amossé, E. Bocher, M. Bonhomme, A. Bourgeois, G. Bretagne, S. Caillerez, E. Cordeau; C. Demazeux; S. Faraut, C. Gallato, S. Haoues- Jouve, M.-L. Lambert, A. Lemonsu, J.-P. Lévy, N. Long; C.-X. Lopez, G. Petit, M. Pellegrino, C. Pignon, C. Plumejeaud, V. Ruff, R. Schoetter, N. Tornay, D. Vye.....	157
Sky Access versus Shading for Pedestrian Comfort in the Hot Tropical Climate of Jeddah , Badia Masoud, Benoit Beckers, and Helena Coch.....	168
Numerical modelling of evaporative cooling using water spray systems for heat stress reduction in urban areas , H. Montazeri, Y. Toparlar, B. Blocken and J.L.M. Hensen.....	178
Impact of the anisotropy of the sky vault emissivity on the building envelope radiative budget , R. Nahon, O. Blanpain, and B. Beckers	188
Impacts Of Realistic Surface Heating On Outdoor Thermal Comfort , Negin Nazarian, Tiffany Sin, Leslie K. Norford	199
Estimating the Urban Heat Island Effect in the City of Guayaquil , Massimo Palme, Geovanna Villacreses, Andrea Lobato, Martín Cordovez, José Macias and Guillermo Soriano.....	210
Daylighting: an approach from urban to room scale , Bernard A. Paule and Jérôme H. Kaempf.....	224
Heat stress in urban area: data fusion of observations, modeling and geospatial information , L. Pinson and V. Masson.....	239

A robust smoothed voxel representation for the generation of finite element models for computational urban physics , Alain Rassinoux, Benoit Beckers.....	249
Downburst Reconstruction using Physical Simulation and Analytical Model with Application to Urban Environments , Djordje Romanic, Dan Parvu, Horia Hangan	260
To evaluate the sustainability of urban planning projects through an LCA approach: example of application of the NEST tool and requirements for its use in the context of Ecuador and Latin America , Nicolas Salmon Grace Yopez-Salmon, Marc Lotteau.....	272
Plenary Session : Object-Oriented Approach to Urban Canyon Analysis , Timofey E. Samsonov, Pavel I. Konstantinov, Mikhail I. Varentsov	283
Solar Cooling in the Ecuadorian Contexts , María A. Sanchez del Hierro, Jairo Acuña, Tannya K. Pico, Jorge D. Czajkowski	301
Real-time material computation in architectural design: Experiments on the development of interactive form finding tools , Seiichi Suzuki Erazo.....	316
Computational analysis of an urban park's impact on the Antwerp microclimate , Yasin Toparlak, Bert Blocken, Bino Maiheu, GertJan van Heijst	325
Radiative Performance Assessment Of Two Roofs In Mediterranean And Equatorial Climates , J. Torres-Quezada, A. Pages-Ramon, H. Coch and A. Isalgué.....	337
Periodic 3D model to optimize urban shapes for solar radiation , T. Vermeulen, C. Knopf-Lenoir, L. Merino, P. Villon, and B. Beckers	349
Pertinence of social inclusion design methods in communities , Enrique V. Villacís, María L. Rodriguez, Cynthia C. Ayarza, and Klaus Rueckert.....	358
Application of Large-Eddy Simulations in Evaluating Ventilation over 3D Building Data Retrieved from Satellite Images , Weiwen Wang, Yong Xu, and Edward Ng.....	367

The urban environment, an anthroposystem in continuous change and evolution, has brought about many advantages to our societies and without doubt, the 21st century will be one of intense urbanization. The mix of social, economic, demographic and environmental aspects within this setting, combined with its physical design, make for a complex arrangement of a large number of variables.

It is in that context that we now turn to science for aid. New technologic tools, combined with the scientific rigor we can find in the field of physics, present us with promising advances that can increase our understanding of the structure and dynamics of the city and can allow us to hope for a future of sustainable urban design and management. A variety of such examples are presented in this publication that consolidates the academic papers presented at the First International Conference on Urban Physics, which was held in the beautiful city of Quito, Ecuador in October 2016. Quito was also the stage for the UN Habitat III conference, in which the United Nations launched their New Urban Agenda.

Last year, the United Nations approved the 2030 Agenda for Sustainable Development with the Sustainable Development Goals as its main focus. In the coming years the UN and all its development partners will work arduously towards making progress in all of the 17 SDG's, including goal no. 11: - Sustainable cities, will allow us to focus on adopting and implementing integrated policies and plans towards inclusion, resource efficiency, mitigation and adaptation to climate change and resilience to disasters in cities.

Our strong commitment to a new and improved urban future will be incorporated into our actions in the coming years. We



realize that the academic sector is a key ally in this process. It can provide us with new methods and sound scientific information to write informed new policy guidelines to be implemented globally.

In this regard, I also applaud the effort of Dr. Beckers in pointing out a crucial element, namely the divergence between the data available for the western hemisphere and the scarcity of data we still have in less developed areas of the world, where a different climate, different social relations and other economic possibilities confront us with different realities. No doubt this will be one of our main challenges, as the urbanization process is present in the whole world.

The United Nations always strive for inclusive change and development for all with the goal of decreasing poverty and inequality and although challenging, our actions are already underway. We thank the organization of the FICUP for aiding us in our efforts.

Diego Zorrilla
Representative of the United Nations
Development Programme (UNDP) in Ecuador

For our University, and for many others, scientific, technologic and economic development will only make sense if it contributes to increase the global commons of mankind instead of creating an economy of exclusion and a culture of the disposable.

We also believe that nature is a gift from God, not our personal quarry / source that can be exploited until its total exhaustion. For this reason, the responsibility to preserve nature becomes a priority before the possibilities of exploiting it. All living beings are connected. Without exception, as members of the same human family, together with all living creatures and future generations we have received this gift that we should not use at our whim and will.

Being coherent with these thoughts we decided to organize and host this international academic conference whose main objective is to meet the highest scientific expectations and expose the most innovative proposals for the development of sustainable cities. As you know, this event seeks to synthesize the recent scientific developments that affect cities, their energy efficiency, their impact on climate change, hence their indisputable importance and relevance.

At the regional level, this conference aims to become a unique opportunity to promote studies on Andean, Amazonian or Islander cities little represented in the scientific literature. At the local level, this conference offers Ecuadorian researchers the opportunity to participate in a high-level academic event, to establish a network with the international scientific community and to become a hub for research aimed at improving life quality in our cities.



Finally, this First International Conference on Urban Physics is articulated perfectly with the Habitat III conference as a preparatory event. In addition is one of the emblematic events celebrating the 70 years of our beloved University. And most important of all, it responds to the call of Pope Francis in the Encyclical *Laudato Si*, to pledge us all for the care of our common house: the earth.

S. J. Fernando Ponce León
Rector of the Pontifical Catholic
University of Ecuador

First International Conference on Urban Physics (FICUP)

Scientific Committee

Chairman:	Benoit Beckers	Université de Pau et des Pays de l'Adour, France
Members:	Daniel Aliaga,	Purdue University, USA
	Pierre Alliez,	Inria Sophia Antipolis – Méditerranée, France
	Viorel Badescu,	Candida Oancea Institute, Polytechnic University of Bucharest and Romanian Academy, Romania
	Pierre Beckers,	Université de Liège, Belgium
	Gonzalo Besuievsky,	Universitat de Girona, Spain
	Philippe Blanc,	Mines ParisTech, France
	Bert Blocken,	Eindhoven University of Technology, the Netherlands and Leuven University, Belgium
	Emmanuel Bozonnet,	Université de La Rochelle, France
	Piotr Breitkopf,	Université de Technologie de Compiègne, France
	Wouter Buytaert,	Imperial College London, London, UK
	Guedi Capeluto,	Technion - Israel Institute of Technology, Israel

Alberto Cardona, Universidad Nacional del Litoral, Santa Fe,
Argentina

Alain Clappier, Université de Strasbourg, France

Raphaël Compagnon, Haute Ecole d'Ingénierie et d'architecture de
Fribourg, Switzerland

Philippe R B Devloo, Universidade Estadual de Campinas – FEC,
Brazil

Eduardo Fernández, Universidad de la República, Montevideo,
Uruguay

Gérard Hégron, IFSTTAR, France

Adnan Ibrahimbegovic, Université de Technologie de Compiègne,
France

Jérôme Kämpf, Ecole Polytechnique Fédérale de Lausanne,
Switzerland

Vincent Lemort, Université de Liège, Belgium

John Mardaljevic, Loughborough University, UK

Alberto Martilli, Ciemat, Madrid, Spain

Valéry Masson, Centre National de Recherches
Météorologiques, Toulouse, France

Edward Ng, Chinese University of Hong Kong, China

Gustavo Patow, Universitat de Girona, Spain

Marius Paulescu, West University of Timisoara, Rumania

Claude Puech, INRIA Chile, Chile

Luis Quiroz, Universidad de Concepción, Chile

Alain Rassinoux, Université de Technologie de Compiègne,
France

François Sillion, INRIA, France

James Voogt, University of Western Ontario, Canada

Why Urban Physics and Why in Ecuador?

Benoit Beckers

Architecture and Urban Physics
Department of Building and Public Works (ISA BTP)
Université de Pau et des Pays de l'Adour
Allée du Parc Montaury
64600 Anglet
France

Keywords: Urban physics, Building physics, Environmental physics, Urban climate, Ecuador

Abstract. *The fundamental question addressed in the first international conference on urban physics is: why study urban physics? This paper allows us to respond to this concern. The subsidiary question is why in Ecuador and the Galapagos. The history of this part of the world shows us that we are not doing more than following the footsteps of prestigious scientists for more than three hundred years.*

1. Introduction

Comparing today's cities worldwide, one is astonished by their many similarities in the form of streets, squares, facades, and other urban structures. This is due to a more and more noticeable convergence in construction techniques, but also in urban planning programs and territorial policies: downtowns with their tall towers of glass and steel, surrounded by large sets of brick and concrete blocks and residential areas sprawling far into the countryside.

In the past, cities were much more diverse: there were cities without streets such as Çatal Höyük, a Neolithic megalopolis of almost 13 hectares whose interiors were accessed from terraces connected to each other. There were also lake or lagoon cities such as the prestigious Venice, underground or semi-buried cities... These configurations were often excellent answers to climate assaults, because although other factors contributed to this (military defense and transport, among others), energy was expensive and the means to locally control the physical parameters of comfort such as temperature, air quality, lighting, and noise level were very limited. So, initiatives were taken in order to have the best general conditions on the urban scale, so that only small local adjustments should be necessary: some heating in homes, an increase of natural ventilation, candles for illuminating at night at the risk of setting fire to the neighborhood. However, neither of these ancient cities exceeded one million people from what we can tell.

Megacities of the Industrial Revolution have had to settle on other schemes and the past original solutions became obsolete, while new solutions were becoming increasingly uniform. Therefore, the new structures, which were very complex with their train networks, roads, running water, sewage, electricity, had to carry out special technology research. Indeed, several major scientific results came from urban problems of that time: the graph theory (anticipated by Euler to solve the problem of the bridges of Königsberg), the formulation of the heat equation by Fourier, which sought to solve Paris heating problems, and even the definition of the black body by Kirchhoff to characterize the new whiteness of electric light in the lighting of cities.

In return, however, the most conscientious planners could hardly benefit from the scientific and technical advances, and only indirectly: metal structures, glazing, the development of transport, the lift and other inventions have allowed for both center densification and periphery sprawl. They were not well thought-out choices: it was not possible to rely on such partial and transitory calculations as the course of shadows, the visuals, the sound rays, or the finding of prevailing winds, to account for the whole power of financials, investors and speculators effectively - or even only a little.

In the second half of the twentieth century, two important ideas have been developed. First, bioclimatic architecture has connected climate with people's activities and their comfort, establishing guidelines for the emergence of building physics. Then, environmental physics has developed its balance sheets of material, energy and momentum over crops and forests and - why not? - cities. At the beginning of this century, the progress of measure (and particularly telemetry) and computing allowed us to finally consider urban physics at the interface between building physics and environmental physics.

2. Urban Physics Worldwide

With these new resources, it becomes possible to map the Urban Heat Island [Pinson 2016], quantify the mutual influence between it and building consumptions [Masson 2016], and develop interdisciplinary studies taking into account air quality, climate comfort, and soundscapes [Gauvreau 2016]. With respect to numerical methods and their application to very large urban models, there are two main starting points: first, shortwave radiation [Beckers 2016] and longwave radiation [Nahon 2016], and, second, Computation Fluid Dynamics (CFD) methods [Montazeri 2016].

CFD simulations allow comprehensive studies on the effect of vegetation on a park in the urban environment [Toparlar 2016], but also on the very specific and potentially devastating phenomena related to windstorms [Romanic 2016].

Methods related to radiation, which can be heat, but also natural light [Paule 2016], give particular importance to the quality of the geometric model [Rassineux 2016], its level of detail [Besuievsky 2016] and are therefore utilized to calculate the specific characteristics of urban forms [Aguerre 2016], which then allow for the automatic optimization process [Vermeulen 2016].

These two steps would soon be combined in Finite Element Method (FEM) platforms applied to the city, which would help to better assess multiple physical aspects [Knopf-Lenoir 2016], but with significant computing time, which will justify in turn the use of methods such as model reduction techniques [Breitkopf 2016].

The most advanced work in this emerging field is often developed in Europe and North America, but also in important centers in Southeast Asia and Oceania. This allows for extensive studies of the urban climate in tropical megacities like Hong Kong [Wang 2016], or equatorial ones like Singapore [Nazarian 2016]. There are also studies on the specific characteristics of cities in arid climates [Massoud 2016] and Nordic ones or on Urban Heat Island in Arctic cities of the Russian far North [Salmonov 2016].

These studies are a fundamental part of the current research because considering the variety of climates on the globe, it is necessary to propose appropriate urban solutions, taking into account what is possible from historical solutions and adapting them to current conditions.

It is disappointing that the corresponding research does not have all the same reach or the same visibility, particularly in sub-Saharan Africa and Latin America; even though these two parts of the world have very important urban growth, with serious problems not only related to natural and industrial hazards, but also to energy supply deficits, air and soil pollution, and often poor quality of construction and maintenance.

The UN-Habitat program [<http://www.unhabitat.org/>] has therefore rightly been established in Nairobi (Kenya). After Vancouver (1976) and Istanbul (1996), the third Habitat conference will be held in Quito in October 2016 [<https://www.habitat3.org/>].

3. UrbanPhysics In Ecuador

In a relatively compact territory (ten times as big as Belgium), Ecuador meets four remarkable and differentiated climates: the Coast, the Andes, the Amazon and the Islands. As the name indicates, the country is located on both sides of the equator, and it is on its coast that the Humboldt Current, having enriched its cold, rich waters from Antarctica, the coasts of Chile and Peru, is changing its bearing to the open sea and the Galapagos Islands. The map in Figure 1, which represents this country, was drawn up in 1942 by the geographic services of the US army, at the time when the Galapagos Islands had acquired strategic importance against Japan. The Americans had set up a base there, and after the war, they left to the Ecuadorians the airport of Baltra and equipment for desalination. Thus populations could settle permanently on these islands, well-preserved so far by the lack of drinking water.

The population, a small forty thousand inhabitants, lives in a unique and much protected nature reserve, where any intervention is particularly exposed, starting with access to energy [Calle 2016] and the development of essential infrastructures, such as Baltra airport [Evans 2016].

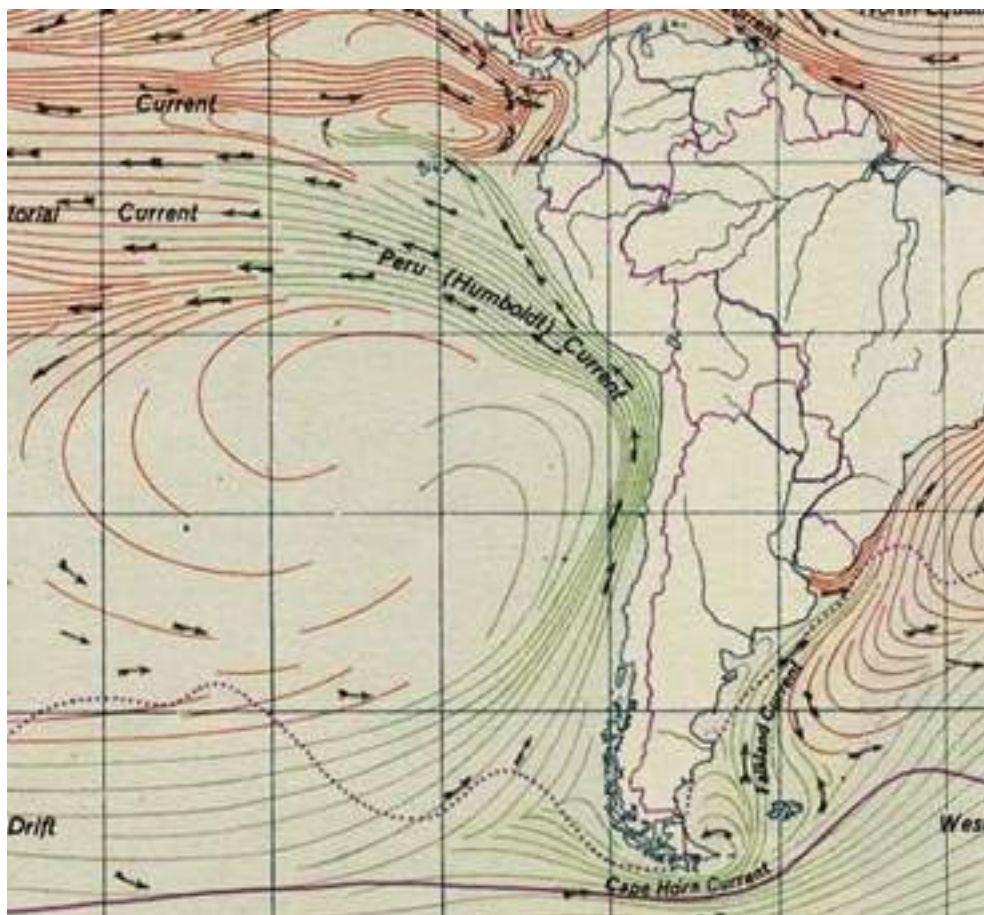


Figure 1: https://commons.wikimedia.org/wiki/File:Humboldt_current.jpg

The Ecuadorian Coast is one of those special places where life proliferates, on land and in the water: cocoa, bananas, shrimp, among many other species of flora and fauna. Some of the most remarkable and oldest cultures of pre-Columbian America have developed there, especially the Valdivias (3500 - 1800 B.C.) and the Chorreras (1200 - 500 B.C.). The “Museo Nacional

Quito” displays these extraordinary achievements. In this very hot and very humid climate, an appropriate architecture is of the essence [Torres Quezada 2016], and the Urban Heat Island of the great city of Guayaquil has to be limited [Palme 2016].

In the early sixteenth century, the Andean Inca civilization, originated from Cuzco, dominated Ecuador. It is in Quito that the emperor Huayna Capac learned of the existence of Spanish people, before dying in the south of the present-day Colombia, probably of smallpox, which shortly preceded the advance of the Conquistadores.

Quito is the second highest capital in the world (2850 meters), after La Paz (3660 meters) and before the megacity of Bogota (2640 meters). With an annual average temperature of 14-15 degrees in Bogota as well as in Quito, solar gains are welcome, but the access to natural light should rule bioclimatic architecture [Franco 2016].

Quito owes its beauty to a remarkably preserved colonial city, but more specifically to a superb location where ravines alternate with volcanoes [Aragundi 2016]. In the eighteenth century, this “volcanoes alley” formed the most accessible and open place around the equatorial line.

That is why Charles Marie de La Condamine (Paris 1701 - Paris 1774) chose to lead the “French geodesic expedition in Ecuador” there from 1735 to 1743 to determine the shape of the Earth. He was accompanied by the mathematician and physicist Pierre Bouguer (Le Croisic 1698 - Paris 1758), who published an “Essai d’optique sur la gradation de la lumière” in 1729 [Bouguer 1729], where he assessed the amount of light lost by passing through a given area of the Earth’s atmosphere. The geodesic expedition left such memories in Ecuador that the country owes its present name to it, after the failure of Simon Bolivar’s “Gran Colombia”.

Another scientific expedition has left a deep impression on the region, that of Alexander von Humboldt (Berlin 1769 - Potsdam 1859) and Aimé Jacques Alexandre Goujaud, known as Bonpland (La Rochelle 1773 - Paso de los Libres 1858). In 1802, they conducted a vegetation survey of Chimborazo, considering altitude, climate, and topography. They began the ascent of the volcano, without reaching the summit at 6310 meters altitude. Nevertheless, they held the world record for altitude until 1804, when Joseph Louis Gay-Lussac passed 7000 meters, but in a hot air balloon.

Before that, Humboldt and Bonpland had met José Celestino Mutis y Bosio (Cádiz 1732 - Santa Fe de Bogotá in 1808). The Spanish doctor was the protagonist of the “Real Expedición Botánica del Nuevo Reino de Granada”, the only genuine high-scale scientific enterprise realized in the American colonies of Spain, under the enlightened reign of Carlos III. This expedition, which lasted thirty years starting in 1783, allowed the scientists to collect and classify 20 000 plant species and 700 animal species in the territory of present-day Colombia. It allowed for the creation a group of scientists and local artists who participated in the independence movement, often paying for that with their lives.

Today, intellectual life has become less dangerous, and Ecuadorian researchers – or researchers

established in Ecuador – are exploring new architectural forms in the Ecuadorian context [Suzuki 2016], the link between architecture and social life [Villacis 2016], the adaptation of sustainable urban planning approaches [Salmon 2016], and the feasibility of the transition to electric vehicles [Davis 2016]. In doing so, they develop, in the very particular physical and socio-economic context of their country, ideas that concern researchers worldwide.

Finally, we must mention one last significant scientific expedition that closely concerns Ecuador, probably the most famous one. In 1831, the young Charles Darwin (Shrewsbury 1809 - Downe 1882) embarked on the Beagle for an expedition that lasted five years. He explored the coasts of Brazil, Uruguay, Argentina, Chile, and Peru, crossing the Andes several times in search of geological strata and fossils of extinct animals. On the way back, during a stop at the Galapagos, he naturalized some birds that seemed to be of different species. After his return to England, John Gould observed that all these birds were finches, differing only by the shape of their beaks. For Darwin, it was the finding that led him, after much verification, to formulate his theory of natural selection.

Ten years ago, on June 23, 2006, the last passenger of the Beagle died in Beerwah, Australia, victim of a heart attack. Harriet was then 175 years old. This Galapagos turtle had been picked up by Charles Darwin, and then offered to a friend who took her to Australia. During the life of Harriet, the human population multiplied by seven. The whalers no longer stop in the islands in the best interest of the turtles. The hard whale fishing has stopped, but the seas are now plowed by container ships and the continents have seen a proliferation of cities and their suburbs, to cover a high percentage of the land surface.

4. Conclusions

If she had lived ten years longer, maybe Harriet would be moved to learn that some researchers would meet in her native country to discuss the future of human cities, their footprint on our planet, and their control by means of physical modeling, satellite imagery, and computers. But we would have ignored it, because the emotions of a turtle remain imperceptible to us.

References

[Aguerre 2016] José Pedro Aguerre, Eduardo Fernández, Gonzalo Besuvievsky, and Benoit Beckers, *Sparse Matrix Solution for Computing Urban Radiation Exchange*, *First International Conference on Urban Physics* (Quito – Galapagos, 2016, Sept. 26-30)

[Aragundi2016] Sheika M. Aragundi, Alexandra P. Mena and Jenny J. Zamora *Historical Urban Landscape as a Descriptive Feature for Risk Assessment: the ‘Quebradas’ of Quito*, *First International Conference on Urban Physics* (Quito – Galapagos, 2016, Sept.

[Beckers 2016] Benoit Beckers and Pierre Beckers, *Fast and accurate view factor generation*, *First International Conference on Urban Physics* (Quito – Galapagos, 2016, Sept. 26-30)

[Besuievsky 2016] Gonzalo Besuievsky, Benoit Beckers, and Gustavo Patow, *Skyline- control Based LoD Generation for Solar Analysis in 3D Cities*, *First International Conference on Urban Physics* (Quito – Galapagos, 2016, Sept. 26-30)

[Bouguer 1729] Pierre Bouguer, *Essai d'optique sur la gradation de la lumière*, Claude Jombert ed., 1729

[Breitkopf 2016] Piotr Breitkopf, Pierre Villon, *Towards reduced-order modeling of complex phenomena in urban physics*, *First International Conference on Urban Physics* (Quito – Galapagos, 2016, Sept. 26-30)

[Calle2016] Pedro Calle, Siebe Broersma, *Energy Strategies towards a Fully Sustainable Galapagos Archipelago*, *First International Conference on Urban Physics* (Quito – Galapagos, 2016, Sept. 26-30)

[Davis 2016] Davis, M.J.M., *An Electrifying Change: The Need to Introduce Electric Vehicles in Ecuador, And Its Potential Impact on the Energy Sector*, *First International Conference on Urban Physics* (Quito – Galapagos, 2016, Sept. 26-30)

[Evans 2016] John Martin Evans and Silvia de Schiller, *From Theory to Practice: Building Physics in Urban Design*, *First International Conference on Urban Physics* (Quito – Galapagos, 2016, Sept. 26-30)

[Franco 2016] A study of solar access in Bogotá: the Las Nieves neighborhood, R. Franco, P. Bright, J Benitez, and B. Beckers, *First International Conference on Urban Physics* (Quito – Galapagos, 2016, Sept. 26-30)

[Gauvreau 2016] Gauvreau B., Guillaume G., Can A., Gaudio N., Lebras J., Lemonsu A., Masson V., Carissimo B., Richard I. and Haouès-Jouve S., *Environmental quality at district scale: A transdisciplinary approach within the EUREQUA project*, *First International Conference on Urban Physics* (Quito – Galapagos, 2016, Sept. 26-30)

[Knopf-Lenoir 2016] Multiphysic Design of a Street Section, Catherine Knopf-Lenoir, David Muñoz, Raphaël Nahon, Benoit Beckers, *First International Conference on Urban Physics* (Quito – Galapagos, 2016, Sept. 26-30)

[Masson 2016] V. Masson , J. Hidalgo, A. Amossé, E. Bocher, M. Bonhomme, A. Bourgeois, G. Bretagne, S. Caillerez, E. Cordeau; C. Demazeux; S. Faraut, C. Gallato, S. Haoues-Jouve, M.-L. Lambert, A. Lemonsu, J.-P. Lévy, N. Long; C.-X. Lopez, G. Petit, M. Pellegrino, C. Pignon, C. Plumejeaud, V. Ruff, R. Schoetter, N. Tornay, D. Vye, *Urban Climate, Human behavior & Energy consumption: from LCZ mapping to simulation and urban planning (the MAPUCE project)* , *First International Conference on Urban Physics* (Quito – Galapagos, 2016, Sept. 26-30)

[Massoud 2016] Badia Masoud, Benoit Beckers, and Helena Coch, *Sky Access versus Shading for Pedestrian Comfort in the Hot Tropical Climate of Jeddah*, *First International Conference on Urban Physics* (Quito – Galapagos, 2016, Sept. 26-30)

[Montazeri 2016] H. Montazeri, Y. Toparlar, B. Blocken and J.L.M. Hensen, *Numerical modeling of evaporative cooling using water spray systems for heat stress reduction in urban areas*, *First International Conference on Urban Physics* (Quito – Galapagos, 2016, Sept. 26-30)

[Nahon 2016] R. Nahon, O. Blanpain and B. Beckers, *Impact of the anisotropy of the sky vault emissivity on the building envelope radiative budget*, *First International Conference on Urban Physics* (Quito – Galapagos, 2016, Sept. 26-30)

[Nazarian 2016] Negin Nazarian, Tiffany Sin, Leslie K. Norford, *Impacts of Realistic Surface Heating on Outdoor Thermal Comfort*, *First International Conference on Urban Physics* (Quito – Galapagos, 2016, Sept. 26-30)

[Palme2016] Massimo Palme, Geovanna Villacreses, Andrea Lobato, Martín Cordovez, José Macias and Guillermo Soriano, *Estimating the Urban Heat Island Effect in the City of Guayaquil*, *First International Conference on Urban Physics* (Quito – Galapagos, 2016, Sept. 26-30)

[Paule 2016] Bernard A. Paule and Jérôme H. Kaempf, *Daylighting: an approach from urban to room scale*, *First International Conference on Urban Physics* (Quito – Galapagos, 2016, Sept. 26-30)

[Pinson 2016] L. Pinson and V. Masson, *Heat stress in urban area: data fusion of observations, modeling and geospatial information*, *First International Conference on Urban Physics* (Quito – Galapagos, 2016, Sept. 26-30)

[Rassineux2016] Alain Rassineux, Benoit Beckers, *A robust smoothed voxel representation for the generation of finite element models for computational urban physics*, *First International Conference on Urban Physics* (Quito – Galapagos, 2016, Sept. 26-30)

[Romanic2016] Djordje Romanic, Dan Parvu, Horia Hangan, *Downburst Reconstruction using Physical Simulation and Analytical Model with Application to Urban Environments*, *First International Conference on Urban Physics* (Quito – Galapagos, 2016, Sept. 26-30)

[Salmon 2016] Nicolas Salmon, Grace Yopez-Salmon, Marc Lotteau, *To evaluate the sustainability of urban planning projects through an LCA approach: example of application of the NEST tool and requirements for its use in the context of Ecuador and Latin America*, *First International Conference on Urban Physics* (Quito – Galapagos, 2016, Sept. 26-30)

[Samsonov 2016] Timofey E. Samsonov, Pavel I. Konstantinov, Mikhail I. Varentsov, *Object-Oriented Approach to Urban Canyon Analysis*, *First International Conference on Urban Physics* (Quito – Galapagos, 2016, Sept. 26-30)

[Suzuki 2016] Seiichi Suzuki Erazo, *Real-time material computation in architectural design: Experiments on the development of interactive form finding tools*, *First International Conference on Urban Physics* (Quito – Galapagos, 2016, Sept. 26-30)

[Toparlar2016] Yasin Toparlar, Bert Blocken, Bino Maiheu, GertJan van Heijst, *Computational analysis of an urban park's impact on the Antwerp microclimate, First International Conference on Urban Physics* (Quito – Galapagos, 2016, Sept. 26-30)

[Torres-Quezada 2016] J. Torres-Quezada, A. Pages-Ramon, H. Coch and A. Isalgué, *Radiative Performance Assessment of Two Roofs in Mediterranean and Equatorial Climates, First International Conference on Urban Physics* (Quito – Galapagos, 2016, Sept. 26-30)

[Vermeulen 2016] T. Vermeulen, C. Knopf-Lenoir, L. Merino, P. Villon, and B. Beckers, *Periodic 3D model to optimize urban shapes for solar radiation, First International Conference on Urban Physics* (Quito – Galapagos, 2016, Sept. 26-30)

[Villacís 2016] Enrique V. Villacís, María L. Rodriguez, Cynthia C. Ayarza, and Klaus Rueckert, *Pertinence of social inclusion design methods in communities, First International Conference on Urban Physics* (Quito – Galapagos, 2016, Sept. 26-30)

[Wang 2016] Weiwen Wang, Yong Xu, and Edward Ng, *Application of Large-Eddy Simulations in Evaluating Ventilation over 3D Building Data Retrieved from Satellite Images, First International Conference on Urban Physics* (Quito – Galapagos, 2016, Sept. 26-30)

Sparse Matrix Solution for Computing Urban Radiation Exchange

José Pedro Aguerre¹, Eduardo Fernández¹, Gonzalo Besuvievsky², and Benoit Beckers³

¹Centro de Cálculo, Universidad de la República, Uruguay
{jpaguerre,eduardof}@fing.edu.uy

²Geometry and Graphics Group, Universitat de Girona, Spain
gonzalo@imae.udg.edu

³Roberval Laboratory, Urban Systems Engineering, Université de Technologie de Compiègne -
Sorbonne University, France
benoit.beckers@utc.fr

Keywords: Urban Radiation Exchange, Radiosity, Form Factors, Sparse Matrix, Daylighting

Abstract. *Numerical simulation of cities generates highly complex computational challenges. Many existing computer models should be adapted to consider the physical and social phenomena that are developed in urban environments. In this paper, a numerical model for urban radiation exchanges is analyzed. In this way, the sparsity of the form factors matrix is studied. This matrix is used to solve problems of radiation exchange (light and heat). It is found that this matrix is usually highly sparse, which enables it to be stored in main memory for models up to 140k patches. A technique is also proposed to estimate the inverse of the radiosity matrix, useful for finding radiation exchange. In this calculation, near-zero elements are removed, leading to a highly sparse approximation. These techniques could be useful for the design of buildings, taking into consideration the characteristics of the surroundings, as well as to help in the definition of city regulations related to urban construction.*

1 Introduction

Due to the increasing need of energy assessment tools at large scale, urban physics simulation has become a major topic of interest. This work focuses on light exchange at urban scale. Thermal radiation is not considered in this paper. The evaluation of annual solar irradiance and the analysis of the spatial variation over building facades has a relevant interest for urban planning and building design. Computational simulation for radiative transfer on an urban scale, where thousands of buildings have to be considered, is a challenge. The main problem is how to deal with the huge amount of data required to represent such models.

One of the mathematical models adapted to predict urban radiation exchange is the use of the radiosity method [Cohen and Wallace, 2012; Beckers, 2013a]. A full solution of this method in a city model may require computing the view factors between all building mesh elements and solving the linear system, which may be an expensive computational task considering a district model domain composed of hundred of buildings. A possible solution to manage the problem is to rough simplify the visibility problem [Robinson and Stone, 2005].

We focus on solving the problem considering all visibility information. By observing that the form factor matrix that represents all view factors is generally sparse for this kind of environments, we propose a novel approach for radiative exchange computation that can approximate the inverse of the radiosity matrix. We formulate the problem as a Neumann series and approximate the matrix by eliminating unimportant terms. Our resulted study on different kinds of urban model configuration shows that, for models composed of thousands of patches, we can provide an accurate approximation of the inverse radiosity matrix that can also be stored in main memory. In this way, it can be used to solve efficiently annual based radiative simulations. This is a promissory result, concerning its potential use for radiative exchange and analysis.

The rest of the paper is structured in the following way. Sec. 2 describes the radiosity method, as well as the main related works. Sec. 3 presents our proposal for solving the described problem. Next, the experimental analyses are shown in Sec. 4, where several study cases are presented and evaluated. Finally, Sec. 5 is dedicated to the conclusions and main lines of future works.

2 Related work

The two main methodologies for solving the urban radiant exchange problems are ray tracing and radiosity. While the former is widely used in rendering, the radiosity method is more suitable because it was originally developed for heat transfer exchange computation. One of the advantages of using this method is that it can obtain results in the whole scene space, which makes it attractive for urban environment analysis. In the rest of this section, we review the radiosity method and the works related to our approach.

2.1 The Radiosity Problem

The radiosity method [Goral et al., 1984] is a technique which allows to compute global illumination on scenes with Lambertian surfaces. It has been applied in many areas of design and computer animation [Dutre et al., 2006]. The continuous radiosity equation can be discretized through the use of a finite element methodology. The scene is discretized into a set of patches,

leading to express the problem using the following set of linear equations:

$$B_i = E_i + R_i \sum_{j=1 \dots n} B_j \mathbf{F}(i, j) \quad , \quad \forall i \in \{1 \dots n\}$$

This set of linear equations is expressed in a succinct manner in Equation 1.

$$(\mathbf{I} - \mathbf{RF})B = E, \tag{1}$$

where \mathbf{I} is the identity matrix, \mathbf{R} is a diagonal matrix containing the reflectivity index of each patch, B is the radiosity vector to be found, and E is the emission vector. $\mathbf{F}(i, j)$ is a number between 0 and 1 expressing the form factor between patch i and j . This value indicates the fraction of the light power going from one to another. Therefore, the form factor matrix is a $n \times n$ matrix, where n is the number of patches in the scene.

\mathbf{F} can be efficiently computed using the hemi-cube algorithm [Cohen and Greenberg, 1985], but its memory requirements ($O(n^2)$) are often an obstacle when working with big models ($n > 50.000$).

Equation 1 can be solved using several approaches. For example, the operator $\mathbf{M} = (\mathbf{I} - \mathbf{RF})^{-1}$ can be calculated, which represents a global transport operator relating the emitted light with the final radiosity of the scene, $B = \mathbf{M}E$. When \mathbf{F} has a low numerical rank, factorization techniques can be used to efficiently compute an approximation of \mathbf{M} [Fernández, 2009]. On the other hand, \mathbf{M} can also be approximated using iterative methods such as Neumann series ([Kontkanen et al., 2006]).

Another approach is to compute B by solving the linear system of equations iteratively, using methods such as Jacobi or Gauss-Seidel ([Cohen and Wallace, 2012]). Eq. 2 presents the radiosity resolution using the Jacobi iteration. Each iteration adds the radiosity of a new light bounce to the global radiosity result.

$$B^{(i+1)} = \mathbf{RF}B^{(i)} + E \quad , \quad \text{where } B^{(0)} = E \tag{2}$$

2.2 Neumann Series

Given an Operator \mathbf{T} , its Neumann series is a series of the form

$$\sum_{k=0}^{\infty} \mathbf{T}^k$$

The expression \mathbf{T}^k is a mathematical notation that means applying the operator \mathbf{T} , k consecutive times. Supposing that \mathbf{T} is a bounded operator and \mathbf{I} the identity operator, if the Neumann series converges, then $(\mathbf{I} - \mathbf{T})$ is invertible and its inverse is the series:

$$(\mathbf{I} - \mathbf{T})^{-1} = \sum_{k=0}^{\infty} \mathbf{T}^k = \mathbf{I} + \mathbf{T} + \mathbf{T}^2 + \mathbf{T}^3 + \dots$$

This property can be used to calculate the radiosity ([Cohen and Wallace, 2012]), by computing an approximate to the inverse of $(\mathbf{I} - \mathbf{RF})$ through l iterations:

$$(\mathbf{I} - \mathbf{RF})^{-1} \approx \mathbf{I} + \mathbf{RF} + (\mathbf{RF})^2 + \dots + (\mathbf{RF})^l$$

In this series, $(\mathbf{RF})^i$ contains the information of the i^{th} bounce of light between the surfaces in the scene. The main computational cost of this approach is the multiplication of matrices. Thus, if \mathbf{RF} is sufficiently big, the method can be prohibitively expensive.

[Kontkanen et al., 2006] use a variant of this method to compute a global transport operator for radiance calculations. This operator expresses the relationship between the converged and incoming incident lighting. In this process, the matrices are compressed using the following strategy: at each step, all the coefficients below a certain threshold are removed. This results in sparse matrices, which allow to speed up the calculation. The computation is stopped when all the coefficients in $(\mathbf{RF})^i$ are smaller than the threshold.

2.3 Sparse Matrices in Radiosity Problems

A *sparse matrix* is any matrix with enough zeros that it pays to take advantage of them [Wilkinson, 1971]. Generally, using sparse representations allows to save time or memory (usually both) by exploiting the number of zeros. Furthermore, these kind of matrices are applied in problems where the use of full matrices is not possible due to memory restrictions.

The use of sparse matrices in radiosity calculations is still a subject of study. [Gortler et al., 1993] present the Wavelet Radiosity method, which is based on wavelet theory. Expressing the kernel operating in a radiosity function in a wavelet basis leads to a sparse approximation of it. On the other side, [Goel et al., 1991], [Borel et al., 1991] and [Chelle and Andrieu, 1998] solve the radiosity problem using iterative methods (like Gauss-Seidel) taking advantage of the sparsity of the form factors matrix. This property is present in the tested scenes (plant canopies), where there is a high occlusion level between distant polygons.

2.4 Urban Radiative Methods

A previous work for reducing the urban radiosity formulation is the simplified radiosity algorithm (SRA) [Robinson and Stone, 2005]. The basis of the simplification is grouping, for each sky direction, the main obstructions that obscured each surface. Then, for a scene composed of n patches and getting p sky patches, the system matrix can be reduced to a $n \times p$, that can both be inverted or used to solve the system iteratively. This method is embedded in the CitySim package [Robinson et al., 2009], a multi-purpose system for urban models simulation. In [Beckers, 2013b], the idea of using well-known finite element techniques as condensation, is analyzed for being adapted to urban models. In this case, the analysis is done only for longwave radiation.

3 Our Proposal

This section presents the main ideas of the present work, and proposes an algorithm to compute radiosity solutions exploiting the properties of the studied matrices.

3.1 Studying the Sparsity of a City's Form Factors Matrix

The density factor (sparsity) of a matrix is the fraction of non-zero elements over the total number of elements. In the form factor matrices, this factor depends on how many patches are seen from each patch: if patch j sees few patches, then row j of \mathbf{F} has few elements different than zeros, and vice versa. Figure 1 shows two urban scenes where each patch is colored by checking how

many elements are seen from it. For example, the upper elements on the tallest buildings are red while the ones on houses are blue. This result allows to predict that the \mathbf{F} matrix corresponding to a city, where each patch sees few others, is very sparse.

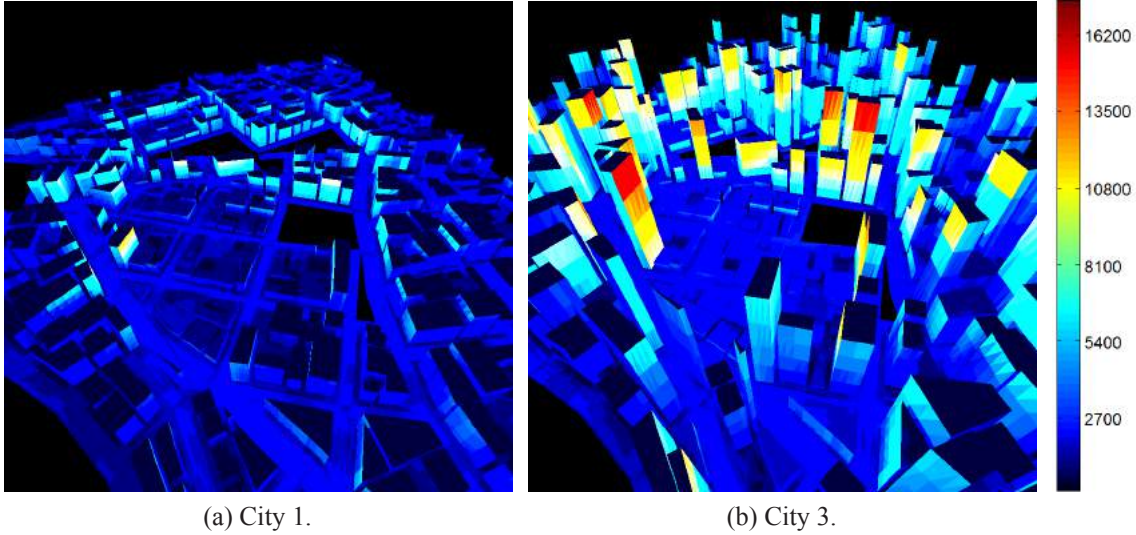


Figure 1: Two example urban scenes. The color of a patch indicates the number of patches that are seen from it.

The previous fact derives into the main conjecture of the present work: different kinds of cities have sparse \mathbf{F} matrices with different density factors. This sparsity depends on many factors. For example, orography, construction type, buildings disposition and heights are expected to have a great influence on the structure of the matrices. In this paper we focus on the variation of building heights. A city with big variance on its buildings height (as a typical contemporary downtown with skyscrapers) should generate less sparse matrices than a city with uniformly elevated buildings (as, for example, Haussmann’s Paris).

3.2 An Approximation of $\mathbf{M} = (\mathbf{I} - \mathbf{R}\mathbf{F})^{-1}$

The inverse of a sparse matrix is usually a full matrix, where its calculation is computationally expensive, and has memory limitations for medium to large size matrices. However, in the case of the radiosity matrix, its inverse \mathbf{M} has many elements below a small threshold. Therefore, in relation to \mathbf{M} , our proposal consists in finding a sparse approximation ($\tilde{\mathbf{M}} \approx \mathbf{M}$) that allows to compute low-error radiosity values.

In order to compute $\tilde{\mathbf{M}}$ efficiently, we use a method based on the work by [Kontkanen et al., 2006]. As described in Sec. 2.2, the algorithm is based on the use of Neumann series and a compression strategy based on removing all elements below a threshold ε . To obtain even sparser matrices, we apply this compression to $\mathbf{R}\mathbf{F}$ before starting the process.

Algorithm 1 describes the proposed method, where the function “remove” eliminates $|\mathbf{T}(i, j)| < \varepsilon, \forall i, j$.

```

 $\tilde{\mathbf{M}} = \mathbf{0};$ 
 $\mathbf{T} = \mathbf{I};$ 
while  $\mathbf{T} \neq \mathbf{0}$  do
   $\tilde{\mathbf{M}} = \tilde{\mathbf{M}} + \mathbf{T};$ 
   $\mathbf{T} = \mathbf{T}(\mathbf{RF});$ 
  remove( $\mathbf{T}, \varepsilon$ );
end

```

Algorithm 1: Calculate $\tilde{\mathbf{M}}$.

Once the sparse approximation is computed, it is relatively inexpensive to calculate the radiosity results for k different emissions (Eq. 3):

$$\begin{aligned}\tilde{\mathbf{M}} &\approx (\mathbf{I} - \mathbf{RF})^{-1} \\ \tilde{\mathbf{B}}_k &= \tilde{\mathbf{M}}\mathbf{E}_k\end{aligned}\quad (3)$$

where the i^{th} column of \mathbf{E}_k is an emission and the i^{th} column of $\tilde{\mathbf{B}}_k$ is the approximation of its corresponding radiosity result, $\forall i \in 1 \dots k$.

3.3 Daylight Simulation

Computing urban radiation exchange can have increasing interest if it is efficiently calculated. In this work, we apply the described techniques on urban daylight simulation, such kind of simulation has been applied in different fields such as design [Baker and Steemers, 2014], building energy consumption [Hviid et al., 2008] or ecology [Longcore and Rich, 2004].

In order to simulate the sky and its interaction with the city, a hemisphere containing the city is added to the model. This hemisphere is divided into m elements and each element is given its corresponding emittance, simulating the skylight. There are several ways to mesh the sky ([Tregenza, 1987], [Mardaljevic, 1999]), though we use a simple division with parallels and meridians ($m=132$) as a proof of concept.

Once the sky is added to the model, we use the strategy described at [Beckers, 2013b] to calculate the first bounce of light from the sky in the city. We use this as the urban emission, which allows us to work only with the form factors between patches of the city. For this purpose, Eq. 1 is re-written in the following way:

$$\mathbf{B} = \mathbf{E} + \mathbf{RF}\mathbf{B}\quad (4)$$

Let us separate sky (index s) and city (index u) contributions in Eq. 4:

$$\begin{bmatrix} B_s \\ B_u \end{bmatrix} = \begin{bmatrix} E_s \\ E_u \end{bmatrix} + \begin{bmatrix} (\mathbf{RF})_{ss} & (\mathbf{RF})_{su} \\ (\mathbf{RF})_{us} & (\mathbf{RF})_{uu} \end{bmatrix} \begin{bmatrix} B_s \\ B_u \end{bmatrix}$$

The sky is considered as a black surface, with zero reflectance, while the city has no emission. Therefore:

$$\begin{bmatrix} B_s \\ B_u \end{bmatrix} = \begin{bmatrix} E_s \\ 0 \end{bmatrix} + \begin{bmatrix} 0 & 0 \\ (\mathbf{RF})_{us} & (\mathbf{RF})_{uu} \end{bmatrix} \begin{bmatrix} B_s \\ B_u \end{bmatrix}$$

In the previous equation, $B_s = E_s$. This leads to the following statement:

$$B_u = (\mathbf{RF})_{us}B_s + (\mathbf{RF})_{uu}B_u = (\mathbf{RF})_{us}E_s + (\mathbf{RF})_{uu}B_u$$

Now, grouping the radiosities from both sides:

$$(\mathbf{I} - (\mathbf{RF})_{uu})B_u = (\mathbf{RF})_{us}E_s$$

The left side of this equation is the radiosity matrix $(\mathbf{I} - (\mathbf{RF})_{uu})$ times the radiosity result for the city. Therefore, following Eq. 1, the first bounce of light coming from the sky in the city is the new emission $E = (\mathbf{RF})_{us}E_s$.

4 Experimental Analysis

The results of the presented set of experiments were conducted on a desktop computer, with Intel quad-core i7 processor and 16 Gbytes RAM. The calculation of each \mathbf{F} matrix was realized using the hemi-cube technique, where the graphic component was executed on a NVIDIA GeForce-780 GPU processor. The code was implemented on C++, OpenGL, CUDA [Kirk and Hwu, 2010], and MATLAB [MATLAB, 2010].

4.1 Example City Models

The following analysis is performed using three different urban scenes, which are generated from the same cadastral plan. The first model contains only flat houses, the second low and middle-sized buildings, and the third is composed of different sized buildings, including tall skyscrapers. The urban scenes can be observed in Fig. 2

As can be seen, the first model has a small variance on building heights, while the third one has a big variance. The three models are composed of 8897 patches.

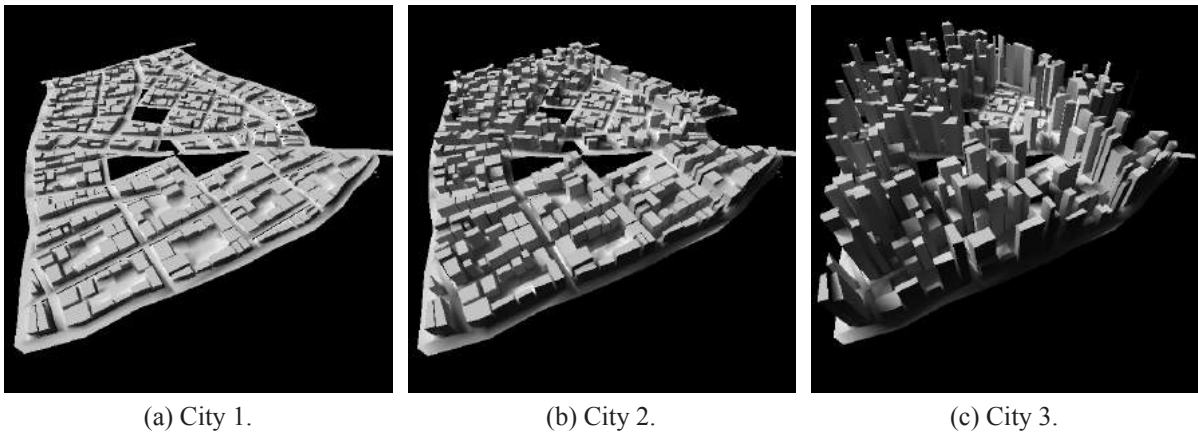


Figure 2: Three different urban scenes to experiment with.

4.2 Sparsity Results for \mathbf{F} and $\tilde{\mathbf{M}}$

We show the sparsity results for the described city models. For each model, three variants are studied: the original ($n=8897$), dividing each patch into 4 ($n=35588$) and into 16 ($n=142352$), where n is the number of patches. This allows to analyze the proposed algorithm for bigger models, as well as the effect of dividing patches in the sparsity factor. The calculation of \mathbf{F} takes about 20s, 90s, and 600s for $n=8897$, 35588, and 142352, respectively.

First of all, we explore the density of \mathbf{M} matrices ($n=8897$, inverted with MATLAB) and the distribution of their elements, for different reflectivity indexes R (Fig. 3). It can be appreciated that most of the matrices elements are non-zero, and also that most of them have very small values. An increment in the value of R is related to an increment in the values of the matrix elements. Finally, the matrices of City 1 have smaller elements than those related to City 3.

In the rest of the paper, a reflectivity index of 0.7 is used. This value is higher than the expected for cities, but it could be useful for challenging the sparsity of the matrices $\tilde{\mathbf{M}}$.

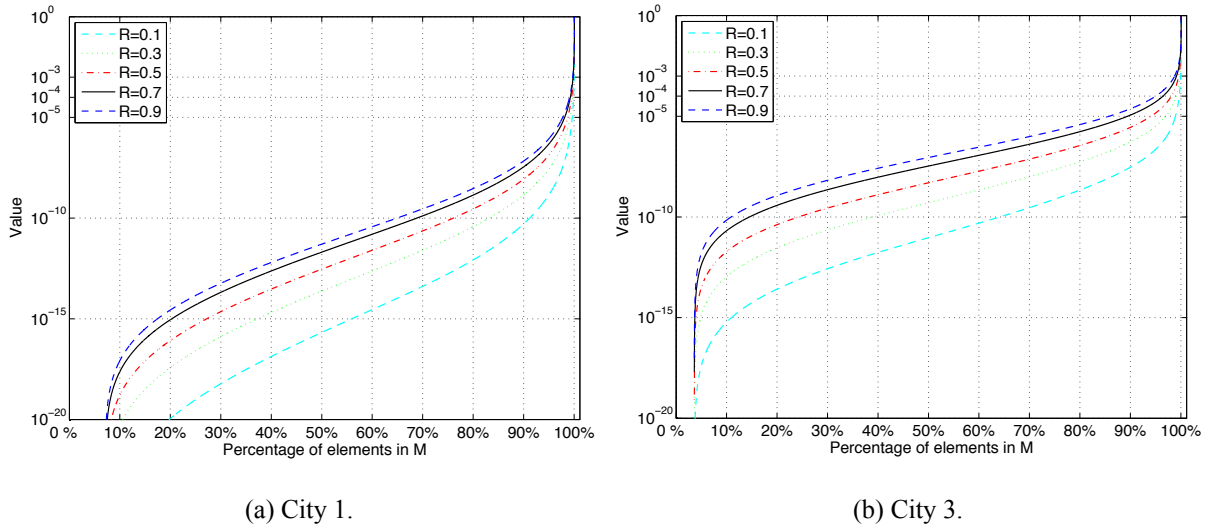


Figure 3: Distribution function of the \mathbf{M} elements, for different reflectivity indexes and cities.

The sparsity results and memory storage for \mathbf{F} and $\tilde{\mathbf{M}}$ matrices can be seen in Table 1. As expected, the density factor of \mathbf{F} grows as the city model becomes less homogeneous, which implies the use of a larger memory space. Nevertheless, the density reported in the worst case (City 3 with $n = 8897$) signifies a storage of 1.23% of the total elements of the matrix. On the other hand, the density factors are shorter for finer meshes of the same city model.

The density factor of $\tilde{\mathbf{M}}$ has a similar behavior to that described for \mathbf{F} . Also, for all cases, the density increases as the threshold ε becomes smaller. The memory required to store the sparse matrices \mathbf{F} and $\tilde{\mathbf{M}}$ is always much less than its full version, for every of the test cases executed.

4.3 Execution Times

In order to study the computational performance of the proposed algorithm, we calculate the daylight illumination for a whole year. For this, we use the 3 city models with the 3 mesh variants,

	n	Density of \mathbf{F}	Density of $\tilde{\mathbf{M}}$			Memory size (GB)		
			$\varepsilon = 10^{-3}$	10^{-4}	10^{-5}	Full	\mathbf{F}	$\tilde{\mathbf{M}} (10^{-5})$
City 1	8897	0.68 %	0.22 %	0.61 %	1.48 %	0.60	0.01	0.02
	35588	0.48 %	0.10 %	0.31 %	0.83 %	9.66	0.09	0.17
	142352	0.35 %	0.04 %	0.15 %	0.45 %	154.60	1.05	1.46
City 2	8897	0.84 %	0.30 %	1.01 %	2.58 %	0.60	0.01	0.03
	35588	0.60 %	0.15 %	0.51 %	1.41 %	9.66	0.12	0.28
	142352	0.44 %	0.05 %	0.24 %	0.75 %	154.60	1.34	2.42
City 3	8897	1.23 %	0.55 %	2.07 %	6.24 %	0.60	0.01	0.08
	35588	0.87 %	0.20 %	0.88 %	2.98 %	9.66	0.17	0.59
	142352	0.64 %	0.06 %	0.36 %	1.40 %	154.60	1.94	4.52

Table 1: Density and memory size of the form factors matrices and the approximated inverse.

along with 3650 sky configurations. The obtained data is compared to the execution times of solving the same radiosity problem iteratively, using the Jacobi iteration (Eq. 2).

Table 2 shows the obtained execution times for the described test cases. The third column shows the speedup over the Jacobi based method. It is important to highlight that this speedup is calculated taking into account both time to compute $\tilde{\mathbf{M}}$ and time to compute $\tilde{\mathbf{M}}\mathbf{E}$. That is: $\text{Speedup} = T_J / (T_{\tilde{\mathbf{M}}} + T_{\tilde{\mathbf{M}}\mathbf{E}})$, where T_J is the execution time needed to calculate the radiosity using Jacobi with the same number of iterations (light bounces) than to compute $\tilde{\mathbf{M}}$, for each case.

As can be appreciated in the table, the execution times depend highly on the correspondent density factor of $\tilde{\mathbf{M}}$. The sparser this matrix is, the lower the execution times are. For the considered example problem, the proposed algorithm works faster than the Jacobi iteration method for all the test cases.

	n	Time for $\tilde{\mathbf{M}}$ ($T_{\tilde{\mathbf{M}}}$)			Time for $\tilde{\mathbf{M}}\mathbf{E}$ ($T_{\tilde{\mathbf{M}}\mathbf{E}}$)			Speedup = $T_J / (T_{\tilde{\mathbf{M}}} + T_{\tilde{\mathbf{M}}\mathbf{E}})$		
		$\varepsilon = 10^{-3}$	10^{-4}	10^{-5}	$\varepsilon = 10^{-3}$	10^{-4}	10^{-5}	$\varepsilon = 10^{-3}$	10^{-4}	10^{-5}
City 1	8897	0.17s	0.68s	2.51s	0.52s	1.22s	2.88s	$47.5 \times$	$27.2 \times$	$14.8 \times$
	35588	1.10s	7.08s	32.80s	3.72s	10.20s	26.70s	$69.4 \times$	$34.4 \times$	$16.7 \times$
	142352	7.33s	60.90s	440.00s	26.40s	89.80s	264.00s	$110.0 \times$	$43.9 \times$	$20.1 \times$
City 2	8897	0.26s	1.49s	5.80s	0.71s	1.99s	4.99s	$45.2 \times$	$22.0 \times$	$10.9 \times$
	35588	2.06s	15.20s	79.60s	5.17s	16.20s	45.70s	$73.4 \times$	$30.7 \times$	$13.5 \times$
	142352	11.80s	136.00s	1180.00s	34.20s	140.00s	442.00s	$124.0 \times$	$41.7 \times$	$16.9 \times$
City 3	8897	0.52s	4.10s	18.40s	1.09s	4.04s	11.90s	$45.3 \times$	$15.9 \times$	$6.7 \times$
	35588	3.35s	38.00s	264.00s	6.91s	29.10s	100.00s	$80.6 \times$	$26.2 \times$	$9.3 \times$
	142352	15.80s	306.00s	4070.00s	37.70s	223.00s	837.00s	$188.0 \times$	$42.2 \times$	$14.7 \times$

Table 2: Execution times (in seconds) of radiosity calculations for the test cases.

4.4 Radiosity Results

In this section we study the impact of the proposed algorithm on the radiosity results. We use 132 different sky configurations, each one with a unique sky element illuminating the scene, to compute 132 radiosity solutions of the city. Given a patch of the city, the radiosity value

calculated for each of the sky configurations is related to the concept of Daylight Coefficient ([Tregenza and Waters, 1983]). The linear combinations of the radiosity solutions for the 132 skies allow to find the radiosity of the city for any other sky configuration. Fig. 2 shows the radiosity values of the three cities for the same sky configuration, when $\varepsilon=10^{-5}$.

Comparison with Jacobi

Table 3 shows the relative errors of the 132 radiosities obtained, comparing $\tilde{B} = \tilde{M}E$ to the solution (B_J) of the Jacobi iteration methodology (Eq. 2). The initial emission is the first bounce of the light emitted from the sky (Sec. 3.3). The mean, standard deviation and maximum values are reported. As expected, the error gets smaller as the city homogeneity increases and as the truncation factor decreases. For every case, the standard deviation is small, as well as the maximum error is close to the mean value.

		Relative error of \tilde{B} : $\frac{\ \tilde{B}-B_J\ }{\ B_J\ } (\times 1000)$								
		$\varepsilon = 10^{-3}$			$\varepsilon = 10^{-4}$			$\varepsilon = 10^{-5}$		
	n	μ	σ	Max	μ	σ	Max	μ	σ	Max
City 1	8897	27.80	2.29	29.40	7.83	0.73	8.29	1.88	0.19	2.00
	35588	53.00	3.17	55.70	16.90	1.25	17.90	4.53	0.36	4.78
	142352	48.60	5.09	52.80	15.30	1.88	16.70	4.15	0.57	4.57
City 2	8897	87.70	6.44	95.20	31.70	2.99	34.20	9.50	1.04	10.30
	35588	86.50	9.15	97.80	35.00	5.42	39.80	11.00	2.20	12.80
	142352	134.00	11.70	154.00	61.80	6.24	69.30	23.00	3.41	25.90
City 3	8897	92.60	3.92	98.20	33.30	2.11	35.30	9.86	0.72	10.50
	35588	141.00	8.67	155.00	59.30	4.80	64.20	19.70	1.93	21.40
	142352	189.67	17.74	221.03	99.20	8.45	113.05	42.14	4.77	47.12

Table 3: Radiosity errors for the test cases (all numbers are $\times 1000$).

Radiosity 3rd and successive bounces

In Fig. 4, the average radiosity values for the 132 different sky configurations are shown (for two city models). All the radiosity curves are sorted from lowest to highest values. In both plots, we present the results using the Jacobi iteration method for computing radiosity (B_J) and only the third and successive bounces (S_J). Also, we show the same results using the proposed algorithm for different truncation thresholds.

As can be appreciated, the illumination is much higher in B_J than in S_J , because the first two bounces are the main component of the total radiosity. Nevertheless, the rest of the bounces together are not negligible, which means that they cannot be discarded in the calculations. Taking a closer look into the results of the proposed algorithm, it is evident that a higher truncation threshold implies a higher error. When compared to the Jacobi solution, the results seem close enough for most practical applications, when $\varepsilon=10^{-4}$ and 10^{-5} . Finally, the errors on the third and successive bounces seem uniform.

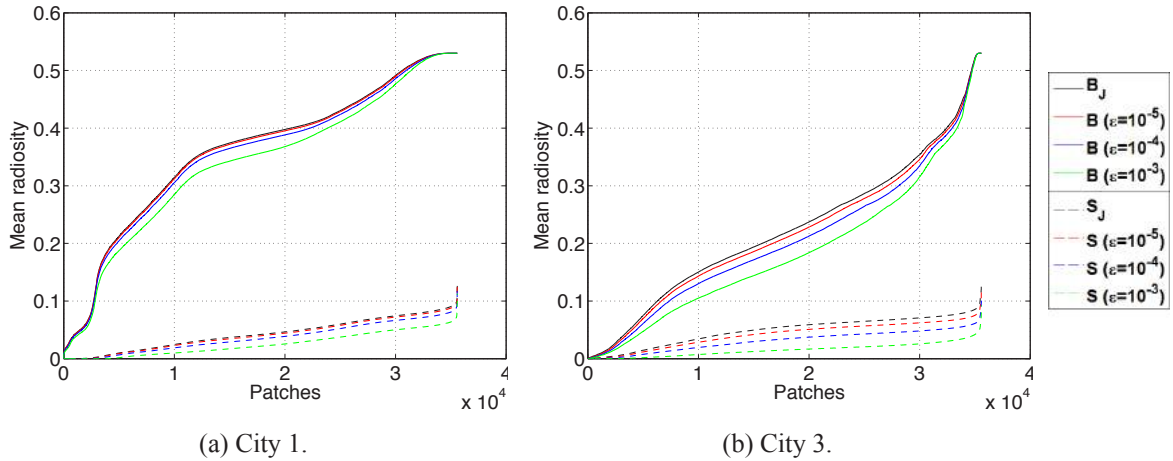


Figure 4: Comparison of radiosity results between Jacobi (B_j), third and successive bounces (S_j), and their approximations using different thresholds.

5 Conclusions and Future Work

This work is a first step into the study of the correlation between the characteristics of a city and the sparsity of its form factors matrix (F). Here we focus on the variation of building heights. We studied three different cities, and found that more homogeneous cities produce more sparse F matrices. The matrices are sparse enough to be stored in the main memory of a desktop computer, considering city scenes that contain up to 140k patches. Another result is the calculation of a sparse approximation to the inverse of the radiosity matrix (\tilde{M}). This approximation is based on the use of Neumann series and the elimination of all terms with lower values than a given threshold. \tilde{M} is also sufficiently sparse as to be stored in main memory. These matrices were tested doing radiosity calculations for several sky configurations. We compared the results with a Jacobi iteration method, and found that the radiosities have low relative errors. Additionally, the proposed method is time efficient.

Further works should address the study of F for real cities, and also to take other characteristics into account. The calculation of \tilde{M} could allow the use of standard skies and meteorological yearly data, to perform statistical analyses related to the use of natural light in cities. These results can have a big influence into the definition of city regulations. Other possible line of work is related to the design of new city elements, like buildings and public places, taking into consideration the main characteristics of the surroundings. Finally, to apply the proposed methods to thermal radiation and heat accumulation on urban environments, we should consider the main aspects related to the heat equation.

Acknowledgments

The work was partially supported by FSE_1_2014_1_102344 project from Agencia Nacional de Investigación e Innovación (ANII, Uruguay) and TIN2014-52211-C2-2-R project from Ministerio de Economía y Competitividad, Spain.

References

- [Baker and Steemers, 2014] Baker, N. and Steemers, K. (2014). *Daylight design of buildings: A handbook for architects and engineers*. Routledge.
- [Beckers, 2013a] Beckers, B. (2013a). *Solar energy at urban scale*. John Wiley & Sons.
- [Beckers, 2013b] Beckers, B. (2013b). Taking advantage of low radiative coupling in 3d urban models. In *Proceedings of the Eurographics Workshop on Urban Data Modelling and Visualisation*, pages 17–20. Eurographics Association.
- [Borel et al., 1991] Borel, C. C., Gerstl, S. A., and Powers, B. J. (1991). The radiosity method in optical remote sensing of structured 3-d surfaces. *Remote Sensing of Environment*, 36(1):13–44.
- [Chelle and Andrieu, 1998] Chelle, M. and Andrieu, B. (1998). The nested radiosity model for the distribution of light within plant canopies. *Ecological Modelling*, 111(1):75–91.
- [Cohen and Greenberg, 1985] Cohen, M. F. and Greenberg, D. P. (1985). The hemi-cube: A radiosity solution for complex environments. In *ACM SIGGRAPH Computer Graphics*, volume 19, pages 31–40. ACM.
- [Cohen and Wallace, 2012] Cohen, M. F. and Wallace, J. R. (2012). *Radiosity and realistic image synthesis*. Elsevier.
- [Dutre et al., 2006] Dutre, P., Bala, K., Bekaert, P., and Shirley, P. (2006). *Advanced Global Illumination*. AK Peters Ltd.
- [Fernández, 2009] Fernández, E. (2009). Low-rank radiosity. In *Proceedings of the IV Iberoamerican symposium in computer graphics. Sociedad Venezolana de Computación Gráfica*, pages 55–62.
- [Goel et al., 1991] Goel, N. S., Rozehnal, I., and Thompson, R. L. (1991). A computer graphics based model for scattering from objects of arbitrary shapes in the optical region. *Remote Sensing of Environment*, 36(2):73–104.
- [Goral et al., 1984] Goral, C. M., Torrance, K. E., Greenberg, D. P., and Battaile, B. (1984). Modeling the interaction of light between diffuse surfaces. In *Proceedings of the 11th annual conference on Computer graphics and interactive techniques, SIGGRAPH '84*, pages 213–222, New York, NY, USA. ACM.
- [Gortler et al., 1993] Gortler, S. J., Schröder, P., Cohen, M. F., and Hanrahan, P. (1993). Wavelet radiosity. In *Proceedings of the 20th annual conference on Computer graphics and interactive techniques*, pages 221–230. ACM.
- [Hviid et al., 2008] Hviid, C. A., Nielsen, T. R., and Svendsen, S. (2008). Simple tool to evaluate the impact of daylight on building energy consumption. *Solar Energy*, 82(9):787–798.
- [Kirk and Hwu, 2010] Kirk, D. B. and Hwu, W.-m. W. (2010). *Programming Massively Parallel Processors: A Hands-on Approach*. Morgan Kaufmann Publishers Inc., San Francisco, CA, USA, 1st edition.

- [Kontkanen et al., 2006] Kontkanen, J., Turquin, E., Holzschuch, N., and Sillion, F. X. (2006). Wavelet radiance transport for interactive indirect lighting. In *Rendering Techniques 2006 (Eurographics Symposium on Rendering)*, pages 161–171.
- [Longcore and Rich, 2004] Longcore, T. and Rich, C. (2004). Ecological light pollution. *Frontiers in Ecology and the Environment*, 2(4):191–198.
- [Mardaljevic, 1999] Mardaljevic, J. (1999). *Daylight simulation: validation, sky models and daylight coefficients*. De Montfort University.
- [MATLAB, 2010] MATLAB (2010). *version 7.10*. The MathWorks Inc., Natick, Massachusetts.
- [Robinson et al., 2009] Robinson, D., Haldi, F., Kämpf, J., Leroux, P., Perez, D., Rasheed, A., and Wilke, U. (2009). CitySim: Comprehensive micro-simulation of resource flows for sustainable urban planning. In *Proc. Building Simulation*.
- [Robinson and Stone, 2005] Robinson, D. and Stone, A. (2005). A simplified radiosity algorithm for general urban radiation exchange. *Building Services Engineering Research and Technology*, 26(4):271–284.
- [Tregenza, 1987] Tregenza, P. (1987). Subdivision of the sky hemisphere for luminance measurements. *Lighting Research and Technology*, 19(1):13–14.
- [Tregenza and Waters, 1983] Tregenza, P. and Waters, I. (1983). Daylight coefficients. *Lighting Research and Technology*, 15(2):65–71.
- [Wilkinson, 1971] Wilkinson, J. (1971). The algebraic eigenvalue problem. In *Handbook for Automatic Computation, Volume II, Linear Algebra*. Springer-Verlag New York.

Historical Urban Landscape as a Descriptive Feature for Risk Assessment: the ‘Quebradas’ of Quito

Sheika M. Aragundi¹, Alexandra P. Mena^{1,2}, and Jenny J. Zamora¹

¹ Pontificia Universidad Católica del Ecuador
Av. 12 de Octubre 1076 y Roca, Quito
e-mail: saragundi@puce.edu.ec

² Municipio del Distrito Metropolitano de Quito
Venezuela entre Chile y Espejo, Quito
amena001@puce.edu.ec, jjzamora@puce.edu.ec

Keywords: Historical cartography, Aerial photography, Geometric Correction Model, Quebradas, Urban landscape, Risk Assessment.

Abstract. *Over the last decades the city of Quito has undergone notable spatial transformations, most of which have not been recorded given the unplanned nature of the city’s growth. Amongst the various unplanned changes that have shaped the modern Quito, the filling of ravines or ‘quebradas’, is one of major concern due to the numerous hazardous events associated to it. Determining the exact location of these areas and assessing their extent is therefore crucial for the city development planning. This paper assessed the potential of historical cartography and aerial photography to document urban landscape change and to determine risk areas in a digital geospatial environment. Historical planimetric cartography (1932) and aerial photography (1956) were rectified using a DLT Geometric Correction Model in order to reconstruct the historical urban landscape of Quito and locate ancient ravines or ‘quebradas’ which have been filled over the last century. The results show that the DLT Geometric Correction Model performed by ERDAS v10 renders high accuracy raster coverages from historical cartography which can be efficiently used in change detection. This study also emphasizes the importance of historical cartographic documents as the sole source of reliable information on urban historical landscape before aerial photography and the need for making this information available also in a vector format to government and academic institutions for decision making and research purposes.*

1 Introduction

The city of Quito has a long history of hazardous events caused by alluviums, floods, collapses and slides originated from the morphology of the terrain, the intensity of rainfall and the alterations to the water drainage by urbanization [De Noni, 1986; Peltre, 1989; Perrin, 2001]. According to a report by De Noni [1986] a total of 260 of such events occurred between 1900 and 1986, and the vast majority of these were related to the filling of the *quebradas* which ran through the urban territory.

The filling of the *quebradas* in Quito seems to have started in the early decades of the seventeenth century and then the practice continued over the colonial era [Terry 1834; Orton 1870]. In 1832, Terry mentions the existence of extensive underground vaults under the Jesuits' church and convent which were once a natural chasm and water-course that have been filled with stone arches on which the edifices are supported [Terry, 1834]. Later in 1870, in the account of his journey across South America, Orton reports "Two deep ravines come down the mountain, and traverse the city from west to east. They are mostly covered by arches, on which the houses rest; but where they are open, they disclose as fit representatives of the place of torment as the Valley of Hinnom". A preliminary analysis of historical maps of Quito also reveals the spreading of this activity over subsequent decades [Cf. Ortiz Crespo, 2007].

During the second half of the twentieth century when the major urban sprawling took place, numerous remaining *quebradas* were filled in order to allow mobility between zones that were separated by their courses [Peltre, 1989; Carrion, 1994; Metzger 1994; Porras, 2008]. This pattern of transformation of the city did not take into account technical criteria such as the kind of material that should be used for this purpose, or the process of compaction and stabilization which are mandatory in this type of works [Peltre, 1989; Carrion, 1994; Metzger 1994; Porras, 2008]. These ravine fillings are characterized by heterogeneous and loose soils, unable to gain stability over time and support cementation [Peltre, 1989; Porras 2008] as determined through sounding procedures in the *quebradas Los Gallinazos* and *La Pradera* underneath the Cumandá bus station and the interoceanic road [Porras, 2008]. Being natural catchments, the *quebradas* will still perform their function even if filled; consequently, water will tend to drain towards the original course through natural crevices [Peltre, 1989; Porras, 2008]. Although water is drained through collector systems underneath the filling, inadequate capacity of the collectors to cope with intensive rain and runoff has resulted in floods, mudflows and debris flows of high socioeconomic and environmental costs [Peltre, 1989; Metzger, 1996; Porras, 2008].

In a climate change scenario, it has been predicted that changes in precipitation patterns are likely to increase current discharge in the tropical Andes [Buytaert, 2008] which could in turn augment runoff in urban areas [Cf. Perrin, 2001] and exacerbate the risk associated to filled *quebradas*.

Peltre [1989] provides an exhaustive account of the *quebradas* of Quito from historical maps (i.e. 1932-1934), however the cartographic format of the data does not allow monitoring of the sites or comparison with present geographic raster and vector data. Updating geospatial data in a consistent manner is considered a critical task for the planning and decision making processes [Li, 2002; Ramirez, 2005; Recio, 2011], however it can be expensive and time consuming. In this respect it has been suggested that an efficient approach to this task would be to detect, identify and update changes only [Recio, 2011]. Airborne and satellite imagery from high spatial and spectral resolution sensors have proven to be adequate data for this task, however, they are limited in the historical time frame. Thus, in those areas of the world where

major landscape changes took place before the availability of aerial photography, the only source of reliable information on past landscape scenarios are historical maps.

In this context, the aim of this study was to assess the potential of historical cartography and aerial photography to document urban landscape change and to determine risk areas in a digital geospatial environment.

2 Study Area, Historical, and Ancillary Data

The study area encompasses the central part of Quito the capital city of Ecuador (Figure 1). The city is located at 0°10' S and 2800 meters above sea level on the slopes of the Pichincha volcano. It stretches approximately 50 km in length (North- South) and 4 to 10 km in width over the inter Andean valley (Figure 1). Over the last 4 decades the city has undergone important changes with scant planning, particularly the filling of quebradas which has resulted in numerous hazardous events [Peltre, 1989; Carrion, 1994; Metzger 1996; Porras, 2008].

The historical data used in the study included (1) a 1978 reprint of the Planimetric Map of Quito elaborated in 1932 by the Geographical Military Service (Servicio Geográfico Militar , today Instituto Geográfico Militar, IGM) as a 200 dpi TIF file format, (2) a single aerial photography of the area of Guápulo, scale 1:10 000 acquired in May 1956 and purchased to the IGM as a 1200 dpi TIF file format and (3) a single aerial photography of the area of El Itchimbía acquired in May 1956, scale 1:5000 and purchased to the IGM as a 1200 dpi TIF file format (Figure1).

The reference source for the study was a mosaic of 10 panchromatic orthophotographs of 2011, scale 1:5000, WGS 84S 18Z and the elevation source was the associated DEM WGS 84S 18Z of 1,0 meter resolution, both provided by the SIGTIERRAS Program (affiliated the Ministerio de Agricultura, Ganadería, Acuacultura y Pesca, MAGAP) under an inter institutional cooperation agreement. Finally, the vector file of the Metro Quito route scheduled for July 2019 (provided by the Secretariat of Mobility of the Quito Metropolitan District, Secretaría de Movilidad del Distrito Metropolitano de Quito, 2016) was used to identify zones where the route intersects old filled ravines and which should be given special consideration in risk studies.

3 Methodology

The area of interest (AOI) was cropped from the digital Planimetric Map of Quito in Adobe Photoshop CS6, the resulting file was then enhanced through brightness/contrast adjustment and sharpen filter. The historical aerial photographs were also cropped in Adobe Photoshop CS6 but the resulting files did not undergo image enhancement processing before photogrammetric restitution.

3.1 Photogrammetric Restitution of Historical Data

Photogrammetric restitution was carried out in the three raster files in ERDAS v 10 (a raster-based software package designed to process and extract information from images, Hexagon Geospatial ERDAS IMAGINE) using the Direct Linear Transformation DLT [Abdel-Aziz 1971] Model:

$$\begin{aligned} x' &= \frac{p_{11}X + p_{12}X + p_{13}Z + p_{14}}{p_{31}X + p_{32}Y + p_{33}Z + p_{34}} \\ y' &= \frac{p_{21}X + p_{22}Y + p_{23}Z + p_{24}}{p_{31}X + p_{32}Y + p_{33}Z + p_{34}} \end{aligned} \quad (1)$$

A mosaic of 8 panchromatic orthophotographs scale 1:5000 was used for *X* and *Y* coordinates reference and a 1m resolution DEM was used as *Z* reference with a 0,01 convergence value and Image Point SD of 0,33 for *X* and *Y*. The model was set to 50 iterations and the resampling method was set to Nearest Neighbor. The model was set to account for lens distortion for the aerial photography files only.

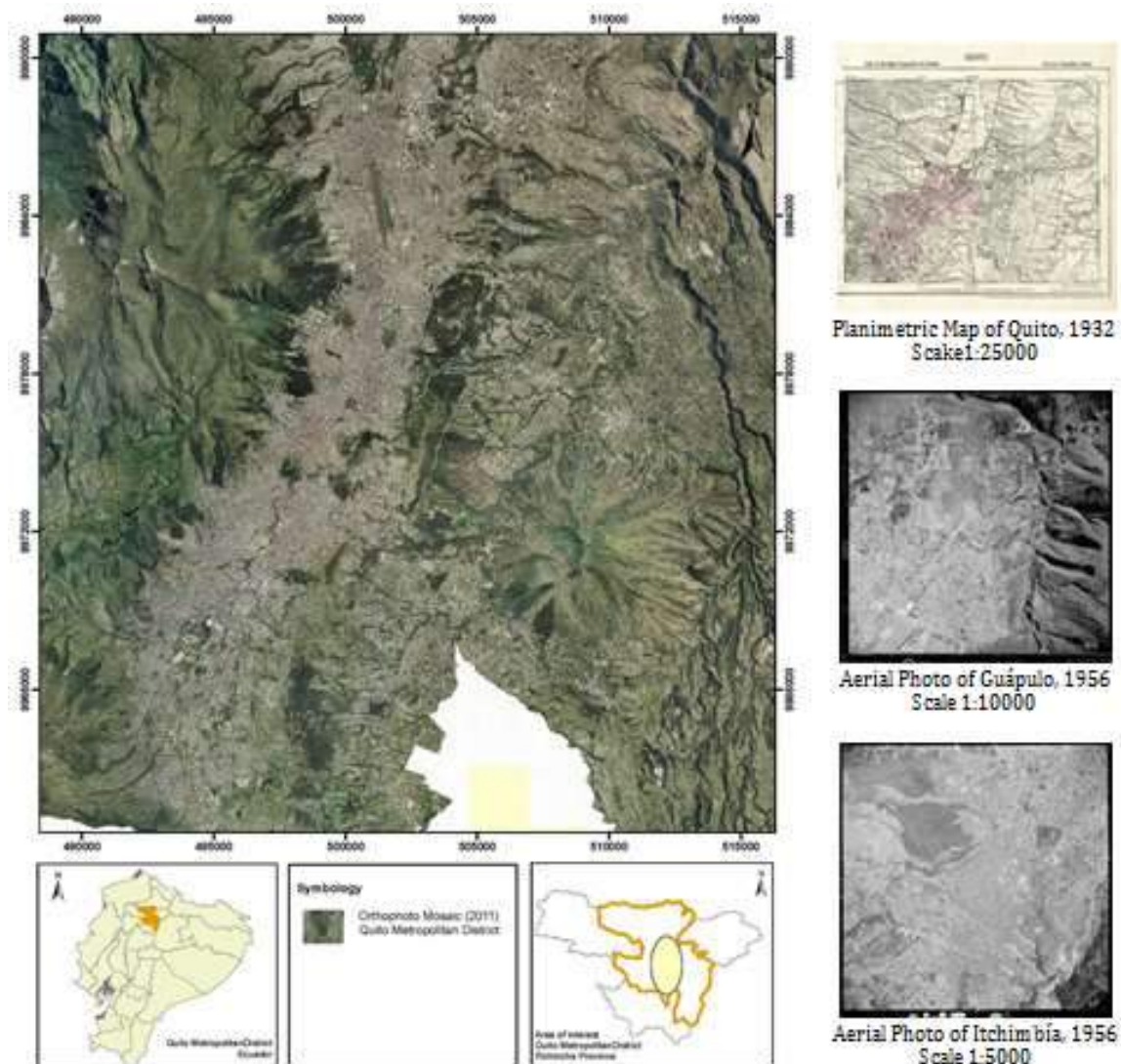


Figure 1 : Study area and historical data

3.2 Historical Urban Landscape and Location of risk areas

In order to check for accuracy, the rectified historical files were imported to ArcMap 10.3 along with the 2011 orthophoto mosaic. The rectified planimetric raster was used for on screen digitizing of the 1932 quebradas map for the AOI. The planimetric map, the historical aerial photographs, the 1932 quebradas map and the Metro Quito route were then overlaid on top of the 2011 orthophoto mosaic in order to locate risk areas and urban infrastructure built on top of old filled quebradas (Figures 2 and 3) .

4 Results and Discussion

4.1 Direct Linear Transformation Model Accuracy

The planimetric map of Quito of 1932 and the historical aerial photography from the sites in the central area of the city were rectified with 47 to 63 control points (CP's) per file and an error ranging from 0.0255 to 0.560 meters in x' , from 0.0366 to 0.9525 meters in y' and a total error ranging from 0.0366 to 1.1053 meters. The accuracy attained with the DLT Image Geometric Correction model is therefore very high.

The errors most probably responded to the fact that the high spatial resolution DEM used as Z reference was derived from 2011 LIDAR data and, therefore, areas where slides and/or gravel mining took place before 2011, although avoided when collecting CP's, could not be resolved and showed distorted in the rectified imagery (Figure 3). Other sources of error were probably nonlinear image errors such as scanner and lens distortion.

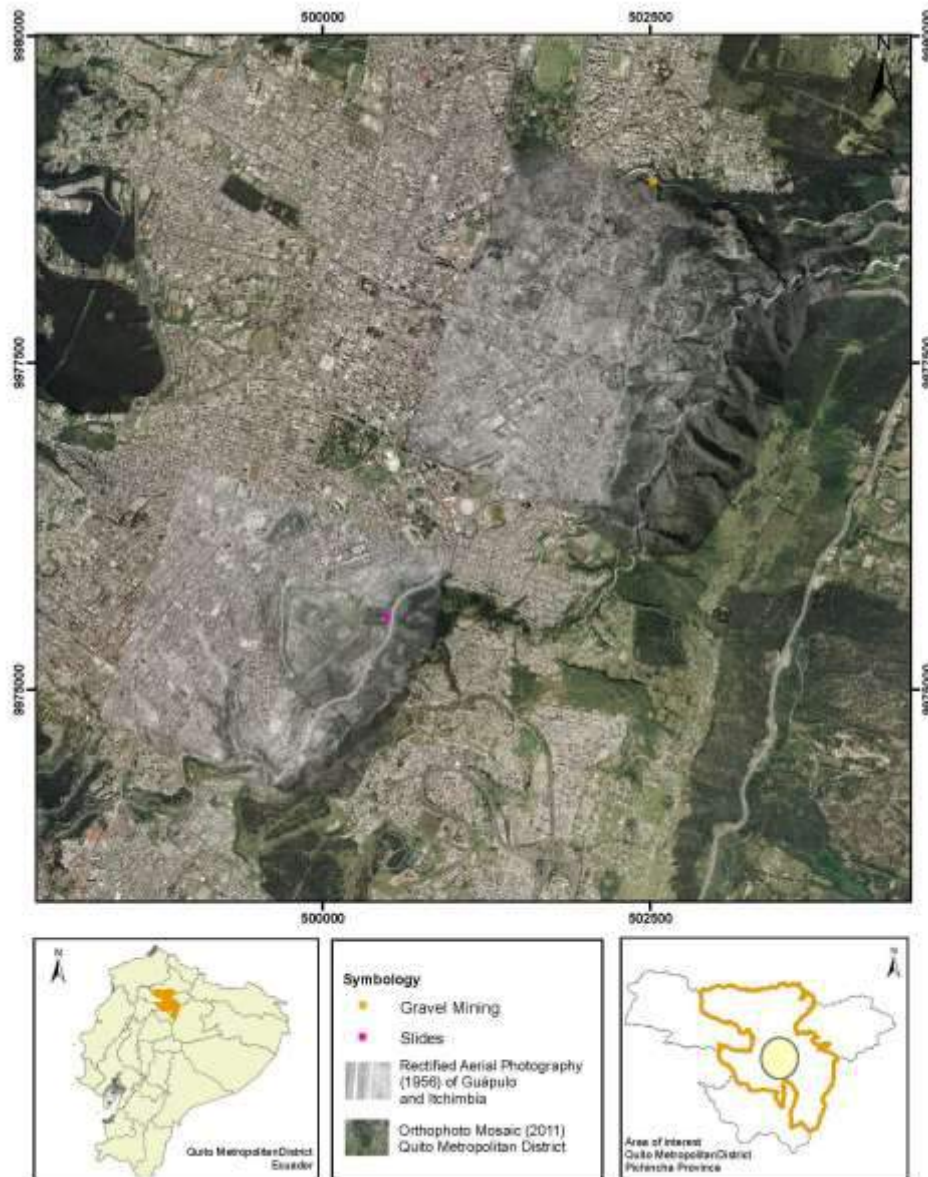


Figure 2: Aerial Photography of 1956 Showing Slides and gravel mining

4.2 Location of risk areas

Figure 3 shows (1) the map of the quebradas, (2) the planned metro Quito route and the 1932 planimetric map of the city overlaid on top of the 2011 ortophoto mosaic. Urban infrastructure which rests on top of old filled quebradas and are considered risk areas, are:

- Av. 24 de Mayo, La Ronda, Plaza de Cumandá, *quebrada Jerusalem*
- The colonial urban infrastructure, *quebrada del Tejar*
- Av. Patria and Ladrón de Guevara street, *quebrada de Miraflores*
- The northern part of the city, *quebrada del Batán*

Zones where the Metro Quito route intersects old filled ravines(intersection points) are:

- Av. 10 de Agosto y Pérez Guerrero, *quebrada Miraflores*
- Calle Pérez Guerrero, *quebradas Ascázubi y La Alcantarilla*
- Universidad Central, *quebrada Vásquez*
- Seminario Mayor, *quebradas Alpallana y De la Comunidad*

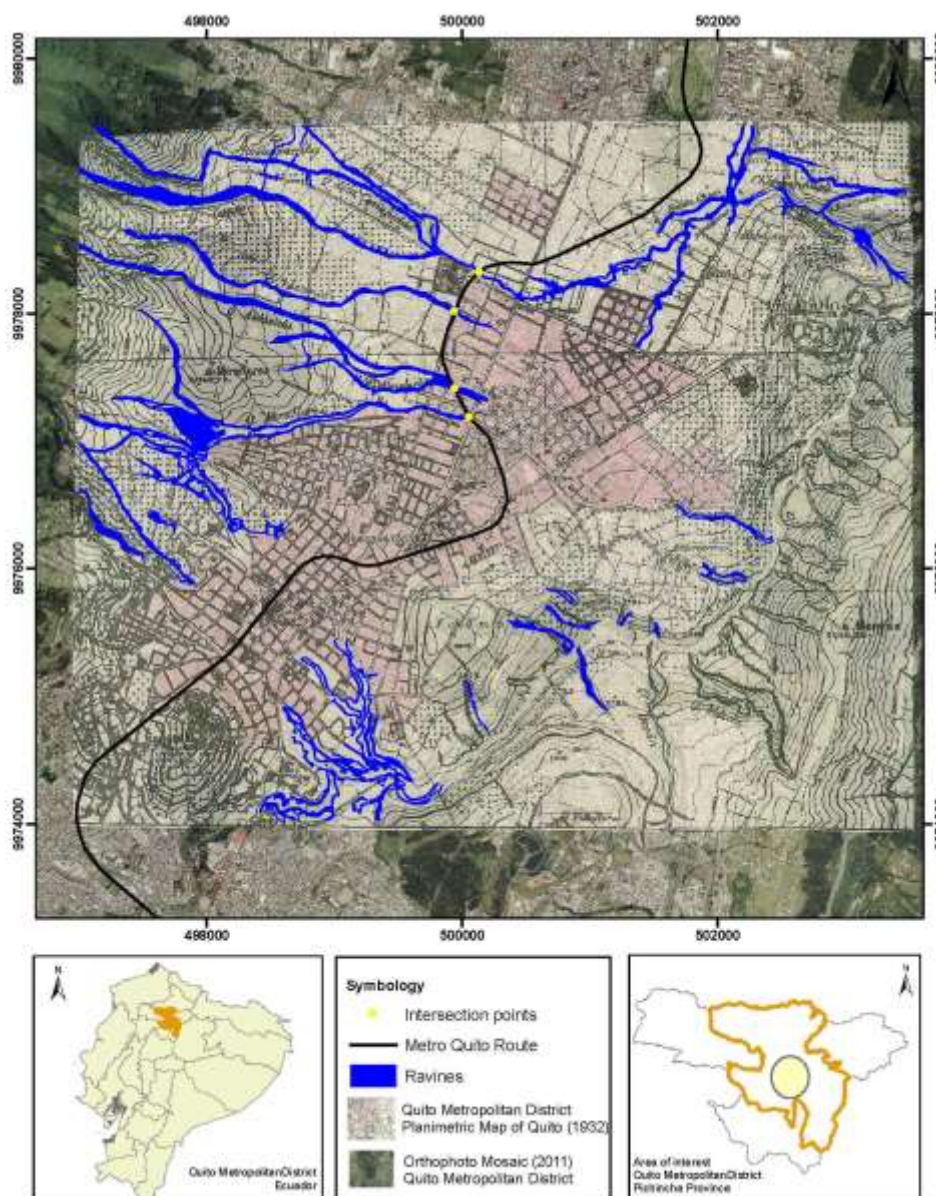


Figure 3: Location of urban infrastructure on filled quebradas

5 Conclusions

- Historical cartography and aerial photography can be successfully and reliably used for change detection with different purposes and in different landscape settings
- The accuracy attained with the DLT Image Geometric Correction Model of ERDAS v10 allows the use of historical cartography for risk assessment. Photogrammetric correction with DLT also proved to be a cost efficient method for updating geospatial data.
- Better accuracy could be attained from digital elevation models derived from historical contour maps. This should actually be a requirement for urban planning in mountain cities which have undergone dramatic landscape changes which is the case of Quito.

References

- [Abdel-Azis 1971] Y.I Abdel-Azis, H.M. Karara, Direct Linear Transformation from Comparator Coordinates into Object Space coordinates in Close-range Photogrammetry, *Proceedings of the Symposium on Cross range Photogrammetry*, American Society of Photogrammetry, pages 1-18, 1971
- [Buytaert 2008] Wouter Buytaert, Rolando Célleri y Luis Timbe, Predicting Climate Change Impacts on Water Resources in the Tropical Andes: Effects of GCM Uncertainty, *Geophysical Research Letters*, pages L07406 - L07408, 2008
- [Carrión 1994] Fernando Carrión, René Vallejo, La planificación de Quito, del Plan Director a la Ciudad Democrática, Quito Transformaciones Urbanas y Arquitectónicas, Series Quito, 237 pages, 1994
- [De Noni 1986] B. y G. de Noni, M. A. Fernández y P. Peltre, Accidentes Climáticos y Gestión de las Quebradas de Quito. Análisis del ‘aluvión’ de la Raya del 23 de Enero de 1986, *Paisajes Geográficos Revista del CEPEIGE*, pages 25-44, July 1986
- [Li 2002] D. Li, H. Sui, P. Xiao, 2002, Automatic Change Detection of Geospatial data from imagery, *The International Archives of the Photogrammetry, Remote Sensing and Spatial Information Sciences*, vol. 32 n° 2, pages 241 – 255, 2002
- [Metzger 1996] Pascale Metzger, Nury Bermúdez, El Medio Ambiente Urbano de Quito, municipio del Distrito Metropolitano de Quito, Institut Français de Recherche Scientifique por le Développement en Coopération (ORSTOM), 178 pages, 1996
- [Ortiz Crespo, 2007] Alfonso Ortiz Crespo, Matthias Abram, José Segovia, *Damero*. FONSAL, Quito, Ecuador, 207 pages, 2007
- [Orton 1870] James Orton, *The Andes and the Amazon: or, Across the Continent of South America*, 349 pages, 1870
- [Peltre 1989] Pierre Peltre, Quebradas y Riesgos Naturales en Quito, período 1900-1988, *Riesgos Naturales en Quito; Lahares aluviones y el Derrumbe del Pichincha y el Cotopaxi*. Estudios de Geografía vol. 2, pages 46-66, 1989
- [Perrin 2001] J. L. Perrin, C. Bouvier, J. L. Janeau, G. Ménez, F. Cruz, Rainfall/Runoff processes in a small periurban catchment in the Andes Mountains. The Rumihurcu Quebrada, Quito Ecuador, *Hydrological Processes*, pages 843-854, 2001
- [Porras 2008] Carlos Porras, *Examen especial, al Sistema de Prevención, Mantenimiento, Construcción, y Rehabilitación de los colectores, así como a las acciones realizadas por las emergencias en los sectores: Trébol, Ferroviaria, Aeropuerto de Quito*,

Guápulo, y en la Parroquia de Amaguaña, por el período comprendido entre el 1 de enero al 31 de mayo del 2008, pages 1-8, 2008

[Ramírez 2005] J.R. Ramírez, Updating of Geospatial Data: a theoretical Framework, *Surveying and Land Information Science*, vol. 65, pages 245-254, 2005

[Recio 2011] J.A. Recio, T. Hermosilla, L.A. Ruiz, A. Fernández-Sarría, Historical Land Use as A feature for image Classification, *Photogrammetric Engineering and Remote Sensing*, vol. 77, n°4, pages 377-387, April 2011

[Terry 1832] Adrian Terry *Travels in the Equatorial Regions of South America in 1832*, 302 pages, 1834

Fast and accurate view factor generation

Benoit Beckers¹ and Pierre Beckers²

¹Compiègne University of Technology – Sorbonne University

Rue Roger Couttolenc, CS 60319
60203 Compiègne - France
Benoit.Beckers@utc.fr

²University of Liège

7, rue des Erables, 4122 Plainevaux - Belgique
Pierre.Beckers@ulg.ac.be

Keywords: View Factor, Ray Tracing, Uniform Mesh, Radiative Heat Transfer, Stratified Sampling.

Abstract. *This document explains how to mesh the hemisphere with equal view factor elements. The main characteristic of the method is the definition of elements delimited by the two classical spherical coordinates (polar and azimuth angles) similar to the geographical longitude and latitude. This choice is very convenient to identify the localization of the elements on the sphere; it also simplifies a lot the determination of rays for either deterministic or stratified sampled Monte Carlo ray tracing. The generation of the mesh is very fast and consequently well suited for ray tracing methods. The quality of the set of rays spatially very well distributed is a fundamental element of the whole process reliability.*

1 Introduction

The main radiative phenomena considered in urban physics are: light, sound and heat. In thermal radiation, we must distinguish between exchanges that occur in short wavelengths (including visible light) and those that take place in the long wavelengths [Beckers 2011]. The objects of the urban scene only emit in long wavelengths, with an intensity that is proportional to the fourth power of their temperature. Thermal loads due to Sun are totally provided in shortwave, and their interaction with the city surfaces is independent of the temperatures.

The fundamental differences between these problems come from the wave propagation behavior and the human perception: light is considered instantaneous, sound is perceived delayed, and heat involves inertia [Beckers 2014a].

To solve radiative problems, we distinguish two completely different approaches. The first one is using some kind of mesh generated in CAD systems (typically the wide used “stl” files), finite element or radiosity methods [Beckers 2016]; the second deals only with discretized sources and uses ray tracing techniques, typically in the frame of Monte Carlo methods.

In the first approach, the problem is based on the discretization of the objects into elements or patches that will be used to model the scene and simulate the physical behavior. The basic ingredients are the view factors. These are purely geometrical parameters that describe how objects are seen from each other. They can be computed by algebraic or Monte Carlo ray tracing methods.

The paper is mainly based on [Beckers 2012], where the idea of using spherical equal area cells was introduced for the first time. The concept of coverage index, initially introduced in [Tregenza 1987] and enhanced in [Beckers 2014b], is actually giving valuable information on the cells aspect ratios. The geometric backgrounds of the method are fully developed in [Beckers 2014a].

2 View Factor

The *view factor* (also called *form factor*) is the basic element of the radiative studies [Beckers 2014a, Beckers 2012, Sillion 1994]. It defines the fraction of the total power leaving patch A_i that is received by patch A_j . Its definition is purely geometric. The angles θ_i and θ_j relate to the direction of the vector connecting the differential elements with the vectors normal to these elements; r_{ij} is the distance between the differential elements.

$$F_{ij} = \frac{1}{A_i} \int_{A_i} \int_{A_j} \frac{\cos \theta_i \cos \theta_j}{\pi r_{ij}^2} V(y_i, y_j) dA_i dA_j \quad (1)$$

Except in particular situations [Howel 2010], it is not possible to compute the view factors explicitly. An additional difficulty appears in presence of obstructions represented in the above expression by the visibility function $V(y_i, y_j)$. This function is equal to 0 or 1 according to the possible presence of an obstacle that does not allow seeing an element y_j from an element y_i .

It is much easier to compute the differential view factor by removing the external integration that will be taken into account thereafter in order to achieve the evaluation of the view factor, using, for instance, Gaussian quadrature rule. The differential view factor in a point y_i surrounded by the element area dA_i is given by:

$$F_{dA_i-A_j} = \int_{A_j} \frac{\cos \theta_i \cos \theta_j}{\pi r_{ij}^2} V(y_i, y_j) dA_j \quad (2)$$

This expression can be interpreted as the result of two successive operations known as Nusselt analogy, where we will momentarily disregard the visibility term $V(y_i, y_j)$ not required for the explanation:

1. The element is projected on the unit hemisphere centered on the point y_i . This step is represented by the factor $\cos \theta_j / r_{ij}^2$ of relation (2). The solid angle completed by the element dA_j , which is also the area of the spherical polygon built from the same element, is given by

$$d\omega_j = \frac{\cos \theta_j}{r_{ij}^2} dA_j \quad (3)$$

2. The spherical polygon is orthogonally projected on the base plane dA_i . This projection corresponds to the term $\cos \theta_i$ of relation (2), which is now transformed into:

$$F_{dA_i-A_j} = \int_{\Omega_j} \frac{\cos \theta_i}{\pi} d\omega_j \quad (4)$$

The term Ω_j represents the solid angle or the spherical polygon area subtended by A_j . The view factor is expressed in percents (projected area over unit disk area by 100).

3 Computing the View Factor

The view factor can be calculated principally in two ways: algebraic methods or ray tracing methods. In the first situation, the geometry of the scene has to be modeled. In the second case, we do not need the deep description of the scene: it is sufficient to give a set of simple patches or triangles like in the “stl” format, which comes from the stereolithography CAD software and is widely used for rapid prototyping, 3D printing and computer-aided manufacturing.

So, the first way to calculate the differential view factor, shown in relations (3) and (4), is to project it onto the hemisphere defined at the concerned point and then to project the spherical polygon orthogonally on the plane tangent to the surface (the disk which is the base of the hemisphere). This projection is compared to the area of the disk. The calculation method is in principle easy to implement. Both steps are easy to perform for any shape that can be decomposed in small line segments. This procedure is applicable for any parameterized shape.

The foundation of the first step is a central projection on a unit sphere centered at origin, which consists in dividing the positions by their modules:

$$P' = \frac{P}{|P|} \quad (5)$$

The second step, which is the orthogonal projection of P' , is straightforward provided we are working in axes defined with respect to the projection plane (normal vector n).

$$P'' = P' - (P' \cdot n)n \quad (6)$$

Let us start with the computation of the view factor of a polyline $P_{i-1} P_i P_{i+1} \dots$ which is not necessarily in a plane. It is shown in blue lines in Figure 1. To compute from point O the view factor of this figure, we have to proceed in two steps. First, we project it on the unit sphere

represented in the figure by its base and two orthogonal semi-meridians, respectively in the plane $x = 0$ and $y = 0$.

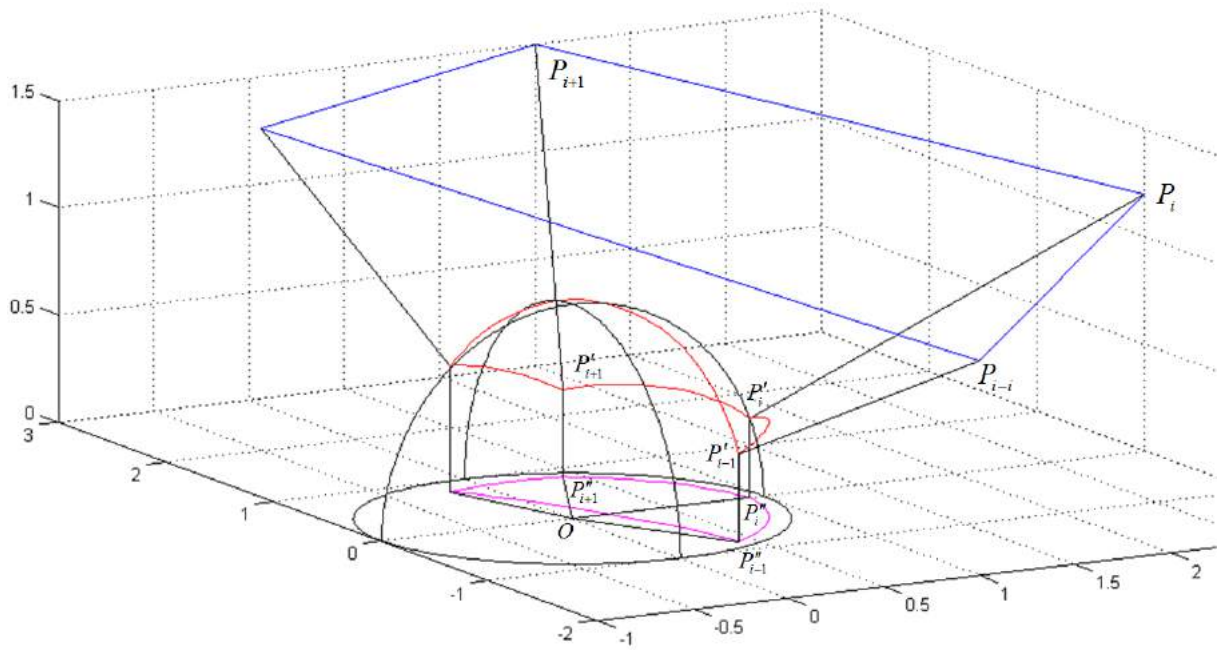


Figure 1: View factor: Point to patch

The spherical projection drawn in red is composed of great circle arcs. In the figure, P'_{i-1} , P'_i and P'_{i+1} are the spherical projections (5) of P_{i-1} , P_i and P_{i+1} . In a second step, we build the orthogonal projection of the spherical polygon on the base of the hemisphere: plane $z = 0$. The circular arcs are transformed into elliptical ones (with the two limiting cases of straight lines or circular arcs). In the figure, P''_{i-1} and P''_i are the orthogonal projections (6) of P'_{i-1} and P'_i .

To compute the view factor, we have first to define the unit vectors f_i normal to the faces of the spherical pyramid $OP'_{i-1}P'_iP'_{i+1}$... where OP'_{i-1} , OP'_i , ... are unit vectors computed from the apex O to the vertices of the studied contour $P_{i-1}P_iP_{i+1}$... The vertices sequence of the pyramid base is defined in such a way that the spherical polygon representing its projection on the sphere is always situated on the left side of its boundary composed of great circles segments.

$$f_i = \left(\frac{OP'_{i-1} \times OP'_i}{|OP'_{i-1} \times OP'_i|} \right) \quad (7)$$

The length l_i of the circular segment $P'_{i-1}P'_i$ is given by:

$$l_i = \arcsin (|OP'_{i-1} \times OP'_i|) \quad (8)$$

It is always positive because the arc length is greater than zero and less than π . Because the area of a unit disk sector of angle α is equal to $\alpha/2$, the arc length of the spherical pyramid face $OP'_{i-1}P'_i$ is equal to twice its area. The orthogonal projection a_i of the face area on the base plane with normal vector n is then given by:

$$a_i = \frac{l_i}{2} (f_i \cdot n) \quad (9)$$

The vector n is normal to the surface supporting dS and on which we calculate the view factor. As defined in (7), the vectors f_i are normal to the faces of the pyramid: $OP_{i-1}P_i$, OP_iP_{i+1} ... The dot products of (9) are multiplied by the quantities l_i , equal to the angles of the faces of the pyramid at the apex O . This expression can be positive or negative, depending on its orientation given by the dot product.

If we add algebraically the expressions (9) for all the contour segments, we obtain the area of the orthogonal projection $P_{i-1}'' P_i'' P_{i+1}'' \dots$ of the spherical polygon, which must be divided by π (area of the base) to obtain the relative area:

$$F_{dS-P_j} = \frac{1}{\pi} \sum_i a_i = \frac{1}{2\pi} \sum_i l_i (f_i \cdot n) \quad (10)$$

For a shape $P_{i-1} P_i P_{i+1} \dots$, the formula is giving a result that depends only on the accuracy of its evaluation. This shape can be as simple as a polygon or it can be extracted from the outline of a solid and expressed as a polyline. The precision also depends on the precision of the computation of the obstructions. In complex situations, these computations can be very heavy.

If the patches do not cover the full hemisphere, the complement to 1 of the sum of their view factors is called sky view factor (closure property of the view factors). The sky view factor is linked to the visible part of the vault of heaven; it is often used as design parameter in architectural applications. When the skyline is available, (10) can provide an easy and fast method to compute the sky view factor.

4 Meshing the Hemisphere

Before considering the second method used for computing the view factors, we have first to consider the spherical support used to generate the rays for the casting process. There are several methods to mesh a sphere: in the first one, it is covered with spherical polygons that are figures of the sphere delimited by great circles. In practice, these structures are based on some of the five regular spherical polygons.

In another one, we build elements bounded by segments of parallels and meridians. The choice of this kind of mesh is justified by the fact that the spherical coordinates based on polar and azimuth angles (where the polar angle may be called co-latitude, zenith angle, normal angle, or inclination angle) or the geographical coordinates are widely used to describe the sphere. A direct advantage of this choice is that the azimuthal projections centered on the poles of these elements are figures of the circle bounded by arcs of concentric circles and radii segments [Beckers 2014b, Leopardi 2006]. For these reasons, it is our preferred meshing method.

But before addressing the problem of the hemisphere, we first examine how to define equal area cells within a disk. The full disk is divided into a central one surrounded by concentric rings, each one containing a certain number of cells. For a mesh where all elements have the same area, one realizes immediately that the sequence of cells differs on the different rings.

Let assume that N equal cells have to be defined in a unit disk. Starting from a central disk composed of a single cell and whose radius is equal to $r_1 = 1/\sqrt{N}$, we easily perform the computation in the ring surrounding it. This disk is composed of n cells, so that the disk that is the sum of the inner disc and this one contains ($k_2 = k_1 + n$) cells (or $k_{i+1} = k_i + n$). The radius of this disc is given by $r_{i+1} = r_i \sqrt{k_{i+1}}$. The number of cells added to each ring is arbitrary, provided that the total amount of cells does not exceed the value N .

As the filling sequence of the successive disks is arbitrary, we deduce that it is possible to impose at each step an additional condition, for example imposing the aspect ratio of the cells, either in the ring to be inserted on the disk (Figure 2), or on the hemisphere (Figure 3). This procedure only needs a few statements in Matlab and gives the sequence of cells in the different rings, from the spherical cap on the top of the dome to its base. For the example of 100 imposed cells of Figure 2, we have the non optimized sequence:

$$S = [1 \ 8 \ 22 \ 42 \ 68 \ 100] \quad (11)$$

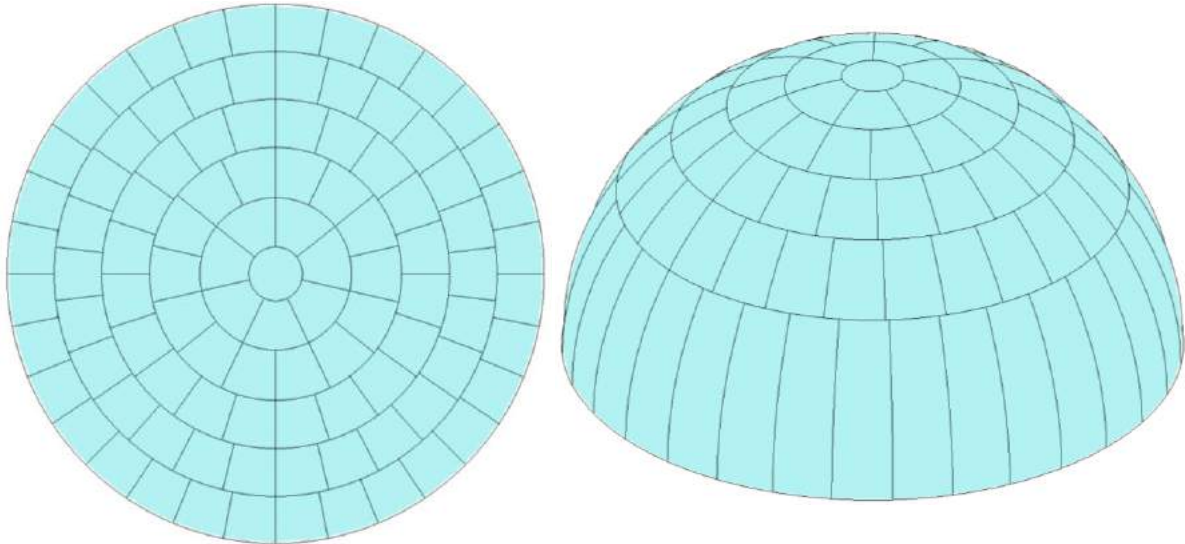


Figure 2: 2D and 3D views of 100 cells with equal areas and aspect ratio equal to 1 on the disk

In the optimized case of Figure 3, obtained with the functions developed in [Beckers 2016b], we obtain the sequence:

$$S = [1 \ 8 \ 22 \ 40 \ 62 \ 84 \ 100] \quad (12)$$

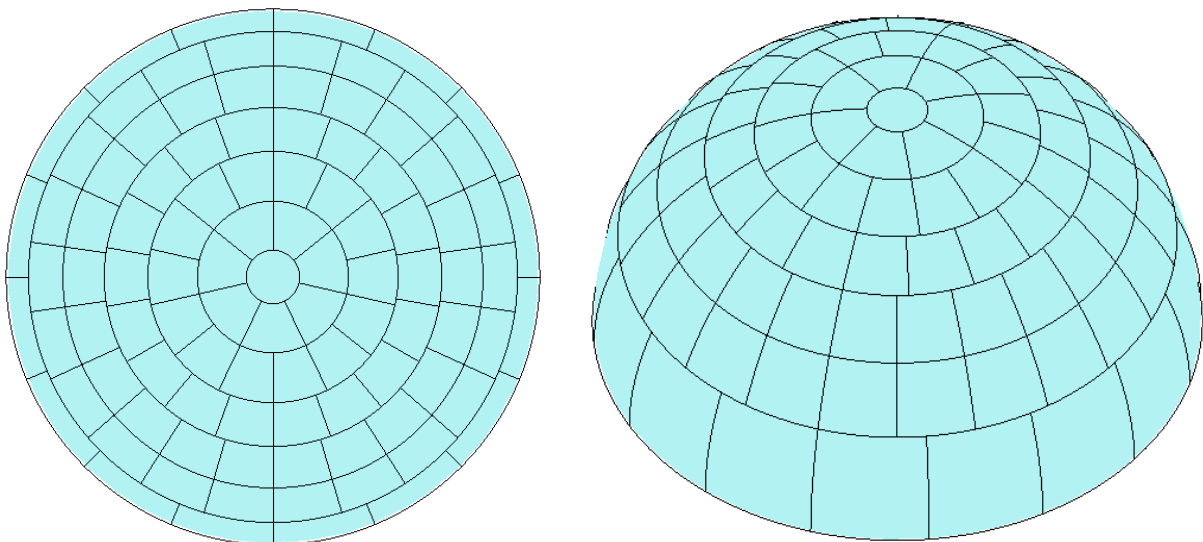


Figure 3: 100 cells with same areas on the disk and aspect ratio equal to 1 on the hemisphere

Once the sequence of cells is defined on the disk, it is easy to use an inverse azimuthal projection to obtain the mesh on the sphere. In the case of azimuthal orthogonal projection,

the relationship between the polar angle θ on the unit hemisphere measured in radians and the radius in the projection is:

$$r = \sin \theta \quad (13)$$

On the left side of [Figure 2](#), we see the orthogonal projection of the hemisphere on its base. Here, both the areas and the aspect ratios of the projection are equal. The drawback of this choice is the important distortion of the cells close to the base of the hemisphere. In [Figure 3](#), the areas of the projection are required to be equal while the aspect ratios are required to be equal to one on the hemisphere. The important distortion of the cells close to the base is now removed.

When we significantly increase the number of cells, we observe first that the processing time needed to generate the sequence of cells is negligible and secondly that the main difference between optimized ([Figure 4](#), left) and non optimized ([Figure 4](#), right) situations is occurring mainly close to the base.

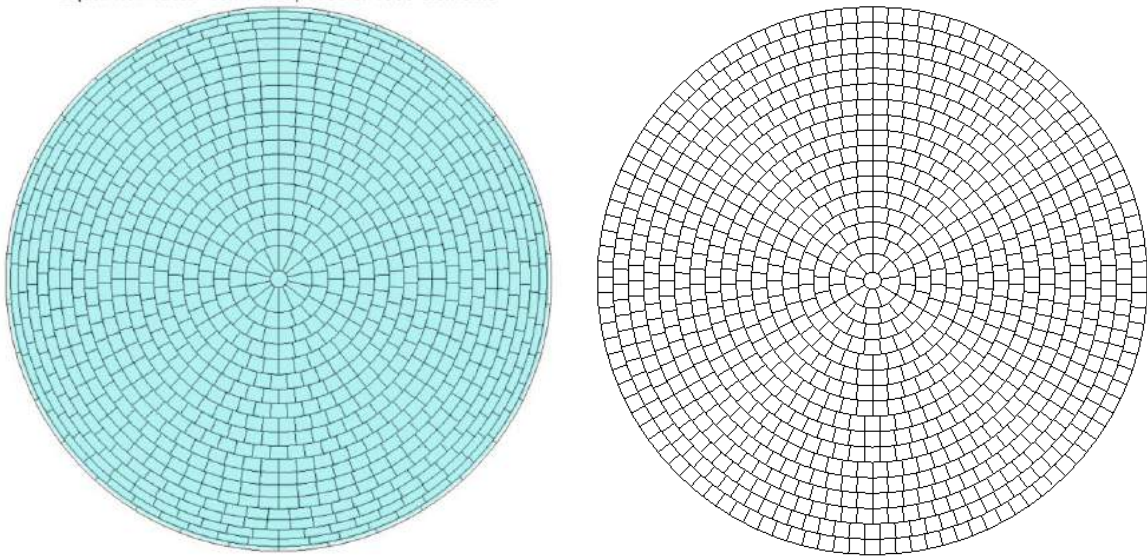


Figure 4: Comparison of the 2 solutions for a generation of 1000 cells

5 Generating rays

After the generation of equal view factor cells, it is possible to generate rays that will allow computing view factors of the scene elements. The rays are generated, for instance from the origin to each cell and traced to the scene, and the number of collisions with the elements is accounted. The view factor of an element is the ratio between the number of impacting rays and the total number of traced rays. If the number of traced rays is sufficient, the result tends to the exact solution [[Vujicic 2006](#)].

The first method used to define the rays is deterministic, for instance, the rays pass through the center of each cell. It is the situation shown in the orthogonal projections [Figure 5](#) & [Figure 6](#) of the optimized cell sequence [1 15 32 54 80 107 133 151].

In a non optimized sequence [1 9 22 41 64 91 120 151], we observe the bad aspect ratio of the lower ring ([Figure 7](#)); it is confirmed by the diagram of [Figure 8](#) showing the relative coverage index in each ring. This index is defined as the ratio of the area of the greatest inscribed circle and the cell area, compared to the same ratio computed in a plane square and equal to $\pi/4$ [[Beckers 2014b](#)]. It also appears clearly that the density of points is lower in the bottom of the dome ([Figure 6](#)). The same is occurring for the random rays of [Figure 10](#).

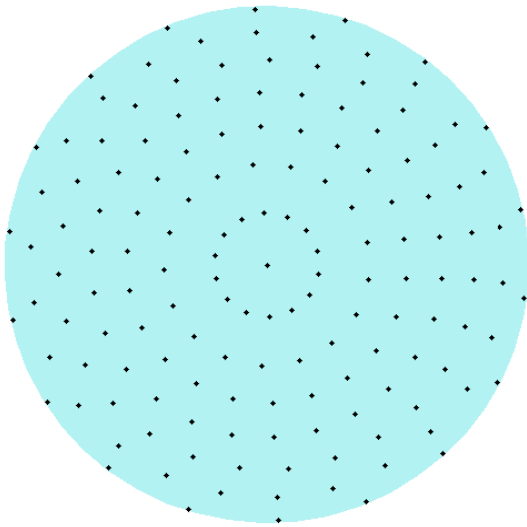


Figure 5: Deterministic 151 cells centers

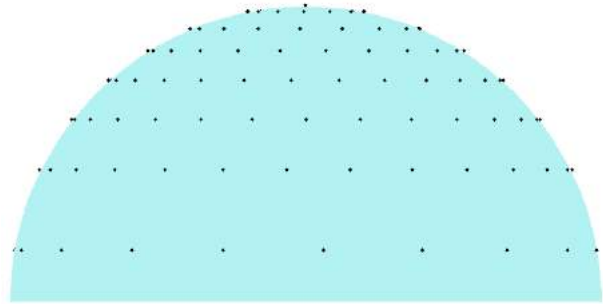


Figure 6: Side view of the dome composed of 151 rays generated from equal view factor cells

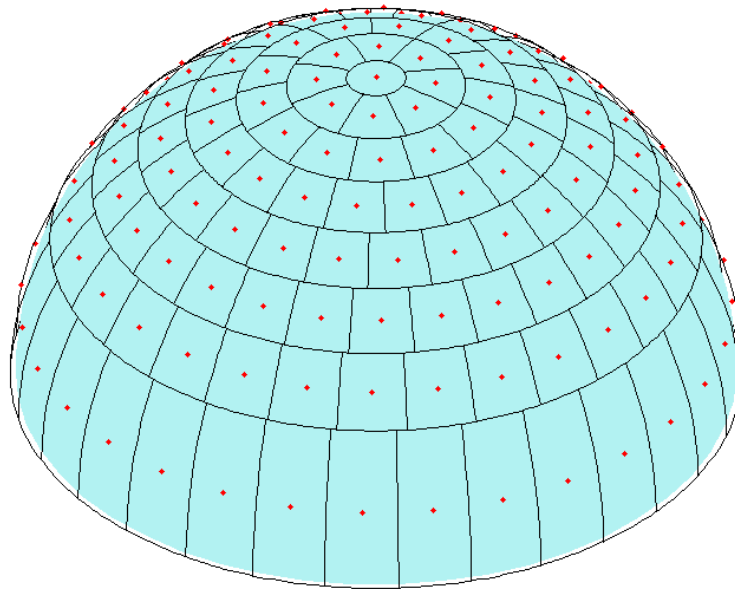


Figure 7: Mesh and deterministic rays for the non optimized 151 cells dome

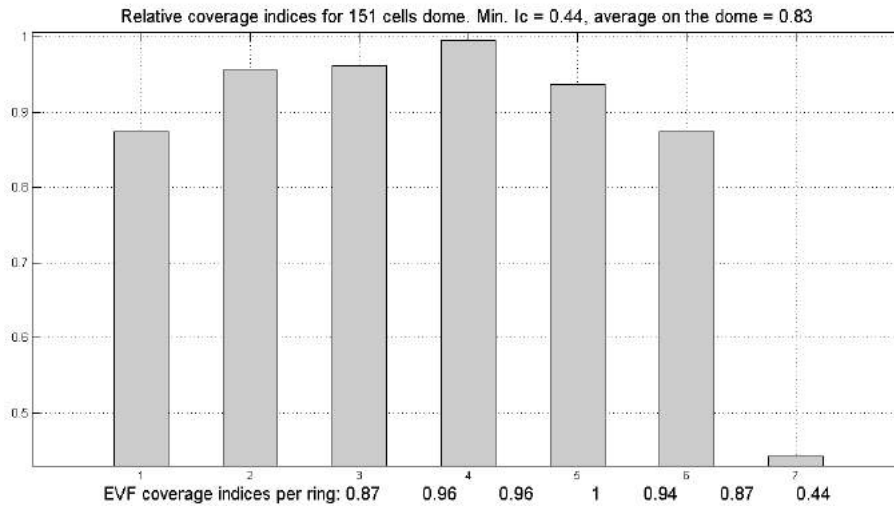


Figure 8: Equal view factor (EVF), 151 cells mesh without cells aspect ratio optimization

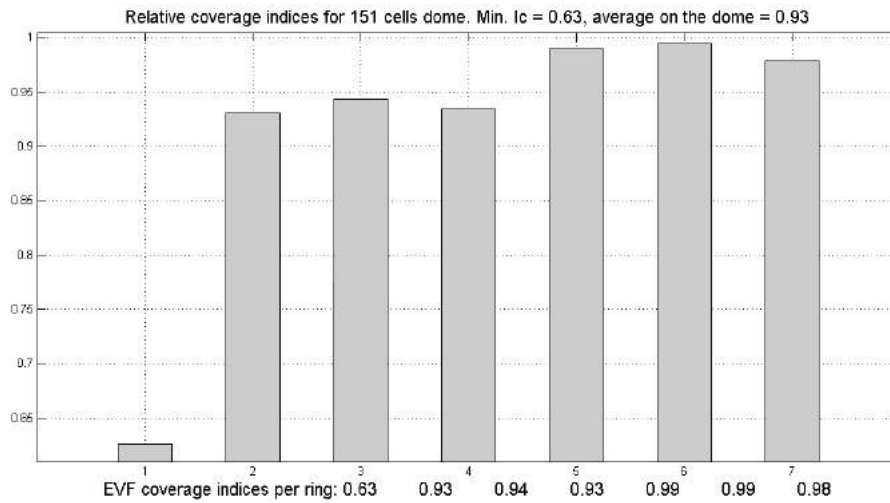


Figure 9: Equal view factor (EVF) optimized 151 cells mesh

In the optimized mesh where the cells aspects ratios on the sphere are close to 1, we obtain the new cells sequence [1 15 32 54 80 107 133 151] and the coverage indices of Figure 9. We observe that the worse coverage index occurs in the ring close to the top of the dome while it occurs in the bottom ring of the non optimized sequence. Anyway, the optimized sequence is better both for the minimum value and for the average.

In the second ray tracing method, the position in each cell is defined randomly. Because all the cells are defined between two latitudes and two longitudes, this procedure is very reliable and easy to implement. This method pertains to the category of stratified sampled Monte Carlo methods. An example of this kind of ray distribution is shown on a side view of a dome in Figure 10. It appears clearly that the density of points is lower close to the base of the dome, which reflects the behavior of importance sampling methods.

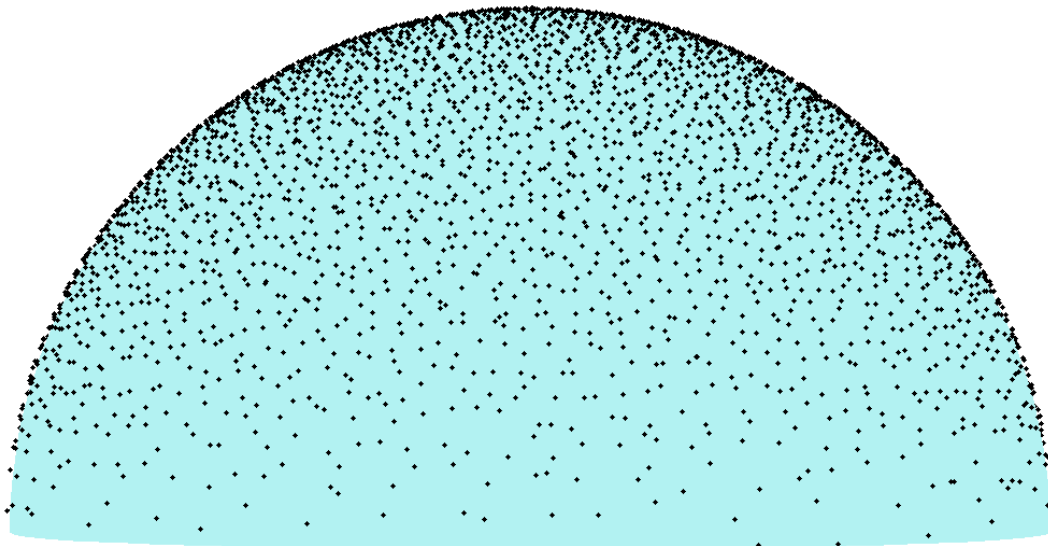


Figure 10: Side view of a dome composed of 5000 random rays

The proposed method is also the most convenient one to generate uniform equal solid angle rays on the sphere. In this case, as proposed in [Beckers 2012], it is similar to that of [Leopardi 2006], but according to the performed comparative tests, we feel that it is faster, because it is using a pure algebraic procedure.

6 Conclusion

Two methods are proposed for computing the view factors. The first one, often called Lambert method [Beckers 2014a], uses an explicit formulation of the point to patch view factor. It is very efficient and exact in the case of lack of obstacle between the point and the patch. The second one is based on an original method of mesh generation on the sphere or the hemisphere. This kind of mesh allows using both importance and stratified sampling in Monte Carlo ray tracing methods. It provides an efficient method to compute the view factors in complex urban environments because due to its geometrical simplicity, it is naturally well suited to deal with complex spatial configurations.

References

- [Beckers 2011] Benoit Beckers, “Impact of solar energy on cities sustainability”, PLEA 2011 - 27th Conference on Passive and Low Energy Architecture, Louvain-la-Neuve, Belgium, 13-15 July 2011.
- [Beckers 2012] Benoit Beckers, Pierre Beckers, “A general rule for disk and hemisphere partition into equal-area cells”, *Computational Geometry: Theory and Applications*, Vol. 45, Nr. 7 2012, p. 275-283.
- [Beckers 2014a] Benoit Beckers, Pierre Beckers, *Reconciliation of Geometry and Perception in Radiation Physics*, John Wiley and Sons, Inc., 192 pages, July 2014.
- [Beckers 2014b] Benoit Beckers, Pierre Beckers, “Sky vault partition for computing daylight availability and shortwave energy budget on an urban scale”, *Lighting Research and Technology*, vol. 46 n°6, Pages 716-728, December, 2014
- [Beckers 2016] Benoit Beckers, “Multiscale Analysis as a Central Component of Urban Physics Modeling”, in: *Computational Methods for Solids and Fluids, Multiscale Analysis, Probability Aspects and Model Reduction*, Adnan Ibrahimbegovic (Ed.), Springer International Publishing, 2016, Pages 1- 27.
- [Beckers 2016b] Benoit Beckers, Pierre Beckers, “Complete set of Matlab procedures for achieving uniform ray generation”, 2016, Website: <http://www.heliodon.net/>
- [Howel 2010] J.R. Howell, R. Siegel, M.P. Menguc, *Thermal Radiation Heat Transfer*, 5th ed., Taylor and Francis / CRC, New York, 2010.
- [Leopardi 2006] Paul Leopardi, “A partition of the unit sphere into regions of equal area and small diameter“, *Electron. Trans. Numer. Anal.* 25 2006 309–327.
- [Tregenza 1987] Tregenza Peter R., “Subdivision of the sky hemisphere for luminance measurements”, *Lighting Research & Technology*, 1987; 19: 13–14.
- [Sillion 1994] François Sillion, Claude Puech, *Radiosity and Global Illumination*, Morgan Kaufmann Publishers, Inc., 1994.
- [Vujicic 2006] Mile R. Vujicic, Nicholas P. Lavery, S. G. R. Brown, “Numerical Sensitivity and View Factor Calculation Using the Monte Carlo Method”, *Proceedings of the Institution of Mechanical Engineers, Part C: Journal of Mechanical Engineering Science* 2006, 220:697

Skyline-control Based LoD Generation for Solar Analysis in 3D Cities

Gonzalo Besuievsky¹, Benoit Beckers², and Gustavo Patow¹

¹Geometry and Graphics Group, University of Girona, Spain

²Urban System Engineering Department, Compiegne University of Technology, France

Keywords: Level of Detail, 3D City model, Solar simulation

Abstract. *Solar simulation for 3D city models may be a complex task if detailed geometry is taken into account. For this reason, the models are often approximated by simpler geometry to reduce their size and complexity. However, geometry details, as for example the ones provided in a roof, can significantly change the simulation results if not taken into account. The classic solution to deal with a detailed city model on a district scale is to use a Level-of-Detail (LoD) approach for geometry reduction.*

In this paper, we present a new LoD method for 3D city models for performing accurate solar simulation with detailed geometry models. Given a Point of Interest to analyze, the method works by automatically detecting and preserving all roofs that really have significant impact on the simulation and simplifying the rest of the geometry. We perform a test for a detailed district model showing that for this case our method can reduce the geometry size to 5% of the original model, preserving almost the same accuracy.

1 Introduction

The estimation of the solar potential and the access to sunlight in urban areas is a very important issue in building energy performance. The computation accuracy for solar simulation is directly influenced by the urban geometry, both at the neighborhood and at the building scale. Because of this, a well-defined geometrical model of the urban environment is mandatory for accurate analysis and assessment.

One of the main difficulties concerning geometry detailed models is the amount of data to deal with, affecting the memory storage and the time processing. The classical solution is to introduce Levels of Detail (LoD) into the model in order to simplify it. Most of the simplification methods for simulation work by rough approximating the buildings to simple shapes like bounding boxes and basic roof geometry. As a consequence, building elements that influence the simulation, like a roof water tank or an antenna, may propagate errors in a lighting assessment or in a Sky View Factor (SVF) study.

In this paper, we propose a new LoD method for urban models. Our main goal is to provide models for performing solar simulation at full geometry resolution. Given a 3D detailed city model and a region of interest, the method can obtain a simplification model feasible for computing solar radiation for that region. By computing the skyline impact over the urban geometry, the method preserves all important roof details. A fast ray-casting engine is used against a rough approximation of the model to decide which geometry level should be instantiated.

The main contribution of our work is that it provides a fast, accurate and automatic model simplification for dealing with solar simulation in detailed urban models. We tested our reduced model results to perform an annual daylight simulation. Our results show that, for the district model used, we can obtain accurate values with the model reduced to 5% of the original size, improving considerably the execution time.

2 Previous Work: LoD in Urban models

Level-of-detail techniques have been largely developed in computer graphics with the aim of reducing geometry since the first work presented by [Clark, 1976], followed by the seminal work by [Luebke and Erikson, 1997]. The interested reader can refer to the book at [Luebke et al., 2002] for a more exhaustive and complete survey of general LoD techniques.

As far as urban models are concerned, a few LoD proposals come from the use of a semantically well-defined dataset structure, as for example the CityGML schema as defined at [Kolbe, 2009]. CityGML differentiates between five consecutive LoD-levels, where objects become more detailed with increasing LoD

regarding both geometry and thematic functionality differentiation. They range from a coarsest level in LOD0, which is essentially a two and a half dimensional digital terrain, to full interior structures like rooms, stairs, and furniture in the top level LOD4. In that approach, the different levels of detail are pre-made and not adapted for specific simulation purposes.

For procedural modeling, [Parish and Müller, 2001] presented an initial proposal intended for city generation based on the L-system recursive nature. Automatic LoD-generation is obtained by starting from the building envelope as axiom, and the output of each rule iteration represents a refining step in the building generation. Although it is simple and automatic, this approach does not provide control on geometric building details. Recently, new approaches have been proposed to integrate LoDs mechanism in the procedural processing. In [Besuievsky and Patow, 2013a], the authors developed a rewriting method of the rulesets for the buildings for further replacing the geometric operators, which produces the right level of detail for each asset according to some user-defined criteria. In [Besuievsky and Patow, 2013b], they propose a highest level of detail by enabling selection, from entire buildings up to whole blocks, for geometric reduction. These works focus more on solving rendering problems, whereas in our approach we target more on the model preparation for simulation analysis.

Concerning solar energy simulation, defining the optimal LoD at the neighborhood scale is not a simple problem and most of the approaches are taken from an empirical perspective. In [Rodriguez et al., 2012], a study of the sensitivity of the geometry used is carried out taking into account the solar flux computation, where different levels of detail elements (windows and roofs) are evaluated for a neighborhood-scale model. In [Besuievsky et al., 2014], a configurable LoD system based on procedural models is presented for daylight simulation. The system allows the configuration of different criteria for approximating the full geometry for different computations. [Biljecki et al., 2014] provided a formal and consistent framework to define discrete and continuous levels of detail (LODs), by determining six metrics that constitute it, and discussed their quantification and relations. Following this initial work, in [Biljecki et al., 2015], they studied the propagation of positional error in 3D GIS, and applied this computation to the estimation of the solar irradiation of building roofs. Next, [Biljecki et al., 2016] studied the variety of LOD1 and LOD2 geometric references that are commonly employed in LoD models, and performed numerical experiments to investigate their relative difference when used as input for different spatial analyses of a 3D building model. Their results show that two different models generated from different geometric references, but with the same LoD, may yield substantially different results when used in a spatial analysis.

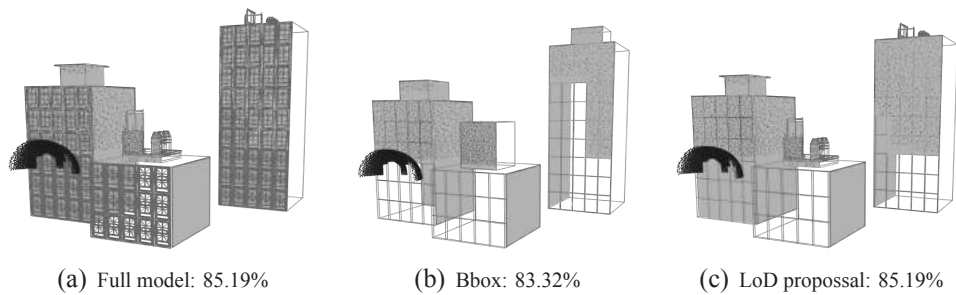


Figure 1: Sky View Factor test for three different model representations.

3 Skyline Approximation Foundation

In this section, we analyze the influence that the city skyline details have on the simulation. For this analysis, we use the Sky View Factor (SVF) as a metric for studying the influence of the roof details on a given building. The SVF, currently used in daylight assessment, is defined as the percentage of sky visible from a surface, taking into account the angle of inclination to the sky vault. It is a pure geometrical parameter that has a physical meaning. Fig. 1 shows three simple buildings modeled at different detail resolutions: full detail resolution, bounding box approximation represented by the envelope of each building, and a mix of the previous ones, putting full resolution only to the roof. We compute the SVF for a virtual point in front of the buildings, getting the same value for both the full model and for the last approximation. We noted that most of the relevant details for solar analysis belong to the skyline given by the roof, and that could be obtained from the silhouette. We complete our test by computing the average SVF with Heliodon [Beckers and Masset, 2008] on two virtual surfaces on a 3D city model: an horizontal plane at the street level and a vertical plane in front of the facade of a building (see Fig. 2). By comparing the results of the bounding box approximation with full roof resolution city against the full model, we observe a relative error lower than 10^{-2} in both cases. Considering that the number of polygons used in the approximation representation is 10 times smaller than the original model, we tuned our LoD proposal following these observations.

4 LoD Generation Method

Given a 3D city model, the method works in two steps. In a first pre-processing step, all geometry assets (like windows, balconies or roofs) are replaced by their respective bounding boxes. We call the resulting model the *rough* model. In the second step, a LoD operator decides, from a given Point of Interest (POI), the simplification level according to a defined criteria by intersecting a bundle of rays

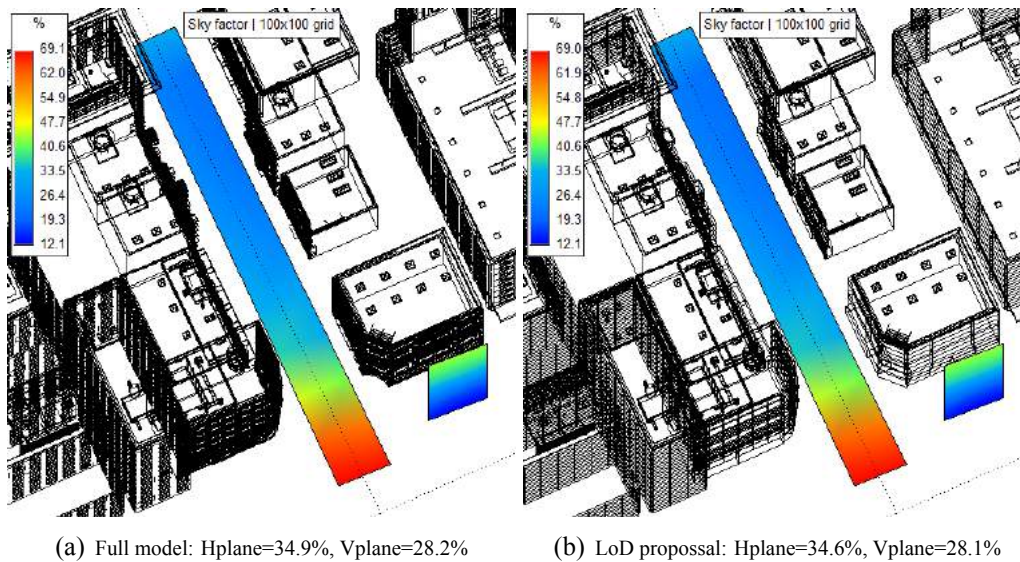


Figure 2: Average Sky View Factor for horizontal and vertical planes in two different representations of a 3D city model.

from the POI with the rough model. The rest of this section describes the method in detail.

4.1 Criteria

For our geometry selection/replacement to work, we designed a simple criteria based on the observation that the relevant details for solar computation are the ones that belong to the building silhouettes (see Section 3). For the rest of the geometry, in most cases it will be enough to approximate it by its visible bounding box planes. We also noted that silhouettes are more relevant at the city skyline. Our LoD model define then three particular geometry levels:

- **Level 0:** The geometry is omitted from the model
- **Level 1:** The geometry is instantiated as its bounding box
- **Level 2:** The geometry is represented in full details.

4.2 LoD algorithm

The algorithm that sets the corresponding simplification levels using the previous criteria is presented at Algorithm 1. The algorithm takes as input a fully detailed city model and a POI, to obtain the simplified representation. After generating the bounding boxes for the rough model (method *generateBBox*, see Section 4.3) it

casts a bundle of rays from the POI (Section 4.4). The algorithm automatically replaces all affected roofs with geometric details (method *isSilhouette*, see Section 4.5), and discards all geometry not participating in the SVF computation (level 0 in the above criteria).

Algorithm 1 LoD Algorithm

Require: *3DCM*: 3D City Model

Require: *POI*: Point of Interest

$P \leftarrow generateBBox(3DCM)$

$rayCastBundle(POI, P)$

for each p_i **in** P **do**

$n \leftarrow p_i.hits()$

if $n = 0$ **then**

$p_i.setLevel(0)$

else

if $p_i.isRoof()$ **and** $p_i.isSilhouette()$ **then**

$p_i.setLevel(2)$

else

$p_i.setLevel(1)$

end if

end if

end for

4.3 Bounding box Building Generation

The bounding box city model is generated in a pre-processing step. It is assumed here that the building models are well structured into assets that represent the basic constructive elements, like windows, doors, balconies or roofs. In general, these elements concentrate most of the geometric complexity. These assumptions about the building structure are reasonable, considering that the 3D building models used in practice are usually generated by Architectural CAD systems that already provide these structures. However, if the models are given as a raw polygon soup, as for example when obtained from acquisition techniques (e.g., with LIDAR), a detection and classification step should be applied to structure the model. Our current implementation is based on procedural urban models [Müller et al., 2006], which implicitly provide this organization: the buildings are generated from the iterative application of a set of rules, each one resulting in a product subject to further processing by successive rules. In this model, the constructive geometric elements are attached to the model in a final ruleset application to the final products by use of the *Insert* command.

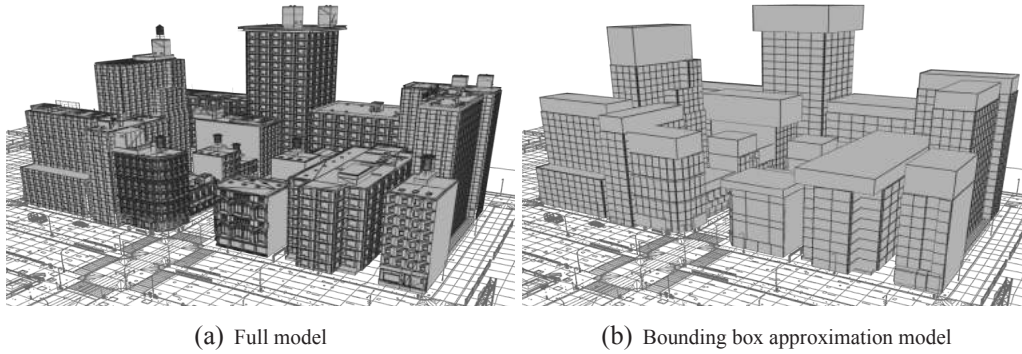


Figure 3: The urban model.

Here we describe the algorithm for procedural models, and a similar procedure should be followed for other kind of 3D models after a structuring stage, as mentioned above. Given a detailed procedural urban model, the bounding box generation algorithm iterates over all products of each building detecting the *Insert* command placements. For each asset, a bounding box of the corresponding insertion is then computed. Then, new building instances are generated, replacing all geometry insertions by their corresponding bounding boxes (see Fig. 3(b)).

4.4 Bundle distribution

We generate the ray bundle distribution by randomly sampling the sky vault using the equal-area cell distribution method described in [Beckers and Beckers, 2014]. By using such specific distribution, we can quickly approximate the SVF directly by just counting the number of impacts with the city model from a given POI.

4.5 Silhouette detection

The problem for detecting the silhouette of an object has been solved by several geometric techniques. One of the widest uses is for visualization in non-photorealistic rendering [Markosian et al., 1997]. In our case, we can simplify the problem with the observation that we are only interested in impact detection in the upper hemisphere of directions with the city skyline and that all candidates to analyze are rectangles produced by the bounding box building approximation described above.

With these considerations, we use the bundle of rays to build a routine for silhouette detection. After casting rays from a given POI, we can split the rays of the obtained distribution into two sets: the ones that impact the geometry and the ones that go straight to the sky. We used this last set to decide if a polygon roof belongs to the silhouette or not: our algorithm works by projecting such candidates to the

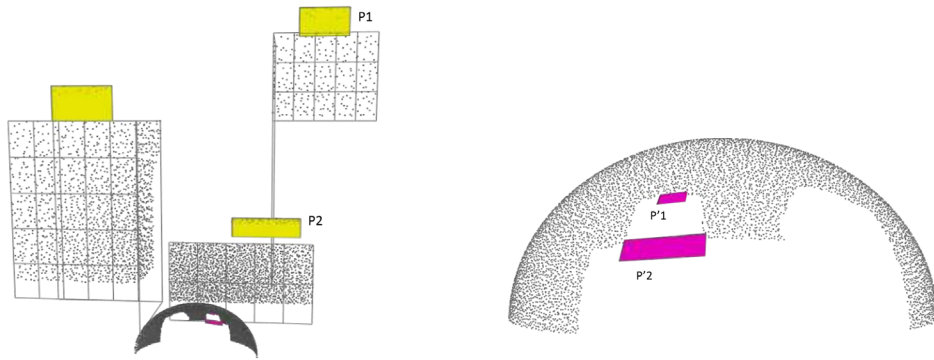


Figure 4: Silhouette algorithm. Top candidate polygons are projected onto a sphere center at the POI (left). By comparing their projection to the sky points, P1 is classified as silhouette and P2 not (right).

POI distribution bundle of rays. When analyzing the projection of the top line of the polygon, if there is any sky point of the distribution close enough (i.e., whose distance is below a given user-defined threshold) to the line, then we can conclude that the polygon is part of the skyline, otherwise it is not. Fig. 4 shows a graphic example using the same buildings models of Fig. 1. The yellow top polygons of the left are candidates for being silhouette from a given POI. Projecting P1 and P2 to the bundle distribution of the sky points, our algorithm discards P2 from the skyline and includes P1.

4.6 Model Aggregation

The final step of the method is to merge all instances of geometry obtained in Levels 1 and Level 2 into a single model. The resulting geometric model is then exported for being used by any daylight simulation application.

5 Results

In this section, we analyze the performance of our LoD approximation. First of all, it should guarantee that the solar simulation will not be affected by the simplification method. We use the SVF computation to validate our approximation. To show its potential use, we compute the solar impact at the windows of a facade for a given model. We also analyze the importance of using detailed geometry by comparing the simulation result to a rough approximation model.

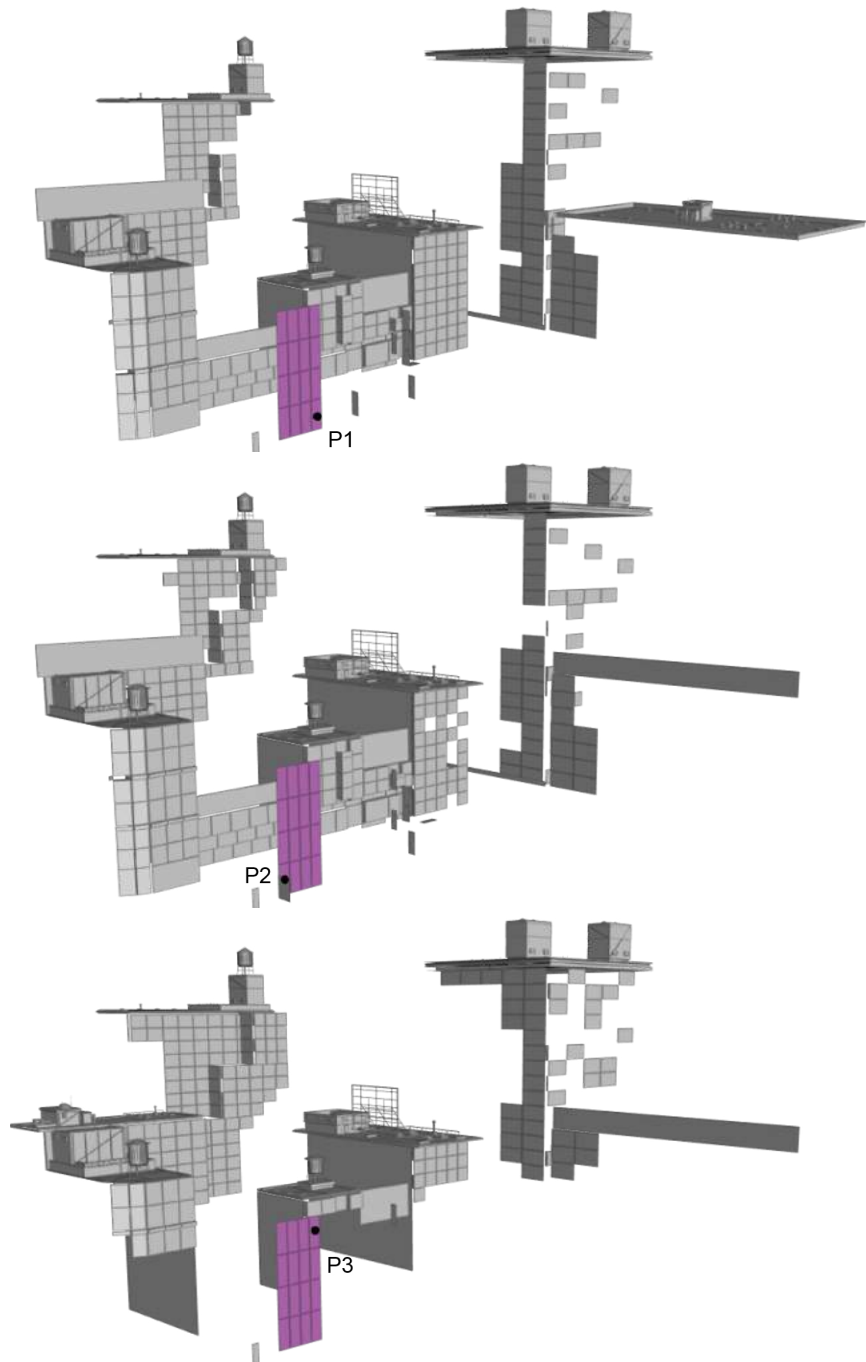


Figure 5: Simplified model for 3 window selected in the facades. The POI is set at each center of the corner's window of the facade.

5.1 LoD from POI

To analyze the accuracy of our method, we computed the SVF using a detailed model composed by 297K polygons (see Fig. 3(a)). We tested our LoD model for a virtual facade. We generated the LoD model for the corner windows of the facade, and the POIs were set at the center of each window. For the resulting models (see Fig. 5) we computed the SVF for both the full and the approximated models. The relative error is computed as $E_r = \|SVF_{Full} - SVF_{LoD}\| / SVF_{Full}$ (see Table 1). On average, the model is reduced to 16.8K polygons, which represents around only 5% of the full input model. The processing time to generate the reduced models is around 10 seconds. Our implementation is written with Python routines using SideFX's Houdini [Side-Effects-Software, 2015] as a development platform.

	P1	P2	P3	P4
SVF_Full	12.59	15.02	24.57	25.59
SVF_App	13.31	14.70	26.60	24.22
Error	0.027	0.021	0.082	0.053
# Polygons	20039	16881	19201	11388

Table 1: Sky View Factor results comparison for the reduced models.

5.2 Solar Impact Computation

To test the usability of the models, we performed a solar impact computation for the whole year using Heliodon [Beckers and Masset, 2008]. The model is localized in Barcelona, Spain. We compute the total daylight hours each window receives using a 15-minute time step. Table 2 shows the resulting hours using the full model and each LoD model for the corresponding window at the corners facade (see Fig. 6). We observe that the relative error in average is around 2%, which is significantly small. The savings in the simulation processing time are also significant: for the full model, the simulation takes around 5 minutes for each window, while the same simulation takes only 15 seconds using the approximated models. Finally, we did the same simulation with the bounding box building models (Fig. 3(b)) to analyze the relevance of using geometric details. In this case, the error, on average for the four windows, is around 13%, too large for accurate simulation purposes. This demonstrates, again, the validity of our assumption, that details should be preserved, but only for the skyline silhouettes.

	P1	P2	P3	P4
Daylight_Full (h)	889.1	923.6	1272.6	1357.8
Daylight_LoD (h)	875.8	932.9	1230.5	1299.7
Daylight_Bbox (h)	784.9	774.9	1084.3	1142.6
Error(Full-LoD)	0.015	0.009	0.033	0.042
Error(Full-Bbox)	0.117	0.191	0.033	0.188

Table 2: Daylight hours comparison for the whole year.

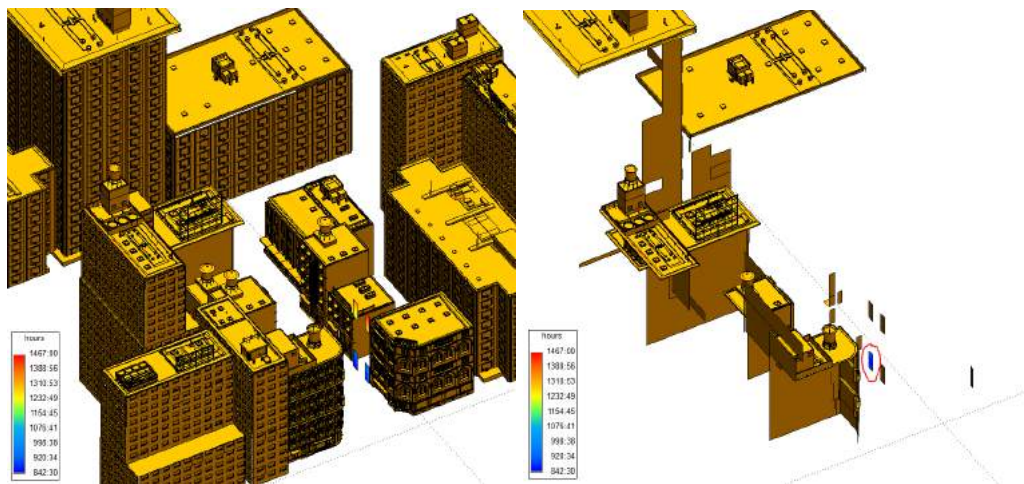


Figure 6: Year-daylight simulation: Full detailed urban model (left) and LoD model for P1 (right).

6 Discussion and Perspectives

Although several LoD techniques were developed to simplify city models for different purposes, only a few of them focus on actual solar simulations for driving the simplification of the model. Comparing our approach to the POI method presented in [Besuievsky et al., 2014], we can observe a significant improvement in the accuracy of the simplification. Whereas in the mentioned technique simplification is implemented by a set of configurable distances to the POI, here we drastically simplify the model by keeping only the geometry that has the largest impact on the final calculation. If visualization of the simulation results is desired, then they can easily be mapped to the original model.

Another important result of this work is the analysis of the relevance the geometric details may have on solar simulation. As it is shown in [Biljecki et al., 2015], among the different applications of 3D city models, the solar impact, like computing solar panels irradiance, is frequently needed. However, building models are usually simplified to LoD1 or LoD2 in CityGML format using only basic

roof geometry, which may lead to significant differences from the real models, and thus seriously distorting the subsequent calculations. We show here that certain detailed geometry may be important in the impact study, and we provide a method to handle it. Our technique for detecting the skyline can be extended for other relevant architectural elements, as for example balconies and other protruding elements, necessary for other kinds of simulations (e.g., wind, pollution, pedestrian simulations).

Our simplification is point-of-view based, as we use the POI for reference. For further development we plan to extend the technique for simplifying the model from an area of interest, like a whole facade or a street. This would allow more general calculations than with a single POI without the burden of repeating the same simplification over and over again, but from slightly different origins.

Acknowledgements

This work was partially supported by grant TIN2014-52211-C2-2-R project from Ministerio de Economía y Competitividad, Spain.

References

- [Beckers and Beckers, 2014] Beckers, B. and Beckers, P. (2014). Sky vault partition for computing daylight availability and shortwave energy budget on an urban scale. *Lighting Research and Technology*, 46(6):716–728.
- [Beckers and Masset, 2008] Beckers, B. and Masset, L. (2008). Heliodon2 software, references & manuals. <http://www.heliodon.net/> (in French & Spanish).
- [Besuievsky et al., 2014] Besuievsky, G., Barroso, S., Beckers, B., and Patow, G. (2014). A Configurable LoD for Procedural Urban Models intended for Daylight Simulation. In Besuievsky, G. and Tourre, V., editors, *Eurographics Workshop on Urban Data Modelling and Visualisation*. The Eurographics Association.
- [Besuievsky and Patow, 2013a] Besuievsky, G. and Patow, G. (2013a). Customizable lod for procedural architecture. *Computer Graphics Forum*, 32(8).
- [Besuievsky and Patow, 2013b] Besuievsky, G. and Patow, G. A. (2013b). City-level level-of-detail. In Association, E., editor, *XXIII Congreso Español de Informática Grafica*, pages 29–36.
- [Biljecki et al., 2015] Biljecki, F., Heuvelink, G. B. M., Ledoux, H., and Stoter, J. (2015). Propagation of positional error in 3D GIS: estimation of the solar

- irradiation of building roofs. *International Journal of Geographical Information Science*, 29(12):2269–2294.
- [Biljecki et al., 2016] Biljecki, F., Ledoux, H., Stoter, J., and Vosselman, G. (2016). The variants of an LOD of a 3D building model and their influence on spatial analyses. *ISPRS Journal of Photogrammetry and Remote Sensing*, 116:42–54.
- [Biljecki et al., 2014] Biljecki, F., Ledoux, H., Stoter, J., and Zhao, J. (2014). Formalisation of the level of detail in 3D city modelling. *Computers, Environment and Urban Systems*, 48:1–15.
- [Clark, 1976] Clark, J. H. (1976). Hierarchical geometric models for visible surface algorithms. *Commun. ACM*, 19:547–554.
- [Kolbe, 2009] Kolbe, T. H. (2009). Representing and exchanging 3d city models with citygml. In *Lecture Notes in Geoinformation and Cartography*, page 20. Springer Verlag.
- [Luebke and Erikson, 1997] Luebke, D. and Erikson, C. (1997). View-dependent simplification of arbitrary polygonal environments. In *Proceedings of the 24th annual conference on Computer graphics and interactive techniques*, SIGGRAPH '97, pages 199–208.
- [Luebke et al., 2002] Luebke, D., Watson, B., Cohen, J. D., Reddy, M., and Varshney, A. (2002). *Level of Detail for 3D Graphics*. Elsevier Science Inc., New York, NY, USA.
- [Markosian et al., 1997] Markosian, L., Kowalski, M. A., Goldstein, D., Trychin, S. J., Hughes, J. F., and Bourdev, L. D. (1997). Real-time nonphotorealistic rendering. SIGGRAPH '97, pages 415–420, New York, NY, USA.
- [Müller et al., 2006] Müller, P., Wonka, P., Haegler, S., Ulmer, A., and Van Gool, L. (2006). Procedural modeling of buildings. *ACM Trans. Graph.*, 25:614–623.
- [Parish and Müller, 2001] Parish, Y. I. H. and Müller, P. (2001). Procedural modeling of cities. In *Proceedings of the 28th Annual Conference on Computer Graphics and Interactive Techniques*, pages 301–308. Press.
- [Rodriguez et al., 2012] Rodriguez, D., Besuievsky, G., Patow, G., and Beckers, B. (2012). Procedural models to better compute solar flux at the neighbourhood scale. In *Proceedings of Flow modeling for urban development*.
- [Side-Effects-Software, 2015] Side-Effects-Software (2015). Houdini.

Towards reduced-order modeling of complex phenomena in urban physics

Piotr Breitkopf, Pierre Villon
Laboratoire Roberval, UMR-T337 UTC-CNRS
Universite de Technologie de Compiègne, France

Abstract

Effective use of numerical modeling in the design of complex systems is hindered by the time required to perform the simulations. In the present work, we foster a new computational paradigm coupling simulation, reduced-order modeling and machine-learning to provide tools for decision making for design and optimization. This methodology, based on manifold-learning, finite element and Proper Orthogonal Decomposition has been successfully used in several domains ranging from design of terrestrial/aerospace vehicles, coupled systems optimization and inverse identification. We hope, that it may be extended to the emerging domain of urban systems multiphysical modeling.

1 Introduction

Physical-based modeling of urban systems involves taking into account several disciplines in order to support decision-making process in such domains as urban development, eco-design and optimization. Consider thermal modeling involving solar irradiance, wind, coupled with meteorology, human-generated sources: heating/air conditioning, transportations... Intelligent design requires the multiple-scale of phenomena, from the level of a single building to the level of a district. The latter one may be considered from the scratch within a new project or, more frequently, is highly constrained when improvements of an existing district is considered.

The numerical models are by nature multiphysical. Thermal convection and radiation is coupled with fluid mechanics when considering urban canyons. High-fidelity CFD (Computational Fluid Dynamics) models for such systems are beyond the capacity of current and forthcoming simulation infrastructure. Multi-scale approach allows to consider various levels of simplification ranging from 0D (scalar), through 1D, 2D up to 3D models. Reduced order modeling offers an interesting framework, allowing to generate new simulations from sets of data pre-computed off-line. These data may be then interpreted on-line in a much more interactive manner, compatible with time constraints of a decision-making process. Moreover, the database may be potentially enriched by experimental data coming from real-world measurements.

Such kind of models require three ingredients: simulators, reduction tools and machine learning techniques. In our former work, we have applied these concepts to computational mechanics problems. The overall idea is to use industry standard simulators as black-box solutions according to design of computer experiments allowing for the generation of a series of *snapshots* of the full-scale solution for a predefined set of parameters. Then, Principal Component Analysis is applied to find a reduced-order representation of the database in terms of a set of eigenvectors of the covariance matrix. Finally, *intrinsic dimensionality* is estimated, allowing us to explicitly construct a low-dimensional *shape manifold* embedding of the full-scale solution space.

2 Reduced Order Modeling

2.1 Concept of shape space

Basically, the "solution space" (the vector space in which the solution to the physical problem evolves) is determined by the problem as well as the manner in which the problem is posed. While this concept, as an abstract notion, has been used in the field of Riemannian geometry [8] – there was, at the time the authors began their research, no tangible way to manipulate this solution space in the context of real life problems. To get a tangible description of solution space for a design problem, we first assume a discrete representation of "solution" $\Gamma \in \mathcal{R}^N$, where N is the number of points of discretization of the physical field.

Now let $\mathcal{S} \subset \mathcal{R}^N$ be a set such that any $\Gamma \in \mathcal{S}$ is an *admissible* solution, and any

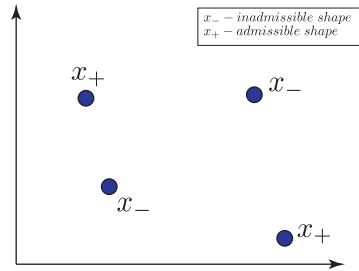


Figure 1: Concept of solution space

solution lying outside \mathcal{S} is an *inadmissible* solution. This means that any possible set of M "admissible" solutions are simply individual elements that have been sampled from \mathcal{S} . In Fig. 1 the admissible and inadmissible solutions are denoted by x_+ and x_- , respectively.

2.2 Hypothesis of the solution manifold

Our fundamental hypothesis [5, 7] has been the existence of a smooth "solution manifold" \mathcal{M} connecting all admissible solution. \mathcal{M} approaches the true "solution space" of the particular problem with increasing N . We call this as the "solution manifold" (Fig. 2). Furthermore, we make the assertion that it is a p -dimensional manifold embedded in \mathcal{R}^N space, where $p \leq N$. This p is the *intrinsic* dimensionality of the design problem.

In summary, the characteristics of the solution manifold are:

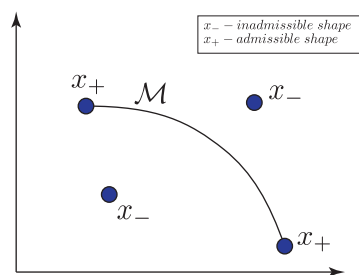


Figure 2: Concept of solution manifold

1. All points on the manifold correspond to admissible solutions.
2. Any point that lies outside the manifold corresponds to a NON admissible solution for the given problem.
3. The manifold approaches the true solution space for a given design problem with increasing dimension.
4. The manifold dimensionality p is the *intrinsic* problem dimensionality.

2.3 Solution interpolation

In the optimization problems we will be looking for an admissible solution that minimizes a given cost function. We thus need to develop a way to interpolate between admissible instances of solution while *staying* in the *solution space* restricted to \mathcal{M} . This means that the interpolation must implicitly satisfy the full set of problem constraints so as to generate solely admissible solution.

The reason for this is that a simple linear combination of two admissible solutions will not

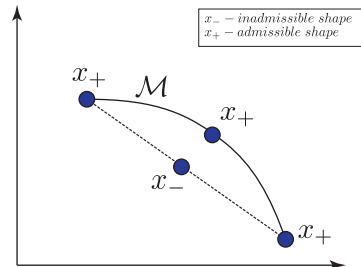


Figure 3: Solution interpolation

necessarily be an admissible solution. This situation is illustrated in Fig. 3, where linear interpolation between two admissible solutions x_+ gives an inadmissible solution x_- , while an interpolation on the manifold \mathcal{M} gives an admissible solution x_+ . This interpolation would in turn give the numerical expression of the manifold in the neighborhood of an admissible solution (say Γ_1).

2.4 Step-by-step manifold construction

According to our fundamental hypothesis, a *global manifold* is defined as a smooth hyper surface that connects *all* the admissible solutions for a given problem in applied mechanics. However, generating this for a large problem would entail heavy off-line simulations for sufficient accuracy, since it is always high-dimensional and nonlinear. The main idea here is to project the desired solution onto the surface of the solution manifold \mathcal{M} *without* explicitly constructing the global manifold.

Therefore, we have proposed an *on-line* approach which constructs only the *useful* portion of \mathcal{M} (local manifold) progressively. Choosing an initial point x^0 (Fig. 4), we generate the

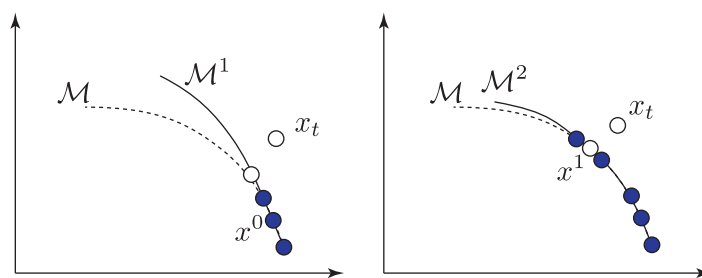


Figure 4: Walking along the solution manifold

local neighborhood of m neighbors (depending on the problem) and approximate the manifold locally around x^0 . We then project the desired shape x_t on this local manifold to get x^1 and the first estimate of the solution. We then generate the local manifold for the new point x^1 and project x_t on this new neighborhood iteratively till convergence.

2.5 Proper Orthogonal Decomposition

Consider a set of M discrete vectors $(\chi^1.. \chi^M)$ corresponding to M *admissible* solutions for a given design problem. We first perform POD directly on $\chi^1.. \chi^M$ by calculating the deviation

matrix D_S for the snapshots $\chi^1.. \chi^M$ where χ_0 is the mean snapshot:

$$D_S = [\chi^1 - \chi_0 \quad \chi^2 - \chi_0 \quad \dots \quad \chi^M - \chi_0] \quad (1)$$

and covariance matrix C_v :

$$C_v = D_S \cdot D_S^T \quad (2)$$

allowing us to express any χ^i in terms of the eigenvectors $\bar{\phi}_j$ of C_v where M is the number of snapshots.

$$\chi^i = \chi_0 + \sum_{j=1}^M \alpha_j^i \bar{\phi}_j \quad (3)$$

and obtain a set of M projection coefficients α_j^i for the i^{th} snapshot individual snapshot χ^i .

2.6 Estimation/detection of dimensionality p

In the great majority of real life problems, we will have an intrinsic dimensionality of $p \geq 3$ thus preventing detection by visual inspection of the shape manifold. In such cases, we turn to statistical methods involving data sets and dimensionality estimation. There are two main classes of methods that may be used to estimate p : the number of non-zero eigenvalues of a covariance matrix for the data set and "near neighbour" methods. In the first group, we have the Fukunaga-Olsen algorithm [2] for a local neighborhood of $b \leq M$ points $\alpha^1.. \alpha^b$ around the design point α^{ev} in α -space. The linear basis matrix P is assembled according to

$$P = \begin{bmatrix} 1 & \alpha_1^1 - \alpha_1^{ev} & \alpha_2^1 - \alpha_2^{ev} & \dots & \alpha_M^1 - \alpha_M^{ev} & \dots \\ \vdots & \vdots & \vdots & \dots & \vdots & \dots \\ 1 & \alpha_1^b - \alpha_1^{ev} & \alpha_2^b - \alpha_2^{ev} & \dots & \alpha_M^b - \alpha_M^{ev} & \dots \end{bmatrix} \quad (4)$$

followed by assembling the moment matrix $A = P^T W P$, where W is the diagonal matrix whose elements correspond to the weighted contributions of the nodes $\alpha_1.. \alpha_b$.

Next, we detect the local rank of the manifold by calculating the singular values of the moment matrix A , this gives us the dimensionality $p \leq M$ which is the rank of A (number of non-zero singular values). While the eigenvalues from $p+1..M$ most theoretically vanish, in practice we will need to establish a threshold value to determine p due to numerical errors. Again, there are several ways to detect p (*e.g.* Pettis "near neighbour" algorithm). One advantage of the LLE approach [3] for manifold learning is purportedly its ability to estimate p as part of the learning approach.

2.7 Local interpolation over a p -dimensional manifold

Now that we have established a p dimensional manifold for the design problem, we can use this to move along the manifold by interpolating between neighboring snapshots, and thus move from a point-set snapshot-based description to a smooth space. This can be achieved by using a local coordinate system $(t_1..t_p, h)$ with the local expression of the manifold given by $h = h(t_1..t_p)$. We may obtain the *natural* co-ordinates $t_1..t_p$ by calculating the eigenvectors of the covariance matrix C_α (centered over the evaluation point α^{ev}) for the local neighborhood:

$$C_\alpha = (1/b) \sum_{i=1}^b (\alpha^i - \alpha^{ev})(\alpha^i - \alpha^{ev})^T \quad (5)$$

giving the local principal directions $\mathbf{v}_1, \mathbf{v}_2.. \mathbf{v}_{p+1}$:

$$(\mathbf{v}_1, \mathbf{v}_2.. \mathbf{v}_p) = \text{eigenvectors}(C_\alpha) \quad (6)$$

followed by projecting the points of the neighborhood onto these principal directions giving:

$$\alpha = \alpha^{cen} + t_1 \mathbf{v}_1 + \dots + t_p \mathbf{v}_p + h(t_1..t_p) \mathbf{v}_{p+1}$$

where α_{cen} is the centroid of the neighborhood in α -space.

At this stage we have the local coordinates $(h, t_1 \dots t_p)$ of the b snapshots in the neighborhood. To move to the continuous description, we need to be able to interpolate between these instances and pass a smooth manifold through these points, or sufficiently close in a minimized weighted-error sense. This can be done in several ways: kriging, cokriging, radial basis functions, moving least squares, etc. We have always stood by the Diffuse Approximation [4] because of the ease and flexibility in using it to perform a local moving least squares fit with an appropriate weighting function for a given number of neighbors (or radius of influence). The Diffuse Approximation is then performed for a general point α^* belonging to this neighborhood (*i.e.* not one of the snapshots) using these b neighboring points to get the local surface $h = \tilde{h}(t_1 \dots t_p)$ using a polynomial basis centered around α^* with weighting w .

The basic idea here is to represent $\tilde{h}(t_1 \dots t_p) = \beta_0 + t_1 \beta_1 + \dots t_p \beta_p$ with $\beta_0 \dots \beta_p$ solution of the Diffuse Approximation problem

$$E(\beta) = \frac{1}{2} \sum_1^b w(t^i, t) (\beta(t^i)^T \mathbf{a} - h(t^i))^2 \quad (7)$$

where $w(t^i, t)$ is the weighting function for the i^{th} neighbor snapshot [1]. For a Gaussian weighting function this could be of the form:

$$w(i) = e^{-c \|t^* - t^i\|^2} \quad (8)$$

where c is a constant to control the weighting factor. This equation gives us $h, t_1 \dots t_p$ where h is height over the centroidal plane for the neighborhood.

The local parametric expression for the α -manifold in this local neighborhood of α^{ev} using p local parameters $t_1 \dots t_p$ is then given as:

$$\alpha_1 = \alpha_1(t_1 \dots t_p), \dots, \alpha_M = \alpha_M(t_1 \dots t_p) \quad (9)$$

meaning that the projection coefficients are controlled locally by p parameters that allow us to move along the tangent plane to the manifold.

We do not specifically *need* truncation of the POD basis, although we do implement it for global manifolds resulting in high numbers of modes, most of them with marginal contribution. In the local manifold approach, as the number of modes is limited by the number of available samples, we favor retaining all the modes, avoiding thus the truncation error commonly associated with the POD method, especially when the POD truncation error does not drop off quickly enough when meta-modeling structural shapes [6].

Also the estimation of p needs a sufficiently close neighborhood as explained in [5], and the number of neighbors b needed depends on the expected value of p and the order of polynomial chosen for the matrix P .

3 Numerical example

Here we employ the presented reduced-order approach in the cope of an optimization problem. An air conditioning duct is parameterized with 7 shape variables. First, a set of simulations is performed according for the test configurations chosen according to Latin Hypercube Sampling. Then, the shape optimization is carried out in order to get the most uniform flow at the output section. The result presented in (Fig. 5) shows the streamlines for such an optimal configuration, obtained with 6 POD modes.

4 Conclusion and prospects

We have presented the conceptual basis and some numerical tools to handle complex problems within a reduced-order modeling framework. These concepts were successfully applied to numerous applications in computational mechanics and the urban physics simulation is promising domain of application.

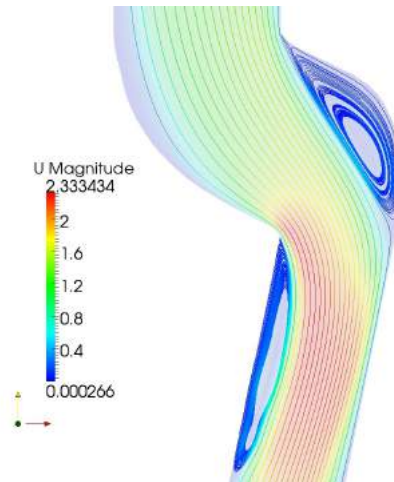


Figure 5: Flow in an optimized duct (6 modes).

References

- [1] P. Breitkopf, A. Rassineux, G. Touzot, and P. Villon. Explicit form and efficient computation of mls shape functions and their derivatives. *International Journal for Numerical Methods In Engineering*, 48(3):451–466, 2000.
- [2] K. Fukunaga and D.R. Olsen. An algorithm for finding intrinsic dimensionality of data. *IEEE Transactions on Computers*, 20:176–183, 1971.
- [3] David Gonzalez, Elias Cueto, and Francisco Chinesta. Computational patient avatars for surgery planning. *Annals of Biomedical Engineering*, pages 1–11, 2015.
- [4] B. Nayroles, G. Touzot, and P. Villon. Generalizing the finite element method: diffuse approximation and diffuse elements. *Computational Mechanics*, 10(5):307–318, 1992.
- [5] B. Raghavan, P. Breitkopf, Y. Tourbier, and P. Villon. Towards a space reduction approach for structural shape optimization. *Structural & Multidisciplinary Optimization*, 2013.
- [6] B. Raghavan, P. Breitkopf, and P. Villon. Pod-morphing: an a posteriori reparametrization approach for shape optimization. *European Journal of Computational Mechanics*, 19(5-7):671–697, 2010.
- [7] B. Raghavan, L. Xia, P. Breitkopf, A. Rassineux, and P. Villon. Towards simultaneous reduction of both input and output spaces for interactive simulation-based structural design. *Computer Methods in Applied Mechanics and Engineering*, 2013.
- [8] V. Schulz. A riemannian view on shape optimization. *Foundations of Computational Mathematics*, 2012.

Energy Strategies towards a Fully Sustainable Galapagos Archipelago

Pedro Calle¹, Siebe Broersma²,

¹ Technical University of Delft
Julianalaan 134, NL-2628 BL Delft, the Netherlands
soroche@lycos.com

² Technical University of Delft
Julianalaan 134, NL-2628 BL Delft, the Netherlands
S.Broersma@tudelft.nl

Keywords: Energy Potential Mapping, Galapagos Archipelago, New Stepped Strategy, Sustainable Energy Matrix, bottom-up approach, Self-sufficient Island.

Abstract. *An average inhabitant of the Galapagos consumes a fifth of the energy of an English citizen, therefore one could state that this is a very sustainable community; however, the inhabitants live under poor conditions. Bad energy, water and waste management, together with increasing tourism have led the most preserved archipelago of the world into an endangered natural ecosystem. As a response, the government of Ecuador presented an energy master plan that replaces the fossil fuel matrix with imported biofuels while leaving the production pattern unchanged. This research is based on the starting point that the uniqueness of this environment requires and offers more possibilities for smarter local interventions.*

Its focus lies on an integral energy system based on different local energy strategies applied to the Island of Santa Cruz and can serve as the core of sustainable development of the entire archipelago. First an energy study has been executed mapping local demands and sustainable potentials. Next, The New Stepped Strategy has been applied to identify suitable sustainable energy interventions that ensure more community participation based on the reduction of the demand, the use of waste as energy, and a sustainable energy production.

It was discovered that 55% of the energy demand of the Island could be reduced, and half of the remaining demand could be supplied by waste streams of biomass converted into energy and the other half by renewable energy production. These strategies served as basis to create sets of interventions based on governmental and community initiatives that led to a sustainable energy master plan that improves and solves energy, waste and water management.

This research clearly shows how a sustainable energy master plan that considers waste as energy can solve environmental threats and improve living conditions. Furthermore these strategies could be repeated and adapted to other islands.

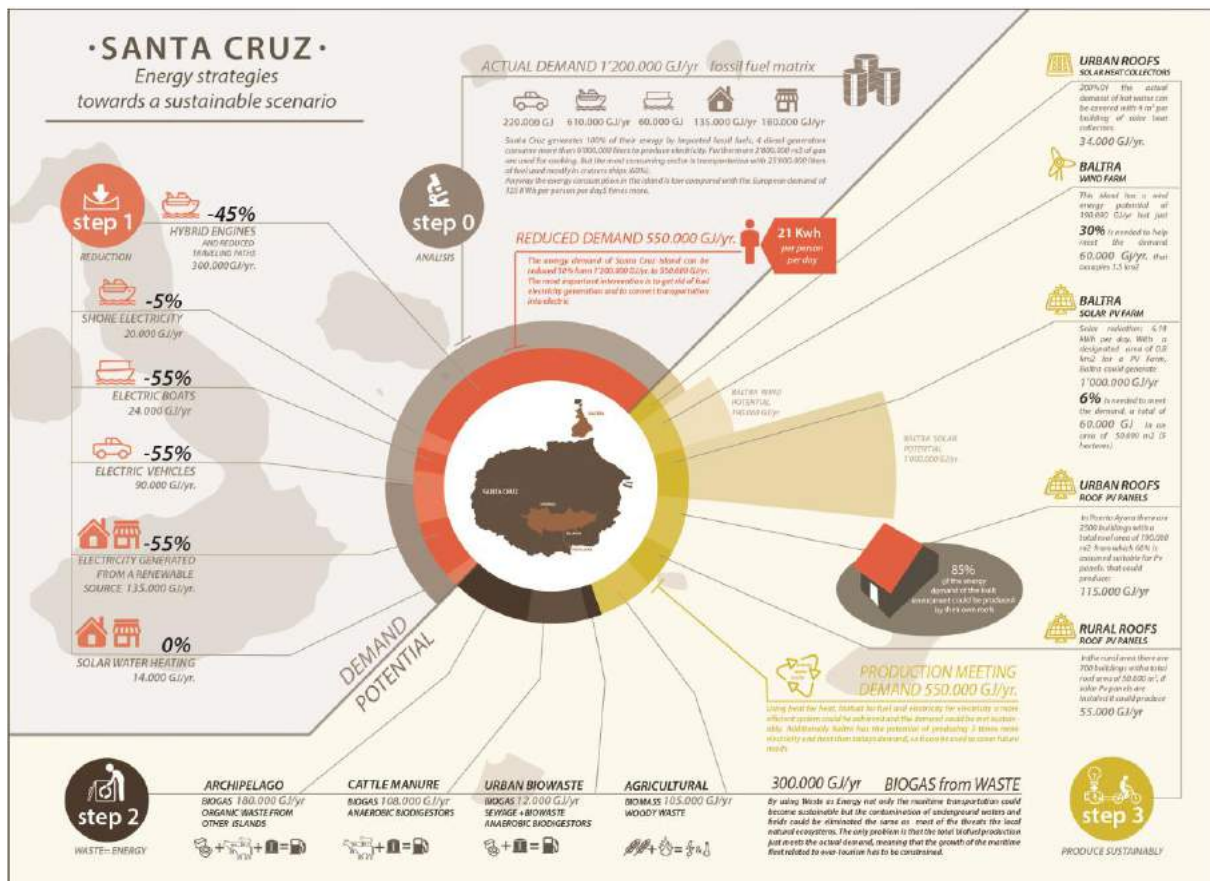


Fig 1: Sustainable Energy Master Plan for Santa Cruz Island. A “Combined Approach Scenario”. This graph shows how energy balance could be achieved by a set of interventions made by collaboration between the government and citizens. Step 0: actual demand; Step 1: reduction strategies of the demand by interventions in each sector (total of -50%); Step 2: the use of urban and agricultural waste as biomass or biofuel for energy production (covering 50 % of the reduced demand); Step 3: the production of energy from renewable (covering remaining demand).

1 Introduction

Islands are especially vulnerable to environmental change, because they have extremely limited resources. In terms of energy, they depend heavily on imported fuels [UNDP 2012]. Therefore, evolving islands into green and self-sufficient ecosystems provides very specific challenges. Several projects in developed countries have shown that this can be done. Example is the island of Tokelau [Powersmart. 2012] in the Pacific Ocean, which has changed its entire energy matrix into renewables.

The Galapagos is known as the most preserved archipelago of the world. It is a living lab of evolution and an iconic piece of natural heritage. Many species living in the archipelago cannot be found anywhere else in the world. However, this unique range of endemic species of flora and fauna is threatened by the unsustainable way of living of local communities and the growing tourism [DPNG 2013]. Thus, the situation on the Galapagos requires urgent attention. The isolation of the archipelago offers the opportunity to develop a system that demonstrates that nature and humans can live in harmony.

Unfortunately, the current efforts of the local government towards sustainability are lacking consistency. Big projects with low effectiveness are executed in a patriarchal way, using a universal solution for various endemic problems. The situation of the Galapagos

requires a specific approach and the participation of the community [Municipality of Santa Cruz. 2014].

This research project creates an integral energy plan for Santa Cruz, the most densely populated island of the Galapagos, which can serve as a model for the sustainable development of the other islands. This plan is based on an energy study that maps the demands and potentials of the island. “The New Stepped Strategy” towards sustainable design [Dobbelsteen. 2009] is introduced to develop two different scenarios: Top-down and bottom-up. The final energy plan combines those two scenarios, ensuring that it is both self-sufficient and feasible.

2 Energy Study

A diagnostic study is the starting point of this research. The demand of Santa Cruz Island regarding energy, waste and water and the potential energy production from renewable resources have been measured, quantified and compared.

In order to compare and quantify all the energy demands and potentials, the Joule is used as the measuring unit in a year based time period.

2.1 Energy Demand

Today more than 25.000 people live in the Galapagos, compared with a few hundred inhabitants 40 years ago. Also, more than 180.000 tourists visit every year. Up until 2007] all the energy provided to the islands was generated by fossil fuel; transportation, houses, hotels and even tap water relied on fuel to work. Because the islands have no oil production of their own, all fossil fuel is imported, creating a huge dependency on the main land.

The study is divided into three main sectors, namely transportation, residential and non-residential, with the following outcomes:

- Transportation consumption: 900.000 GJ/yr., of which 75% are used by cruiser-ships and tourist related vehicles.

- Residential consumption: 82.000GJ/yr., which is extremely low compared to European standards, a fifth of an average English household (almost no heating or cooling are used).

- Non-residential consumption: 92.000 GJ/yr., related to tourism, business and industry.

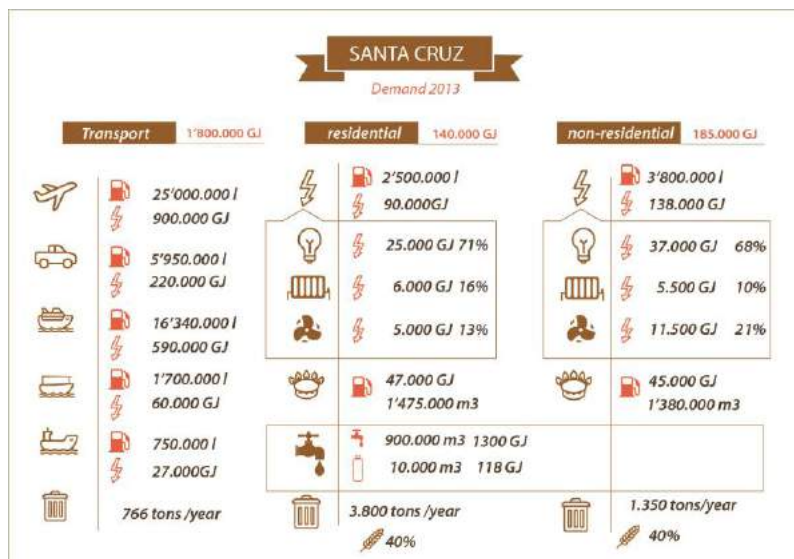


Fig 2: Energy demand chart 2013

2.2 Energy Potential

The method of energy potential mapping (EPM) analyses the spatial plans of land based on the energy production techniques that can be used.

For this study six different renewable energy sources were analyzed that can be utilized in this island: Solar photovoltaic, solar thermal, wind, geothermal, tidal and biomass. Three main areas in Santa Cruz Island, which are not part of the national park Baltra Island, an agricultural zone in the high lands and the urban areas, represent the only potential places available to generate renewable energy without big environmental impact. These areas have already been occupied and affected by inhabitants. Therefore, they are considered human lands even though birds, reptiles and other species are still frequently present in these lands.

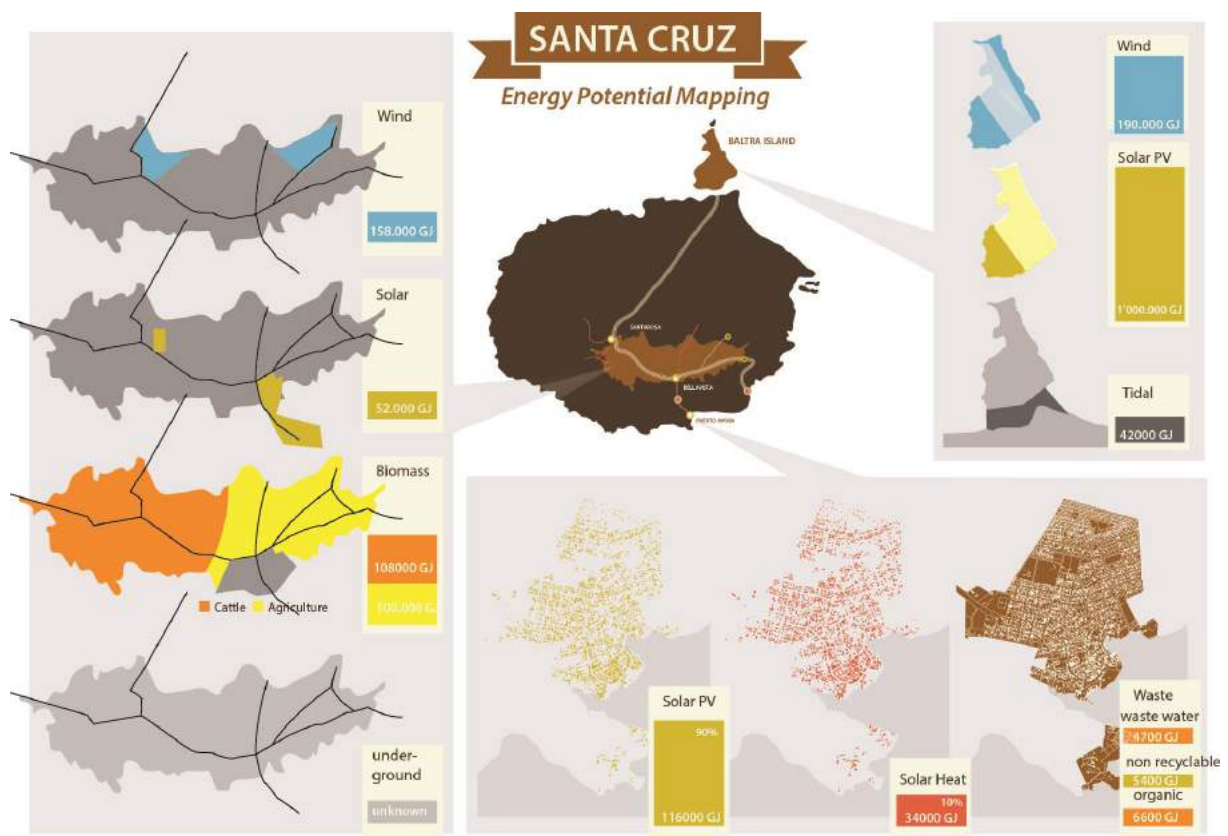


Fig 3: Layered energy potential mapping of the three areas of intervention non-part of the national park.

2.3 New Stepped Strategy

The "New Stepped Strategy" was implemented in order to improve sustainably Santa Cruz's energy balance. This strategy follows three steps:

-The "Reduction" of energy, water and waste demand. After a process of filtering layers of interventions (fig. 4) the demand drops from 1'200.000 GJ/yr. to 565.000 GJ/yr., which is a reduction of more than 50%; this is a big step towards sustainability.

-The "Reuse" of waste streams as energy supply (waste = food). Waste has an important potential that is being dismissed in the Galapagos. By reusing this waste from urban and rural areas, 225.000 GJ per year could be generated from biogas or biomass combustion.

-The "Production of renewables" potentially could supply 1.720.000 GJ per year, which is more than enough to satisfy the demand of the island. The importance of running the first two previous steps allows a minimized production of just 300.000 GJ, which in turn reduce dramatically the necessary energy, space and fiscal investment.

3 Sustainable Scenarios

After running the EPM a new energy scope appeared with a reduced demand and local production potentials. This outcome has been used to create and compare five scenarios which explore different approaches to achieve an energy balance in Santa Cruz Island.

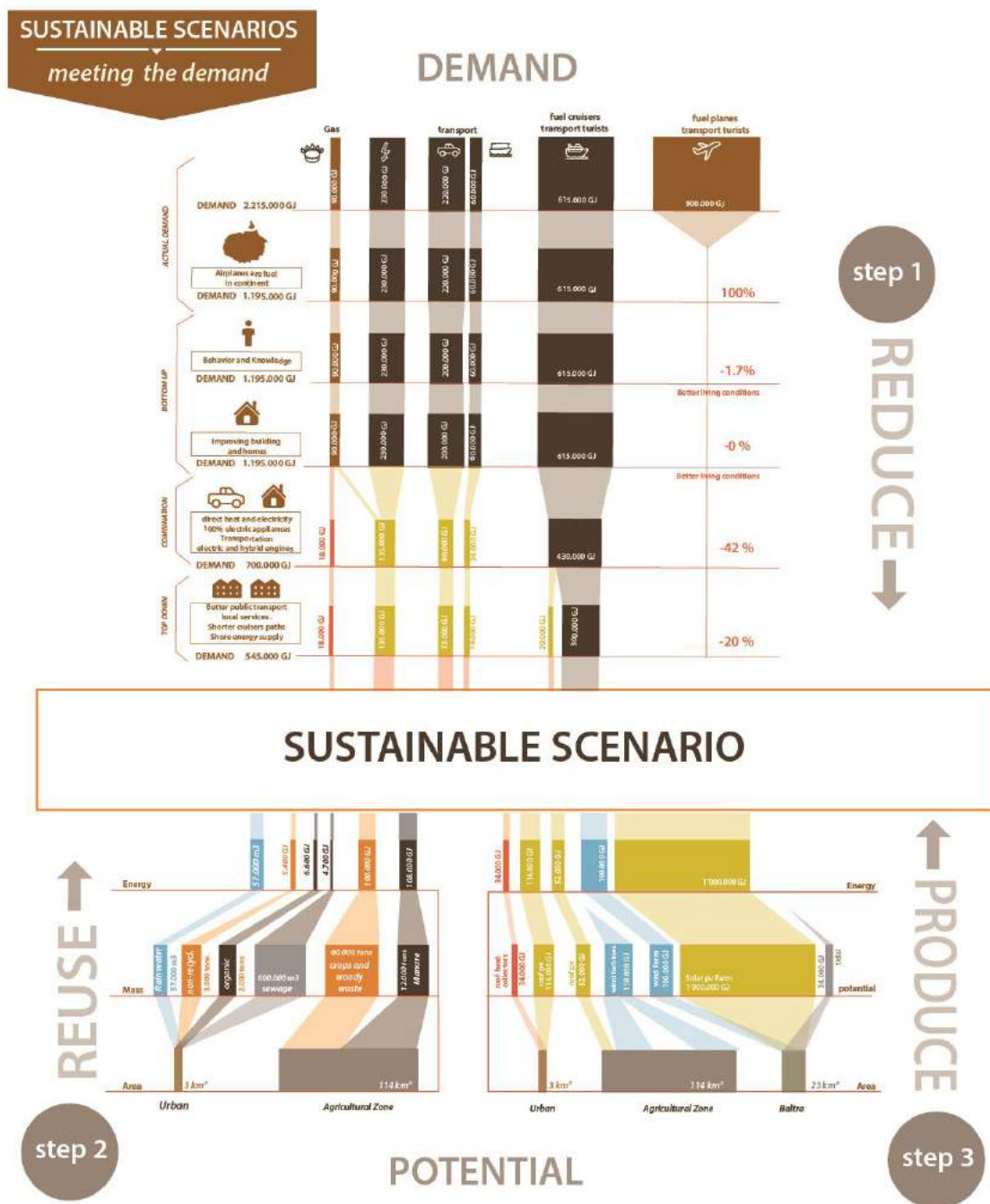


Fig 4: The New Stepped Strategy applied in the EPM leading to a sustainable scenario.

3.1 Top-down Scenario Government Plan

From The Government also called Top down, a centralized core of actions that are easy to control and run. This scenario represents the actual governmental approach over the new scope of demand. A small wind farm in combination with a huge load of imported biofuel and fossil fuel would satisfy the energy demand. This is the cheapest and most simple way of eliminating fossil fuels in the Island. However the risk of fuel spills stays the same, as does the contamination in air and water. In the long term this scenario based on bio fuel is not sustainable, since the amount of biofuel that has to be produced competes directly with food production. Next to that, only a small part of the energy potential of the island is used, so energy is being wasted.

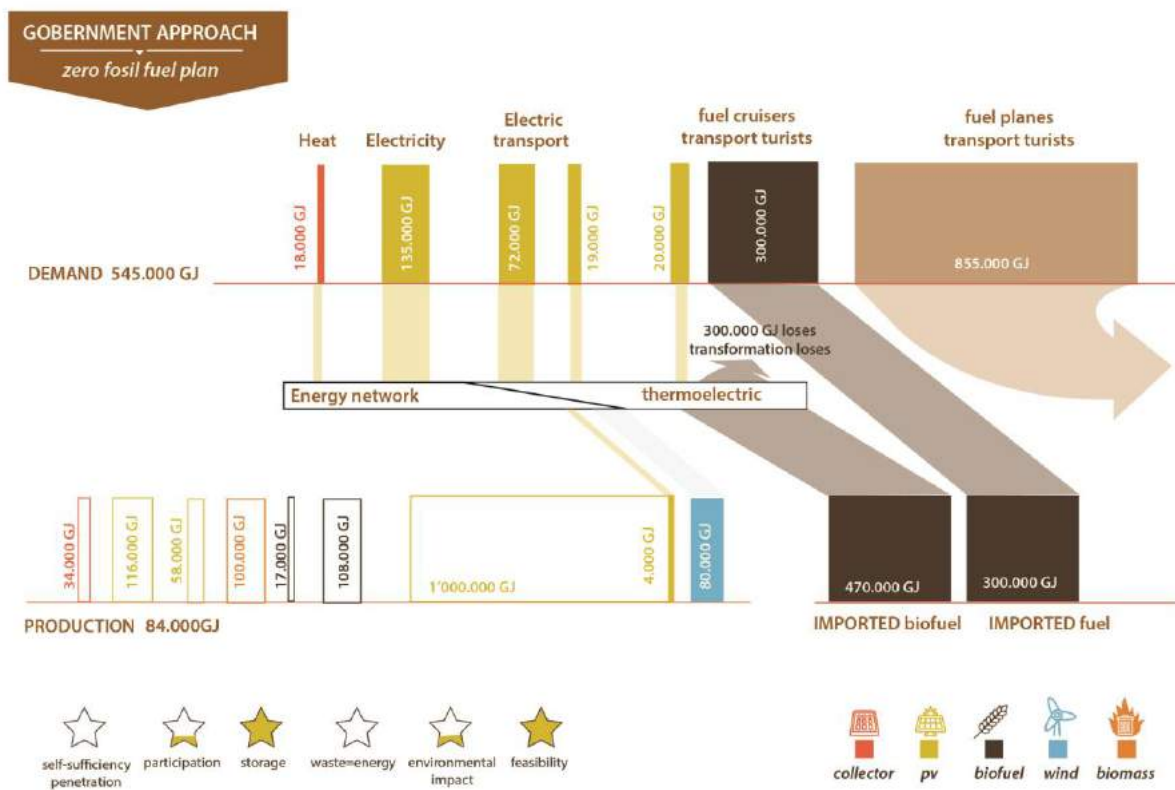


Fig 5: Actual Government’s plan applied to the EPM

3.2 Top-down Scenario, solar plus wind.

This Scenario adds a big solar photovoltaic farm to the government’s approach, so all electrical demand can directly be satisfied with renewables. In this case, the imported biofuel demand is reduced, but still needed for the maritime fleet. The incorporation of solar energy as the main renewable source is a good step towards sustainability but the requirements of energy storage, the risks of imported biofuels and the ignored waste potential as energy creates a scenario far from sustainable.

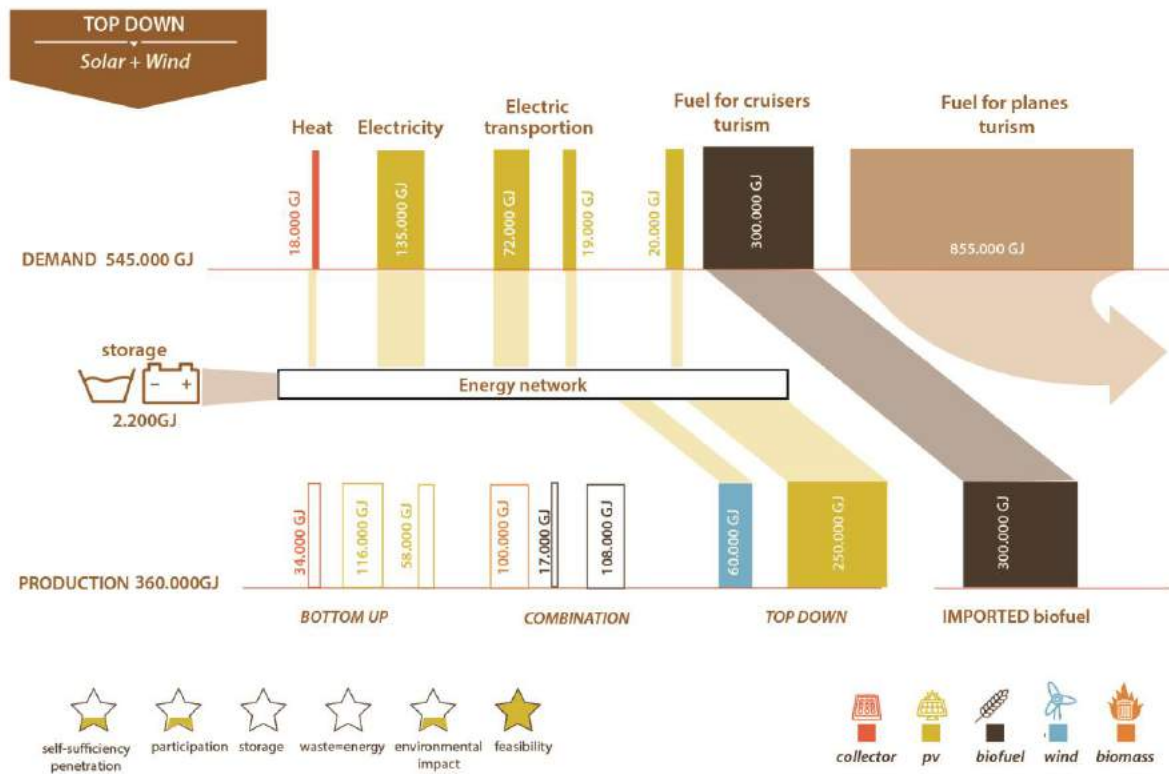


Fig 6: Top-Down approach Scenario, solar plus wind.

3.3 Bottom-up Approach Scenario

From the people, the user, also called Bottom-up, were decentralized actions, interventions or initiatives come from the mass and the public sector creating in this case the inclusion of the inhabitants into the energy matrix as producers. This scenario shows clearly a bigger and more diverse energy input which is generated by solar panels on building roofs, the use of urban and rural waste and the incorporation of the inhabited islands into the biofuel production.

This scenario starts using the over production of bio-waste from other islands to add up to the grid so the imported biofuels disappear, a big step towards self-sufficiency. The only problem is that the production just reaches balance, and without any backup, this creates a weak system.

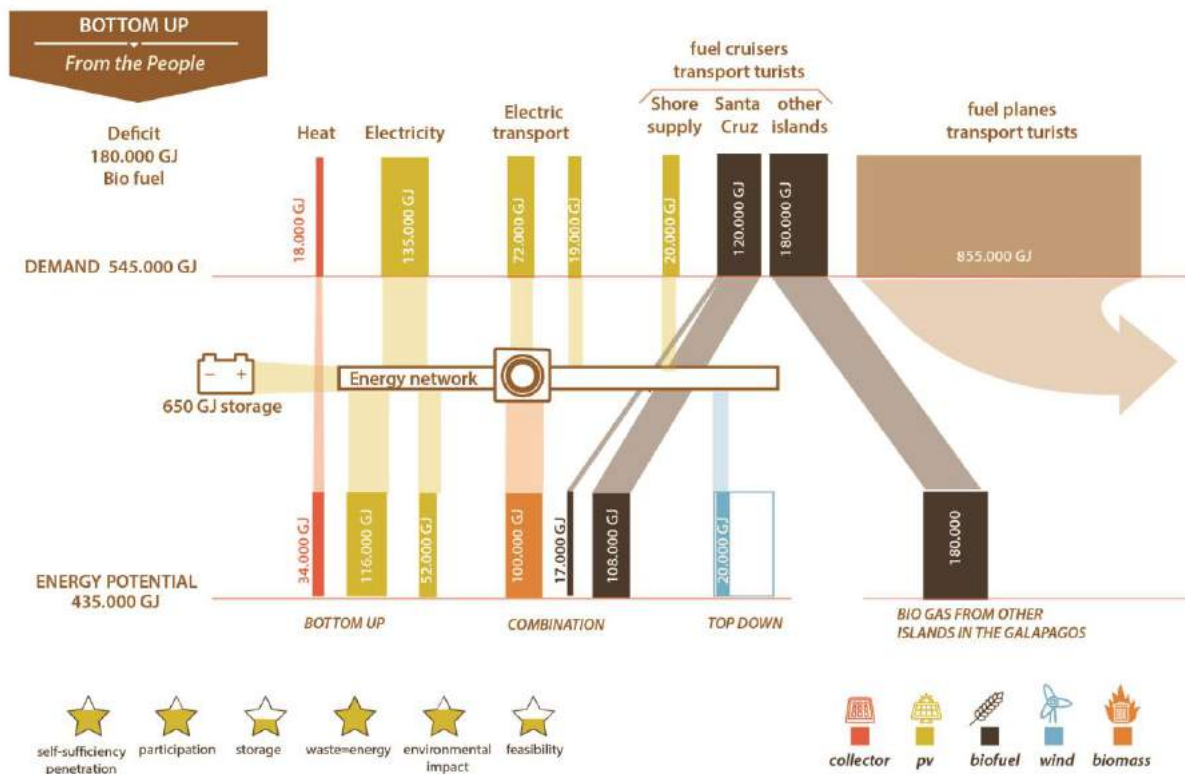


Fig 7: Bottom-up Scenario applied to the EPM.

3.4 Combination Approach Scenario

By combining the best qualities of the previous scenarios a new fused approach appears, where people and government participate as a team. In this case the participation of the public sector remains as the core energy generation, but the government also executes projects to support and sum up into the grid, allowing reducing energy storage and creating a much more diverse energy system which creates a more stable grid. However the entire archipelago needs to collaborate in the production of biogas to satisfy the cruisers demand, which seems reasonable since the cruisers travel around most of the island and can reload gas in very port.

A bottom-up approach supported by the government clearly reaches the goal of a sustainable island based on renewable energy and even achieves energy self-sufficiency. But more important requires that rest of the populated islands follows the same steps generating a fully sustainable archipelago.

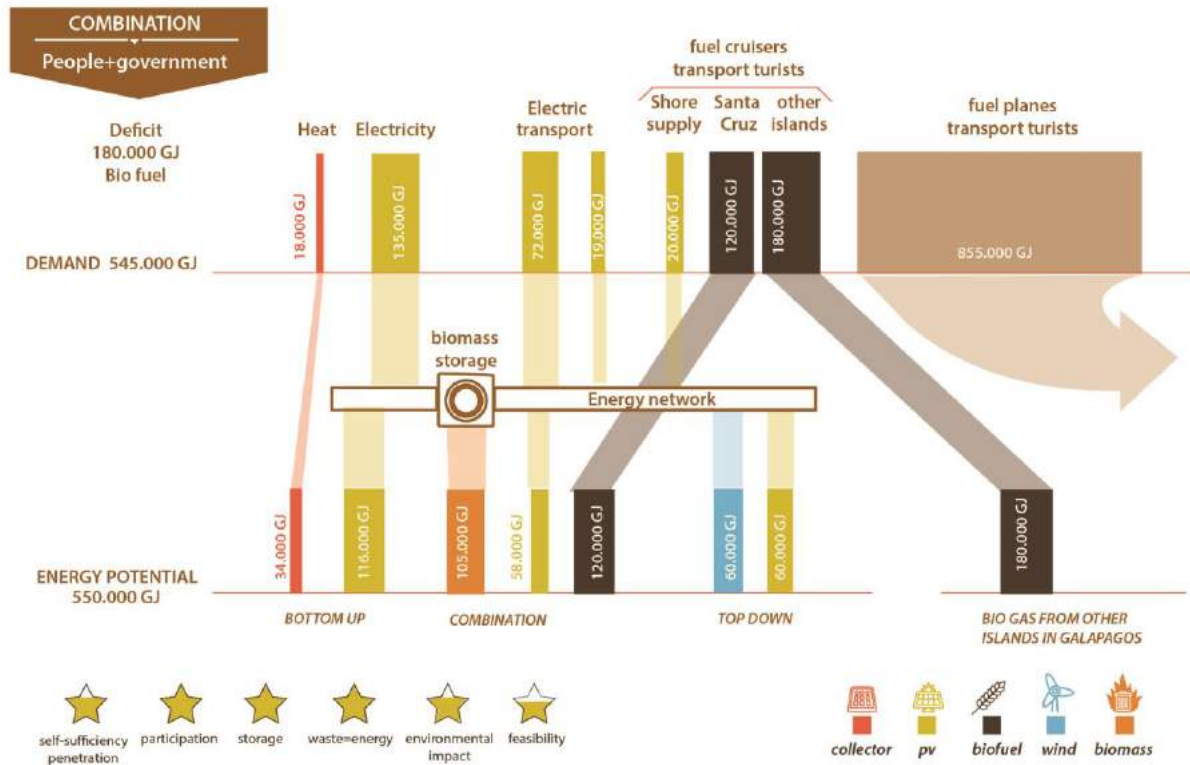


Fig 8: Combined Scenario applied to the EPM.

3.5 Ultimate Self-sufficiency Scenario

This scenario shows how Santa Cruz can reach energy self-sufficiency without the input of the rest of the archipelago. Based on “Power to Gas” technology [California Hydrogen Business Council. 2015] and the high potential of solar energy this island could produce enough natural gas with electricity to supply the entire cruises fleet fuel demand.

This scenario requires technology that is under development and has not yet been implemented on this scale, so it seems unfeasible but could be used in a near future.

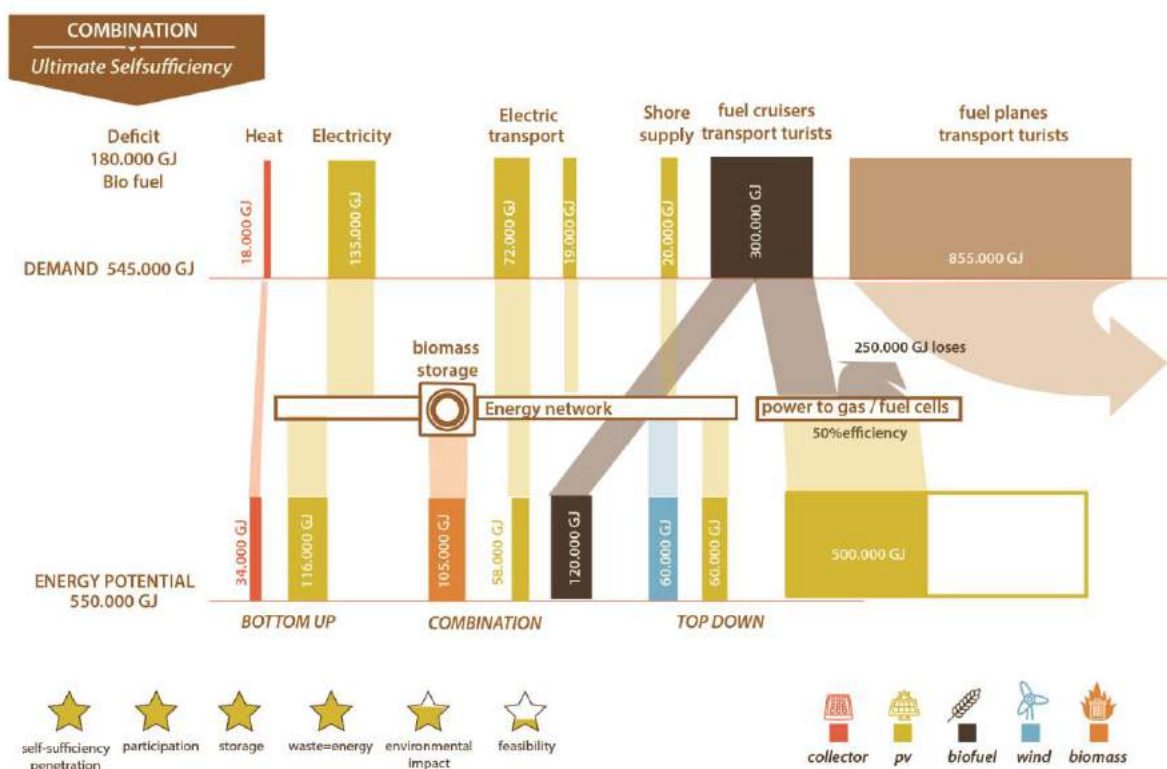


Fig 9: Ultimate Scenario applied after the EPM.

4 Conclusions

- A self-sufficient energy plan is developed for Santa Cruz, the most densely populated island of the Galapagos. This energy plan is based on reduction, reuse and production of energy. First of all, the energy demand can be reduced by 50%. The burden of ships on the energy demand is noteworthy (about 60%), mostly caused by tourism. With regard to the production of energy, using waste cycles is very beneficial: It can generate 50% of the energy demand. The remaining energy demand can be met with renewable energy. There are a lot of potentials for the production of renewable energy. The most outstanding example is solar energy, since the island is on the equator. However, it is important to keep in mind that such energy production is expensive.
- Using the New Stepped Strategy, a top-down and bottom-up scenario was developed. The top-down strategy refers to governmental interventions. These are mostly massive interventions that are aimed at the production of green energy. These interventions could be implemented without the support of any other parties, making it a highly feasible scenario. However, there is a medium environmental impact, mostly because the land that is required for the production of energy (f.e. for a windmill park or solar panels). The bottom-up scenario is based on the participation and investment of people. Reducing and recycling are more central to this scenario. Especially the use of waste cycles makes this scenario more sustainable. An additional advantage is that it helps to get rid of waste, which is problematic for an island like Santa Cruz. This decreases waste contamination threats. The production of energy is also incorporated in the bottom-up scenario, albeit in a less massive way than in the top-down scenario (f.e., solar panels could be placed on

roofs of existing houses). Papers should be written following the format of the Latex or Word macros for submission that can be found at the conference website.

- The master plan is a bottom-up approach, supported by the government. By applying this energy plan, Santa Cruz can become a self-sufficient island. A diverse system is created that relies on different sources and in that way achieves grid stability. However, this also implicates more interventions and a more complex system to manage. Governmental support is required to make the energy plan feasible. For example, the government plays a key role in offering the right incentives to the inhabitants of the island to participate in the reduction of energy demand and the reuse and production of energy.
- This research clearly shows how and why the government can apply the new stepped strategy to their energy master plan in order to be more consistent in their intentions to turn the Galapagos into a zero fossil fuel archipelago. Also, it shows that it is essential to include the inhabitants into the energy plan, because this makes sustainable interventions possible, particularly the inclusion of waste cycles in the energy plan and the reduction of demand.
- Although an energy plan is designed and proposed that succeeds in making Santa Cruz a self-sufficient island, there are some lasting concerns for the future. First of all, the impact of ships on the energy demand has already been pointed out. The growing tourism will only enlarge this problem in the future. At this moment, it is not possible to power ships with renewable sources. Without new technologies that can eliminate fossil fuels from ships, the only way to control the energy demand, is by imposing restrictions on tourism. This is a complex issue, since tourism is also the primary source of income for the inhabitants of the Galapagos. However, finding a balance between environmental and economic concerns seems to be essential for the preservation of this unique archipelago.

References

- [UNDP 2014]. United Nations Development Programme, Stanislav Saling, *Reducing dependence on fossil fuels essential for progress in SIDS*, UNDP New York, 2014.
- [Dobbelsteen 2012] Andy Van den Dobbelsteen, S. Broersma., B. Geldermans. *Energy Neutral Design. Energy Neutral Design step3: Generating Renewable Energy*. TuDelft, 2012
- [Lysen 1996] Lysen, E., *The Trias Energica: Solar Energy Strategies for Developing Countries*, 1996.
- [Mackay 2009]. Mackay, D. J. SEWTHA (pp. 300), 2009. Retrieved from www.withouthotair.com,
- [Powersmart 2012]. Powersmart. "TOKELAU - 100% SOLAR POWERED", 2012, Retrieved 14 April, 2014, from http://powersmartsolar.co.nz/our_projects
- [G.M.S.C. 2015]. Gobierno de la Municipalidad de Santa cruz, *Plan de Desarrollo y Ordenamiento Territorial del Cantón Santa Cruz 2014-2025*, 2015
- [DPNG 2013] DPNG, CGREG, FCD y GC. *Informe Galapagos 2011-2012*, Puerto Ayora, Ecuador, 2013.
- [California Hydrogen Business Council. 2015]. Power-to-Gas: The Case for Hydrogen, California Hydrogen Business Council, October 8, 2015. Retrieved from <https://californiahydrogen.org/sites/default/files/CHBC%20Hydrogen%20Energy%20Storage%20White%20Paper%20FINAL.pdf>

AN ELECTRIFYING CHANGE: THE NEED TO INTRODUCE ELECTRIC VEHICLES IN ECUADOR, AND ITS POTENTIAL IMPACT ON THE ENERGY SECTOR

Davis, M.J.M.^{1,2}

¹Pontificia Universidad Católica del Ecuador (PUCE), Facultad de Arquitectura, Diseño y Artes (FADA), Av. 12 de Oct 1976 y Roca, Pichincha, Quito, Ecuador, mdavis930@puce.edu.ec

²Evolution Engineering, Design and Energy Systems Ltd., 5 Silver Terrace, Exeter, Devon, UK, davismaks@evolutionecoengine.com

Keywords: Transport, Urban Planning, Renewable Energies, Hydropower, Ecuador.

***Abstract.** Private cars are turning electric, with a global increase of 50% between 2013 and 2014. Additionally, Ecuador stands to greatly benefit from a move away from fossil fuels to electric transport. Transport makes up 49% of the national annual energy demand, the fuel for which needs to be imported into the country and is then heavily subsidized. This paper sets out to quantify the potential electricity demand that would be generated from a mass conversion to electric vehicles. Wind and solar power are then compared with hydropower potential to meet this demand. It is found that wind and solar are competitive with hydropower, but where large areas of between 1.24% to 2.51% of the Ecuador's total territory would be required. Finally, the need is recognized to drastically reduce the potential energy demand from electric cars, by decreasing the number of private vehicles on the road in favor for electric public transport systems.*

1 INTRODUCTION

The World Energy Outlook of 2015 highlighted the recent boom in the electric vehicle (EV) market, with a 50% increase in light-duty passenger electric vehicles between 2013 and 2014 (IEA, 2015). This in turn has implications for the national installed electricity production capacity. For example Tran, Banister, Bishop and McCulloch (2012) highlighted the potential need to install between 2 to 18 GW from 2030 to 2050 in the UK, given the EV market shares envisaged. They added that the global electricity demand could rise from 142 to 580 Mtoe from 2035 to 2050, due to the introduction of electric vehicles into the mainstream automotive markets. This is then related to the potential increase or decrease in CO₂ emissions, which is directly linked to the CO₂ intensity of the electricity sector. In China and India for example, it was shown that mass electric vehicles could in fact lead to higher CO₂ emissions overall, due to the manner in which the electricity is produced (Doucette & McCulloch, 2011).

Ecuador presents an interesting case study. On the one hand it is a country whose economy relies on oil extraction and export, where crude petroleum makes up some 55% of the total products exported (Simoes, Hidalgo & Landry, 2014). On the other hand, Ecuador is currently unable to refine its crude oil to the amount of diesel and gasoline needed, in order to satisfy the demand from the transport sector. To make matters worse, the refined oil used by transport is heavily subsidized. In the most recent National Energy Balance published by the Ministry of the Coordination of Strategic Sectors (MCSE, 2014), it was shown that transport makes up 49% of national energy demands (Figure 1). It was also shown that 64% of diesel and 59% gasoline is imported from abroad. The Ministry of Finance then tells us how in their planning for the period of 2015 to 2018, subsidies of fossil fuels account for an expenditure of 3,494.84 million USD. This figure represents 3% of Ecuador's GDP (World Bank, 2014). As such, it can be concluded that Ecuador exports the raw material of crude oil, then imports practically all the refined gasoline and diesel it needs to satisfy its main energy demand of transport, then subsidizes this heavily. Overall, it is therefore of national interest for the country to drastically reduce the energy demand for fossil fuels from its transport sector. Furthermore, the country is pushing towards being a hydroelectric powerhouse of the region. In 2013 Ecuador produced 46% of its electricity from hydropower plants (MCSE, 2014). By the end of 2016 it aims to increase this to 93%, by which time a series of hydropower plants will be brought online (CONELEC, 2013).

Therefore, with expensive imports and subsidies in place, in addition to 49% of national demand from the transport sector, as well as with a large hydroelectric infrastructure providing cheap electricity production, it could be said to be of interest for Ecuador to change from fossil fuel transport to electric vehicles. This was reflected in the news in 2015 that the government planned to import up to 15,000 electric vehicles (Jaramillo, 2015), which would not have any import taxes imposed on them (El Universo, 2015).

This paper sets out to assess the theoretical demand from a mass, national conversion from fossil fuel to electric cars. It does not examine to what extent the use of cars might increase or decrease, nor the role of public transport systems. Whilst this is recognized as a limitation, it is nevertheless felt that by showing the electricity demand that would need to be met, new fields of study are opened into a) how to meet such a demand, and b) strategies to reduce the dependency on travel by car.

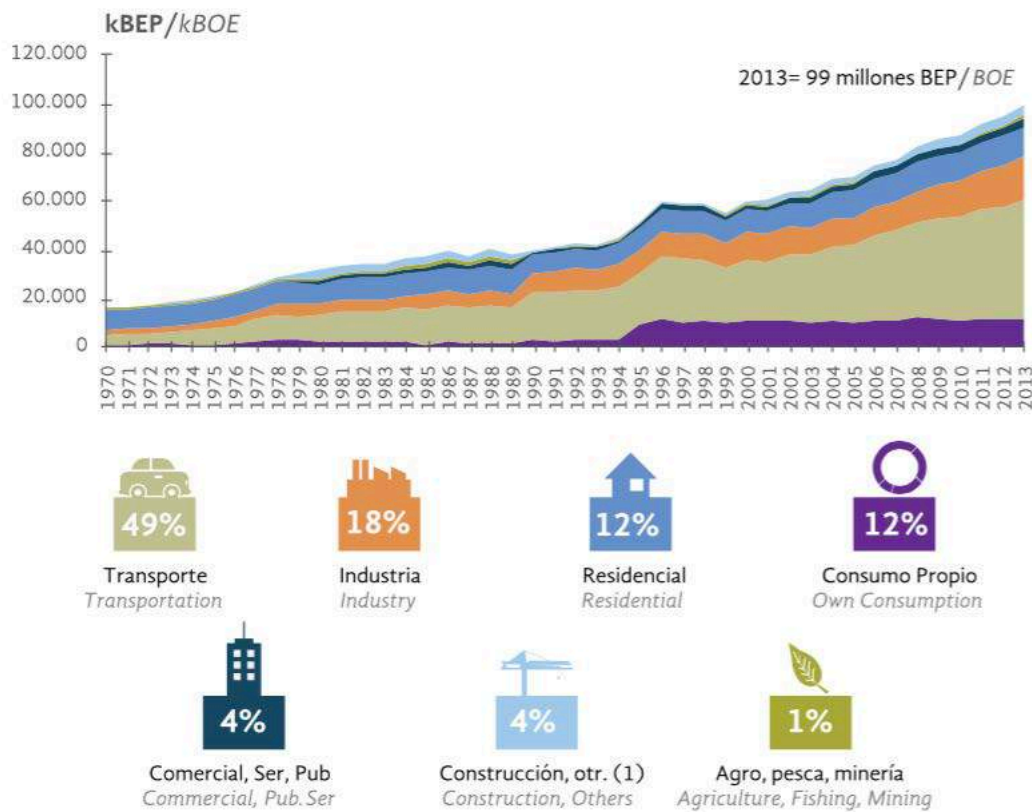


Figure 1. Energy demands in Ecuador by Sector (MCSE, 2014)

2 METHODOLOGY

The paper begins with quantifying the potential electricity demand that would be generated from a mass conversion to electric vehicles. It then goes on to compare this with the electricity generation capacity of Ecuador. This is then followed up by a series of possible scenarios using solar and wind power, after which a brief cost comparison is carried out.

3 CHANGING TO ELECTRIC VEHICLES

In this section a study is carried out to attempt to quantify the electricity demand from the mass conversion of fossil fuel cars to electric vehicles. This is first done through a consideration of the efficiency gains between an internal combustion engine and electric motor. This is then followed up by an analysis of the electricity demands given the MPGe of electric cars, coupled with the overall distances travelled by automobiles in Ecuador.

3.1 Total demand through efficiency gains

Let us consider three types of automobile, which cover the spectrum of small cars, medium size cars and SUV's. The research draws on a small car from Chevrolet, a medium size car from Ford and an SUV from Kia. The examples have been chosen where the car models are commercially available in either a gasoline or fully electric version. For the efficiency comparison, 1 gallon of gasoline has been taken as 33.7 kWh. The data for the MPG and MPGe was taken from the official U.S. government source for fuel economy information for cars of 2016 (fuel economy.gov, 2016).

	Fossil fuel vehicle (MPG)	Electric vehicle (MPGe)	Times more efficient
Chevrolet Spark (1.4l automatic vs. electric)			
City	31	128	4.13
Highway	41	109	2.66
Ford focus (2.0l vs. electric)			
City	26	110	4.23
Highway	38	99	2.61
Kia Soul (2.0l automatic vs. electric)			
City	24	120	5.00
Highway	31	92	2.97

Table 1: Efficiency gains for small, medium and SUV car types for fossil fuel vs. electric

From Table 1 the following scenarios can be deduced for the efficiency gains from changing from a gasoline to an electric car:

- Overall best case = 5 times more efficient.
- Overall worst case = 2.61 times more efficient.
- Overall average case = 3.6 times more efficient.

The next step is to assess how much the energy demand for transport would be reduced if this change were made. In 2013 the overall energy consumption of the transportation sector was 49 million BOE, 16% of which was due to cars and jeeps (MCSE, 2014). Given that the ratio between BOE and kWh is 1:1,628.2, this gives a total of 12,765,088,000 kWh for cars and jeeps in 2013. In terms of the energy efficiency gains outlined above, this would give total prospective annual electricity demands of:

- Overall best case (5 times more efficient) = 2,553,017,600 kWh/year (80% reduction).
- Overall worst case (2.61 times more efficient) = 4,890,838,314 kWh/year (62% reduction).
- Overall average case (3.6 times more efficient) = 3,545,857,778 kWh/year (72% reduction).

3.2 Total demand through mileage

Another way to determine the predicted energy demands from a mass change to electric cars is by considering the total mileage driven. By considering the data from Table 1, let the following scenarios for MPGe be assumed:

- Overall best case = 128 MPGe.
- Overall worst case = 92 MPGe.
- Overall average case = 109.7 MPGe.

The National Institute of Statistics and Census Data of Ecuador (INEC) tells us the number of automobiles in circulation to be 795,711 (INEC, 2014). This can then be coupled with the total mileage data from Cevallos (2015), which tells us 21,176 km are driven per year per

automobile. As such, it can be concluded that a total of 10,470,086,522 miles are driven annually for all the cars in circulation in Ecuador. For the electricity demands, it is once again assumed that one gallon equivalent is equal to 33.7 kWh. Overall, the electricity demands are shown in Table 2.

Scenario	Total Gallons (equivalent)/year	Total kWh/year
Best case (128 MPGe)	81,797,550.95	2,756,577,467
Worst case (92 MPGe)	113,805,288.30	3,835,238,215
Average Case (109.7 MPGe)	95,442,903.57	3,216,425,850

Table 2: Total electricity demands through mileage travelled

In terms of reduction in energy demands, this would give the values of:

- Overall best case = 78% reduction.
- Overall worst case = 70% reduction.
- Overall average case = 75% reduction.

Given the differences between the two methodologies, it is clear that a more in-depth study needs to be carried out. It is suggested that for now the overall worst case scenario is adopted, where there is a 62% reduction in demand, and 4,890.84 GWh/year would need to be produced.

3.3 The impact on the Ecuadorian national electricity production capacity

As mentioned in Section 1, Ecuador is currently undergoing a transition in the energy sector where it aims to have 93% of its electricity produced from hydroelectric plants by the end of 2016 (CONELEC, 2013). According the MSCE (2014) in 2013 Ecuador produced a total of 23,923 GWh electricity, of which 11,004.58 GWh (46%) came from hydraulic plants and 291.86 GWh (1.22%) from renewables.

In the worst-case scenario depicted in Section 3.2, 4,890.84 GWh electricity would need to be produced annually. This would represent 44.4% of current hydropower, or require an 18-fold increase in renewable energy production.

The demand could also be met through an increase in fossil fuel plant capacity, but in this paper it is argued to not be recommendable. It would increase Ecuador's dependence on imported fossil fuels, as most processed oil is currently imported from abroad (MSCE, 2014). It would also counteract gains in reduction of Carbon Dioxide emissions. This has been shown in scenario planning studies for electric vehicles in China, where the CO₂ emissions were found to be related directly to the electricity generation mix and only loosely linked to driving distances and charging habits (Liu & Santos, 2015).

4 DISCUSSION OF RESULTS

In this section the results of a mass conversion to electric cars in Ecuador and its impact on the national electricity production capacity is examined. It is put forward that it would be of interest to install renewable energy plants on a large scale.

4.1 The solar photovoltaic potential in Ecuador

The National Advisory Bureau for Electricity of Ecuador puts the average national global radiation as 4,574.99 Wh/m²/day (CONELEC, 2008). Regarding efficiency of solar PV, the National Renewable Energy Laboratory sets the record at 46.0% (NREL, 2015). Conventional solar panels made from multicrystalline cells however, tend to have efficiencies ranging from 14.4% (Peek, 2015) to 22.1% (Hanley, 2015). Let us take an efficiency of 15% as a reasonable point of departure. This would give an average electricity production from solar PV to be estimated at:

$$4.57499 \times 0.15 = 0.686 \text{ kWh/m}^2/\text{day} \quad (1)$$

We can then estimate the surface area needed to meet the demand for the worst-case scenario, where all cars in Ecuador are be changed to electric vehicles:

$$4,890,838,314 / 0.686 = 7,127.92 \text{ km}^2$$

This is a substantial area, making up some 2.51% of the country's total.

4.2 Wind power potential in Ecuador

Ecuador has good wind resources, mainly due to the Andean mountain range that runs through the country. Currently there is a 16.5 MW wind farm installed in the Loja region, which produces 64.0 GWh per year (CONELEC, 2013). The Ministry of Electricity and Renewable Energies recently published the wind power atlas of Ecuador. In the short term, it identified the potential for 1,518.17 GWh annual production from prospective wind farms over an area of 294.74 km² (low wind scenario). In the longer term up to 2,868.98 GWh could be produced from 556.99 km² of wind power plants. This would be insufficient to cover the total potential demand from a mass conversion to electric cars.

4.3 Wind plus Sun

Let us assume that the complete transition to electric cars would be a long-term strategy, and that complete wind power potential would be mobilized. If 2,868.98 GWh were produced from wind turbines using 556.99 km², then the remaining 2,021.86 GWh could be produced with solar PV over an area of:

$$2,021.86 \times 10^6 / 0.686 = 2,946.25 \text{ km}^2$$

This would give a total area of 3,503.24 km² for wind and solar power, or 1.24% of the country's total territory.

It is worth noting here that the paper does not enter into the study of variable electricity production from renewable sources, and how this is able to meet the variable demands from the transport sector. This would be an area of further study. To date it was found in Beijing that the impact of plug-in hybrids would be negligible given correct charging time management (Liu, 2012). It is suggested that similar strategies are looked into for the impacts of electric vehicles in Ecuador, where the possibilities for Smart Grids are opened up.

4.4 Considering the costs and centralized vs. decentralized electricity production.

The CONELEC Masterplan for Electrification between 2013 and 2020 tabulates the predicted costs for various hydropower, thermal power, wind power and solar power electricity generation plants (CONELEC, 2013). The costs are estimated, and there exist a far

greater number of hydroelectric projects than for wind and solar. We can nevertheless use the data to estimate the costs per GWh for wind, solar and hydro power plants. The results are shown in Table 3.

Type	MUSD/GWh	GWh/MUSD
Hydro	4.38	0.23
Wind	4.45	0.22
Solar	1.49	0.67

Table 3: Estimated costs of hydro, wind and solar power (adapted from CONELEC, 2013)

It can be seen that wind and solar power are competitive with hydropower. If the total estimated demand from a mass change to electric cars were to be met by either of these sources, or the wind/solar mix described in Section 4.3, the costs would be:

- Hydro: 21,410.53 MUSD.
- Wind: 21,752.16 MUSD.
- Solar: 7,267.28 MUSD.
- Wind/Solar: 15,764.16 MUSD.

What is also of interest is the fact that solar and wind power have more potential to be implemented as a decentralized power source, given that the solar/wind potential are more dispersed than hydropower sources. This opens up a whole new area of research, where not only a study is carried out into meeting the energy demands from electric transport, or solely the costs in doing so, but to see how the energy production could be carried out in such a manner as to promote poverty relief in developing countries. It was put forward by Davis, Jácome and Lamour (2016) that urban metabolism cycles, where city waste is turned into energy sources, should be harnessed in such a manner that it brings about sustainable economic development in vulnerable urban communities. Their work centered on Quito, the capital of Ecuador. A vulnerability index analysis was carried out, where the parish of Calderón was identified as having a population that was both large and particularly vulnerable (in terms of the number of dependents per adult and the level of informality in the job market). An investigation was carried out to determine the potential economic benefits if the organic waste for Quito were used to make biogas and to generate electricity. It was found overall that there was a potential for Calderón to be a renewable energy center of Quito, where the electricity produced could potentially initiate the socio-economic development of the parish. It would be interesting to extend this work on a national scale for the electricity demands studied, especially in consideration of the development needs faced following the recent earthquakes.

4.5 The need to reduce demand by reducing private vehicles on the road

Special mention needs to be given to the fact that this paper only looks at the consequences of a mass change to private electric vehicles. As such, it does not consider the need to reduce the use of private cars for transport. Cars present an urban problem, not only for their energy demands, but also for the need of far greater spaces and infrastructure. MacKay (2008) tells us how a single person in a Lexus 4 x 4 private vehicle uses 8 kWh/10km travelled, whereas the same person in a train would require but 0.6 kWh/10km and on a bicycle would need a mere 0.24 kWh/10km. In addition, the use of cars puts an incredible pressure on the space available

in cities (see Figure 2). It is therefore argued in this paper that the study carried out is valuable in quantifying the impact of electric cars. However, a holistic solution needs to be further researched into, where transport is not only electrified but the use of private cars is drastically reduced in Ecuador.

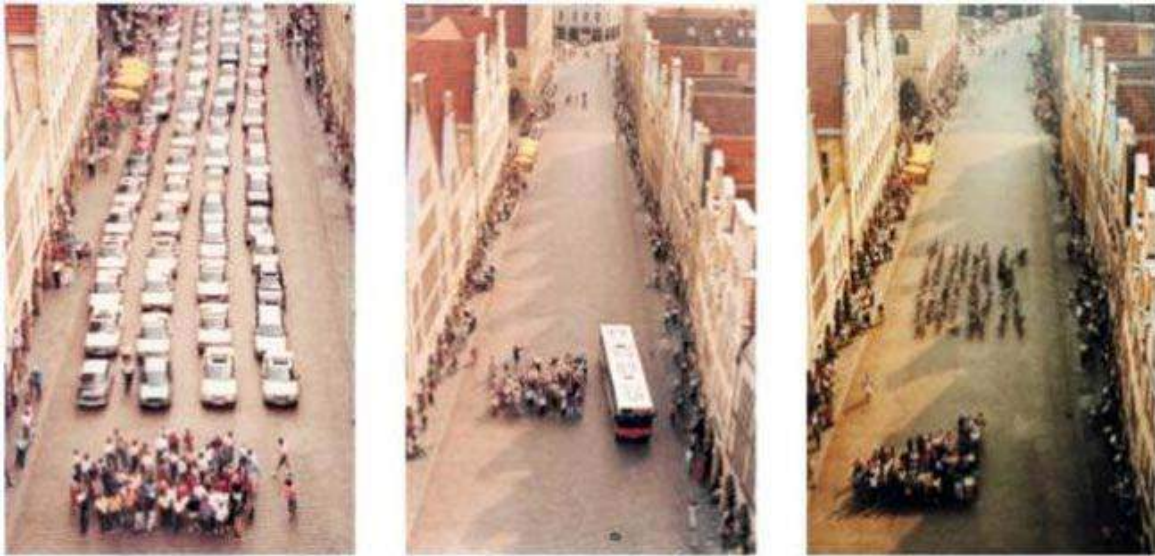


Figure 2: the space taken up a group of people in Munich, Germany - each in their own car, all in a single bus, or each with their own bicycle (Vanderbilt, 2010)

5 RECOMMENDATIONS FOR FURTHER RESEARCH

Amongst the points raised in the text, the following areas for further research are highlighted:

- Further work is needed in quantifying the potential electricity demands from electric vehicles. Additionally, the variability of the electricity produced from solar and wind power should be assessed in greater detail in its ability to meet the charging demands for electric vehicles.
- The opportunities for the socio-economic development of vulnerable urban communities, via the implementation of nation-wide decentralized electricity production should be investigated further.
- Overall, there is a need to consider not only electric vehicles, but look into holistic transport systems for Ecuador, which are based on electricity but have incorporated other public transport technologies.

6 CONCLUSIONS

There is a global tendency to move away from fossil fuel cars to electric vehicles. Furthermore, Ecuador finds itself in the uncomfortable position of having to export raw crude oil, to then import the refined gasoline and diesel it needs to meet the demands of the transport sector (49% of its national energy requirements). To make matters worse, diesel and gasoline are heavily subsidized by the government. In addition, Ecuador has a huge hydroelectric potential, where it aims to increase national electricity production through hydropower from 43% to 93%. Overall, it can be said that the country stands to greatly benefit by changing from fossil fuel vehicles to electric transport. Should all of the private cars in Ecuador change to electric vehicles en-masse however, the electricity demand created

would be 44% of the current hydropower capacity, or an 18-fold increase in renewables. Whereas wind and solar are competitive with hydropower in terms of the costs of meeting this demand, large areas amounting between 1.24% and 2.51% of Ecuador's total would be needed. On the other hand, wind and solar offer the potential for decentralized electricity production, where possibilities for the socio-economic development of deprived urban areas open up.

Overall, it becomes clear that not only does Ecuador need to move to electric transport, but that there also needs to be a decrease in the number of cars in circulation, and an increase in public transport systems.

7 ACKNOWLEDGEMENTS

The research project would not have been possible without the dedication, support and patience from a team of undergraduate students from the Department of Architecture, Arts and Design from the Pontificia Universidad Católica de Ecuador. In particular, thanks are extended to Daniel Esteban Naranjo Holguin, Andrea Enríquez Herrera, Giselle Aguirre, Johanna Cuito, Zaoky Guanoluisa, Jimena Román and Dario Silva.

8 REFERENCES

- Cevallos, J. Estimación del consumo de combustibles en el transporte terrestre en Ecuador (No. 2015_05). Instituto de Altos Estudios Nacionales, Centro de Prospectiva Estratégica. Recuperado de [http://ceproec.iaen.edu.ec/download/wps\(2\)/2015_05.pdf](http://ceproec.iaen.edu.ec/download/wps(2)/2015_05.pdf), 2015.
- CONELEC. Atlas Solar del Ecuador con Fines de Generación Eléctrica. CIE. Ecuador, 2008.
- CONELEC. Plan Maestro de Electrificación. Resumen Ejecutivo. Ministerio Coordinador de Sectores Estratégicos y Ministerio de Electricidad y Energías Renovables. Quito, Ecuador, 2013.
- Davis, M.J.M., Jácome Polit, D., Lamour, M. 2016. Social Urban Metabolism Strategies (SUMS) for Cities. Procedia Environmental Sciences. Elsevier, USA, (in progress).
- Doucette, R. T., & McCulloch, M. D. Modeling the CO₂ emissions from battery electric vehicles given the power generation mixes of different countries. *Energy Policy*, 39(2), 803-811, 2011.
- El Universo. Autos eléctricos sin aranceles anuncia el Gobierno ecuatoriano. El Universo (12 January 2015). Retrieved from: <http://www.eluniverso.com/noticias/2015/02/12/nota/4549911/autos-electricos-aranceles-anuncia-gobierno-ecuatoriano>, 2015.
- fueleconomy.gov. The Official U.S. government source for fuel economy information for cars. U.S. Department of Energy & U.S. Environmental Protection Agency. USA, 2016.
- Hanley, S. Panasonic Quickly Beats SolarCity's Solar Module Efficiency Record. 09 October 2015. Retrieved from: <http://cleantechnica.com/2015/10/09/panasonic-quickly-beats-solarcity-solar-module-efficiency-record/>, 2015.
- INEC. Anuario de Estadísticas de Transportes 2014. Cuadros Estadísticos de Resultados. Retrieved from: <http://www.ecuadorencifras.gob.ec/documentos/web->

inec/Estadisticas_Economicas/Estadistica%20de%20Transporte/Publicaciones/Anuario_de_Estad_de_Transporte_2014.pdf, 2014.

- International Energy Agency (IEA). World Energy Outlook 2015. Paris, France, 2015.
- Jaramillo, A. USD 35 000 costará un auto eléctrico. El Comercio (23 February 2015). Retrieved from: <http://www.elcomercio.com/tendencias/autoelectrico-ecuador-costos-tecnologia-electrolinas.html>, 2015.
- Liu, J. Electric vehicle charging infrastructure assignment and power grid impacts assessment in Beijing. *Energy Policy*, 51, 544-557, 2012.
- Liu, J., & Santos, G. Plug-in hybrid electric vehicles' potential for urban transport in China: The role of energy sources and utility factors. *International Journal of Sustainable Transportation*, 9(2), 145-157, 2015.
- MacKay, D. Sustainable Energy-without the hot air. UIT Cambridge, 2008.
- Ministerio Coordinador de Sectores Estratégicos (MCSE). Resumen Balance Energético 2014. Quito, Ecuador, 2014.
- Ministerio de Finanzas. Programación Presupuestaria Cuatrienal 2015-2018 (p. 73). Quito: Ministerio de Finanzas. Retrieved from: <http://www.observatoriofiscal.org/docs/ analisisopinion/Presupuesto2015ProgramaCuatrienal.pdf>, 2015.
- National Renewable Energy Laboratory (NREL). Best Research Cell Efficiencies. Retrieved from: http://www.nrel.gov/ncpv/images/efficiency_chart.jpg, 2015.
- Peek, S. Sharp ND-F2Q235 Review. 26 March 2013. Retrieved from: <http://solar-panels-review.toptenreviews.com/sharp-solar-panels-review.html>, 2013.
- Simoes, A., Hidalgo, C., Landry, D. A proportional representation of Ecuador's exports. Atlas of Economic Complexity, MIT Media, Lab, Boston, USA, 9 May 2014.
- Tran, M., Banister, D., Bishop, J. D., & McCulloch, M. D. Realizing the electric-vehicle revolution. *Nature climate change*, 2(5), 328-333, 2012.
- Vanderbilt, T. How we drive. Retrieved from: <http://www.howwedrive.com/2010/06/28/german-efficiency/>, 2010.
- World Bank. Ecuador, Country at a Glance. Retrieved from: <http://www.worldbank.org/en/country/ecuador>, 2014.

From Theory to Practice: Building Physics in Urban Design

John Martin Evans¹ and Silvia de Schiller²

^{1,2} Research Centre Habitat and Energy, Faculty of Architecture, Design and Urbanism
University of Buenos Aires, Pabellón 3, Piso 4, Ciudad Universitaria, Av., Castillo S/N
Buenos Aires, C1428BFA, Argentina
e-mail¹: evansjmartin@gmail.com - email²: sdeschiller@gmail.com

Keywords: Equatorial climate, Galapagos, Sustainable Building, Urban Planning.

Abstract. *This paper presents concepts of architectural physics applied during the design process to achieve a low impact naturally conditioned built environment of particular concern in a highly sensitive natural heritage site, the Galapagos Islands, declared World Natural Heritage by UNESCO. These concepts were applied in the new ecological airport project and National Park Directorate buildings. They offer the opportunity to develop new guidelines for both situations, which, in turn, provide the basis for design criteria and tools for implementation on a larger scale with the aim of applying theory in practice, generating passive bioclimatic design and low energy architecture. The Seymour Airport Terminal, Galapagos Islands, Ecuador, is therefore based on principles of building physics, the application of bioclimatic design strategies, optimizing natural resources and achieving a very low energy, naturally conditioned building, with daylight and cross ventilation, throughout the 7.000 m² covered area. Design development involved extensive laboratory model testing in artificial sky, wind tunnel and sun movement simulator, combined with numerical simulation. Design strategies include total solar protection of all openings, high solar reflection and thermal insulation in roofs, cross ventilation, thermal stratification and extraction of warm air by stack effect, modification of temperature variation with thermal capacity of building materials, shaded roof lights and reflective internal surfaces. The building integrates solar installations, supplying 100 % of hot water requirement with solar thermal systems, while photovoltaics contribute 25 % to the electricity demand. The challenging innovation of this project is the application of these principles in a deep plan airport building, with specific functional and security requirements for the physical separation of circulation on land and airside. The building achieved Sustainable Building LEED Gold certification. Measurements and studies carried out for the Galapagos National Parks Directorate provided further evidence of the architectural requirements for thermal comfort in naturally conditioned buildings in Galapagos. The application of lessons from these cases and the physical phenomena are applied to the urban scale, to guide the principles of sustainable urban development in an equatorial island climate. Orientation of urban subdivisions, building height control, space between building, treatment of outdoor spaces with local vegetation and integration of solar energy in buildings will promote sustainable development in architectural and urban practice.*

1 Introduction

Urbanization, tourism, new buildings, and increasing energy use generate impacts that threaten the Galapagos Islands, with a unique and vulnerable ecosystem designated a World Natural Heritage site by UNESCO as well as the status of the largest and oldest Ecuador National Park. The energy demand for air-conditioning in buildings is an important part of this impact, as, in addition to the emission of greenhouse gases, oil spills from ships supplying conventional fossil fuels have already caused serious damage to marine ecosystems. As a result, the energy policy for the islands is to achieve an energy supply based exclusively on renewable sources. However, this policy does not yet include effective measures to reduce the demand, with great potential based on passive and low energy building and urban design.

In this context, the paper presents the application of architectural physics in the design process to achieve a low impact naturally conditioned building: the Seymour Ecological Airport Passenger Terminal (de Schiller, 2015), the first airport terminal to be certified LEED Gold (USGBC, 2014). The 7,000 m² airport terminal, handling 70,000 passengers a year, with high internal gains in a demanding equatorial island climate, achieves comfortable indoor environment with natural air conditioning, based on natural daylight and ventilation, in all public spaces, during all hours of operation throughout the year.

The paper follows the design development sequence, from climatic variables studies through the physical phenomena that contribute to the favourable modification of environmental variables, the selection of bioclimatic design strategies, initial design proposals, testing the initial project concept with physical and numerical models, achieving the final design, construction procedures and verification in the completed building. The bioclimatic design resources and low impact measures include total solar shading of all windows and skylights, cross ventilation, insulated and reflective roofing, extensive floor to ceiling heights for thermal stratification and natural extraction of hot air through stack effect. Internal spaces also have natural daylight, with patios and well-protected skylights. Additionally, the building includes recycled wastewater and materials, and provides universal accessibility in all public spaces with no steps or lifts. Solar collectors provide all the hot water and PV panels on the covered walkways not only provide shade for passengers but also supply a significant proportion of the electrical energy demand.

The experiences and results of the design of the airport terminal contributed to subsequent studies carried out for the Galapagos National Park Administration in the framework of the Prometeo Programme (SENECyT, 2015). These included environmental measurements and diagnosis of environmental conditions in the Galapagos National Park buildings and the preparation of design recommendations for new and existing buildings of the National Park. The same recommendations are applicable to residential and other buildings in the private and public sector.

The conclusions use these experiences to draw recommendations for design requirements at urban design scale, with factors such as: predominant orientation of sub-divisions, spaces between buildings in relation to their height, roofs treatment and thermal performance, conditions for outdoor spaces and the prevision of solar energy systems at the urban scale. These recommendations determine basic urban indicators such as population and building density, ground coverage, functional use of local vegetation. These conclusions are compared with urban design guidelines for warm humid climates (Givoni, 1998; de Schiller, 1998;

Baker, 1987), in the context of compact urban development in developing countries (de Schiller, 2000). Study of applied physics to urban scale will influence design requirements at different architectural scales and, as this paper shows, the study of applied physics at the building scale should positively influence urban planning.

2 Environmental context

The Galapagos Islands, located in the centre of the Pacific Ocean about 1000 km from the South American Continent, on and close to latitude 0° , show a typical warm humid equatorial climate, moderated by the temperate Humbolt current with low seasonal temperature variation. Monthly average temperatures range from 24° to 31° C in March and 19° C to 27° C in September, while absolute values range from 34° maximum and 14° C minimum, outside the acceptable comfort range, Figure 1 (Evans, 2015; Pearce, 1990; Wunderground, 2016). In the Island of Baltra, the rainfall is low with an annual average of about 100 mm, concentrated between January and April. Relative humidity is high, especially in the early morning.

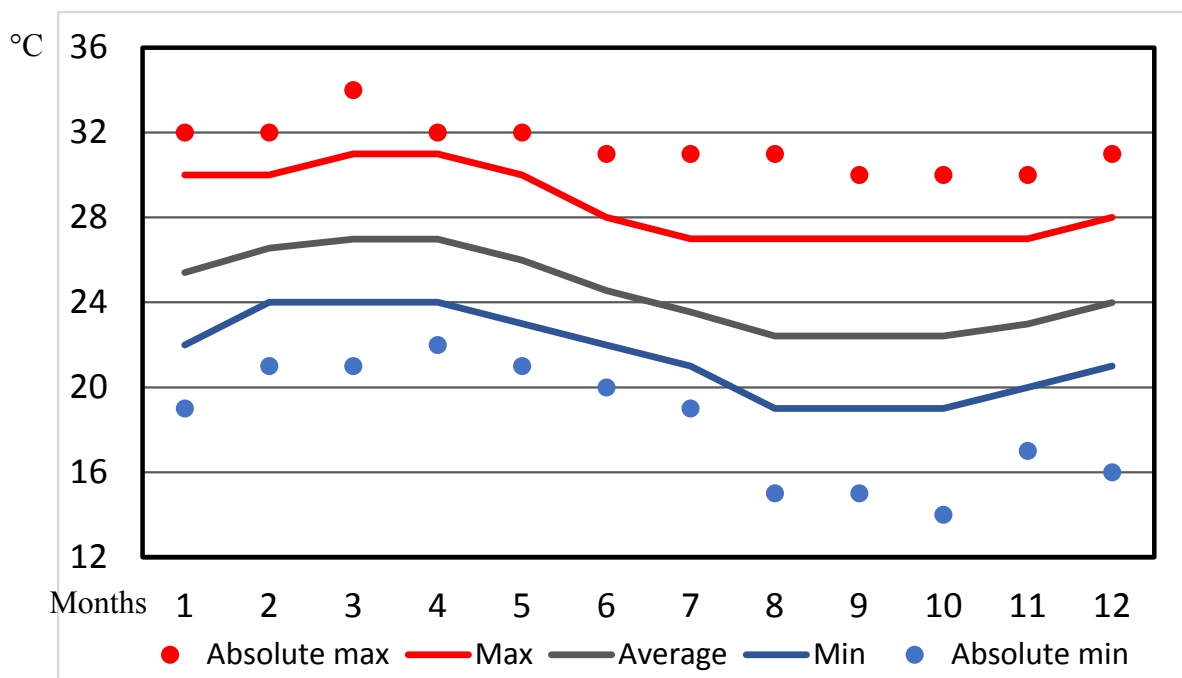


Figure 1. Average and extreme monthly temperatures at the Seymour Airport, Island of Baltra, Galapagos.

The outdoor comfort conditions in the shade and with normal air movement are within the comfort zone nearly all the time and, in well-designed buildings, the indoor conditions can be maintained within the comfort limits. In conventional buildings with poor roof insulation, inappropriate window orientation and lack of cross ventilation, air conditioning is needed to achieve comfortable indoor environment. Extensive use of artificial conditioning leads to high electricity demand in the islands, exceeding the per capita national average.

However, in an airport terminal, there are three additional challenges:

- For functional and economic reasons, airport terminals have deep plans with considerable distances between opposing facades, a severe challenge for natural lighting and cross ventilation design strategies.
- Airport terminals have a high concentration of passengers in confined spaces with a high internal thermal load.

- In addition, the functional and security requirements for physical separation between air-side and land-side further complicate the possibilities of natural conditioning.

The design challenge of the Seymour Airport Passenger Terminal was to achieve thermal comfort and daylighting in a naturally conditioned building without mechanical air conditioning. This paper explains the development of the design to respond to this challenge.



Figure 2. Previous airport passenger terminal

At the start of the design process, the design team measured temperatures in the original Airport Terminal Building, Figure 2, an open sided space with poor roof insulation and internal spaces without cross ventilation. Part of the building was a remnant of the US Airforce base built on the island during the Second World War, with additions and changes. The results showed the poor level of thermal comfort achieved and indicated environmental issues to be resolved in projected building.

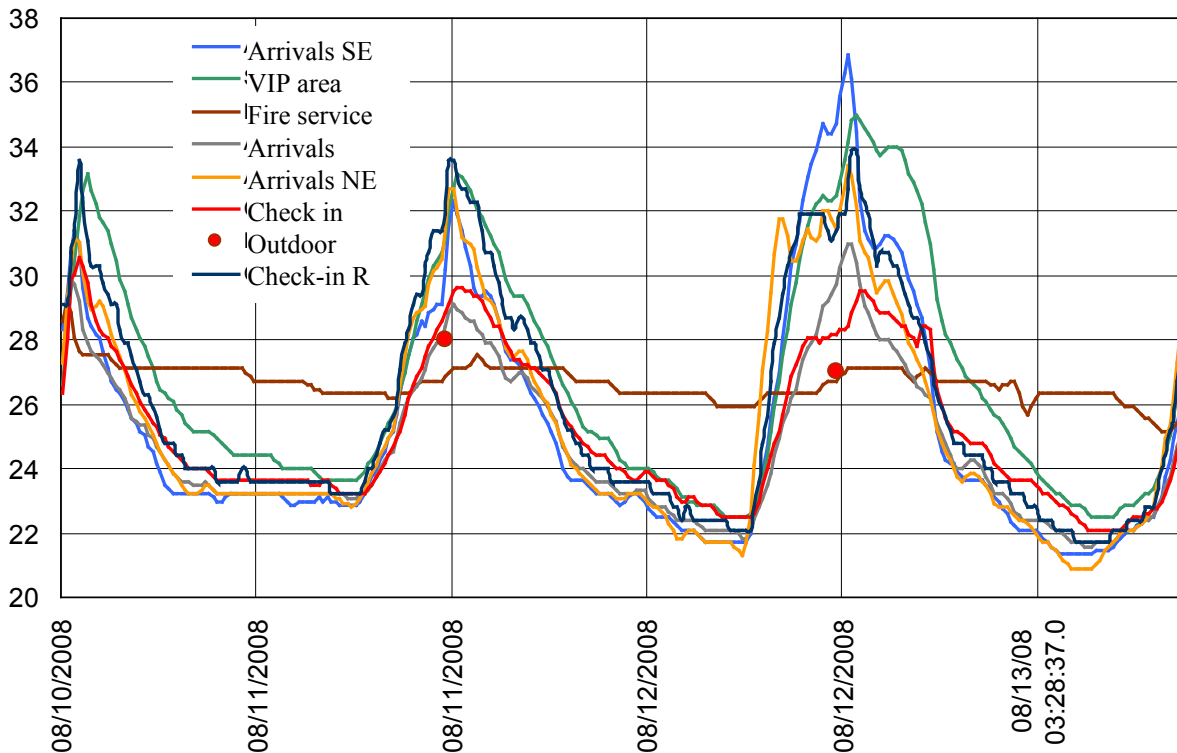


Figure 3. Temperature measurements in the old terminal building.

An analysis of the temperature measurements showed that indoor night temperatures in a well-ventilated building are similar to outdoor conditions but daytime temperatures vary widely, Figure 3. The highest temperatures were measured close to the roof (Check-in R), in spaces receiving direct sun (Arrivals SE) and with roof lights and poor ventilation (VIP area). The firemen's accommodation, with blockwork walls, had a limited temperature swing but poor ventilation without air movement does not favour cooling at night or daytime comfort.

Climate analysis and temperature measurements showed the importance of full solar protection and natural lighting, cross ventilation, insulated and reflective roofs and building forms and orientation that respond to sun and breeze. The first design proposals, Figure 4, adopted roof forms to favour the extraction of rising warm air and improve internal daylight in a deep plan building. Another early relevant decision was to orientate the building with the main facades facing north and south to avoid solar gains, orientation which also catches the prevailing winds from the southeast.

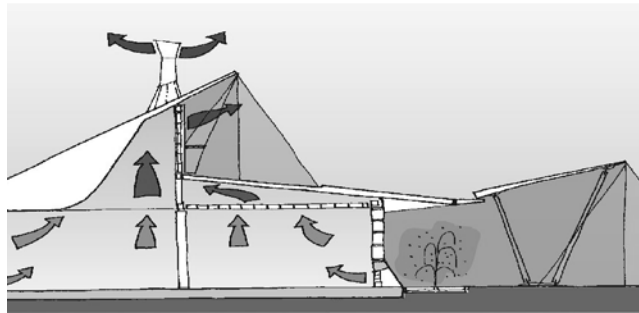


Figure 4. Initial design proposals with roof forms for ventilation

3. Building Physics for Natural Conditioning

In artificially conditioned buildings, the design of artificial lighting and air conditioning can correct or overcome design deficiencies, ensuring adequate level and distribution of light and air temperature throughout the building. The design of these conventional buildings often ignores energy efficiency measures, which consequently increases energy use and at the same time, environmental impact. This option was not acceptable in a sensitive site without conventional energy supply.

Design of naturally conditioned buildings requires a continuous testing and verification of design strategies to ensure appropriate thermal and daylight quality. These were carried out on a regular basis with lab tests, using a mirror type artificial sky for natural lighting studies, a heliodon for testing solar protection while controlling solar gains and a low speed boundary layer wind tunnel for testing cross ventilation, Figure 5. Numerical simulations were used to complement physical scale model tests.

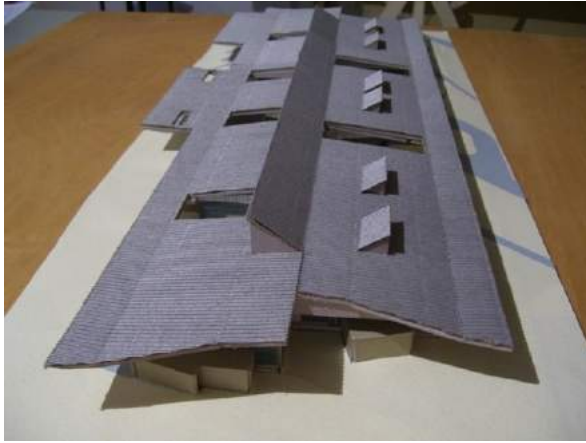


Figure 5. Laboratory tests: heliodón, solar simulator for sun protection studies and artificial sky daylight studies.

The design of naturally conditioned buildings thus requires a close cooperation between designers and environmental consultants. In the case of the Seymour Airport, the design team was skilled in bioclimatic design, with post-graduate studies and specialised teaching experience.

From the initial stages, Figure 6, the team incorporated a series of design resources in order to achieve high level of thermal comfort and natural daylight in all public spaces of the new terminal building, while ensuring low energy demand and minimum environmental impact.



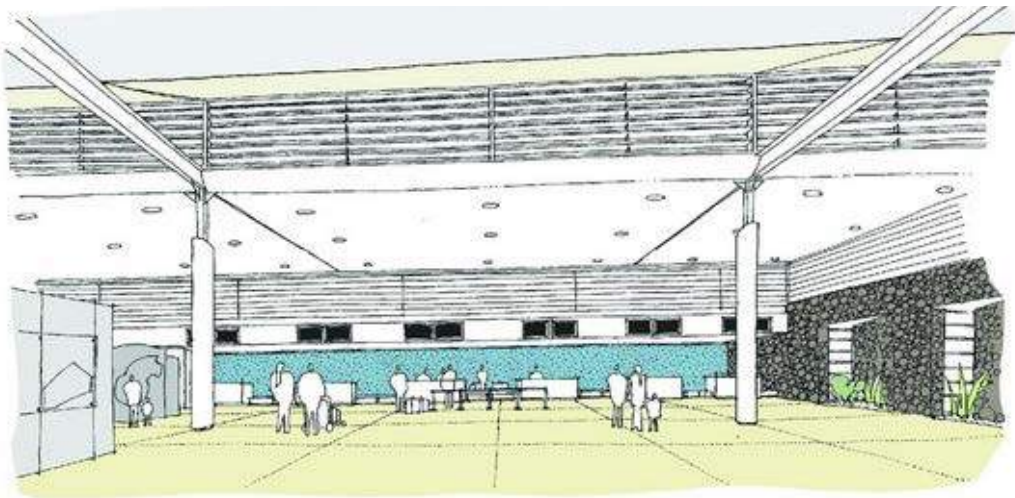


Figure 6. Concept sketches of the central spine and check-in area.



Figure 7. Daylight simulations in the check-in area

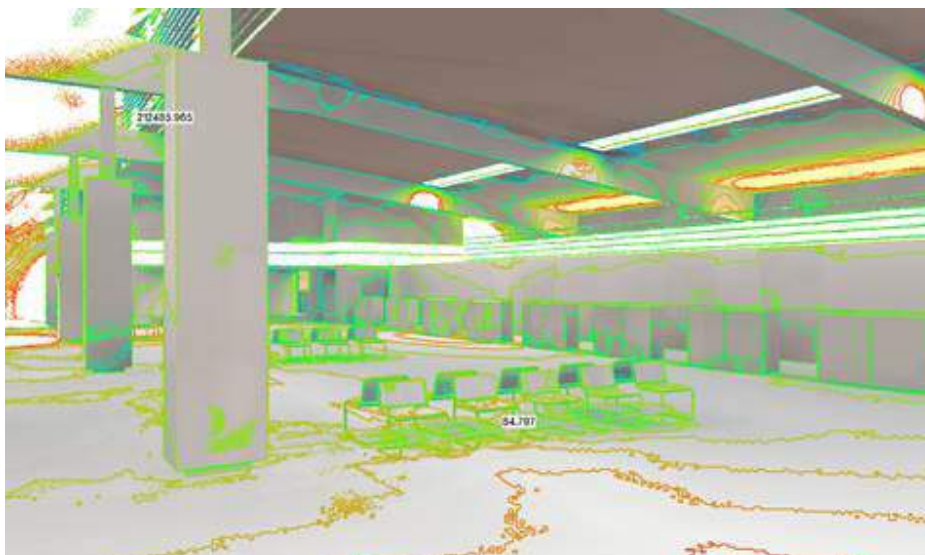




Figure 8. Two complementary daylight studies.

- Above, simulation using Radiance to check for distribution at floor level and check glare from roof openings with solar protection.
- Below, testing a central section of the terminal with a model in the artificial sky.

The following environmental strategies were developed and implemented in the project.

3.1. Solar protection, roof.

While the external air temperature may reach 34° C, the combination of high air temperature and solar radiation can produce a sol-air temperature of 60° C, considering a white painted flat roof and peak solar radiation of 1000 W/m² at midday on the equator. The sol-air temperature is the fictitious external air temperature, which represents the combined impact of solar radiation and external air temperature (Koenigsberger, 1971). The calculation of heat gains through the roof depend on two key variables of sol-air temperature: solar radiation absorption and thermal transmittance. The roof thermal performance is therefore a key building component to achieve comfortable indoor temperatures.

The sandwich roof panel consists of a 100 mm core of thermal insulation between two corrugated aluminium sheets with a white external surface reflecting a high proportion of the incident solar radiation, while the high emissivity of the painted surface readily emits part of the heat absorbed, figure 9. An aluminium surface would reflect a higher proportion on the incident radiation but the low emissivity would retain a high proportion of the heat generated by the absorbed incident radiation, transmitting a higher proportion to the underside of the roof.

The thermal insulation reduces the transmission of heat to the underside of the roof, while the inner aluminium sheet with a lower emissivity reduces the indoor mean radiant temperature. The overall performance of the roof can be measured by the solar heat factor, the proportion of the incident solar radiation transmitted through the roof. In a naturally ventilated building with cross ventilation, the indoor and outdoor air temperature are very similar, so heat flow through the roof due to difference in air temperature is limited.

The roof thermal transmittance or U value is 0,28 W/m²K and the solar heat factor is 0,7 %, so less than 1 % of the incident solar radiation is transmitted through the roof, a maximum thermal load of 7 Watts/m² at midday, though much less in the early morning. The roof component of internal radiation, contributing to a possible increase in the internal mean radiant temperature is therefore controlled.



Figure 9. Airport passenger terminal showing the reflective white roof and the southern façade in total shade. The wind turbines to the north of the terminal provide part of the electricity demand.

3.2. Building orientation for sun and wind.

The location of the airport very close to the equator implies intense solar radiation on the roof at midday and on eastern facades in the morning and west facing facades in the afternoon, with lower incidence on northern and southern facades. The existing runway is orientated to the prevailing winds from the northeast when normally, passenger terminals are located parallel to the runway. However, in this case, the conventional orientation has serious disadvantages: the principal facades would be orientated to the NW and SE.

This orientation does not catch the prevailing winds effectively, and the facades receive higher solar radiation intensities, as they are difficult to shade from low angle morning and afternoon sun. The orientation of the airport building is therefore by 45° turned with the longer facades facing north and south to minimize solar impact in this equatorial location as shown in Figure 10. The impact of prevailing winds from the NE is less intense, but the change in angle reduces the effectiveness by only 30 %, following the cosine law, as $\cos 45^\circ = 0,707$.

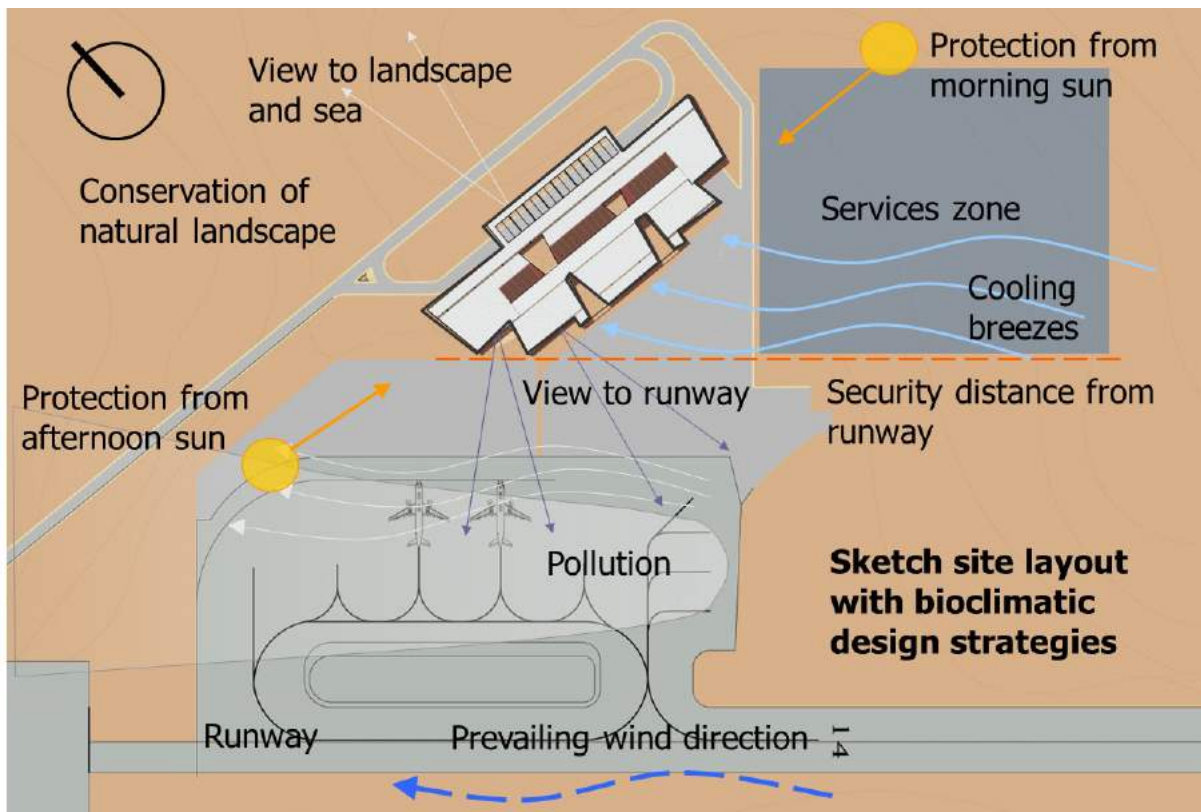


Figure 10. Schematic site layout showing bioclimatic design strategies, with orientation related to the impact of the sun on east and west facades, and the improved exposure wind to south-west winds parallel to the runway.

3.3. Solar protection, openings.

Openings are another route for solar heat gain, though the maximum solar radiation intensity on vertical surfaces is about 660 W/m^2 . On the equator, this occurs on western and eastern facades at about 9:00 in the morning and 15:00 in the afternoon. The latter case is the most critical as the peak radiation coincides with high external air temperature.

Three relevant and combined measures reduce solar radiation incidence through openings: in addition to the building orientation, large roof overhangs shade the north and south facades, also providing shade to the circulation spaces outside the building. Additional horizontal sunshades protect sections of the facades where the roof does not shade completely. These two basic and essential measures eliminate the ingress of direct solar radiation. The horizontal sunshades also reduce diffuse radiation from overcast skies and mosquito screens on windows provide additional protection from diffuse sky and reflected ground radiation, reducing the transmitted radiation by a further 30 %.

3.4. Solar protection, walls.

Most facades are open to the breeze to catch natural air movement, but some offices and the toilets require opaque walls. Various measures reduce the impact of solar radiation on these surfaces. The roof overhangs provide partial protection to most opaque walls, the orientation of the building reduces the areas of walls facing east and west, and white painted external surfaces reflect solar radiation, while the hollow concrete block construction delay and further reduce thermal transmission through the walls.

The U value of white painted concrete block walls is $2.57 \text{ W/m}^2\text{K}$ while the solar heat factor is about 4 %. This is acceptable considering that the external surfaces are partially shaded, the peak radiation does not occur during hours of airport use and the walls provide a time lag of various hours.

3.5. Solar protection of outdoor spaces.

The extensive overhangs on the north and south facades and the covered vehicle access on the landside not only shade the facades but also the external surfaces. This provides improved comfort for pedestrian circulation in outdoor spaces and reduces the air temperature around the building, figure 11.



Figure 11. Shading of outdoor circulation spaces and building facades. Louvres on the east façade and white painted walls also reduce solar gains.

3.6. Cross ventilation

Cross ventilation is another key strategy to provide cooling air movement when temperature exceeds the comfort zone. Air movement can achieve the equivalent of 1 to 2° degree decrease in the apparent air temperature. However, this air movement must reach the occupants, as the breeze produces a cooling effect as it passes over the skin, improving evaporation and dissipating heat by convection.

This requirement presents a serious challenge in a deep plan building, which requires physical separation between arriving passengers before passing sanitary and migration controls, and departing passengers after screening and ticket checks. The first measure is the location of openings on the windward side at low level. This allows air movement through the spaces on the windward side. The second measure is the design of a physical barrier that is permeable to airflow. The project achieves this with two rows of vertical bamboo posts separated by 60 cm. A wire grid achieves further security to avoid the possibility of passing objects across the barrier. Finally, openings on the leeward side allow the air to exit on the

landside. The combination of these three measures promotes air movement at occupant level in all public spaces.

The design adopts two further measures to improve air movement at critical times and in spaces with design limitations. Large ceiling fans improve air movement when temperatures are high and natural breeze is insufficient for comfort. The check-in area has air movement blocked by the airline offices behind the check-in desks; these offices are small and need to be closed for security. So above the check-in desk, a high level screen including louvres diverts the high level air movement down to the queuing passengers.

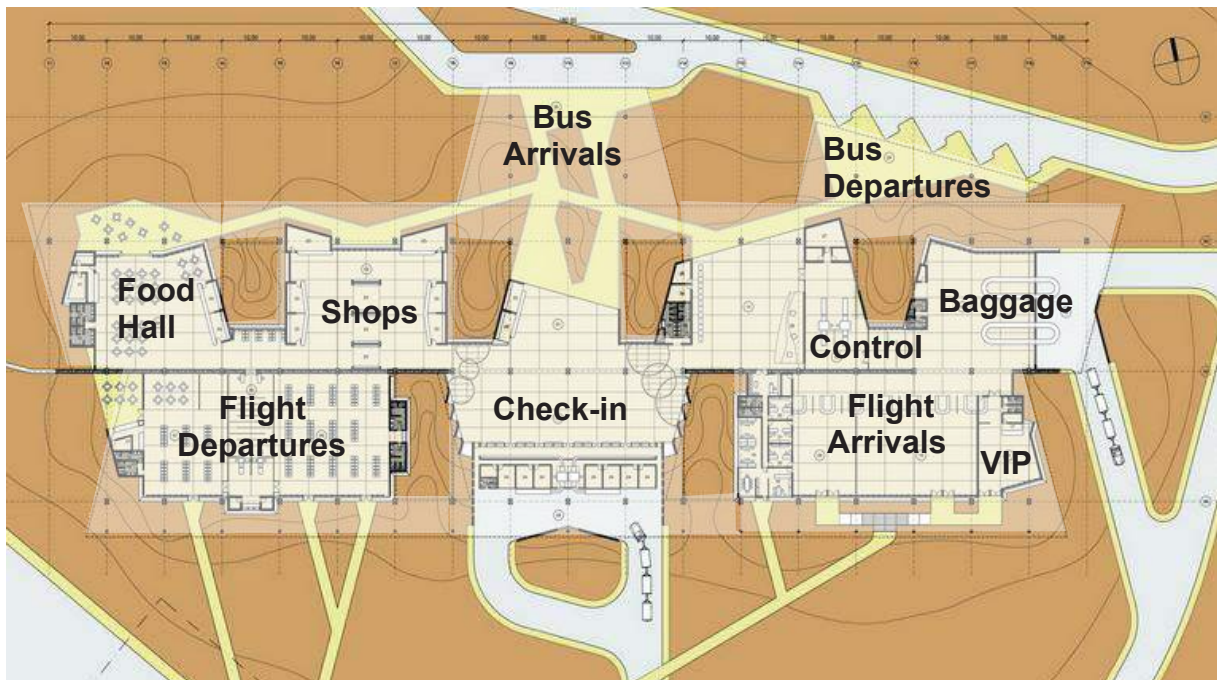


Figure 12. Floor plan showing outline of high level roof, 6 patios and shaded outdoor areas

3.7. Avoiding the greenhouse effect.

In most climates, glass is a key material for achieving natural light with temperature control, visual contact to the outside, rain protection and a favourable transmission of solar radiation while reducing heat losses. However, in the special case of the Seymour air terminal, with outdoor air temperatures close to or within the comfort zone in all hours of operation, the designers took the unusual decision of eliminating glass in windows. Glazed buildings will allow high temperature long wave radiation to pass through the glass to the interior spaces, and limit the out-going low temperature short wave radiation. Thus, glazed buildings will catch part of the radiation and retain the heat in the interior.

The airport building therefore has no glass, to encourage cross ventilation, to reduce the heat concentration due to radiation gains and to allow outgoing low temperature radiation from the interior to the outside. The challenge posed by this decision is to ensure adequate conditions of thermal comfort at all times in an open building with cross ventilation.

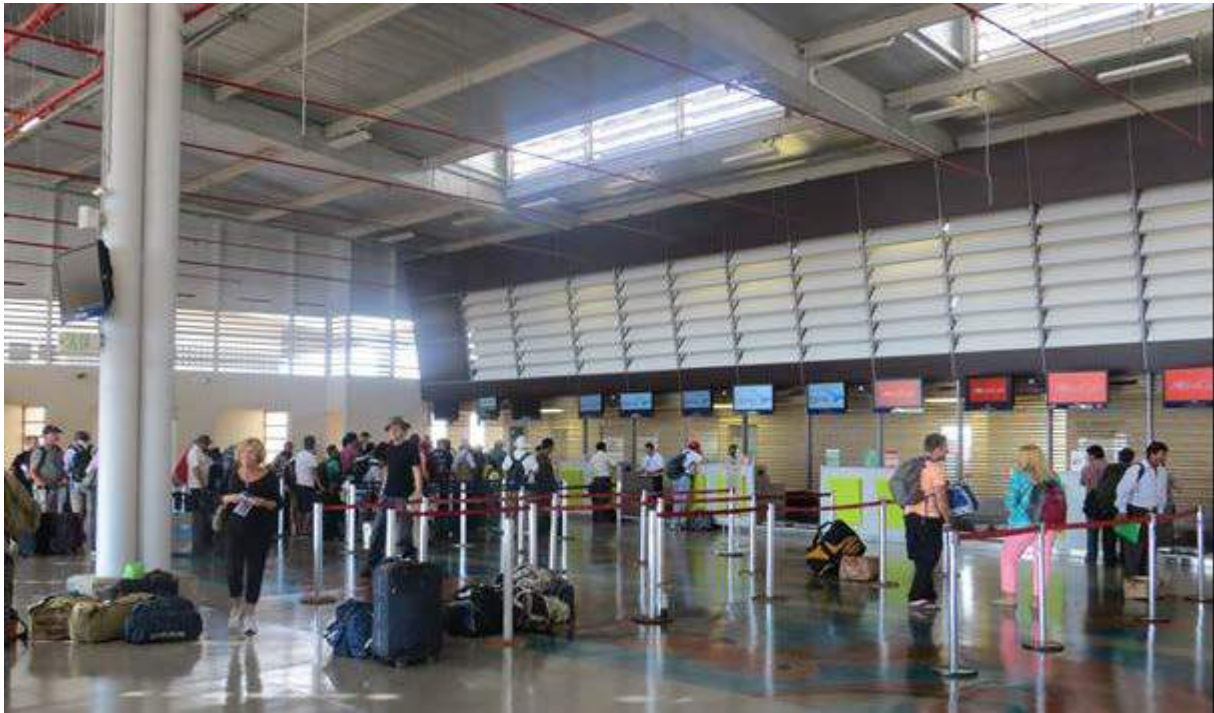


Figure 13. Check-in area, showing good daylight distribution and louvers above the check-in stands to direct natural airflow over the queuing passengers.

3.8. Acoustic control indoors.

The absence of glass has a further advantage: airport terminals normally require considerable surfaces of acoustic absorbance to reduce reverberation but the unglazed windows act as perfect absorbers with negligible reflected sound. The permeable bamboo barriers also act as good sound absorbers. These characteristics offer a special advantage in warm humid climates where absorptive materials can deteriorate and collect dust.

3.9. Control of excessive wind speeds.

As the building is open to breeze, it is important to avoid excessive wind speeds in the interior of the building when external wind speeds are high, although these events are not frequent. The design adopts three strategies to moderate internal air velocity:

- Mosquito screening on all window openings reduces wind speeds.
- Openings areas on the windward side are limited in relation to the average internal section, thus controlling the average internal air velocity.
- Roof openings in the central spine are orientated to the leeward side of the building producing a suction effect, avoiding an increase of internal wind speed that a windward opening would produce. As the outlet area is larger than in inlet areas, the design naturally moderates indoor air movement.

3.10. Patios to catch breeze and daylight.

In the deep-plan building with a considerable distance between the east and west façade, the design incorporates patios to improve the access to daylight and introduce breeze to the central areas of the building. They also allow natural ventilation of toilet areas. The east and

west facing facades of these spaces includes effective sun shading. These outdoor spaces also provide additional views to outdoors from the central circulation and other central spaces.

3.11. Control of noise and pollution.

The design of the building, open to the prevailing wind, also raises the problem of the pollution caused by the movement of aircraft and the operation of jet engines, close to the terminal building on the airside. The new layout for movement and parking of aircraft, in relation to the location of the airport terminal reduces this problem.

In outdoor situations without earth berms or thick vegetation barriers, distance is the most effective noise attenuator. The distance from the aircraft to the new terminal is therefore more than twice the distance of the previous building. The disadvantage is a longer walk from the aircraft to the terminal. Direction of persistent prevailing winds also blows the exhaust from the jet engines of taxiing and parked aircraft away from the airport building.

On the landside, the problem of traffic noise and pollution is minimized due to the special situation of this island airport. Airport busses transport all passengers from the airport to the ferry to the island of Santa Cruz, and there is no access for private cars, so traffic noise and pollution are limited. The prevailing southeasterly winds carry the exhaust fumes of busses away from the building.

3.12. Air volume.

High floor to ceiling heights, Figure 14, with a minimum value of 6 m, increases to 9 m in the centre and southwestern end of the building. This large air volume provides a thermal buffer, reducing the increase in indoor air temperature caused by internal and external heat gains. Large air volume increases effectiveness due to the cross ventilation with a high level of air renovation. The large air volume also contributes to the acoustic performance, providing additional absorbance.

The continuity of the air internal volume also allows a distribution of the heat load, connecting spaces with high and low internal gains. For example before the flights, passengers use the shopping area and restaurants, while concentrating in the adjacent space for flight departures when their flight is announced.

3.13. Stratification.

The generous floor to ceiling height also promotes stratification, allowing the separation of layers of warmer air at higher level and conservation of cooler air at lower levels. This separation means that the higher air temperatures at the upper level do not affect the thermal comfort of passengers. The distance between roof and floor also moderates the roof component of the mean radiant temperature.

Hot air plumes from local heat sources, such as coffee machines and ovens in the restaurants, can rise to roof level without affecting the occupants at low level.



Figure 14. Central spine with indirect lighting and extraction of hot air by stack effect.



Figure 15. Openings with mosquito screening, without glass.

Figure 14 shows the central circulation with gentle non-slip ramps with a 1:15 gradient to achieve changes in level without steps, as the floor follows the natural slope of the land. To the left, the permeable bamboo barrier allows air movement at low level. The columns constructed with recycled petrol pipelines.

Figure 15 shows openings without glass to ensure cross ventilation while sun shading eliminates ingress of solar radiation. Overhangs also shade outdoor spaces and white painted wall reflect solar radiation.

3.14. Stack effect for extracting hot air.

A long central spine opening in the roof is orientated away from the prevailing wind, as the object is not to catch more air movement at high level but to encourage the extraction of rising hot air. The stack effect complements the suction effect of wind. In this case, this design resource is effective due to the constant direction of the prevailing wind, which comes from the NE for over 90 % of the time and part of the remaining periods correspond to calms. The stack effect improves the extraction of hot air as the inside air gets hotter.

3.15. Reducing heat gains from artificial lighting.

Artificial lighting produces heat, although advances in technologies such as LEDs have reduced this impact. Therefore, the terminal building is designed for natural daylight in all public spaces. This required extensive model testing and simulation at the design stage in order to assure correct levels of light at occupant level and to achieve visual comfort. Multiple design resources were incorporated in the project as a result of these studies.

Light coloured surfaces contribute to the internally reflected component and reduce glare. This is a significant problem in equatorial climates where overcast skies are a source of high illuminance, especially when visible through high-level windows.

As explained in previous sections, the design ensures that no direct sunlight enters the building, eliminating this source of visual discomfort. The sunshading and mosquito screens also reduce glare. In the central building spine, large north facing skylight with louvered sunshades also allows good daylight without direct sun, in addition to the ventilation function. The project included additional windows in the roof where needed to increased daylight levels.

3.16. Thermal capacity to reduce temperature variation.

Climate data shows comfortable temperatures most of the time, with limited periods with maximums and minimums outside the comfort zone, taken to be 18-28° C, and up to 30° with cross ventilation in a naturally conditioned building.

Use of thermal inertia, using materials with high thermal capacity, can reduce daily temperature swings. Building surfaces with high thermal capacity, such as floor and walls, cool during the night and maintain lower temperatures during the morning. These cooler surfaces absorb heat from the air at low level and avoid rapid heating of the indoor the air. The denser cool air remains at low level, promoting comfort for the occupants in the lower air zone. The use of thermal capacity complements the stratification strategy.

3.17. Using average hourly temperature variation.

The airport operates from 7:30 in the morning to 13:00, with a capacity of 10 inward and outward flights each day¹, with a maximum capacity of 100 to 120 passengers on each flight. The flights arrive at half-hourly intervals and the turn-round time is about one hour. This schedule avoids use of the airport at times of peak outdoor temperature at 15:00 in the afternoon, and most passenger pass through the building between 8:30 and 12:00, times when the outdoor air temperatures are always comfortable.

3.18. Using average hourly wind speed variation.

The times of airport operation also allow for the effect of average hourly wind-speed variation on thermal comfort. In the early morning, when air temperatures are lower, the average wind-speed is low with frequent calms. Using this natural variation, the wind-chill effect is minimized when air temperatures are cool or comfortable. Air temperatures increase during the morning and convective mixing in the boundary layer increases wind velocity near the ground. This relation between wind speed and temperature promotes thermal comfort, as higher temperatures require higher velocities of air-movement and air velocity increases naturally as temperatures rise.

3.19. Rain protection.

The design of the roof ensures slopes to the outside of the building, with all gutters and downpipes outside the building perimeter. This avoids potential problems of leakage and blocked rainwater pipes inside the building. It also allow for rainwater collection, though the very low rainfall does not justify the reuse of rainwater for watering plants or other uses such as flushing toilets. Main ventilation outlet and north-facing skylight in the central spine of the roof have adjustable louvers that are closed during occasional rainstorms.

¹ The airport does not provide for future expansion as the daily maximum passenger volume is determined by the environmental capacity of the Galapagos Islands

The orientation of this opening faces away from the prevailing breeze, reducing ingress of rain. However, all internal surfaces are resistant to droplets of water, and, with high ambient temperatures, moisture quickly evaporates.

3.20 Site topography and drainage.

The lineal form of the building, over 200 m long requires a significant variation in levels to ensure adequate gradients for rainwater and wastewater drainage. The natural slope of the land allows a 1.3 m difference in levels from the higher east end to the lower west end. The difference in levels is accommodated by a series of gentle ramps, designed to facilitate passengers movement and totally avoiding steps in all public areas. Figure 11 shows the ramps with change of floor colour and handrails for additional security. There is one set of stairs for the limited access to a first floor airport administration offices and security room with closed circuit security surveillance system. The difference in level is also used for a gravity roller system for delivering luggage to passengers, avoiding conventional mechanical carousel and reducing energy demand. An additional benefit is the avoidance of large-scale earth movement, an important factor in achieving a sustainable design.

3.22. Photovoltaic panels

Photovoltaic panels provide shade and protection from occasional rain, forming covered walkways that link aircraft with the terminal building, Figure 16. They also generate 25 % of the energy requirement for the building, a high proportion of the total demand considering the limited surface of the photovoltaics. This is possible due to the exceptionally low energy demand of the building, without air-conditioning or artificial lighting in public spaces.



Figure 16. Two walkways, with photovoltaic roofs, provide 25 % of the electrical energy demand, as well as shade and rain protection for the path between parked aircraft and the terminal building.

3.21. Solar collectors

In a warm humid equatorial climate, the demand for hot water is limited to showers for personnel, and bars and restaurants. Small individual thermal solar systems installed on the roof to supply hot water directly to each point of use. In this location, the optimum slope for maximum solar radiation is horizontal, but an inclination of 10° does not affect performance. The architectural design incorporates solar collectors in the gently sloping roof to achieve architectural integration. This slope also allows natural cleaning of the collectors when it rains.

3.22. Integration

Figure 17 shows a representative cross section through the check-in hall. The design of the roof form promotes the integration of a series of environmental control strategies including louvres and extensive overhangs to avoid direct sun indoor, outdoor shade, cross ventilation, stack effect, roof suction effects and solar collectors.

This form was developed as a result of an extensive series of simulations and laboratory tests.

A special baffle above the check-in stands deflects the air downwards over the queuing passengers, as the offices behind the stands block air movement.

At the same time, the roof was designed to cover the large spans with structural steel components of limited length, according to the maximum size that could be transported by the available shipping.

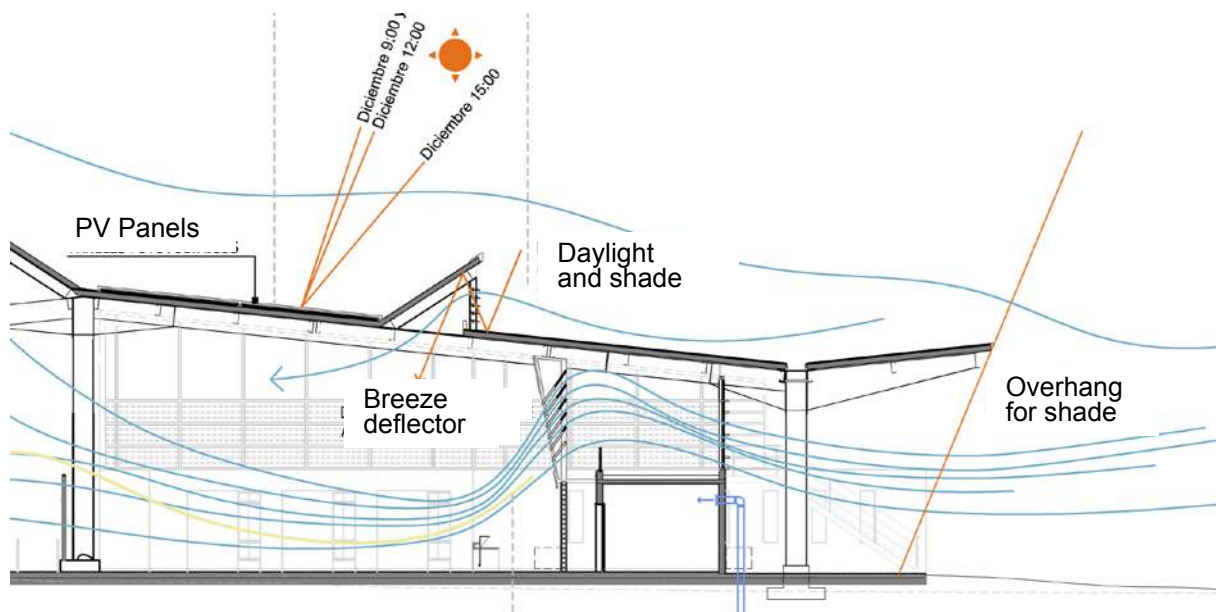


Figure 17. Section through the check-in hall showing air flow and shading

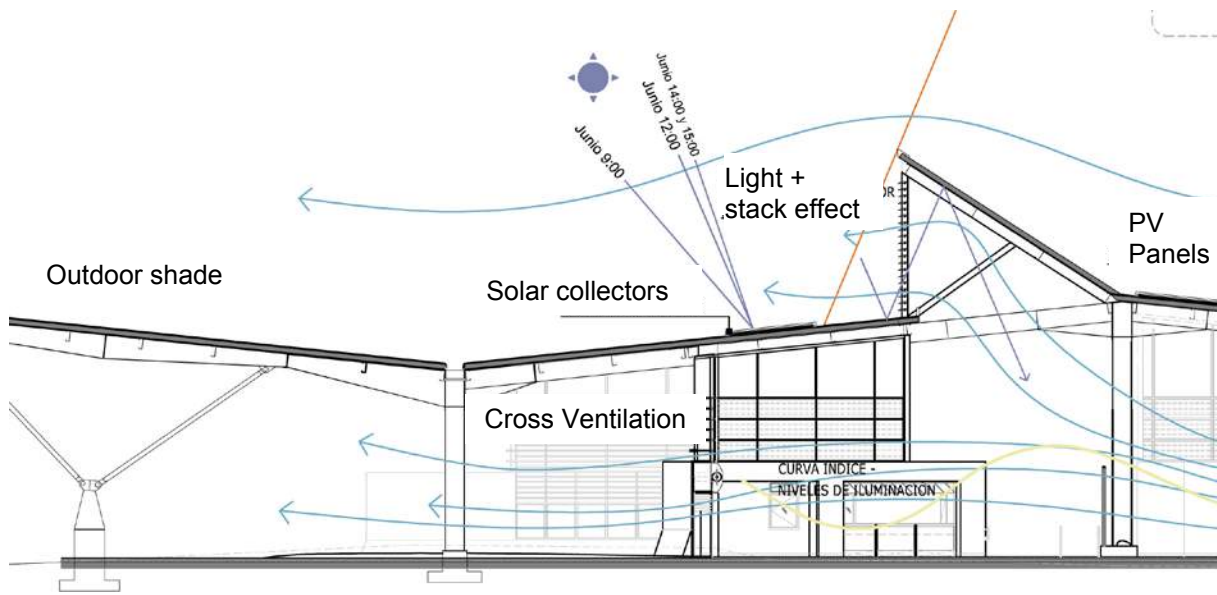


Figure 18. Section through the central spine and main entrance: cross ventilation and stack effect.

Figure 18 shows a section through the central spine with inclined roof to extract rising hot air and provide daylight. Solar collectors are located on the roof to provide hot water to bars and showers for personal.

4. Challenges of natural conditioning.

The Comfort Triangles (Evans, 2005) show the way in which the building modifies the outdoor temperature, Figure 19. This representation emphasises the daily variation of temperature, an important factor in naturally conditioned buildings. Red dots show the average monthly outdoor temperature swing on the horizontal scale and the average monthly outdoor temperature on the vertical scale in relation to the combination that provides comfort, the red comfort triangle.

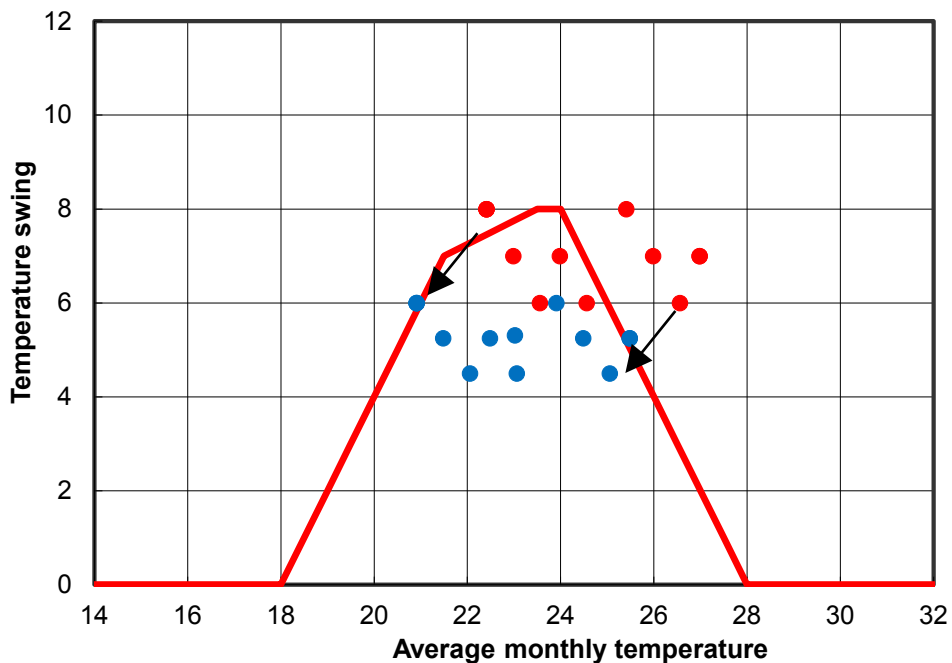


Figure 19. The comfort triangles showing average external (red) and estimated indoor temperatures (blue) in

relation to requirements for thermal comfort, the red comfort zone.

The blue dots show monthly average indoor conditions obtained with key bioclimatic strategies, cross ventilation, thermal inertia and stratification. The cross ventilation can reduce the apparent temperature by an average of 1,5° C, while the thermal inertia reduces the temperature swing, considering indoor variations about 75 % of the external variation. The black arrows show the effect of this modification, moving the thermal sensation into the comfort zone.

The design of this naturally conditioned solves many of the problems of thermal and visual comfort, without recourse to artificial air conditioning, but also introduces a series of new challenges not evident or considered in conventional buildings.

Breeze raises dust, especially after midday when wind speeds increase, due to low rainfall and slow growth of vegetation, combined with construction earth movement. Fine dust entering through windows without glass and settle on the floor is still a difficulty to solve and, as it was expected, being reduced by the outdoor ground cover with local grass and vegetation. This is a delicate issue challenging the strict prohibition of imported vegetation, even from neighbouring islands. However, the cost of cleaning the screed floors is less than the cost of maintenance and energy for an air conditioning system. The cleaning of mosquito screening and exposed installations is more complicated due to the high ceilings.

Strict regulations of the Natural Park prohibit the introduction of flora from outside the islands and even between islands. This also includes a prohibition on transporting grass seeds between the islands of Santa Cruz and Baltra, separated by a 300 m channel. This measure, to protect the unique flora and fauna on each island and avoid the ecological damage caused by the introduction of exotic species, means that plants for ground cover can only be obtained from the island of Baltra. Therefore, it is hoped that, over time, local vegetation will develop to improve dust control, a significant problem at present. The same argument was also used to exclude the use of grasses from the Island of Santa Cruz for the biological treatment of sewage in the airport.

Another ecological problem is the rapid adaption of local birds to the favourable conditions in the new building with open doors during operating hours. The open nature of the building also provide outdoor tables and benches related to the restaurant sector. The indoor restaurant area is also especially attractive due to the crumbs, food left on tables and tourists feeding birds.

The National Park Directorate is concerned about alterations of natural ecosystems, considered acceptable in conventional urban situations but undesirable in the special conditions of Galapagos, an unforeseen consequence of an opened naturally ventilated building. The toilet areas, designed with natural ventilation, are provided with solar chimneys for air extraction. Due to problems with recycled water from hand wash basins used for toilet flushing, small electric extract fans were installed to remove odours and achieve adequate air quality.

The building was LEED certified by the United States Green Building Council (USGBC, 2015), achieving LEED Gold, the first airport terminal to obtain this distinction. The certification involved many other factors, such as the use of low impact building materials, efficient use of water, installations with low energy demand and sustainable practices in site development and construction. However, the low energy requirements and indoor environmental quality contributed vital points, with high score on energy efficiency and use of renewable energy. The certification process required extensive simulation to demonstrate the low energy performance and the effectiveness of the cross ventilation strategy to achieve a good distribution of air movement for thermal comfort at all times.

A key requirement of the LEED certification process is the achievement of closely controlled indoor thermal conditions, complying with the same standards of air-conditioned buildings at all times. This required extensive simulation to show that the combination of indoor air temperature, relative humidity, mean radiant temperature and air movement provide comfort throughout the building. This was achieved and will be verified by measurements.

5. Buildings of the Galapagos National Park.

The experience of the design of the Seymour Airport passenger terminal contributed to the Galapagos National Park Sustainable Building Study to reduce environmental impacts, applying natural conditioning in buildings with different functions, including offices, housing, interpretation centres, and research laboratories. This was carried out by the authors in the framework of the Prometeo Programme financed by SENEcyT (2014).

A survey of existing buildings and temperature measurements shows the importance of applying bioclimatic design strategies to improve comfort and reduce the dependence on imported fossil fuels.

Improvement of existing housing for visiting scientists, volunteers and park staff and a manual for sustainable building design contribute to the conservation of this unique ecosystem, demonstrating the potential of bioclimatic design, renewable energy and sustainable building criteria (Evans, 2015). These were presented to the Galapagos National Park Authority in a series of reports.

Measurements and observations in houses for The Galapagos National Park staff confirmed the importance of building orientation for solar protection and cross ventilation. Measurement in the roof also showed the problem excessive heat flow through poorly insulated roofs. The result is the use of air-conditioning in the majority of the park buildings such as offices, housing and interpretation centres.

The indoor temperature swing was 60 % of the external variation in a well-ventilated house of lightweight timber construction with the same orientation as the airport. But the maximum temperature in the base of the roof cavity was 39,1° C when the maximum outdoor temperature was 29,3° C and the maximum indoor temperature was 28.2° C (Evans, 2014). However, in a blockwork house with east and west facing windows, the maximum indoor air temperature was 37.3° C when the maximum outdoor air temperature was 32.9° C.

This confirms the importance of orientation, solar protection and insulated roofs. It is ironic that in Galapagos, solar energy photovoltaic panels are generating electricity used in air conditioning units to remove heat caused by excessive transmission of solar energy through inadequately insulated roofs.

Better roofs thermal insulation could reduce energy demand and improve thermal comfort at a lower cost than the expensive imported solar panels.

Photovoltaic electricity injected in the distribution network is also used to produce domestic hot water, which could have been produced by solar thermal collectors with much higher efficiency and significantly lower cost.

6. Lessons for Planning in warm humid island climates.

This section explains the requirements for sustainable urban planning in warm humid climates, based on the experience of the airport terminal design and the recommendations presented to the Galapagos National Park Authority.

These supplement the results and recommendations of the following previous studies and guidelines for urban design made by the authors:

- Basic design requirements for warm humid climates were defined in the United Nations study (Koenigsberger, et al, 1971).
- Studies for sustainable urban development in Haikou, China (Wiesman, 1994) were also presented in Urban Design International (de Schiller, 1998).
- Studies of the Urban Heat Island in Tampico, on the Caribbean coast of Mexico, (Evans, 2005) show the importance of protecting green spaces and water surfaces in urban areas, as well as the avoidance of dark paved surfaces and excessive air-conditioning use.
- Analysis of climate impacts on urban growth in developing countries (de Schiller, 2000) show different requirements in varying climates. In warm humid climates, the importance of spaces between building to encourage air movement and provide space for vegetation may limit higher urban densities.

The Galapagos experience shows the need to respect favourable building orientations, especially at the stage of planning urban sub-division, as the size and orientation of plots will determine possible building form and orientation. In equatorial regions close to the equator, the north and south facing facades are easily shaded while low angle morning and afternoon sun will produce an undesirable impact on east and west facades. Permissible urban densities will also affect the possibility of achieving effective cross ventilation. This will depend on adequate spaces between buildings, based on the relation between building height and space between facing facades. An open urban texture, avoiding continuous linear blocks will also improve air movement at the urban scale.

In warm humid climates, where open windows are required to catch the breeze, acoustic factors also require increased spaces between buildings to reduce annoyance due to noise. Vegetation and ground cover therefore provide an important contribution to evaporative cooling, acoustic absorption, and shade for outdoor surfaces. With cross ventilation, the cooling of outdoor air also improves indoor conditions. Ground cover is a particular challenge in Galapagos, with limited rainfall and a ban on the use of exotic plants, and even the use of local plants from neighbouring islands.

This paper shows the importance of design requirements at the building scale and their influence at the urban scale. While the environmental and ecological conditions of Galapagos represent a special case, the need to achieve sustainable low impact urban development is a global requirement. An understanding of the physical phenomena and their application in practice at the building and urban scale can contribute to achieve a more sustainable future.

Acknowledgments

The design development of the Seymour Ecological Airport Terminal involved close collaboration between client representatives, design team, consultants and government authorities.

Javier Sartorio, member of the design team in the first and second stage, and the Studio Alvorado-Font-Sartorio, in charge for detailed plans and contract documentation. Members of the Research Centre Habitat & Energy, University of Buenos Aires: Guillermo Adamo and Diego Abalsamo for numeric simulations and studies in the Bioclimatic Design Laboratory, and Jorge Marusic for thermal solar installations.

Landscape designers, Monica Dazzini and Marcelo D'Andrea, and Architects Nélida Balmaceda, Adriana Apolonio and Martin Giordano for universal accessibility requirements.

The authors would also like to acknowledge the following important contributions: Eugenio Periset, Project Coordinator, Corporación America, Ezequiel Barrenechea, administrative director and Jorge Rosillo, representative of Ecogal, Alejandro Muchanoff, airport engineering, currently airport manager Seymour Airport, with Architects Tannya Pico and Ana Vergara in the construction stage, and Veronica Reed for LEED certification.

The Prometeo Programme, supported by SENESCYT, the Ecuadorian Secretary for Higher Education, Science, Technology and Innovation, provided the authors the opportunity to undertake sustainable building studies for the Galapagos National Parks Authority, acknowledging the support of the Director of the National Park, Arturo Izurrieta, and Silvina Albuja, infrastructure coordinator.

References

- [Baker 1987] Baker N. V., *Passive and Low Energy Building Design for Tropical Island Climates*, Commonwealth Science Council, Commonwealth Secretariat Publications, London.
- [de Schiller 1988] de Schiller, Silvia, and Evans, John Martin, *Healthy buildings in a new city: bioclimatic studies for Argentina's new capital*, in Planning, Physics and Climate Technology for Healthy Buildings, Vol 2, edited by Birgitta Berglund and Thomas Lindvall, Healthy Buildings, Stockholm. ISBN 91-540-4933-4.
- [de Schiller 1998] de Schiller, Silvia, and Evans, John Martin, *Sustainable Urban Development: design guidelines for warm humid cities*, Urban Design International, Vol 3, N° 4, Joint Centre for Urban Design, Oxford Brookes University. E & FN Spon, London. ISSN 1357-5317.
- [de Schiller 1998] de Schiller Silvia, Evans John Martin *Sustainable Urban Development: Guidelines for sustainable urban development* Urban Design International, Vol 3, N° 4, December 1990, Joint Centre for Urban Design, Oxford Brookes University. E & FN Spon.
- [de Schiller 2000] de Schiller Silvia, Evans John Martin, *Urban climate and Compact cities in Developing Countries*, pp 117-124 in Jenks Mike, Rod Burgess, *Compact Cities, Sustainable Urban Forms for Developing Countries*, , E & FN Spon, London and New York.
- [de Schiller 2015] de Schiller, S. and Evans J. M. *Proyecto Demostrativo de Edificación Sustentable*, pp 94-99, Revista Summa+ 145, Sustentabilidad y Reuso, Septiembre 2015.
- [Evans 1994] Evans J. M. and de Schiller S. *Sustainable Urban development for Haikou: design guidelines for a warm humid city* pp 165-184 in [Wiesman 1994] Wiesman B., Xiaowei L and Xiang L, Eds. *Urban design: Tropical Coastal Cities*, China Architecture and Building Press, Beijing.
- [Evans 2015] Evans J. M. and de Schiller, S, *Sustainable design and natural conditioning for a sensitive site: Seymour Airport and National Park Buildings in Galapagos*. Book of Abstracts, Architecture in (R)evolution, 31st International PLEA Congress, Passive and Low Energy Architecture, Bologna.
- [Evans 2005] Evans J. M. and de Schiller S. *La isla de calor de ciudades con clima cálido-humido: el caso de Tampico*, AVERMA Avances en Energía Renovable y Medio Ambiente, Vol 9, ISSN0329-5184.

[Evans 2005] Evans, J. M. *The Comfort Triangles, a new tool for bioclimatic design*, PhD Thesis, Technical University of Delft, Delft.

[Evans 2014] Evans, J. M. *Temperaturas interiores en vivienda en distintos climas: medición, simulación y calibración de un modelo AVERMA* Avances en Energía Renovable y Medio Ambiente, Salta.

[Givoni 1994] Givoni B, *Passive Low Energy Cooling of Buildings*, Wiley, New York

[Givoni 1998] Givoni B, *Climate Considerations in Building and Urban Design*, Wiley, New York.

[Pearce, 1990] Pearce E. A. and Smith C. G. *World Weather Guide*, Hutchinson, London.

[SENECyT 2015] Secretaria de Educación Superior Ciencia, Tecnología y Innovación, *Programa Prometeo*, retrieved 2015, <http://prometeo.educacionsuperior.gob.ec/que-es-prometeo/>

[United Nations, 1971] Koenigsberger O. H., Mahoney K. and Evans. J. M. *Climate and house Design: Design of low cost housing and community facilities*. Department of Economics and Social Affairs, United Nations Publication, ST/SOA/93, E.69.IV.11. New York.

[USGBC 2015] United States Green Building Council, *LEED NC New Construction Version 4*, USGBC, Washington D. C.

[Wunderground 2016] Weather Underground, (Seymour climate data) retrieved 2016, <https://www.wunderground.com/ec//seymour/zmw:00000.1.84001>.

A study of solar access in Bogotá: the Las Nieves neighborhood

R. Franco¹, P. Bright¹, J Benitez¹, and B. Beckers²

¹Universidad de Bogotá Jorge Tadeo Lozano
address: Carrera 4 N° 22-61, Bogotá - Colombia. <http://www.utadeo.edu.co/es>
e-mail: (ricardo.franco, p.bright, javier.benitezb)@utadeo.edu.co

²Université de Technologie de Compiègne-Sorbonne University
address: Rue Roger Couttolenc, CS 60319 60203 Compiègne – France. <https://www.utc.fr/>
e-mail: benoit.beckers@utc.fr

Keywords: *solar access, urban morphology, solar rights, energy and sun.*

Abstract. *It was during the 1970's that interest for searching and exploiting solar energy came up as a clean, safe and unlimited alternative source, as opposed to nuclear energy, coal, oil and its by-products and their environmental and speculative impact on markets. The concept of solar access was first used in the US as a way of legally protecting a building's present and future rights to sunlight availability and the collection and use of solar energy.*

This paper presents an on going research on solar access for the city of Bogotá, Colombia (4,38' North) applying the descriptive method, according to Knowles' concept of the solar envelope [Knowles 1999]. From this point of view the geometry and projection of shadows seek to establish the maximum height of buildings so that buildings access to sunlight is not obstructed.

Introduction

This article is the result of the on going research project at the Architecture Programme of the "Jorge Tadeo Lozano" University: "A study of solar access for the Las Nieves neighbourhood". Las Nieves is a traditional neighbourhood of the Colombian capital which has been object of a continuous process of urban transformation in the last 40 years, including building or renovating public space, renovation and reactivation of deteriorated areas. The consolidation of the cultural and educational uses as well as private investment have widened the commercial and real-estate offer, added to the pressure for taller buildings in order to increase density and the proposed urban renovation of this area of the city. These processes have brought, as a consequence, the construction of high rise towers of up to 60 stories in this traditional zone where the top heights were 5 stories within the neighbourhood and 20 stories on avenues as the Calle 19. The consequences of the construction of one of those new towers, the BD Bacatá, will be analysed in this article in terms of solar access (shadow projection, hours of sun, solar irradiation, and sky view factor).

Solar energy, more than any other type of renewable energy, has direct effects on shape, habitability, comfort and the volumetric planning of buildings, distance between buildings, their heights and recoils. Therefore, if a building has solar access, the energy received can be used and integrated in the building through active or passive systems with the goal of reducing CO₂ emissions and its demand of energy; trying to keep a sustainable dimension in the architecture. The use of solar energy as a main source for the human life requires a space condition, the solar access, since without it, it is not possible to reach a dimension of the urban sustainability [Cárdenas 2012].

Background

Primitive use of sunlight: orientation and passive use

The idea of solar access is older than the research projects and laws passed in the previous century. Inhabitants in ancient China, Greece, Rome and Pre-Hispanic America (all localized in the northern hemisphere) used solar energy to heat spaces in winter and to avoid overheating in summer. The technique to obtain the best from solar energy consisted in understanding that sunlight changed according to seasons, and so they acted accordingly with proper building orientation and placing windows towards the south, as well as the proper use of materials and their thermal inertia.

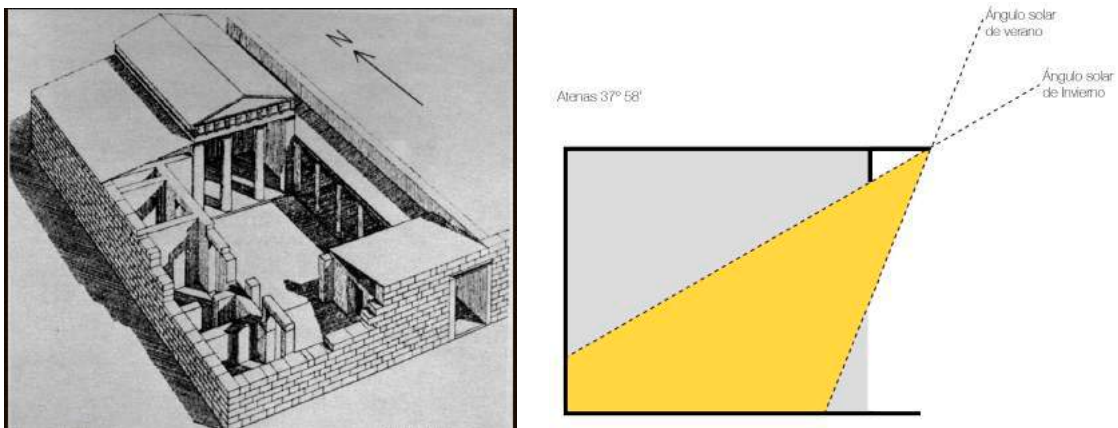


Figure 1: Greek house facing south (right), taken from [Butti 1980], page 5.
 (To the left) Bioclimatic control exercised by the portico for this latitude.

In ancient Greece, Socrates explained "In the houses that look toward the south, the sun penetrates the portico in winter, while in summer the path of the sun is right over our heads and above the roof so that there is the shade." [Butti 1980]

This Socratic principle of design served as a base for Greek architecture to gain advantage of solar resources in a passive manner, thanks to proper orientation and the effective disposition of rooms behind the portico which let the sun in during the winter while keeping the sun out in the summer.

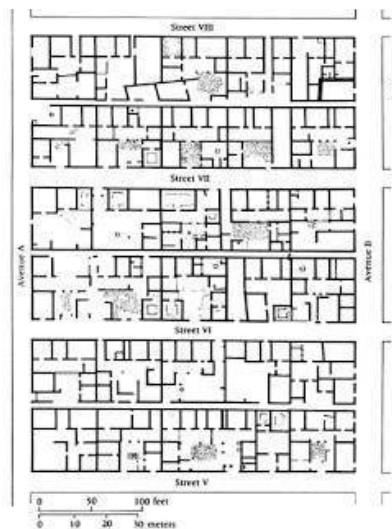


Figure 2: Plan of the city of Olynthus facing south, taken from [Butti 1980], page 6

The city of Olynthus is an example of how these principles were practiced in a dense community. Approximately 2500 people lived there with limited resources, wood for heating homes with fire was scarce and the Greeks had no glass in their windows, thus the necessity of gaining advantage with solar resources.

Solar access concept:

[McCann 2008] defines solar access as a building's continuous availability of direct sunlight without obstructions from other buildings, properties, trees, etc. Solar access is calculated using a solar path diagram for each building.

Solar access description:

According to [Muller 2009], in America every owner must have access to direct sunlight, with the right to install a device that turns solar energy into usable energy. In consequence, solar access is divided into two categories: the Solar Easement Law of 1976 concerning solar access and the Solar Rights Act of 1978 that concerns the right to install a solar energy system.

The link between urban form and solar access has not been addressed clearly or convincingly in urban standards and normativity for the design of Colombian cities. This paper seeks to address the issue of solar access and its importance for buildings and the well being of people everywhere.

Solar access study for the Las Nieves neighbourhood in Bogotá, Colombia (4°38' North)

The city of Bogotá is the capital of Colombia, located in the centre of the country on the eastern ramification of the Andes, located in 4°38' latitude North and 74° longitude West, and a height of 2650 metres above sea level (8694 ft).



Figure 3: Location of the Republic of Colombia and Bogotá city , taken from www.worldatlas.com

Bogotá has a moderately cold weather due mainly to the altitude, the average temperature is 14° C and there are no seasons or significant changes in climate. There are two periods of rain, from March to May and from September to November. The lowest temperatures happen in December and January, sometimes reaching -4° C before dawn and increasing up to 24° C at noon. With daily temperature variations of up to 12° C.

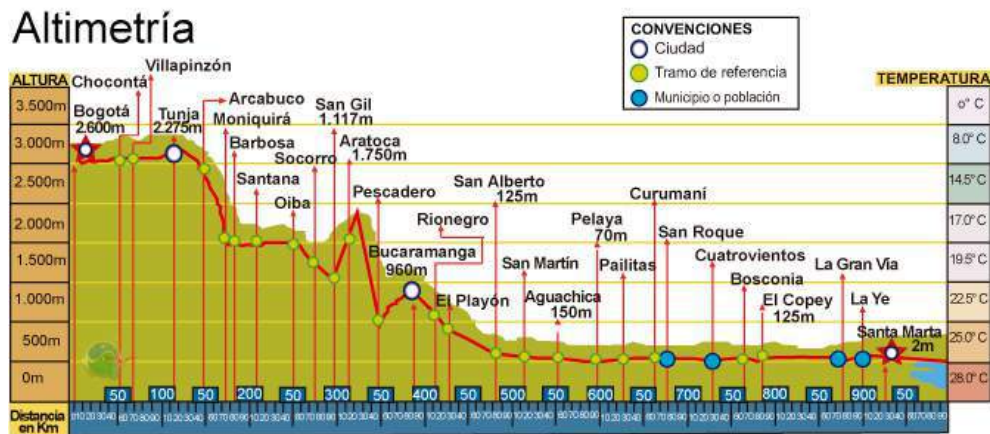


Figure 4: Altimetry Bogotá city, taken from www.destinosyplanes.com

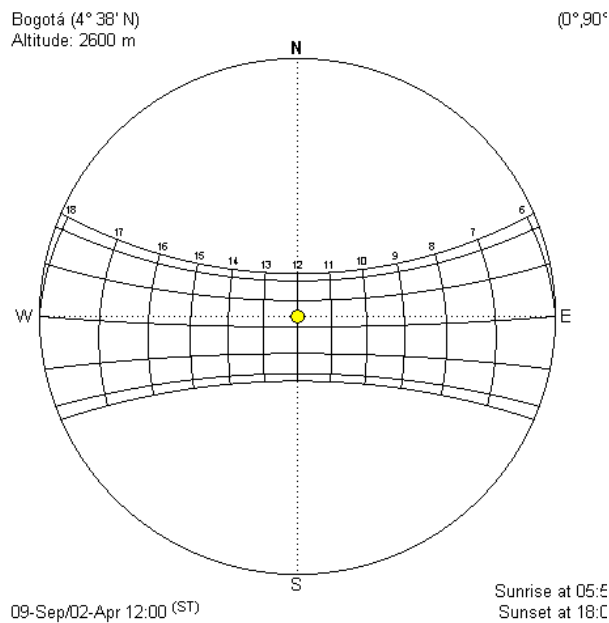


Figure 5: Solar Charter of Bogotá city, generated by the software Heliodon, [Beckers 2006]

The solar chart for Bogotá shows sunrise at 6:08 and sunset at 17:52. The height of the sun at noon is 62°, on December 21st. For the 21st of June sunrise is at 5:52, sunset at 18:08 and the sun's height is 71° at noon, establishing a 9° difference between December and June.

April 2nd and September 9th last the same, for those days the sun height is 90°. The difference between the longest day (June 21st) and the shortest (December 21st) is only 32 minutes.

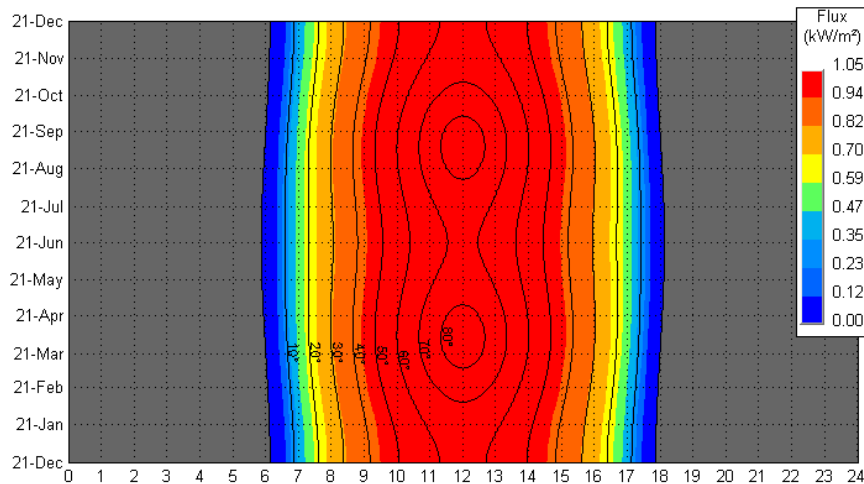


Figure 6: The isochronous projection for Bogotá, generated by the software Heliodon, [Beckers 2006]

The isochronous projection for Bogotá shows that the sun's height is above 40° during the whole year between 9:00 and 15:00. The direct solar flux exceeds 940 W/m², reaching 1050 W/m² at noon close to the equinoxes.

The need for sun and radiation in Bogotá

Givoni's higrathermic diagram for Bogotá recommends the use of passive gains in order to obtain energy within living spaces [Givoni 1969]. This extra energy can be exploited by architecture to increase inside temperature and so, without the use of other mechanisms, produce a better sensation of thermal comfort. This is particularly important due to the differences in temperature during the day.

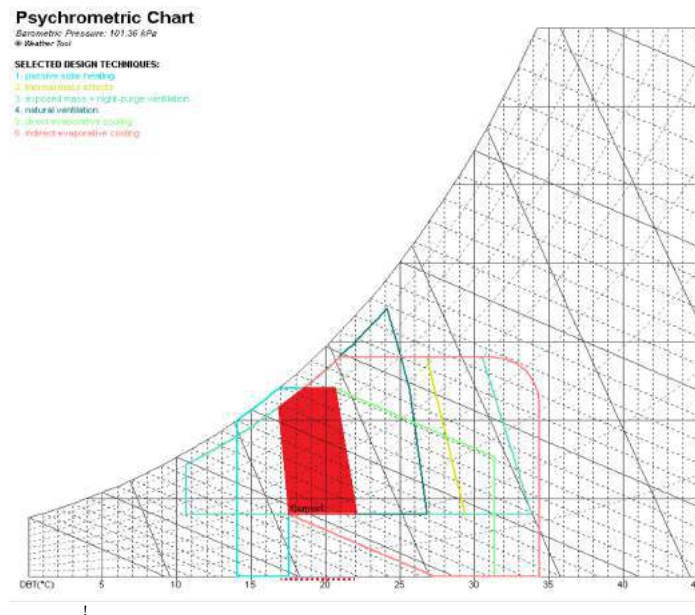


Figure 7: Givoni's higrathermic diagram for Bogotá, generated by the software Ecotect, versión 2011

According to [Knowles 1999], well-being and the joy of life are related to the sun and quality of life in our cities. The sun is an important determination in both physical and psychological comfort; it is important in architecture and can reduce public health issues.

Las Nieves

The Las Nieves Neighbourhood is linked to Bogotá's economic and cultural development. In 1598 Las Nieves was the northernmost Parish. Previously inhabited by natives, it grew since the XVII century thanks to civil and religious buildings. During the XVIII century artisans and industrial uses added to the area's religious character. In the XX century the neighbourhood was known for its cultural activity thanks to the appearance of several theatres and cinemas.

After 1970's the Las Nieves neighbourhood continues its transformation thanks to the appearance of other cultural centres and universities that keep the sector alive. New denser projects are being built now adding to the neighbourhood's potential, hence the need to include high rise buildings.

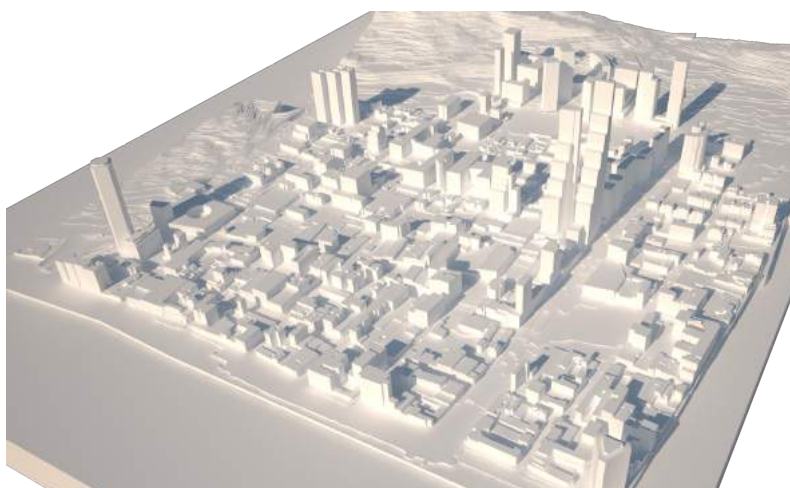


Figure 8: Images of the 3D model of the neighborhood Las Nieves

The model

These characteristics were taken into account in order to build the model

- Each floor is 3.00 metres height. There are no facade details or percentages of glass surfaces.
- All roofs were assumed as flat.
- Projects being built or already designed were included
- The model includes the terrain and mountains to the east
- The model was constructed by students within the "Espacios temporales" workshop, at the Jorge Tadeo Lozano University.
- The model consists of 632814 triangles, 308658 points and measures 1537.6 x 1153.3 x 325.4 metres.

The solar access study

The analysis was made using the descriptive method because it is one of the most important points of view in the regulations as well as the concept of solar envelope by [Knowles 1999]. From this angle the geometry and projection of shadows seek to establish the maximum height of buildings so that they do not obstruct the access of sunlight to existing buildings [Franco 2014].

Section lines

Bogotá is located in the Torrid zone, therefore there are no seasons but rainy months. The model will be analysed with the lower sun angles and the extreme periods: on December and June 21st, from 9:00 to 15:00 (These time spans are consistent with US and Australian regulations).

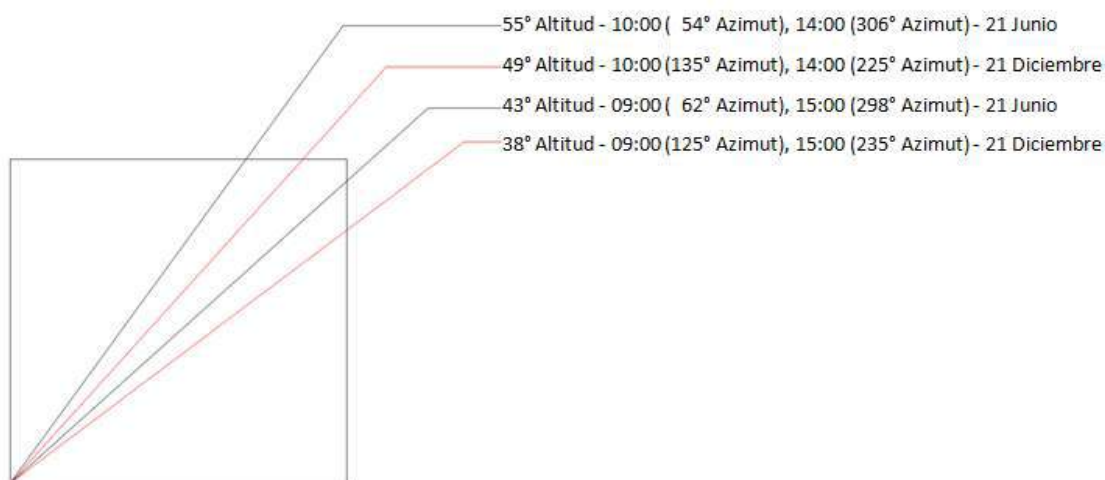


Figure 9: Section lines for Bogotá city

According to [Capeluto 2005] Section lines are used to:

- Determine solar access and rights by defining a base point in the lowest residential floor and use it to draw the section lines to limit the height of the building directly in front.
- Determine and uphold solar access and rights in public spaces: sidewalks, streets, squares and parks.

Case study: BD Bacatá Downtown Building

The BD Bacatá is being built in a lot previously occupied by the Bacatá Hotel, a 15 stories height building built by the architectural firm Meléndez Páez. The new building has multiple uses: hotel, housing, a commercial centre, office spaces and parking basements, designed by the Spanish Grupo Alonso Balaguer.



Figure 10: Plant location case study

The consequences of building a 67 floors (240 metres) building on the Calle 19 where no building is higher than 20 stories (60 metres) are shown in the following analysis. These consequences are exposed through graphic comparisons generated with the Heliodon software: shadow projection, hours of sunlight on facades and sidewalks, solar irradiation and the sky view factor taken on several points on the street.

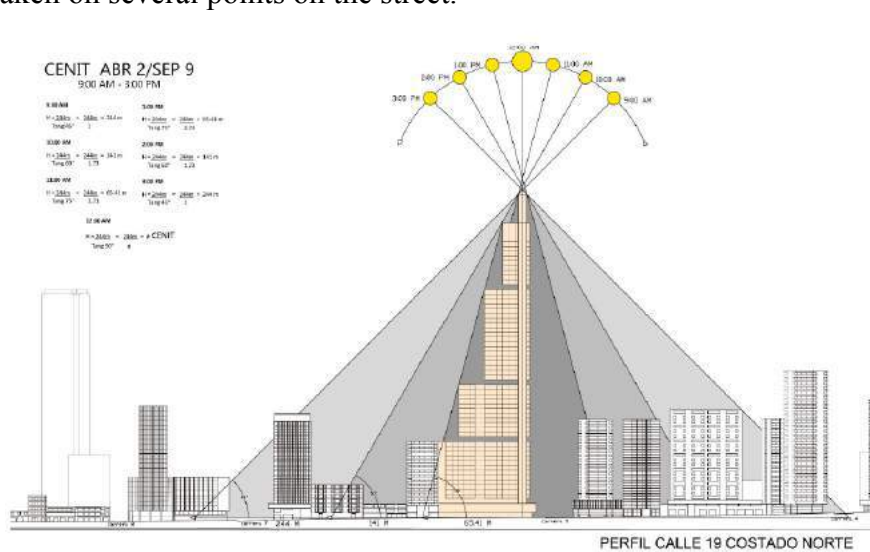
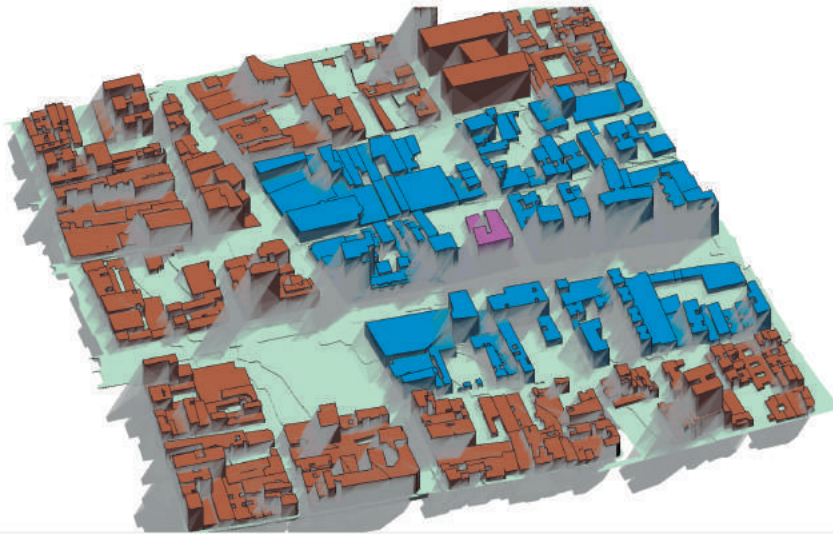


Figure 11: Shadow projection BD Bacatá Downtown on Calle 19, April 2, sun height 90. Graphic by students: Martín Diego, Martínez José y Riapira Steven

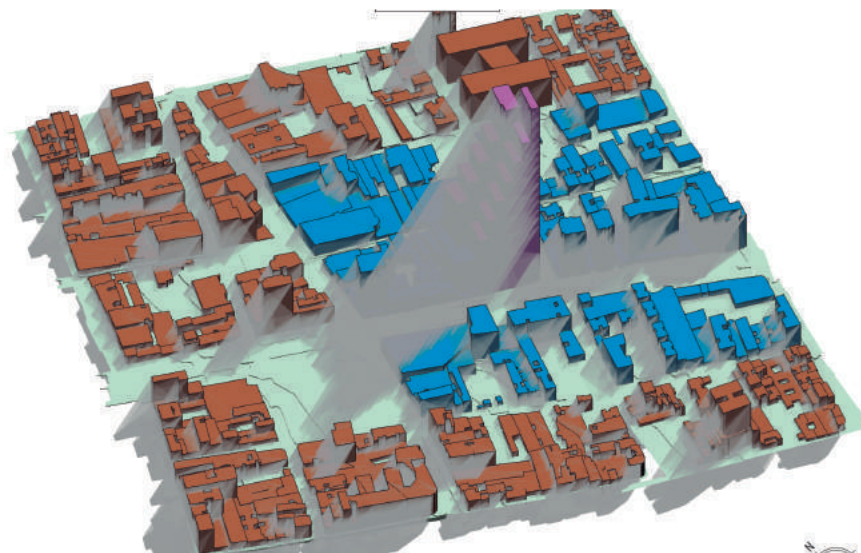
Shadow projection comparison on June 21st, at 9:00 a.m.

The graphs for the 21st of June at 9:00 a.m., show how the new BD Bacatá's shadow (below) is projected to the Southeast onto Calle 19 and some neighbouring buildings, even reaching the 7th avenue to the west. The projected shadow is approximately 260 metres in length. In the previous image the demolished hotel and its neighbours cast a uniform shadow onto Calle 19th, without affecting other buildings.

Comparativo proyección sombras.



Antiguo Hotel Bacatá
Fecha correspondiente a 21 de Junio
Hora 9:00 am



Nuevo BD Bacatá
Fecha correspondiente a 21 de Junio
Hora 9:00 am



Figure 12: Comparison between shadow projections on June 21st, at 9:00 am

Shadow projection comparison on June 21st, at 3:00 p.m.

The graphs show the new BD Bacatá's shadow on Calle 19 to the Southeast reaching some of the neighbouring buildings. The previous hotel's 48-metre shadow does no affect other buildings.

Comparativo proyección sombras.

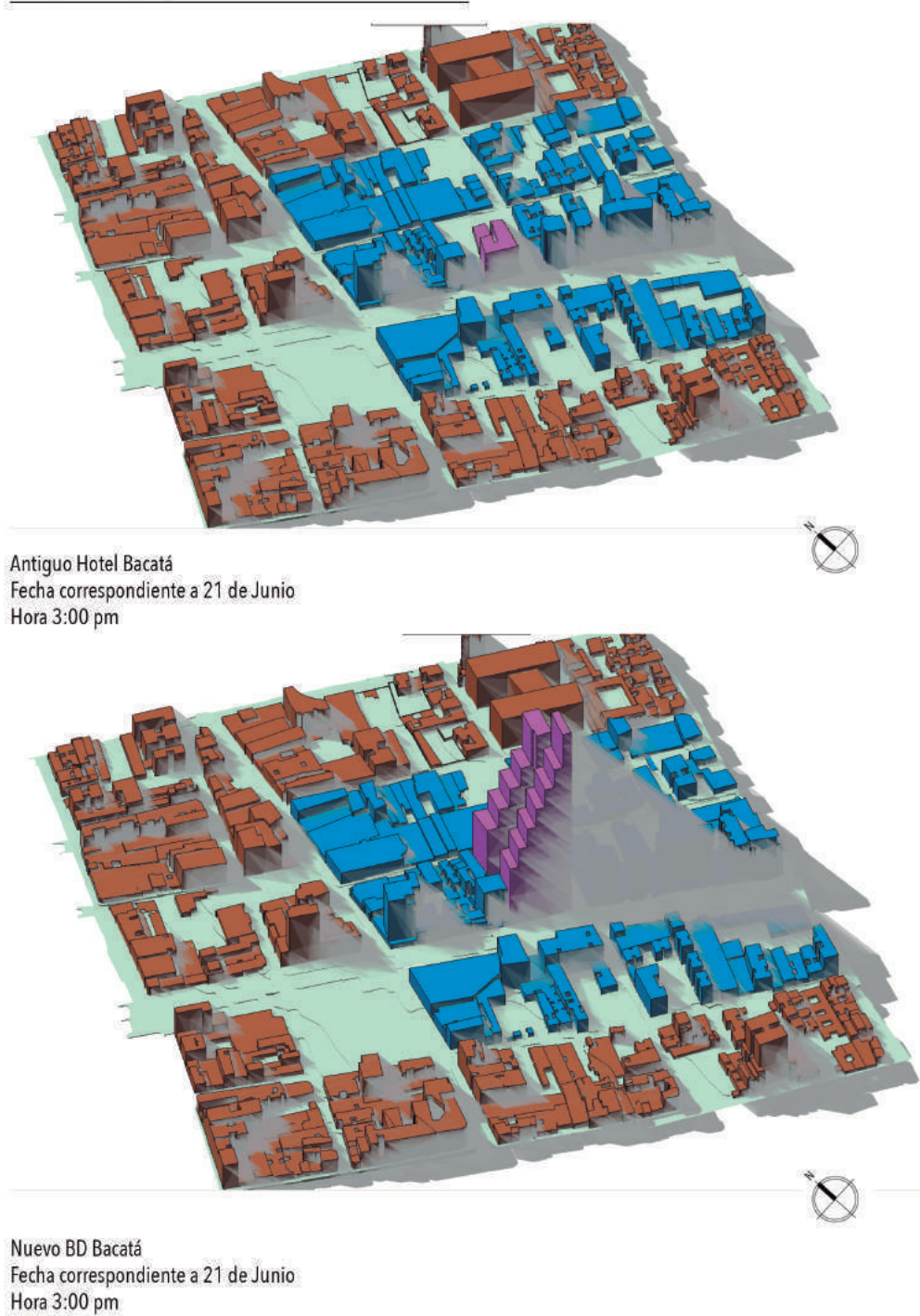
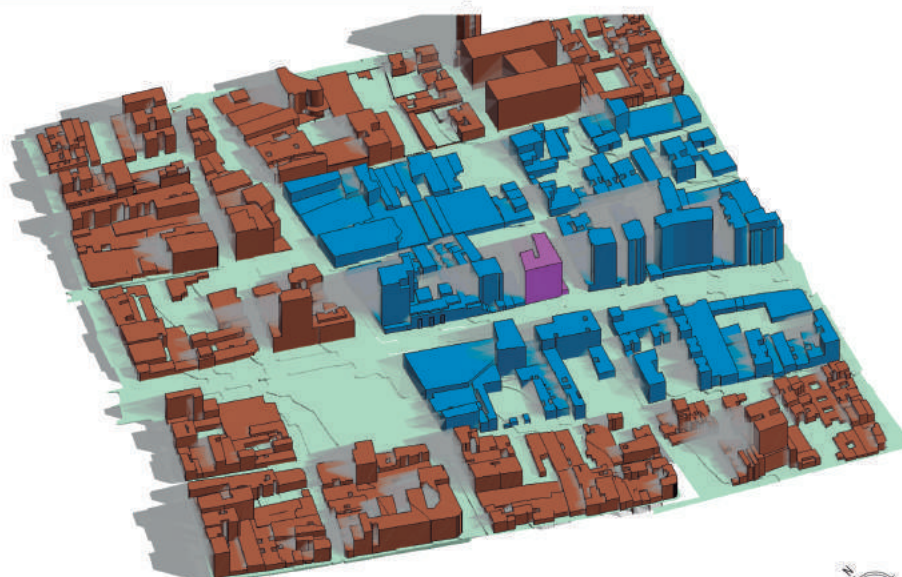


Figure 13: Comparison between shadow projections on June 21st, at 3:00 pm

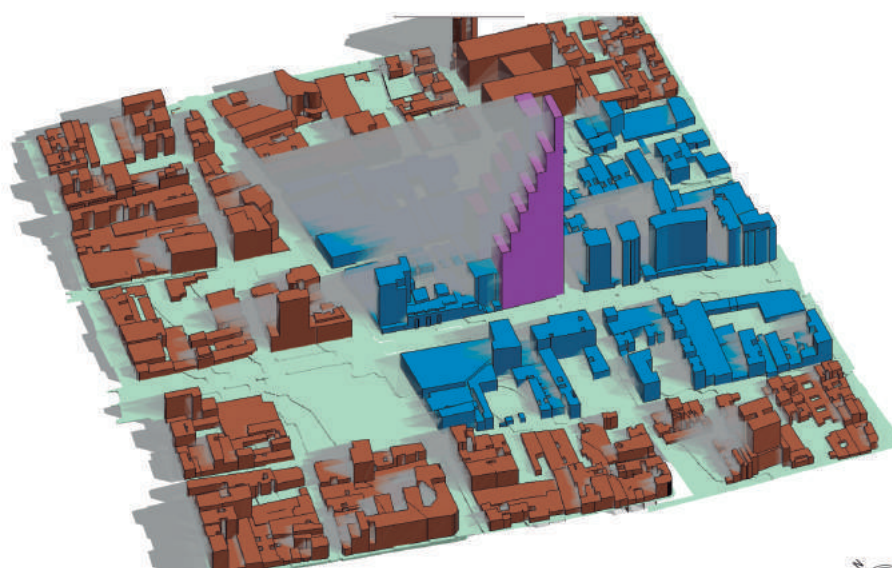
Shadow projection comparison on December 21st, at 9:00 a.m.

The projected shadows of the BD Bacatá move to the Northwest affecting many of the neighbouring buildings, sidewalks and streets. The 307 metres extended shadow reaches Carrera 8a and 21st street. The previous building's extended shadow was 57 metres long, reaching 20th street.

Comparativo proyección sombras.



Antigo Hotel Bacatá
Fecha correspondiente a 21 de Diciembre
Hora 9:00 am



Nuevo BD Bacatá
Fecha correspondiente a 21 de Diciembre
Hora 9:00 am



Figure 14: Comparison between shadow projections on December 21st , at 9:00 am

Shadow projection comparison on December 21st, at 3:00 p.m.

The 307 metres projected shadows of the BD Bacatá to the Northeast reach Carrera 3rd and Calle 21st. The old hotel's shadow reached up to Carrera 5a.

Comparativo proyección sombras.



Figure 15: Comparison between shadow projections on December 21st, at 15:00 pm

Comparison of hours of sun on surrounding facades and rooftops

The following graphs show the number of sunlight hours on facades and rooftops surrounding the case study. In June the demolished hotel the rooftops and north facades oriented to Calle 20 received between 10 and 12 hours of sun. With the BD Bacatá highrise the same rooftops and facades receive between 2.5 and 11 hours of sun, which means an average loss on 38.7%.

The situation for December is worse. The facades on Calle 19 receive between 6 to 11 hours of direct sun, a reduction of 17% compared to the demolished hotel. The facades on Carrera 5 receive between 0 to 5 hours of sun, compared to 2.6 to 6 in the previous situation. On average this means a loss of 71.3% in hours of direct sunlight, on December 21st.

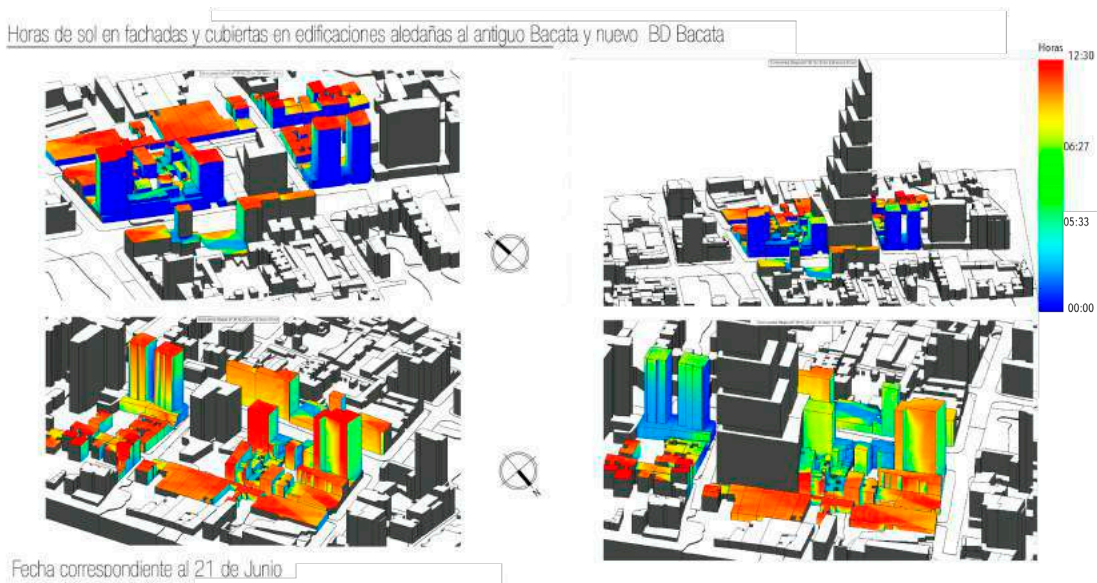


Figure 16: Comparison of hours of sun on surrounding facades and rooftops on June 21st

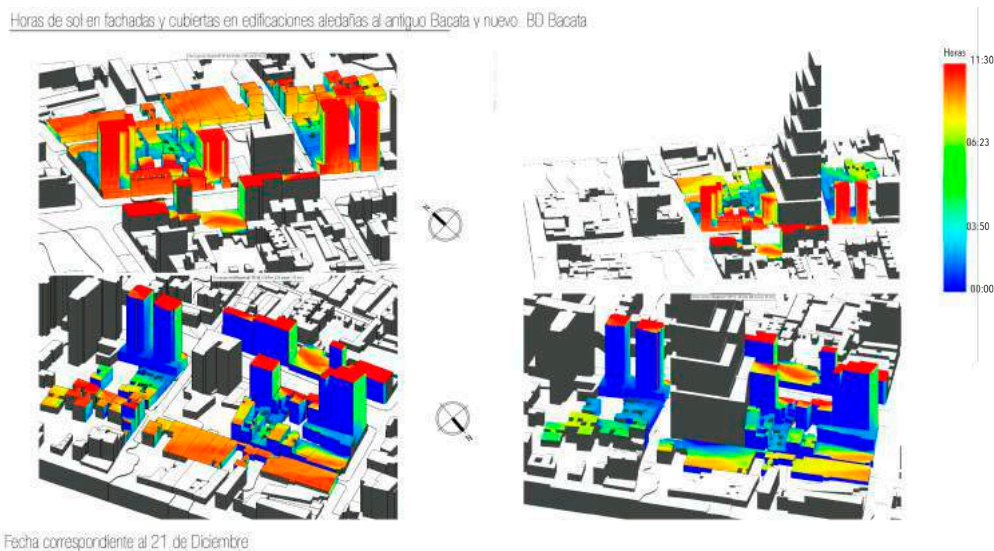


Figure 17: Comparison of hours of sun on surrounding facades and rooftops on December 21st

Solar irradiation comparison on surrounding facades and rooftops on June 21st

For this day the BD Bacatá affects the surrounding buildings, implying losses of up to 37% hours of sunlight and up to 50% in solar radiation. No evident losses occur on Carrera 5ta or Calle 20.

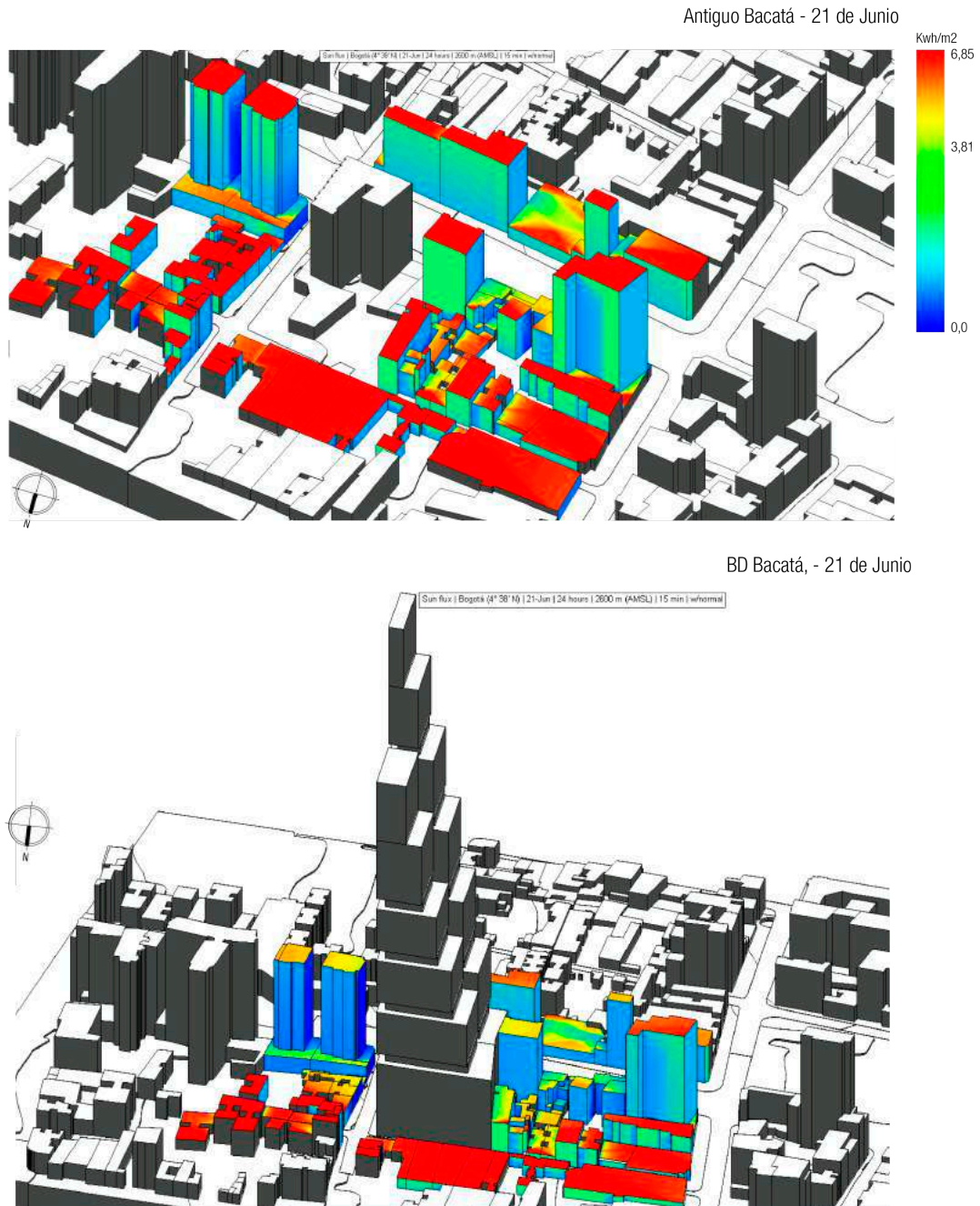


Figure 18. Solar irradiation comparison on surrounding facades and rooftops on June 21st

Solar irradiation comparison on surrounding facades and rooftops on December 21st

For this day the solar irradiation simulation results are contrasted, with less losses on neighbouring rooftops, between 10.5% reduction of sunlight and 33.6% radiation reduction. More losses occur then on Calle 20 where the rooftops receive up to 75% less energy, 32% less sunlight and 28% radiation. The worst situation occurs at the corner of Carrera 5ta and Calle 20 where the reductions in energy are 49.5% hours of sunlight and 50.5% in solar radiation.

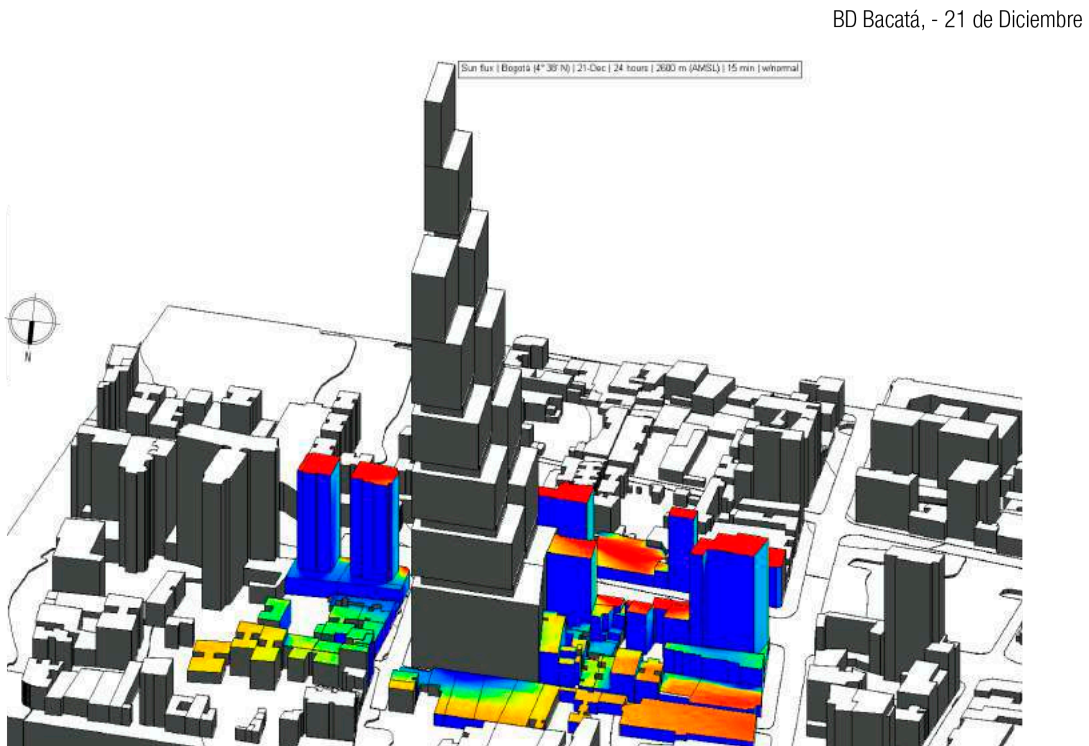


Figure 19. Solar irradiation comparison on surrounding facades and rooftops on December 21st

Comparison of sun hours on sidewalks

The building of the BD Bacatá skyscraper, in comparison to the demolished hotel, implies a reduction in hours of sun on sidewalks of 11.3% for the 21st of June. Stereograph 3 shows a reduction of sun on the sidewalk from 1 hour 45 minutes to zero. The problem is similar on December 21st, showing a reduction of 42.42% of sun reduction, as well a reduction from three and a half hours to zero in graph 2.

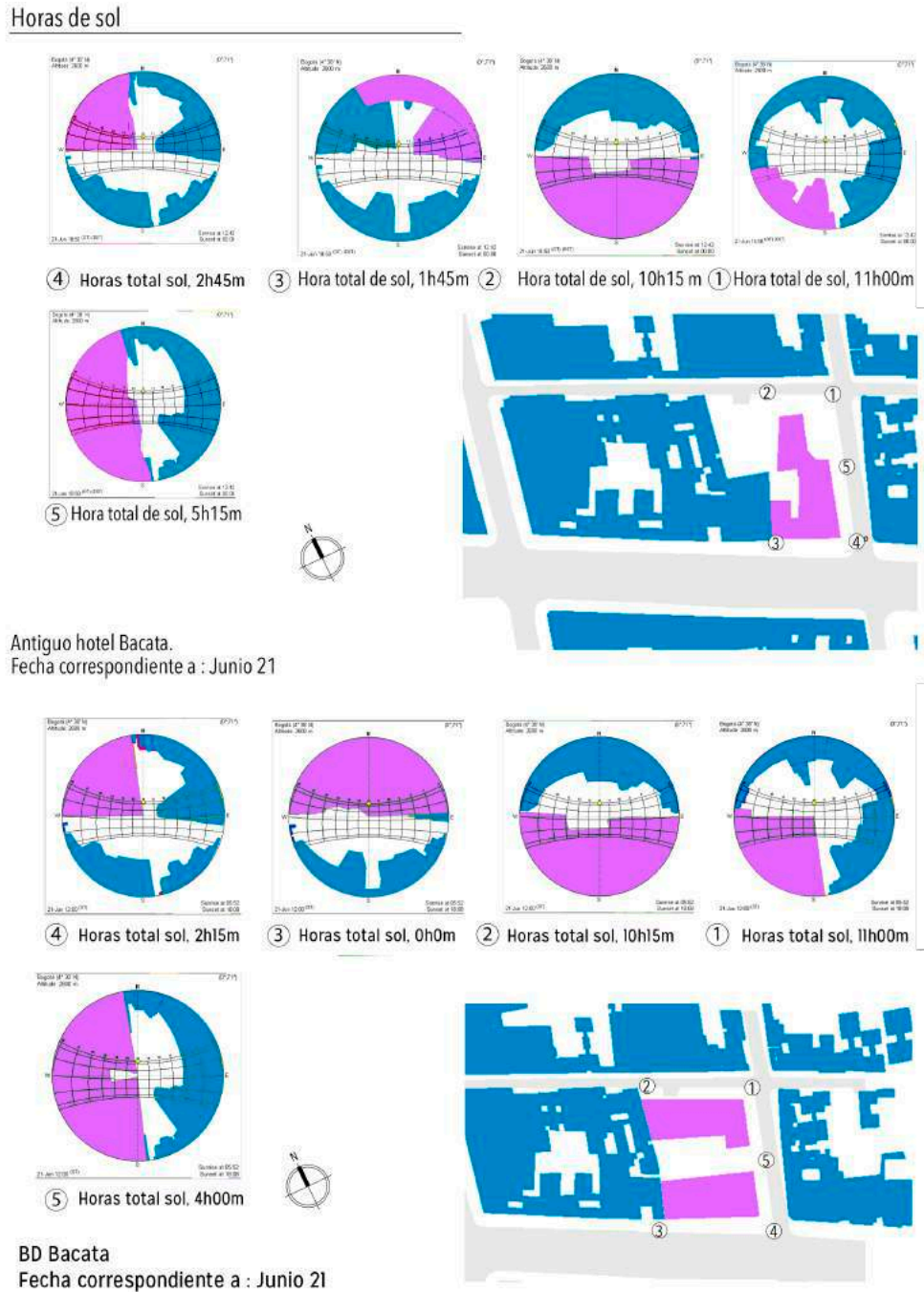


Figure 20: Comparison of sun hours on sidewalks on June 21st

Horas de sol

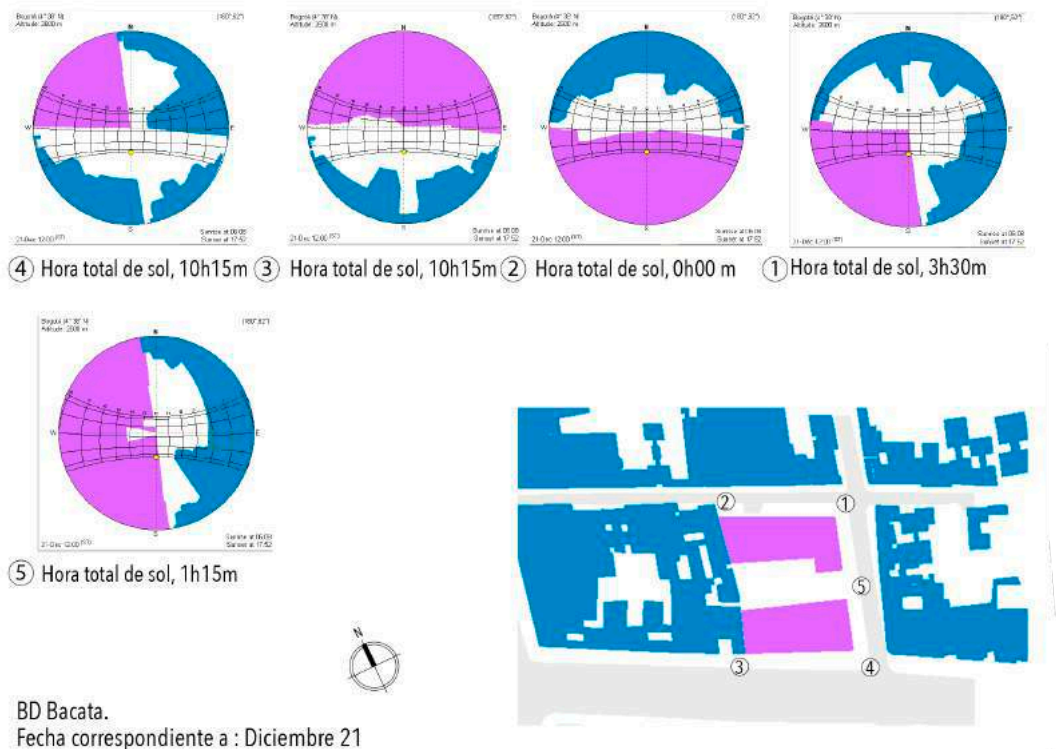
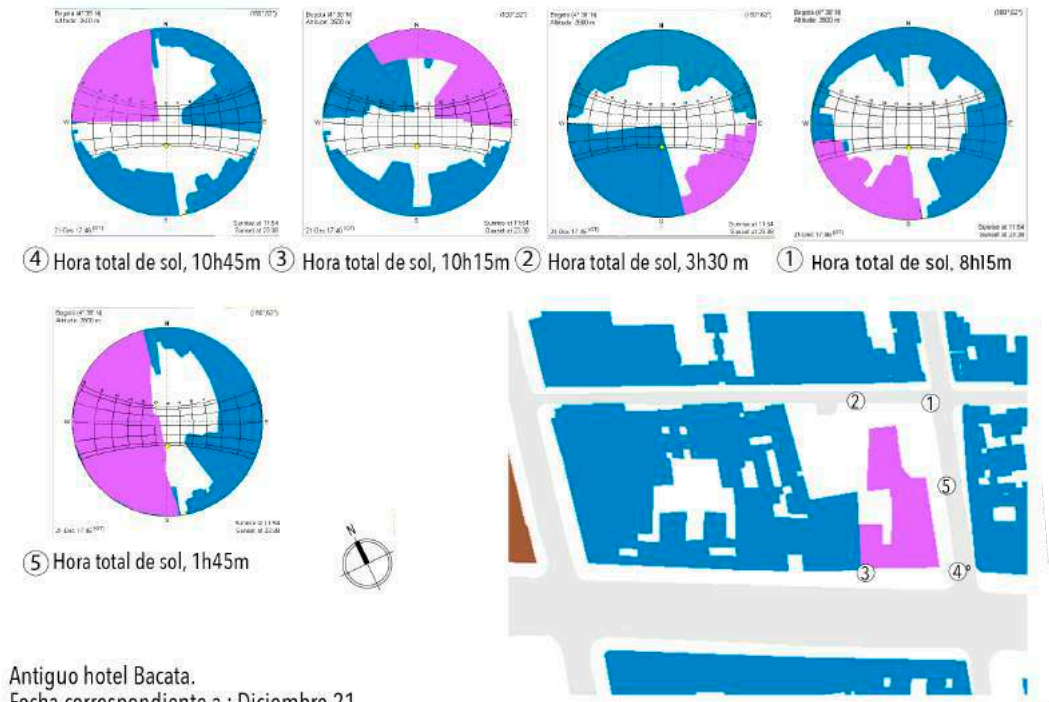


Figure 21: Comparison of sun hours on sidewalks on December 21st

Sky view factor

These graphs show the comparison between the demolished hotel and the new BD Bacatá building and evidence a maximum reduction of 23.3% in sky view factor. The factor varies according to the relative distance to the new building.

Factor de vista de cielo, antiguo hotel Bacata.



Figure 22: Sky view factor hotel Bacatá

Factor de vista de cielo, nuevo BD Bacata.

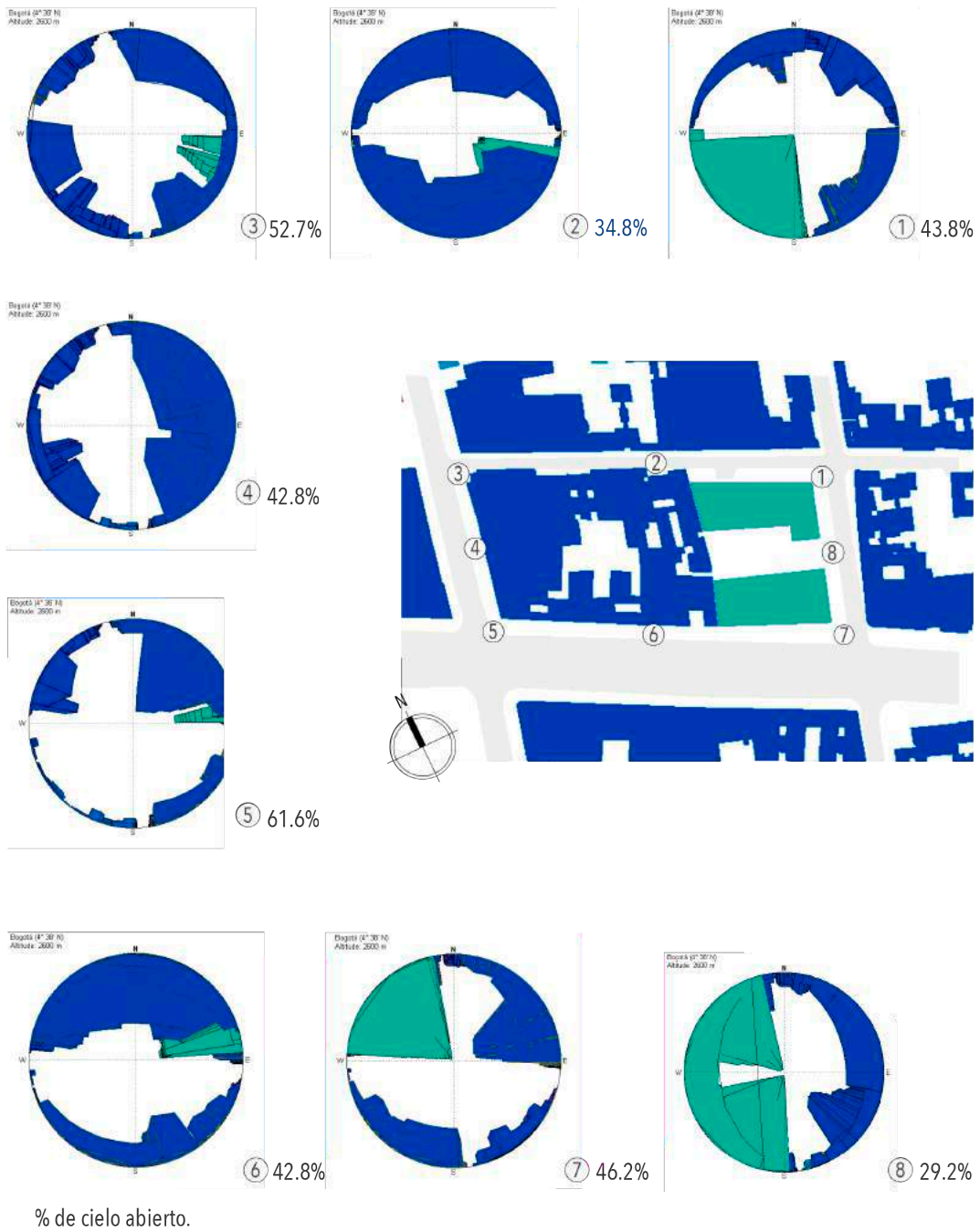
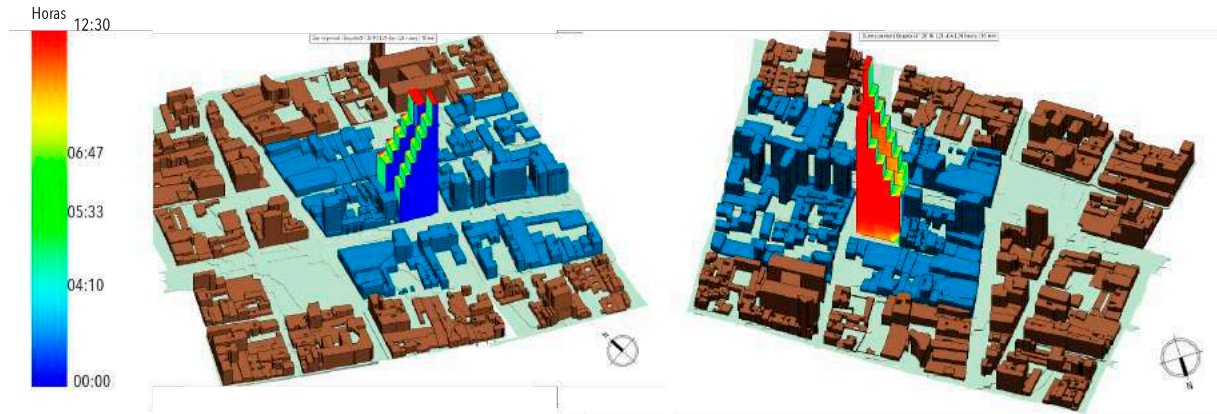


Figure 23: Sky view factor BD Bacatá

BD Bacatá Analysis of sunlight and irradiation hours on June 21st

On this day the BD Bacatá receives a maximum number of hours of sunlight, due the position of the sun for this period. The north facing facades and higher rooftop receive the highest amount of sunlight, the lower rooftops receive up to 50% less sunlight.

Horas Sol Bd Bacata, para el periodo correspondiente a 21 de Junio.



KWH /m2 BD Bacatá, para el periodo correspondiente a 21 de Junio.

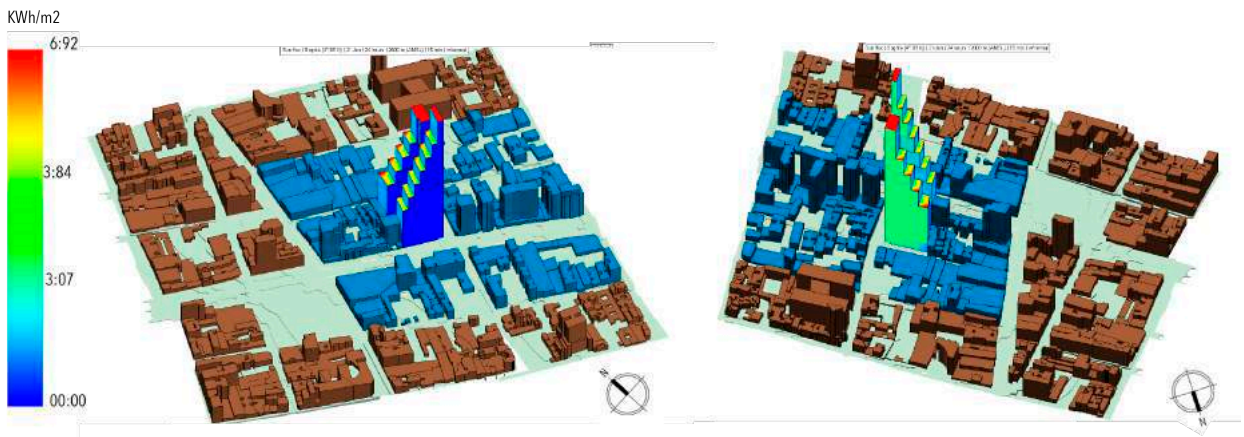


Figure 24: BD Bacatá sunlight and irradiation hours on June 21st

BD Bacatá Analysis of sunlight and irradiation hours on December 21st

On December 21st the buildings situation changes, although it is not absolutely inverse. Energy is concentrated on the southern facades and rooftops, with the same reduction in the lower rooftops.

Horas Sol Bd Bacata, para el periodo correspondiente a 21 de Diciembre.



KWH/m2 BD Bacatá, para el periodo correspondiente a 21 de Diciembre.

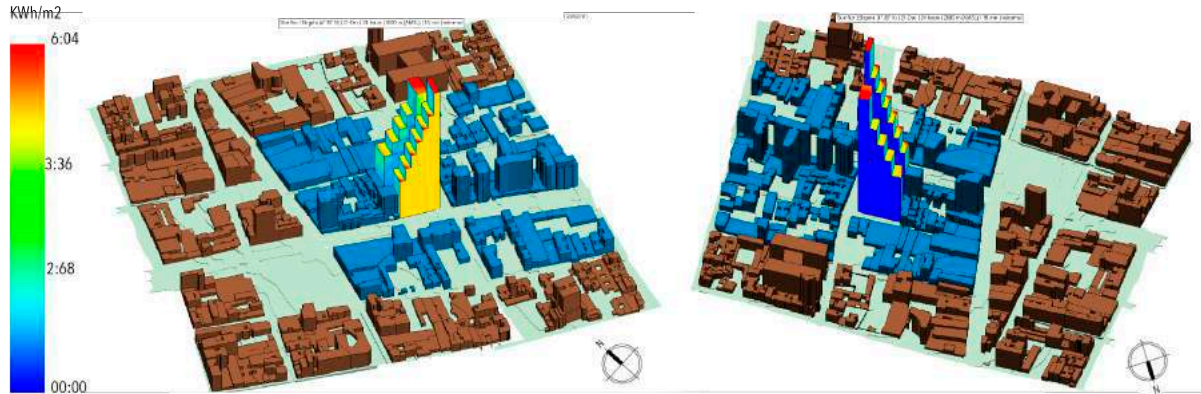
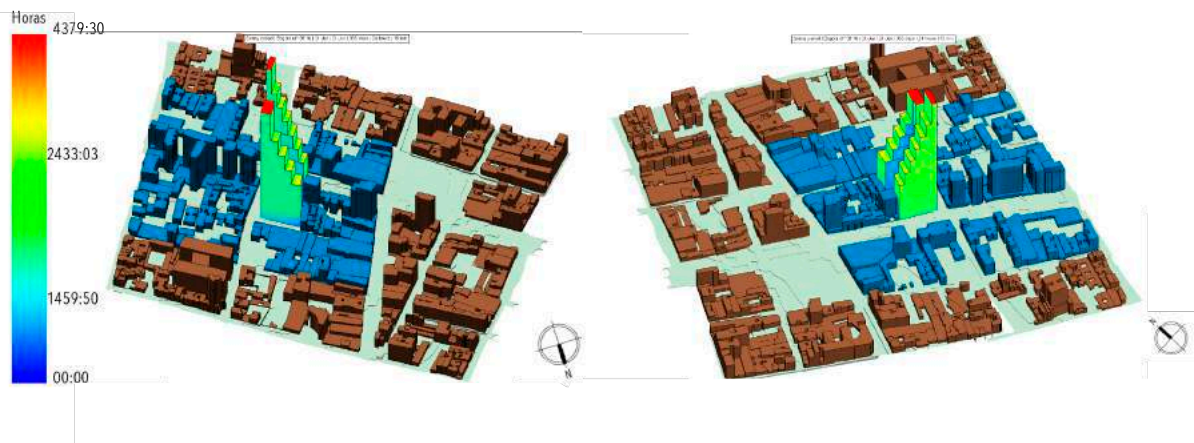


Figure 25: BD Bacatá sunlight and irradiation hours for the 21st of December

BD Bacatá Analysis of sunlight and irradiation hours during the whole year

According to the sunlight and irradiation analysis the BD Bacatá is a better solution as an architectural project than as an urban solution to existing energy conditions. The buildings largest facades oriented 120° North allow the building benefit from sunlight during the whole year, reaching an energy balance between the north and south facades.

Promedio anual de horas de sol.



Promedio anual de KWH/m2.



Figure 26: BD Bacatá sunlight and irradiation hours during the whole year

Conclusions

- According to the case study, the Las Nieves neighborhood, we can conclude that the building of the BD Bacatá has a negative effect on the surrounding urban fabric in key factors such as direct sunlight hours, sky view factor and solar irradiation.
- The new BD Bacatá building has a negative energetic impact on the surrounding urban fabric. The sky view factor from the sidewalks is reduced in 23.3%, its orientation and form affect the hours of sunlight on the facades and rooftops on Carrera 5 where the average loss of sunlight hours is of 71.3% on December 21st.
- The shadow projected by the new BD Bacatá during the year, specially during the cold days, prevents the passive solar gains required by the neighbouring buildings to increase their inside temperature, affecting social dynamics, comfort and health of the inhabitants.
- The buildings around the new BD Bacatá receive between 38.7% and 71.3% less hours of sun compared to the demolished Bacatá Hotel, designed on a platform and tower typology that permitted a higher solar access to the neighbouring buildings.
- The BD Bacatá's design consists of two towers facilitating shadows between them, decreasing possible sunlight and irradiation hours by 3.6% and 6% respectively. Under the same analysis, the building decreases sunlight by 6.8% and radiation by 7.4% in a radius close to 150 metres. It can be argued that the BD Bacatá is better as an architectural project than as an urban project in its response to existing energy conditions.
- The construction of the new building of BD Bacatá in Las Nieves neighborhood leads to at least two types of definitive reflections for growing and densification of the city; but this can be addressed in future articles. ¿What is the maximum possible height for new buildings in the Las Nieves Neighborhood according to US or Australian policies? ¿If high-rise buildings are permitted, how much free public space should be proposed below the buildings' projected shadow?
- As a final conclusion it can be said that taking into account the analysis above, the initial hypothesis is confirmed: The solar energy, more than any other type of renewable energy has direct effects on shape, habitability, comfort and the volumetric planning of our buildings, the distance between buildings, their heights and recoils. Therefore, if a building has solar access, the energy received can be used and integrated in the building through active or passive systems with the goal of reducing CO2 emissions and its demand of energy; trying to keep a sustainable dimension in the architecture.

I would like to express my sincere gratitude to all of those have participated in the making of this article.

Dirección de Investigación, Creación y Extensión

Facultad de Artes y Diseño and Programa de Arquitectura de la Universidad de Bogotá Jorge Tadeo Lozano.

Javier Benitez , Omar Niño, Ángela Pachón research assistants

Student workshop Espacios temporales, period 2016-1:

ALVARADO CARRILLO, DANIELA
AMAYA SABOGAL, WILVER CAMILO
ARIAS LUQUE, NICOLÁS ALEJANDRO
BORDA RUEDA, ADRIANA MILENA
CAMACHO GARCÍA, JOHANNA ANDREA
CASTRO LATORRE, MARIO ADRÉS
CRUZ MUSUSU, MARÍA CAMILA
GARAVITO LÓPEZ, JONATHAN CAMILO
GARCÍA BETANCUR, PAULA ANDREA
GUZMÁN RAMÍREZ, LEONARDO ANTONIO
LUNA MOTATO, JOHANNA CAROLINA
MOSQUERA CASTELLANO, JORHELIS G.
OVALLE BARRERA, DANIEL ENRIQUE
PERDOMO BARBOSA, MARÍA CAMILA
PIÑEROS AGUDELO, ANDREA CATALINA
PRIETO ARÉVALO, KATHERINE JULIETTE
RAMÍREZ CÁRDENAS, ÁNGELA PATRICIA
RAMÍREZ RIAÑO, DANIELA
TERREROS PERDOMO, SEBASTIÁN E.
TORRES NARANJO, LAURA NATALIA
VILLALBA MORENO, JUAN DAVID
VITERI TORO, LUISA FERNANDA
ZULETA OLAYA, ANDRÉS FERNANDO

And finally students :

MARTÍN BUITRAGO, DIEGO ALBERTO
MARTÍNEZ MENESES, JOSÉ LUIS
RIAPIRA MORENO, LUDWIG STEVEN

References

- [Beckers 2006] Benoit Beckers & LucMasset. *Heliodon2*. software and user's guide, www.heliodon.net. (2006)
- [Butti 1980] Ken Butti. *A Golden thread : 2500 years of solar architecture and technology*. Palo Alto: Cheshire Books ; New York : Van Nostrand Reinhold. (1980)
- [Cárdenas 2012] Luz Cárdenas & Paula Uribe. *Acceso solar a las edificaciones: El eslabón pendiente en la legislación urbanística chilena sobre la actividad proyectual*. Revista de Urbanismo, 14 (26), Pág. 21-42. doi:10.5354/0717-5051.2012.20922. (2012)
- [Capeluto 2005] Capeluto, G., Yezioro, A., Bleiberg, T. &Shaviv, E. *From computer models to simple design tools: solar rights in the design of urban streets*. Cominiación presentada en: Ninth International IBPSA Conference. Montréal, Canada, (2005, Agosto).
- [Franco 2014] Ricardo Franco. Tesina: Acceso solar: estudio comparativo de acceso solar por el método descriptivo entre las ciudades: Jerusalén, Israel (31,8' Norte) y Bogotá, Colombia (4,38' Norte). Universidad Politécnica de Cataluña, Barcelona. (2014)
- [Knowles 1999] Ralph Knowles. *The Solar Envelope*. California, USA. University of Southern California. [en línea][consulta: 19 mayo 2014] Disponible en: http://www-bcf.usc.edu/~rknowles/sol_env/sol_env.html. (1999).
- [McCann 2008] ColleenMcCann. *A Comprehensive Review of Solar Access Law in the United States*. Florida. Ed., Florida Solar Energy Research and Education Foundation. (2008).
- [Muller 2009] Hannah Muller. "Solar Access: Recommendations for the City and County of Denver," U.S. Department of Energy: 5. (2009).

Environmental quality at district scale: A transdisciplinary approach within the EUREQUA project

Gauvreau B.¹, Guillaume G.¹, Can A.¹, Gaudio N.², Lebras J.², Lemonsu A.², Masson V.², Carissimo B.³, Richard I.⁴ and Haouès-Jouve S.⁵

¹ LUNAM, Ifsttar, Laboratory of Environmental Acoustics (LAE)
CS4, 44344 Bouguenais Cedex, France
{benoit.gauvreau, gwenael.guillaume, arnaud.can}@ifsttar.fr

² Météo-France, CNRM/GMME/TURBAU, CNRS
BP 45712, 31057 TOULOUSE Cedex 1, France
{noemie.gaudio, julien.lebras, aude.lemonsu, valery.masson}@meteo.fr

³ CERE, ENPC, EDF R&D,
6 Quai Watier, 78400 CHATOU Cedex, France
bertrand.carissimo@enpc.fr

⁴ Environnons consulting
<http://www.tfconsultant.fr/nous-sommes/isabelle-richard>
environnons@gmail.com

⁵ Université J. Jaurès, LISST
5 Allée A. Machado, 31000 Toulouse, France
sinda.haoues-jouve@univ-tlse2.fr

Keywords: Environmental Physics, Acoustics, Urban Climate, Experiment, Simulation.

Abstract. *This paper presents a research project entitled EUREQUA (Multidisciplinary Assessment and Environmental Requalification of districts) that adopts an original methodological approach relying on a multidisciplinary team of researchers in physics, environmental, human and social sciences (geographers, sociologists, atmospheric physicists, acousticians, architects, etc.) in collaboration with officials of urban living. The EUREQUA project (2012-2017) implements a transdisciplinary approach because it focuses on 3 main observables (climate comfort, air quality and sound environment) and because it combines experimental, numerical and statistical methods. This paper focuses on one district particularly studied within the EUREQUA project, both experimentally and numerically. This paper also briefly expose the methodology and how qualitative and quantitative results are jointly processed and combined in order to make environmental criteria emerge in scenarii conception, through statistical data cross-analysis, feedback meetings with inhabitants and participative workshops.*

15 Introduction

Together with issues such as access to natural spaces and amenities, electromagnetic radiation exposure and other psycho-socio-economic parameters, several physical topics contribute strongly to the environmental quality of urban spaces, *e.g.* air quality, climate comfort and sound environment (“soundscape”). This is especially the case at the *district scale* that is both a fundamental living territory for the inhabitants and a privileged public action area. Thus a current research project entitled EUREQUA (Multidisciplinary Assessment and Environmental Requalification of districts) is currently carried out (2012-2017). It adopts an original methodological approach relying on a *multidisciplinary* team involving researchers in physics and environmental sciences (atmospheric physicists, fluid mechanics, acousticians, geographers, etc.), researchers in human sciences (environmental psychologists, sociologists, architects, urbanists, etc.) and professional partners (design offices, technical consultants) in collaboration with public stakeholders of urban living. The first phase of the project led to the selection of three relevant districts in Toulouse, Paris and Marseille (France), namely those with specific environmental nuisances (microclimate, noise, air pollution, road traffic...), social and morphologic differentiations (private buildings, individual houses, social housing...), and potential rehabilitation projects (areas likely to be re-qualified in the medium term). The concept of environmental quality of life has then been addressed by combining approaches from two different scientific traditions: *(i)* a geographical and social approach mobilizing different techniques of social surveys to understand how people perceive the environmental quality of their district, and *(ii)* an approach based on measurements and numerical modelling of physical phenomena in urban environment (microclimate, noise, air quality), their interactions and impacts [Richard et al. 2013]. For more information: <http://w3.lisst.univ-tlse2.fr/programmes/eurequa.htm>

The crucial stage of the research project was to conceive a strong interdisciplinary protocol and to carry out *in-situ* campaigns that combine measurements (urban climatology, acoustics, and air pollution) and surveys (questionnaires) in the three selected districts. The project also includes an important part of numerical development in order to model, with a fine spatial scale, the urban microclimate, air pollutant diffusion and acoustic propagation. This paper focuses on one district studied within the EUREQUA project (in the city of Toulouse), both experimentally (Section 2) and numerically (Section 3). Finally, this paper will briefly expose the EUREQUA methodology, *i.e.* how all those qualitative and quantitative results are currently jointly processed and combined in order to make environmental criteria emerge in *scenarii* conception, through statistical data cross-analysis, feedback meetings with inhabitants and participative workshops (Section 4).

25 In-situ measurements

2.15 Design of experiments

An interdisciplinary field experiment associating researchers in environmental, human and social sciences was carried out in a district of the city of Toulouse (France). The area covered about 1 km x 0.5 km and was composed of different urban fabrics (Figure 1). From January to June 2014, a permanent network was setup, composed of 10 weather stations recording near-surface temperature, humidity, wind speed and direction, and completed by 1 roof-level reference station in order to document larger scale atmospheric variables including the incoming short- and long-wave radiation (Figure 2). Moreover, 3 intensive observational periods (IOP) were conducted in January, April and June 2014 on the district of the city of Toulouse. For 3 successive days, every 3 hours, mobile measurements of temperature,

humidity and wind were continuously recorded along a predefined itinerary through the district, with a GPS recording associated. Furthermore, black and grey globes were used to appreciate the “perceived” temperature (Figure 3).



Figure 1 : EUREQUA Project, district of Bordelongue in the city of Toulouse (F); (a) satellite view (www.geoportail.gouv.fr) ; (b) cartographic representation after importation from IGN database via OrbisGIS, SIG validation and vegetation enrichment (<http://orbisgis.org>)



Figure 2 : EUREQUA Project, in-situ experimental campaign; fixed sensors



Figure 3 : EUREQUA Project, in-situ experiment; urban climate, air quality and acoustic mobile sensors

These atmosphere-related observables have been completed by infrared mobile measurements through a dedicated camera (Figure 3). Additional atmospheric measurements have been carried out to quantify air quality (NOx), through fixed sensors (Figure 2) and mobile sensors, *i.e.* embedded on pedestrian system (Figure 3), on probe balloon and on equipped vehicle (Figure 4). Regarding acoustic observables, each sound level meter (fixed or mobile) was also synchronized to GPS data logger and configured to give access to L_{eq1s} for all $\frac{1}{3}$ octave bands in the range [50Hz – 20kHz]. This allowed the extraction (or calculation) of classical and original sound indicators (See Section 2.2).



Figure 4 : EUREQUA Project, in-situ experimental campaign; probe balloon and vehicle embedded sensors

Finally, during specific measurements periods identified as “instrumented and commented walks”, the inhabitants completed a social survey (simultaneously to measurements) about their feeling perception at some specific “stop points” (previously identified through collaborative diagnostics together with inhabitants [Berry-Chikhaoui et al. 2014]), in terms of environmental comfort assessment related to climate, air quality and sound (Figure 5).



Figure 5 : EUREQUA Project, in-situ experimental campaign; “environmental quality” questionnaires

During several days and 3 times per day, some groups formed by scientists and inhabitants walked along a defined itinerary through the chosen districts. While physical scientists working on urban climate, noise and air pollution collected continuous data (leading to temperature, humidity, wind, sound and air pollutants indicators, see Figure 3), the social scientists were conducting a survey with the inhabitants through a questionnaire administered at each relevant place of the itinerary (Figure 5). After each “Instrumented and commented walks”, a focus group was carried out with the same participants to deepen and broaden the issues raised in the questionnaire. Note that, during the walk (about 1h, *i.e.* about 2-3km), the climate, air quality and sound environment are assumed to be “frozen” and representative of the considered period. This strong assumption can sometimes mask some specific and stochastic events such as wind gusts, air pollution fluctuations, noisy emergences, etc. Finally, for each district and for each intensive observation period (IOP), additionally to fixed measurements (Figure 2), this experimental protocol allowed collected about 20 “instrumented walks” (*i.e.* mobile measurements, see Figure 3) and about 9 “instrumented and commented walks” (*i.e.* mobile measurements + synchronous questionnaires, see Figure 5) for each 3-day IOP.

2.25 Data post-processing and analysis

The data analysis of urban climate has first focused on the objective detection of a microclimate variability at this study scale, which is assumed to combine the influence of synoptic meteorological conditions and the effect of urban landscape heterogeneities [Le Bras 2015]. A robust statistical relationship has been found between the temperature range observed at the scale of the districts for each instrumented walk, and the general conditions of temperature, wind speed, incident global radiation, and cloud cover at the same time.

The fine spatial variability in temperature which is superimposed to this signal (Figure 6) has been compared to a set of indicators related to land-cover fractions and morphological parameters (computed from a high-resolution geospatial database using <http://orbisgis.org>). Whereas a statistical analysis has made it possible to link the vegetation density and some cooling effects for Marseille, and the urban density to local warming effects for Paris, no significant relationship has been found at this time for Toulouse. Additional finer-scale indicators (*e.g.* sky-view factors) are currently being tested to understand the observed variability of microclimate.

The meteorological measurements have also been used to address the issue of climatic atmosphere or “ambiance” through the coupling of different measured meteorological parameters, and the evaluation of a perceived temperature computed using grey globes.

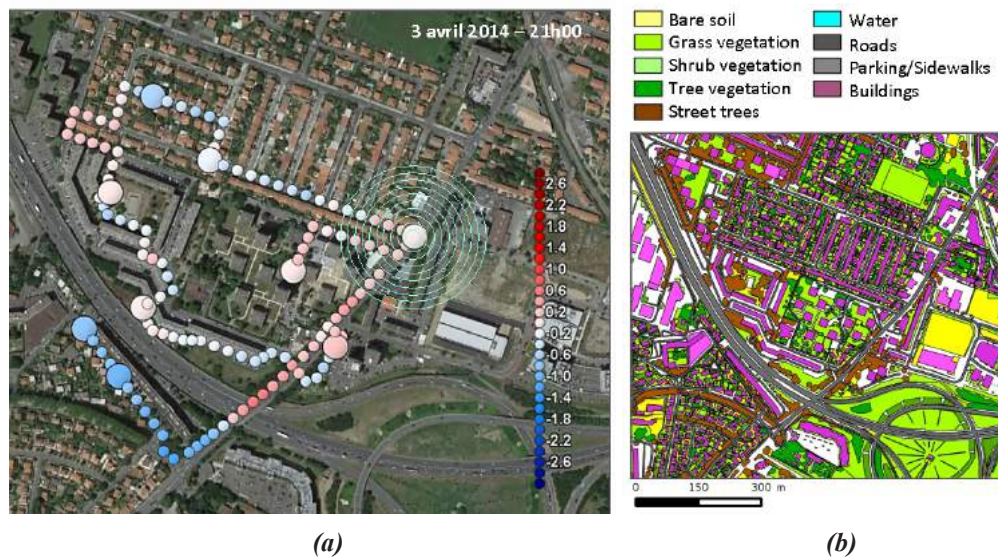


Figure 6 : EUREQUA Project, District of Toulouse (F); (a) mobile measurements of air temperature evolution in space, (b) high-resolution geospatial database of land cover

Figure 7 from [Carissimo et al. 2015] shows two examples of data processing of the thermal images for 2 of the 8 stop points. The first point is a square with trees surrounded by apartment buildings and the second is a crossroad in an area surrounded by little houses with very little vegetation. For each of these plots the infrared images have been processed to obtain the brightness temperature grouped and plotted using the same color scale. The differences between the two points illustrate the higher temperatures of the non vegetated area.

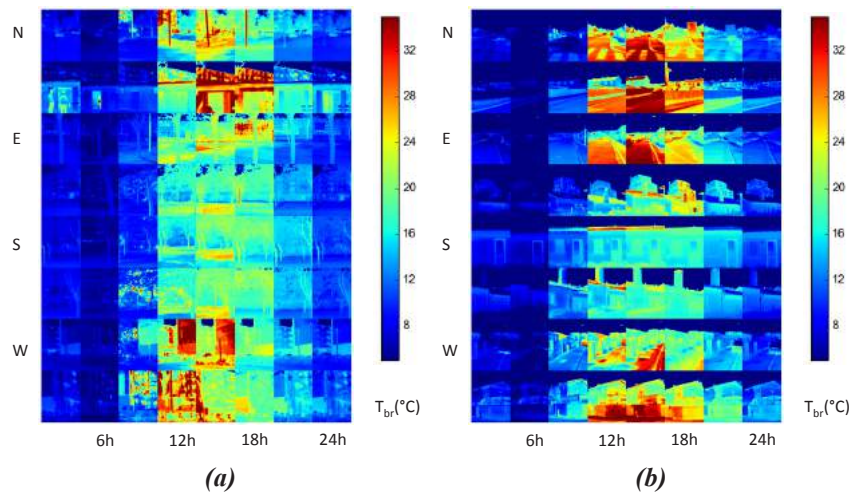


Figure 7 : EUREQUA Project, District of Toulouse (F), mobile measurements, evolution of IR radiation in direction (toward the North and then clockwise toward the NE) and time (every 3h); (a) a square surrounded by buildings (vegetal + mineral zone), (b) a crossroad with very little vegetation (fully mineral zone)

Regarding acoustical data, post-processing operations consisted of (i) filtering invalid data (overloads, GPS erroneous data, etc.) and (ii) extracting or calculating numerous acoustic indicators from raw data (L_{eq1s} for all $\frac{1}{3}$ octave bands in the range [50Hz – 20kHz]). Thus,

those acoustical measurements allowed filling the experimental database with energetic indicators (e.g. L_{\min} , L_{\max} , $L_{\max}-L_{\min}$, etc.), statistical indicators (e.g. percentiles L_1 , L_{10} , L_{50} , L_{90} , $L_{10}-L_{90}$, etc.), spectral indicators (e.g. spectrum gravity center – SGC) and dynamic indicators related to the time evolution of sound pressure levels (e.g. standard deviation – STD). Using an adapted combination of those numerous “soundscape” indicators, the analysis has shown next that some “acoustically homogeneous” zones can be distinguished through a robust method [Can et al. 2015a, 2015b, 2015c]. Thus this method has been applied to the district of Toulouse, leading to 4 groups for the day and 2 groups for the night (Figure 8), whatever the season (winter/spring/summer). Note that this method is powerful to identify the “transition” zones (from a group G_i to a group G_j), which have been shown very determinant zones for the inhabitants’ perception of their sound environment [Brocolini et al. 2013].

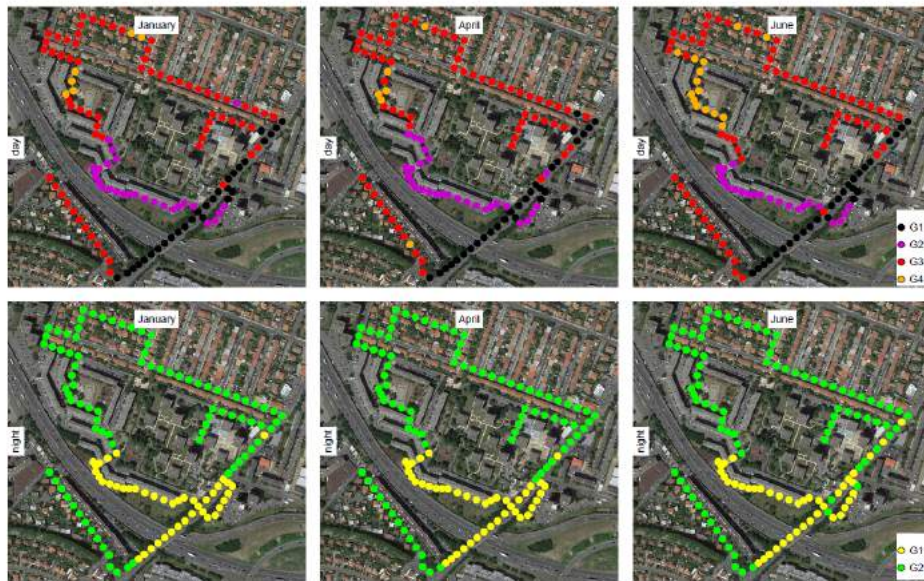


Figure 8 : EUREQUA Project, District of Toulouse (F), mobile measurements, evolution in space and time of statistically calculated “homogeneous sound groups” G_i

35 Numerical simulations

3.15 Chaining principle

Computational Fluid Dynamics (CFD) simulations were carried out with Code_Saturne (See Section 3.2). Input and initial data are provided by Large Eddy Simulation (LES) performed with the Meso-NH meteorological model (Lafore et al 1998, <http://mesonh.aero.obs-mip.fr>) with a 100-m spatial resolution, and a realistic description of the orography and the city (and of its energy exchanges with the atmosphere). They were validated against the observations.

Next, output data from CFD simulations (*i.e.* at the district scale in space) can be used either for the modelization of air pollutant dispersion (see example in Section 3.2) or as input data for the model of acoustic propagation (see example in Section 3.3). The latter is based on the Transmission Line Matrix (TLM) method, which can deal with urban propagation conditions, by modeling 3D physical phenomena such as multiple reflection, built-up diffraction, ground absorption, temperature/wind-induced refraction, turbulence scattering, etc. [Guillaume et al. 2014][Aumond et al. 2014]. The chaining principle between the 3 models LES/CFD/TLM is synthetized in Figure 9.

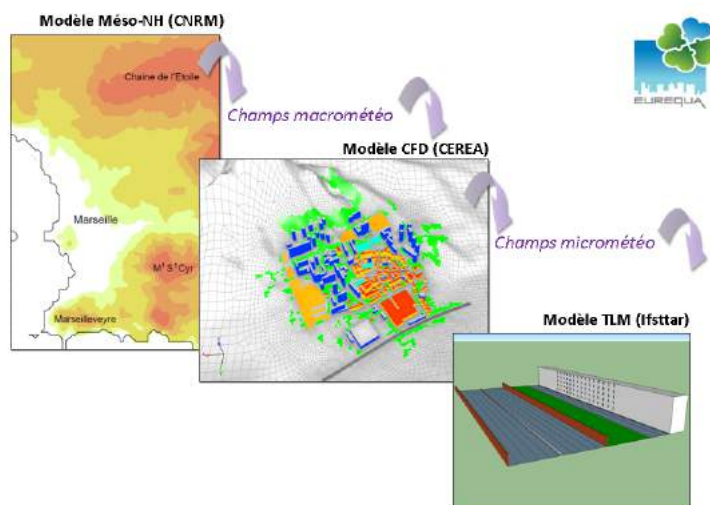


Figure 9 : principle of the "chaining cascade" for meso-scale model (Meso-NH / CNRM-GAME), micrometeorological model (CFD / CERE) and acoustic propagation model (TLM / Ifsttar)

This chaining procedure between atmospheric and acoustical models requires a delicate and sensitive compromise between time, space and frequency resolutions [Lihoreau et al. 2006][Aumond et al. 2014]. It allows numerical simulations for both air pollutants dispersion (Section 3.2) and sound propagation in urban area (Section 3.3).

3.25 Air pollutants dispersion

Code_Saturne [Archambeau et al. 2004], [Chahine et al. 2015] (<http://code-saturne.org>) is used for general computational simulations of fluid dynamics and has been adapted to micro-scale meteorological simulations (Figure 10) including local air pollutants dispersion (Figure 11) [Gao et al., 2015]. *Code_Saturne* is initialized and driven at the boundaries with meteorological profiles from Meso-NH calculations (see Section 3.1) and from background pollutant concentrations estimated from measurements outside the local simulation domain.

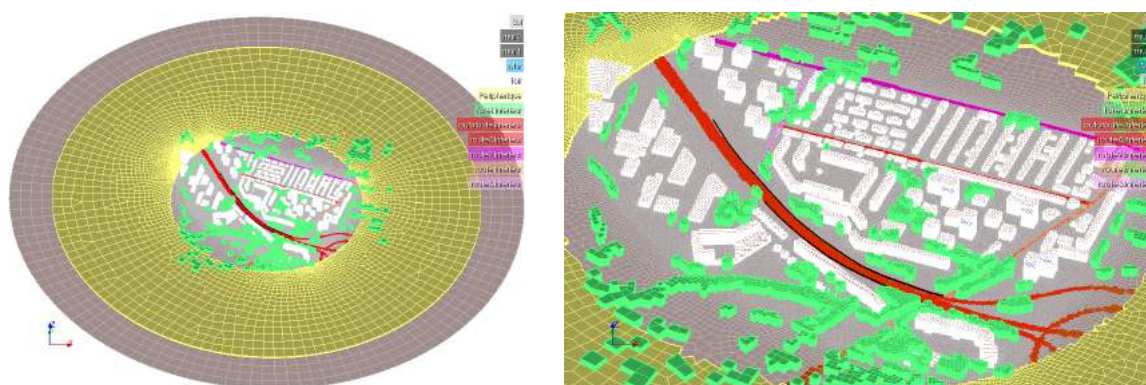


Figure 10 : Toulouse Bordelongue district mesh for the Computational Fluid Dynamics (CFD) simulations using *Code_Saturne* [Gao et al. 2015]. The green area is the vegetation taken into account as a porous zone.

Next, *Code_Saturne* is used to compute air pollutants dispersion for different scenario of district improvements (Figure 11). Compared to the base case, Fig. 11a illustrates the impact of doubling the height of the noise wall (to 6m), a very local impact, and Fig. 11b the impact of removing one of the buildings to create more space in the district but allowing pollution from the highway to penetrate more deeply.

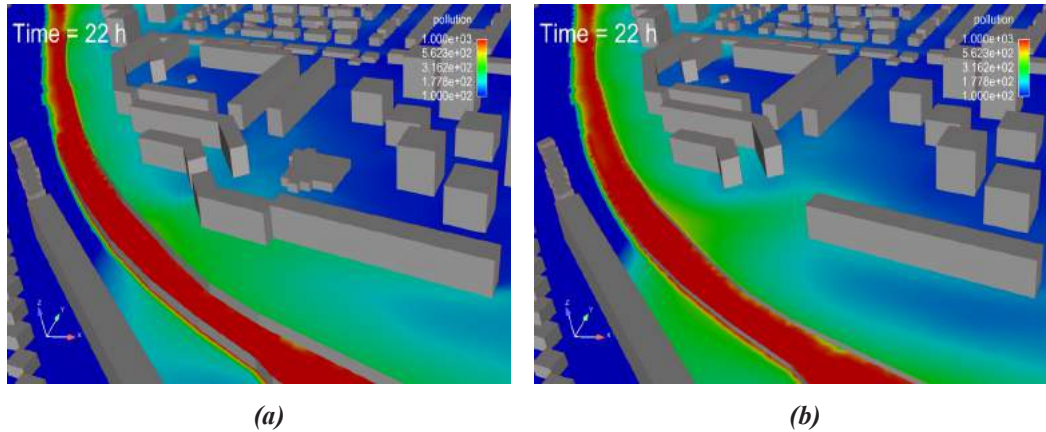


Figure 11 : Computational simulations of air pollutants dispersion in an “improved” district using Code_Saturne; (a) with a 6m high sound wall along the highway, (b) with the existing 3m high sound wall along the highway but modification of the built-up environment

3.35 Noise propagation

This part of the EUREQUA research work was carried out within the framework of a post-doctoral position (G. Guillaume, 2013-1014). It mainly consisted of integrating specific micrometeorological effects on urban sound propagation at the *street scale* using a reference code developed at Ifsttar based on the Transmission Line Matrix (TLM) method [Guillaume et al. 2015][Aumond et al. 2014]. Thus wind and temperature input data can be issued from either *in-situ* experimental observations or CFD calculations (“methods chaining”, cf. Section 3.1). This technique was applied on the district of Toulouse using the built-up model generated by a free CAD tool and the notations given in Figure 12.

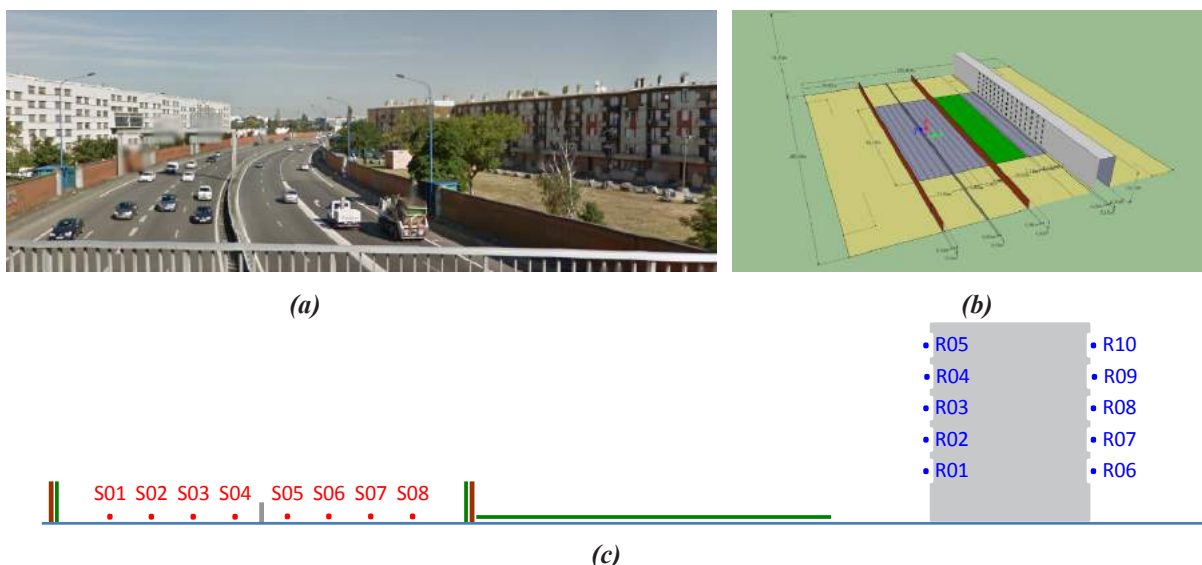


Figure 12 : EUREQUA Project, District of Toulouse (F); (a) photographic view, (b) schematic representation, (c) sources and receivers positions for TLM numerical simulations

An example of urban temperature gradients effects on sound pressure levels at receiver R04 is given in Figure 13 in the case of a stable urban boundary layer (night). As a first approximation, the temperature profiles are here idealized (log-lin profiles) although they were simulated *via* CFD, validated by experimental observations and next extrapolated to urban boundary layer (UBL) with the Monin-Obukhov similarity theory (MOST).

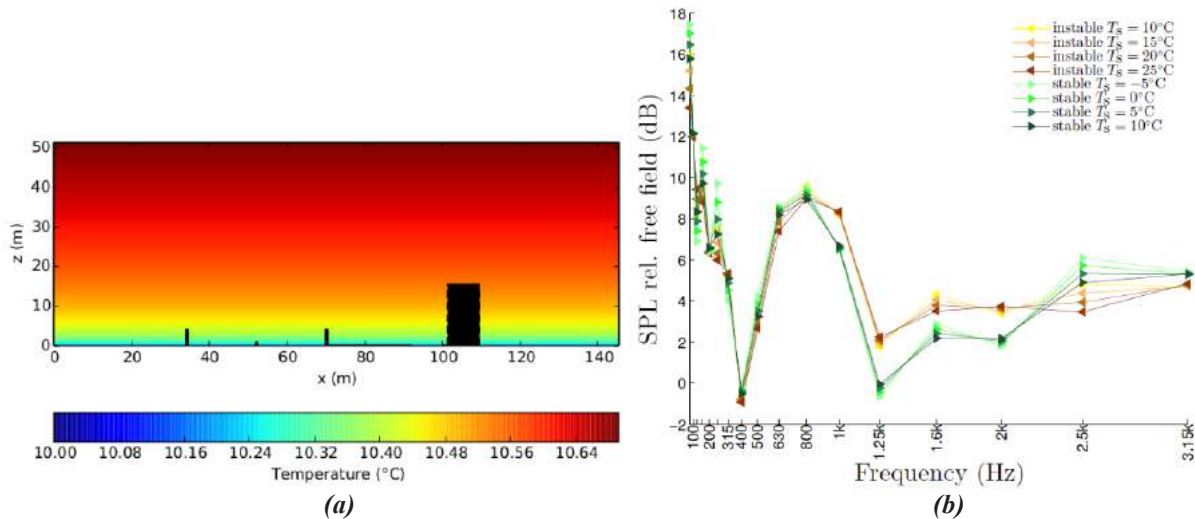


Figure 13 : micrometeorological effects on urban sound propagation; **(a)** in-situ temperature gradients (experimental + theoretical MOST) for stable atmosphere (night), **(b)** sound pressure levels relative to free field at the receiver R04

Many TLM simulations were carried out for different micrometeorological conditions (stable and unstable atmospheres), for different sound source characteristics and for different acoustic indicators (sound pressure level and reverberation time) calculated at different positions (cf. R0i in Figure 12). All those TLM calculations have confirmed – and quantified – the influence of the stratified atmosphere on sound propagation, even in urban (*i.e.* dense built-up) area.

Although this numerical work was carried out within a partnership limited to researchers mainly involved in engineering sciences, it remains a transdisciplinary approach in terms of scientific exchanges between acousticians, atmosphere physicists and fluid dynamics specialists. This work is still under progress in order to adapt automatically – and instantaneously – the grid meshing (in space and time) between CFD and TLM codes. Last but not least, for a larger scale in space (*i.e.* the district scale rather than the street scale), one can use classical engineering methods (*e.g.* NMPB2008 [Dutilleux et al. 2010]) and associated softwares in order to evaluate the acoustic impact of different urban *scenarii*. In this objective, another part of the work at Ifsttar within the EUREQUA project was dedicated to the improvement of the open-source and freeware “NoiseM@p” (<http://noisemap.orbisgis.org>). Nevertheless, it should be noticed that such simplified methods do NOT take into account all the physical phenomena involved in urban acoustic propagation (*e.g.* roughness diffusion, turbulence scattering and other micrometeorological effects in presence of specific wind and temperature profiles in urban zones) and do NOT give access to time-related sound indicators such as reverberation time.

45 Statistical data analysis, feedback meetings and participative workshops

As the EUREQUA project aims at revisiting the concept of environmental quality of life through a participative methodology and through geographical and social approaches, it has mobilized different techniques of social surveys to understand how people perceive the environmental quality of their district (cf. Section 2). Thus currently, experimental data collected during the intensive observational periods (IOP) are post-processed and statistically cross-analyzed in order to identify and characterize potential relationships between physical (*i.e.* “objective”) measurements, numerical simulations and people’s feelings and perceptions (questionnaires) [Gaudio et al. 2015].

The EUREQUA project scheduled feedback meetings with district inhabitants and users, elected officials, local actors, etc.; it also scheduled participative workshops in order to make environmental criteria emerge in *scenarii* conception. Thus feedback meetings and collaborative workshops have been carried out for each studied district (*i.e.* for each area which might be re-qualified in the mid-term). Some illustrations of such a collaborative rehabilitation project can be found in Figure 14.



Figure 14 : feedback meetings and collaborative workshops with inhabitants, in partnership with "Environnons" consulting (<http://www.tfconsultant.fr/nous-sommes/isabelle-richard>) and the architecture and urbanism office "Ateliers Lion Associés" (<http://www.atelierslion.com>), and with acknowledgments for graphic facilitation and collaborative design from P. Bellenoue (<http://wildisthgame.com>)

55 Conclusion and outlooks

The EUREQUA project (2012-2017) implements a transdisciplinary approach because (i) it merges researchers from different topics (in physics, environmental, human and social sciences), (ii) it focuses on 3 main observables (climate comfort, air quality and sound environment), (iii) it leverages experimental, numerical and statistical methods, (iv) it considers environmental quality as both an objective (collective) and subjective (individual) fact and (v) it combines quantitative and qualitative data. Currently, the EUREQUA team focuses its efforts on cross-analysis of IOP data for the 3 observables (climate comfort, air quality and sound environment), coming from *in-situ* measurements (objective data) and

synchronous questionnaires (subjective data). As this work is currently ongoing, more insights on the methodology to aggregate the results will be presented during oral session.

Thus a lot of work remains to be done, particularly on the development of an innovative methodology for *scenarii* conception and for merging experimental diagnostic, numerical predictions and participative workshops with district inhabitants and users, elected officials, local actors, etc. The final objective is to capitalize the results of the EUREQUA research to build a decision support tool. Moreover, one of the next and final issues of the EUREQUA project will stand in the multidimensional representation (cartography) of *all* the reliable criteria for the assessment of the environmental quality.

References

- [Aumond et al. 2014] P. Aumond, G. Guillaume, B. Gauvreau, C. Lac, V. Masson, M. Bérengier, (2014), "Application of the Transmission Line Matrix method for outdoor sound propagation modelling - Part 2: Experimental validation using meteorological data derived from the meso-scale model Meso-NH". *Applied Acoustics*, Vol. 76, pp 107-112
- [Archambeau et al. 2004] Archambeau, F., N. Mehitoua, and M. Sakiz. 2004. "Code_saturne: a Finite Volume code for the Computation of Turbulent Incompressible Flows — Industrial Applications". *Intern. J. on Finite Volumes* 1: 1–62
- [Berry-Chikhaoui et al. 2014] Berry-Chikhaoui I., Dorier E., Haouès-Jouve S., Flamand A., Chouillou D., Hoornaert S., Marry S., Marchandise S., Richard I., Rouquier D., Rouyer A., (2014), "La qualité environnementale au prisme de l'évaluation par les habitants. Un effet de quartz", *Revue Méditerranée*, n°123
- [Brocolini et al. 2013] Brocolini, L., C. Lavandier, M. Quoy, and C. Ribeiro. 2013. "Measurement of Acoustic Environments for Urban Soundscapes: Choice of Homogeneous Periods, Optimization of Durations, and Selection of Indicators". *J. Acoust. Soc. Amer.* 134 (1): 813–21
- [Can et al. 2015a] A. Can, B. Gauvreau, (2015), "Describing and classifying urban sound environments with a relevant set of physical indicators", *J. Acoust. Soc. Amer.*, Vol. 137(1), pp 208–218
- [Can et al. 2015b] A. Can, G. Guillaume, B. Gauvreau, (2015), "Noise indicators to diagnose urban sound environments at multiple spatial scales", *Acta Acustica united with Acustica*, Vol. 101(5), pp. 964-974
- [Can et al. 2015c] A. Can, B. Gauvreau, (2015), "Spatial categorization of urban sound environments based on mobile measurements", invited paper, *Proc. Euronoise 2015*, Maastricht (NL), may 31 – june 3 2015
- [Carissimo et al. 2015] B. Carissimo, Y. Qu, R. Bresson, N. Daviau, N. Gaudio, M. Milliez, (2015), "Spatial variability, horizontal anisotropy and diurnal evolution of measured infra-red fluxes in a city neighborhood of Toulouse", *Proc. ICUC9*, Toulouse (F), 20-24 july 2015

- [Chahine et al. 2015] A. Chahine, P. Matharan, D. Wendum, L. Musson-Genon, R. Bresson, and B. Carissimo. 2015. 'Modelling Atmospheric Effects on Performance and Plume Dispersal from Natural Draft Wet Cooling Towers'. *J. Wind Engineering and Industrial Aerodynamics* 136: 151–64
- [Dutilleux et al. 2010] G. Dutilleux, J. Defrance, D. Écotière, B. Gauvreau, M. Bérengier, F. Besnard, E. Le Duc, (2010), "The revision of the French method for road traffic noise prediction", *Acta Acustica united with Acustica*, Vol. 96(3), pp. 452-462
- [Gao et al. 2015] Z. Gao, Y. Qu, M. Milliez and B. Carissimo, (2015), "High resolution numerical study of wind, thermal effects and pollution dispersion in an urban neighborhood in Toulouse", *Proc. ICUC9, Toulouse (F)*, 20-24 July 2015
- [Gaudio et al. 2015] N. Gaudio, S. Marchandise, J. Le Bras, A. Lemonsu, S. Haouès-Jouve, D. Legain, J. Hidalgo, B. Tudoux, "Observation of urban climate variability at local scale and comparison with human perception", *Proc. ICUC9, Toulouse (F)*, 20-24 July 2015
- [Guillaume et al. 2014] G. Guillaume., P. Aumond, B. Gauvreau, G. Dutilleux, (2014), "Application of the Transmission Line Matrix method for outdoor sound propagation modelling - Part 1: Model presentation and evaluation". *Applied Acoustics*, Vol. 76, pp 113-118
- [Lafore et al. 1998] Lafore, J. P., J. Stein, N. Asencio, P. Bougeault, V. Ducrocq, J. Duron, C. Fischer, P. Hereil, P. Mascart, J. P. Pinty, J. L. Redelsperger, E. Richard, and J. Vila-Guerau de Arellano, (1998), "The Meso-NH Atmospheric Simulation System. Part I: Adiabatic formulation and control simulations", *Annales Geophysicae*, 16, 90-109
- [Lihoreau et al. 2006] B. Lihoreau, B. Gauvreau, M. Bérengier, Ph. Blanc-Benon, I. Calmet, (2006), "Outdoor sound propagation modeling in realistic environments: Application of coupled parabolic and atmospheric models", *J. Acoust. Soc. Amer.*, Vol. 120(1), pp. 110-119
- [Le Bras 2015] J. Le Bras, (2015), *Le microclimat urbain à haute résolution : mesures et modélisation*, PhD Thesis, University of Toulouse (F)
- [Richard et al. 2013] I. Richard, M. Pellegrino, B. Gauvreau, A. Flamand, J.-P. Lévy, S. Haouès-Jouve, (2013), "Approches croisées pour la modélisation acoustique en milieu urbain : une proposition méthodologique", invited paper and keynote lecture, *Proc. EcHoPolis Conference, Athens (G)*, 29 sept – 3 oct 2013

CLIMATE COMPARSION IN THE URBAN AREAS OF THE OYAMBARO AND QUITO VALLEYS

Jiménez R., Sylvia¹; Van Sluys, Christine²

¹ Pontificia Universidad Católica del Ecuador
e-mail: svjimenez@puce.edu.ec

² Pontificia Universidad Católica del Ecuador
christine@jaramillovansluys.com

Keywords: Urban Climate, Climate Comparison, Climate Classification.

Abstract. *The microclimates in the Andean valleys of Oyambaro and Quito in Ecuador can present a wide diversity within a few kilometers apart. For urbanists and architects the climatic analysis available of Quito Metropolitan District as one city with several microclimates can be of significant importance as the use of space can change within each administrative zone. This paper discusses the difference comparing four microclimates, the data availability, administrative zoning and basic passive measures using a locally developed precipitation based climate stratification.*

1. Introduction

The Oyambaro and Quito Valleys are several plateaus at an altitude that varies from 1200 to 2900 meters above sea level. The populated areas located in these valleys have more than 10000 years of history (Lozano,1991) and since 2008 constitute the Municipal District of Quito (DMQ). These valleys represent an interesting case study for their unique climatic conditions of high altitude at the Equator, according to the Köppen-Geiger classification of the subtropical highland climate *Cwb* or *Cfb*, is infrequent and found in remote locations such as the highland in Argentina, Copacabana, Bolivia and parts of the Himalayas (Peel,2007).

During the XXth century, the accelerated urban sprawl in Latin-American cities has triggered a deep morphological inflexion in the existing urban structures, to name the main impacts, residential typology changed, and the role of infrastructure and urban services won relevance as autonomous systems. The concept of infrastructure was introduced as a support of this process of urban expansion resulting in land speculation and fragmentation between urban spaces. Especially at the DMQ, the urbanizing process is characterized by a vast and disperse urban fabric of low density and often unarticulated of its geographical reality. Thus, it is fundamental to identify criteria for decision making that respond accordingly to the existing urban and climatic diversity.

At the present time, architecture and urban design are looking more closely to climate responsive design principles based on data than the previous decades. Passive design is regaining more importance as a necessity rather than a foreign consideration. However, passive techniques developed for centuries in different locations do not fit completely in an infrequent and scarcely studied location such as the DMQ, where vernacular buildings disappeared during the Spaniard expansion in the Americas. Thus, this study tries to analyze the climatic conditions of four administrative zones consolidated as low-density urban areas, in two different microclimates no more than fifteen kilometers apart.

2. Methodology

Several climate classifications for the DMQ were analyzed selecting one that provided a framework that considers simple variables and corresponds with local perceptions of climate by the general population.

For comparison purposes GIS data bases were used combining data sets for the geographic location of meteorological stations of the National Institute for Meteorology and Hydrology of Ecuador (INHAMI) and Metropolitan Network of Environmental Monitoring (REMMAQ) within the Administrative zoning of the DMQ. Four stations were selected due to their relevance in the analysis of the expansion of the urban areas and their relative short distance within the different climatic zones.

Daily and hourly data sets were analyzed through climate software without iteration and extrapolation for missing data. Givoni psychometric charts were used to show the main strategies and to illustrate the comparison. A table with the variables and results synthesizes the work.

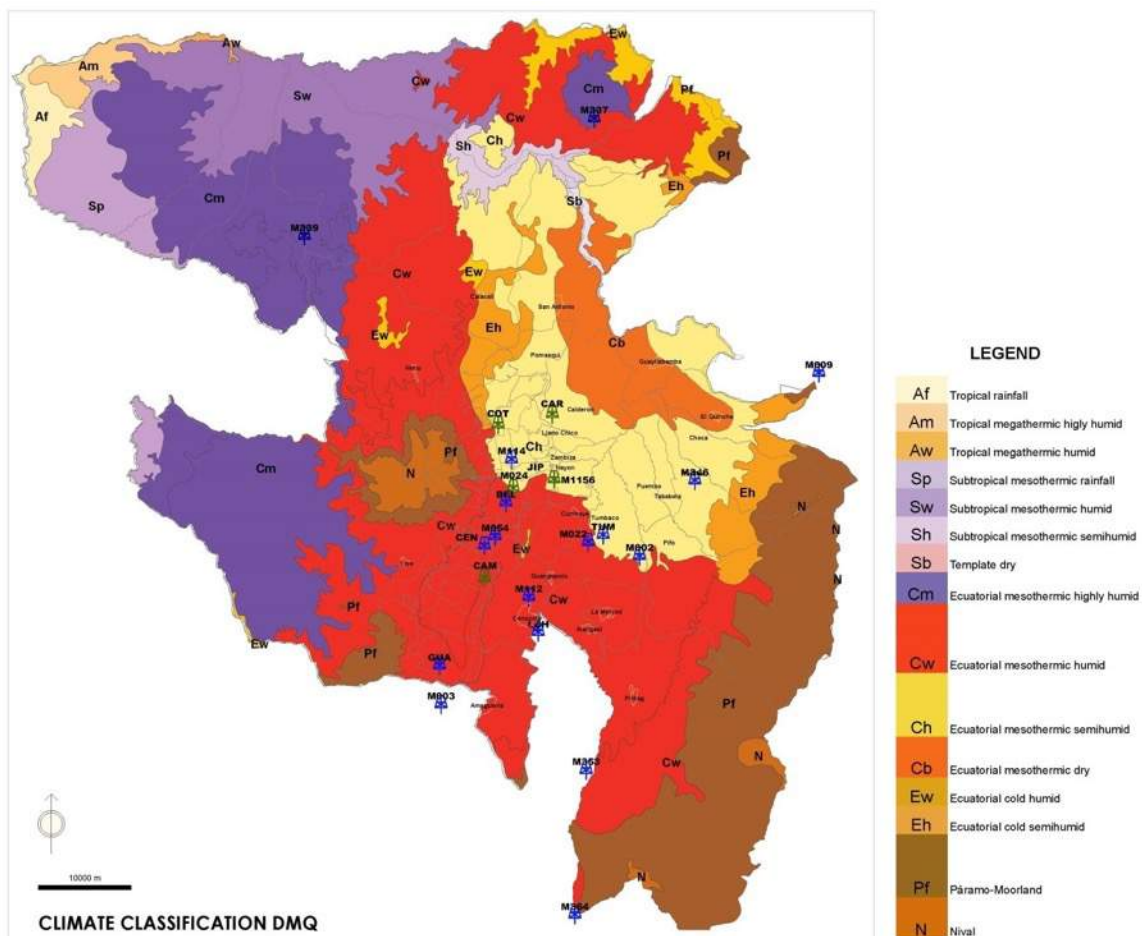
3. Climate Comparison

3.1. Climate Stratification at the DMQ

Weather in the equatorial region of the Andes is influenced by the Coriolis effect and the masses of air moving from the Pacific Ocean intertropical front colliding at the Andes westward (Porruat, 1995 a) (Porruat, 1995 b). This phenomenon causes important fluctuations of variables like wind, precipitation, humidity and temperature variations of 1.3°C every 200 meters in altitude (Egescio, 1994). At the Oyambaro and Quito Valleys part of the Municipal District of Quito (DMQ) the changes of surface temperature by radiation and different materials, can cause a connective system of precipitations and condensation (DMA, 2009), that combined with the trade winds can cause precipitation in the extreme east and higher parts of the DMQ and climatic inversion during the early hours of the morning (INHAMI, 2010).

Climatic variations at these valleys have been studied since 1970. Thus, in order to determine the baseline for these comparisons several climate stratifications have been revised: Miller's with the over simplified categorization with 5 climates (Naranjo, 1989) Holdridge – Tosi climatic ranges with 13 regions (Cañadas, 1978) (Estrada et al, 1983), Köppen-Geiger (Blandin, 1977) determining mainly a subtropical highland *Cwb* or *Cfb*, and the hydro climatological classification by Pourrut and Leiva with 15 zones (1989).

Pourrut and Leiva hydro climatological classification, developed on site, considers simple variables such as: temperature, evapotranspiration potential determined by Thornthwaite and maximum annual precipitation based in hydrological regions determined by Dubreil



Guiscafré (Pourrut, 1995a). This hydro climatological classification was selected as a framework that used simple variables as stated below, it was studied onsite and corresponds with “climate perceptions by the general population” (DMA, 2009) .

3.2. Climate Analysis

In order to select the stations for the study, as explained in the methodology, the criteria used included: location within each climatic zone represented (DMA,2009), availability of complete data sets (INAMHI,2011), and their importance in analyzing areas with potential for densification in the DMQ.

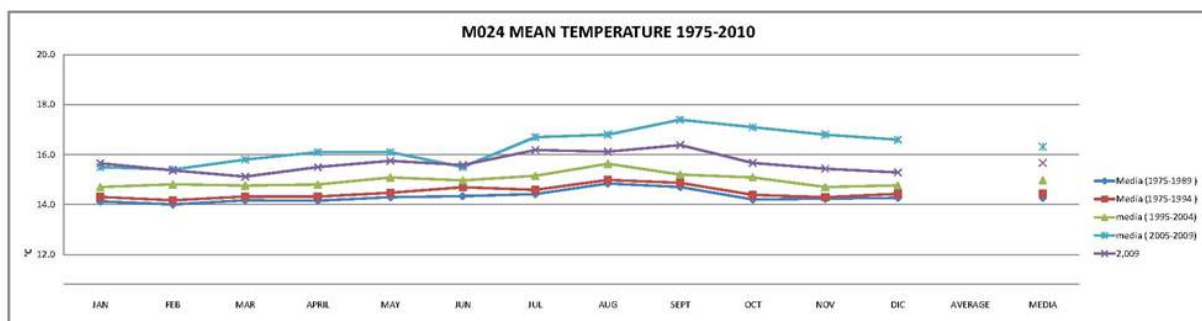
In table 2, the list of public meteorological stations is detailed, including the availability of complete data sets and automatic digital stations. For the purpose of this study five stations were selected: M1156 –Nayon, CAM- Camal, CAR- Carapungo COT-Cotocollao and M024 –Iñaquito as a control station to identify the annual data set used for the analysis.

INDEX OF METEOROLOGICAL STATIONS WITH PUBLISHED INFORMATION

CODE	NAME	TYPE	LATITUD DD MM SS	LONGITUDE DD MM SS	HEIGHT (m)	OWNER
M003	IZOBAMBA	AP	0° 22' 0" S	78° 33' 0" W	3058	INAMHI
M002	LA TOLA	AP	0° 13' 46" S	78° 22' 0" W	2480	INAMHI
M024	QUITO INAMHI-INNAQUITO	CE	0° 10' 0" S	78° 29' 0" W	2812	INAMHI
M009	LA VICTORIA INERHI	AP	0° 3' 36" S	78° 12' 2" W	2200	INERHI
M337	SAN JOSE DE MINAS	PV	0° 10' 32" N	78° 24' 30" W	2417	INAMHI
M339	NANEGALITO	PG	0° 4' 0" N	78° 40' 35" W	1633	INAMHI
M364	LORETO PEDREGAL	PV	0° 33' 41" S	78° 25' 35" W	3620	INAMHI
M353	RUMPAMBA-PICHINCHA	PV	0° 25' 39" S	78° 24' 57" W	2940	INAMHI
M346	YARUQUI INAMHI	PV	0° 9' 35" S	78° 18' 55" W	2600	INAMHI
M114	AEROPUERTO	DAC	0° 13' 00" S	78° 48' 00" W	2812	DAC
M112	CONOCOTO		0° 16' 02" S	78° 28' 08" W	2252	INAMHI
M1156	NAYON SANTA ANA – PUCE	CO	0G 10' 37" S	78G 25' 39" W	2450	IN-PUCE
M022	TUMBACO	CO	0° 13' 00" S	78° 24' 50" W	2348	INAMHI
MA2T	TABACUNDO	CO	0° 02' 00" N	78° 14' 00" W	2790	INAMHI
M054	QUITO OBSERVATORIO	CP	0° 12' 40" S	78° 30' 00" W	2820	OAQ
MA02	COCHASQUI PICACHO	CO	0° 05' 00" N	78° 18' 00" W	3540	INAMHI
M605	COCHASQUI HACIENDA	PV	0° 03' 22" N	78° 18' 35" W	2980	INAMHI
LCH	LOS CHILLOS	O3, PM10, MET	0°18'00" S	78°27'36" W	2453	REMMAQ
TUM	TUMBACO	SO2,O3, MET	0°12'36" S	78°24'00" W	2331	REMMAQ
GUA	GUAMANÍ	CO,NOX,O3, PTS	0°19'51" S	78°33'5" W	3066	REMMAQ
CEN	CENTRO	SO2, CO, NOx, PM2.5, SO2, CO, O3, NOx, PM2.5, PTS, MET	0°13'12" S	78°30'36" W	2820	REMMAQ
CAM	EL CAMAL	SO2, CO, NOx, PM2.5, PM10, SO2, CO, O3, NOx, PM2.5, PM10, MET	0°15'00" S	78°30'36" W	2840	REMMAQ
JIP	JIPUAPA	SO2, CO, NOx, PM2.5, PM10, SO2, CO, O3, NOx, PM2.5, PM10, MET	0°09'36" S	78°28'48" W	2781	REMMAQ
BEL	BELISARIO	SO2, CO, NOx, PAR, MET	0°10'48" S	78°29'24" W	2835	REMMAQ
CAR	CARAPUNGO	SO2, CO, NOx, PAR, MET	0°5'54" S	78°26'50" W	2660	REMMAQ
COT	COTOCOLLAO	SO2, CO, O3, NOx, PAR, PM10, MET	0°6'28" S	78°29'50" W	2793	REMMAQ

TYPE	
AP	Agricultural
CE	Climate Especial
PV	Pluviometric
PG	Pluviografic
DAC	Aeronautical
CO	Climate Complete
CP	Climate Principal
PARTICULATE	
SO2	Sulfure Dioxide
	Nitrogen Oxide
CO	Carbon Dioxide
O3	Ozone
PTS	Particulate<=1 µm
PM2.5	Particulate<=2.5 µm
PM10	Particulate<=10 µm

Table 1 Meteorological Stations of the DMQ .Data Sets: INAMHI, 2000 – 2010, REMMAQ 2010, PUCE 2010.



A representative climatic year was selected analyzing 35 years of data from the control meteorological station out of the study M054-Iñaquito, choosing an annual data set that best illustrated the variability (Figure 2) discarding years affected by abnormal climatic events such as El Niño, la Niña, major floods or draughts. The data used was of calendar year 2009 as it represents the tendency of analysis of the period stated above rather than a typical meteorological year combining a decade, mainly as the stations where recently installed and detailed data was unavailable.

Figure 2: Climate Analysis M054 1975-2010 . Data Bases: INHAMI, 2010

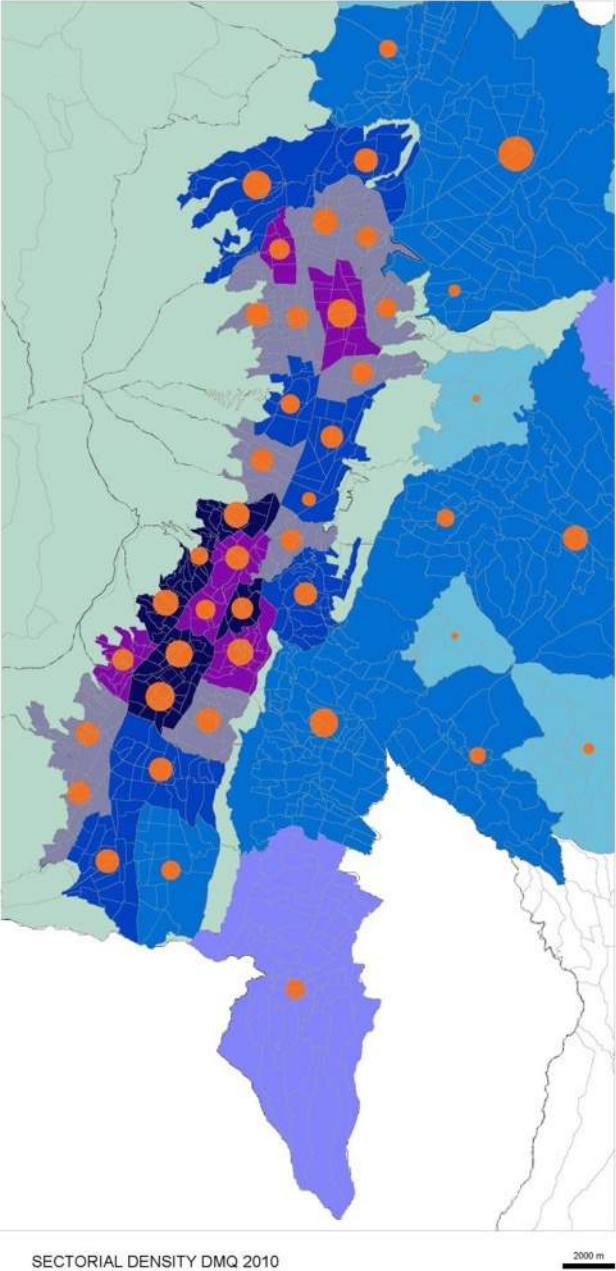


Figure 3: Sectorial Density DMQ. (Jaramillo, et al, 2011). Data Bases: DMQ, INEC 2010

As shown in figure 3, the analysis of the density of the urban area was calculated using GIS to analyze population data from the Census of 2010. The areas were divided in Barrio-sectores an administrative subunit used to identify areas of lower density, and lower population that have an higher urbanizing potential with an inhab/ ha ratio of 4.0-6.7. The sectors selected were: Nayón and Quitumbe in the south and Cotocollao in the north of the city.

3.3. Climate Comparisons and Passive Strategies

Daily and hourly data sets were analyzed through climate software without iteration and extrapolation for missing data. The analysis used was the main graphs used by architects and urbanist for decision makers, such as climate summary, prevailing winds, precipitation and Givoni psychometric charts. The first charts were used to check for consistency of the data and strategies, while the latter Givoni Psychometric Charts (ISO 7730) were generated to analyze strategies and to visualize better the climate comparison according to climate zones: Equatorial meso thermic humid and Equatorial meso thermic semi humid .

The charts used the complete data sets of temperature and humidity for sedentary activity of 1 MET (58.2 W/m²) and insulation by clothing of 1 CLO (0,155 m²;×K/W).

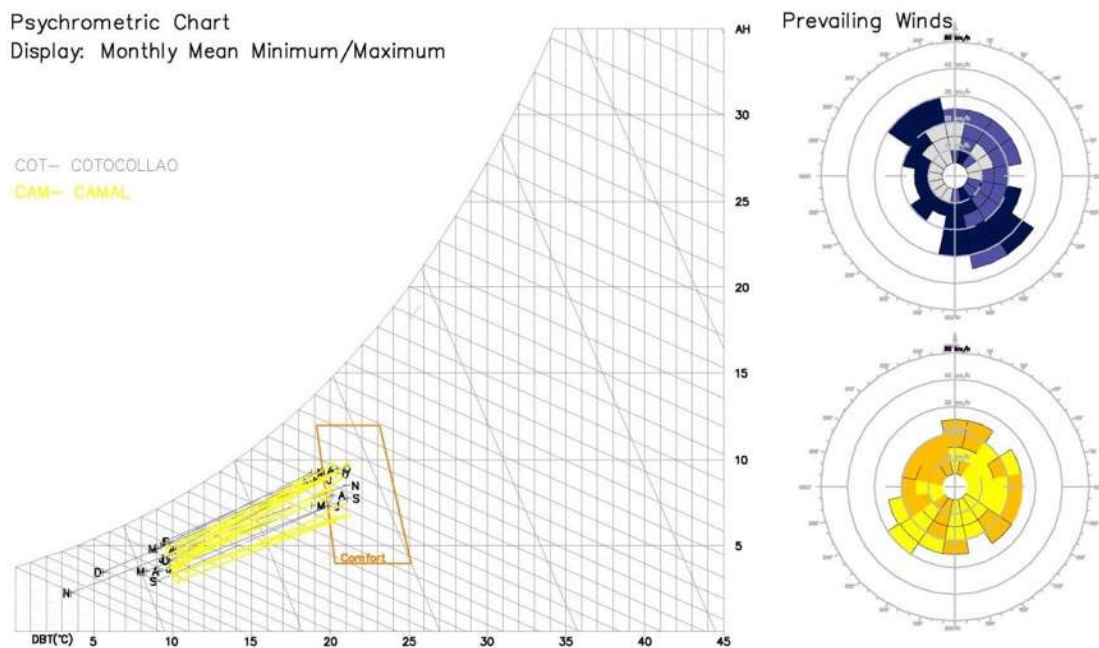


Figure 4: Climate Comparison COT-CAM.. Data Bases: REMMAQ

The data in the Image 4 above shows the monthly temperature and humidity ranges, of two stations CAM-Camal and COT-Cotocollao within the climate classification Equatorial mesothermic humid, the mean temperature ranges between 12 and 20°C with rainfall around 1.000 y 2.000 mm with two rainy seasons between February-May and October-November, covering the 21% of the net area of the DMQ (DMQ ,2009).

As shown in the graph the conditions of comfort are met only 10 % of the time, the main strategies suggested for buildings are: high thermal mass to warmup during night all year long, active solar gain during the day and dehumidification.

The comparison of the prevailing winds shows the higher frequency westward, with differences due to topography and their location north and south within 15 Km from each other. Wind from the northwest in Cotocollao and south west in Camal.

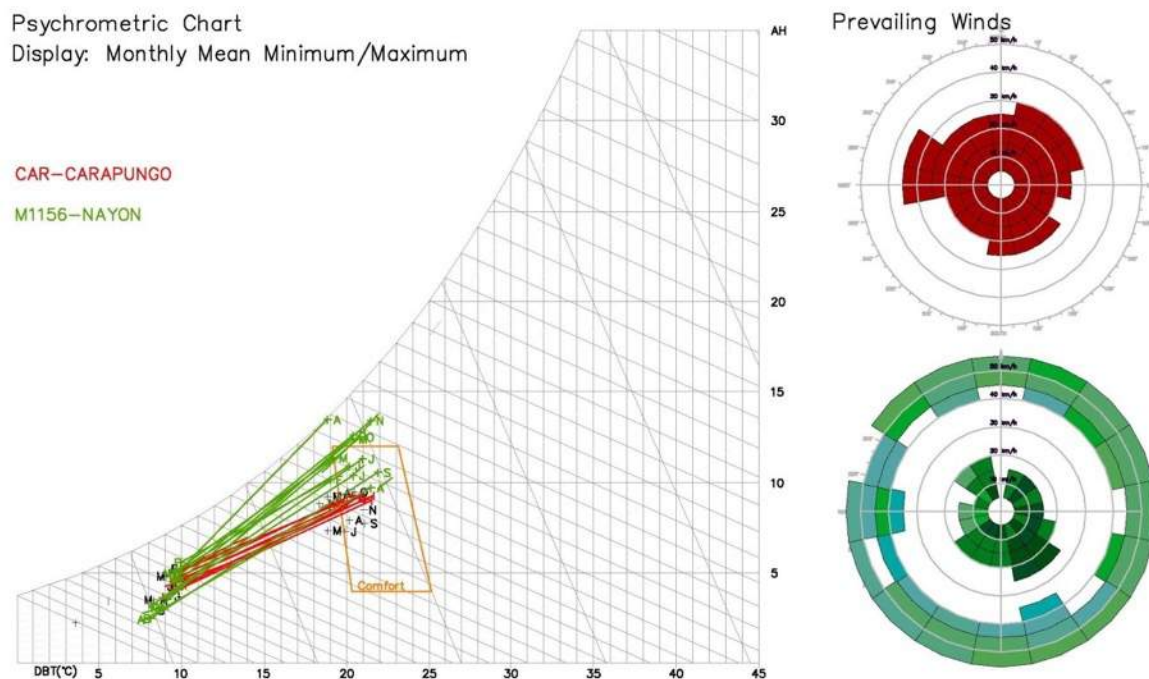


Figure 4: Climate Comparison CAR-M1156. Jiménez 2015. Data Bases: REMMAQ -INAMHI

The comparison of stations CAR-Carapungo and M1156-Nayon are within the climate classification Equatorial mesothermic semi humid with temperature ranges between 12 and 18°C, rainfall around 500 and 1.000 mm with a dry season between July through September. This climate represents the 13% of the net area of the DMQ (DMQ, 2009).

As shown in the graph the conditions of comfort are met 20 % of the time, the main strategies suggested for buildings are: high thermal mass to warm up during night all year long, active solar gain during the day and ventilation between 13h00 and 15h00 when solar gain is at its maximum. Nayón presents a high peak in humidity during April when the wind westward brings higher precipitation.

The comparison of the prevailing winds shows main differences due to topography and their location within 8 Km from each other. Wind from the northwest and east in Carapungo and stronger winds from all directions in Nayón, since its location in the first high elevation to encounter the winds moving from the eastern planes at the Amazon basin.

4. Discussion of Results for Urbanism and Architecture

Climate uniformity within extensive territorial zones is an important parameter for urban planners and designers as well as for architects. The following table (Table 3) summarizes the results of the criteria used in this climatic comparison. The data shows the different climatic zones with the same color coding of Figure 1, for visual comparison. The surface area within each zone is presented in comparison to the net area of the DMQ. Main populated districts and sites within the climate zone are stated by name for easy identification. Average Climatic

data is presented with annual rainfall mean temperature and the codes of the main climatic stations with published data.

Passive strategies for buildings are stated for the four stations analyzed as well as climatic features for the other stations. Thermal mass, or air tightness is recommended for the climates: Equatorial mesothermic semi humid (**Ch**) and Equatorial mesothermic humid (**Cw**). The daily temperature difference of 8 to 10°C between day and night suggests heat accumulation during the day for the night as a passive strategy. Additionally, shade is recommended in dry zones and between 11h00 to 15h00. Morning strategies differ between stations as dehumidification and ventilation are recommended. The recommendations and main climatic features in this table should be used as guidance for rapid analysis and schematic design.

CLASIFICATION		LOCATION			CLIMATE DATA				PASSIVE STRATEGIES
HYDRO CLIMATIC CLASSIFICATION	LEGEND PORROUT	AREA OF THE DMQ%	ADMINISTRATIVE ZONES	MAIN CITIES, SITES	ANNUAL RAINFALL mm	AVERAGE TEMPERATURE E °C	STATION CODE	MAIN CLIMATE FEATURES	
Af	Tropical rainfall		Adm. Zonal Nor Occidente- La Delicia	Limite con San Miguel de los Bancos	>	3000	>	22	
Am	Tropical megathermic highly humid	0,8	Adm. Zonal Nor Occidente	Vertientes exteriores de la cordillera occidental	2000	3000		22	HEAVY Rainfall (dec-jun) NO Rainfall (jul- nov)
Aw	Tropical megathermic humid	0,9	Adm. Zonal Nor Occidente	Pacto	1000	2000	>	22	Rainfall (dec-may) dry rest of the year
Sp	Subtropical mesothermic rainfall	,1	Adm. Zonal Nor Occidente	Pacto	>	3000	18	22	No dry season, mild rainfall Aug
Sw	Subtropical mesothermic humid	3,00	Adm. Zonal Eloy Alfaro- Nor Occidente	Gualea, Nanegal	1000	2000	18	22	
Sh	Subtropical mesothermic semihumid	7,00	Adm. Zonal Aeropuerto	Perucho	500	1000	18	22	Medium Rainfall (jan-May), 4 to 8 months Dry
Sb	Temperate dry	1,1	Adm. Zonal Norte- La Delicia	San Antonio, Perucho	<	500	18	22	NO Rainfall all year long
Cm	Ecuatorial mesothermic highly humid	,2	Alfaro - Centro- Quitumbe -Eugenio	Pacto, Gualea, Nanegal, Nanegalito, Santa Elena y las zonas aledañas Chiriboga, Lloa	>	2000	12	18	M339 Constant Rainfall , Mid Rainfall(jul-sep)
Cw	Ecuatorial mesothermic humid	17,4	Adm. Zonal Valle de los Chillos Tumbaco Aeropuerto	Chavezpamba, San José de Minas, Perucho, Atahualpa y San Carlos de Palma Real, Nono, Calacali, Cumbayá, Pifo, Puengasi, Pintag, Lloa, Amaguaña, Conocoto, Guagopolo, Alangasi, La Merced, Quitumbe, Turubamba, El Condado	1000	2000	12	18	M337, JIP, M024, BEL, M054, CEN, CAM, M112, M022 , M002, M353 High thermal mass during night all year long , Active Solar Gain, Dehumidification
Ch	Ecuatorial mesothermic semihumid	13,4	Adm. Zonal Tumbaco-Centro-Eugenio Espejo - Quitumbe	Perucho, Puéllaro, Pomasqui, Guayllabamba, San Antonio, El Quinche, Checa, Tababela, Tumbaco, Yaruquí, Puembo, Pifo, Amaguaña, Pintag, La Merced, Conocoto, El Condado, Calderón		500	12	18	CAR, COT, M346, M114, M1156, TUM High thermal mass during night all year long , Active Solar Gain, Ventilation
Cb	Ecuatorial mesothermic dry	20,8	Adm. Zonal Calderon - La Delicia	Calderon , San Antonio, Guayllabamba	500	1000	12	18	High thermal mass during night all year long , Humidification, Ventilation. Shade from 11h00 -15h00
Ew	Ecuatorial cold humid	12,00	Adm. Zonal Quitumbe- La Delicia	Calacali, Nono, San José de Minas	500	1000	8	12	
Eh	Ecuatorial cold semihumid	3,5	Adm. Zonal Quitube-Centro-Eloy Alfaro	Checa, Yaruquí, El Quinche, Calacali, Pomasqui, San Antonio, Guayllabamba, El Condado		500	4	8	
Pf	Páramo-Moorland	14,2	Adm. Zonal Eloy Alfaro - Centro- Quitumbe -Eugenio Espejo	Pintag, Pifo, Volcan Pichincha, San Alfonso, Quitumbe, La Ecuatoriana, Guamaní, Belisario Quevedo, Cochapamba, Rumipamba, San Juan		500	<	4	MOO3
N	Nival	1,6	Adm. Zonal Eloy Alfaro - Centro- Eugenio espejo	Volcan Pichincha, Atacazo y Antisana, Belisario Quevedo, Cochapamba, Rumipamba, San Juan					

Table 3: Summary of Climate Classification and Passive Strategies DMQ .Data Bases: DMQ,DMA,INHAMI, REMMAQ

As stated above in the climate comparison, wind analysis should be done for every station due to its seasonal variability increased by topographic conditions. However the main peaks Rucu and Guagua Pichincha volcanos stop winds from the west and allow movement of air masses mainly from north to south.

5. Recommendation for Further Research

As stated before along the article, the main opportunities and challenges for further research might be:

Further investigation towards locally develop a climate stratification seems necessary not only for large urban areas, but also for regions, as bigger urban districts and cities rely on contiguous smaller and satellite cities in neighboring states.

Additional work to consolidate a typical meteorological year of the main meteorological stations with condensed data for ten years should be programmed by local authorities, not only for research and comparison purposes but also for simulation and closer approximation to understanding the complexity of meteorological phenomena at the urban scale.

Detailed analysis of all the climatic zones at the DMQ is needed, perhaps including one typology of building such as a housing standard typology in the different 15 climate zones within a city evaluating their performance under a locally available passive performance system.

6. Concluding Remarks and Discussion

As Iñaki Abalos (2008) states in his text *The Thermodynamic Beauty*, two different trends in design strategies largely linked to different latitudes are identifiable in sustainable urbanism and architecture: the first based on the construction of a highly technical environment, and the artificial achievement of comfort, and the second, a model from the subtropics based on “solar geography” with the analysis of resources from a minimum resource approach.

The main aim of this study was to establish a basic climatic framework that shows the climate variation in Quito as it is perceived by the general population. This perception often acknowledges that the weather in Quito is so variable that rains in areas as small as neighborhoods and general climate stratification do not correspond to the reality perceived by their inhabitants.

The division of a medium sized climatic zone such as Porroút’s between main classifications of hundreds of kilometers such as Köppens, can serve the perceptions determined by inhabitants and could give insights to city planners as well as professional of the built environment when they are complimented by passive strategies and summarized results.

This analysis represents a rapid initial assessment tool of passive strategies for urbanism and architecture. Public spaces should involve wind and solar radiation to meet comfort and to locate gathering spaces. Strategies for architectural design point towards heat gains in the main climates studied, that could be of use in a sustainable development and densification in the DMQ.

7. Acknowledgements

This research paper is a result of several research endeavors financed by the Pontificia Universidad Católica del Ecuador and University College London. We would like to acknowledge the work of the following research assistants: Rashid Saá, Tatiana Armijos, and

Carlos Ortega. Additional thanks for their contribution and professional advice and review to Anibal Robalino, and Zhohana Rodriguez.

8. References

- (Ábalos, 2008). ÁBALOS, Iñaki. La Belleza Termodinámica. Madrid 2008, España: Luis Mansilla, Luis Rojo y Emilio Tuñón (ed.). Revista Circo, number 157. page. 6
- (Blandin ,1977) BLANDIN Landivar, Carlos. El clima y sus características en el Ecuador. Quito, Ecuador 1977: Instituto Panamericano de Geografía e Historia.
- (Cañadas, 1978) CAÑADAS Cruz, Luis. El Mapa Bioclimático y Ecológico del Ecuador. Quito: s.n., 1983. ISN: 6649.
- (Estrada et al, 1983), Estrada, Eduardo; Cañadas Luis Clasificaciones climáticas. En CAÑADAS Cruz, Luis. El Mapa Bioclimático y Ecológico del Ecuador. Quito: s.n., 1983.
- (DMA, 2009) Dirección Metropolitana de Ambiente MDMQ. Atlas Ambiental del Distrito Metropolitano de Quito. [ed.] María Luz Albuja. Quito: MDMQ, 2009. Vol. 1. Vol2.
- (Egesco, 1994) EGESCO. Hidrología. Caracterización Físico-Climática. Estudios definitivos del control de escurrimientos en las laderas del Pichincha. Tomo II. Quito, Ecuador. 1994.
- (Pourrut, Leiva ,1989) .PORROUT Pierre, CADIER Eric, et al “Estudio Hidro climatológicos: Marco, Crónica y Aspectos Metodológicos Sucintos” in “El Agua en el Ecuador” Corporación Editora Nacional .Quito 1989.
- (Pourrut, 1995a) PORROUT Pierre, ROVERE Oscar, et al “Clima del Ecuador” in “El Agua en el Ecuador” Corporación Editora Nacional .Quito 1995
- (Pourrut, 1995b) PORROUT Pierre, NOUVELOT Jean Francois “Anomalías y Fenómenos Climáticos Extremos” in “El Agua en el Ecuador” Corporación Editora Nacional .Quito 1995.
- (INHAMI, 2010) INAMHI, Instituto Nacional de Meteorología e Hidrología. Análisis Climatológico: 01 - 10 de agosto de 2009. Quito: INAMHI, 2009. pág. 10.
- (INHAMI, 2010) INAMHI, Dirección de Gestión Meteorológica. Anuario Meteorológico 2009. Quito, Ecuador: INAMHI, 2010. Vol. 45.
- INAMHI, Sección Educativa. Sección Educativa: Fenómeno del Niño. [Cited: 02 de Septiembre de 2012.] Available at: <http://www.inamhi.gov.ec/educativa/elnino.htm>.
- INEC, Instituto Nacional de Estadísticas y censos. Data set for population Census 2010
- ISO-7730, Ergonomía del ambiente térmico. Determinación analítica e interpretación del bienestar térmico mediante el cálculo de los índices PMV y PPD y los criterios de bienestar térmico local. 2005. International Standard Organization.
- (Jaramillo, et al, 2011). JARAMILLO, Esteban, VAN SLUYS, Christine, JIMÉNEZ, Sylvia. Manual de tipologías urbano-arquitectónicas para un desarrollo urbano sustentable con incidencia sobre el cambio climático en el DMQ. Quito 2011, Ecuador. Trabajo de consultoría realizado para la Gesellschaft für internationale zusammenarbeit (GIZ)-(MDMQ).
- (Lozano, 1991) LOZANO, Alfredo. Quito, ciudad milenaria. Editorial Abya Ayala 1991.Pg 30.

(Naranjo, 1989)NARANJO, Plutarco. El clima del Ecuador. Quito 1989, Ecuador : Casa de la Cultura Ecuatoriana.

(Peel, 2007)Peel M. C., Finlayson B. L., and McMahon T. A. Updated world map of the Koppen-Geiger climate classification:Hydrol. Earth Syst. Sci. Discuss., 4, 439–473, 2007. [Cited : 02 de Septiembre de 2012.] Available at :www.hydrol-earth-syst-sci-discuss.net/4/439/2007/.

REMMAQ; Red Metropolitana de Monitoreo Ambiental de Quito. [Cited : 02 de Septiembre de 2012.] Available at: <http://190.152.144.75/reportes/Reporte10MinutoGraph.aspx>
<http://www.quitoambiente.gob.ec/ambiente/index.php/datos-descarga-mensual>

Multiphysic Design of a Street Section

Catherine Knopf-Lenoir¹, David Muñoz², Raphaël Nahon³, Benoit Beckers¹

¹ Compiègne University of Technology - Sorbonne University
Rue Roger Couffolenc, CS 60319
60203 Compiègne – France
catherine.vayssade@utc.fr, benoit.beckers@utc.fr

² Geometry and Graphics Group, Universitat de Girona, Spain
davidmunoznovo@gmail.com

³ Université de Lille 1
Cité Scientifique 59655 Villeneuve d'Ascq, France
raphael.nahon@ed.univ-lille1.fr

Keywords: Multi-physics, Heat transfer, Urban Acoustics, Solar Radiation and Optimization.

Abstract. *The objective of the present work is to illustrate and discuss how numerical models can be used to simulate different physical phenomena that have a great impact on the comfort of buildings: acoustics and solar radiation, in order to:*

- 1) get estimations of the noise level, temperature and natural light on any facade as functions of the noise sources in the street and the local climate,*
- 2) evaluate the sensitivity of these quantities with respect to some basic shape features,*
- 3) and propose an approach to optimize the shape considering different requirements on the levels of noise (to minimize), temperature and/or natural light at the ground floor (to maximize).*

1 Introduction

Ventilation, inertia, shading and insulation are ingredients of the four main strategies of bioclimatic architecture. It is also necessary to consider the characteristics of a particular climate, so as to compose these resources [Beckers 2012a]. Ventilation predominates in the hot and humid climates mainly found in the tropical regions. Where there is a large daily temperature variation, as in the tropical deserts, inertia is particularly welcome. Mediterranean architecture is mainly determined by the combined influences of light and shadow. Insulation is the key word in the cold regions.

With these principles, it is possible to design buildings where life is always better than outside, where maximum comfort is achievable at low energy cost. With the help of renewable energy, we can even consider “positive energy buildings”.

The urban scale introduces an additional difficulty, because the city itself is altering the climate locally. From the patterns of environmental physics, we begin to be able to quantify the evolution of the temperature of the urban air (Urban Heat Island) [Masson 2013]. From the patterns of building physics, we can manage the heat exchanges across the block or the district [Beckers 2012b]. Now, these two problems are linked. In addition to various physical couplings (solids, fluids, water cycle ...), multiscale aspects necessarily appear, which remain today a major challenge for modeling [Beckers 2016]. However, the inhabitants of the cities, their architects and their political representation do not see things in such a comprehensive way. For them, living in urban areas has essentially two consequences: less natural light and more noise. We might add: the quality of the views (privacy), the air quality (smelling, pollution), and the availability of transportation ... Most of these problems have a clear physical basis, but they are not coupled together by the physics: however, they are by the architecture and its usage. Thus, the sound waves and the heat do not interfere with each other, but excessive noise is forcing residents to close windows, even in summer, when cross ventilation would avoid air conditioning...

To address such issues, we have at our disposal tools to assist us for the efficient design, especially in the field of solar radiation [Beckers 2006]: we can design a solar protection, assess the photovoltaic potential on roofs, study light distribution in complex spaces. The contribution of optimization techniques then allows to dimension the openings [Fernández 2016] or to seek the optimal shape of a set of buildings [Vermeulen 2013] or a whole neighborhood [Vermeulen 2015].

However, to really accomplish the urban dimension, it is necessary to progress in three areas:

- Improving the quality and flexibility of the geometric model, built by procedural methods to wisely simplify the level of details of near [Besuievsky 2014] and far objects [Muñoz 2015];
- Define convenient parameters to quantify and qualify the light that reaches simplified interiors [Nahon 2015] or even just outside the windows, when the size of the geometric model makes no longer possible to model the interior [Nahon 2016];
- Improve and accelerate computational algorithms, using the best available projections [Beckers 2014b], in particular to distribute the incident energy on the sky vault [Beckers 2014c].

To include other areas in this process, starting with heat transfer in solids and urban acoustics, it must be agreed about the lowest common denominator to the models that we believe necessary. The natural candidate is the finite element method [Beckers 2016]. Today there are environments such as "Comsol Multi-physics" [Comsol 1998] where we can find all the necessary tools. The purpose of this paper is to present a first exploration of these

environments applied to the simplest urban problem: find a street profile that gives the best compromise between sound, heat and light fields.

2 Physical Models

As a starting point, the first observation is that any street generates shadows. If it is oriented from north to south, as in the case studied here, the buildings have facades eastward, and they are sunny in the morning, or westward, and they directly capture sun rays in the evening. Sun radiation is composed of photons in short wave (their wavelength is ranging from UV to visible light and to near infrared, always below 4 microns). These photons can be absorbed by the surface they intercept. They then contribute to warming. If the surface is light in color, they are likely to be reflected, in general diffusely. In this case, the so called techniques of "radiosity" allow calculating at reasonable cost the full set of reflections [Beckers 2011].

Sound rays have very different behavior. In architectural and urban acoustics, reflection is mainly specular, and then it is necessary to capture this behavior in the design phase: the facades and balconies can be considered as a first approximation, as reflectors that guide sound reflection in the same way as mirrors do with light. The so called "geometric" methods (sound rays) then correspond to the right answer to the modeling task [Beckers 2009].

In general, the windows are the main places of exchange between the outside and inside (thermal and acoustic) and even the only one for light. The here studied configuration is shown in Figure 1. This is a street lined with two-story buildings equipped with balconies. It is proposed that these balconies have a form such that specular reflections from the street noise cannot reach the top floor (Figure 1 left). The upper windows will still have a good view of the sky factor (Figure 1 right), but the lower windows do not have anymore, because of the balcony. Seeing less of the sky, they also lose some of the direct solar radiation that would reach them either in the morning (east facing windows) or at night (west facing windows).

We imagine that the street is located in Quito, on the equator, and we are studying it on 21 September at the Autumn Solstice. That day, the sun rises exactly in the east, reaches the zenith at noon, and sets exactly in the west, after a journey of 12 hours (on the equator, every day is twelve hours long). So, the solar journey is exactly in the street section plane, and the thermal problem could, exceptionally, be fully solved in two dimensions.

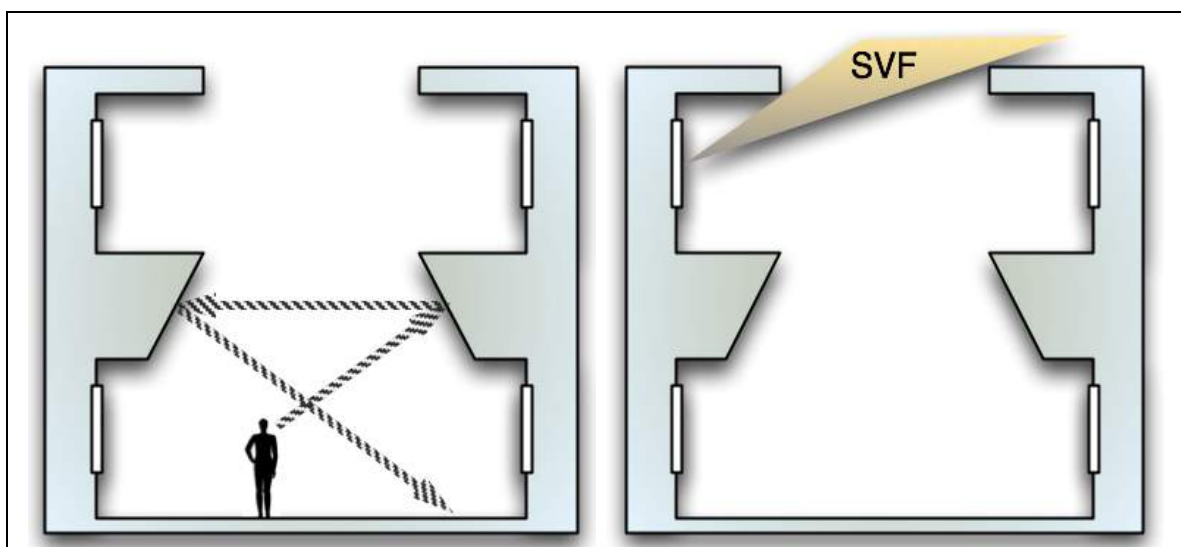


Figure 1: General configurations

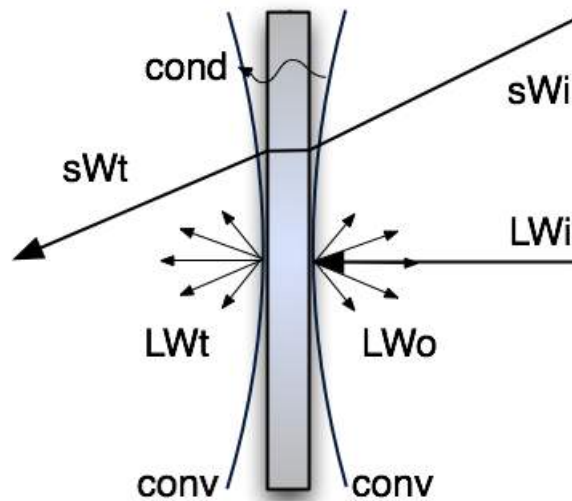


Figure 2 : Scheme for a window

Figure 2 shows the thermal balance on a surface. The incident shortwave radiation (sWi) reaches the surface, and partly crosses it (sWt) in the case of a window. Another part of the radiation is absorbed, as well as the incident long wave (LWi) radiation, which comes from the ground, the opposite façade and the sky. The absorbed heat passes through the wall by conduction and both surfaces of the wall in turn emit long-wave (LWo and LWt), according to the fourth power of their temperature (Stefan Boltzmann law). Finally, convection takes place on both sides of the wall.

3 Case Study

Figure 3 shows a symmetric 3D model of two buildings facing in a narrow street. The façade walls have a part overhanging in the street, which is parameterized with 2 design variables $x1$ and $x2$ (Figure 4).

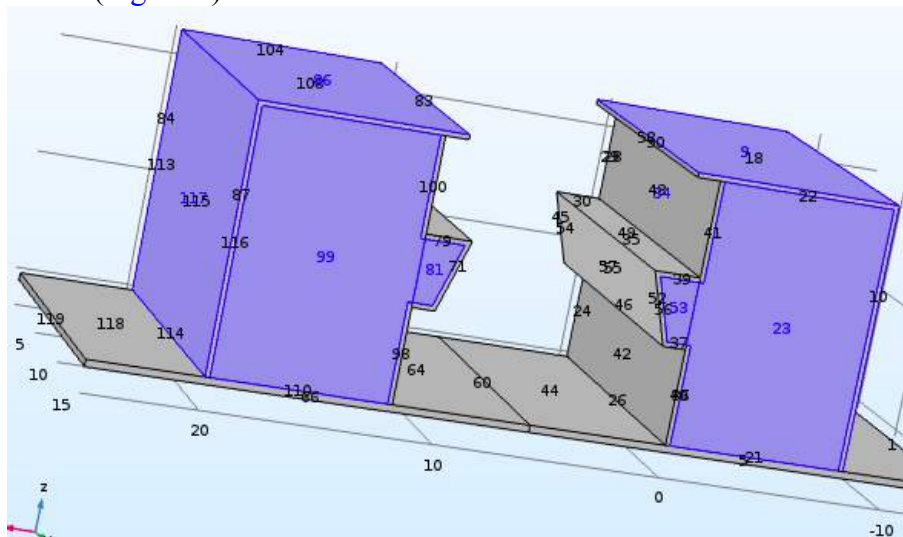


Figure 3: Model for 3D thermal analysis

Two physics are considered: acoustics and thermics. We choose to characterize the sound level by the sound intensity integrated on the first floor wall, and the thermal effect by the temperature of the wall at the ground floor.

The objective of the study is to evaluate the influence of the shape of the façades on these two criteria and to show how a final shape could be found in order to get the best compromise, depending on the two performance requirements that are imposed.

The acoustics model is defined by the surfaces which represent both façades and the ground between them; two “side” and one “top” virtual surfaces are necessary to close the domain.

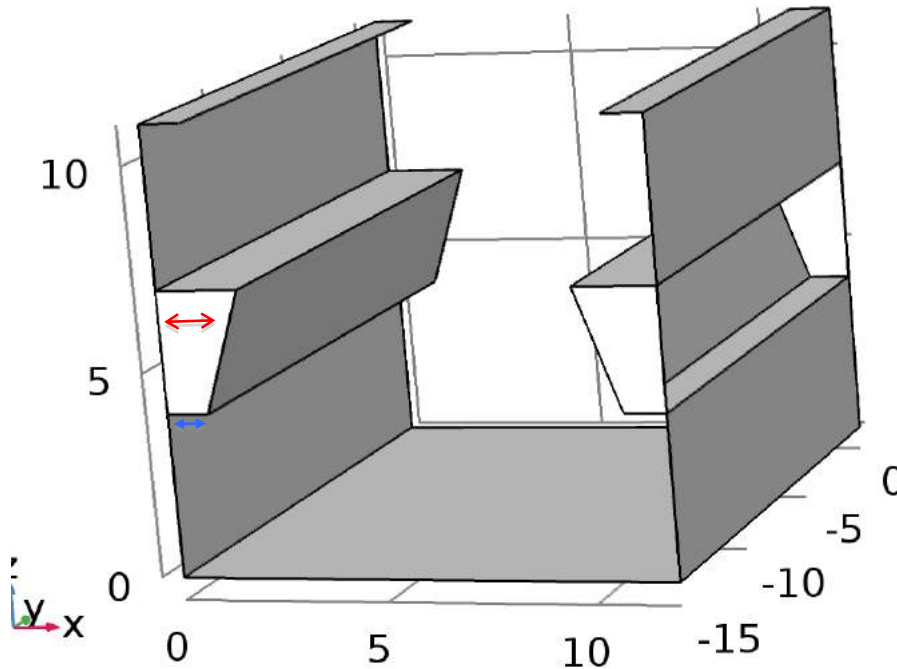


Figure 4 : Model for acoustic simulation

4 Optimization

4.1 Acoustical model

The acoustic model is defined by the surfaces which represent the two façades and the ground between them; two “side” and one “top” virtual surfaces are necessary to close the domain.

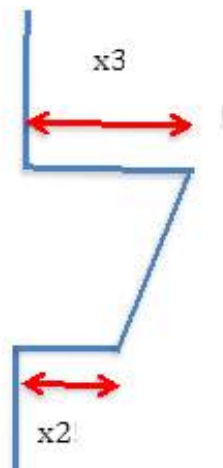


Figure 5 : Design variables

Shape	Intensity on upper floor wall, left side (W)
1 : no balcony (x2, x3)=(0, 0)	$19.66 \cdot 10^{-4}$
2 : balcony with inclined wall (x2, x3)= (0.5 m, 1m)	$3.12 \cdot 10^{-4}$
3 : (x2, x3)= (1m, 2m)	$2.61 \cdot 10^{-4}$
4 : balcony with vertical wall (x2, x3)= (2m, 2m)	$5.37 \cdot 10^{-4}$

Table 1 - Sensitivity of noise level with respect to the shape

The sound source ($0.001[W]$) is located at the point S ($x=4, y=-10, z=1.5$) (Figure 4 and Figure 5); the walls are supposed to be made of concrete (specular reflection, absorption coefficient: 0.05); the sound intensity on the left wall, upper floor, is computed by using 40000 rays, which is the lowest number to get convergent values of the results; Table 1 presents the intensity corresponding to 4 balcony shapes.

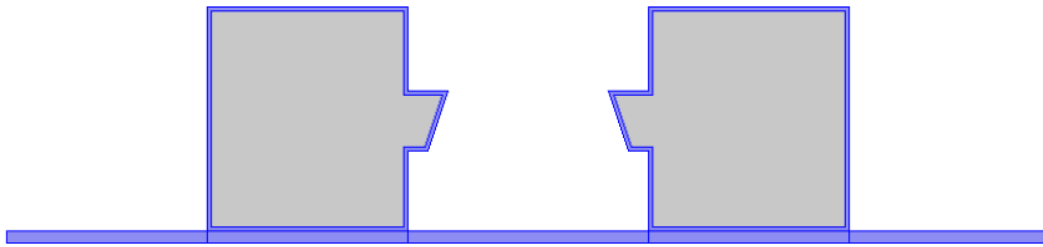


Figure 6 : Thermal study, 2D model

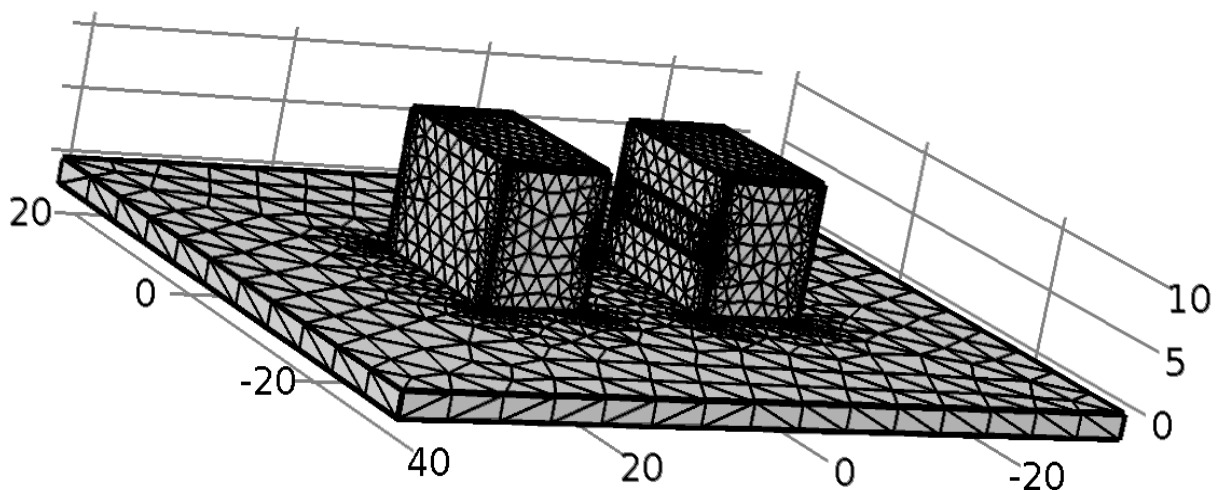


Figure 7 : Thermal study, 3D model

We observe that the presence of a balcony allows reducing the sound intensity by a factor up to 85 %; the lowest intensity is obtained for the shape 3.

4.2 Thermal Model

We consider now the thermal problem. The street is assumed to be located at (Lat: 0° , Long: 78°). In a first step, as we need only global quantities (average temperature on the surface of the walls), we simplify the problem by taking a 2D representation (Figure 6). In this case, the solar source is not considered; the variation of the temperature field with respect to the shape is very low, and it is not possible to determine the best solution because the precision of the model itself is not sufficient.

Therefore, we choose now a transient 3D model taking into account surface to surface radiation. It is necessary to mesh all the walls as 3D components, which gives a high number of degrees of freedom in the finite element system to solve (~ 50000 degrees of freedom, Figure 7), at each time step (every 30' from 5 a.m. to 7 p.m.).

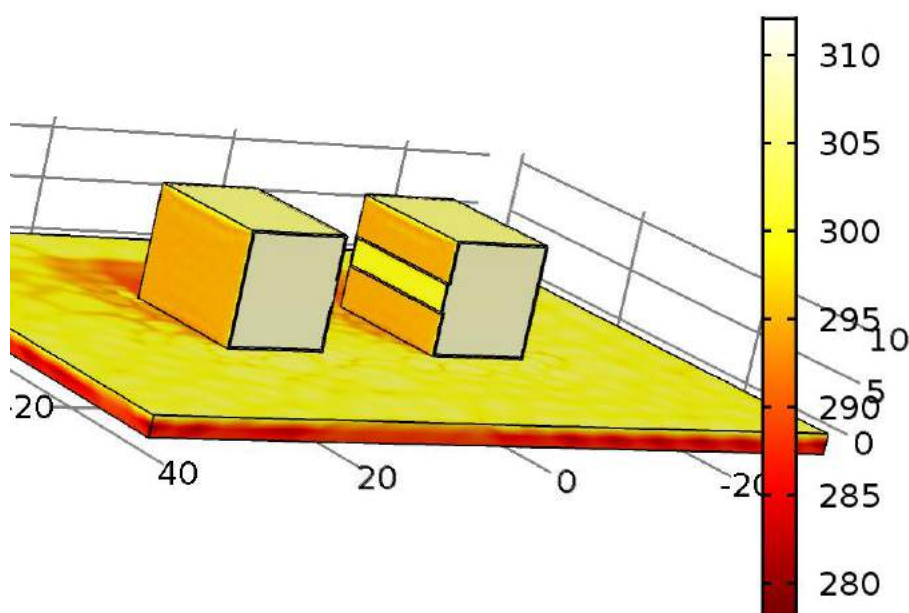


Figure 8 : Temperature field at 1 p.m.

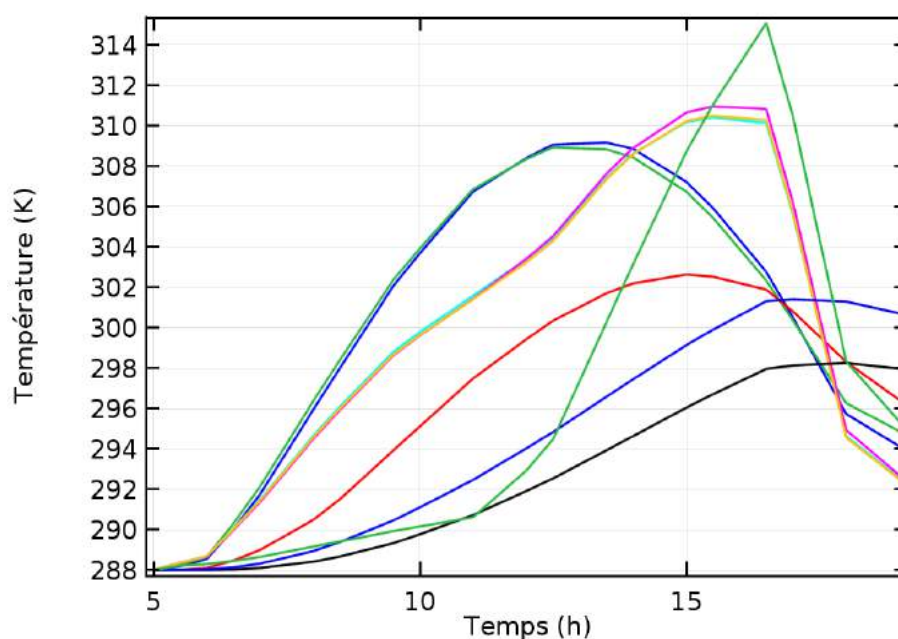


Figure 9 : Evolution of the temperature at different locations on the facades

As we can expect, this model provides more complete and more precise information (Figure 8 and Figure 9). The question is now: how to choose the type of responses to calculate: temperature, energy... and the time or location to consider: maximum/average/point values ... to get “performance criteria” which are significant for architects or engineers? Even if some quantities seem almost equivalent, the optimal solution can be different for these criteria. In our example, if we are looking for the shape providing the highest average temperature on the wall of the ground floor, we find that the shape without balcony is clearly the best one. On the contrary, the average value on all external walls is almost insensitive to the shape.

4.3 Multicriteria solution

If we come back to our initial aim: to consider both acoustics and thermics, we see that the best solution for the thermal problem is in contradiction with the best solution for acoustics. It means that, in a general case, optimization has to find a compromise between the main physical phenomena that we consider as important. The easiest way to solve this kind of problem is to convert it into a constrained problem:

$$\begin{aligned} & \text{Minimize (or maximize) } f(x) \\ & \text{with: } g_j(x) \leq 0 \quad j = 1, \dots, m \\ & x = (x_1, x_2, \dots, x_m): \text{shape variable} \end{aligned}$$

$$\begin{aligned} & f(x): \text{objective function} \\ & g_j(x): \text{constraint functions} \end{aligned}$$

In the test example presented before, the objective function can be associated to acoustics (Min noise), and then the constraints could be defined by imposing a minimum level of temperature to satisfy at a given time $T(t_0) \geq T^{imp}$

There are very efficient numerical methods to solve this type of problem; moreover, some methods exist to estimate how the optimal solution varies depending on the limit value T^{imp} . Other approaches, which need a high number of numerical simulations, allow to find at the same time all the best trade-offs between the criteria.

5 Conclusions

Because optimization problems are dealing with iterative algorithms, a large number of simulations must be performed. So, fast numerical procedures are needed to solve the acoustic and thermal problems. They can be obtained by model reduction techniques or by response surface methods, which are both using a small number of high precision solutions to build explicit approximations, or by simplified models, for instance, models based on basic physics.

Today, new alternatives are also open. Indeed, the deep experience gained in the use of finite element method in the last fifty years for the solution of most engineering problems suggests revisiting old techniques to solve this application.

We have shown [Beckers 2015] that the heat flow element models, dual to the temperature ones, have an excellent behavior and allow performing error analysis. These elements are built with a set of degrees of freedom located on the sides in 2D or on the faces in 3D. For this reason, and because the simulations are dealing with radiative loads often related to radiosity methods [Beckers 2013], these models could give some improvement in the interpretation and the processing of the results.

With the same focus of improving the performance of the solvers, the superelement technique [Beckers 2113, 2014a] is expected to help in the handling of massive transient thermal problems including non linear boundary conditions.

References

- [Beckers 2006] Benoit Beckers & Luc Masset, Heliodon2, Software, references & manuals (in French & Spanish), **2006**, <http://www.heliodon.net>
- [Beckers 2009] Benoit Beckers & Nicoletta Borgia, *The Acoustic Model of the Greek Theatre*, Protection of Historical Buildings - PROHITECH 2009, June 21-24 **2009**, Roma, Italy.
- [Beckers 2011] Benoit Beckers, Impact of Solar Energy on Cities Sustainability, in *Architecture & Sustainable Development*, (vol.2, 395-400), Ed. M. Bodart & A. Evrard, Proc. 27th Int. Conf. on Passive and Low Energy Architecture (PLEA 2011), July, 13-15, **2011**, Louvain-la-Neuve, Belgium.
- [Beckers 2012a] Benoit Beckers, "Worldwide aspects of solar radiation impact", in *Solar Energy at Urban Scale*, chap. 5, Ed. B. Beckers, John Wiley and Sons, Inc., **2012**.
- [Beckers 2012b] Pierre Beckers & Benoit Beckers, Radiative Simulation Methods, in *Solar Energy at Urban Scale*: 205-236, ed. B. Beckers, John Wiley and Sons, Inc., **2012**.
- [Beckers 2013] Benoit Beckers, "Taking advantage of low radiative coupling in 3D urban models." *Proceedings of the Eurographics Workshop on Urban Data Modelling and Visualisation*. Eurographics Association, **2013**.
- [Beckers 2014a] Benoit Beckers and Pierre Beckers, Super Element Technique for Solar Energy Optimization at Urban Level, *OPT-i, International Conference on Engineering and Applied Sciences Optimization*, 4-6 June **2014**, Kos Island, Greece.
- [Beckers 2014b] Benoit Beckers, Pierre Beckers, Reconciliation of Geometry and Perception in Radiation Physics, John Wiley and Sons, Inc., 192 pages, July **2014**.
- [Beckers 2014c] Benoit Beckers, Pierre Beckers, Sky vault partition for computing daylight availability and shortwave energy budget on an urban scale, *Lighting Research and Technology*, vol. 46 n°. 6, Pages 716-728, December, **2014**.
- [Beckers 2015] Pierre Beckers, Benoit Beckers, A 66 line heat transfer finite element code to highlight the dual approach, *Computers & Mathematics with Applications*, Volume 70 Issue 10, November 2015, Pages 2401-2413.
- [Beckers 2016] Benoit Beckers, Multiscale Analysis as a Central Component of Urban Physics Modeling, in *Computational Methods for Solids and Fluids, Multiscale Analysis, Probability Aspects and Model Reduction*, Adnan Ibrahimbegovic (Ed.), Springer International Publishing, 2016, Pages 1- 27.
- [Besuievsky 2014] Gonzalo Besuievsky, Santiago Barroso, Benoit Beckers, Gustavo Patow, A Configurable LoD for Procedural Urban Models intended for Daylight Simulation, *Eurographics Workshop on Urban Data Modelling and Visualization*, April 7-11, **2014**, Strasbourg, France.
- [Comsol 1998] Introduction to COMSOL Multiphysics®, Version: COMSOL 5.1, **1998**

- [Fernández 2016] Eduardo Fernández, Benoit Beckers, Gonzalo Besuievsky, A fast daylighting method to optimize opening configurations in building design, *Energy and Buildings, Volume 125, 1*, August **2016**, Pages 205–218.
- [Masson 2013] Masson V., Y. Lion, A. Peter, G. Pigeon, J. Buyck, E. Brun, "Grand Paris" : Regional landscape change to adapt city to climate warming, *Climatic Change* (**2013**) 117:769–782
- [Muñoz 2015] David Muñoz, Benoit Beckers, Gonzalo Besuievsky and Gustavo Patow, Far-LoD: Level of Detail for Massive Sky View Factor Calculations in Large Cities, *3rd Eurographics Workshop on Urban Data Modelling and Visualization*, November 23, **2015**, Delft, the Netherland.
- [Nahon 2015] Raphaël Nahon, Gonzalo Besuievsky, Eduardo Fernández, Benoit Beckers, Olivier Blanpain, Exploring metrics on the evaluation of the bioclimatic potential at early stages of urban project, *International conference CISBAT on "Future buildings and districts sustainability from nano to urban scale"*, September 9-11, **2015**, EPFL - Lausanne, Switzerland.
- [Nahon 2016] Raphaël Nahon, Benoit Beckers, Olivier Blanpain, Modélisation de l'éclairage naturel dans les premières étapes d'un projet d'aménagement, *34^{èmes} Rencontres de l'AUGC*, Université de Liège, Belgique, May 25-27 **2016**.
- [Vermeulen 2013] Thibaut Vermeulen, Jérôme Henri Kämpf, Benoit Beckers, Urban Form Optimization for the Energy Performance of Buildings Using Citysim, *International conference CISBAT on "Clean Technology for Smart Cities and Buildings"*, September 4-6, **2013**, EPFL - Lausanne, Switzerland.
- [Vermeulen 2015] Thibaut Vermeulen, Catherine Knopf-Lenoir, Pierre Villon, Benoit Beckers, Urban layout optimization framework to maximize direct solar irradiation. *Comput. Environ. Urban Syst.* **2015**, 51, 1–12.

Urban Climate, Human behavior & Energy consumption: from LCZ mapping to simulation and urban planning (the MApUCE project)

V. Masson¹, J. Hidalgo², A. Amossé⁵, E. Bocher⁷, M. Bonhomme⁵, A. Bourgeois⁸, G. Bretagne³, S. Caillerez³, E. Cordeau³; C. Demazeux⁴; S. Faraut⁵, C. Gallato³, S. Haoues-Jouve², M.-L. Lambert⁴, A. Lemonsu¹, J.-P. Lévy⁸, N. Long⁶; C.-X. Lopez², G. Petit⁷, M. Pellegrino⁹, C. Pignon⁶, C. Plumejeaud⁶, V. Ruff³, R. Schoetter¹, N. Tornay⁵, D. Vye⁶

¹ Centre National de Recherches Météorologiques, Météo-France/CNRS
42 av Coriolis, 31057, Toulouse, France
e-mail: valery.masson@meteo.fr



² Solidarity, Society and Territory Interdisciplinary laboratory, Toulouse, France



³ French National Federation of Urban Planning agencies, Paris, France



⁴ Urban Planning & Law laboratory, Aix-Marseille University, Aix-en-Provence, France



⁵ Laboratory of Research in Architecture, Toulouse, France



⁶ Laboratory on coastal environment and society, La Rochelle, France



⁷ Laboratory on Sciences of Information Transfert and Communications, Lorient, France



⁸ Laboratory on technics, territories and societies, Univ. of Paris-East, Marne-La-Vallée, France



⁹ Lab'Urba, Univ. of Paris-East, Marne-La-Vallée, France

Keywords: Urban database, Urban climate, Energy consumption, Urban planning, Behaviors

Abstract. *The goal of the project is to propose a methodology to integrate quantitative energy and climate data in urban policies. In order to achieve this, the first objective is to obtain data from numerical simulations, focusing on urban microclimate and building energy consumption. Both aspects are physically coupled as domestic heating and air-conditioning are highly meteorologically dependent and heat waste impacts the Urban Heat Island. For this we develop a generic and automated method for generating Local Climate Zones (LCZ) for all cities in France at the scale of each urban block, including the urban architectural, geographical and sociological parameters necessary for the energy and microclimate simulations. Human behavior being a very potent level to address energy consumption reduction, a model of energy consumer behavior is also developed inside our coupled microclimate building energy model, and is linked to the social information from the database. The second objective is to define vectors, understandable by urban planners, to include quantified energy-climate data to legal urban planning documents. This is done by analysis of legal and planning documents, of a few “best cases” and based on urban planning agencies requirements. The urban database, tools and models will be available as open-source.*

Introduction

The MApUCE project aims to integrate in urban policies and most relevant legal documents quantitative data from urban microclimate, climate and energy.

The primary objective of this project is to obtain climate and energy quantitative data from numerical simulations, focusing on urban microclimate and building energy consumption in the residential and service sectors, which represents in France 41% of the final energy consumption. Both aspects are coupled as building energy consumption is highly meteorologically dependent (e.g. domestic heating, air-conditioning) and heat waste impact the Urban Heat Island. We propose to develop, using national databases, a generic and automated method for generating Local Climate Zones (LCZ, see figure 1) for all cities in France, including the urban architectural, geographical and sociological parameters necessary for energy and microclimate simulations.

As will be presented, previous projects on adaptation of cities to climate change have shown that human behavior is a very potent level to address energy consumption reduction, as much as urban forms or architectural technologies. Therefore, in order to further refine the coupled urban climate and energy consumption calculations, we will develop within TEB (and its Building Energy Module) a model of energy consumer behavior.

The second objective of the project is to propose a methodology to integrate quantitative data in urban policies. Lawyers analyze the potential levers in legal and planning documents. A few “best cases” are also studied, in order to evaluate their performances. Finally, based on urban planning agencies requirements, we will define vectors to include quantified energy-climate data to legal urban planning documents. These vectors have to be understandable by urban planners and contain the relevant information.

To meet these challenges, the project is organized around strongly interdisciplinary partners in the following fields: law, urban climate, building energetics, architecture, sociology, geography and meteorology, as well as the national federation of urban planning agencies.

In terms of results, the cross-analysis of input urban parameters and urban micro-climate-energy simulated data will be available on-line as standardized maps for each of the studied cities. The urban parameter production tool as well as the models will be available as open-source. LCZ and associated urban (and social!) indicators may be integrated within the WUDAPT database, that aims to describe many cities in the world using the LCZ terminology.

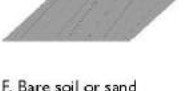
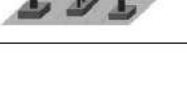
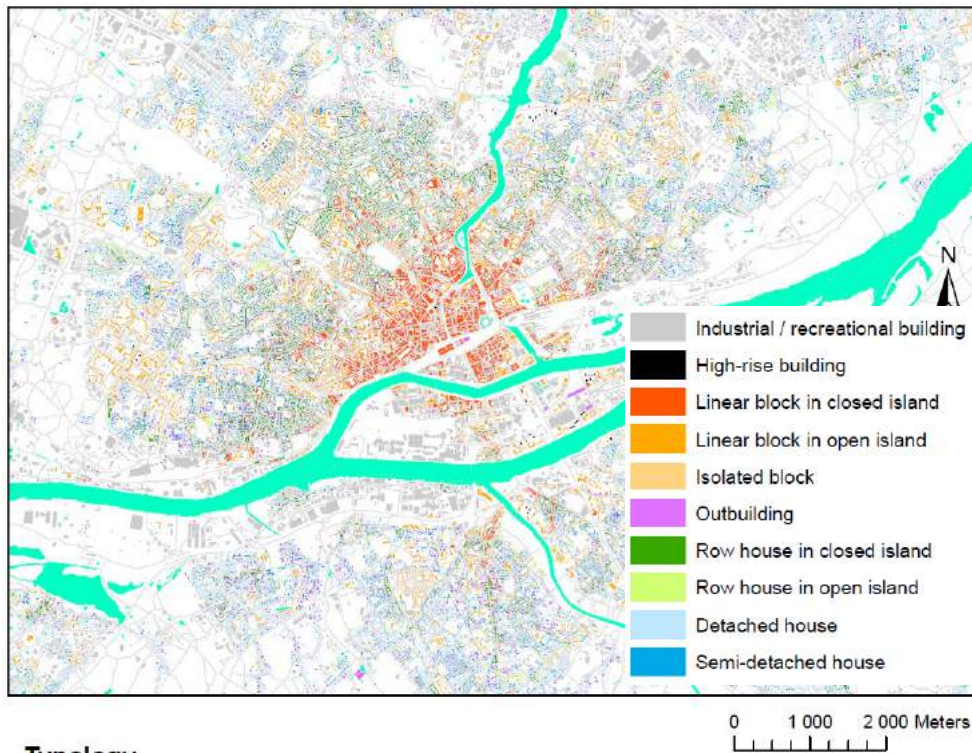
Built types	Definition	Land cover types	Definition
 <p>1. Compact high-rise</p>	Dense mix of tall buildings to tens of stories. Few or no trees. Land cover mostly paved. Concrete, steel, stone, and glass construction materials.	 <p>A. Dense trees</p>	Heavily wooded landscape of deciduous and/or evergreen trees. Land cover mostly pervious (low plants). Zone function is natural forest, tree cultivation, or urban park.
 <p>2. Compact midrise</p>	Dense mix of midrise buildings (3–9 stories). Few or no trees. Land cover mostly paved. Stone, brick, tile, and concrete construction materials.	 <p>B. Scattered trees</p>	Lightly wooded landscape of deciduous and/or evergreen trees. Land cover mostly pervious (low plants). Zone function is natural forest, tree cultivation, or urban park.
 <p>3. Compact low-rise</p>	Dense mix of low-rise buildings (1–3 stories). Few or no trees. Land cover mostly paved. Stone, brick, tile, and concrete construction materials.	 <p>C. Bush, scrub</p>	Open arrangement of bushes, shrubs, and short, woody trees. Land cover mostly pervious (bare soil or sand). Zone function is natural scrubland or agriculture.
 <p>4. Open high-rise</p>	Open arrangement of tall buildings to tens of stories. Abundance of pervious land cover (low plants, scattered trees). Concrete, steel, stone, and glass construction materials.	 <p>D. Low plants</p>	Featureless landscape of grass or herbaceous plants/crops. Few or no trees. Zone function is natural grassland, agriculture, or urban park.
 <p>5. Open midrise</p>	Open arrangement of midrise buildings (3–9 stories). Abundance of pervious land cover (low plants, scattered trees). Concrete, steel, stone, and glass construction materials.	 <p>E. Bare rock or paved</p>	Featureless landscape of rock or paved cover. Few or no trees or plants. Zone function is natural desert (rock) or urban transportation.
 <p>6. Open low-rise</p>	Open arrangement of low-rise buildings (1–3 stories). Abundance of pervious land cover (low plants, scattered trees). Wood, brick, stone, tile, and concrete construction materials.	 <p>F. Bare soil or sand</p>	Featureless landscape of soil or sand cover. Few or no trees or plants. Zone function is natural desert or agriculture.
 <p>7. Lightweight low-rise</p>	Dense mix of single-story buildings. Few or no trees. Land cover mostly hard-packed. Lightweight construction materials (e.g., wood, thatch, corrugated metal).	 <p>G. Water</p>	Large, open water bodies such as seas and lakes, or small bodies such as rivers, reservoirs, and lagoons.
 <p>8. Large low-rise</p>	Open arrangement of large low-rise buildings (1–3 stories). Few or no trees. Land cover mostly paved. Steel, concrete, metal, and stone construction materials.	VARIABLE LAND COVER PROPERTIES	
 <p>9. Sparsely built</p>	Sparse arrangement of small or medium-sized buildings in a natural setting. Abundance of pervious land cover (low plants, scattered trees).	Variable or ephemeral land cover properties that change significantly with synoptic weather patterns, agricultural practices, and/or seasonal cycles.	
 <p>10. Heavy industry</p>	Low-rise and midrise industrial structures (towers, tanks, stacks). Few or no trees. Land cover mostly paved or hard-packed. Metal, steel, and concrete construction materials.	<p>b. bare trees</p>	Leafless deciduous trees (e.g., winter). Increased sky view factor. Reduced albedo.
		<p>s. snow cover</p>	Snow cover > 10 cm in depth. Low admittance. High albedo.
		<p>d. dry ground</p>	Parched soil. Low admittance. Large Bowen ratio. Increased albedo.
		<p>w. wet ground</p>	Waterlogged soil. High admittance. Small Bowen ratio. Reduced albedo.

Figure 1 : definition of LCZ typology (from Stewart and Oke 2012)



Typology

Figure 2 : exemple of typology of each buildings, estimated automatically using a random forest algorithm.

1 From Local Climate Zones (LCZ)...

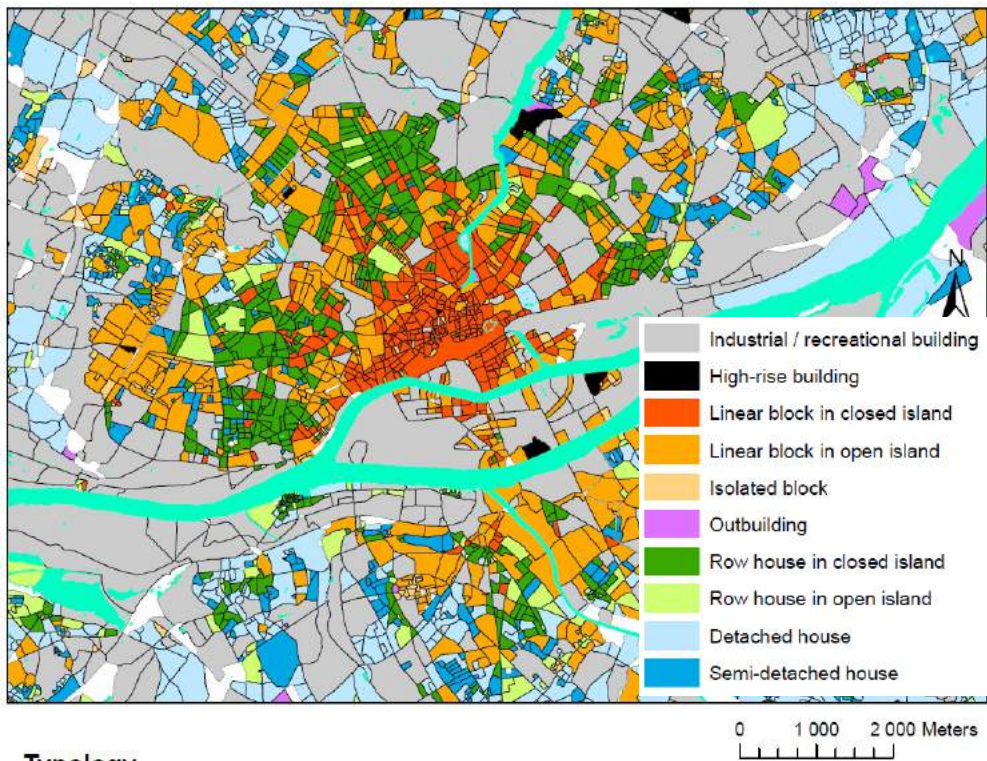
The objective is to define each neighbourhood from a point of view understandable by both urban planners and modellers. The concept of 'Local Climate Zone' (Stewart & Oke 2012) describes both urban morphology and its impacts on local micro-climate.

An automatic platform under a Geographical Information System is built in order to derive 80 urban & social indicators, at building and neighborhood scale (figures 2 & 3). The methodology is :

1.1 to use buildings&social national databases

In order to have a methodology available for all cities in France, we have chosen databases that are homogeneous and simply available on the entire country (from INSEE and IGN institutions). These databases are at several spatial resolutions: the finest is the building scale, with some morphological information (especially building height and shape) but also some usage information (industrial or not). We have then the cadastral parcel scale, with its delimitation for all private domain, and many information about land use (water and road network, vegetation). Using these topographic sources, we compute a new zoning made of the contiguous street-blocks, that can be aggregated then to upper levels to transform it into LCZ (cf infra). Social information is available statistically for surfaces with at least 2000 households each, or on a grid of cells of 200 m by 200 m, with fewer information but useful, like number of inhabitants, or households for instance. Finally, information on architectural

technics and methods are available at larger scale (for example, red bricks are usually used in historical construction in south-West of France).



Typology

Figure 3 : example of typology of each LCZ, estimated automatically from the typology of buildings within.

1.2 to derive the limits of the islets

The islets are continuous street blocks, a scale that is very understandable by urban planners, as it is intimately linked to the structure of the city. In order to define continuous islets, one first aggregates contiguous parcels. Then, as one wishes to include roads and other extra-parcel surfaces in their neighborhoods, a Voronoï algorithm (figure 4) is used to determine the limits between two islets.

1.3 to compute the indicators

Several indicators, covering morphologic ones (example: mean and distribution of building heights), social ones (age of people and family sizes, buildings uses...), and architectural ones (type of material used for walls or roofs,...) are computed at several scales (buildings, bulding blocks, islets). For further modeling, the typology of each neighborhood is defined, which allows them to be then treated as small LCZ.

Such spatial scale is too small for a LCZ from the point of view of the urban climatologist, true, but this is understandable as such for urban planners, which appropriated the concept of LCZ. Furthermore, as can be seen on figure 3, LCZ of the same color can be spatially aggregated in order to reflect the concept of urban climatologists LCZ concept better. The

advantage is that there is more details for each LCZ indicator (e.g. mean building height in the LCZ) when spatial scale is smaller.

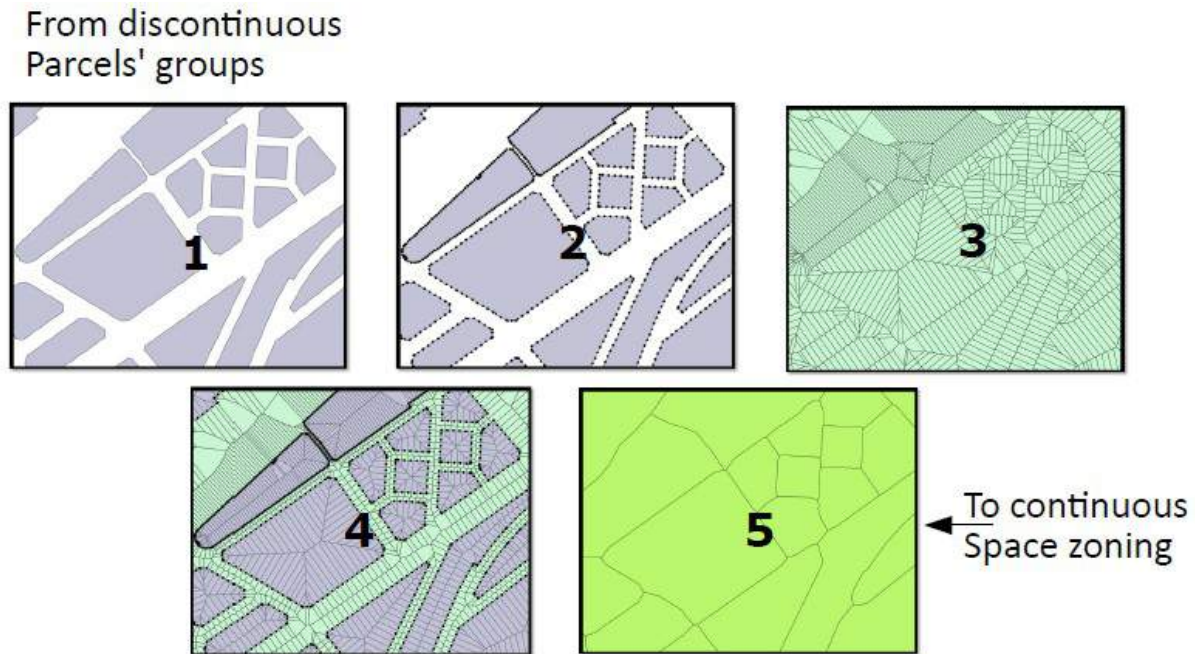


Figure 4 : methodology to define continuous islets

2 ... for modelling of behaviours, energy and micro-climate ...

2.1 Behaviors

Past projects (e.g. MUSCADE, Masson et al 2014) showed that energy consumption can sometimes be more reduced by behaviors than buildings improvements.

The objective is to model behavior, using existing specific databases on relationship between energy consumption & inhabitants practices (e.g. from ENERGIHAB project). Example of behaviors are: target temperature for heating or air-conditioning, occupancy of the building, regulation of heating systems, closing/opening the windows at night, possession of equipment, frequency of use of some appliances (i.e. washing machine) etc.. The method to model each of these behavior or use of the building is to link them to typologies of household and housing using a statistical approach (logistic regression), as these are data we can project (with some hypotheses) at LCZ scale.

Behaviour = function (household, housing)

The behavioral model created in the basis of the ENERGIHAB database (referred to the Ile de France Region only) will be tested and validated on other databases at the national scale, and finally translated to the islet scale through successive adjustments.

The main advantage of islets for such estimation is that they are more homogeneous in their content for housing and households: most of the time, contiguous parcels group similar activities. This, plus the fact that some proxies are precomputed at this scale (number of inhabitants, households, collective housing ...) allows for an more efficient estimation method of households behavior.

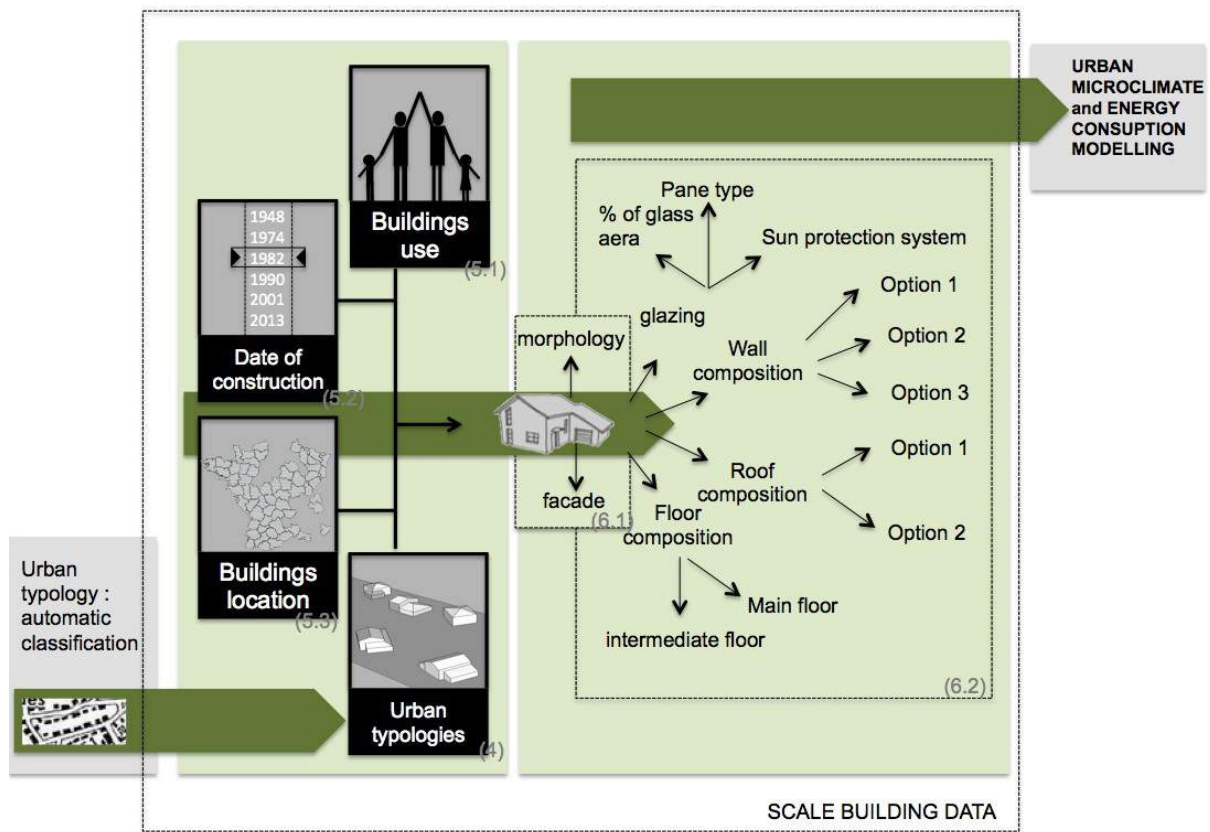


Figure 5 : methodology to define architectural characteristics for the models

2.2 Architectural characteristics

Accurate simulation of the city energy balance requires studying the thermal behavior of buildings and therefore requires knowing many details: at least the buildings geometries, their envelope materials and surroundings ground covering. For instance, information on shape and location of a building are useful to assess the performance of solar panels; information on the materiality of the facades, make it possible to estimate solar gains through the windows and therefore to perform building energy balance simulations (Masson, 2000); etc.

The main issue in integrating this type of information to urban scale simulations is the lack of precision of the available data for buildings (Ching et al., 2009). If a limited number of buildings can be very precisely described (through existing Building Information Model (BIM) for instance (Ferries et al., 2014), but also through historical studies or architectural inventories), the data at the city scale remains broadly heterogeneous.

Our methodology, called GENIUS (GENERator of Interactive Urban blockS), was to perform a literature review combined with interviews of urban planners to characterize a typology of urban forms in the whole French territory, and to associate it with a wide

database. The key theme of our work concerns the integration of building scale data into urban microclimate and energy consumption modeling. It leads us to formulate the question “how can we characterize the building scale in order to update, and to make full use of urban simulation tools?”. An extensive bibliographical study of building materials and systems, architecture and building cultures, conservation, etc. has been done. This describes more than 400 architectural structures of the buildings, that are associated to buildings use, age, location and typology (figure 5). This allows to give information to the urban simulation tools.

3 ... to Urban Planning and Laws

Besides the tasks related to the production of climate and energy consumption data, research on how to integrate energy, micro-climate and climate change issues in urban planning are also being addressed in parallel. This section of the project is titled “Urban planning plans: general framework and transfer”. It is composed by four tasks dealing with: the legal French framework analysis; the analysis of “exemplary cases” from the point of view of their governance and the legal translation of local actions; the analysis of the experience of use and needs of data by the French planning agencies; and finally the development of transferable tools adapted to the French urban planning standards.

3.1 Analysis of legal documents

In this sense, more than twenty planning legal tools have been analyzed from the French urban planning and land management laws; the energy and climate planning documents; documents from the sustainable development field; and finally some specific scoping papers.

The legal analysis shows that:

- Legislative texts provide that the majority of those tools can or should include actions related with mitigation and/or adaptation to the climate change.
- However, each of them is submitted to some levers and obstacles as the precision of the applicable actions, the legal force of the measures and the cross competencies within the stakeholders.
- The study concludes that to efficiently take into account microclimate, building energy consumption and energy human behavior, actions should be addressed not only by one but with several complementary legal documents.

3.2 Analysis of exemplary cases

The objective of the “exemplary cases” task, is to analyze the levers that permit the transfer from climatic knowledge to practices. And also, to understand what is the applicable scale of such information and what are the obstacles. In summary, why the transfer of climate information is successfully done in some places and not in others?

At the beginning a large panel of cases were identified in France and abroad (Europe, America, Asia and Oceania) based on scientific and grey literature as well as some preliminary interviews with researchers. In a second time the focus was put on a panel of cases that seemed particularly interesting: Germany and Japan due to their high degree of expertise at both research and implementation levels; Spain and Netherlands due to an incipient practice in this sense. In France the cities of Paris, Grenoble, Lyon, Marseille, Frontignan and Agen were also deeply analyzed.

Methodologically, the analysis was based on literature, institutional websites and interviews with both practitioners and producers of climatic data, almost always researchers. Three types of targets were considered: implementation at the urban politics level through planning documents, implementation at the operational level (operations of urban spaces) and the development of dedicated agencies and transfer tools (climatic maps or atlas).

The analysis of exemplary cases showed that, **financial means are not the main factor** that inhibits the consideration of energy and climate in city planning. Good practices seem being favored by key persons that make the link between several city services and some other institutions (as laboratories). This work is being completed in coordination with the urban environmental lawyers team that analyze for the same study cases the legal framework at the national, regional and local levels.

3.3 Urban planning agencies survey

To obtain inputs to the tasks related with the exemplary cases and the transfer tools, a survey to all 51 French urban planning agencies has been done. The objective was to analyze how climate and energy issues are being integrated in city planning and urban design and to characterize potential user needs. 25 agencies have been answer the survey showing a large heterogeneity in the practices depending on the local context (size of the city, historical relations with the municipality, ...).

The result shows that there are a multiplicity of concerns related to energy consumption that are currently addressed but micro-climate is less taken into account. It has been pointed out the difficulty of data access and, when they exists, their unadapted spatial scale to perform territorial diagnostics. The weak use of Geographical Information Systems to cope with this issues was pointed out.

Concerning the expectations related to the MAPUCE project, agencies confirms the necessity of the climatic and energy consumption data from the project, but, they point out the importance to produce indicators applicable to all type of cases, from big to little cities, including rural or poor densely built territories. Needs on thematic training and generic tools are also often indicated.

3.4 Urban Climate Maps

The work on tools for transferring energy and climate data in a comprehensive way are currently underwork and will be nourished by the precedent results. Identification of the lacks of knowledge transfer related to climate and energy consumption as well as Environmental Urban Climate Maps will be produced. Methodological sheets and guides will be also produced. Feasibility of the proposed tools will be tested during the project over three terrains, Toulouse, LaRochele and Aix-Marseille. An example of information that can be used, among other, to build Urban Climate Maps for stakeholders is the urban heat island. Spatial interpolation (figure 6) and methodologies to cross various information of different nature are being developed using the MApUCE database.

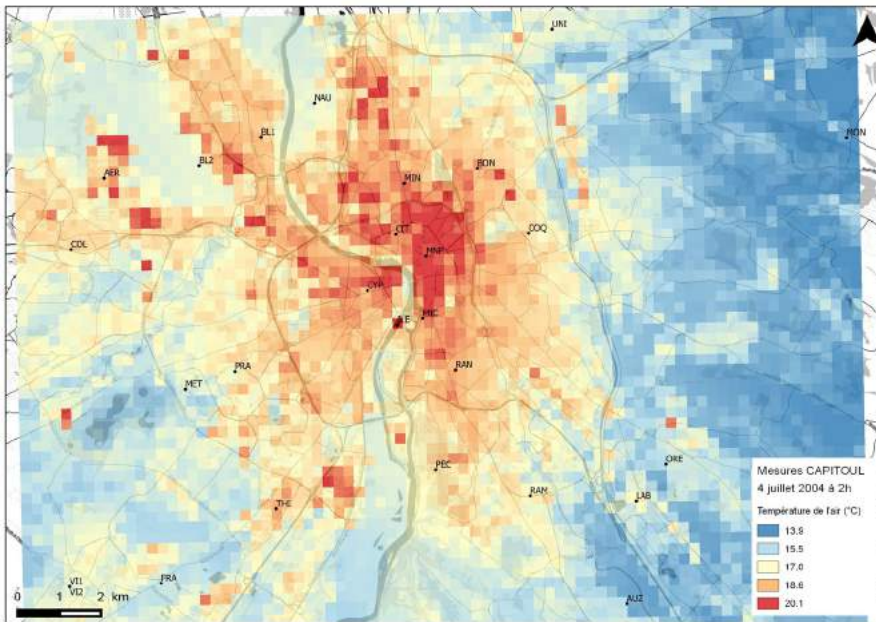


Figure 6 : example of Urban Heat Island on Toulouse (interpolated from CAPITOU data, Masson 2008)

4 Conclusion : what next ?

The project started March 2014. It will last 4 years. After the completion of the urban database over French cities (indicators are already computed on 80 agglomerations, figure 7), simulations of energy and micro-climate will be done with the TEB model. The sociologists and lawyers of the project will analyze urban planning processes in Toulouse, La Rochelle & Marseilles and propose ways to include quantitative data in legal documents 'at the right place, the right moment, with the right tool'.

In terms of results, the cross-analysis of input urban parameters and urban micro-climate-energy simulated data will be available on-line as standardized maps for each of the studied cities. The urban parameter production tool as well as the models will be available as open-source. The fine data obtained within the project can also be used within the frame of the WUDAPT initiative (Mills et al, 2015, See et al 2015). On the one hand, it can be used to validate WUDAPT products, that are produced at larger scale and with much less input information. On the other hand, the LCZ and associated urban (and social!) indicators may be integrated within the WUDAPT database.

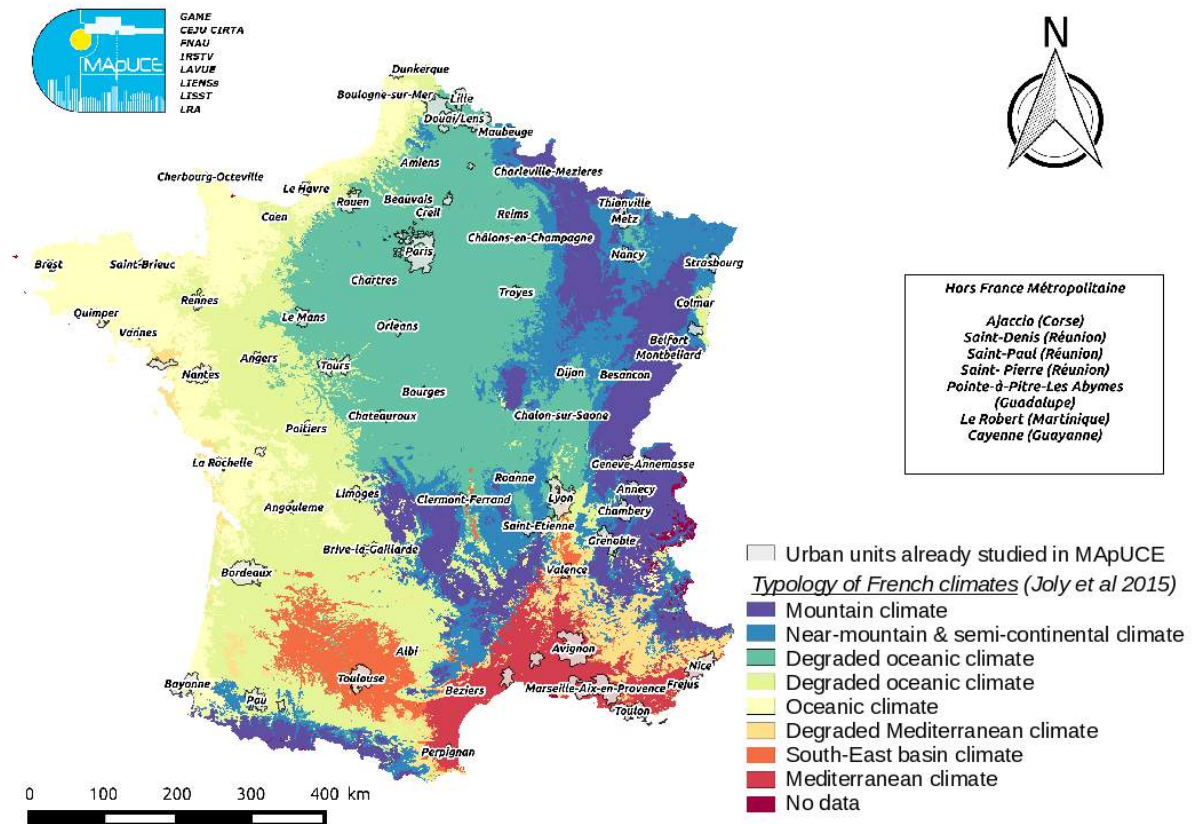


Figure 7 : The agglomerations already computed in the MapUCE database, and their climatic environment

5 References

- Bueno, B., G.Pigeon, L. Norford, K. Zibouche, C. Marchadier 2012: Development and evaluation of a building energy model integrated in the TEB scheme, *Geosci. Model Dev.*, **5**, 433–448.
- Ferries, B., & Bonhomme, M., 2014. La maquette numérique, un moyen d'augmenter la densité informationnelle d'un territoire ? (Building Information Model, a way to increase informational density of a territory?) [in French] In the proceedings of the 6th Seminar of Numerical Architecture Conception - SCAN'14. Luxembourg.
- Masson V., 2000 : A Physically-based scheme for the Urban Energy Budget in atmospheric models. *Boundary-Layer Meteorol.*, **94**, 357-397.
- Masson V., C. Marchadier, L. Adolphe, R. Aguejdad, P. Avner, M. Bonhomme, G. Bretagne, X. Briottet, B. Bueno, C. de Munck, O. Doukari, S. Hallegatte, J. Hidalgo, T. Houet, J. Le Bras, A. Lemonsu, N. Long, M.-P. Moine, T. Morel, L. Nologues, G. Pigeon, J.-L. Salagnac, K. Zibouche, 2014 : Adapting cities to climate change : a systemic modelling approach. *Urban Climate*, **10**, 407-429, doi:10.1016/j.uclim.2014.03.00
- Mills G., J. Ching, L. See and B. Betchel, 2015: An introduction to the WUDAPT project, *9th International Conference on Urban Climate*, **GD2**, 20th-24th July 2015, Toulouse, France.
- Pigeon G., K. Zibouche, B. Bueno, J. Le Bras, V. Masson, 2014 : Evaluation of building energy simulations with the TEB model against EnergyPlus for a set of representative buildings in Paris. *Energy and Buildings*, **76**, 1–14, doi : 10.1016/j.enbuild.2013.10.038
- See L., J. Ching, V. Masson, J. Feddema, G. Mills, M. Neophytou, M. Foley, M. O'Connor, C. Perger, M. Duerauer, S. Frtiz, B. Bechtel 2015, Generating WUDAPT's Specific Scale-dependent Urban Modeling and Activity Parameters: Collection of Level 1 and Level 2 Data, *9th International Conference on Urban Climate*, **GD2**, 20th-24th July 2015, Toulouse, France.
- Stewart I. D. and T. R. Oke, 2012: Local Climate Zones for Urban Temperature Studies. *Bull. Amer. Meteor. Soc.*, **93**, 1879–1900. doi: <http://dx.doi.org/10.1175/BAMS-D-11-00019.1>

Sky Access versus Shading for Pedestrian Comfort in the Hot Tropical Climate of Jeddah

Badia Masoud¹, Benoit Beckers², and Helena Coch³

^{1,3} Architecture energy and environment Group, School of architecture Barcelona UPC, Spain
Av. Diagonal, 649-651, 08028 Barcelona
Badia_masoud@hotmail.com, helena.coch@upc.edu

² Compiègne University of Technology – Sorbonne University
Rue Roger Coultolenc, CS 60319
60203 Compiègne – France
benoit.beckers@utc.fr

Keywords: Pedestrian Comfort, Urban Morphology, Compact City, Solar Radiation, Urban Climate.

Abstract: *Many urban studies have been done to demonstrate that urban sprawl is not the right approach in hot climate cities. On the contrary, a compact design is recommended to enhance human thermal comfort. This research aims to clarify the relation between urban morphology and outdoor thermal comfort of Jeddah, Saudi Arabia. The aim is to develop an outstanding future strategic compact morphology that would facilitate a dynamic development of the city.*

Jeddah city will soon have a subway that is expected to radically change the habits of its inhabitants. Our idea is to consider the main stations of the future metro as nodes, creating more densely inhabited localities and also defining transitional spaces for pedestrian activities. Microclimates generated in and around these activity nodes must be particularly studied to encourage residents and visitors to reclaim a pedestrian life that was clearly noticeable in the old city, but has virtually disappeared in most recent neighborhoods, entirely devoted to automobile transport. Services and facilities around metro nodes should become the transitional thermal comfort areas of the metro station exits.

This paper will provide numerical modeling simulations that are used to assess the solar radiation in the urban layout (the old compact area and the modern sprawl area) by the software "Heliodon 2" (direct shortwave, Sky View Factor) and "Heliodon plus" (climatic data) to clarify the differences between the old and the new layout and why the change to compactness needs to be put into effect.

1 Introduction

Every year, the Saudi Arabian population is increasing by about 2% and the energy demand by 4–5% [Al-Hadhrami 2013]. Due to a rapidly escalating population and a high level of economic growth, the Kingdom of Saudi Arabia is experiencing a strong infrastructure expansion [Taleb 2015]. However, more than half of the country's energy demand has been created by the increased urban density together with the rise of consumerism, and these have not only led to an increase in environmental degradation locally, but they have also meant that the country's traditional primary energy is under used and consequently carbon emissions are set to rise and to play a larger role in global climate change. Electricity generation in Saudi Arabia is completely dependent on the unsustainable practice of burning fossil fuels, which has major environmental consequences.

However, when compared to other countries, the issue of energy efficiency is not generally given serious consideration with regard to Saudi urban building designs. In addition, the Kingdom of Saudi Arabia is one of the driest regions in the world and is facing serious challenges relating to a rapid growth [Kamal 2014]. Last, but not least, there are no regulations, or compulsory building codes, that incorporate the principles of sustainable architecture in the country [Taleb 2015]. It has been argued by many scholars that setting a coherent set of these codes and standards is one of the most important and cost-effective ways to promote the widespread of sustainable practices [Awawdehl 2014].

The government has adopted concepts and solutions from western nations in its architecture and physical planning. Rapid changes have taken place in the Kingdom of Saudi Arabia following the discovery of oil in commercial quantities and the country's opening up to the western world. The speed with which development has occurred and the rapid advance in technology experienced in the seventies, in every field, including construction, planning, industry, education, etc., have affected all aspects of living in the country. One aspect of life which has suffered most has been the traditional environment. The attraction of the western way of life and the western concept of development have drawn Saudi attention away from the development of a clear understanding of their traditional residential environment, and away from the value of its continuity.

With the introduction of automobiles, new building techniques and materials, the whole urban fabric of the city has been changed. A completely new form of housing has emerged and new physical communication networks have become necessary to accommodate the new mechanical means of transportation, with different housing types, wide dual carriageway roads, street intersections, flyovers and large areas of car parking spaces. Moreover the indigenous society has changed from being a highly traditional Islamic society into a semi-cosmopolitan environment of the twentieth century [Alharbi 1989].

According to [Brown 2010], many outdoor urban environments, especially in hot countries, tend to be poorly regulated and not thermally comfortable. [Lin 2009] indicated that few people visit squares or other public spaces in hot and humid regions when the thermal index is high.

During the day, the incoming solar (short-wave) radiation increases the surface and air temperatures. At night the surface is cooled due to the net outgoing long-wave radiation. This outgoing long-wave radiation diminishes with lower SVF, (higher H/W ratio). In concise terms, the narrower a street is, the less heat will be gained during the day, and less heat will be lost at night. [AL-Asir 2009]

From ancient times, a key strategy for thermal comfort and pollution dispersal in hot climates has been to maximise airflow and thereby achieve maximum ventilation. However, the low levels of wind speeds in the tropics during the passing of the inter-tropical

convergence zone twice a year make it necessary to carefully map out the ventilation strategy at a citywide level to induce sufficient air movement, both for pollution dispersion as well as thermal comfort. It will also enhance the cooling potential of naturally ventilated buildings (which is the common approach to indoor cooling in the warm, humid tropics)[AL-Asir 2009, Beckers 2012].

[Dalman, 2011] evaluated the microclimate principles of two different fabrics, one traditional and the other modern in the South East of Bandar Abbas. The study affirms the important following findings: canyon orientation, with effective shade and ventilation, was found to be the main contributor to thermal comfort in the selected area. In this regard, the usual wind and sea breeze, in combination with canyon orientation, play a significant role in providing a thermally comfortable situation. The streets height to width ratio (H/W ratio) in traditional fabrics is higher than in the modern one, and the traditional fabric was found to be more thermally comfortable. Hence, Shading and ventilation factors are not embedded in the design process in the modern fabrics of Bandar Abbas, which reveals scant consideration for these factors. The calculated values of thermal comfort indices (Physiological Equivalent Temperature (PET), Predicted Mean Vote (PMV), Standard Effective Temperature (SET) and Mean Radiant Temperature (MRT)) show a lower ratio in modern fabrics than in traditional areas; this is the effect of the lower H/W ratio and inadequate wind circulation and shading.

[Radhi2013] Investigates urban expansion in Bahrain over the last few decades and assesses its impact on atmospheric urban heat islands. The results show that network grids with structure and high density building developments that increase shelter and reduce wind velocity can lead to higher levels of stored heat on surfaces.

One of the most important urban parameters which affect solar access is urban density [Sanaieian 2014]. [Johansson 2006] examined the influence of urban geometry on outdoor thermal comfort by comparing an extremely deep street canyon and a shallow one in Fez, Morocco, making a comparison between an old and a new area. Continuous measurements during the hot summer and cool winter seasons show that, by day, the deep canyon was considerably cooler than the shallow one. The results indicate that, in hot dry climates, a compact urban design with very deep canyons is preferable.

2 Jeddah and its Climate

2.1 Jeddah:

The city of Jeddah is located in the western part of Saudi Arabia, where it overlooks the east coast of the Red Sea. With 3.9 million of inhabitants, Jeddah is considered the second largest city in Saudi Arabia in terms of population after Riyadh city. Jeddah is the most important seaport of Saudi Arabia on the Red Sea.

The history of Jeddah as a place of pilgrimage contributed to the development of its urban pattern. The rapid growth in population (natural and transient) in the last four decades coincided with the Kingdom's huge increase in wealth. This resulted in Jeddah City expanding physically at an unprecedented rate. This expansion was in part due to the limited success of spatial planning and regulatory frameworks that attempted to constrain development to certain areas of the city.

Without effective regulation and a coordinated, strategic approach, the urban area of Jeddah grew beyond the capacity of its infrastructure, leading to structural problems in the provision of water, sewage and roads. This growth also left the city with a number of structural challenges, including large quantities of vacant land and a dependency on the private car. Insensitive development, pollution, high energy consumption and lack of awareness damaged Jeddah's marine environment, while the relics of Jeddah's remarkable

heritage, in particular Albalad (la Medina) fell into decline [Khan 2012, Habibullah 2014, Fatta 2014].

2.2 Climate:

The city is located at latitude 21° 32' North, 39° 10' East. It has a hot climate, the Average Low/High temperatures usually vary between 18°C and 39°C, rarely going below 16°C or above 41°C. There are almost only clear skies, with cloud cover varying between 2% and 18%; the relative humidity varies between 30% and 89%, so the air is mostly humid. Rainfall in Jeddah is generally sparse, and usually occurs in small amounts in November and December, According to the Holdridge life zone system of bioclimatic classification, Jeddah is close to the tropical desert scrub biome (Khan 2012).

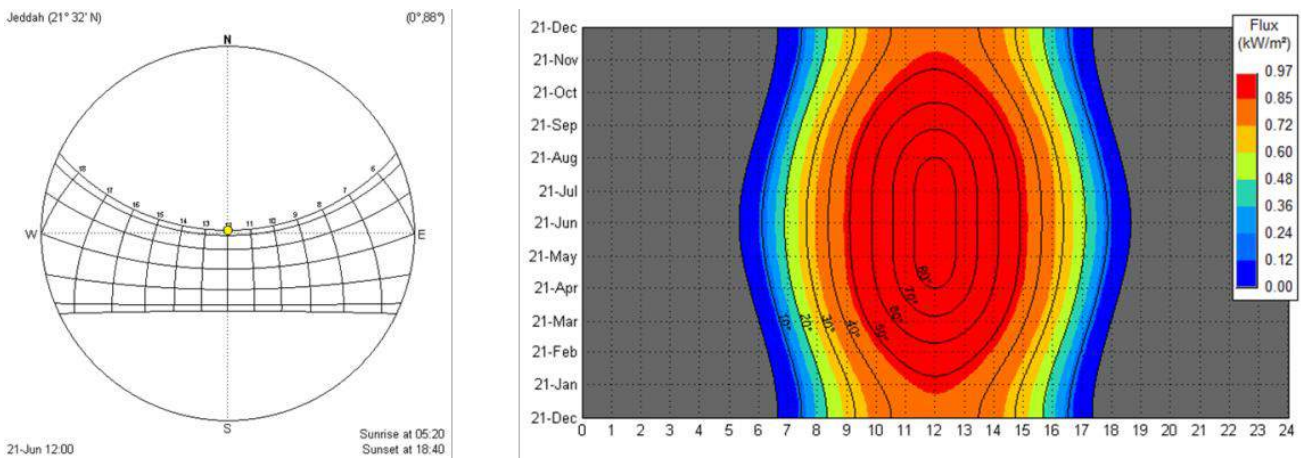


Figure 1: stereographic and isochronal solar diagrams for Jeddah

	Sunrise	Sunset	Solar height at noon
21 June	05:20	18:40	88°
21 December	06:40	17:20	45°

Table 1: Sunrise, Sunset and solar height at noon for 21st June and 21st December.

Jeddah is very close to the Tropic of Cancer. As shown in Table 1, the sun almost reaches the zenith in the summer solstice, reaching 45° at the winter solstice. The difference in day length between the two solstices is two hours and forty minutes. As shown on the isochronal projection of Figure 1 [Beckers, 2006], solar height is up to 40° between 10:30 and 13:30 during the entire year, and the direct radiation is then up to 800 kW/m² in sunny hours, reaching 1000 kW/m² in summertime.

[Khan & Duris, 2012] Studied Jeddah, Saudi Arabia urban structure and the amount of solar energy registered at ground level. Results have shown that the values of solar energy tend to be higher in the modern urban fabric than in the old one because of the significant differences between these two areas. These results show that modern districts with straight streets and large avenues receive more energy than the old city with its curved and narrower streets. The wider the street is, the easier it is for the sunlight to penetrate it. The fact that the modern city has almost only straight streets and avenues allows solar radiation to penetrate,

whilst the old city has narrower and more curved streets that cast enough shadow to considerably reduce direct sunlight.

3 Case studies:

3.1 Description:

Two areas of Jeddah have been chosen for the analysis, according to their contrasting morphology. The first one is in the south part of Jeddah, which is the old area (Albalad). The second area is in the north part of Jeddah, which represents the modern urban layout of the city (Al Salamah district).

As shown in Figure2, both chosen urban patterns have distinctive characteristics, related to density, H/W ratios and building organization.

The old area is characterized by its narrow streets, with a width varying between 2m and 5m. Building heights are from one to six levels. It is a mixed use urban area (residential and commercial). The old area has a dense, compact and irregular pattern.

The selected case in the modern area is residential. The housing in Al Salamah district consists of two storey detached villas and apartment buildings ranging from five to seven stories. The typical lot size is 20 x 30 meters and most blocks are 60 x 180 meters. The district was laid out in a rectangular grid system, with rectangular and square lots. Such development consists of parallel alignments, simple geometrically shaped patterns of streets designed for adequate vehicle movement, with width ranges from 10 to 20 meters. The architecture is distinctly American in style and built according to zoning regulations that stipulate distances from the street, detached rather than attached buildings.

The simulation and analysis will be done on two intersecting streets on the two layouts (the old and new)The analysis in the modern area will take place in the apartment building zone, which has been selected because it is denser than the villa areas.

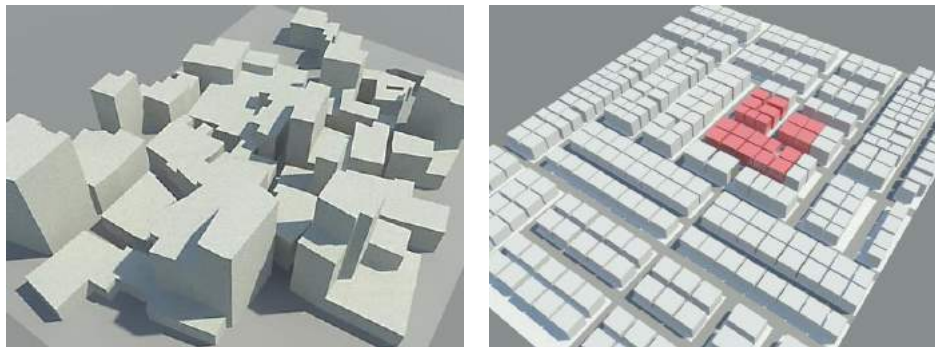


Figure 2: The 3D modeled on Rrvit Autodesk 2016 on the old area (Al Balad) and the modern area of Jeddah (Al Salamah)

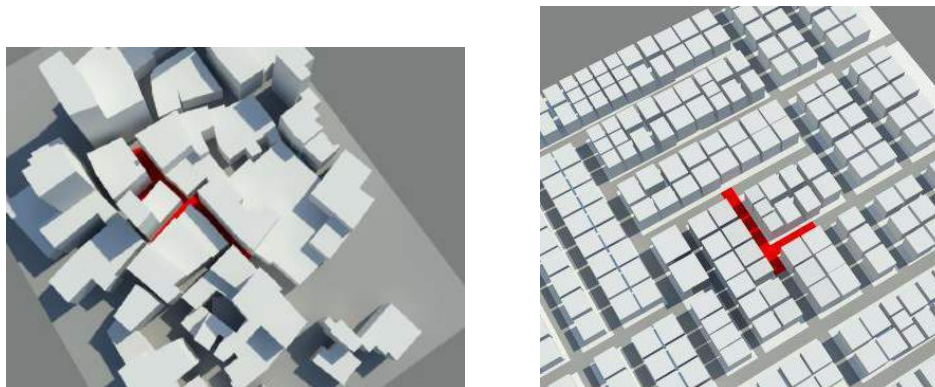


Figure 3: The 3D modeled on Rrvit Autodesk 2016 on the old area (Al Balad) and the modern area of Jeddah (Al Salamah) with the chosen intersection streets

3.1 Methodology:

The main analysis is realized with the Heliodon 2 software [Beckers 2006]. The program performs calculations in theoretical cloudless conditions, without taking into account the diffuse radiation emitted by the sky, nor the radiation reflected from nearby surfaces. It is completed by computations with the Heliodon Plus tool [Nahon 2016], which allows taking into account the climatic data.

4 Results:

4.1 Case study 1: old city urban layout:

The old area, as shown in Figure 4, has a mean sky view factor of 10.3%. Moreover, in Figure 5, we have a mean radiation value of three hours of sun in summer at street ground level, and only half an hour in winter.

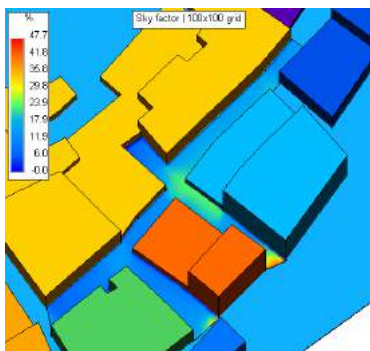


Figure 4: Mean SVF.

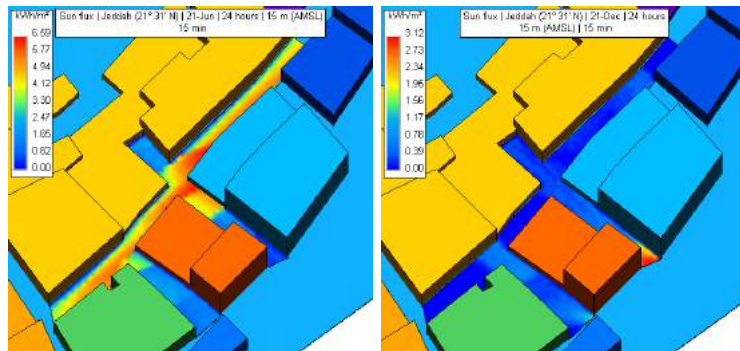


Figure 5: Mean Solar radiation value on 21st June and 21st December

Mean Solar period in summer	3h09 (429m ²)
Mean Solar period in winter	0h31 (429m ²)
Mean Sky view factor (SVF)	10.3%

Table 2: Old area Heliodon calculation (Mean Solar period on 21st June (Summer) and 21st Dec (Winter) and Mean SVF)

4.2 Case study 2: modern city urban layout

The modern area, as shown in Figure 6, has a mean sky view factor of 23.5%. Moreover, in Figure 7, we have a mean radiation value of six hours of sun in summer at street ground level, and only one hour in winter.

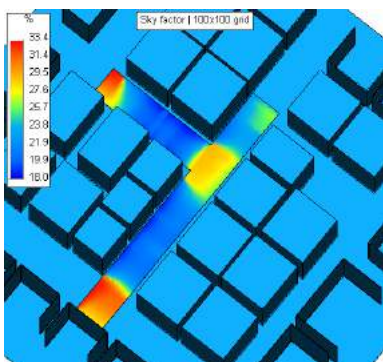


Figure 6: Mean SVF.

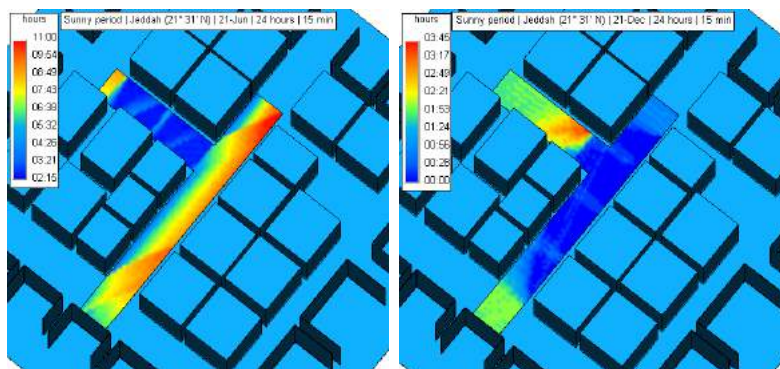


Figure 7: Mean Solar radiation value on 21st June and 21st December

Mean Solar period in summer	6h18 (1702.9 m ²)
Mean Solar period in winter	0h54 (1702.9 m ²)
Mean Sky view factor (SVF)	3.5 %

Table 3: Modern area Heliodon calculation (Mean Solar period on 21st June (Summer) and 21st Dec (Winter) and Mean SVF)

5 Discussion:

We investigated sky Access versus shading for pedestrian comfort in the hot tropical climate of Jeddah. Our results show that 10% SVF at street level could be a good compromise, and that it could be a target for the new transition areas in the metro nodes.

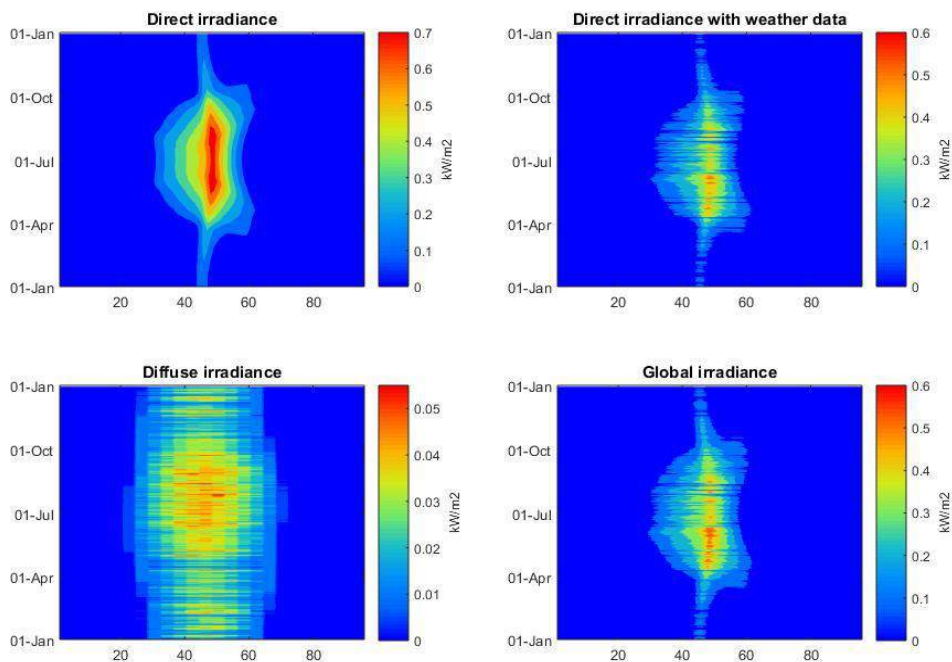


Figure 8: Solar Evolution Old area done by: Heliodon plus.

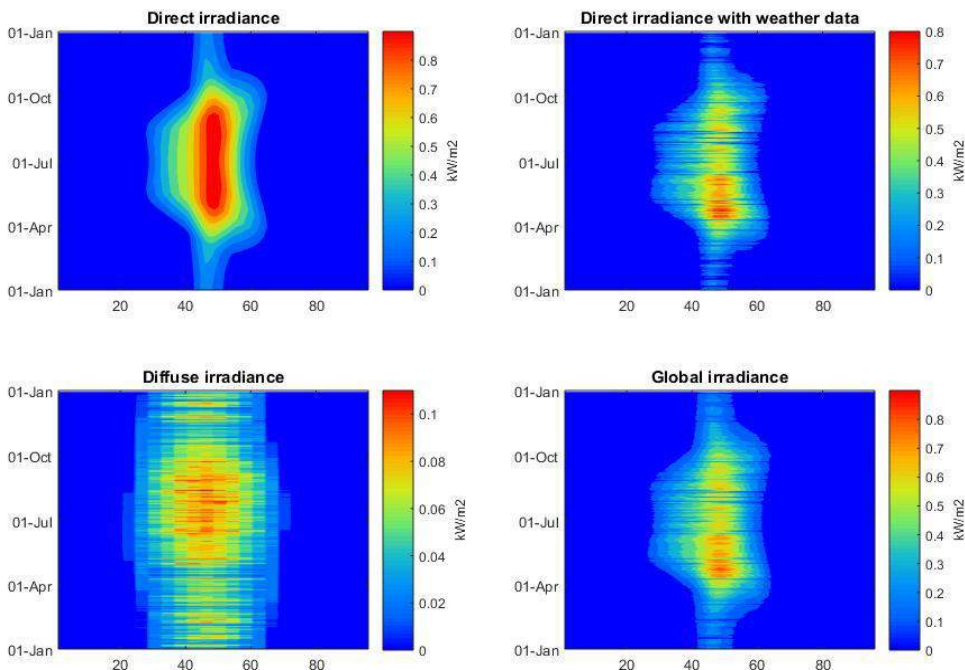


Figure 9: Solar Evolution Modern area (al Salamah) done by: Heliodon plus.

The study of the presence of clouds was obtained from the meteorological station, the theoretical energy data obtained are compared with Heliodon with actual data measured by the local weather station and a correction factor is established. Seeing the difference between the theoretical values and means of direct radiation, it proceeds to establish a correction factor with the following formula [Nahon 2016].

$$\text{Correction factor} = \frac{\text{Solar radiation calculated from the measured value}}{\text{Solar radiation calculated by Heliodon}}$$

	Jan	Feb	Mar	Apr	May	Jun	Jul	Aug	Sep	Oct	Nov	Dec
Correction	0.64	0.76	0.82	0.83	0.72	0.57	0.55	0.52	0.68	0.81	0.75	0.66

Table 4: Heliodon plus correction factor of each month.

6 Conclusion:

Our demonstration of the analysis of solar penetration, in both layouts in Jeddah city indicates and confirms the existence of the urban sprawl problem. Therefore, shading and densifying Jeddah city is essential, but a balance must be maintained. The idea is to consider the main stations of the future metro as nodes, creating more densely inhabited localities and also defining transitional spaces for pedestrian activities. Therefore, in continuing the study, we will model the extra extrusions on the facades of the old area, to evaluate their participation to shading.

7 References:

[AL-Asir 2009] AL-Asir, Hala Shaker, Awadallah, Tala. Climate Conscious Architecture and Urban Design in Jordan, Towards energy efficient buildings and improved urban microclimate. *Housing Development & Management and the Royal Scientific Society and the authors*, 2009.

[AL-Hadhrami 2013] L. M. Al-Hadhrami, Comprehensive review of cooling and heating degree days characteristics over Kingdom of Saudi Arabia, *Renewable and Sustainable Energy Reviews*, vol. 27 (2013), p. 305–314.

[Alharbi 1989] Alharbi, T.H. The development of Housing in Jeddah, changes in built form from the traditional to the modern. *Doctorial Study* (1989), p.392.

[Ali-Toudert 2005] Ali-Toudert, Fazia. Dependence of Outdoor Thermal Comfort on Street Design in Hot and Dry Climate. *Berichte des Meteorologischen Institutes der Universität Freiburg*, (2005).

[Awawdehl 2014] Awawdehl, Siba Adel and Tweed, Aidan Christopher. Buildings' energy efficiency and building energy codes: *International Journal of Applied Science and Technology* Vol. 4 (2014). p. 37–46.

[Beckers 2006] Benoit Beckers, Luc Masset, Heliodon 2, software and user's guide, <http://www.heliodon.net>.

- [Beckers 2012] Benoit Beckers, *Worldwide Aspects of Solar Radiation Impact*, in *Solar Energy at Urban Scale*, chapter 5, Ed. B. Beckers, John Wiley and Sons, Inc., 2012.
- [Dalman, 2011] Dalman, Salleh, Elias, Sopian, Abdul Razak, Tahir, Osman Mohd, Dola, Kamariah and Saadatian, Omidreza. Microclimate and thermal comfort of urban forms and canyons in traditional and modern residential fabrics in Bandar Abbas, Iran. *Modern Applied Science*. Vol. 5, no. 2 (2011) p. 43–56.
- [Fatta 2014] Fatta, Ghadi. *The Effect of Land Speculation on the Housing in the City of Jeddah, A research paper submitted to the graduate school Ball university, Munich, Master of urban planing*. (2014).
- [Habibullah 2014] Habibullah, Amir Mohammed. . *Sustainable strategies for urban water management for arid region: the case study of Jeddah city Saudi Arabia* .*Submitted in partial fulfillment of the requirements for the degree of Master of Landscape Architecture in Landscape Architecture in the Graduate College of the University of Illinois at Urbana-Champaign* (2014).
- [Johansson 2006] Johansson, Erik. Influence of urban geometry on outdoor thermal comfort in a hot dry climate: A study in Fez, Morocco. *Building and Environment*. Vol. 41, no. 10,(2006) p. 1326–1338.
- [Kamal 2014] Kamal, Mohammad Arif. *The morphology of traditional architecture of Jeddah, Climatic design and environmental sustainability, global built environment* . Vol. 9, (2014).
- [Katzschner 2006] Katzschner, Lutz. Microclimatic thermal comfort analysis in cities for urban planning and open space design. *Institute of Environmental Meteorology, University Kassel, Department of Architecture and Urban Planning, Kassel, Germany*, (2006) p. 31–36.
- [Khan& Duris 2012] Khan, Ahmed and Duris, Kevin. *The impact of the urban pattern on solar radiations. International Scientific Journal Architecture and Engineering*(2012).
- [Lin 2009] Lin, Tzu-Ping, De Dear, Richard, Matzarakis, Andreas and Hwang, Ruey-Lung. Prediction of thermal acceptability in hot-humid outdoor environments in Taiwan. *The seventh International Conference on Urban Climate, 29 June - 3 July 2009, Yokohama, Japan* (2009), p. 3–6 .
- [Nahon 2016] Raphaël Nahon, David Muñoz, Benoit Beckers, Heliodon Plus, software and user's guide, <http://www.heliodon.net>.
- [Radhi 2013] Radhi, Hassan, FIKRY, Fayze and Sharples, Stephen. Impacts of urbanization on the thermal behavior of new built up environments: A scoping study of the urban heat island in Bahrain. *Landscape and Urban Planning, Landscape and Urban Planning* Vol. 113, (2013), p. 47–61.
- [Sanaieian 2014] Sanaieian, Haniyeh, Tenpierik, Martin, Linden, Kees Van Den, Mehdizadeh Seraj, Fatemeh and Mofidi Shemrani, Seyed Majid. Review of the impact of urban block form on thermal performance, solar access and ventilation. *Renewable and Sustainable Energy Reviews*. Vol. 38, (2014) .p. 551–560.

[Taleb 2015] Hanan Taleb, Mousa Musleh, Applying urban parametric design optimization processes to a hot climate: Case study of the UAE, *Sustainable Cities and Society*, Vol. 14 (2015), p. 236–253.

[Wei Zhang & Sarkar 2010] Zhang, Wei and Sarkar, Partha P. Influence of surrounding buildings on the flow around a low-rise building in ABL and tornado-like winds. *The Fifth International Symposium on Computational Wind Engineering*, (2010).

Numerical modelling of evaporative cooling using water spray systems for heat stress reduction in urban areas

H. Montazeri¹, Y. Toparlar^{2,3}, B. Blocken^{1,2} and J.L.M. Hensen²

¹ University of Leuven
Leuven, Belgium
hamid.montazeri@kuleuven.be

² Eindhoven University of Technology
Eindhoven, The Netherlands
b.j.e.blocken@tue.nl; j.hensen@tue.nl

³ Flemish Institute for Technological Research
Mol, Belgium
y.toparlar@tue.nl

Keywords: Computational Fluid Dynamics, Wind comfort, Thermal comfort, Built Environment.

Abstract. *Evaporative cooling by water spray systems is increasingly used to reduce heat stress in urban areas. To our knowledge, a systematic investigation of the cooling potential of such a system in an actual urban area has not yet been performed. This paper presents high-resolution Computational Fluid Dynamics (CFD) simulations based on the 3D unsteady Reynolds-Averaged Navier-Stokes (URANS) equations to assess the cooling potential by a water spray system with 15 hollow-cone nozzles. The system is numerically implemented for a courtyard in the Bergpolder Zuid region of the Dutch city of Rotterdam and operated during the heat wave period of July 2006. To simulate the two-phase flow, the Lagrangian-Eulerian approach is implemented. The CFD simulations are validated based on wind-tunnel measurements of an evaporative cooling process and on field measurements of surface temperatures during the heat wave period (without water spraying). The Universal Thermal Climate Index (UTCI) is used to assess the heat stress reduction due to evaporative cooling.*

15 Introduction

To reduce the negative effects of heat waves and the UHI effect in urban areas, several adaptation measures can be considered such as vegetation, high-albedo surfaces and evaporative cooling. Evaporative cooling by water spray systems can be considered as an environmental-friendly and cost-effective technique to improve the quality of indoor and outdoor environments with relatively simple system components. Water sprays give building designers and urban planners much flexibility for innovative system design concepts, and easy integration in existing city infrastructures or renovation projects. The effect is controllable and can be employed in a dynamic way to operate only when cooling is desired. Most other climate change and/or urban heat island (UHI) mitigation/adaptation approaches, such as high-albedo surfaces, have an effect all year long, which implies they have a positive effect in warm seasons, but also negative side-effects such as increased building energy consumption in winter.

The two-phase flow in water spray systems is very complex as the evaporation process depends on several physical parameters, which are not easily varied independently. Given the complexities involved in evaluating the performance of water spray systems, most previous studies were performed using field measurements. They evaluated the influence of different physical parameters on the performance of water spray systems, such as ambient air temperature and air humidity, solar radiation, elapsed time under influence of spray and nozzle spray characteristics. However, field measurements are usually only performed in a limited number of points in space. In addition, there is almost no or limited control over the boundary conditions. This is, however, very important given the wide range of parameters influencing the performance of evaporative cooling systems.

Numerical simulation by Computational Fluid Dynamics (CFD) can be a useful tool to investigate the two-phase flow in spray systems. However, to our knowledge, a systematic investigation of the cooling potential of water spray systems in an actual urban area has not yet been performed. Therefore, the current paper presents CFD simulations on a high-resolution grid to assess the cooling potential of a water spray system with hollow-cone nozzles for a courtyard in the Bergpolder Zuid region of the Dutch city of Rotterdam in July 2006, when one of the major European heat waves occurred. In addition, the impact of the injected water flow rate and the height of the spray system on its cooling performance is investigated.

In Section 2, the Bergpolder Zuid region is described. Section 3 presents briefly the validation study for the evaporative cooling model. In Section 4, the CFD simulations for Bergpolder Zuid are outlined. Finally, results (Section 5) and conclusions (Section 6) are provided.

25 Urban area and surroundings

The region consists of both residential and office buildings with narrow streets and surrounded by large avenues. Most of the streets in the region are narrow with an aspect ratio between 1:1 and 2:1. The average building height is about 12.6 m where the lowest building is 2.8 m and the highest building is 51.0 m. No significant vegetation or water bodies are present in the region (Fig. 1).

The Bergpolder Zuid region is bordered by the central district of Rotterdam in the south and mainly green fields to the north, until the city of Delft (located in the northwest).

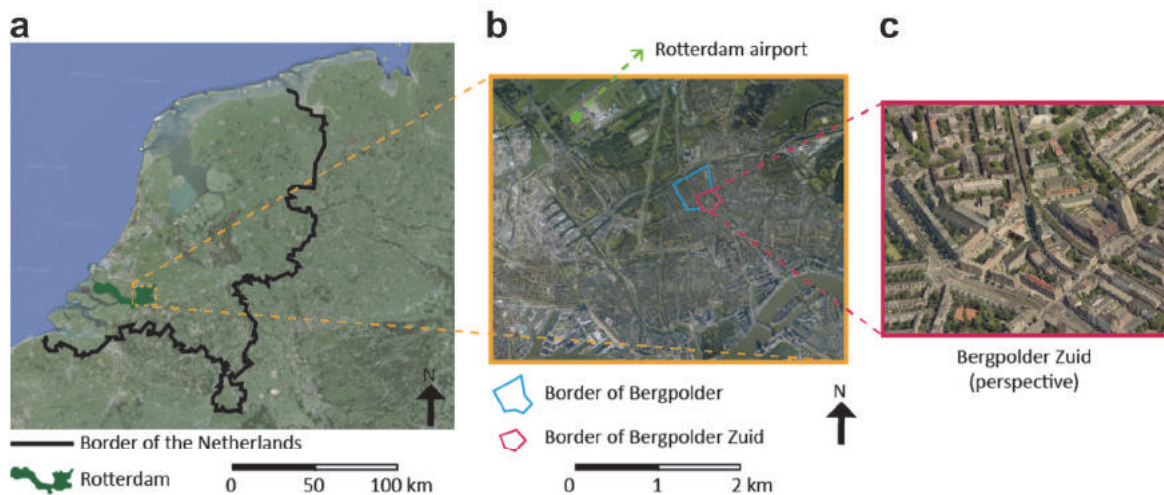


Figure 1: (a) Location of Rotterdam. (b) Top view with indication of border of Bergpolder and Bergpolder Zuid (modified from Google Maps). (c) Aerial view of Bergpolder Zuid (view from south)

35 Evaporative cooling validation study

Due to lack of high-resolution experimental data for water spray systems in urban areas, the wind-tunnel measurements of dry-bulb temperature (DBT) and wet-bulb temperature (WBT) during evaporative cooling by a hollow-cone nozzle spray system by Sureshkumar et al. [16] are used for CFD validation. The CFD results show a good agreement, within 10% for DBT and 5% for WBT. More information on the results and sensitivity of the results to the computational parameters can be found in Ref. [Montazeri et al., 2015].

45 CFD simulations of urban microclimate

4.15 Computational geometry and grid

The computational domain is the combination of a circular inner subdomain, which contains the explicitly modeled buildings, i.e. with their actual shape and size, and a surrounding outer hexagonal subdomain (Fig. 2a). The diameter of the circular subdomain is 1200 meter. The edges of the hexagon are 1200 m and the height is 400 meter. The buildings inside the computational domain are represented in three levels of detail depending on their distance to the area of interest, which is the Bergpolder Zuid region. The buildings within the Bergpolder Zuid region are modeled with high resolution where geometrical details as small as 1 meter edge length are explicitly represented (Fig. 2). For the buildings located in the remaining regions of Bergpolder, the resolution detail is lowered to 3-meter edge length. Finally, the remaining surrounding buildings are included with a resolution of 8-meter edge length and some of the courtyards are omitted from representation. Outside the circular subdomain, the obstacles that might affect the flow are not modeled explicitly but implicitly using appropriate roughness parameters in the standard wall functions, as recommended by best practice guidelines [Blocken, 2015].

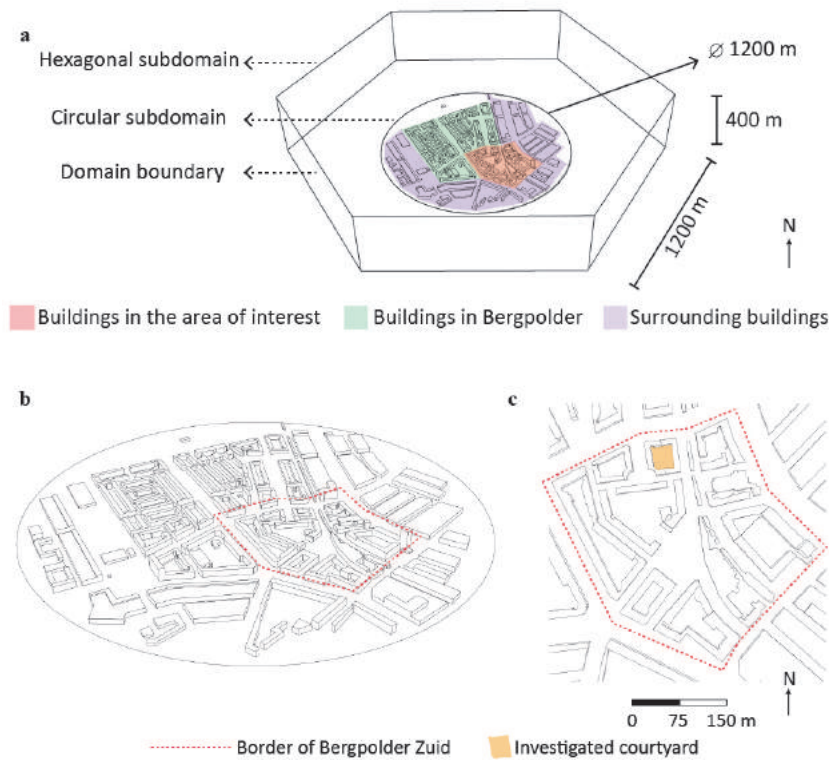


Figure 2: (a) Computational domain and geometry. Different colors represent different categories of buildings in terms of detail in modeling; (b) Building and street surfaces as in the computational domain; (c) top view of the Bergpolder Zuid region

A water spray system is employed in a courtyard where a relatively high air and surface temperature is observed from the simulations without water spray. The location of the courtyard is shown in Fig. 2c. The system consists of 15 hollow-cone spray nozzles, which are installed equidistantly at 0.5 m intervals on a single horizontal line at $H = 3$ m from ground level (Fig. 3).

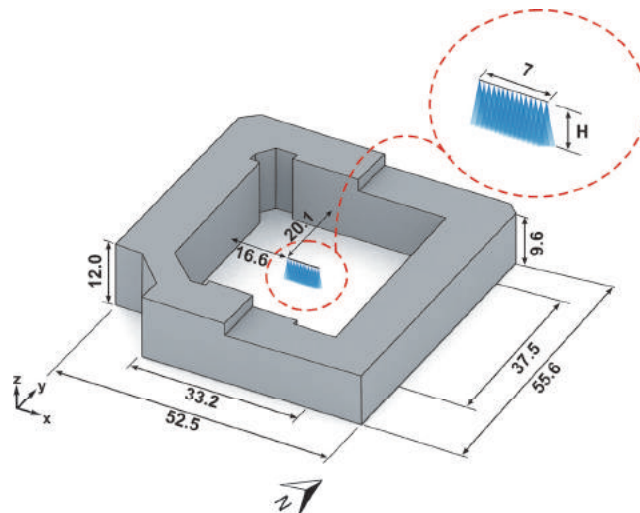


Figure 3: Perspective view and section of the courtyard along with the water spray system (dimensions in meter)

The computational grid is generated by the surface-grid extrusion technique by van Hooff and Blocken [van Hooff and Blocken, 2010]. This procedure allows a large degree of control over the quality of the grid and its individual cells. It consists of only hexahedral and prismatic

cells and does not contain any tetrahedral or pyramid cells. The grid on the building and ground surfaces of Bergpolder Zuid and immediate surroundings is shown in Fig. 4b. It is important to note that the grid has been constructed in agreement with best practice guidelines [Franke et al., 2007; Tominaga et al., 2008]. This includes the use of only hexahedral and prismatic cells, a minimum number of 10 cells along building edges and between neighboring buildings and wall-adjacent cell faces that are as much as possible either parallel or perpendicular to the walls. The computational domain contains a total of 6,610,456 cells.

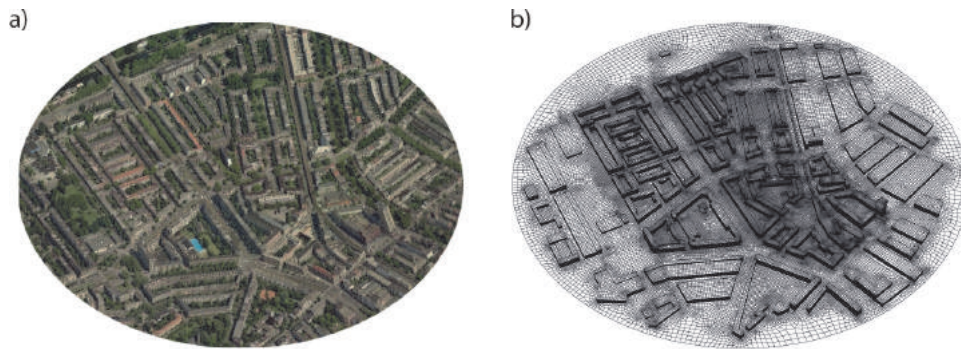


Figure 4: (a) Aerial view of the Bergpolder Zuid region (Source: Google Maps). (b) Computational grid on the building surfaces and on part of the ground surface. The intensity of black lines indicates areas with a higher grid resolution (total number of cells: 6,610,456)

4.2 Boundary conditions

For each of the outer faces of the hexagonal subdomain, a velocity inlet or pressure outlet boundary condition is imposed, depending on the hourly wind direction. Hourly meteorological data for the days under study are acquired from the Royal Dutch Meteorological Institute (KNMI). The meteorological data were recorded by the KNMI Rotterdam weather station, located 4 km northwest of Bergpolder Zuid (Fig. 1b).

At the inlets, vertical profiles for the mean wind speed ($U(z)$ (m/s)), turbulent kinetic energy ($k(z)$ (m^2/s^2)) and turbulence dissipation rate ($\epsilon(z)$ (m^2/s^3)) are imposed using the equations by Richards and Hoxey [Richards and Hoxey, 1993].

In addition, a constant air temperature is imposed at the inlets. For the simulations with evaporative cooling, also a constant vapor mass fraction is imposed. For the discrete phase, the escape boundary condition is used for the walls and the outlets.

The standard wall functions by Launder and Spalding [Launder and Spalding, 1974] are employed. The roughness height (k_s) and the roughness constant (C_s) are calculated based on the appropriate relationship with z_0 derived by Blocken et al. [Blocken et al., 2007] for ANSYS/Fluent.

A 10 m thick earth layer is modeled implicitly for the ground surface of the domain and at 10 m depth of this layer, a constant temperature of 10°C is imposed. The building walls are represented by brick layers with 0.4 m thickness and inside the buildings, a constant indoor air temperature of 24°C is imposed. The interior surface has a constant convective heat transfer coefficient and emissivity of $8 \text{ W}/\text{m}^2\text{K}$ and 0.95, respectively. The top of the computational domain is modeled as a free slip wall and zero static pressure is imposed at the outlets.

55 Results

5.15 CFD simulations of urban microclimate without evaporative cooling

The 3D Unsteady Reynolds-Averaged Navier-Stokes (URANS) equations are solved in combination with the energy equation. Closure is obtained by the realizable k - ϵ model. Conduction, convection and radiation are considered in the simulations, fully coupled with the wind flow. At the solid boundaries, a one-directional conduction equation is used. Natural convection is modeled with the Boussinesq approximation and for the radiation the P-1 radiation model is employed. Solar load parameters such as the sun direction vector and the diffuse portion of the total radiation approaching the surface are calculated with the implemented solar calculator of ANSYS/Fluent. Pressure-velocity coupling is performed with the Semi-Implicit Method for Pressure Linked Equations (SIMPLE). For all convection and viscous terms, second-order discretization schemes are used. Unsteady simulations are performed with a time step of 900 seconds and with 60 iterations per time step, based on a time-step sensitivity analysis. For the temporal discretization, second-order implicit time integration is used.

The CFD simulations are performed for 15-19 July, 2006. To compare the simulation results with satellite imagery results, 90 sampling points are specified on the building roofs and street surfaces of the computational domain of Bergpolder Zuid to extract spatially averaged values from the CFD simulations. The sampling points are positioned on the building and ground surfaces. The selection and number of these sampling points are based on a sensitivity analysis reported in Toparlar et al. [Toparlar et al., 2015]. The comparison between the CFD simulations and the satellite imagery data is provided in Fig. 5. The simulations can repeat the diurnal variation with a fairly good agreement. The surface temperatures by the CFD simulations show an average deviation of 7.9% with the measurements, whereas the minimum deviation is 0.27% and the maximum deviation is 24.2%.

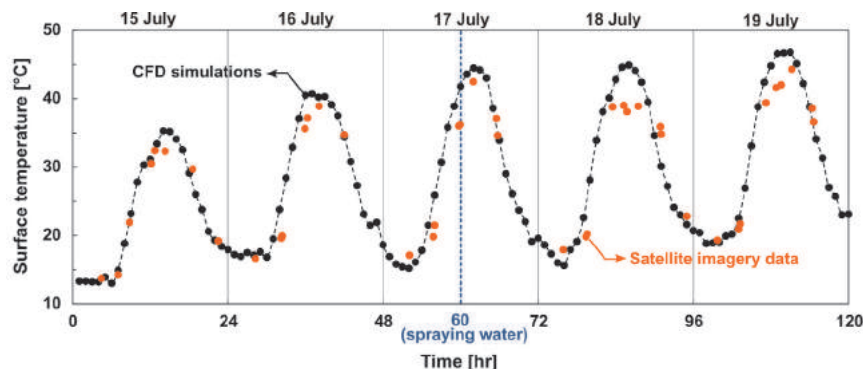


Figure 5: Urban climate validation study: Comparison of average surface temperatures for five consecutive days from CFD simulation and satellite imagery (without water spray)

Contours of wind speed and air temperature at 1.75 m height (pedestrian height) at 12:00 h on July 17 are provided in Fig. 6. The temperature distribution is consistent with the wind speed distribution. In the regions with low wind speeds, air temperatures are relatively higher. This is the case for courtyards, for example, where wind speed can be significantly reduced.

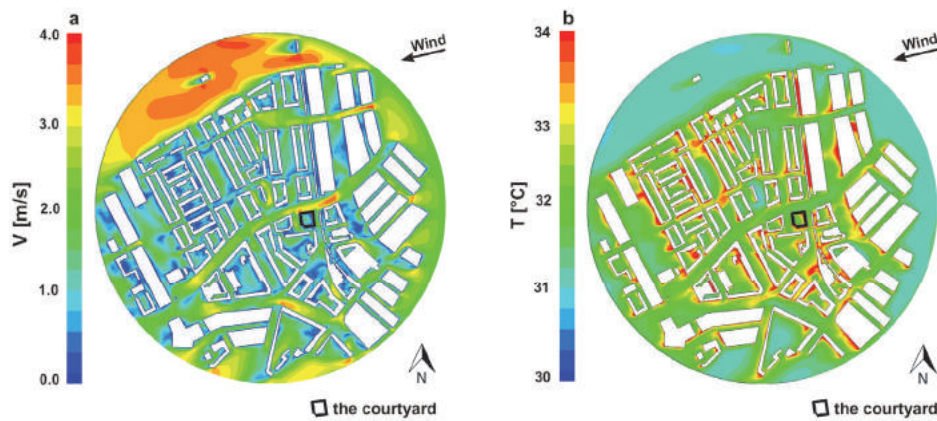


Figure 6: (a) Air velocity and (b) air temperature distribution at pedestrian height (1.75 m) for July 17, 2006: 12:00 h

Fig. 7a shows the wind speed distribution at pedestrian height inside the courtyard where the spray system will be employed (Fig. 3). The velocity vector field in a vertical plane along the spray line is shown in Fig 7b. The flow in the courtyard is dominated by a recirculation zone.

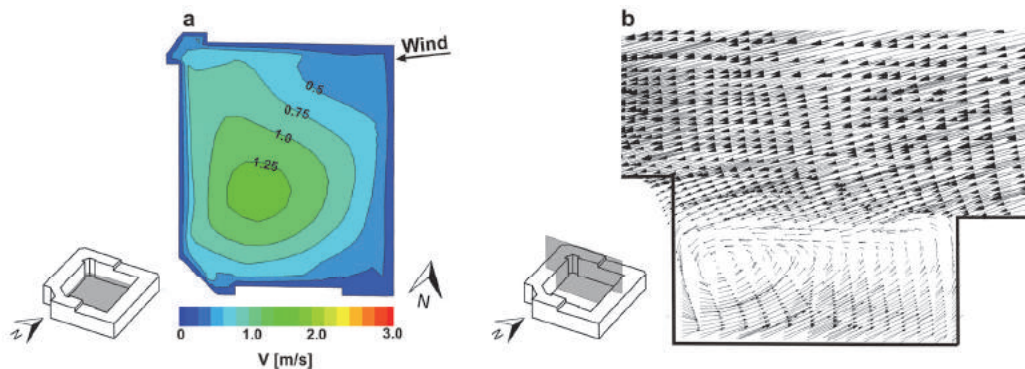


Figure 7: (a) Wind speed distribution in a horizontal plane at a height of 1.75 m above ground level, and (b) velocity vector field in a vertical plane in the courtyard for the case without spray.

5.2 CFD simulations of urban microclimate with evaporative cooling

For the simulations with evaporative cooling, the Lagrangian model for droplets and the species equations for water vapor are added.

The total injected water flow rate from the nozzles is 9.0 l/min. The Rosin-Rammler model [Rosin and Rammler, 1933] is used to describe the size distribution of the droplets in the CFD simulations. The smallest and largest droplet diameters to be considered in the size distribution of the Rosin-Rammler model are 10 and 60 μm , respectively. The mean of the Rosin-Rammler distribution, \bar{D} and the spread parameter, n are 20 μm and 3.5, respectively. The injected water temperature is 25 °C.

The droplets are injected into the domain and trajectory calculations are performed at 12:00 h on July 17. The 3D steady RANS equations are solved for conservation of momentum, heat and mass. Note that all boundary conditions (i.e. meteorological conditions) are fixed, identical to those at 12:00 h. Inlet mean wind speed is 3 m/s, wind direction is 80°, inlet air temperature is 29.7 °C and inlet air relative humidity is 33%. The droplets are treated in a steady-state fashion. The discrete phase interacts with the continuous phase in a fully coupled manner and the discrete phase model source terms are updated after each continuous phase iteration. The

correlation by Morsi and Alexander [Morsi and Alexander, 1972] is used for the droplet drag coefficients.

The impact of evaporative cooling by a water spray system on human heat stress depends on the complex interaction between different climatic variables and spray characteristics [Montazeri et al., 2015b]. It can be assessed by the Universal Thermal Climate Index (UTCI) [Fiala et al., 2012] which is a heat stress/thermal comfort indicator for outdoor and semi-enclosed environments. It reflects the human physiological reaction to meteorological parameters including air temperature and humidity, wind speed and mean radiant temperature, T_{mrt} [Bröde et al., 2012]. In this study, the first three quantities are a direct output of the CFD simulations. T_{mrt} is assumed to be constant in the entire courtyard before and after spraying water, $T_{mrt} = 45\text{ °C}$, in accordance with the observations from previous on-site measurements for similar urban areas. The UTCI values can be categorized into ten levels of thermal stress ranging from “extreme cold stress” to “extreme heat stress”.

To evaluate the cooling performance of the spray system inside the courtyard, the results are compared for two cases, with and without spray system. Figs. 8a and c show the distributions of air temperature and relative humidity across a horizontal plane (1.75 m from ground height) for the case without spray system. The results are provided for 12:00 h on July 17. A relatively uniform air temperature and relative humidity distribution can be observed at this height, where the wind speed is relatively low (0.5 – 1.5 m/s) (Fig. 7a). Note that the air temperature is 2-4 °C higher than the inlet air temperature (meteorological data) at the same time (i.e. 30 °C). In this case, the average UTCI at this height is almost constant (34.4 °C), which indicates the “strong heat stress” level.

Figs. 8b and d present the results when the spray system is in operation. In this case, the injected water flow rate is $\dot{m}_w = 9.0\text{ l/min}$ and the system is installed at $H = 3\text{ m}$. It can be seen that the maximum temperature reduction (about 7 °C) occurs underneath the spray system in the middle of the spray line. From these figures, the relatively symmetric air temperature and relative humidity distributions on both sides of the spray line can be clearly observed. However, a clockwise circulation flow, when viewed from the positive y-axis (Fig. 8b), in the courtyard leads to the advection of the cool air and moisture to the right-hand side of the courtyard. The spray system retains some cooling effect away from the nozzles. For example, the temperature reduction is more than 2 °C up to a distance of 8 m away from the spray line.

65 Conclusions

This paper presents high-resolution Computational Fluid Dynamics (CFD) simulations based on the 3D unsteady Reynolds-Averaged Navier-Stokes equations to assess the cooling potential and heat stress reduction by a water spray system with 15 hollow-cone nozzles. The system is numerically implemented in the Bergpolder Zuid region of the Dutch city of Rotterdam and operated at a specific moment during the heat wave period of July 2006. To simulate the two-phase flow, the Lagrangian-Eulerian approach is implemented. The CFD simulations are validated based on wind-tunnel measurements of an evaporative cooling process and on field measurements of surface temperatures during the heat wave period (without water spraying). The Universal Thermal Climate Index (UTCI) is used to assess the heat stress improvement due to evaporative cooling.

The results show that for given values of injected water flow rate ($\dot{m}_w = 9.0\text{ l/min}$) and height of the spray system ($H = 3\text{ m}$), a maximum temperature reduction and UTCI reduction of about 7 and 5 °C are achieved at pedestrian height (1.75 m) in the courtyard. In addition, a thermal comfort improvement from strong heat stress (without spray system) to moderate heat stress up to a distance of 5 m from the spray line is observed.

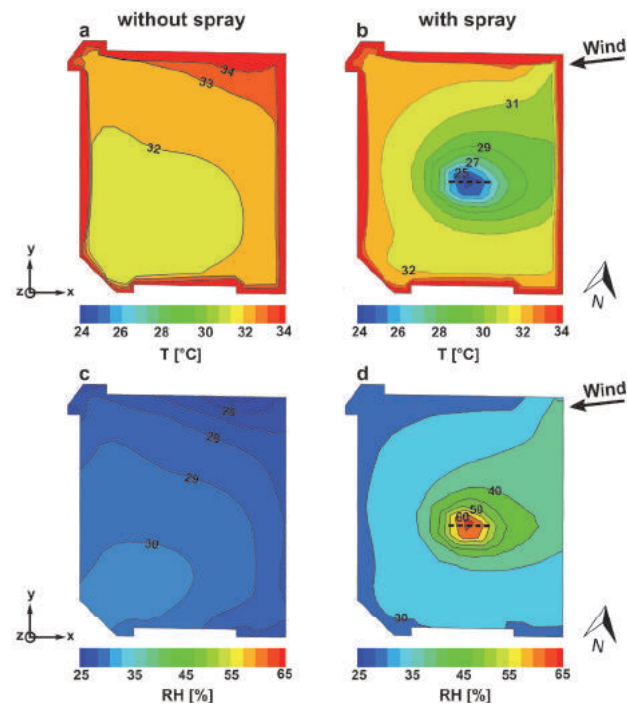


Figure 8: Air temperature distribution in a horizontal plane at a height of 1.75 m above ground level for the case (a) without and (b) with spray (July 17, 2006: 12.00 h). (c,d) Same for relative humidity

Acknowledgments

Hamid Montazeri is currently a postdoctoral fellow of the Research Foundation – Flanders (FWO) and acknowledges its financial support (project FWO 12M5316N).

References

- [Blocken 2015] B. Blocken, Computational Fluid Dynamics for Urban Physics: Importance, scales, possibilities, limitations and ten tips and tricks towards accurate and reliable simulations. *Building and Environment*, 91, Pages 219–245, 2015.
- [Blocken 2007] B. Blocken, T. Stathopoulos, J. Carmeliet, CFD simulation of the atmospheric boundary layer: wall function problems, *Atmospheric Environment*, 41, Pages 238–252, 2007.
- [Bröde 2012] P. Bröde, D. Fiala, K. Błażejczyk, I. Holmér, G. Jendritzky, B. Kampmann, B. Tinz, G. Havenith, Deriving the operational procedure for the Universal Thermal Climate Index (UTCI), *International Journal of Biometeorology*, 56, Pages 481–494, 2012.
- [Fiala 2012] Fiala, D., Havenith, G., Bröde, P., Kampmann, B., Jendritzky, G., 2012. UTCI-Fiala multi-node model of human heat transfer and temperature regulation, *International Journal of Biometeorology*, 56, Pages 429–441, 2012.
- [Franke 2007] J. Franke, A. Hellsten, H. Schlünzen, B. Carissimo, Best practice guideline for the CFD simulation of flows in the urban environment. *COST action 732: quality assurance and improvement of microscale meteorological models*, 2007.

- [Launder 1974] B.E. Launder, D.B. Spalding, The numerical computation of turbulent flows. *Computer Methods in Applied Mechanics and Engineering*, 3, Pages 269–289, 1974.
- [Montazeri 2015a] H. Montazeri, B. Blocken, J.L.M. Hensen, Evaporative cooling by water spray systems: CFD simulation, experimental validation and sensitivity analysis, *Building and Environment*, 83, Pages 129–141, 2015.
- [Montazeri 2015b] H. Montazeri, B. Blocken, J.L.M. Hensen, CFD analysis of the impact of physical parameters on evaporative cooling by a mist spray system, *Applied Thermal Engineering*, 75, 608–622, 2015.
- [Morsi 1972] S.A. Morsi, A.J. Alexander, An investigation of particle trajectories in two-phase flow systems. *Journal of Fluid Mechanics*, 55, Pages 193–208, 1972.
- [Richards 1993] P.J. Richards, R.P. Hoxey, Appropriate boundary conditions for computational wind engineering models using the k- ϵ turbulence model. *Journal of Wind Engineering and Industrial Aerodynamics*, 46, Pages 145–153, 1993.
- [Rosin 1933] P. Rosin, E. Rammler, The Laws Governing the Fineness of Powdered Coal. *Journal of the Institute of Fuel*, 31, Pages 29–36, 1933.
- [Tominaga 2008] Y. Tominaga, A. Mochida, R. Yoshie, H. Kataoka, T. Nozu, M. Yoshikawa, T. Shirasawa, AIJ guidelines for practical applications of CFD to pedestrian wind environment around buildings, *Journal of Wind Engineering and Industrial Aerodynamics*, 96, Pages 1749–1761, 2008.
- [Toparlar 2015] Y. Toparlar, B. Blocken, P. Vos, G.J.F. van Heijst, W.D. Janssen, T. van Hooff, H. Montazeri, H.J.P. Timmermans, CFD simulation and validation of urban microclimate: A case study for Bergpolder Zuid, Rotterdam, *Building and Environment*, 83, 79–90, 2015.
- [Van Hooff 2010] T. Van Hooff, B. Blocken, Coupled urban wind flow and indoor natural ventilation modelling on a high-resolution grid: A case study for the Amsterdam ArenA stadium. *Environmental Modelling & Software*, 25, Pages 51–65, 2010.

Impact of the anisotropy of the sky vault emissivity on the building envelope radiative budget

R. Nahon¹, O. Blanpain¹, and B. Beckers²

¹ Université de Lille 1
Cité Scientifique 59655 Villeneuve d'Ascq, France
raphael.nahon@ed.univ-lille1.fr, olivier.blanpain@univ-lille1.fr

² Université de Technologie de Compiègne (UTC), Sorbonne Universités
Rue du Dr Schweitzer, 60200 Compiègne, France
benoit.beckers@utc.fr

Keywords: Urban modelling, long-wave radiation, atmospheric radiation, sky temperature, directional emissivity, mean radiant temperature

Abstract. *Atmospheric radiation is commonly taken into account as isotropic when modelling the thermal behaviour of a building's envelope. In this article, we study the distribution of the sky temperature along the year under different climates. We show the strong variation between the zenith and the horizon, especially under a dry climate, and point out the interest of taking it into account in the estimation of the walls surface temperatures for the characterization of the thermal comfort and the building's energy needs.*

1 Introduction

According to the United Nations, the Earth's population will reach 9.3 billion in 2050. The demographic growth is combined to the urban one; each year, a crop area equivalent to Italy is taken over by cities [Beckers, 2013]. In 1800, only 2% of the world population was living in urban areas, against more than 50% nowadays. According to the United Nations, this portion will reach 75% in 2050, 20% of which living in megalopolis counting more than 4 millions of habitants. In this context, it is today necessary to build cities of high densities ensuring the comfort of its inhabitants.

[Dollfus, 1954] shows that, until the end of the ninetieth century, building typologies were mainly guided by the local climate and the search of thermal comfort. The advent of new construction processes, such as reinforced concrete, air conditioning or elevators, combined to the boom of automobile and the cheap energy led to the *globalisation of architecture* : the same processes are used under different climates and the use of energetic systems insure the comfort of the population. The global energy crises following the oil shocks of 1971 and 1978 led to a first questioning of this way of doing and to the search of an urban layout optimal regarding energy efficiency and thermal comfort.

A building's energy efficiency is mainly characterized by its warming and cooling needs. The analysis of both aspects implies the modelling of the heat transfers between the building and its environment. The *mean radiant temperature*, the mean temperature of a fictitious enclosure, is a key parameter of the thermal comfort [Huang 2014]. Therefore, it seems necessary to use physical models which permit the analysis of surfaces temperatures and heat flows in order to guide the urban planners when defining the urban geometry.

The analysis of the thermal behaviour of buildings' envelopes at the urban scale can be achieved through different methods, mostly through the use of simplified models [Kampf 2007]. The latter ensure the dynamic modelling of the air temperature inside the buildings with low data requirement and calculation costs. The geometry is summarily taken into account; the vertical walls, roof and ceiling of each building are represented as a unique branch and it is not possible to estimate directly the surfaces temperatures.

The atmospheric radiation, the long wave radiation (above 4 μm) from the sky, plays a significant part in the cooling of buildings. [Givoni 2011] shows for instance that the use of a passive radiant roof may maintain the interior temperature below 21°C for an exterior temperature of 34°C. The sky vault is usually considered as isotropic; its *radiance* is constant in every direction. However, [Kruczek 2015] shows through sky thermography the anisotropy of clear skies; he observes *sky temperatures* of 10°C at the horizon and -50°C at the zenith. [Bliss 1961] proposes a simplified model to take into account this phenomenon. On the basis of this work, [Awanou 1998] establishes the expression of the directional emissivity for clear skies.

This article analyses the distribution of temperature on the sky vault at different periods and under different climates in order to initiate a discussion on a thermal model for the modelling of heat flows and surfaces temperatures at the urban scale.

2 The atmospheric radiation

The sun can be assimilated to a blackbody at a temperature of 5780K. It emits energy as electromagnetic waves with short wavelengths (inferior to 4 μm); nearly 50% of which in the visible spectrum (380 to 780 nm), with a maximum at 500 nm (wavelength of the yellow), 50 % in the near infrared (780 to 4000 nm) and 1% in the ultraviolet (inferior to 380 nm). Part of the radiation reaching the atmosphere is absorbed and reflected by the clouds (23% and 23%), and by the Earth (47% and 7%). The absorbed energy is returned essentially in the far infrared (wavelengths superior to 4 μm) [Beckers 2012].

As the sun, the sky vault can be assimilated to a black body at a varying temperature; the term *sky temperature* (T_{sky} [K]) is used. It can as well be assimilated to a grey body at the air temperature T_a [K]; we use the term *sky emissivity* (ε_{sky}), to denote its capacity to absorb and return radiative energy. The sky vault emits energy to the Earth as electromagnetic waves with long wavelength (LW); the *atmospheric radiation* (φ_{sky}) [W/m^2] is mainly due to the atmosphere water content, which is a function of the air temperature, relative humidity and altitude.

$$\varphi_{sky} = \sigma T_{sky}^4 \quad (1)$$

$$\varphi_{sky} = \varepsilon_{sky} \sigma T_a^4 \quad (2)$$

$$T_{sky} = \varepsilon_{sky}^{1/4} T_a \quad (3)$$

[Angström 1915] proposes a first model for the estimation of the atmospheric radiation on an horizontal plane as a function of: the air temperature T_a , the water vapour pressure V_p [hPa] and the degree of cloudiness N [oktas].

$$\varphi_{sky} = (0.82 - 0.25 \cdot 10^{-0.0945 \times V_p}) \left(1 + 0.21 \left(\frac{N}{8}\right)^{2.5}\right) \sigma T_a^4 \quad (4)$$

Since the presentation of this formula, various models have been proposed for the estimation of atmospheric radiation. Meanwhile, [Tang 2004] indicates that their correlation with observed sky temperatures is poor and that each of them can only be applied under specific weather conditions.

The measurement of sky temperature can be done directly using a pyrgeometer or indirectly using a pyrriometer. However, [Tang 2004] indicates that these instruments are expensive and need frequent calibrations; meteorological observatories are not always equipped with those instruments. In the next parts of this article, we use the weather data available at <https://energyplus.net/weather>. Each data is associated to a source and an uncertainty class. For the files used in this article, the source of the infrared radiation on an horizontal plane is unknown (class "?") and associated to an uncertainty range from 35 to 50%. T_a , V_p and N are associated to classes A to C, corresponding to a measured data, with an uncertainty consistent with the instrument used for its acquisition.

We compare the atmospheric radiation calculated with the Angström formula and the one extracted from the weather database of Paris-Orly observatory (cf. Figure 1). We choose a range of fifteen days with clear and overcast skies, from the 10th to the 25th of January. The parameter V_p is calculated using the expression proposed by [Buck 1981], with R_h [%] the air relative humidity and T_a (expressed here in $^{\circ}\text{C}$) the air temperature :

$$V_p = \frac{R_h}{100} 6.1121 \exp\left(\left(18.678 - \frac{T_a}{234.4}\right) \left(\frac{T_a}{257.14 + T_a}\right)\right) \quad (5)$$

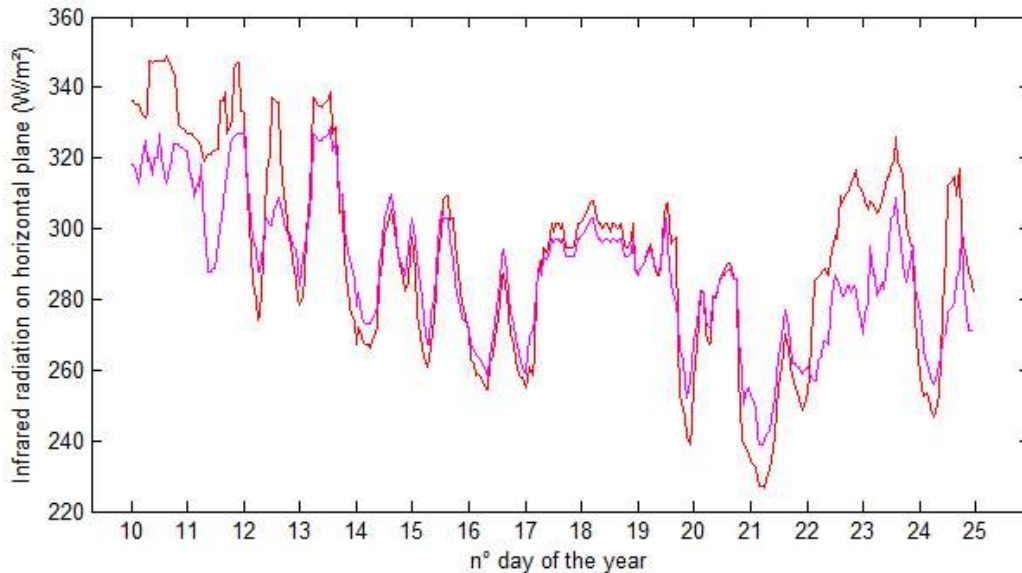


Figure 1: Comparison of modelled (red) and measured (magenta) infrared radiation

The correlation between these curves tends to indicate that the atmospheric radiation extracted from the weather file is calculated through a similar model. This is why in this article, we choose to use the Angström formula in order to analyse the respective impact of T_a , V_p and N on the atmospheric radiation.

We study the evolution of the sky temperature along the year for the city of Paris. We obtain values from -29 to 25°C for an air temperature from -6 and 30°C . We illustrate in Figure 2 the respective impacts of the air temperature and cloud cover on the sky temperature. We note that ε_{sky} tends to 1 for an overcast sky, and so T_{sky} tends to T_{air} . The observed differences for a cloud cover of 100% come from the water vapour pressure V_p (cf. equation 4). The latter fluctuates between 2.5 and 23.5 hPa for the city of Paris; that is to say a minimal and maximal difference between the air and sky temperatures of 2 and 14°C for an air temperature of 15°C . The sky temperature strongly decreases for clear skies; the minimal and maximal values of ε_{sky} are 67 and 82%, that is to say a minimal and maximal difference between the air and sky temperatures of 14 and 27°C for an air temperature of 15°C .

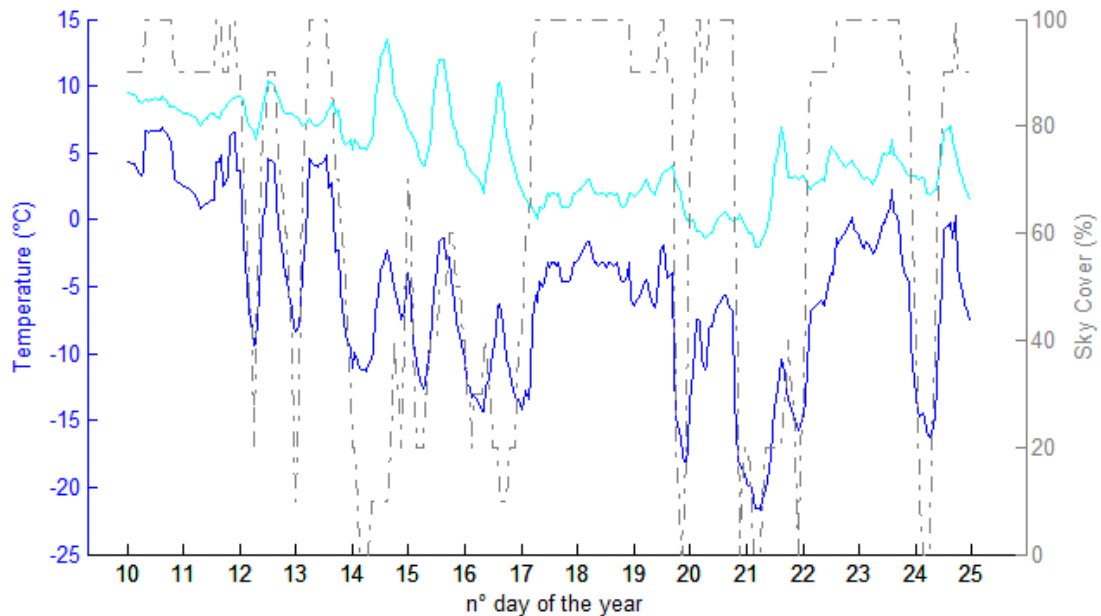


Figure 2: Evolution of the sky temperature (*blue*), air temperature (*cyan*) and cloud cover (*grey*)

We note that the sky temperature cannot be greater than the air temperature; the long wave radiative budget of a surface at the air temperature is always negative. The buildings' walls are cooled by the atmospheric radiation throughout the whole year ; we speak of *passive radiative cooling*. The inhabitants of the Persian desert benefited from this phenomenon to produce ice for an exterior temperature of up to 9°C [Tang 2004].

3 Anisotropy of the sky vault emissivity

The sky temperature is commonly considered isotropic for the modelling of the thermal behaviour of the buildings' envelope, and more generally for the calculation of the energy budget of a surface at the ground level. [Bliss 1961] shows that the sky emissivity depends on the zenith angle. He makes the hypothesis that, in the absence of clouds, the atmosphere is made of parallel layers at uniform temperature, pressure and composition; on this basis, he establishes a first link between the emissivity of a fragment of the sky vault and its zenith angle. [Kruczek 2015] illustrates this phenomenon through the thermography of the sky vault for a clear and an overcast sky (cf. Figure 3).

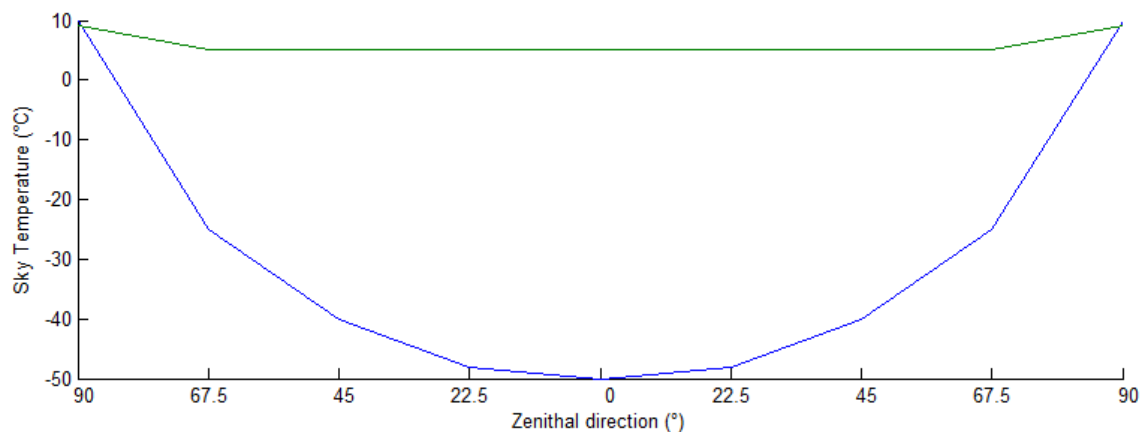


Figure 3 : Sky temperatures observed by Kruczek for a clear (*blue*) and an overcast (*green*) sky

Since Bliss, many authors, such as [Berdhal 1982] and [Berger 2003] studied the anisotropy of the sky emissivity. [Awanou 1998] proposes the following expression of ε_θ , the sky emissivity for the zenith angle θ , as a function of the mean emissivity of the sky vault ε_{sky} :

$$\varepsilon_\theta = 1 - \left(1 - \varepsilon_{sky}\right)^{\frac{\cos(56.25)}{\cos(\theta)}} \quad (6)$$

He identifies a frontier for a zenith angle of 56.25° : above this value, the directional emissivity is inferior to the mean sky emissivity and vice versa. He shows a convergence between theoretical results obtained following this model and the observations of the sky radiance made by [Berdhal 1982] for zenith angles of $0, 60, 75, 90^\circ$ in six cities of the United States.

We note that ε_{sky} tends to 1 for a sky cover of 8 oktas (okta is the fraction equal to one eighth of the celestial dome, used in the coding of cloud amount) and a high relative humidity, and so does ε_θ ; the model seems then valid for extreme cases. We study the sky temperature in Paris in winter for a clear and an overcast sky (cf. Figure 4). The sky vault is divided in 1000 of tiles following the partition proposed by [Beckers 2014]. We consider each tile at a uniform temperature, equal to that of its centre.

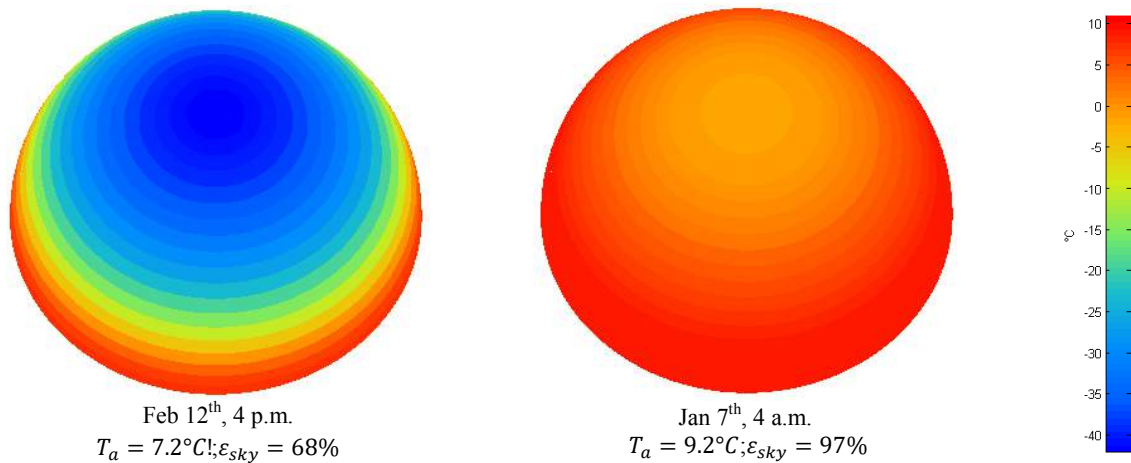


Figure 4 : Sky temperatures for a clear (*left*) and an overcast (*right*) sky in winter in Paris

For a clear sky, we obtain sky temperatures of -42°C at the zenith against 7°C at the horizon for an air temperature of 7.2°C ; for an overcast sky, we obtain a relatively uniform sky temperature, close to that of the air. We obtain for these extreme cases ($\varepsilon_{sky} = 68\%$ and 97%) the behaviour observed by Kruczek.

The taken into account of cloud cover on the repartition is difficult because of the multiple types and heights of clouds. We have seen that ε_{sky} can be of 82% both for:

- a cloud cover of 8 oktas when V_p is low;
- a cloud cover of 0 oktas when V_p is high.

If we apply the formula proposed by [Awanou 1998], we obtain in this case a similar temperature gradient for a clear and an overcast sky (cf. Figure 5).

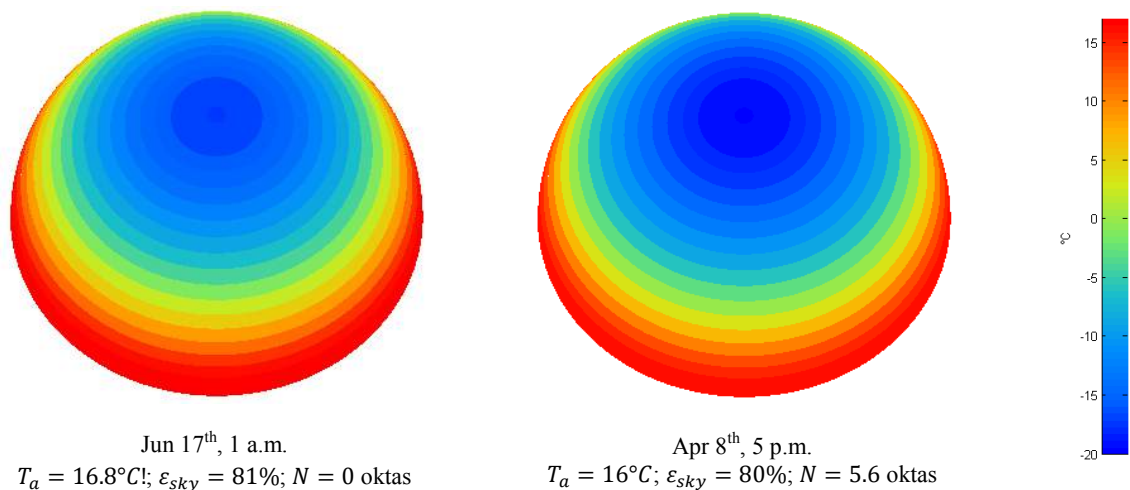


Figure 5 : Sky temperatures for a clear (*left*) and an overcast (*right*) sky in Paris

To date, there is no model for the correct estimation of the sky temperature of an overcast sky. The lack of data makes this last result difficult to analyse. Meanwhile, the differences of temperature between the zenith and the horizon for a clear sky are so important that it seems necessary to take this variation into account when calculating the energy budget of the buildings' envelope. The model proposed by [Awanou 1998] permits a good estimation of the sky temperature both for clear and strongly overcast skies; it appears reasonable to prefer this to an isotropic one, even though the one obtained for partially overcast sky may be wrong.

4 Climate influence

[Clark 1981] and [Argiriou 1992] illustrate the impact of the local climate on the atmospheric radiation; they show that the passive radiative cooling of buildings has a strong potential in most of the cities of the southwest of Europe but not in the southeast of United States.

The city of Paris is characterized by a relatively cold and wet winter, with a mean air temperature of 5°C and a relative humidity of 80%, and a relatively hot and dry summer, with a mean temperature of 20°C and relative humidity of 70%. We compare the sky temperature in winter and in summer for a clear and an overcast sky (cf. Figure 6). The minimal value of ε_{sky} is of 78% in summer against 67% in winter; the sky temperature is generally colder and the difference between the zenith and the horizon is more important in winter than in summer.

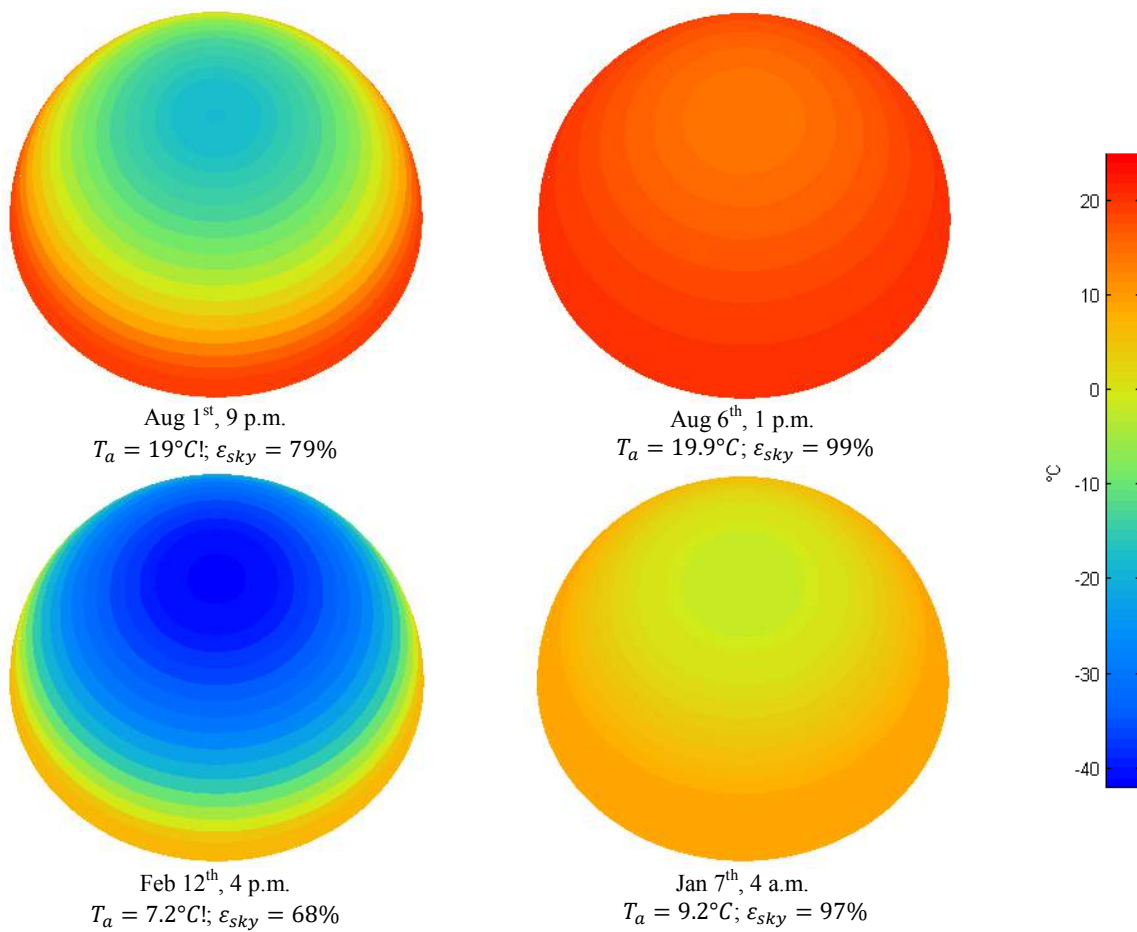


Figure 6 : Sky temperature in summer (*up*) and in winter (*down*), for a clear (*left*) and overcast (*right*) sky

We compare the evolution of the cloud cover during the course of a year for the cities of Paris, Montreal and Quito (cf. Figure 7). In order to do so, we compare the theoretical values of the incoming shortwave radiation from the sun for a clear sky, calculated following the model proposed by [Liu 1962], and the ones from the weather database.

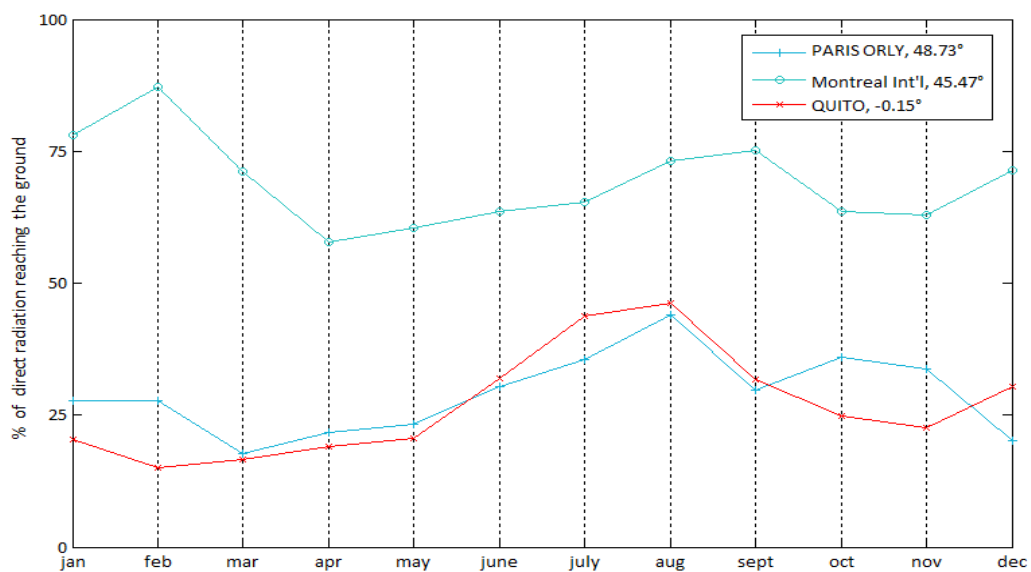


Figure 7 : Evolution of the cloud cover (monthly average)

We note a similar profile in the cities of Paris and Quito, with respectively 70 and 73% of the sun direct radiation intercepted by the clouds over a year, a minimum of 56 and 54% in August and a maximum of 82 and 85% in March and February. In Montreal, only 32% of the sun direct radiation is intercepted by clouds over a year, with a minimum of 13% in February and a maximum of 42% in April.

We compare for these three cities the sky mean temperature from the 1st of January to the 21st of March and from the 21st of June to the 21st of September (cf. Figure 8). The mean air temperature and relative humidity are displayed on the figure.

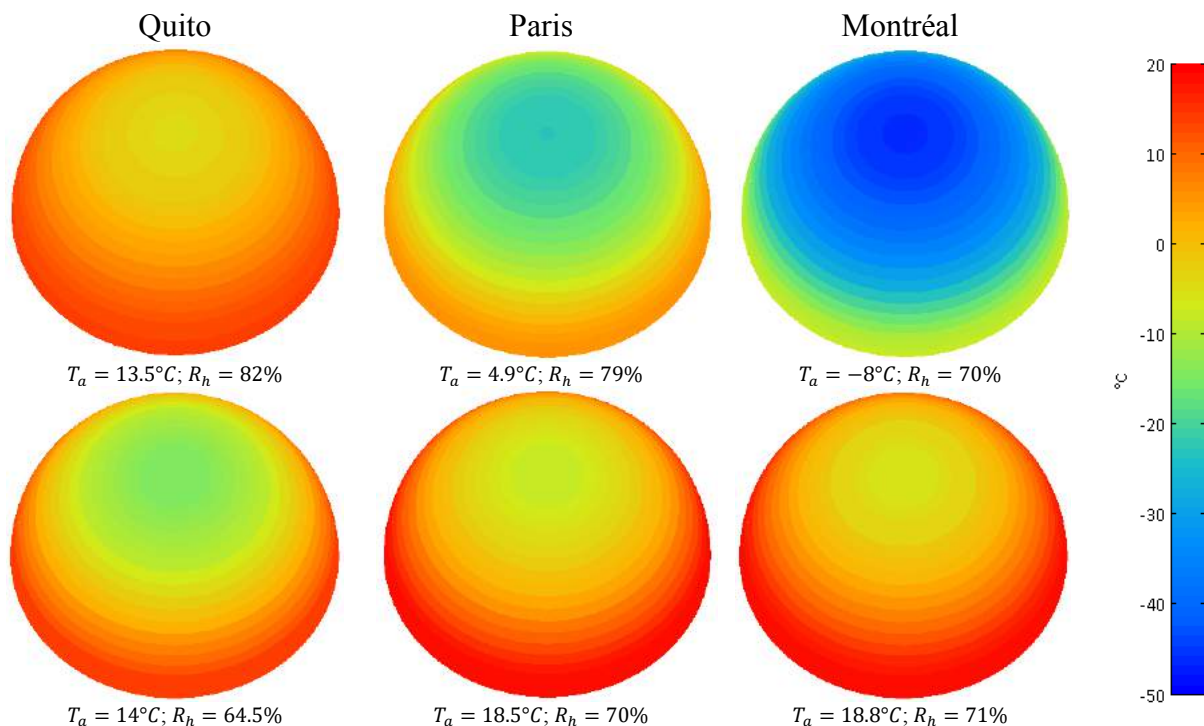


Figure 8 : Mean sky temperatures from the 1st of January to the 21st of March (*up*) and from the 21st of June to the 21st of September (*down*)

We note a similar mean sky temperature in Paris and Montreal in summer, with respective temperatures of -8 and -5°C at the zenith and 18.5°C at the horizon. On the same period, the sky temperature is of -14°C at the zenith and 14°C at the horizon in Quito. In winter, the temperature are clearly inferior in Montreal, with -46°C at the zenith, against respectively -23 and -4°C in Paris and Quito, and -8°C at the horizon, against 5 and 13.5°C.

In Figure 8, the potential for passive radiative cooling of buildings appears limited in Montreal and Paris. Meanwhile, the cooling of the buildings' wall exposed to the zenith and its potential impact on the heating needs appears important.

[Nahon 2016] studies the distribution of light on the sky vault and identifies the most useful areas regarding the access to daylight in an interior; he shows that it is possible to define a *useful* sky factor regarding daylight access. Given those results, it seems possible to identify for a given climate the sky vault areas that favour thermal comfort and limit the energy needs for heating and cooling of buildings.

5 Conclusion

In this article, we illustrate the strong variation of the sky vault emissivity along the year and under different climates. We point out the interest of taking it into account for the estimation of external surfaces temperatures and the calculation of a building's energy budget. The long wave radiative balance of the building's envelope in the modelling of its thermal behaviour is usually done through the estimation of a mean exterior surface temperature, considering an isotropic atmospheric radiation. The authors will present during the conference a comparison of the exterior surfaces temperatures and energy budget obtained following that method and considering differentiated surfaces temperatures and an anisotropic sky.

6 Acknowledgement

The authors are most grateful to the enterprise **CDI Technology** which financed this work.

References

- [Argiriou 1992] Athanassios A. Argiriou, Mat Santamouris, Constantinos Balaras, Sheldon Jeter, Potential of radiative cooling in southern Europe, *International Journal of Solar Energy*, vol. 13, Pages 189-203, January 1992.
- [Awanou 1998] Cossi Norbert Awanou, Clear sky emissivity as a function of the zenith direction, *Renewable Energy*, vol. 13 n°2, Pages 227-248, February 1998.
- [Beckers 2012] Benoit Beckers, *Solar Energy at Urban Scale*, Wiley-ISTE, 384 pages, May 2012.
- [Beckers 2014] Benoit Beckers, Pierre Beckers, Sky vault partition for computing daylight availability and shortwave energy budget on an urban scale, *Lighting Research and Technology*, vol. 46 n°. 6, Pages 716-728, December, 2014
- [Berdhal 1982] Paul Berdhal, Richard Fromberg, The thermal radiance of clear skies, *Solar Energy*, vol. 29 n°4, Pages 299-314, 1982.
- [Berger 2003] Xavier Berger, Bathiebo, J., Directional spectral emissivities of clear skies, *Renewable Energy*, vol. 28, Pages 1925–1933, 2003.
- [Bliss 1961] Raymond W. Bliss Jr., Atmospheric radiation near the surface of the ground, *Solar Energy*, vol.5 n°.3, Pages 103-120, September 1961.
- [Buck 1981] Buck, Arden L., New equations for computing vapor pressure and enhancement factor, *Journal of Applied Meteorology*, vol. 20, Pages 1527–1532, 1981
- [Clark 1981] Clark G., *Passive/hybrid comfort cooling by thermal radiation*, Proceedings of the international passive and hybrid cooling conference, Miami Beach, Pages 682–714, 1981.
- [Dollfus 1954] Jean Dollfus, Les aspects de l'architecture Populaire dans le monde, Albert Morancé, 30 pages, 1954.
- [Givoni 2011] Baruch Givoni, Indoor temperature reduction by passive cooling systems, *Solar Energy*, vol. 85 Pages 1692–1726, 2011.
- [Kämpf 2007] Jérôme-Henri Kämpf, Darren Robinson, A simplified thermal model to support analysis of urban resource flows, *Energy and Buildings*, vol. 39 n°4, Pages 445-453, April 2007.

[Kruczek 2015] Tadeusz Kruczek, Use of infrared camera in energy diagnostics of the objects placed in open air space in particular at non-isothermal sky, *Energy*, vol. 91, Pages 35–47, November 2015.

[Liu 1960] Benjamin Y.H. Liu, Richard C. Jordan, The interrelationship and characteristic distribution of direct, diffuse and total solar radiation, *Solar Energy*, vol. 4, Pages 1–19, 1960.

[Tang 2004] Runsheng Tang, Y. Etzion, I.A. Meir, Estimates of clear night sky emissivity in the Negev Highlands, Israel, *Energy Conversion and Management*, vol. 45 n°11-12, Pages 1831–1843, July 2004.

IMPACTS OF REALISTIC SURFACE HEATING ON OUTDOOR THERMAL COMFORT

Negin Nazarian¹, Tiffany Sin², Leslie K. Norford³

¹ Singapore-MIT Alliance for Science and Technology
1 CREATE Way, #10-01 CREATE Tower, Singapore 138602
E-mail: negin@smart.mit.edu

²Yale-NUS College
E-mail: tiffany.sin@u.yale-nus.edu.sg

³ Massachusetts institute of technology, Cambridge, USA
E-mail: lnorford@mit.edu

Keywords: Computational Fluid Dynamics, Guideline Maps, Outdoor thermal comfort, Realistic heating distribution, Standard Effective Temperature

Abstract. *Outdoor thermal comfort is of growing concern in the urban areas, and is influenced by various factors such as urban morphology, surface characteristics, and non-uniform surface heating that is caused by solar insolation and inter-building shadowing. Although urban design and planning can be employed to enhance the thermal experience of urban dwellers, comprehensive analysis of the outdoor thermal comfort and its link to urban design factors is scarce. To address this shortcoming, we aim to employ the Computational Fluid Dynamic modeling of thermal and flow field, and further investigate the outdoor thermal comfort by calculating the Standard Effective Temperature (SET) as a comprehensive metric for human thermal sensation. Additionally, the differential heating of urban surfaces is parameterized using sets of horizontal and vertical Richardson numbers (Ri_h and Ri_v , respectively), and the variation of SET as a function of this parameterization method is evaluated. Because the defined buoyancy parameters, Ri_h and Ri_v , depend on ambient conditions, material properties, and urban build-up density, quantifying the change in SET in the street canyons based on these parameters aims to improve our understanding of the effect of design on urban microclimate, and ultimately inform urban designers and architects of the impact of their design on human health and comfort. Additionally, this study introduces an example of obtaining guideline maps of thermal comfort and city breathability with respect to climate and design factors in urban streets.*

1. Introduction

Urbanization necessitates expansion and densification of cities, and brings about detrimental modifications to the characteristics of outdoor environments. One major environmental consequence of urbanization is the Urban Heat Island (UHI), i.e., the relative rise of temperature in densely built areas, which is responsible for a variety of health and economic concerns due to the exposure to the elevated air temperature and increased energy demand [Kim, 1992; Oke, 1981; Bornstein, 1968; Oke, 1973]. Additionally, wind flow is obstructed and modified by the configurations of buildings, their orientation with respect to the wind, and the thermal forcing on the building surfaces and roads [Nazarian, 2016a]. Airflow modification also contributes to the UHI formation and air quality concerns in urban neighborhoods. Other categories contributing to modifications of the outdoor microclimate are the reduction of vegetation areas, and introduction of built materials as opposed to the natural land cover, both altering the radiation balance as well as the transpiration and humidity level of urban areas. What humans experience in the urban environments is a combination of all these factors.

Thermal comfort has been evaluated by means of measurements, surveys, and numerical methods; and thermal comfort indices that incorporate numerous microclimate factors have been introduced [Mayer, 1987; Chen, 2012; Johansson, 2014]. Several field studies [Nikolopoulou, 2001; Lin, 2009; Chow, 2016] combined microclimate measurements and surveys from pedestrians in order to evaluate thermal comfort through both objective (microclimate) and subjective (physiological, psychological and behavioral) parameters. Such field studies have verified the role of urban design on the thermal sensation of urban dwellers, and are invaluable for understanding the complex nature of human comfort in urban area. However, field measurements fall short in 1) identifying and isolating the controllable variables in urban microclimates, and 2) representing the detailed spatial variability of thermal comfort indices. Numerical methods can further address these shortcomings, but also face several challenges in computations. Among the factors that add to the complexity of thermal comfort analysis are a) the three-dimensional distribution of surface heating, and the consequent modification of the airflow and thermal fields; and b) the radiation exposure of pedestrians influenced by the urban forms and materials. Accordingly, a recent study by Fan et al. [Fan, 2016] has addressed these challenges by employing detailed CFD simulations of urban flow with realistic thermal forcing on urban surfaces, while calculating the thermal comfort index of Standard Effective Temperature (SET) with an improved Mean Radiant Temperature (T_{mrt}) model.

In this study, we aim to employ the SET calculation method discussed by Fan et al. (2016), and further investigate the effects of climate and design factors on thermal comfort. In order to extend the results to more general scenarios, the SET is evaluated as a function of previously defined buoyancy parameters, Ri_h and Ri_v [Nazarian, 2016a], that are each correlated with ambient conditions (ambient air temperature, wind speed, and wind direction), material properties (surface albedo and window fraction), and urban build-up density (canyon aspect ratio). Using this methodology, we aim to answer the following questions: What is the correlation between design factors, such as the material properties of urban facets, and

outdoor thermal comfort; and how does this correlation change with the location, time of day and stability conditions? How do these correlations compare to the effect of design factors on city breathability [Nazarian, 2016b]? Answering these questions aims to provide the framework for guideline maps that can ultimately inform designers, architects and urban planners on the environmental effects of their design on thermal comfort and breathability, without the explicit need for detailed numerical modelling.

2 Methodology

An overview of the research methodology is shown in Figure 1. In summary, a detailed urban energy balance model (TUF-IOBES, Section 2.1) is employed to incorporate the diurnal and spatial variations of surface heating in the urban flow field simulations (PALM, Section 2.1). In parallel, the parameterization method introduced by Nazarian & Kleissl [Nazarian, 2016a] is used to comprehensively characterize the flow field under unstable conditions, and the sensitivity of non-dimensional numbers to the design and climate factors is evaluated. In the next phase, the detailed distribution of surface and air temperatures, wind flow, and pressure fields will be used for the calculation of the thermal comfort index, SET (Section 2.2), and the correlation of SET with the previously defined characterization methods will be evaluated. Following this methodology, the guideline maps of thermal comfort as varied by various climate and design factors can be produced, and compared with guidelines given for air quality and city breathability.

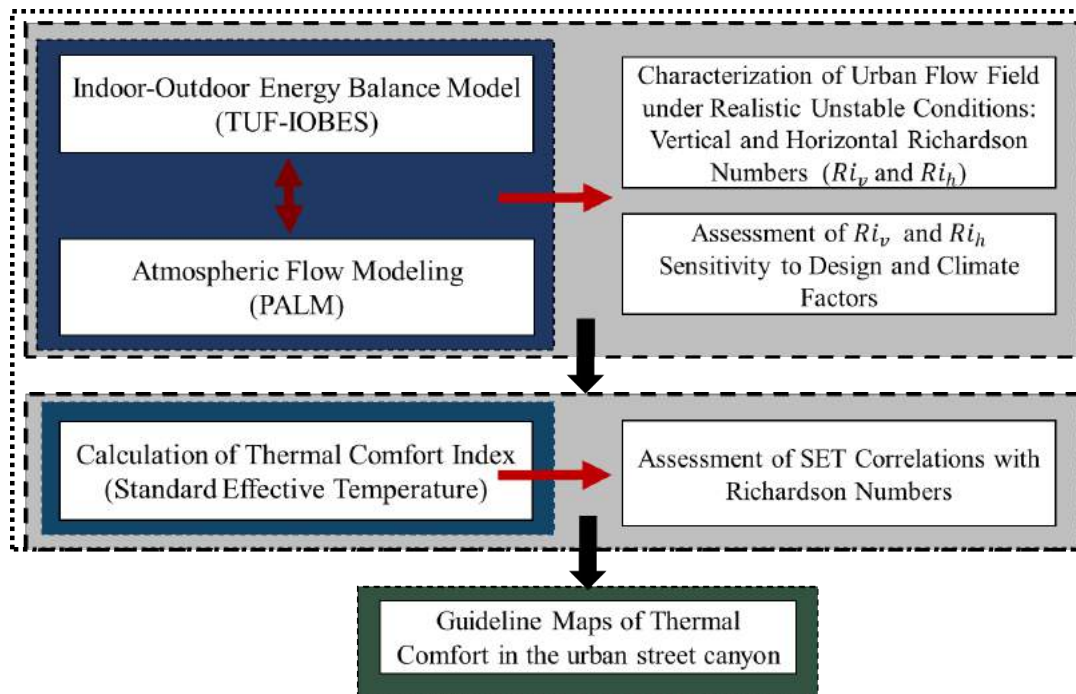


Figure 1- Flowchart of the research methodology for obtaining guideline maps of thermal comfort

2.1 CFD Simulation of Urban Environment with Realistic Surface Heating

Series of fluid flow and thermal field simulations are performed using the PARallelized Large-Eddy Simulation Model [Raasch, 2001; Letzel, 2008; Maronga, 2015] with realistic thermal boundary conditions extracted from Temperature of Urban Facets Indoor-Outdoor Building Energy Simulation [Yaghoobian, 2012]. TUF-IOBES is a building-to-canopy model that dynamically solves for indoor and outdoor energy processes, including effects of real weather conditions, indoor heat sources, building and urban material properties, composition of the building envelope (e.g. windows, insulation), and waste heat from air-conditioning systems on urban canopy temperature. The PARallelized Large-eddy simulation Model (PALM), on the other hand, solves the filtered, incompressible Boussinesq equations, the first law of thermodynamics, the equation for subgrid-scale (SGS) turbulent kinetic energy (TKE)

and passive scalar (pollutant) equation. TUF-IOBES, PALM and the coupling of the two have been previously validated [Yaghoobian, 2012; Park, 2012; Yaghoobian, 2014].

The building configuration used is an aligned array of uniformly spaced cubes with $\lambda_p = 0.29$, $\lambda_f = 0.25$, and aspect ratio of 1 with no vegetation, representing the compact low-rise urban zone based on the LCZ categorization [Stewart, 2011]. Periodic boundary conditions are used in horizontal directions, and for the top boundary condition a sink term of heat is imposed corresponding to the diurnal variation of surface heat fluxes. The focus of this study is on unstable atmospheric stratification and the simulations are done for a temperate mid-latitude climate (Boston, Massachusetts with latitude of 42.36 N), while the results can be expanded to various locations and time of the years using the characterization method further explained in Section 2.3.

2.2 Predicting Thermal Comfort

Thermal comfort is measured in terms of different indices that incorporate the physiological response of humans to microclimate parameters, such as wind flow, air temperature, humidity, and radiation exposure. One such index is SET, which can be calculated as

$$H_{sk} = h_s(t_{so} - SET) + wh_{e,s}(P_{s,sk} - 0.5P_{SET}), \quad (1)$$

where H_{sk} ($W m^{-2}$) is the heat loss from skin, h_s ($W m^{-2}K^{-1}$) is the standard heat transfer coefficient, t_{so} (K) is the standard operative temperature, w (-) is the fraction of the wetted skin surface, $h_{e,s}$ ($W m^{-2}K^{-1}$) is the standard evaporative heat transfer coefficient, $P_{s,sk}$ (kPa) is the water vapor pressure at skin assumed to be that of saturated water vapor at t_{so} , and P_{SET} (kPa) is the saturated water vapor pressure at Standard Effective Temperature (K). In this study, SET is analyzed as a steady-state condition without significant heat storage within the body. Therefore, H_{sk} is assumed to be zero. For SET calculation in this study, the spatial variation of urban microclimate parameters will be provided from the coupled CFD analysis of flow and thermal field in an idealized configuration explained in Section 2.1.

In order to accurately calculate the standard operative temperature (t_{so}) in Equation (1), the mean radiant temperature (T_{mrt}) which accounts for the pedestrian exposure to the net radiation, should be predicted accurately. However, the complexity of T_{mrt} calculation results in simplified models for pedestrian radiation exposure. For instance, T_{mrt} is assumed to be equal to T_{air} in the thermal comfort analysis of Ali-Toudert and Mayer [Ali-Toudert, 2006; Ali-Toudert, 2007] or the reflected solar radiation is neglected in the model proposed by Andreou [Andreou, 2013]. Therefore, the accuracy of many similar thermal comfort models suffers from inaccurate prediction of human radiation exposure from the urban surfaces as well as the sky. Accordingly, Fan et al. [2016] has developed a comprehensive and detailed model for the T_{mrt} calculation that represents the spatial variability of radiation exposure in the urban streets. To do so, shading effects, sky view factor, and surface visibility are modelled in detail. Figure 2 represents the flow and thermal fields, and the corresponding SET distribution at 1000 PST of a clear summer day in southern California (taken from [Fan, 2016]). It can be seen that the distribution of each parameter separately does not reflect the thermal comfort and fails to incorporate the inter-building shadowing effects that significantly influence the mean radiant temperature and the subsequent SET calculation. In the proposed study, the improved model of the mean radiant temperature by Fan et al. [Fan, 2016] will be used to calculate the spatial variability of the thermal comfort index in an idealized configuration of a compact mid-rise urban area.

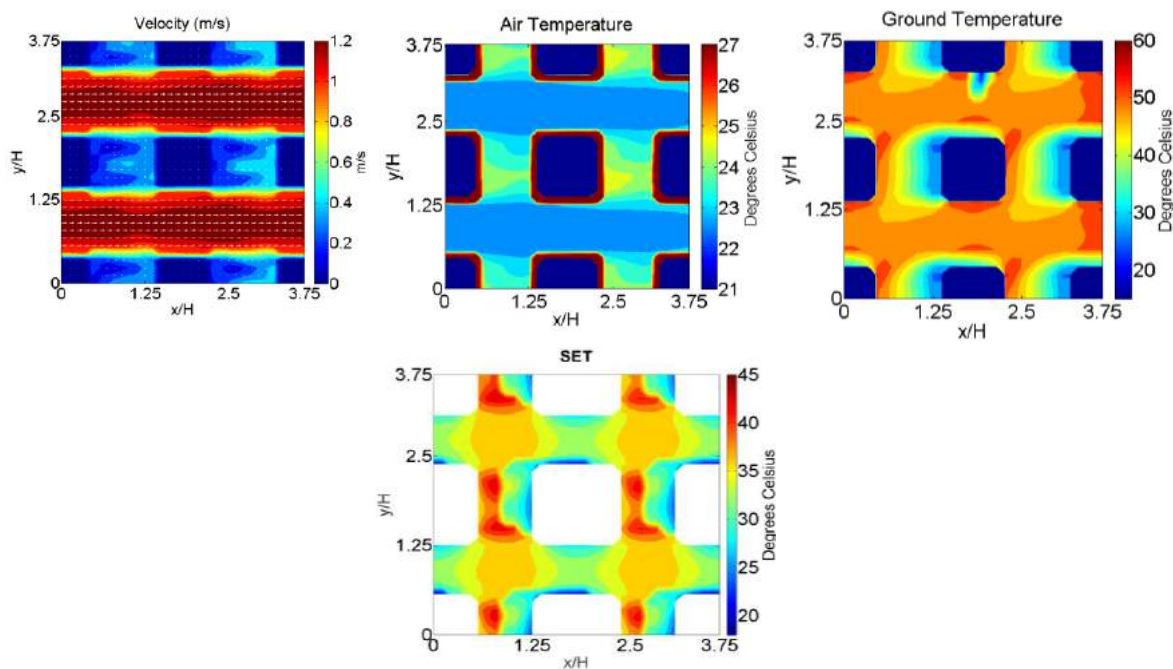


Figure 2. Parameters contributing to spatial variation of standard effective temperature (SET)

2.3 Characterization Method: Momentum Versus Buoyancy Forcing

The differential heating of the urban facets is parameterized using sets of horizontal and vertical Richardson numbers (Ri_h and Ri_v , respectively) as follows:

$$Ri_v = \frac{gH(\overline{T_H} - \overline{T_g})}{U_b^2 T_a} \quad (2)$$

$$Ri_h = \frac{gH(\overline{T_L} - \overline{T_W})}{U_b^2 T_a} \frac{H}{W}$$

where $g=9.81 \text{ m s}^{-2}$ is the gravitational acceleration, H is the building height, W is the canyon width, T_W , T_L , and T_g , are the surface temperature at the windward wall, leeward wall, and ground surface inside the building canyon, respectively, T_a and T_H indicate the air temperature at a reference height and roof level, respectively, and U_b is the bulk wind velocity with zero wind angle from the east-west axis ($\cos\theta=1$).

Accordingly, Ri_v is used to indicate atmospheric stability due to the temperature difference in a vertical direction and incorporates the effect of ground and roof heating in the building canyon. Ri_h compares the ratio between thermal forcing and inertial forcing in the canyon and conveys information regarding the directionality of thermal forcing in relationship to the canyon vortex, as well as incorporating the effect of canyon aspect ratio H/W . Both Richardson numbers depend on the free-stream conditions above the building canopy, such as air temperature, and wind speed and direction. The validity of this choice of non-dimensional numbers is previously analyzed through simulations with different wind speed and surface radiative properties, but the same sets of Richardson numbers, and the similarity of results are seen [Nazarian, 2014a].

2.4 Urban Flow Characterization and Design Factors: An example of guideline maps

In order to draw conclusions from the thermal comfort analysis that can be further used for alternative urban planning strategies, it is important to quantify the modification of prescribed

Richardson numbers due to such design and climate factors as wind speed, surface material properties and urban built-up density. An example of surface radiative properties is discussed here, although this project aims to extend the analysis to other climate and design parameters, including canyon aspect ratio and wind direction.

Figure 3 shows the modification of Richardson numbers where wall and ground albedo, α_w and α_g , respectively, are varied from 0.1 to 0.5. When increasing α_g , Ri_v increases while Ri_h is not significantly modified. This is due to the fact that with increasing ground albedo, the reflected shortwave radiation is imposed on both walls equally; therefore, although wall temperature increases, the horizontal temperature gradient remains unchanged. Similarly, when increasing α_w , Ri_v is only changed slightly. Additionally, it is shown that the effect of ground albedo on the bulk Richardson number is larger than wall albedo, due to the higher view factor.

In the example shown here, the slope of Ri_h and Ri_v as a function of albedo, incorporates the effects of various parameters including U_b , H/W , and T_a , so that $Ri_v \propto \frac{gH}{T_a} \cdot \frac{1}{(U_b \cos\theta)^2} \cdot a\alpha_g$, $Ri_h \propto \frac{gH}{T_a} \cdot \frac{1}{(U_b \cos\theta)^2} \cdot \frac{H}{W} \cdot b\alpha_w$, where a and b are the coefficients for surface temperature based on albedo. This example can be repeated for other parameters to fully analyze the response of Richardson numbers to design and climate factors.

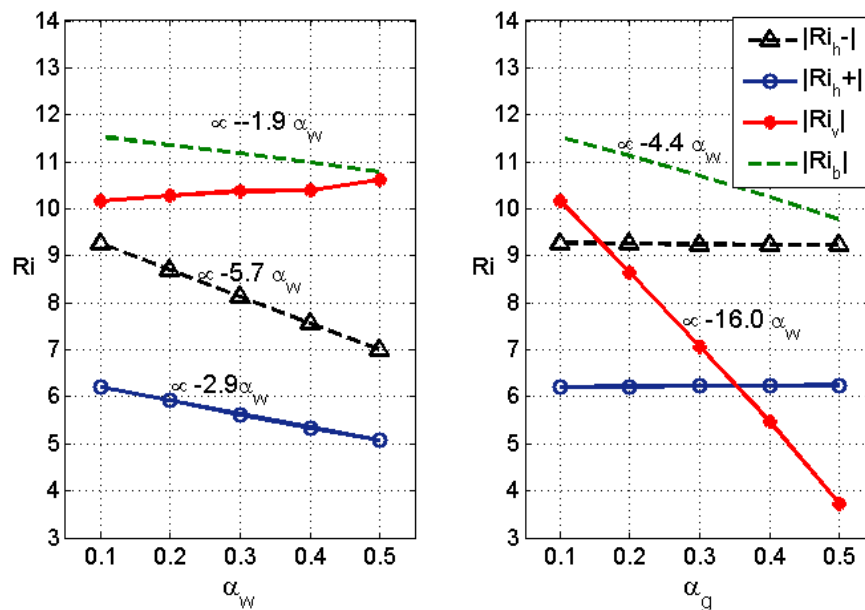


Figure 3. Variation of maximum value of Richardson numbers with wall and ground albedo. For horizontal Richardson number, the maximum value of windward ($|Ri_h^+|$) and leeward ($|Ri_h^-|$) heating are presented separately. Ri_b is calculated based on the average surface temperature of urban facets (T_s) compared to T_a , the free stream wind temperature.

Figure 4 shows the variation with Richardson numbers of the average air temperature in the pedestrian level (a horizontal plane at $z \sim 1.5-2m$). The most notable correlation is seen between the temperature in the building canyon and the vertical Richardson number, Ri_v , while the correlation with Ri_b is also apparent. When comparing the horizontal Richardson number, Ri_h , however, the variation in temperature is more complex as it exhibit differences based on the sign of the Ri_h , as well as the corresponding Ri_v . These results then suggest that investing the correlation with only one horizontal or vertical Richardson number can be

misleading, as Ri_h and Ri_v are dynamically changing throughout the day and do not occur independently of each other. To avoid this, Figure 5 shows the scattered contour of air temperature as a function of both Richardson numbers.

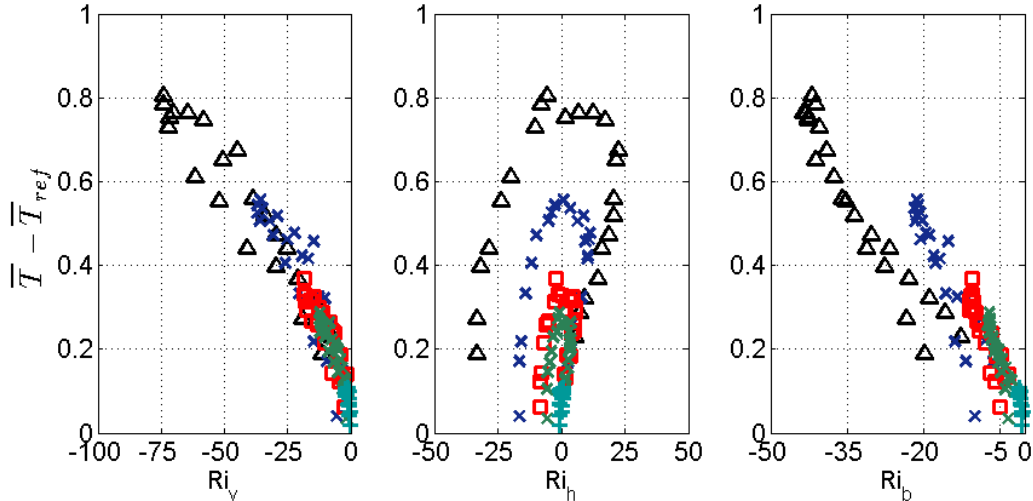


Figure 4. Variation of temperature difference, $\bar{T} - \bar{T}_{ref}$, with Richardson numbers, in the volume between the buildings in the spanwise canyon (BC). Ri_v , Ri_h and Ri_b represent the vertical, horizontal and bulk Richardson numbers, respectively. The results are averaged in the horizontal plane at which the pedestrian breathe in ($z \sim 1.8m$). Data points with different colors represent the scaled range of instability condition that is achieved by scaling surface convective fluxes.

In Figure 5 each curve represents a simulation case with a different range of atmospheric instability achieved by scaling the surface heat fluxes. Due to the high computation cost of the LES model, the instability range is only covered by 5 simulations, although a series of simulations with a more computationally-efficient model, yet accurate in representing the average values (such as RANS), can be carried out to cover the complete physical spectrum of Richardson numbers.

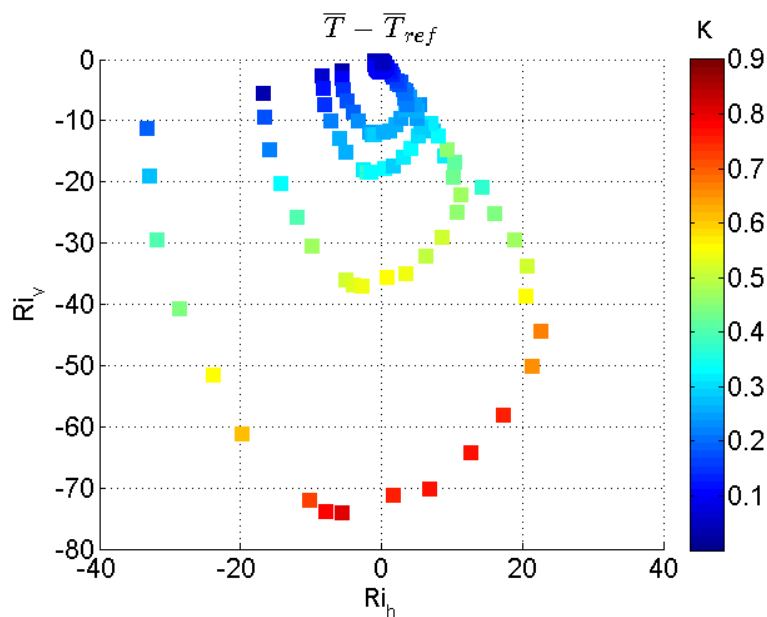


Figure 5 Map of temperature difference at the pedestrian level with horizontal and vertical Richardson numbers.

In order to estimating the qualitative response of the human comfort to design and climate factors, the knowledge of Richardson numbers variations (example given in Figure 3) can be combined with the information given in **Figure 5**. Therefore, guideline maps can be produced that inform the community of designers and urban planners on the environmental effect of their design. Additionally, as demonstrated in Section 2.2, urban air temperature is only one determinant of human comfort, and cannot fully represent the human experience in the thermal environment. Therefore, we aim to employ the SET model by Fan et al. [2016], and extend this study to do a comprehensive calculation of thermal comfort for the flow simulation cases presented in Section 3. Therefore, by repeating the methodology explained in Figure 4 and Figure 5, an example of guideline maps of thermal comfort in urban streets can be produced. Alternatively, in order to fully evaluate the effect of urban design and climate on the experience of humans in urban areas, this project will do a comparison with the guidelines given on the effect of design on city breathability and air quality.

3 Conclusions

The current study describes the framework of obtaining guideline maps of thermal comfort in urban streets. Detailed simulations of flow field and energy balance in an idealized urban environment are performed, which can be used to extract qualitative and quantitative information to be provided to designers and urban planners, and thereby remove the need for detailed modeling. The study also aims to extend the analysis of thermal comfort from solely evaluating the air temperature or flow field, and use comprehensive metrics of thermal comfort, such as SET. Accordingly, this study uses the SET model of Fan et al. [Fan, 2016] that incorporates the spatial and temporal variability of microclimate parameters, as well as calculating the detailed Mean Radiant Temperature at all pedestrian positions. The correlation between SET and previously defined buoyancy parameters, Ri_h and Ri_v , is then investigated. These non-dimensional numbers depend on the local climate as well as design factors; therefore, investigating the correlations between Richardson numbers and thermal comfort aims to connect the microclimate with urban design factors.

References

- [Ali-Toudert, 2006] Fazia Ali-Toudert, Helmut Mayer, Numerical study on the effects of aspect ratio and orientation of an urban street canyon on outdoor thermal comfort in hot and dry climate, *Building and environment*, 41(2):94-108, 2006.
- [Ali-Toudert, 2007] Fazia Ali-Toudert, Helmut Mayer, Thermal comfort in an east–west oriented street canyon in Freiburg (Germany) under hot summer conditions, *Theoretical and Applied Climatology*, 87(1-4):223-237, 2007.
- [Andreou, 2013] E. Andreou, Thermal comfort in outdoor spaces and urban canyon microclimate, *Renewable energy*, 55:182-188, 2013.
- [Bornstein, 1968] Robert D Bornstein, Observations of the urban heat island effect in New York City, *Journal of Applied Meteorology*, 7(4):575-582, 1968.
- [Chen, 2012] Liang Chen, Edward Ng, Outdoor thermal comfort and outdoor activities: A review of research in the past decade, *Cities*, 29(2):118-125, 2012.
- [Chow, 2016] Winston TL Chow, Siti Nur‘Assyakirin Binte Ali Akbar, Su Li Heng, Matthias Roth, Assessment of measured and perceived microclimates within a tropical urban forest, *Urban Forestry & Urban Greening*, 16: 62-75, 2016.

- [Fan, 2016] Jipeng Fan, Negin Nazarian, Tiffany Sin, Leslie Norford, Jan Kleissl, Predicting Thermal Comfort in Urban Environments, *Urban Climate*, In preparation, 2016.
- [Johansson, 2014] Erik Johnson, Sofia Thorsson, Rohinton Emmanuel, and Eduardo Krüger, Instruments and methods in outdoor thermal comfort studies–The need for standardization, *Urban Climate*, 10: 346-366, 2014.
- [Kim, 1992] Hongsuk H. Kim, Urban heat island, *International Journal of Remote Sensing*, 13(12):2319-2336, 1992.
- [Letzel, 2008] Marcus Oliver Letzel, Martina Krane, Siegfried Raasch, High resolution urban large-eddy simulation studies from street canyon to neighbourhood scale, *Atmospheric Environment*, 42(38):8770-8784, 2008.
- [Lin, 2009] Tzu-Ping Lin, Thermal perception, adaptation and attendance in a public square in hot and humid regions, *Building and Environment*, 44(10): 2017-2026, 2009.
- [Mayer, 1987] Helmut Mayer, Peter Höppe, Thermal comfort of man in different urban environments, *Theoretical and applied climatology*, 38(1):43-49, 1987.
- [Moranga, 2015] Björn Maronga, Micha Gryschka, Rieke Heinze, Fabian Hoffmann, Farah Kanani-Sühring, Marius Keck, K. Ketelsen, Marcus Oliver Letzel, Matthias Sühring, Siegfried Raasch, The Parallelized Large-Eddy Simulation Model (PALM) version 4.0 for atmospheric and oceanic flows: model formulation, recent developments, and future perspectives, *Geoscientific Model Development Discussions* 8, 2:1539-1637, 2015.
- [Nazarian, 2016a] Negin Nazarian, Jan Kleissl, Realistic solar heating in urban areas: Air exchange and street-canyon ventilation, *Building and Environment*, 95:75-93, 2016.
- [Nazarian, 2016b] Negin Nazarian, Alberto Martilli, Leslie Norford, Jan Kleissl, Impacts of Realistic Urban Heating: Part II, Air Quality and City Breathability, *Boundary-Layer Meteorology*, Submitted, 2016.
- [Nikolopoulou, 2001] Marialena Nikolopoulou, Nick Baker, Koen Steemers. Thermal comfort in outdoor urban spaces: understanding the human parameter, *Solar energy*, 70(3):227-235, 2001.
- [Park, 2012] Seung-Bu Park, Jong-Jin Baik, Siegfried Raasch, Marcus Oliver Letzel, A large-eddy simulation study of thermal effects on turbulent flow and dispersion in and above a street canyon, *Journal of Applied Meteorology and Climatology*, 51(5):829-841, 2012.
- [Oke, 1973] Tim R. Oke, City size and the urban heat island, *Atmospheric Environment*, 7(8):769-779, 1973.
- [Oke, 1981] Tim R. Oke, Canyon geometry and the nocturnal urban heat island: comparison of scale model and field observations, *Journal of climatology*, 1(3):237-254, 1981.
- [Raasch, 2001] Siegfried Raasch, Michael Schröter, PALM—a large-eddy simulation model performing on massively parallel computers, *Meteorologische Zeitschrift*, 10(5):363-372, 2001.
- [Stewart, 2012] Ian D Stewart, Tim R. Oke, Local climate zones for urban temperature studies, *Bulletin of the American Meteorological Society*, 93(12):1879-1900, 2012.
- [Yaghoobian, 2012] Neda Yaghoobian, Jan Kleissl, An indoor–outdoor building energy simulator to study urban modification effects on building energy use–Model description and validation, *Energy and Buildings*, 54: 407-417, 2012.

[Yaghoobian, 2014] Neda Yaghoobian, Jan Kleissl, Kyaw Tha Paw U, An Improved Three-Dimensional Simulation of the Diurnally Varying Street-Canyon Flow, *Boundary-Layer Meteorology*, 153.2:251-276, 2014.

Estimating the Urban Heat Island Effect in the City of Guayaquil

Massimo Palme^{1,2}, Geovanna Villacreses², Andrea Lobato², Martín Cordovez², José Macias^{2,3} and Guillermo Soriano³

¹ Universidad Católica del Norte, Escuela de Arquitectura
Av. Angamos 610, Oficina 205, Antofagasta, Chile, +56 552 355188
e-mail: mpalme@ucn.cl, massimo.palme@iner.gob.ec

² Instituto Nacional de Eficiencia Energética y Energías Renovables
C. Ñaquito, Quito, Ecuador
e-mail: geovanna.villacreses@iner.gob.ec, andrea.lobato@iner.gob.ec, martin.cordovez@iner.gob.ec,
jose.macias@iner.gob.ec

³ Escuela Politécnica del Litoral
Guayaquil, Ecuador
e-mail: gsorian@espol.edu.ec

Keywords: Urban Heat Island, Ecuador, Urban Weather Generator, Cooling.

Abstract. *Urban Heat Island effect (UHI) is a very important study aspect regarding the future of tropical cities. Guayaquil is the most populated city of Ecuador and leads on the river Guayas, close to the Pacific Ocean, in a very hot humid climatic emplacement. The climate of Guayaquil affects drastically the built environment, especially regarding the cooling demand of buildings and the related electricity consumption. In the future, cooling needs are expected to increase: predictions by the Intergovernmental Panel for Climate Change (IPCC) suggest that the atmosphere temperature will rise up to 6 °C to the end of the century in this region, so the temperatures are expected to increase in at least 4 °C to the middle of the century and 8°C to the end of the century. Moreover, all the South-American countries are experimenting a period of fast economic growth and people are continuously increasing their acquisitive power. Today, only a 15% of the built environment of Guayaquil uses air-conditioning to cool inside, but it is very probable that in the future there will be a significant increase in the use of active systems by the people in their homes and workplaces. This work explores the urban heat island effect on the city. The paper explores the spatial distribution of the city in order to parametrize the urban geometry and materials properties, then a set of simulations is done by using the Urban Weather Generator (UWG) tool. Eight spatial configurations are simulated, representing the different city sectors and a map of the urban parameters is generated and correlated with the heat island expectations. Materials properties of construction elements commonly used in Ecuador are tested to obtain emissivity and reflectivity coefficients to be inserted in the UWG. Results confirm the existence of a UHI effect in Guayaquil, with variable intensities within specific emplacements. Simulations results suggest a probable increase in urban temperatures between 6 and 10 degrees Celsius, considering the combined effect of global warming and urban heat island.*

1 Introduction

The Urban Heat Island Effect (described as the temperature increase of a city respect to the rural environment close to the same city) is a phenomenon that involves many factors, like the presence of impervious materials, the metabolic activity in the streets (people, cars, etc.) and the operation of any kind of appliances in buildings. In the general context of global warming, UHI effect could increase even more the temperatures in the cities worldwide. In some climates, like the cold climates of Northern Europe or Canada, UHI could be regarded as a partially positive effect, because a warmer environment reduces the cold season and the associated heating consumption of buildings. In hot climates, both dry and wet, things change: the UHI should be regarded always as a negative phenomenon forcing temperatures and exacerbating the effect of global warming. Other factors to be taken into account are the considerations that many cities of the developing world lead in the intertropical zone and these cities are experimenting a fast urban growth. Especially in South American region, inhabitants of the mentioned cities are experimenting at the same time an economic growth never known before: it is very probable that the comfort standards of people will change in the next years. All these facts, suggest that the building energy consumption of the region will drastically increase in the next future, like observed in other parts of the world [Kolokotroni 2012, Sailor 2014, Santamouris 2015]. The UHI phenomenon will transform itself in a recursive phenomenon: the warmer the environment, the higher the cooling demand of buildings, the more the electricity consumption and the higher the heat released into the urban canopies, which contributes to a warmer environment and so on.

The figure 1 describes how the Daule and Guayas rivers confine the city of Guayaquil on the east and south boundaries, while the north and west edges are expanding continuously. Guayaquil is a city located very close to the Equator line ($2^{\circ}16'51''$ South & $79^{\circ}54'49''$ West), and an average altitude of 3.80 on the sea level [Interagua 2015] in a hot and humid environment. The city has had a very irregular urban development in the last century, characterized by certain degree of sprawl and, more recently, a change in buildings typologies, introducing the tall buildings for both residences and offices. The urban area of Guayaquil covers around 340 km² at the South American Pacific Coast on the Guayaquil's gulf. Early in the 20th century, Guayaquil's population reached 70,000 people in a 25 years period. An area known as Savannah of the City was occupied in the period between 1930 and 1960; the area is the current downtown, figure 1. From 1969 to 1975, new non-legal territories were populated at the South zones due to a constant migratory flux. At present, the regions are identified as Mapasingue and Guasmo.

In the 80's, the urban scene experienced dramatic changes, some of the sea estuaries were filled (Estero Salado), and some hills disappeared from the landscape. In the next decade, the city realized new highways among them the urban ring. In consequence, a new suburban sector named Isla Trinitaria was populated. Non-legal territory establishment became a problem again. The areas of Prosperina and Pascuales were occupied. The building of commercial malls increased; however, public dwellings programs and the industrial infrastructure decreased. The urban area kept growing to the North and West between 2000 and 2009. Additionally, the city perimeter surpassed its East limits; thus, Guayaquil city joined the municipalities Daule and Samborombon to form one urban community. Relevant improvements were carried out such as sanitary works and a new public transport system. Non-legal territory occupancy persisted as a social problem [Interagua 2015, Moncayo 2015].

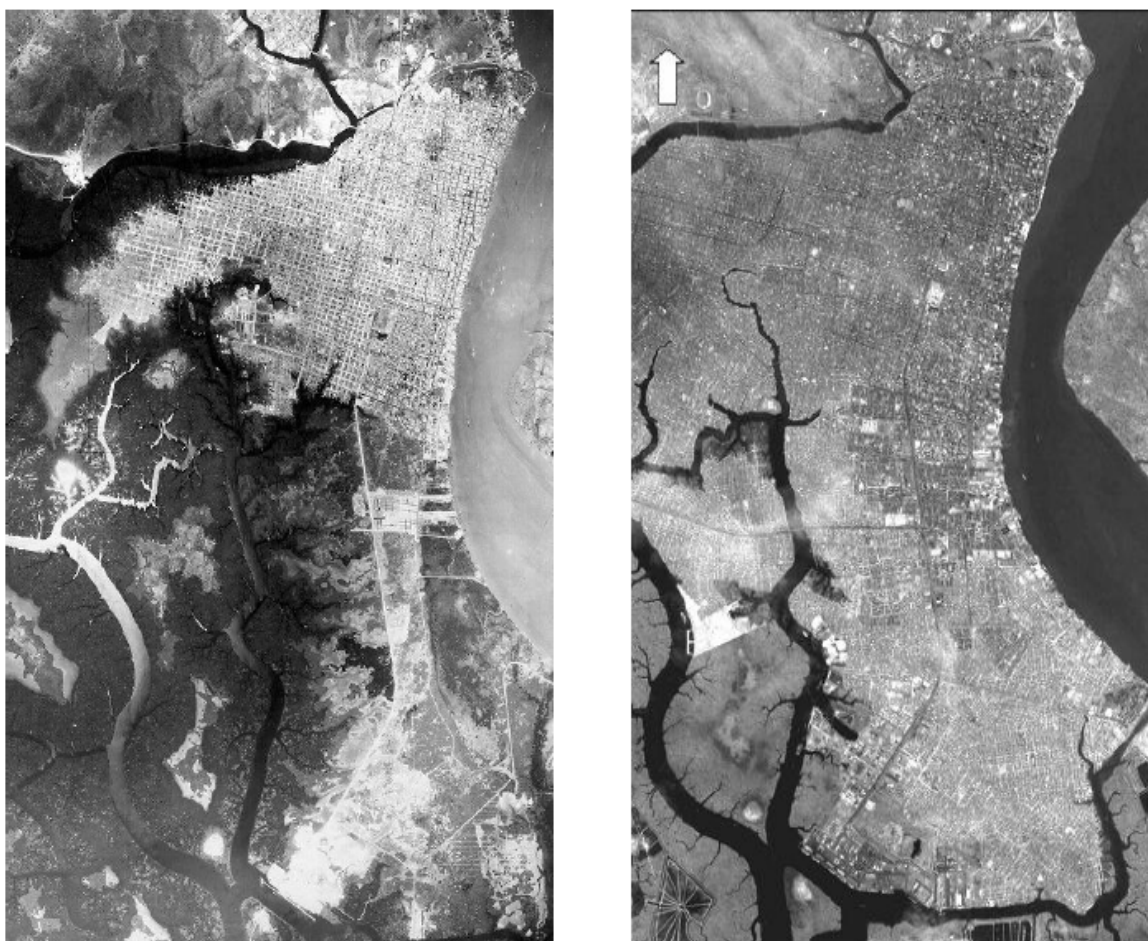


Figure 1. Urban perimeter change, the period from 1961 to 2001

In the last years Guayaquil experienced several improvements focused on the urban environment, e.g. the Estero Salado was recovered, new green zones such as the Samanes Park and the Santay Island project were built. Furthermore, public dwelling programs increased. The urban boundaries have been expanding to the North and West regions, and municipalities as Daule, Samborombon and Duran have enhanced their public facilities, and their populations increased twice since 90's decade, [INEC 2016]. Nowadays, Guayaquil has 2.366.902 inhabitants, which represents 15% of the total Ecuadorian population. Figure 2 shows the entire city with the different zones identified. In the last years, urbanization appears in the right side of the river Gayas. At the same time, the urbanization of the outskirts of Guayaquil is continuing, in this case the typical construction are small houses with poor materials.

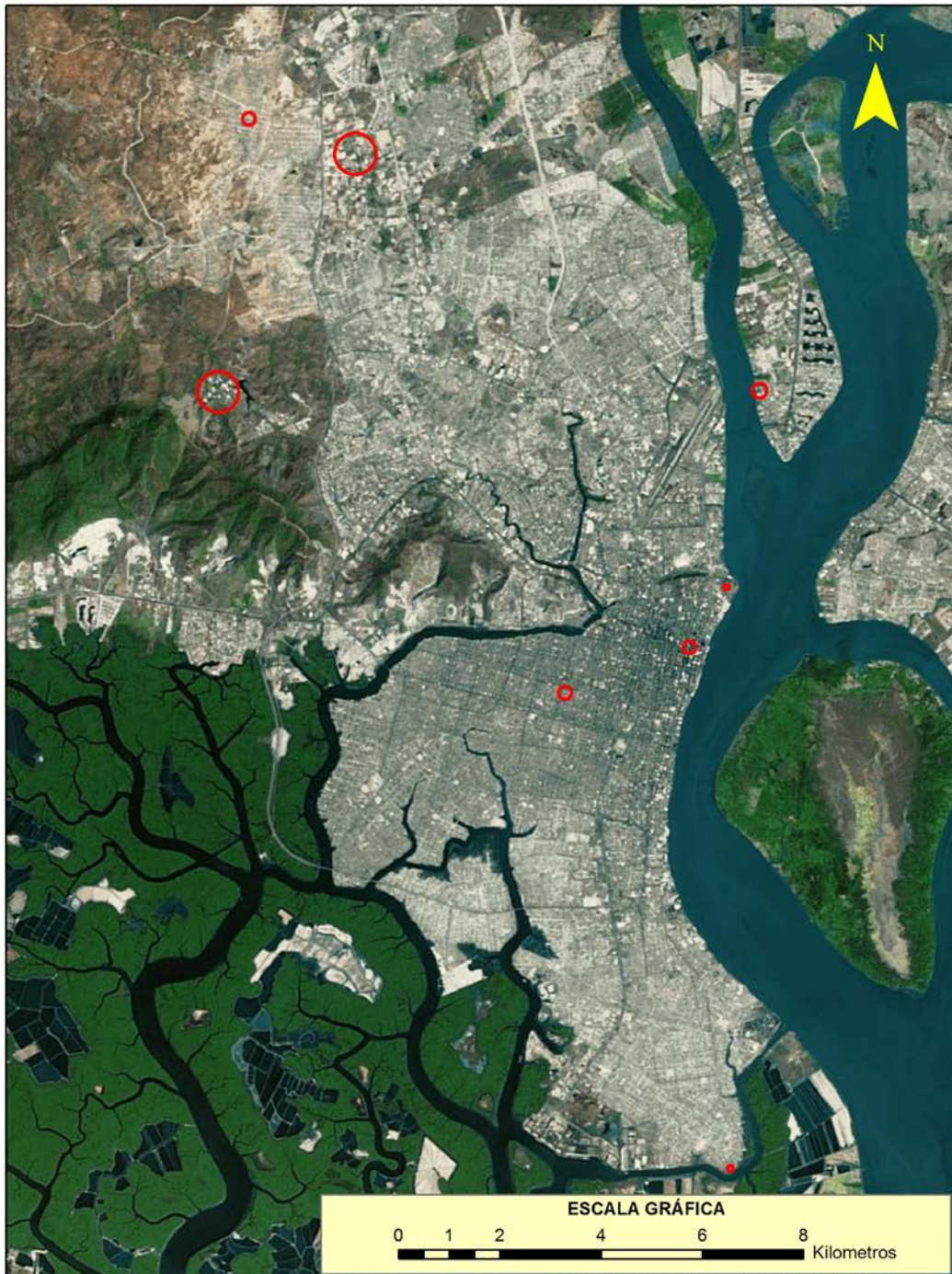


Figure 2: Map of the city of Guayaquil

2 Materials and Methods

UWG tool is a coupled atmospheric-building simulator developed by Bueno [2010, 2012a, 2012b] at MIT. The tool considers a lot of variables, divided in: construction parameters (building materials properties), building parameters (schedules, systems efficiency), urban morphology (density, height, green areas, non-buildings anthropogenic heat generation), and reference site (latitude, longitude, weather data). A parameter sensitivity analysis of the tool is still ongoing [Nakano 2015], but until now it considers the high influence of the following parameters on the resulting urban temperatures: materials emissivity and reflectivity (roofs, soils and walls), urban parameters (density, façade-site ratio, green areas) and anthropogenic heat generation in the street (cars, people). In this work, the UWG parameters considered more effective on the calculation (which are estimated with more detail) are:

- The built-up ratio or site coverage defined by equation (1):

$$\text{site coverage} = \frac{\sum A_{bldg}}{A_{site}} \quad (1)$$

Where A_{bldg} is the footprint of each building in the site and A_{site} is the total site area;

- The facade to site ratio defined by equation (2):

$$\text{facade to site ratio} = \frac{\sum Ph_{wtd}}{A_{site}} \quad (2)$$

Where P is the perimeter of each building in the site, h_{wtd} is the weighted building height (by footprint) and A_{site} is the total site area;

- The tree coverage defined by equation (3):

$$\text{tree coverage} = \frac{A_{green}}{A_{site}} \quad (3)$$

Where A_{green} is the area covered by trees and A_{site} is the total site area;

- The emissivity and albedo properties of vegetation, roads, soils, roofs and walls.

The very influencing parameter “anthropogenic non-building sensible heat generated in the canyon” is very difficult to be estimated. Moreover, the estimation of this heat is inserted in the UWG as an average value, which is obviously a strong limitation, because the car traffic in the street is dynamic and very variable during the day. For this reason, it has been not considered in this first evaluation and a defect value of 50 W/m^2 has been selected.

As exposed, two classes of parameters are definitively needed to obtain a reliable result by these simulations tool: three urban parameters (site coverage, façade to site ratio, tree coverage) and the optical eight materials parameters (albedo and emissivity for walls, roofs, soil and vegetation). In the follow the strategy to obtain the two classes of values is exposed.

First, the representative urban parameters are obtained by analyzing the city morphology. It could be observed in figure 1 a clear fragmentation of the city between the center and the

outside neighborhoods. In the center the average building height is about 30 meters, whilst in the outside the average building height is only 5 meters.

The outside neighbors should also be divided in an historical expansion zone and a new expansion zone. One of the difference between this two zones is the soil typology: asphalt in one case and earth in the other. A very different urbanization process regards the right side of the river Guayas, in this case the upper class residences are big houses or tall buildings.

In this work eight zones are selected and analyzed:

- A reference site placed in the historic center of the city
- A reference site placed in the old neighbor of “Las Peñas”
- A reference site placed in the historical expansion zone north
- A reference site placed in the new expansion zone north
- A reference site of industrial soil use placed in the new expansion zone
- A reference site placed in the new upper-class zone on the right side of the river Guayas
- A semi-rural site corresponding to the University campus
- A reference site placed in the new expansion zone south



Figure 3: historic center of the city

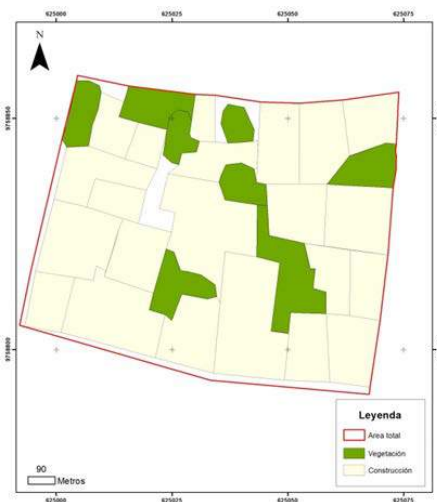


Figure 4: traditional neighbor “Las Peñas”

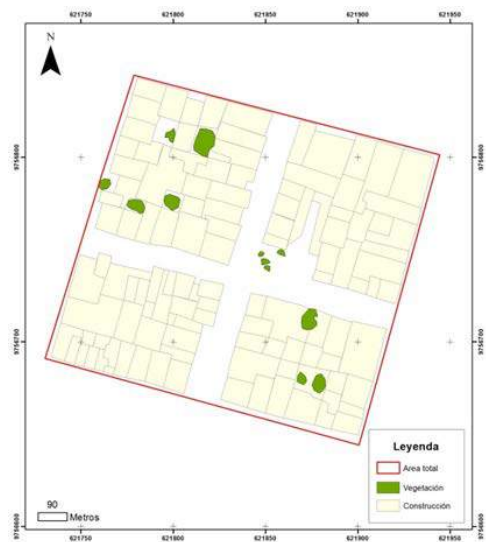


Figure 5: first expansion of the city



Figure 6: new expansion zone

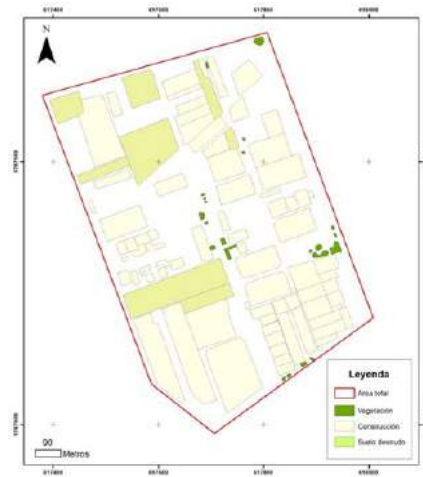


Figure 7: industrial area

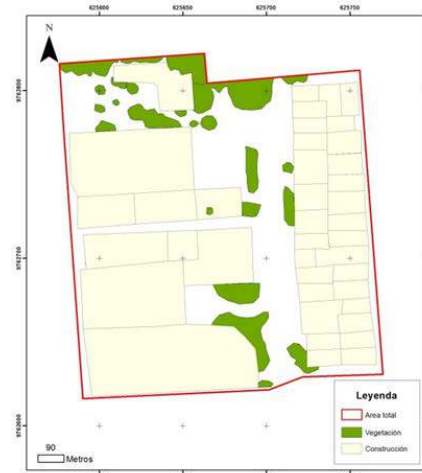


Figure 8: new urbanization on the right side of the river

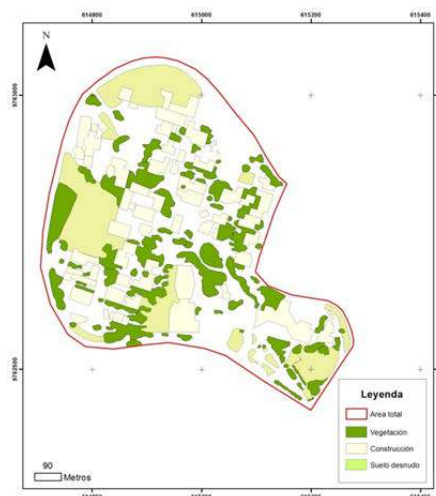


Figure 9: university campus



Figure 10: south expansion zone

Spatial information was obtained by using the photography of the zone realized in 2010 at the scale of 1:5000. A digitalization was done on the eight selected areas by using GIS tool, and the searched parameters were estimated. Table 1 shows the urban parameters obtained and used in UWG simulations.

	Zone description	Site area (m ²)	Weighted height (m)	Site coverage	Façade ratio	Tree coverage
Location 1	Historic center	22793	25.6	0.10	2.6	0.04
Location 2	“Las Peñas”	4443	6	0.77	1.5	0.17
Location 3	Old expansion zone	28133	6.2	0.73	1.4	0.02
Location 4	New expansion zone	22502	6	0.60	1.5	0.04
Location 5	Industrial zone	284146	3	0.41	0.1	0.01
Location 6	Upper-class zone	34389	29.3	0.61	2.9	0.10
Location 7	Semi-rural zone	213794	6	0.20	0.2	0.18
Location 8	South expansion	5928	3	0.71	0.7	0.11

Table 1: Urban parameter used in simulations

With respect to the materials properties, the reflectivity of common roofs materials used in Guayaquil has been assessed by studies in the laboratory of ESPOL University. These results were used to estimate the average reflectivity of the roofs in the UWG simulations. Figure 11 shows the tested materials. The first set was analyzed by using a spectrophotometer as prescribed by the ASTM E903 method [ASTM 2012]. The second set of materials was analyzed by using the Akbari method, that is more useful in field studies on bigger surfaces [Akbari 2008].



Figure 11: materials tested by using spectrophotometer and Akbari method respectively



Figure 12: spectrophotometer UV/Vis/NIR PerkinElmer used in the analysis

Table 2 resumes the reflectivity assessed by ESPOL experiments.

Material	Reflectivity	Method
Steel and zinc, new	0.72	ASTM E903
Aluminium and zinc, new	0.68	ASTM E903
Cement fiber, new	0.48	ASTM E903
Red metal tile	0.23	ASTM E903
Green metal tile	0.20	ASTM E903
Aluminium and zinc, used	0.51	Akbari
Cement fiber, used	0.32	Akbari
Ceramic tile	0.29	Akbari

Table 2: Measured reflectivity of roof materials commonly used in Guayaquil

A visual inspection in the selected areas provides the information about the typical material used for walls, roofs, soils and roads. Table 3 resumes this information.

	Walls	Roofs	Soil	Road
Location 1	Blockwork	Concrete	Asphalt	Asphalt
Location 2	Cement mortar	Zinc	Grass	Asphalt
Location 3	Cement mortar	Zinc	Earth	Asphalt
Location 4	Blockwork/bricks	Zinc	Earth	Earth
Location 5	Blockwork	Eternity	Earth	Asphalt
Location 6	Blockwork	Cement mortar	Earth/grass	Asphalt/earth
Location 7	Blockwork	Cement	Grass	Asphalt
Location 8	Blockwork	Zinc	Earth	Earth

Table 3: Building and street materials

The emissivity was estimated by following bibliographic references [Santamouris 2001 and 2006]. Table 4 resumes the optical properties of buildings and soils materials for the eight city sectors simulated.

	Walls		Roofs		Soil		Road	
	Albedo	Emissivity	Albedo	Emissivity	Albedo	Emissivity	Albedo	Emissivity
Location 1	0.13	0.90	0.32	0.90	0.15	0.91	0.15	0.91
Location 2	0.58	0.90	0.51	0.28	0.30	0.95	0.15	0.91
Location 3	0.58	0.90	0.51	0.28	0.20	0.76	0.15	0.91
Location 4	0.38	0.90	0.51	0.28	0.20	0.76	0.20	0.76
Location 5	0.58	0.90	0.48	0.94	0.20	0.76	0.15	0.91
Location 6	0.58	0.90	0.42	0.90	0.25	0.88	0.10	0.89
Location 7	0.58	0.90	0.42	0.90	0.30	0.95	0.15	0.91
Location 8	0.58	0.90	0.51	0.28	0.20	0.76	0.20	0.76

Table 4: Optical properties of building and street materials

3 Results

The urban canopies climates produced by UWG for the seven zones are compared at different times of the day. In the figure 13 two typical days can be observed: a clear-sky day with maximum temperatures of 33 degrees Celsius and minimum temperatures of 22 degrees Celsius (type “A” day – in the figure corresponds to day 1, day 3, day 4 and day 5) and a covered-sky day with maximum temperatures of 29 degrees Celsius and minimum temperature of 26 (type “B” – corresponding to day 2, day 7 and partially to day 6). The rural temperature is the red line, whilst the other lines are the eight urban temperatures at the street level obtained by UWG.

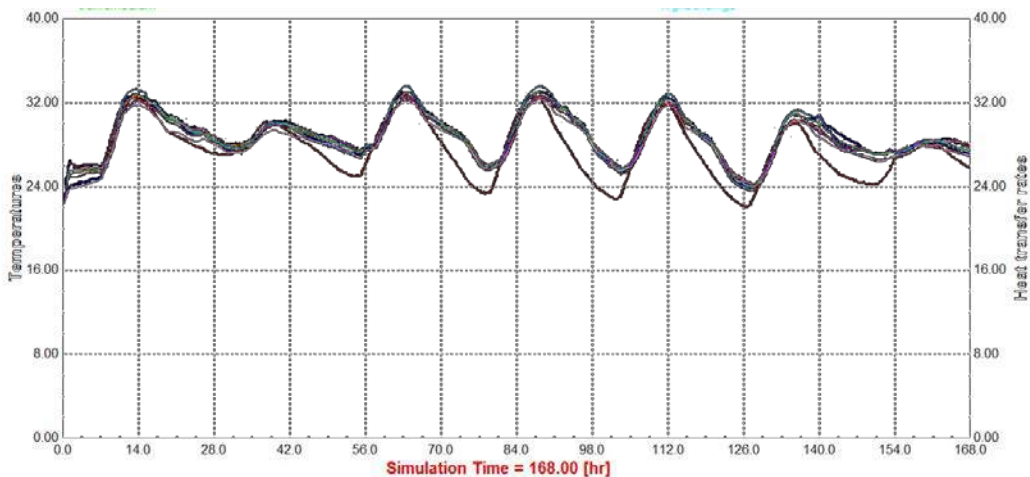


Figure 13: simulation results for the first week of January (TMY)

Analysis of the day type “A”: It could be noticed that all locations present night urban heat island effect, with intensities between 4.0 and 4.7 degrees Celsius. During the day, all the locations show a negative urban heat island, probably due to the building shadows and to the albedo of the surfaces. T is the temperature at the street level produced by UWG, UHI is the difference between the rural temperature and the urban temperature of each sector.

	6.00		12.00		18.00		24.00	
	T (°C)	UHI (°C)						
Location 1	25.5	1.9	30.0	-0.7	32.5	2.5	30.0	4.5
Location 2	26.2	2.7	29.5	-1.2	32.2	2.2	30.0	4.5
Location 3	26.1	2.6	30.0	-0.7	32.7	2.7	30.2	4.7
Location 4	26.0	2.5	30.0	-0.7	32.7	2.7	30.1	4.6
Location 5	25.6	2.0	30.4	-0.3	33.0	3.0	29.7	4.2
Location 6	25.5	1.9	29.5	-1.2	31.7	1.7	29.5	4.0
Location 7	25.5	1.9	29.7	-1.0	32.3	2.3	29.7	4.2
Location 8	26.1	2.6	30.0	-0.7	32.6	2.6	30.2	4.7

Table 5: Temperature and UHI intensities for 8 locations during a type “A” January day

Analysis of the day type “B”: It could be noticed that all locations present night urban heat island effect, with intensities between 2.2 and 3.5 degrees Celsius. During the day, in many locations the UHI effect is present but with little intensity (0.2-0.6 degrees Celsius).

	6.00		12.00		18.00		24.00	
	T (°C)	UHI (°C)						
Location 1	27.0	2.8	29.0	0.2	30.0	2.0	28.7	3.5
Location 2	27.0	2.8	28.2	-0.6	29.7	1.7	28.0	2.8
Location 3	27.0	2.8	29.0	0.2	30.0	2.0	28.2	3.0
Location 4	27.0	2.8	29.0	0.2	30.0	2.0	28.2	3.0
Location 5	26.2	2.0	29.1	0.3	31.0	3.0	27.8	2.6
Location 6	26.2	2.0	28.2	-0.6	29.5	1.5	27.4	2.2
Location 7	26.5	2.3	28.2	-0.6	29.7	1.7	27.4	2.2
Location 8	27.0	2.8	29.0	0.2	30.0	2.0	28.2	3.0

Table 6: Temperature and UHI intensities for 8 locations during a type “B” January day

The most influencing factor on the resulting UHI seems to be the vegetation cover that indicates that locations two, seven and eight have the lowest intensities during the entire 24-hour cycle. Albedo and emissivity properties of materials play also an important role. Densities and height of buildings are responsible of the result obtained by location 1, in the city center. Location 6, where the tallest buildings locate, mitigate the effect with the different soil and the presence of grass.

4 Conclusions and future work

The paper explored the issue of the urban heat island effect in the city of Guayaquil. By using GIS techniques, 8 sectors of the city were parametrized to be inserted in a UWG simulation. Simulation results show that Guayaquil presents a UHI effect of 3-4 degrees Celsius during the afternoons and nights. At noon, some sector could have higher

temperatures than others, but in general, there are only little differences in the obtained UHI across the city. However, this fact should be corroborated by using monitoring techniques. Future work is needed to estimate in an appropriate manner the UHI intensity in Guayaquil, by using remote sensing or (better) by direct monitoring of temperature in the streets.

Considering global warming, IPCC predicted an increase of up to 6 degrees Celsius for the end of the century in the Amazon Region [IPCC 2014]. This means, a possible increase in up to 10 degrees both considering global warming and urban heat island effect in many city sectors. Temperature could rise up to 45 degrees Celsius, which represents an incredible increase in the air conditioning needs or an unacceptable increase in the population exposed to risks related to heat waves.

Future work should also consider the simulation of the thermal demand of different kind of buildings and the suggestion of mitigation strategies appropriated to the local climate and culture. Ecuador is developing at this time a new construction standard (NEC). It is important that the new regulation consider the heat evacuation, both at building and district level. However, the first stage took in to account only canonic parameters of typical European regulations: thermal transmittance of walls, roofs and windows, infiltration values, etc. Natural ventilation and solar protection are not considered as the most important strategies in managing the efficiency of buildings in the country.

References

- [Akbari 2008] Hashem Akbari, Ronnen Levinson, Stephanie Stern, *Procedure for measuring the solar reflectance of flat or curved roofing assemblies*, Solar Energy 82 (7), p. 648-655
- [ASTM 2012] American Society Testing Materials, *ASTM E903 Standard Test Method for Solar Absortance, Reflectance, and Transmittance of Materials Using Integrating Spheres*
- [Bueno 2010] Bruno Bueno, *An urban weather generator coupling a building simulation program with an urban canopy model*. Msc. Thesis. Available on-line: <http://hdl.handle.net/1721.1/59107>
- [Bueno 2012a] Bruno Bueno, *Study and prediction of the energy interactions between buildings and the urban climate*. PhD Thesis. Available on-line: <http://hdl.handle.net/1721.1/77774>
- [Bueno 2012b] Bruno Bueno, Leslie Norford, Julia Hidalgo, Gregoire Pigeon, *The Urban Weather Generator*. Journal of Building Performance Simulation 6 (4), p. 269-281
- [Kolokotroni 2012] Maria Kolokotroni, Zhibin Ren, Michael Davies, Anna Mavrogianni, *London's urban heat island: Impact on current and future energy consumption in office buildings*. Energy and Buildings 47, p. 302-311
- [IPCC 2014] Intergovernmental Panel for Climate Change, *Fifth Assessment Report: Impacts, Adaptation and Vulnerability. Cap. 27, Regional Scenarios*.
- [INEC 2016] National Institute of Statistic and Censur. Available on line (accessed on 7 April 2016): <http://www.ecuadorencifras.gob.ec>
- [Nakano 2015] Aiko Nakano, Bruno Bueno, Leslie Norford, Christoph F. Reinhart, *Urban Weather Generator User Interface Development: New Workflow for Integrating Urban*

Heat Island Effect in Urban Design Process. Proceedings of the 9th International Conference on Urban Climate, 4 June 2015.

[Interagua 2015] INTERAGUA C. LTDA., «Ajuste y Revisión del Plan Maestro de Agua Potable; Alcantarillado Sanitario y Alcantarillado Pluvial Tomos I y II». 23-jun-2015.

[Moncayo 2015] C. A. S. Moncayo, *Guayaquil, ciudad de soportales: una reflexión acerca de su importancia y su uso actual*. PASOS Rev. Tur. Patrim. Cult. 13 (3), p. 681-696

[Sailor 2014] David J. Sailor, *Risks of summertime extreme thermal conditions in buildings as a result of climate change and exacerbation of urban heat islands*. Building and Environment, 78, p. 81-88.

[Santamouris 2015] Matheos Santamouris, Constantinos Cartalis, Afroditi Synnefa, Denia Kolokotsa, *On the impact of urban heat island and global warming on the power demand and electricity consumption of buildings – a review*. Energy and Buildings 98, p. 119-124

[Santamouris 2001] Matheos Santamouris (Ed.), *Energy and Climate in the Urban Built Environment*. James and James, London.

[Santamouris 2006] Matheos Santamouris (Ed.), *Environmental Design of Urban Buildings*. Earthscan, London.

Daylighting: an approach from urban to room scale

Bernard A. Paule¹ and Jérôme H. Kaempf²

¹ Estia SA
EPFL-Innovation Park, CH-1015, Lausanne, Switzerland
e-mail: paule@estia.ch

² kaemco LCC
La Riaz 6, CH-1426 Corcelles-Concise, Switzerland
jk@kaemco.ch

Keywords: Daylighting, Urban scale versus Room scale approaches.

Abstract. *This paper aims to compare the daylighting results provided by two specific software tools dedicated to the preliminary design stage. The first one, DIAL+, focuses on the room scale while the second one, CitySim, aims to provide a decision support at the urban scale. On one side we have a bottom-up approach, which matches the point of view of architects or building designers and, on the other hand, a "top-down" approach that fulfil the needs of urban planners and energy stakeholders. The case study focuses on a small open-space office that we looked at from three different positions in a given building located in the neighborhood "Barrio de las Nieves" in the city of Bogota. The output of both tools are analysed on a annual basis, through the comparison of the number of hours during which the indoor illuminance exceeds 300 lux for two specific points respectively located at 1.50 and 4.50 m from the glazed façade. This work shows that, if the two approaches yield similar results for the first point (close to the façade), however, for the second point (back of the room) the results are significantly divergent. This leads us to believe that both approaches are useful in assessing the daylight constibution for workplaces located in the "first rank", but, for deeper locations, where the internal reflected component is dominating, a detailed analysis should be preferred.*

1 Introduction

In the current context of cities' densification, the analysis of the daylighting potential at the urban scale is not always an easy issue to address. However, recent works on the beneficial effects of light on the health of occupants showed that it is important to propose concrete methods of approach, so as to incorporate this issue in the early design stages. This paper proposes to compare two possible resolution methods. The first one deals with a rather detailed analysis of the internal space, but incorporating a coarse description of the external environment. It is based on the use of DIAL+¹ software [Paule 2011]. The second approach is based on a detailed analysis of flows on the urban level and offers a simplified analysis of daylight availability in the interior spaces. This approach is based on the use of CitySim² software [Robinson 2011]. This study compares the results of both approaches through the analysis of 3 "typical" offices rooms positioned in one of the existing buildings.

2 Description of the urban context

We chose to perform this comparison in the city of Bogota, in the Barrio de Las Nieves. In this changing neighborhood, the recent construction of large office towers has drastically altered the original urban landscape, made up of small buildings built in the twentieth century. The first step consisted in working on 3D information available for the selected urban area that has been provided by the Universidad Jorge Tadeo Lozano in Bogota³. To be able to use the information for both approaches, we had to convert the original file (stl) into .skp format. We then selected one of the existing buildings which is situated in an intermediate area (see red area on Figure 1). Nearby high buildings are located in the South-East and North-West sectors, and distant but very high towers are located on the West sector.



Figure 1: 3D model of Barrio de las Nieves in Bogota (the selected building is marked in red).

¹ <http://www.dialplus.ch>: last visited 06-23-2016

² <http://citysim.pro> : last visited 06-23-2016

³ Acknowledgement to Prof. Misael Ricardo Franco Medina, Profesor asistente UTADAO-Architectural Program

In order to compare different representative situations, we decided to successively analyze three specific room positions within the selected building (see Figure 2).

- Position A corresponds to a West oriented façade and the reference altitude of the room is 23 m above the outdoor ground (0 ref. = ground floor of the selected building).
- Position B corresponds to the same orientation as previous, but the room is located at 52 m above the ground floor.
- Position C corresponds to a South oriented façade and the room is located at 23 m above the ground floor.

The comparison between A and B is useful to show the influence of the floor altitude within a dense urban context and the comparison between A and C points out the impact of very high buildings on the daylight availability.

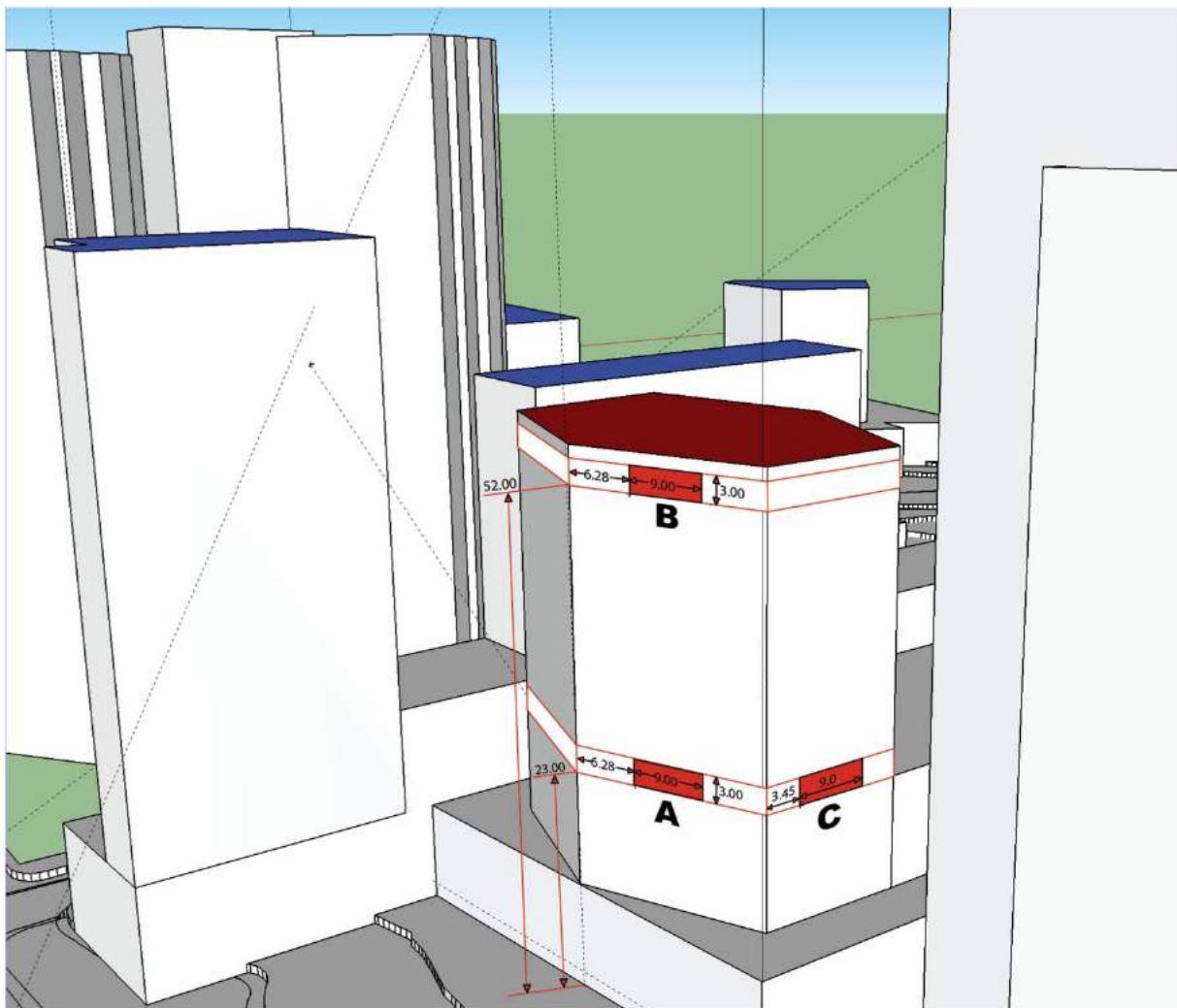


Figure 2: Schematic representation of the selected rooms' positions in the selected building

2.1 Room's parameters

We have then described a reference room to perform the daylighting simulations. This is a small open office (7.80m x 5.20 m) equipped with four windows as shown in Figure 3. The floor area is 54 m² and the glazed area is 14.40 m², which corresponds to a Window to floor

ratio (WFR) of 0.27. In addition to the geometrical parameters, the photometric characteristics of the room are as follows (reflectances, visible and energy transmittances):

- $\rho_{\text{floor}} = 0.30$, $\rho_{\text{walls}} = 0.50$, $\rho_{\text{ceiling}} = 0.70$, $\tau_{\text{glazing}} = 0.70$, $g_{\text{glazing}} = 0.70$

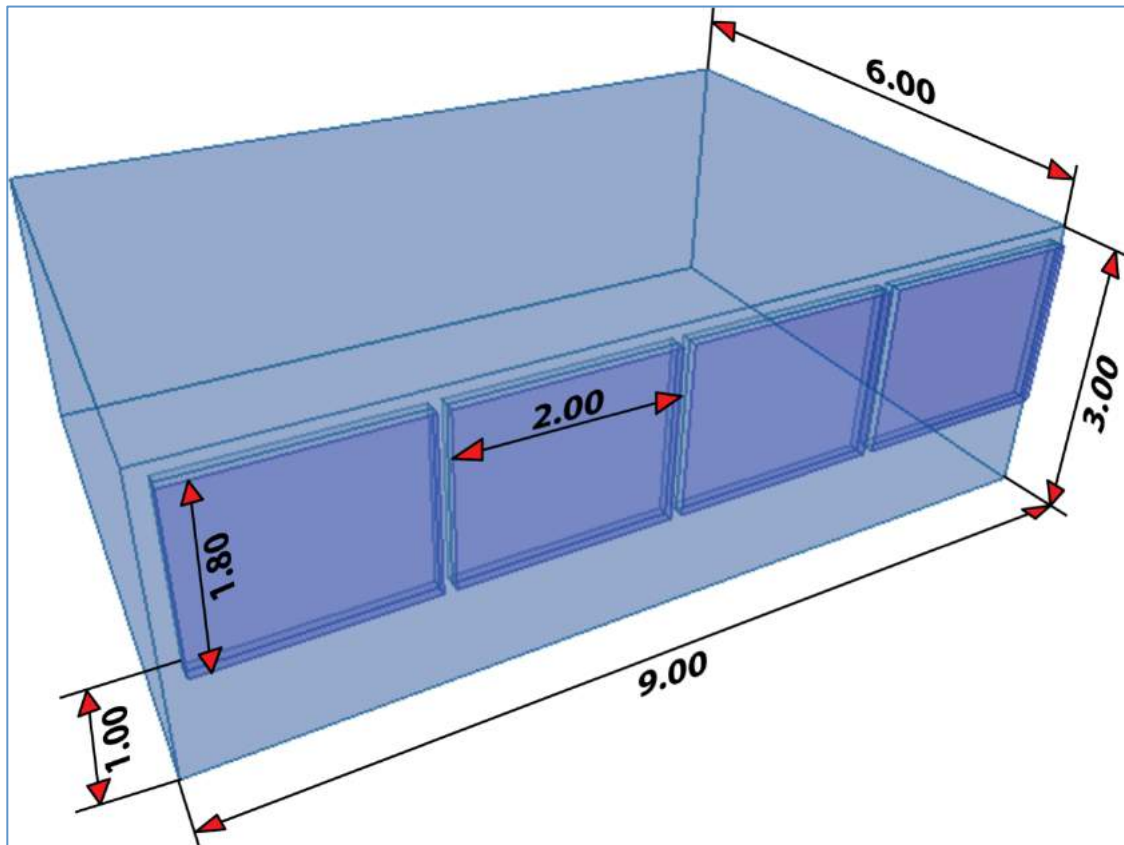


Figure 3: Schematic description of the reference room used for comparison.

2.2 Weather data

The meteorological data used with both methods are strictly the same and have been generated with the software Meteonorm⁴. Concerning the distant horizon, no data was available for Bogota, we have therefore considered that the far-field horizon was 0° in all directions.

2.3 Daylighting appraisal

The methods used by the 2 tools are based on different approaches:

- On one hand, CitySim simulations are based on the hourly calculation of the incident flow on the different surfaces composing the urban scene. The indoor daylight contribution is calculated using a view to the vault provided by the glazing from two reference points at desk level (0.8 m). The first point is situated at 1.5 m from the glazing and the second point at 4.5 m. In the daylight calculation, the direct component is determined using the luminance of the two times 145 Tregenza patches for both the sky and ground and the luminance of the shading surfaces (which include the inter-reflections in the urban canyons). The internally reflected component is determined using the split-flux method [BRE 1996], assuming that the room reacts

⁴ www.meteonorm.com: last visited 06-23-2016

like an integrating sphere. The reflectance of the ceiling, walls and floor are respectively considered to be 0.7, 0.5 and 0.3. Details about the calculation method can be found in [Robinson 2006].

- On the other hand, DIAL+ performs Radiance simulations⁵ to calculate daylight factor values and uses the diffuse outdoor illuminance (hourly step) to estimate the diffuse daylight autonomy according to the required indoor illuminance [Paule 2008]. It thus does not take into account the direct component.

To overcome the issue of the shading device management, which is quite unpredictable, [Paule 2015], we decided to consider that the windows are equipped with a "theoretical" blind device such as:

- When there is no sun, the blinds are raised.
- When the sun hits the façade, the position of the blinds allows blocking the direct component and the incoming light flux (reflected and diffuse components) is high enough to let the electric lighting off.

2.4 Electric lighting

The electric installation is as follows:

- Downwards luminaires
- Luminaires efficacy: 80%
- Dust factor: 80%
- Lamp type: LEDs
- Power: 40 W
- Luminous efficacy: 100 lm/W
- Number of luminaires: 12 (3 rows of 4 luminaires)
- Global installed power: 8.9 W/m²
- Regulation system: Continuous dimming during the opening hours.

Figure 4 below shows the illuminance distribution due to this installation.

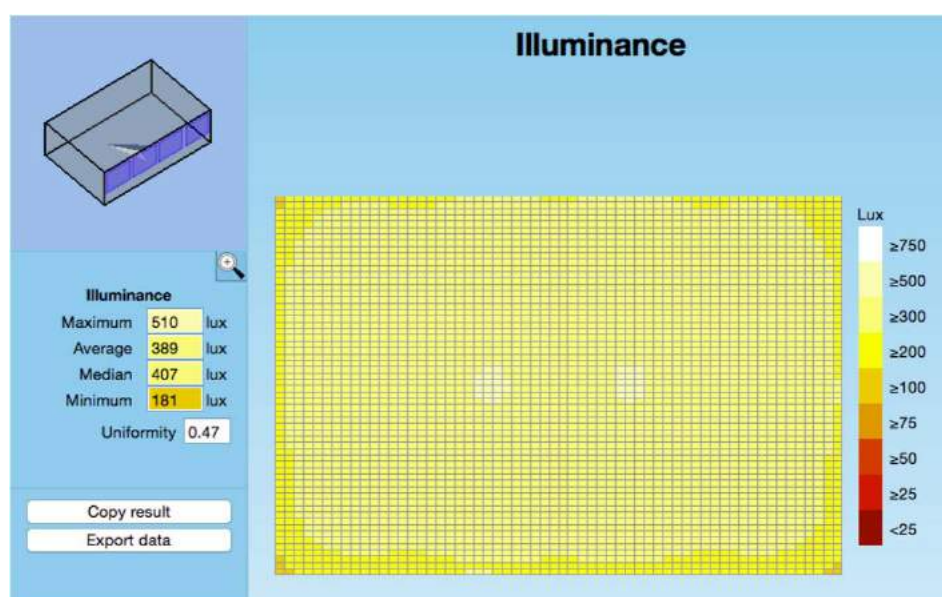


Figure 4: Illuminance value on the work plane due to the electric lighting installation (DIAL+)

⁵ <http://radsite.lbl.gov/radiance/refer/ray.html>: last visited 06-23-2016

2.5 DIAL+ Approach for the description of outdoor environment

The software embeds an intuitive interface allowing the user to quickly specify all the room parameters (geometry, photometry, walls composition and occupation parameters according to the room function).

Regarding the description of the outdoor environment, the process is as follows:

1. Make a screen shot of the studied area (satellite view centred on the selected building),
2. Trace the contour of the surrounding buildings,
3. Enter the height of the surrounding buildings,
4. Locate the centre of the studied room,
5. Enter the altitude of the room (vertical distance from the ground floor).

In this process, the main difficulty lies in the identification of the basis perimeter (ground floor level) of the surrounding buildings. Actually, as the inter-reflection between the different buildings are not considered, the back part of the surrounding buildings has no influence on the daylight simulation, therefore, the precision is only important for the faces that are viewed from the selected rooms (see Figure 5).

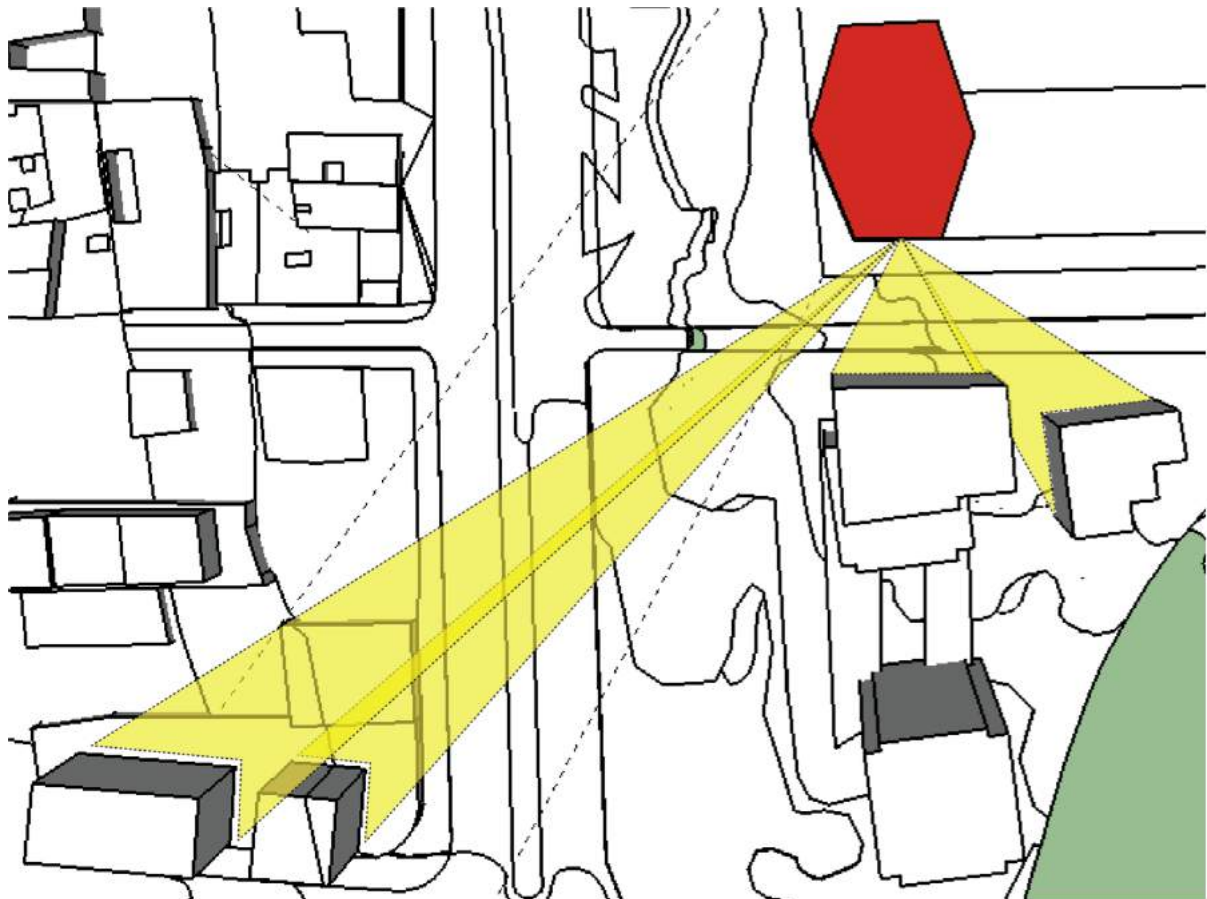


Figure 5: The description of the surrounding buildings should be precise enough only for the faces viewed from the selected room.

Considering that the original file describing the studied area contains a great number of existing buildings, it has been decided to simplify the scene in only keeping the buildings whose maximum height was above 23m (namely the altitude of Room A and C). Figure 6 hereafter shows the corresponding buildings (blue colour). All the lower buildings are considered as part of the outdoor ground and the reflection coefficient has been set to 0.20.

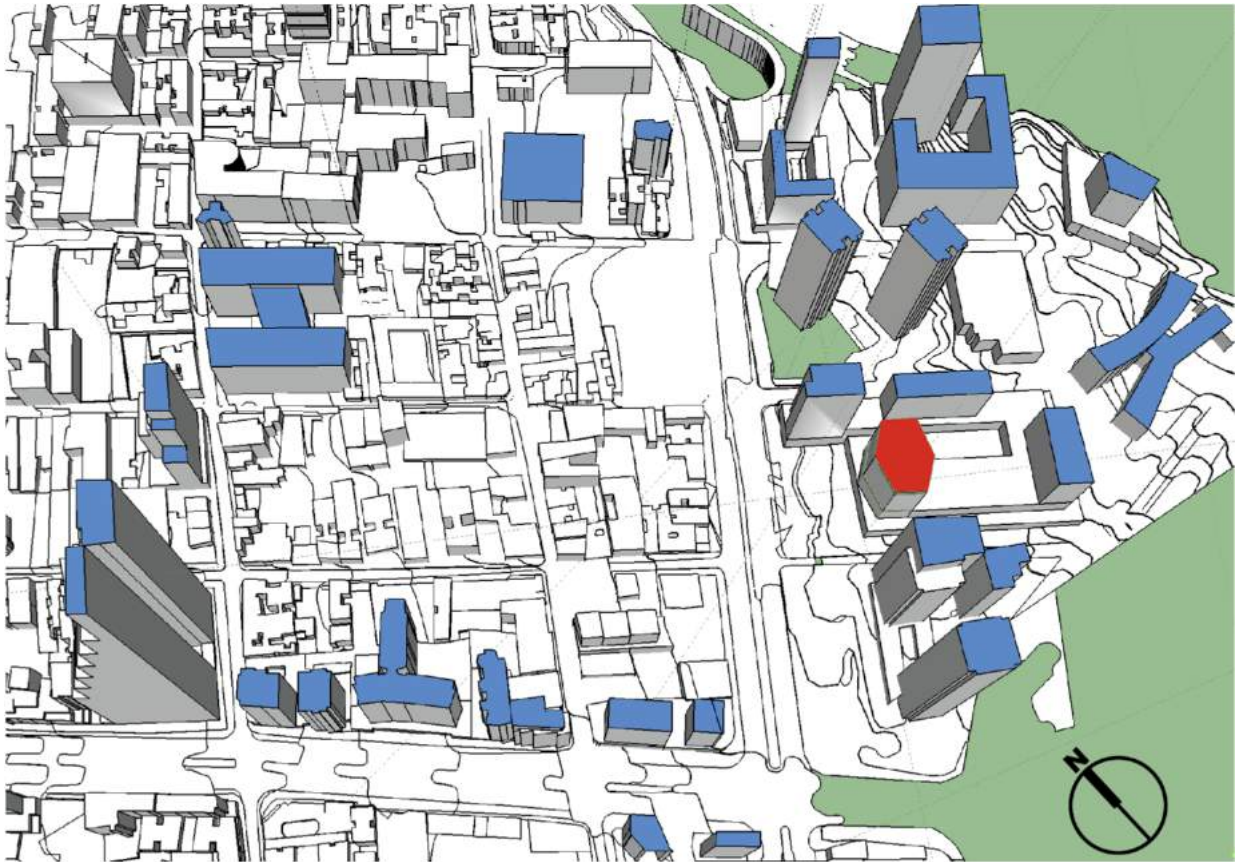


Figure 6: Selection of the surrounding buildings whose altitude is higher than 23m above the reference ground level (blue surfaces).

2.6 CitySim Approach for the description of outdoor environment

The graphical user interface CitySim Pro embeds an import feature of AutoCAD DXF 2000 file format using the 3DFACE primitive. To export the geometrical file from Sketchup, an extension plugin in ruby is provided with CitySim Pro. However, prior to the export, the geometrical file has to be organised in such a way that each building under study lies in a different layer, the ground surfaces in a layer GROUND and the shading surfaces in a layer SHADING. The steps required to produce daylight results from a Sketchup input file is as follows:

1. Simplify the 3D model:
As the simulation time is an increasing function of the number of surfaces for the irradiance and illuminance calculation, limiting the number of surfaces is an essential step to keep a reasonable time frame for the study. Therefore, the initial 3D model was cut to the zone of interest and the grounds (roads, pavements, etc.) were removed from the model.
2. Prepare different layers in the model:
Each building under study must be in a separate layer, and shading buildings must be placed in a layer named SHADING. The resulting scene is then exported to DXF format (using the extension `stp_to_dxf_3DFACE`).
3. Import the DXF file in CitySim Pro:

Use the import feature to import the file in the GUI of CitySim. In our case, only one building is considered in our daylighting study (coloured in yellow and red in Figure 8).

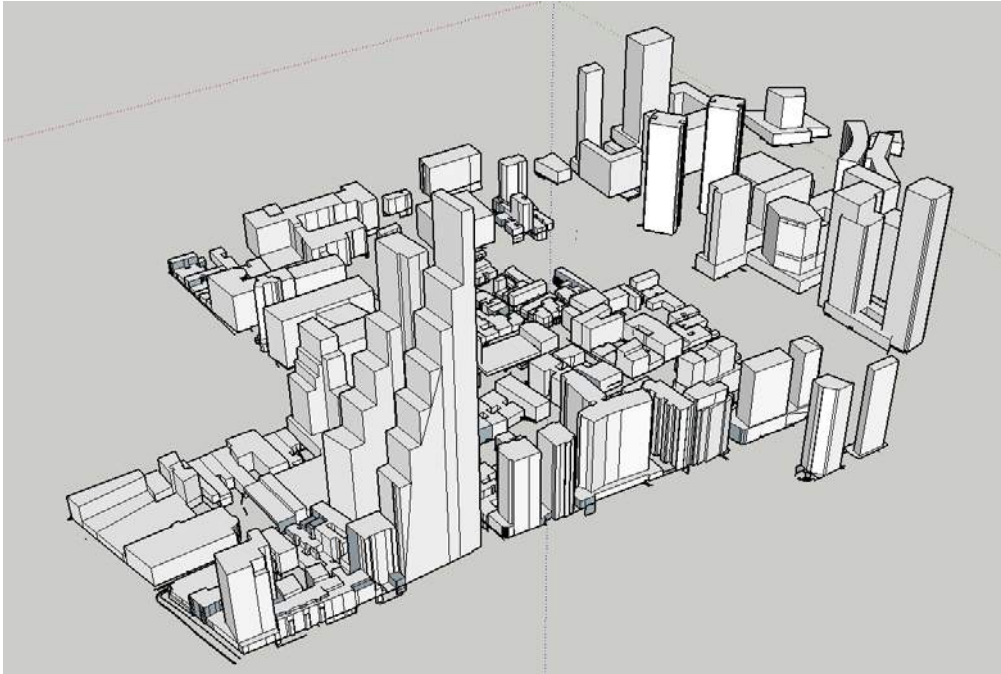


Figure 7: Simplified model for creating an DXF input file for CitySim

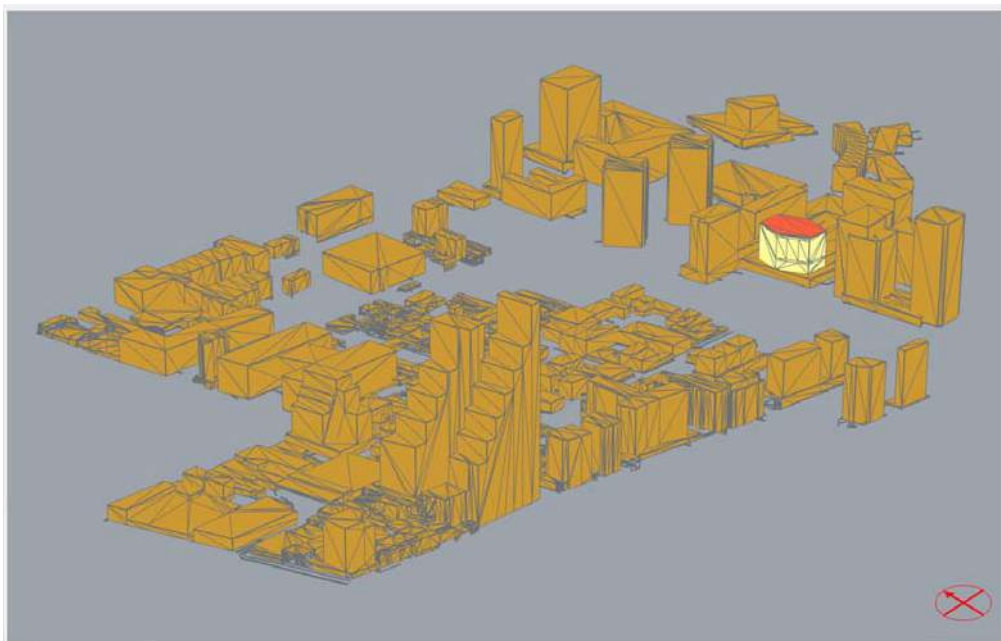


Figure 8: Import of the geometry within CitySim Pro, shading buildings in orange and building under study in yellow and red.

4. Run the simulation:
Save the CitySim XML file and edit the physical characteristics of the surfaces. In our case we consider a shortwave reflectance of 0.2 for all surrounding surfaces and for the ground. Edit the properties of the surfaces of the room under study with providing:

g-value of 0.7 and glazing ratio of 0.5333. After what the simulation is run using the CitySim Solver together with the climate file from Meteonorm.

5. Analyse the results:

The results for daylight are provided in the `_DL.out` file for each surface of the building. The file comprises desk illuminance (0.8 m) for a point near the window (1.5 m away) and in the back of the room (4.5 m away from the window), together with an additional illuminance due to inter-reflections computed using the split-flux method. By using a simple Excel sheet, Daylight Autonomy (continuous or not) can be calculated and the corresponding electric consumption for lighting determined using the installed power for each hour of the year.

In this process, the main difficulty lies in the preparation of the 3D model. The manual work of removing (useless) surfaces and adding buildings in layers is more time consuming than the simulation process itself.

3 Results and discussion

3.1 Outdoor masks

3.1.1. DIAL+

As DIAL+ is dedicated to room-scale analysis, the outdoor environment is represented as viewed from the windows. Figure 9 hereafter shows the respective stereographic projections of the urban landscape viewed from the different rooms. Rooms A and B are facing West and thus are hit by the sun during all the afternoon. The surrounding buildings located in that direction area are quite far and, therefore, the frontal horizon is almost clear. The only high masks are due to buildings located on the North and South. The variation of altitude between Room A and B is expressed by the different angle height of the outdoor buildings on the projection. Room C is South-West oriented and is facing a huge building right in front of it.

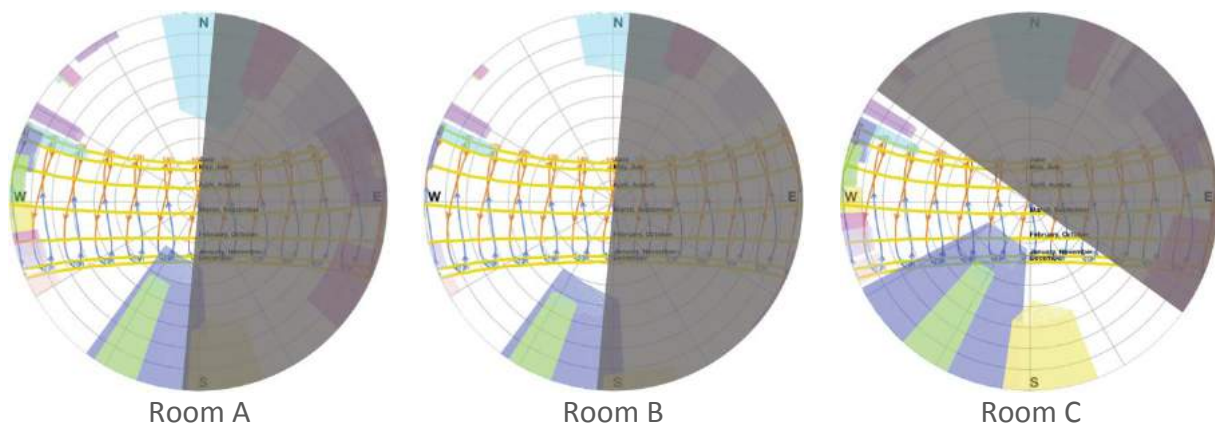


Figure 9: Schematic representation of the outdoor masks respectively viewed from the different rooms.

3.1.2. CitySim

In order to compute the masks due to the surrounding buildings, CitySim considers the view to the outside world through a fully-glazed façade above 0.8 m from two points inside the room. The resulting two masks for each point are superimposed with the luminance distribution of the sky, ground and surrounding façades of other buildings.

3.2 Daylighting contribution

3.2.1. DIAL+Lighting

Figure 10, Figure 11 and Figure 12 displays the results obtained with the lighting module of DIAL+. The comparison between Rooms A and B shows that the daylight availability is identical for the point located at 1.50 m from the façade. Regarding the indoor point (4.50 m from the façade), the difference is still limited. Regarding Room C, the presence of the very high building located right in front of the façade leads to a significant reduction of the daylight availability, particularly in the back part of the room (dist. from façade = 4.50 m). In comparison with Room A, the covering of lighting needs in Room C is divided by 2.5 (29.5% vs. 73.5% of the opening hours).

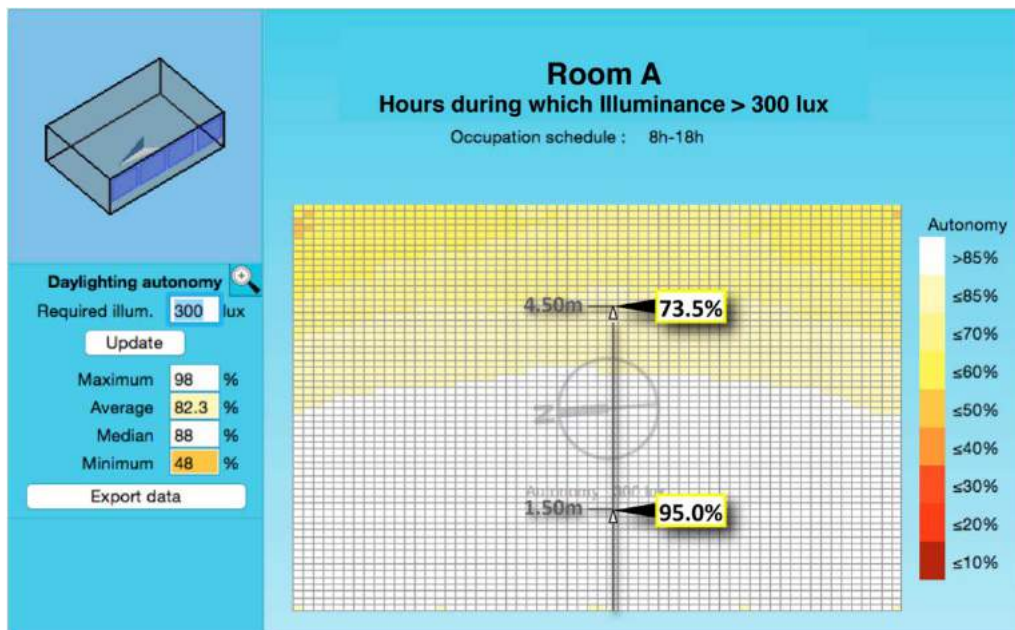


Figure 10: Percentage of time during which the indoor illuminance exceeds 300 lux in room A (8AM-6PM).

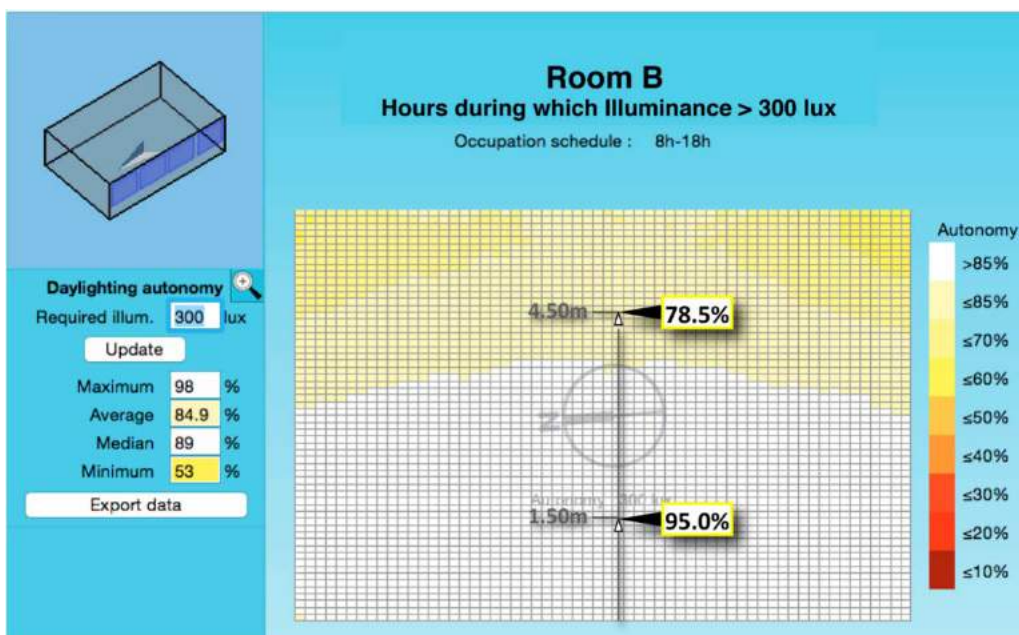


Figure 11: Percentage of time during which the indoor illuminance exceeds 300 lux in room B (8AM-6PM).

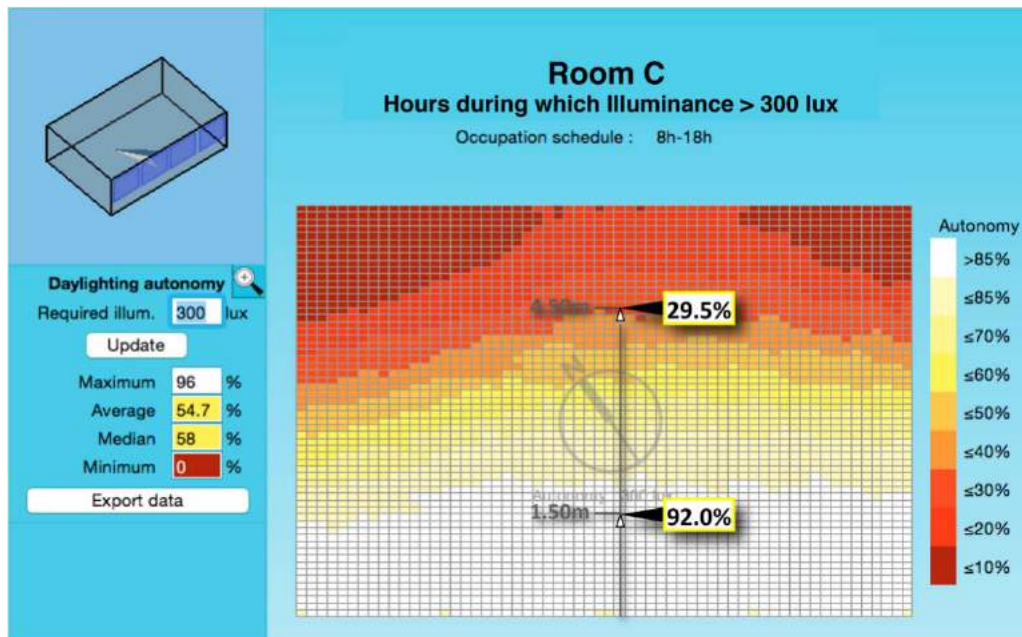


Figure 12: Percentage of time during which the indoor illuminance exceeds 300 lux in room C (8AM-6PM).

3.2.2. CitySim

The daylight contribution for the two reference points in each room is calculated using the sky, ground and surrounding surfaces' luminance. In order to go from the usual radiance calculation (see Figure 13) to the luminance one, the luminous efficacy of the sky from the Perez All-Weather model is considered. Finally, the Simplified Radiosity Algorithm computes the inter-reflections in the urban canyons. When looking at Figure 13, we notice not surprisingly that the horizontal surfaces (roofs) are those that receive the greatest amount of radiation (red color). Figure 14 illustrates that the flux received by room C is significantly reduced by the presence of the surrounding building.

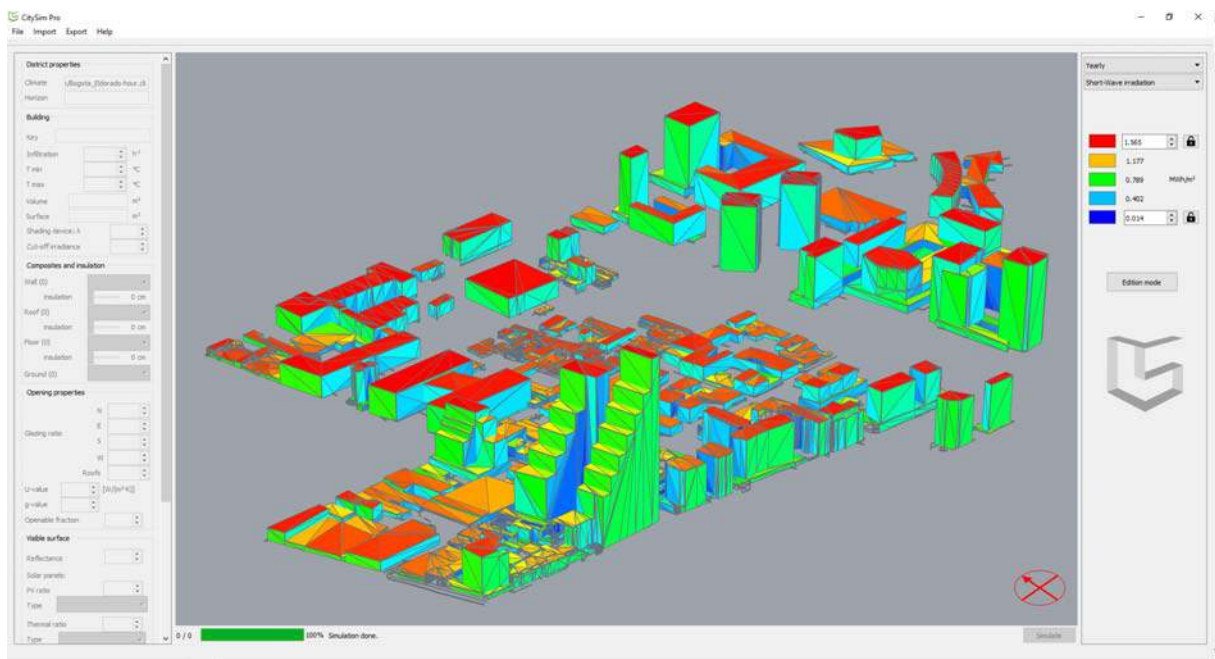


Figure 13: Representation of the annual incident flux on all the surfaces that compose the urban scene (CitySim).

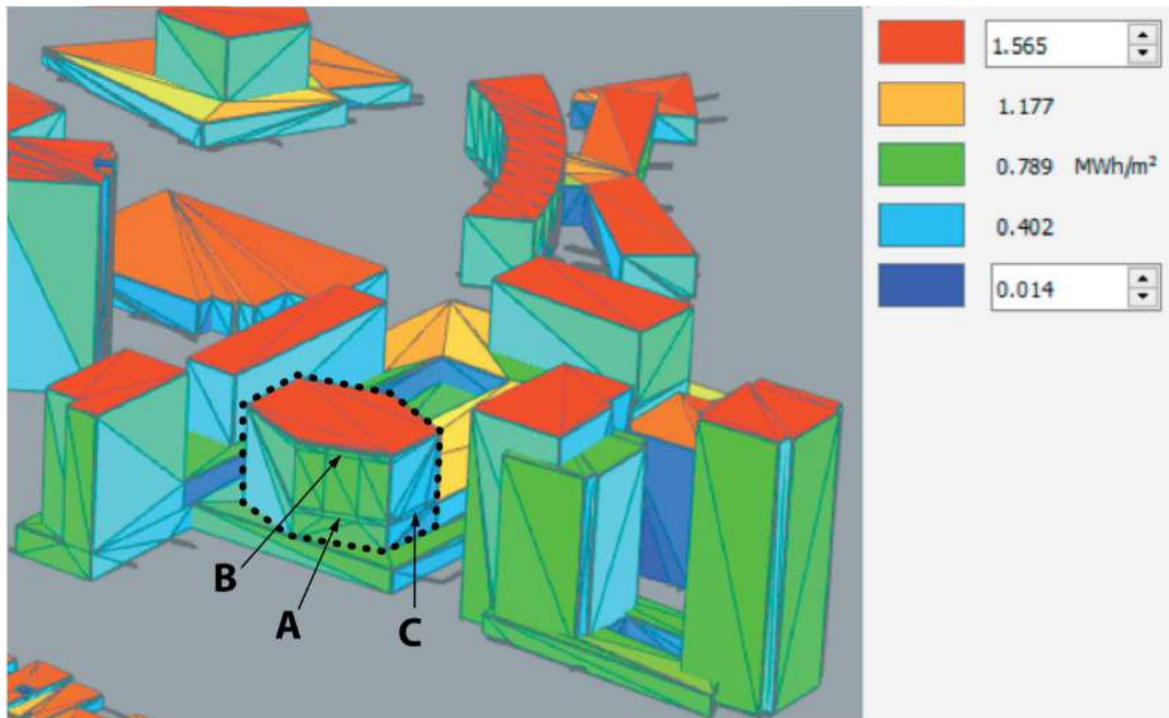


Figure 14: Zoom view on the annual incident flux on the selected building.

3.3 Analysis of the results

3.3.1. Daylight autonomy WITHOUT outdoor masks

Table 1 and Table 2 allow comparing the results obtained with the two methods without outdoor masks. For the point located close to the façade (1.50m) the results are almost identical. For the second point (4.50m from the façade), the difference between the two methods is still limited. It may be noted that without outdoor mask, the daylight contribution of the back part of the room remains significant.

Daylight Autonomy [%]		
Distance from façade = 1.5m	DIAL+	CitySim
Room A	95.0	95.5
Room B	95.0	95.5
Room C	95.0	95.5

Table 1: Comparison of the results for the point located at 1.50 m from the façade WITHOUT outdoor masks. (Annual average percentage of time (8AM-8PM) during which the indoor illuminance exceeds 300 lux)

Daylight Autonomy [%]		
Distance from façade = 4.5m	DIAL+	CitySim
Room A	82.0	93.0
Room B	82.0	93.0
Room C	80.5	92.4

Table 2: Comparison of the results for the point located at 4.50m from the façade WITHOUT outdoor masks (Annual average percentage of time (8AM-8PM) during which the indoor illuminance exceeds 300 lux)

3.3.2. Continuous daylight autonomy WITH outdoor masks

Table 3 and Table 4 allow comparing the results obtained with the two methods with outdoor masks. Here again, for the point located close to the façade (1.50 m) the results are almost identical. However, for the second point (4.50 m from the façade), there is a significant difference between the results obtained with the two methods. This is particularly noticeable for Room C (cf. Table 4).

Daylight Autonomy [%]		
Distance from façade = 1.5m	DIAL+	CitySim
Room A	95.0	95.4
Room B	95.0	95.4
Room C	92.0	93.4

Table 3: Comparison of the results for the point located at 1.50m from the façade WITH outdoor masks (Annual average percentage of time (8AM-8PM) during which the indoor illuminance exceeds 300 lux)

Daylight Autonomy [%]		
Distance from façade = 4.5m	DIAL+	CitySim
Room A	73.5	92.6
Room B	78.5	92.8
Room C	29.5	80.7

Table 4: Comparison of the results for the point located at 4.50m from the façade WITH outdoor masks (Annual average percentage of time (8AM-8PM) during which the indoor illuminance exceeds 300 lux)

3.3.3. Electric lighting consumption

In this section we compare the results obtained with the two methods regarding the annual lighting electricity consumption. In both cases, we made a hourly based analysis assuming that, at each time step, the specific power is linked to the daylighting autonomy and the dimming system (cf. §2.4) just gives the required amount of light in order to reach 300 lux on the work plane. For DIAL+, the mean value of daylight autonomy is used to control the whole room. For CitySim, the room is divided in two zones and the luminaires are controlled according to the values at 1.50 and 4.50 m from the façade.

Table 5 shows that without outdoor masks, the results obtained with the two methods are within the same range. On the other hand, when taking into account the outdoor masks, the gap becomes more important (cf. Table 6). For Room C, which is seriously impacted by surrounding buildings, the ratio between DIAL+ and CitySim is above 2.36.

Annual lighting electricity consumption [kWh/m ²]		
WITHOUT Masks	DIAL+	CitySim
Room A	1.5	1.1
Room B	1.5	1.1
Room C	1.5	1.2

Table 5: Annual lighting electricity consumption WITHOUT outdoor masks (8AM-8PM).

Annual lighting electricity consumption [kWh/m ²]		
WITH Masks	DIAL+	CitySim
Room A	1.9	1.2
Room B	1.7	1.1
Room C	5.2	2.2

Table 6: Annual lighting electricity consumption WITH outdoor masks (8AM-8PM).

3.3.4. Influence of the reflected component

As shown before, the main divergence between the two methods is observed for Room C and the gap is particularly high at the back part of the room (point located at 4.50 m from the façade). This suggests that the problem lies in the calculation of the internal reflected component (IRC), which is dominating in these cases. Actually, in CitySim, the calculation of this component is based on a split-flux method [BRE 1996] and the result is a fixed value assigned to all points of the room. The initial version of DIAL software (DIAL-Europe [de Groot 2003]), which was based on the same calculation technique was facing the same problem and tended to overestimate the results.

In order to test this hypothesis, we relaunched the simulations by setting to 0 the values of the indoor reflectance (floor, walls and ceiling). Table 7 confirms that if the room is completely black (IRC = 0), the results given by DIAL+ and CitySim are much closer.

Annual lighting electricity consumption [kWh/m ²]		
WITH Masks	DIAL+	CitySim
Room A	4.40	4.98
Room B	3.90	4.91
Room C	9.40	11.3

Table 7: Annual lighting electricity consumption in the case of a “Black-Box” with outdoors masks (8AM-8PM).

4 Conclusions

The paper presents a comparative daylighting study between two pre-design tools: DIAL+ and CitySim. Even if each software is based on different methods and assumptions, the idea is to evaluate the order of magnitude of the results provided. For this, the case-study of three rooms in an office building in Bogotá was chosen. Two rooms at different heights on a feebly obstructed façade, and one room on a highly obstructed façade. The results show that the two approaches yield similar results for the three rooms in a zone close to the façade, however, for a zone at back of the room the results are significantly divergent. This leads us to believe that both approaches can be used indistinctively in assessing the daylight contribution for workplaces located in the “first rank” (near the window), even in dense urban context. For deeper locations (workplaces located in the back part of the room) a detailed appraisal of the daylight should be carried out in order to correctly estimate the internally reflected component. However, to the extent of the presence of large urban masks reducing the direct component of natural lighting in these areas, the successive implementation of the two approaches presented here (top-down "with CitySim and" bottom-up "with DIAL +) allows targeting all the daylighting issues in the early stage design.

In the near future, a link between DIAL+ and CitySim could be envisaged, by exporting the obstructing buildings in RADIANCE format from CitySim and importing in DIAL+ whose rendering engine is RADIANCE. This procedure could automate the process of the masks definition.

References

- [BRE 1996] British Research Establishment, *Estimating daylight in buildings : Part 1 - 2 Digest 309, 310*, Building Research Station, Garston, Watford, Hertfordshire WD2 7 JR, England, 1996.
- [de Groot 2003] Ellie de Groot, Laurens Zooneveldt, Bernard Paule, *DIAL-Europe: a decision support tool for early design stage*, Eighth International IBPSA Conference, Eindhoven, Netherlands, August 11-14, 2003.
- [Paule 2008] Bernard Paule, François Bouvier, Gilles Courret, *Eclairage naturel*, Techniques de l'Ingénieur, CC 3315, Fév. 2008.
- [Paule 2011] Bernard Paule, Flourentzos Flourentzou, Samuel Pantet, Julien Boutillier, *DIAL+ Suite a complete, but simple, suite of tools to optimize the global performance of building openings*. Proceedings of the CISBAT'11 Conference, September 2011, Lausanne, Switzerland.
- [Paule 2015] Bernard Paule, Julien Boutillier, Samuel Pantet, *Shading device control: Effective impact on daylight contribution*, Proceedings of the Cisbat'15 Conference, September 2015, Lausanne, Switzerland.
- [Robinson 2006] Darren Robinson, Andrew Stone, *Internal illumination prediction based on a simplified radiosity algorithm*, Solar Energy 80 (2006) pp. 260-267.
- [Robinson 2011] Darren Robinson (Ed.). *Computer Modelling for Sustainable Urban Design*. Earthscan, London, Washington, DC, 978-1-84407-679-6, 2011.

Heat stress in urban area: data fusion of observations, modeling and geospatial information

L. Pinson¹ and V. Masson²

¹ IFSTTAR
Cité Descartes - Marne la vallée
laura.pinson@ifsttar.fr

² Météo-France
Avenue Gaspard Coriolis - Toulouse
valery.masson@meteo.fr

Keywords: Urban Heat Island, Heat wave, Representation, Indoor climate, model

Abstract. *Cities have a direct impact on the local climate. The heating of surfaces and materials in urban area and the production of heat by traffic and human activity contribute to the Urban Heat Island (UHI) effect. This local climate will be even more dangerous with climate change. Climate projections for the world suggest elevated minimum and maximum temperatures and more frequent day with higher temperatures (heat wave). Hence, climate change is threatening human well being and health. Today, more than 50% of the world population lives in urban areas and humans spend more than 80% of their time in confined spaces. This can be affected negatively by indoors temperatures. Indoor temperatures are of special importance for well-being and health in general.*

Quantitative information about outdoor thermal comfort, on various temporal and spatial scales, is required to design better cities and mitigate heat problems not only for warm as well as temperate climates. The overall objective of this study is to explore the relation between indoor and outdoor temperature by urban features such as geometry (type of urban structure), housing areas, building arrangements and several other factors.

We use the SURFEX model (that is implemented in several weather prediction models and can also be used alone) to estimate urban temperatures (in street canyons and inside buildings). Therefore, two questions arise: how to represent the outputs of the SURFEX model both spatially and temporally? This work is part of a study conducted in summer 2015 which gathered data from air temperature sensors in five apartments. So for our study, the information given by the model is completed by measures to study the influence of building characteristics and situation on temperatures. Furthermore, it highlights the importance of thermal comfort in climate scenarios to describe the combined effects of changes in multiple apartments and to more realistically measure its impact on humans.

1 Introduction

Climate change does not only increase temperatures, it is becoming a regular phenomenon with noticeable maximum length of heat waves. Besides, a significant increase in mortality due to heat stress has been proved by Almeida et al. (2013), Gabriel and Endlicher (2011). Thus, heat stress is a serious risk to human societies. For instance, the summer of 2003 was the hottest seen in Europe for 53 years causing 14802 deaths in France (In VS, 2003; World Health Organization Europe, 2003). In urban areas, heat waves are connected to the Urban Heat Island (UHI). This effect can be beneficial in winter, by reducing domestic heating needs; however, it becomes critical for thermal comfort (indoors and outdoors) in summer.

The influence of outdoor climate on indoor climate, especially during heat stress events, has been well investigated [Nguyen et al, 2014; Quinn et al, 2014]. Indoor is mainly influenced by outdoor but its diurnal evolution is inhibited by the physical characteristics of the building (Höppe 1993). Even though the urban spatial variability is not considered in other studies, [Fenner et al. 2014] found significant spatial and temporal differences outdoors during heat waves in Berlin. It is therefore likely that indoors climate differs within the urban areas of any given city.

2 Meteorological data and model

The purpose of our study is to evaluate the heat wave risk in dense urban areas and produce data which could be used as an information tool for cities in the future. For that purpose, we will make an analysis of the data collected (visualize it and realize processing GIS to cross data in the notion of dangerousness). All results will be included into the geographical space. From the meteorological model mesh, we will create several mappings to improve the representation of the heat waves with the aim of estimating exposed areas and to classify their level of dangerousness. An index of dangerousness is calculated from sufficient duration and threshold (night/day and outdoor/indoor), and is computed to this mesh via a compute-dangerousness method. In this section we present the meteorological data we have used to estimate heat wave and series of measures made in specific flats during the heat waves in Paris.

2.1 SURFEX model

In our study, the surface is modeled by the SURFEX model (SURFEX (SURFace EXternalise)), as the first meteorological data. Its goal is to compute the exchanges of momentum, heat, water, CO₂ concentration or chemical species. These exchanges are performed by mean of fluxes. SURFEX has been developed for the representation of surface processes in numerical weather prediction models. So it is designed as a modular scheme that can incorporate various parametrization (via name list options). Each of the following surface is modeled with a specific surface model:

- Nature (natural land surface) with the ISBA model [Noilhan and Planton 1989]
- Towns (built areas) with the TEB model [Masson 2000]
- Lakes treated either with the KLAKE model [Mironov 2010]
- Sea treated with the SEAFUX model [Gaspar and al.1990]

The coverage of each of these surfaces is known through the global ECOCLIMAP database [Masson et al 2003], which combines land cover maps and satellite information. The Surfex fluxes are the average of the fluxes computed over nature, town, sea/ocean or lake, weighted by their respective fraction. These four surface types may occur simultaneously in the same grid with different percentages. SURFEX uses atmospheric forcing to estimate temperature, humidity, wind speed, etc., through the Meso-NH model.

Moreover, thermal comfort (or thermal stress) for inhabitants is calculated during the indoor and outdoor universal thermal climate index (UTCI) implemented in TEB model and depending on air temperature, air humidity, wind and radiation. The assessment scale for the UTCI has been established and categories of heat stress responding the terms from the Glossary of Terms for Thermal Physiology (2003). According to Bröde et al [Bröde et al. 2012] values, ranging from 282.15K to 299.15K, represent conditions with *no thermal stress*, values between 299.15K and 305.15K suggest *moderate heat stress* and values between 305.15K and 311.15K indicate *strong heat stress*. In this project, the thermal comfort is integrated to represent a threshold of discomfort or heat stress.

2.2 Measured data and measurement site

In order to study the variation of temperature inside cities, we installed sensors in specific apartments in Paris during the summer of 2014 and 2015. In this instance, we used measurements from 2015 which was the hottest summer. The aim was to complete the prediction given by SURFEX on indoor temperatures. To assess the variability of indoors heat stress, measurements were executed in five different buildings, with 21 sensors localized in the centre of Paris. The meteorological data comes from the Tynitag sensors (Figure 1). We collected the data using the Tynitag software. The measurement started in 29 June 2015, at 12 am and lasted 34 days.

The The research focuses on the heat stress characterization. Only data from July were evaluated. Indoor temperatures in residential buildings have recently been studied by [Bokenes 2009] and [Kavgic et al 2012]. From this research and studies, we obtained a detailed and deeper knowledge of indoors temperature and its variations. For our experiments, apartments were chosen according to their variability to a priori knowledge on apartments' characteristics on temperature [Bokenes 2009 ; Yohanis 2010] : number of exposition, floor level, ventilation, isolation and sun exposition. These apartments characterize the A variable defined in section 2.2. The number of apartments is limited but our aims is to study the temperature variation between these main building types during a hot summer.

Basic calculations were made (besides graphics) on the data to qualify and quantify the temperature variations and to optimize the mapping. With these statistics, we created 5 types of apartment:

- Apart 1: Old building¹ <1850, one exposition only, ground floor, very poorly ventilated, no sun and isolated
- Apart 2: Haussmann² type building, well isolated and ventilated, 6th floor, N/S orientation

¹ Old building usually have 4/6 floors, in canyon street with a simple architecture, rectangular windows

- Apart 3: Old building <1850, well isolated and well ventilated, sunny and a N/S orientation
- Apart 4: Old building <1850, very well isolated, very poorly ventilated, 3th floor with a North orientation
- Apart 5: Old building <1850, isolated and poorly ventilated, under roof, N/S orientation

The measurements were carried out in various locations in figure 1 the same district in Paris. Measurements were performed, with sensor in several rooms with different exposure (to see the variability if any) and outside when possible to allow comparison with SURFEX model outputs in streets.

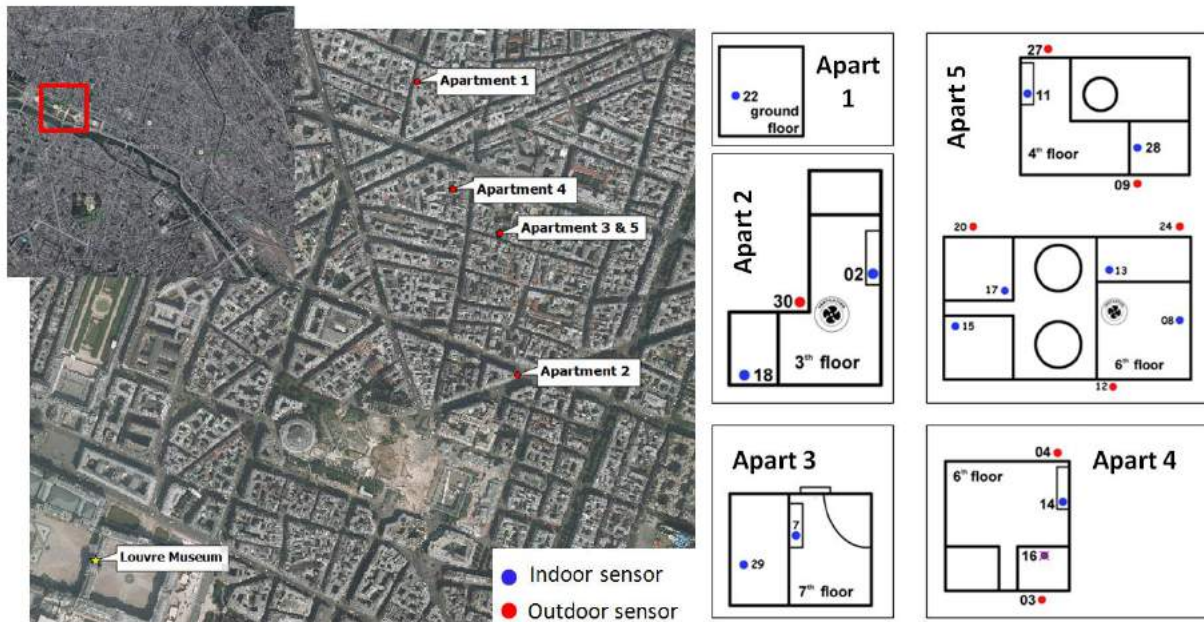


Figure1: Localization and apartments type and sensors for temperature measurements

3 Methodology

3.1 Recontextualization of output's SURFEX

The recontextualization (assignment of estimations in space) of the resulting data is important for a better understanding of the information provided and to visualize several data at the same time. To be able to contextualize this information, we have structured it under a DBMS (DataBase Management System). Every grid cell is described by a set of meteorological indications (stemming from SURFEX) amongst which some represent the temperature in the street 2 metres from the ground, temperature in buildings and on roofs.

There are more than about fifty parameters or indications. The creation of a geo-referenced grid allowed us to allocate to every grid cell of the grid, the value of the punctual datum stemming from SURFEX. For the SURFEX's outputs, we propose to represent the

² Haussmann style building usually have from 5/7 floors, along the wide boulevards, with facades built out of cut stones, possess a continuous balcony on the second and fifth floor and the mansard roof are with roof hatches

temperature in a continuous plan, like apartments. To do so, each point is transformed into a mesh of the same size as the grid cell.

We then allocated the geographical objects (of Topographic data) the values corresponding to this grid. If an object (a building) is located in the intersection of two meshes, we allocate it. We then weighed the average by the surface of the value of both meshes (Figure 2).

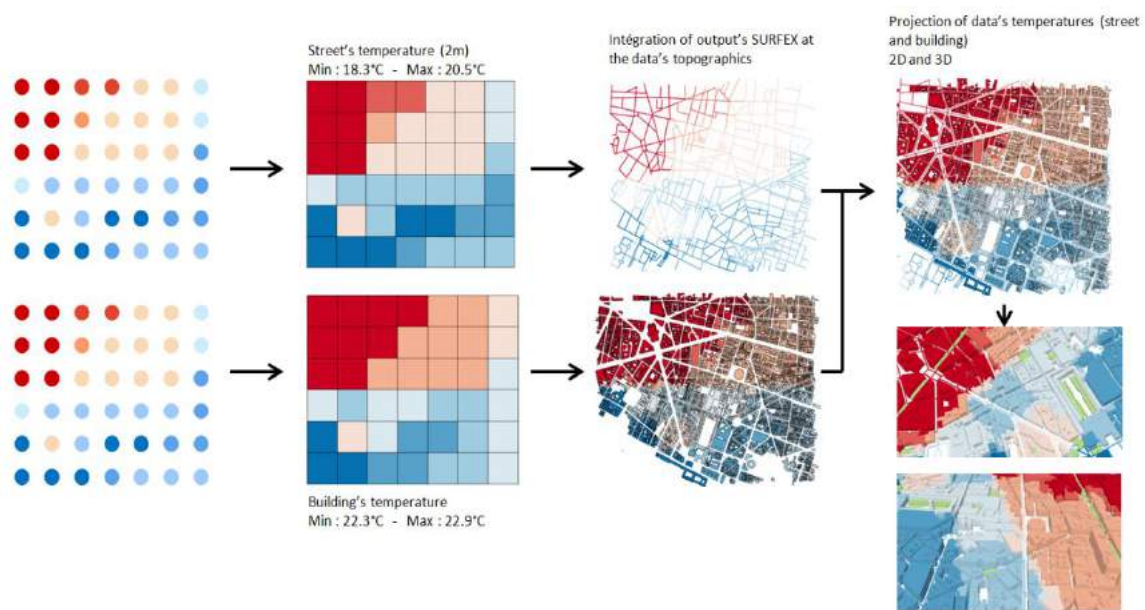


Figure 2: Recontextualisation of output's SURFEX

3.2 Integration of punctual observations

In our study, it is necessary to include sensor measurements and predictive model outputs in the same grid. For the measurements series in Paris, we created 6 categories of apartments by considering various characteristics such as the floor or the exposition, etc. This class is computed from SURFEX prediction and sensors in order to adjust the indoor temperature compute from SURFEX according to each buildings' characteristics type (as SURFEX can run for one type of building only, the dominant one). So, one type of building is described by its attributes. The building's description is given in part 1.2. These apartments are characterized by their indoor and outdoor temperatures. To be able to understand the phenomena more clearly, we represented these data in the meshes below (250m*250m) with an extrapolation. We extrapolate the results obtained in one apartment to the whole mesh. We created surfaces based on measured point. So, from a punctual observation, we move to a mesh in a surface representation.

To observe the punctual observation of the *apart-type* in the *SURFEX's3outputs*, it is necessary to compute the temperature by two types of extrapolation. To integrate punctual observations, our approach is to add SURFEX's outputs in the mesh (*self*) with the difference between the punctual observations and temperatures of the apartment type (Figure 3). Thus each mesh contains a set of values (outdoor – indoor temperatures, UTCI index, etc. for the

SURFEX's outputs) An example is given below to calculate the indoor temperature of the mesh ($mesh$) for the Apartment Type (AT):

$$indoorTemp(AT, mesh) = indoorTemp-surfex-Haus(self) + (indoor-temp-obs(AT, m) - indoor-temp-obs(Haus, m))$$

Indoor-temp-obs corresponds to the punctual observation included in the mesh (*self*)

IndoorTemp-surfex-Haus corresponds to SURFEX's outputs included in the mesh (*self*)
m being the neighbors mesh

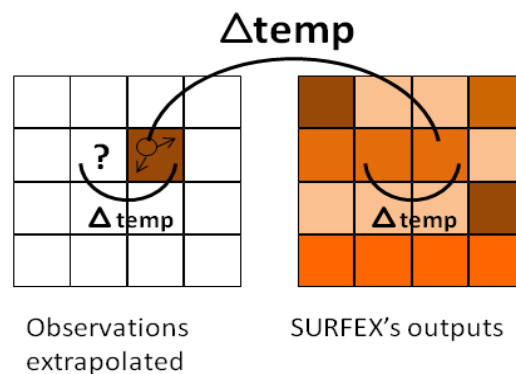


Figure 3: Assimilation's representation

Blending measured data with simulated information is necessary for a better estimation and the mapping of heat wave phenomenon.

4 A more detailed view of the estimation

If the SURFEX's model allows us to calculate temperatures in the streets according to the topography and the surrounding weather conditions, we are completing it with the impact of apartments types on indoor temperature. The output's SURFEX are valid averages in the mesh and a little differentiated. However, we wish to go towards a more accurate estimation. For that purpose, it is necessary to re-interpret the values in light of hypotheses and knowledge. This section aims to map indoors and outdoors temperatures.

4.1 Output's sensors: temperatures spatially differentiated

In order to analyze the huge volume of collected data, we need a well-organized data representation model with a swift data processing which abstracts local data. We used different software. We calculated and represented the thermal behaviour for each sensor.

The first graphs (Figure 4) display the outside temperatures for all sensors; we notice an important homogeneity between temperatures. The thermal amplitude between day and night is present. This amplitude rises in approximately 6K. Even inside the Paris city core, the phenomenon of UHI is visible between different neighbourhoods. The temperatures of the MontSouris Station, located in a park a few kilometers from the city centre, are lower than our sensor's temperatures in the oldest part of Paris centre. Concerning the matrix of outdoor temperature temporal evolution, we notice that the highest temperatures are occurring between 2pm and midnight with a peak of heat at 7pm. The lowest temperatures are concentrated between 3am to 9am.

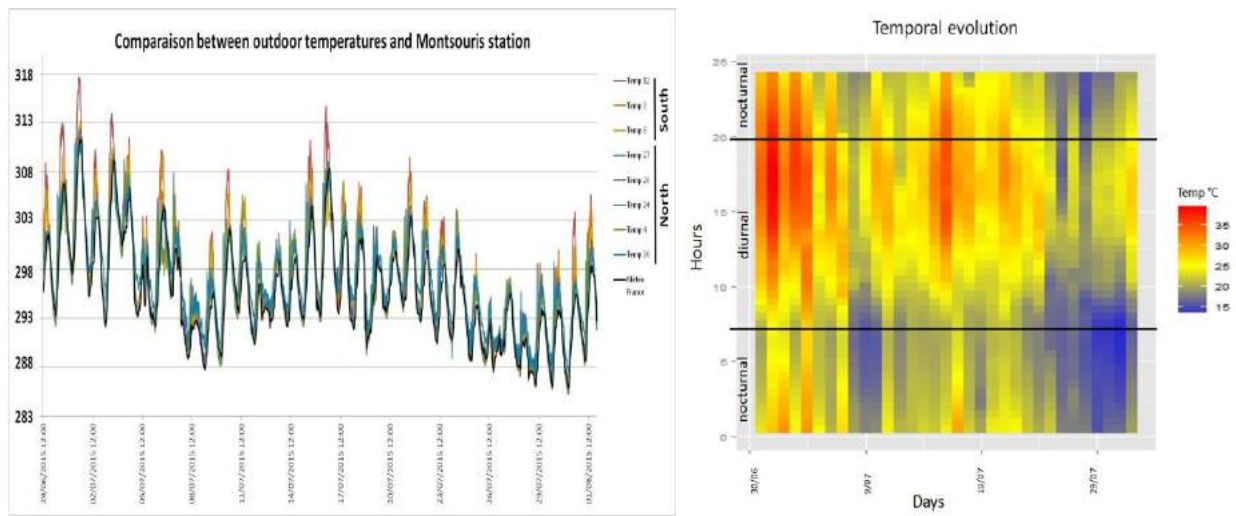


Figure 4: Graphics of outdoors temperature

The second graph (Figure 5) on inside temperatures shows a lower difference between sensor and lower thermal amplitude. Concerning the matrix of inside temperature, we notice that the highest temperatures concentrate between 5pm and 2am with a peak of heat at 8pm. The lowest temperatures concentrate approximately at 10am.

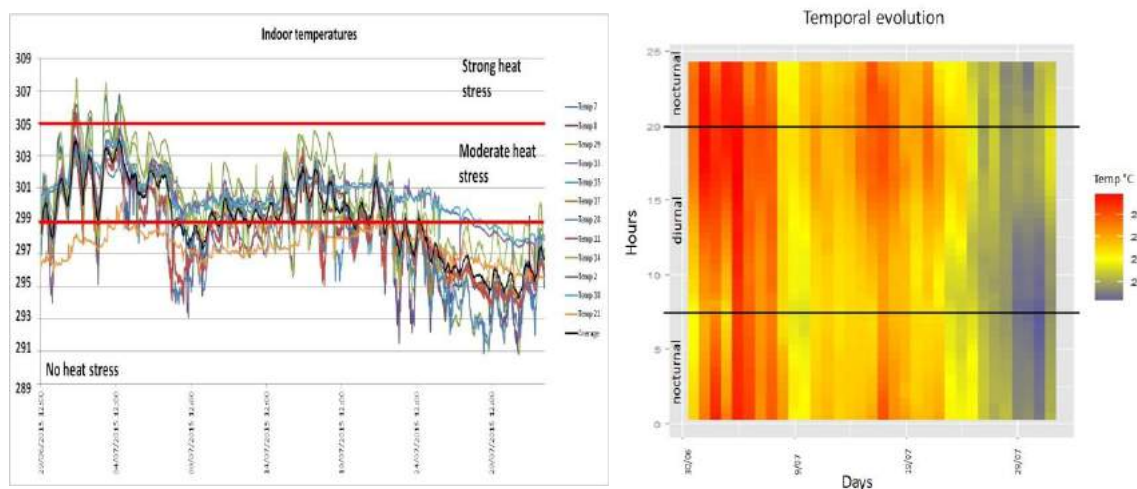


Figure 5: Graphics of indoors temperature

The data analysis shows that various factors such as the double exposure, the insulation, the floor and configuration of an apartment are affecting the changes in indoor temperatures and lead to atypical situations, even extreme configurations. Our findings show that during heat waves, indoor heat stress at night is higher than that outdoors temperature because of the thermal inertness of buildings. Those graphics prove that indoor climate is mainly governed by outdoor climate. In addition, we found temperature variations from one building to another (just a few metres apart) and variations between floors. For a more detailed analysis of the interactions between indoor and outdoor climate and the effect of buildings' characteristics, assimilation must be applied.

4.2 Towards mapping of the dangerousness

In the following, we present six cases to illustrate indoor temperature by using extrapolation and assimilation methods. Both phenomenon are temporal, but in this result, we will concentrate on the representation of one state. Similar to the measurement series, the spatiotemporal representation of the heat wave can be made out of the SURFEX model outputs. It is necessary to structure and store the data under a DBMS (Data Base Management System) then read in a GIS so that we can represent and visualize it. Our analysis also illustrates that the risk is related to the type of apartment. The most dangerous are not the ones exceeding automatically the threshold of 305.15K (UTCI) but those where temperatures remain high and stable during several days. So, the heat wave will not be, thus not lived in the same way. We have a differentiated experience, both specially and temporally (Figure 6).

In this study, we have created five types of building (part 2.2) and one type with the output's SURFEX (type 6). Indeed, figure 6 is represented in the indoor temperatures (average 15h-22h) between 1st and July 5th 2015, in the city of Paris according to types of apartments highlights the impact of the configurations on indoors temperatures. With these maps, we noticed an accumulation of areas of strong heat in the Parisian northwest. These regions of intense heat create zones of dangerousness due to the duration of the phenomenon. The indoor temperature is an aggregation of the temperatures measures over 8 hours to study the phenomenon during daytime or night time. This integration also enhances the results by contextualizing the data (to cross-reference temperatures refereeing to every object in the grid).

The description of the variability of heat stress in the first part of the results indicates that some building characteristics may influence the indoor temperature like the floor level, the orientation and the ventilation. Type 1, situated in the ground floor and receiving no sun rays has low temperatures included on average between 297 and 302K contrary to the type 2 and 3, which have strong indoor temperatures and can achieve more of 310K on two consecutive days. Type 1 is the only one not exceeding the UTCI index thresholds of *moderate heat stress*. It will remain in the *no heat stress*. The third and fourth day, some zone will be in the fateful threshold *very strong heat stress* for type 2, 3 and 6.

So the model SURFEX (type 6), for temperatures is going to overestimate or underestimate the temperature according to the thermal characteristics of buildings.

It's important to know that people within the study rooms are affected by heat stress not only during day but also during night and the ability to cope with heat stress after a disturbed recovery phase at night is likely to decrease due to a possible accumulation effect of heat stress [Parson 2003].

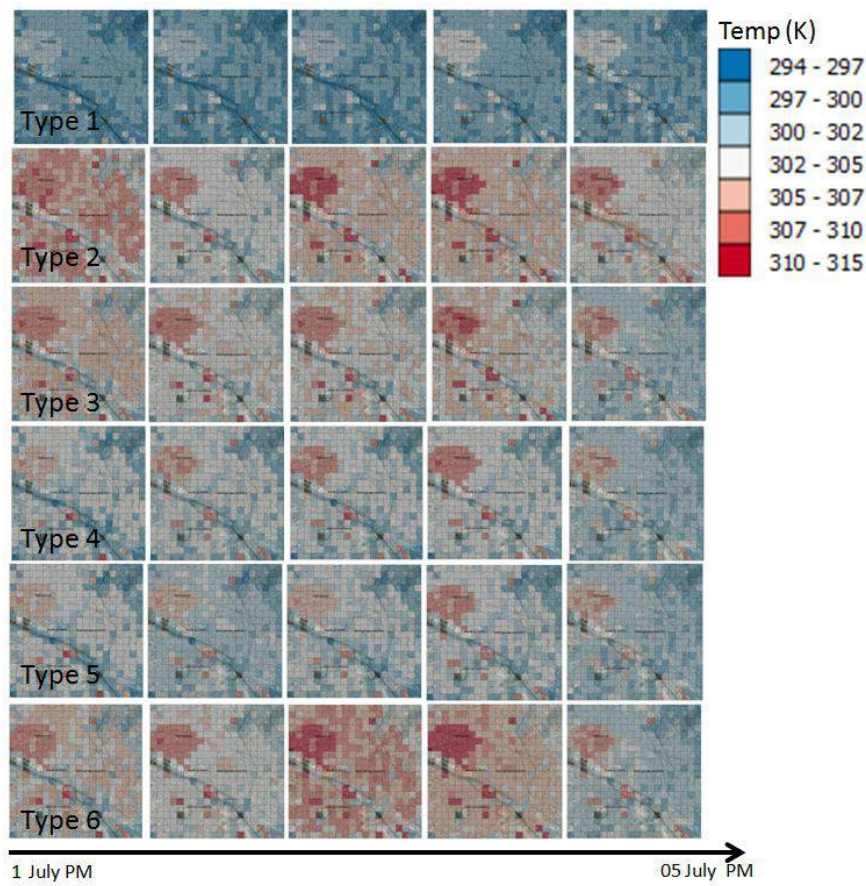


Figure 6: Mapping of indoors temperature by apartments type

5 Conclusion

The analysis shows that indoor heat stress during the summer of 2015 was unequally distributed regarding spatial and temporal variability, especially during the heat waves. The distribution of heat stress in indoor environments showed a small-scaled heterogeneity that was mainly governed by the characteristics of buildings and their surroundings. A significant influence of the outdoor urban heat island could not be found as it is only one factor amongst several other parameters responsible for the development of indoor thermal environment. To isolate and to ventilate the effect of the urban heat island, more buildings must be included in the study. Based on these results, it is suggested that the heat warming to indoor environments be adapted. It is important to recommend adequate adaptation strategies to reduce the heat stress risks. Risk assessments should not only analyze heat stress hazards but spatial variations of vulnerability to heat stress should also be considered.

References

- [Almeida 2013] Almeida S, Casimiro E, Analitis A, Short-term effects of summer temperatures on mortality in Portugal: A time-series analysis. *Journal of Toxicology and Environmental Health, Part A: Current Issues*, Pages 422-428, 2013
- [Bøkenes 2009] Bøkenes L, Mercer J.B, MacEvelly S, Andrews J.F, Bolle R, Annual

- variations in indoor climate in the homes of elderly persons living in Dublin, Ireland and Tromsø, Norway. *European Journal of Public Health*, Pages 526-531, 2010
- [Bröde 2012] Bröde P, Fiala D, Blazejczyk K, Holmér G, Jendritzky G, Kampmann B, Tinz B, Havenith G, Deriving the Operational Procedure for the Universal Thermal Climate Index UTCI. *Int J Biometeorol*, vol. 56, Pages 481-494, 2012
- [Fenner 2014] Fenner D, Meier F, Scherer D, Polze A, Spatial and temporal air temperature variability in Berlin, Germany, during the years 2001-2010, *Urban Climate*, vol.10 , Pages 308-331, 2014
- [Gabriel 2011] Gabriel K.M, Endlicher W.R, Urban and rural mortality rates during heat waves in Berlin and Brandenburg, Germany, *Environmental Pollution*, vol. 159, Pages 2044-2050, 2011
- [Gaspar 1990] Gaspar P, Gregorius Y, Lefevre J.M, A simple eddy kinetic energy model for simulations of oceanic vertical mixing tests at Station Papa and Long-Term Upper Ocean Study Site, *J. Geophys. Res.*, vol.95-16, Pages 179–16,193, 1990
- [Höppe 1993] Höppe P, Indoor climate, *Experientia*, vol. 49, Pages 421-428, 1993
- [Institut 2003] Institut de veille sanitaire, Impact sanitaire de la vague de chaleur d'août 2003 en France. Bilan et perspectives, Pages 120, October 2003.
- [Kavgic 2012] Kavgic M, Summerfield A, Mumovic D, Stevanovi Z.M ,et al, Characteristics of indoor temperatures over winter for Belgrade urban dwellings: Indications of thermal comfort and space heating energy demand. *Energy and Buildings*, Pages 506-514, 2012
- [Masson 2000] Masson V, A physically based scheme for the urban energy budget in atmospheric models, *Bound. Layer Meteor*, vol. 94, Pages 357-397, 2000
- [Masson 2003] Masson V, Champeaux J.L, Chauvin F, Meriguet C, and Lacaze R, A global data base of land surface parameters at 1 km resolution in meteorological and climate models. *J. of Climate*, Pages 1261-1282, 2003
- [Mironov 2010] Mironov D, Heise E, Kourzeneva E, Ritter B, Schneider N, Terzhevik A, Implementation of the lake parameterisation scheme FLake into the numerical weather prediction model COSMO, *Boreal Env, Res.*, vol. 15, Pages 218-230, 2010
- [Nguyen 2014] Nguyen J.L, Schwartz J, Dockery D.W, The relationship between indoor and outdoor temperature, apparent temperature, relative humidity, and absolute humidity. *Indoor air*, vol. 24, Pages 103-112, 2014
- [Noilhan 1989] Noilhan J, Planto S, A simple parameterization of land surface processes for meteorological models, *Weather Rev*, vol. 117, Pages 536-549, 1989
- [Parson 2003] Parson K.C, Human thermal environments : the effects to hot, moderate and cold environments on human health, comfort and performance. *New York*, London, 2003
- [Quinn 2014] Quinn A, Tameriux J.D, Perzanowski M, Jacobson J.S, Goldstein I, Acosta L, Shaman J, Predicting indoor heat exposure risk during extreme heat events. *Sci Total Environ*, vol. 490, Pages 686-693, 2014
- [Yohanis 2010] Yohanis G, Mondol J.D, Annual variations of temperature in a sample of UK dwellings. *Applied Energy*, vol. 87, Pages 681-690, 2010

A robust smoothed voxel representation for the generation of finite element models for computational urban physics

Alain Rassineux¹, Benoit Beckers¹

¹ Sorbonne universités, Université de Technologie de Compiègne, CNRS

Laboratoire Roberval UMR 7337 CNRS/UTC 7337, Centre de Recherche de Royallieu, BP 20529,
F60205 Compiègne
e-mail: alain.rassineux@utc.fr

Keywords: Mesh generation, finite element analysis, large scale city models.

Abstract. *A voxel based methodology to create high quality finite element meshes of large city models for urban computational physics is proposed. Initial data are limited to 3D points cloud or STL files. A voxel grid which provides a rough representation of the outer (visible) surfaces of geometry is first created. The voxel model is then smoothed by a subdivision technique which provides a better representation of the normal vector to the surface than the voxel model. The points smoothed models are thereafter projected on the initial data. The ground, building blocks and the air are identified as volumes and their corresponding closed conforming surface mesh is created. Examples of complex reconstructions are presented.*

1. Introduction

The work proposed here is mostly based on the generation of finite element meshes of complex urban models. When dealing with complex geometry assembly, the major time of the finite element analysis (FEA) is spent on the creation of the mesh model. Mesh generation based on CAD for computational mechanics for instance has been widely investigated [De Cougny 1996]. The model, generally represented by parametric surfaces such as NURBS is meshed patch by patch in a suitable parametric space. Each volume must be represented by a closed BREP which in addition must allow to create a conforming mesh at interfaces between patches. The CAD model must be “cleaned” manually what represents a tedious and time consuming task. In addition, when the number of volumes increases, the cost of the creation of a geometry suitable for meshing becomes prohibitive. Moreover, the CAD model often contains details which are not necessary for the analysis. This may even impede the convergence of the analysis or make the cost of the computation prohibitive. When dealing with explicit analysis for instance, the time step is linked to the smallest element which may be located on a detail of the CAD which has no influence on the FEA. A large amount of time is often spent to remove details from the CAD before creating a relevant mesh.

A second class of techniques which does not use a surface model consists in using a polyhedral representation of the object such as a STL mesh. Most CAD systems can export a surface geometry into a stereolithography (STL) surface mesh file. STL representation provides a good approximation of the surface model into triangles but a very poor mesh for finite element analysis purposes and the mesh must be enhanced [Hassan 2004]. A number of authors have proposed remeshing procedures based on local optimization procedures [Chappuis 2004]. These techniques involve extracting from the surface mesh sets of triangles sharing the same node or the same edge and then remeshing the outer contour to a higher criterion (size or shape). These procedures can be used to refine or coarsen the mesh or more generally to enhance mesh quality with respect to a preset criterion (shape, size, anisotropy). The experience shows that the efficiency of these procedures is considerably reduced when the mesh is highly distorted. Moreover, the initial data mesh must still be conforming; free of intersection, overlappings what remains a severe constraint when dealing with complex heterogeneous urban models. A model composed on hundreds or thousands of buildings, including the ground can hardly be represented with these previous techniques, what explains the use of other techniques in the context of urban modelling such as the use of procedural modeling [Müller 2006], [Lienhard 2014] which enables to create a wide range of architectural detailed model or model reconstruction based on 3D-points clouds [Berger 2016] obtained from aerial data for instance

Lafarge and Mallet [Lafarge 2012] have proposed a survey on a number of these techniques together with an approach based on an energy minimization criterion to reconstruct large scale city models from 3D-points clouds. Geometrical features usually met in urban architecture (façade, roof) such as planes, cylinders, sphere and cones are identified. Complex environments at different scales are rebuilt with accuracy as often required by architects. Most of these techniques allow a very realistic representation of the geometry what may not be the major requirement when dealing with FEA as mentioned previously.

Another class of technique frequently used to create an approximation of complex FE models consists in using a grid [Hello 2014] as a representation model, in most cases when there is no other solution! This grid can be composed of voxels of regular size or be adaptive. In the last case, an octree structure is built [Vo 2015]. The surface to represent can be given by the outer faces of the grid what provides a shagged effect. A smoother surface representation can also be obtained by marching cubes or at a higher cost a level set technique.

A number of simulations such as convection-diffusion can be carried out with a finite difference solver which only requires a grid, usually regular to make the generation easier. However, when dealing with elliptic problems, the Finite Element Method (FEM) has the ability to take into account natural boundary conditions included in the weak form and is therefore much preferred not to mention non linear problems for which FEM must be preferred. In addition, adaptation can be obtained at a much lower cost with FEA. We shall focus here on a technique to generate meshes for finite element analysis. In this context, “Quality” of mesh and especially finite element has been widely discussed [Zienkiewicz 2013]. From a computational point of view, the quality of the mesh is ideally linked to the result of the analysis compared to experimental results provided that these results exist. The accuracy at which the geometry must be described is indeed highly dependent on the physical phenomenon to study and at what scale the phenomenon is studied. For instance, the study of the integrity of a building structure would indeed require an accurate representation of the components on which the loads are applied. The study of direct solar irradiation [Vermeulen 2015] or the calculation of the surface albedo or the compactness of a city may need a much coarser representation of the facade or rooves and a number of details may be eliminated [Beckers 2013]. The choice of the element type in FEA is also an important issue and depending on the simulation, a shell or volume mesh can be chosen for the buildings, ground, or air.

We propose a robust voxel based reconstruction technique dedicated to large scale city models which provides at the same time a high quality finite element mesh for shell or volume simulation while describing all complex boundaries between model components. The approach may use STL file of any quality or 3D point clouds. The technique allow to reconstruct the outer (visible) surfaces of the buildings while removing from the model details which, for a number of applications and at a chosen scale, may not alter the quality of the analysis. Sets composed of adjacent buildings are identified and a closed mesh of each set is created. The technique allows to generate a conforming meshes of both ground and space around the buildings. When the geometry is decomposed into meshable pieces, the same mesh must be created at the interface of shared surfaces in order to create a conforming assembly mesh. This major requirement of traditional FEM is a bottleneck when dealing with large models with noise, gaps, overlap which often require to reconstruct the whole model. Facades and rooves can also be identified. As each component is represented by a closed mesh, all volumes can be easily calculated. Once a mesh is obtained, usual mesh coarsening can be thereafter applied in order to reduce the computational cost if needed. The advantages and drawbacks of the simplified model are discussed and illustrated.

The different steps of the methodology are now described.

2 Voxelisation

In a first step, the initial data (triangles or points) are enclosed in a regularly spaced three-dimensional voxel grid. Voxel size is a user parameter. The resolution of the box in the 3 directions X, Y, Z of the Cartesian coordinate system is given by the triplet (n_x, n_y, n_z) . If a STL file is provided, triangles are discretized using the finite element shape functions so that the maximal space between neighboring points does not exceed 10% of the chosen voxel size. The input data is therefore in all cases a set of points. Point coordinates are mapped in a space of dimension (n_x, n_y, n_z) and origin $(0,0,0)$ denoted as $(0, X, Y, Z)$. Voxels can be easily numbered from 0 to $n_x n_y n_z - 1$.

The number of a voxel of origin (i, j, k) denoted as $V(i, j, k)$ is given by equation (1).

$$i + n_x \times j + n_x \times n_y \times k \quad (1)$$

The 6 neighboring voxels in the 3 directions X, Y, Z (except on the boarder of the grid) are respectively

$$V(i - 1, j, k), V(i + 1, j, k), V(i, j - 1, k), V(i, j + 1, k), V(i, j, k - 1), V(i, j, k + 1)$$

A point of coordinates (x, y, z) in $(0, X, Y, Z)$ is located in the voxel $V(c(x), c(y), c(z))$ where $c(x)$ denotes the smallest integral value that is not less than x .

The only requirement of the technique is to provide a representation of the ground or in other words to give a segmentation of the points into ground and other points to be classified.

Voxels are sorted into 3 categories denoted as ground, building and air voxels. Ground points are first inserted in the grid and ground voxels are defined. The other points are assumed to be building voxels and are also inserted. Indeed, a voxel may contain both ground and building points and priority is given to the ground. As only surfaces points are provided, voxels inside a building with no interior points are not yet classified as building voxels.

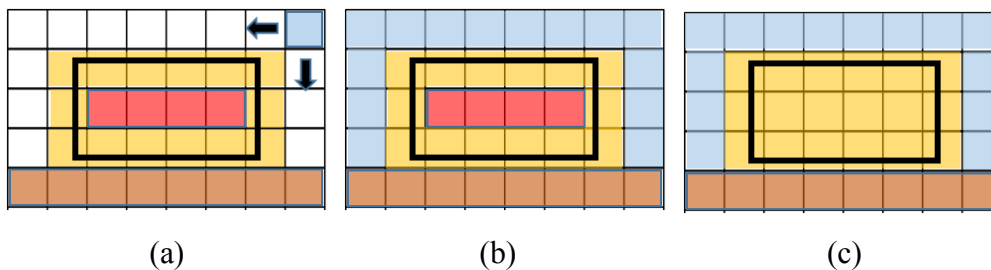
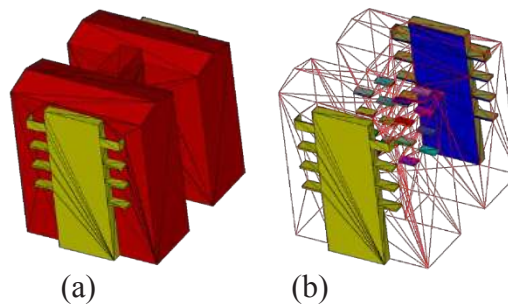


Figure 1. Sorting the voxels: ground, building, air

The sorting process is illustrated in figures 1. The points of the outer surface of a building are represented by a rectangle. In figure 1a, voxels containing ground points have been determined as well as voxels containing building points in a second step.

A prior check is made in order to detect empty cells which may be between the ground and the building. These cells are assigned to buildings. If no ground voxel is found under a building voxel, the cell is reassigned to a ground cell. Voxels (red on the figure) inside the building containing no points have no assignment yet. An empty voxel is chosen on the top of the grid and an advancing front algorithm based on face adjacency easily obtained is applied to fill all cells around the buildings which have not been assigned yet. The result is shown in figure 1b. In practice, a row of empty voxel is added on the top on the grid in order to create a unique volume of air around the buildings. Voxels which have not been assigned are defined as building voxels in a final step. The results is shown in figure 1c.

As represented in figure 2b, STL models may be composed of a high number of simple volumetric shapes which intersects and the model may also contain inner surfaces. The above technique allows to clean easily inner or even spurious surfaces.



Figures 2. STL representation of a building. (a) outer surfaces (b) inner surfaces to remove

3 Creation of building blocks

All cells have been assigned to ground, building or air. We suppose that both ground and air are composed of a single volume.

3.1 Volume determination

An advancing front technique is used again to determine all different volumes (buildings). The algorithm widely used can be easily described as follows.

For all building cells (voxels)

```

{
  If the cell has already been assigned to a volume choose another cell
  Otherwise the front is initially constituted of this unique cell
  While the front is not empty
  {
    Determine for each face of the cell all other adjacent building voxels
    Add these adjacent cells to the front if not yet inside
    Remove the cell from the front
  }
  Increase the number of volumes
}

```

At the end of the process, volumes constituted by a list of cube are created.

3.2 Surface of the building blocks

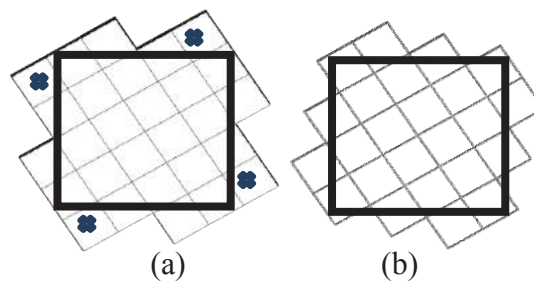
The maximum height, ground surface of a building, volume of each volume can be easily determined. Depending on the voxel size, different thresholds can be given to eliminate “small” buildings.

3.3 Surface of the building blocks

The surface of each building is represented by a quadrangle mesh. A quadrangle face belongs to the outer surface if its neighboring cell is composed of ground or air. In addition, the orientation of the quadrangle face is straightforward since the normal vector to the face must point out of the building cell which contains the face.

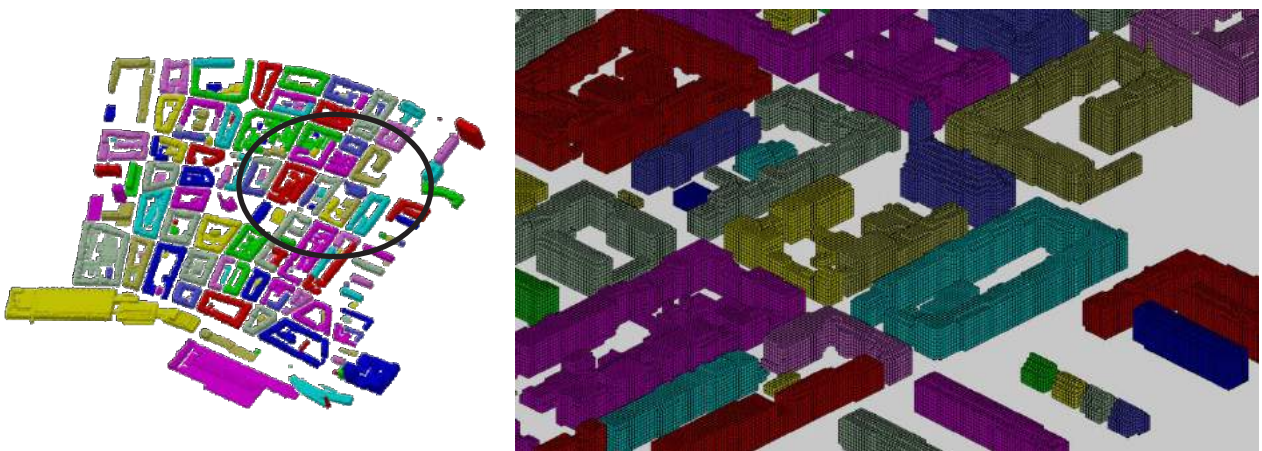
3.4 Elimination of boundary voxels

Building voxels have been assigned to cells which contain other points than ground points. We have identified the volumes and build the outer surface of each volume. The link between a quadrangle outer face and the cell which contains the face is kept. If no building point can be found at a given distance (in practice 0.6) from the outer face, the voxel which contains the face is eliminated. The idea is to keep the voxel if the volume shared with the building is sufficient. This process eliminates from the surface boundary the points which are “far” from the boundary of the building to represent. As shown in figure 3a, 4 cells which are marked by a cross are eliminated.



Figures 3. Elimination of boundary voxels

After the process, for each volume, both list of boundary voxels and outer boundary faces are updated. Volumes of different components can already been calculated. An example of voxel representation of a district of Basel is illustrated in figures 4. Each building blocks is represented. The ground is not displayed on the figure.



Figures 4. Voxel representation of a district of Basel

4 Improving the voxel model

4.1 Smoothing the voxel model

Voxelisation provides an efficient and robust way to build a topology of highly complex models while eliminating unnecessary details, noisy data. Moreover, the mesh obtained can be used for a number of simulations [Hello 2014]. The mesh at the interface between ground/building is conforming. Indeed, the accuracy of the representation is driven by the voxel size and the cost can be quickly prohibitive. In addition, the computation of the normal vector at each face as well as the nodal averaged normal vector is very poor. Many applications [Beckers 2013] require a “decent” computation of the normal vector, especially on the rooves of the buildings. A common idea is to project the points of the voxel model on the set of data points in the direction of the normal vector to the surface. The lack of accuracy of the normal vector makes this procedure quite unreliable. The idea of this work is to smooth the voxel model, not only for esthetical purposes but also to improve the computation of the normal vector at each face and node. Surface smoothing techniques are mainly used for graphics applications, geometric modeling or even film animation. Among them, subdivision techniques [Catmull 1978] are very popular because they can be easily implemented. As in laplacian smoothing, the principle is to move a point to a location calculated by a weighted combination of its neighbors position. We have applied here a standard Catmul-Clark algorithm in which no additional faces nodes are added but only vertices are updated. In practice, the process of smoothing is repeated 3 times. For some applications, the main drawback is the shrinkage of the volume. As we plan to project the points of the voxel model, we experienced that the shrinkage does not affect the a posteriori projection procedure. The smoothing procedure is applied to the buildings and to the ground. The position of a node located at the interface ground/building and air/building is provided by the smoothing of the building only. The quality of the surface mesh is controlled at each step of the smoothing. The new location is updated only if the quality of the mesh remains acceptable.

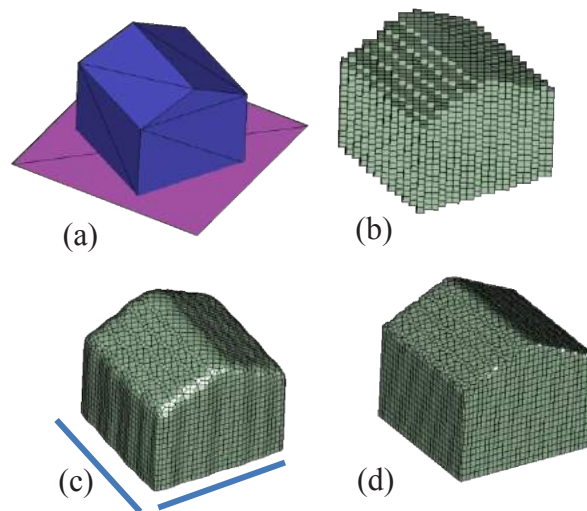
4.2 Projection of the voxel points on the initial data

In order to project the surface voxel points on the initial data, the first step is to calculate the normal vector at each node. This is obtained by averaging the normal vector of all quadrangle faces coincident to that node. In order to compute this normal vector, quadrangles are split into 2 triangles. As two possibilities exist, the solution chosen is the one which maximizes the shape quality criterion defined as the ratio of the inscribed radius and the longest edge [Rassineux 2000]. In a number of cases, the quadrangle mesh can be twisted and only one possibility is acceptable. Then the closest point of the initial data in the direction of the normal vector is chosen. A set of neighboring data point is selected around this point in order to approximate a moving least square plane. If the normal to this plane is compatible with the average normal vector at the voxel point, the voxel point is projected on the estimated plane, otherwise another data point is chosen. The quality of the surface mesh is also controlled. The new location is updated only if the quality of the mesh remains acceptable.

5 Results

A STL mesh of a very simple building is first provided in figure 5a and its voxel representation in figure 5b. In order to test the performance of both smoothing and projection, the facade walls initially parallel to the (X,Y) axis have been rotated by 45°. The result of the

smoothing is shown in figure 5c. The result of the smoothing at the intersection between roof and facades looks like fillets. Some nodes belong to the intersection between ground, the building and the air. On figure 5c, these nodes are closed to the blue lines. For these nodes, the smoothing is applied but their altitude (Z direction) is not changed and only the coordinates in directions X and Y are updated as show in figure 5c. The idea is to keep the façade perpendicular to the ground. The result of the projection is shown is figure 5d. The reconstruction is satisfactory even if angles between planes are smoothed.



Figures 5. Different steps of the methodology. (a) STL mesh (b) Voxel representation (c) Constrained smoothing (d) Final result after projection

A reconstruction and a therefore a full remeshing of a district of Basel is presented. The initial data is a STL file presented in figure 6a. The STL file can be decomposed into sets of triangle surfaces, volumes. A building block can be the assembly of a high number of intersecting volumes and surfaces what explains the different colors for a same building block on figure 6a. The final result of the reconstruction is shown in figure 6b. 140 building blocks have been identified.

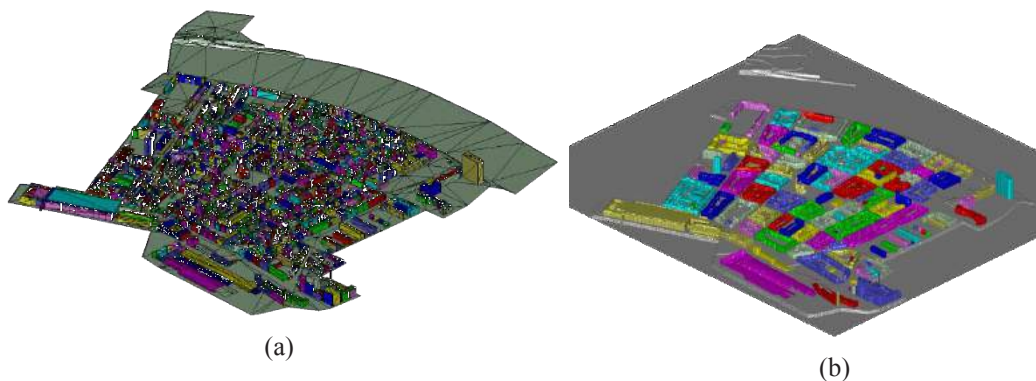


Figure 6. STL representation of a district of Basel- Full model

A more detailed view of the STL (figures 7a) and the smoothed voxel model (figures 7b) is presented thereafter. Apart from angles between planes, the main features of the original model seem to be globally well represented. A selection of complex building is displayed

in figures 8. When shapes become more complex, the projection of the voxel nodes may degrade the quality of the mesh.

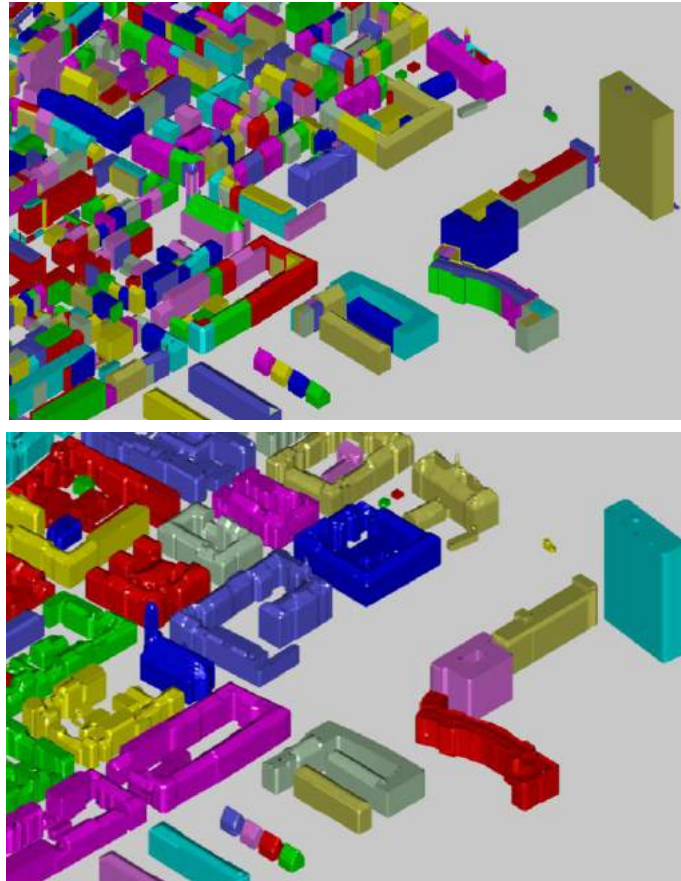
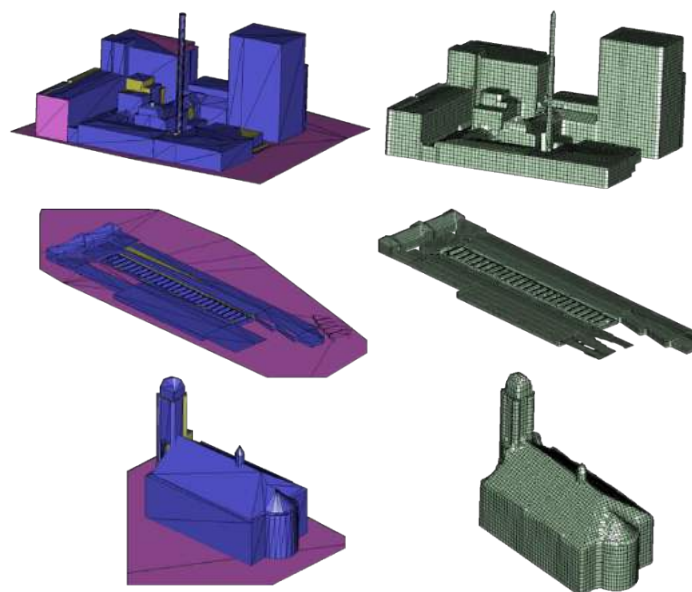


Figure 7. STL representation of a district of Basel- detailed view
(a) STL mesh. (b) rebuild model



Figures 8. Selection of complex buildings. (a) STL meshes (b) Final meshes

6 Conclusions

- A voxel based methodology to create high quality finite element meshes of large city models for urban computational physics from the data of STL files or 3D points has been presented
- The methodology cannot be used if an accurate representation of the geometry is expected. However, the main features of the models presented here are globally well rebuilt.
- The evolving voxel structure which is kept during the process guarantee that conforming meshes are created.
- The surface mesh obtained, once split into quadrangles can be coarsened with standard techniques [Rassineux 2000]
- The closed surface meshes obtained for the air, ground, building can be easily meshed thereafter by any unstructured mesh generator [Rassineux 1997].
- The smoothing procedure allows a better representation of the normal vector to the surface and therefore enables a projection on the initial data
- The process before projection is very robust. The quality of the mesh must be strictly controlled during the projection procedure.

References

- [Beckers 2013] Beckers, B., *Solar Energy at Urban Scale*, pages 1-363, Wiley, 2013
- [Berger 2016] Berger, M., Tagliasacchi, A., Seversky, L.M., Alliez, P., Guennebaud, G., Levine, J.A., Sharf, A., Silva, C.T., *A Survey of Surface Reconstruction from Point Clouds*, Computer Graphics Forum, Article in Press, 2016
- [Catmull 1978] Catmull, E., Clark, J., *Recursively generated B-spline surfaces on arbitrary topological meshes*, Computer-Aided Design, vol. 10 n°6, 1978
- [Chappuis 2004] Chappuis, C., Rassineux, A., Breitkopf, P., Villon, P., *Improving surface meshing from discrete data by feature recognition*, Engineering with Computers, September 2004, Volume 20, Issue 3, pp 202–209
- [De Cougny 1996] De Cougny HL, Shephard MS, *Surface meshing using vertex insertion*, 5th International Meshing Roundtable, pages 243-256 October 1996, Sandia National Laboratories
- [Hassan 2004] O. Hassan, Wang D, Morgan K, Weatherill N P, *Enhanced remeshing from STL files with applications to surface grid generation*, Communications in Numerical Methods in Engineering, vol. 23, pages 227-239, 2004
- [Hello 2014] Hello, G., Schneider, J., Aboura, Z., *Numerical simulations of woven composite materials with voxel-FE models*, 16th European Conference on Composite Materials, ECCM 2014
- [Lafarge 2012] Florent Lafarge, Clement Mallet, *Creating large-scale city models from 3D-point clouds: a robust approach with hybrid representation*, International Journal of Computer Vision, Springer Verlag, 2012, vol. 99 n° .1, pages .69-85.

- [Lienhard 2014] Lienhard, S., Specht, M., Neubert, B., Pauly, M., Müller, P., *Thumbnail galleries for procedural models*, vol. 33 n°2, pages 361-370, 2014.
- [Müller 2006] Müller, P., Wonka, P., Haegler, S., Ulmer, A., Van Gool, L., *Procedural modeling of buildings*, ACM SIGGRAPH 2006 Papers, SIGGRAPH '06, pages. 614-623, 2006
- [Rassineux 2000] Rassineux, A., Villon, P., Savignat, J.-M., Stab, O., *Surface remeshing by local hermite diffuse interpolation*, International Journal for Numerical Methods in Engineering, vol. 49 n°. 1-2, pages 31-49, 2000
- [Rassineux 1997] Rassineux, A., *3D mesh adaptation. Optimization of tetrahedral meshes by advancing front technique*, CMAME vol.141, n°3-4, 1997
- [Vermeulen 2015] Vermeulen, T., Knopf-Lenoir, C., Villon, P., Beckers, B., *Urban layout optimization framework to maximize direct solar irradiation*, Computers, Environment and Urban Systems, vol. 51, pages. 1-12., 2015
- [Vo 2015] Vo, A.-V., Truong-Hong, L., Laefer, D.F., Bertolotto, M., *Octree-based region growing for point cloud segmentation* (2015) ISPRS Journal of Photogrammetry and Remote Sensing, vol. 104, pages. 88-100.
- [Zienkiewicz 2013] Zienkiewicz, O.C., Taylor, R.L., Fox, D., *The Finite Element Method for Solid and Structural Mechanics: Seventh Edition*, Elsevier, 2013

Downburst Reconstruction using Physical Simulation and Analytical Model with Application to Urban Environments

Djordje Romanic¹, Dan Parvu¹, Horia Hangan¹

¹ Wind Engineering, Energy and Environment (WindEEE) Research Institute
Western University
2535 Advanced Avenue
London, Ontario, N6M 0E2
Canada
e-mail: dromanic@uwo.ca
email: dparvu@uwo.ca
e-mail: hmhangan@uwo.ca

Keywords: Coupling Methodology, Downbursts, Analytical Model, WindEEE, Urban Winds, Wind Tunnels, Extreme Winds, Resilience.

Abstract. *Urban environments are frequently exposed to severe wind conditions and stormy weather, such as downbursts. This study proposes a new methodology for coupling an analytical model of downburst winds with a physical simulator capable of reproducing non-synoptic winds. The applications of the method are numerous, but most importantly in the improvement of the resilience of cities to sustain severe winds. A modified version of an analytical model of downburst winds is considered. The physical simulator presented in this study is the Wind Engineering, Energy and Environment (WindEEE) Dome at Western University, Canada. A user-friendly code of the modified analytical model is supplemented with the fluctuating wind component. The proposed methodology may be used to investigate the interaction between urban environments and downbursts in various ways.*

1 Introduction

Downbursts can be defined as a strong downdrafts originating from thunderstorms, and sometimes other cumulonimbus clouds, which result in vigorous starburst outflows at or near the surface (Fujita 1981). Based on the horizontal scale of the diverging winds close to the surface, downbursts are divided into macrobursts (outburst winds exceeding 4 km in horizontal dimension) and microburst (outburst winds below 4 km in horizontal dimension) (Fujita 1985). Damaging winds in intense microbursts can be as high as 75 m s^{-1} ; which for example corresponds to EF3 tornados. It has been observed that dry downbursts are typically produced in weak cumulonimbus or altocumulus clouds (Wakimoto 1985) whereas wet downbursts are usually associated with well-developed thunderstorms (Atkins and Wakimoto 1991).

Cities impact weather and climate in a number of different ways. Urban environments are complex systems made out of irregularly spaced, shaped and oriented obstacles. Therefore, cities act as extremely rough surfaces which have complex interaction with the incoming wind flows. Oke (1988) and Rotach (1993) demonstrated that the urban morphology modifies the spatial structure of rural (open country) boundary layer. For instance, the urban canopy layer, which spans from the surface up to about the average height of buildings, is characterized with an exponential wind profile. This sub-layer is not present in rural environments. A methodology for investigating the influence of synoptic wind systems through coupling numerical weather prediction models and physical simulations is described in Romanic and Hangan (2015). In this study, however, the focus is to explore the possibility of coupling an analytical modeled of non-synoptic winds systems, such as downbursts, and a physical simulator.

The mean velocity profile for downburst winds is substantially different from the standard atmospheric boundary layer (ABL) wind profile (Kim and Hangan 2007). Figure 1 indicates that the maximum wind speeds in the downburst case are observed in the first approximately 200 m above the ground, whereas the wind profile in the typical ABL is logarithmic with the maximum wind speeds observed at the height of the ABL. Note that the reference wind speed in Figure 1 is at 10 m above ground and is equal to 17.5 m s^{-1} for both downburst and ABL profiles. It is also very important to note that while ABL winds are stationary, downburst winds are vortex dominated and non-stationary.

The investigation of downburst winds has mostly been in the realm of analytical models (e.g. Oseguera and Bowles 1988; Vicroy 1991; Holmes and Oliver 2000; Chay et al. 2006), computational fluid dynamics (CFD) models (e.g. Nicholls et al. 1993; Kim and Hangan 2007; Mason et al. 2009) as well as meteorological cloud models (e.g. Straka and Anderson 1993, Orf et al. 2012). For example, Kim and Hangan (2007) modeled a downburst as an impinging jet using Reynolds-averaged Navier–Stokes (RANS) equations and demonstrated that there is a good agreement between their computational results and full-scale measurements in terms of large scale dynamics. The interaction between downburst winds and buildings is of particular importance for urban environments. Kim et al. (2007) investigated the differences between wind loads for tall buildings induced by downburst and ABL winds using again RANS simulations and concluded that downbursts larger than about 2000 m in diameter are likely to produce design wind loads larger compared to the ones resulting from boundary layer winds. Zhang et al. (2013) performed an experimental investigation of downburst induced loads on high-rise buildings and found that the dynamic wind loads exerted on the building model are mainly influenced by the periodical shedding of the primary vortices and the high turbulence levels in downburst flow. Jesson et al. (2015) reviewed both experimental and numerical studies of interaction between downburst-like winds and buildings.

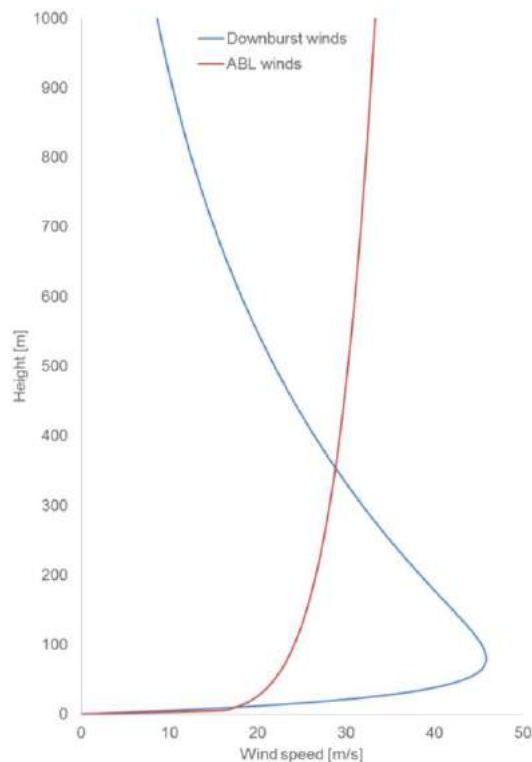


Figure 1: Comparison of a downburst velocity profile and the typical ABL wind profile. The figure is created using the analytical model described in Section 3.1. The following parameters are used: the maximum radial wind speed of 50 m s^{-1} occurring at 1500 m from the downburst center and at a height of 80 m above ground. The downburst profile is plotted at a distance of 1800 m from the downburst center and a stationary downburst is considered. The ABL profile uses the reference wind speed of 17 m s^{-1} at 10 m above ground and the power law exponent of 0.14 .

Small percentage of cumuliform clouds will spawn a downburst. Research on meteorological conditions both inside and outside the parent cloud that lead to the development of downburst is still sparse. Currently it is not possible to estimate the likelihood of downburst occurrences with high precision. Assuming that the severe winds and downbursts are closely related, the map portrayed in Figure 2 might be used as a qualitative indicator of spatial distribution of downbursts across the continental United States. It can be seen that a number of large cities in the United States are affected by severe thunderstorm winds.

Table 1 shows the number of days with thunderstorms in several large cities in the United States. It is interesting to note from Table 1 and Figure 2 that the West Coast of the United States seems to have considerably smaller number of thunderstorms and severe winds than the East Coast. One of the main reasons for this skewed spatial distribution of severe winds across the United States is that the Pacific Ocean is colder than the Atlantic Ocean. The cold water of the Pacific creates very stable air masses along the coast and further inland, thus damping any convection in the atmosphere. The second factor is the low dew point in the stable air above the Pacific. Namely, the lower the dew point, the drier the air, hence no latent heat in the air to supply the energy needed for thunderstorm development.

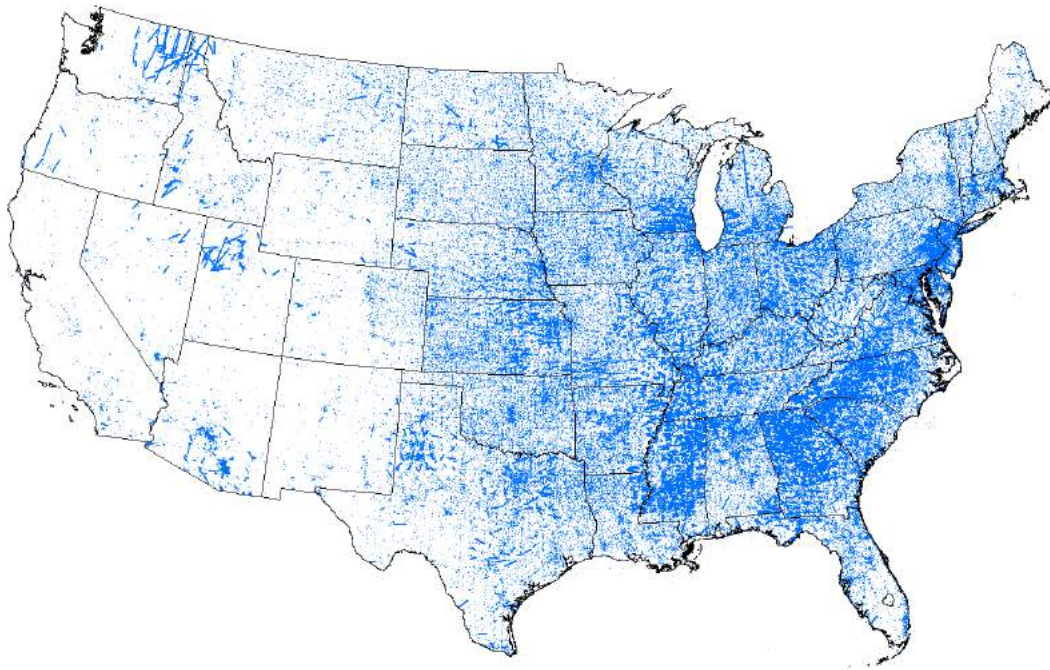


Figure 2: Severe winds over the United States. Source: SPC (2016).

City	2013	2012	2011	1981-2010 average
Los Angeles	1	3	2	3.6
San Francisco	0	6	0	2.9
San Diego	2	1	1	3.0
Sacramento	3	2	2	4.3
Portland	3	7	5	6.7
Seattle	9	5	0	6.4
Chicago	38	36	43	38.0
New York	20	26	28	24.8
Washington DC	30	28	46	31.8

Table 1: Number of days with thunderstorms. Source: NCEI (2016)

The goal of this paper is to present a new methodology for investigating the interaction between downbursts and urban environments. The proposed method combines an analytical model of downburst winds and a physical simulator capable of reproducing non-synoptic wind systems. A 3D physical model of an urban environment can be placed inside of a large multi-fan wind testing chamber capable of reproducing 3D and time-dependent flows such as the Wind Engineering, Energy and Environment (WinDEEE) Dome at Western University. Then, an analytically reconstructed downburst can physically be simulated inside the WinDEEE Dome and the interaction between the downburst and the urban environment can be estimated with great precision. The WinDEEE Dome facility is described in Section 2 and the developed analytical model of downbursts is presented in Section 3 of this paper. Section 4 describes the proposed coupling methodology in more details.

2 Wind Engineering, Energy and Environment (WinDEEE) Dome

WinDEEE is the world's first 3D and time dependent physical wind simulator consisting of a hexagonal test section 25 m in diameter and an outer return dome 40 m in diameter (Hangan 2014). Mounted on the peripheral walls and on top of the test chamber are a total of 116 individually controlled fans and 202 louver systems. Additional systems, including an active boundary layer floor and "guillotine" allow for further manipulation of the flow. These systems are integrated via a sophisticated control system which allows manipulation of the flow with multiple degrees of freedom. WinDEEE can generate straight flows but with a variety of time and space correlations as well as translating tornadoes or downbursts as large as 5 m in diameter. Furthermore, the generated flows can be straight, sheared or swirl winds of variable directionality. Therefore, a large variety of wind fields such as boundary layers, portions of hurricanes, tornados, downbursts, low level currents or gust fronts can be physically simulated. An active topographic capability enables a wide diversity of surface topographies at unprecedented scales allowing wind simulations over areas of the order of 10 km². WinDEEE Dome is equipped with advanced flow measuring techniques such as the Particle Image Velocimetry (PIV) system with local seeding that can measure the wind field over extended urban areas. A traverse mechanism allows for a LASER head to traverse the flow in a multitude of vertical and horizontal sections in order to produce PIV wind field measurements with a full scale equivalent resolution of 10 m. In addition, measurement tools at WinDEEE Dome also include: Pitot tubes with the Pressure Scanner System, Cobra Probes that provide three-component velocity and local pressure as well as the hot-wire anemometers.

In order to generate an impinging flow, six fans located in the upper chamber push the air downward into the test chamber through a bellmouth opening (Figure 3).

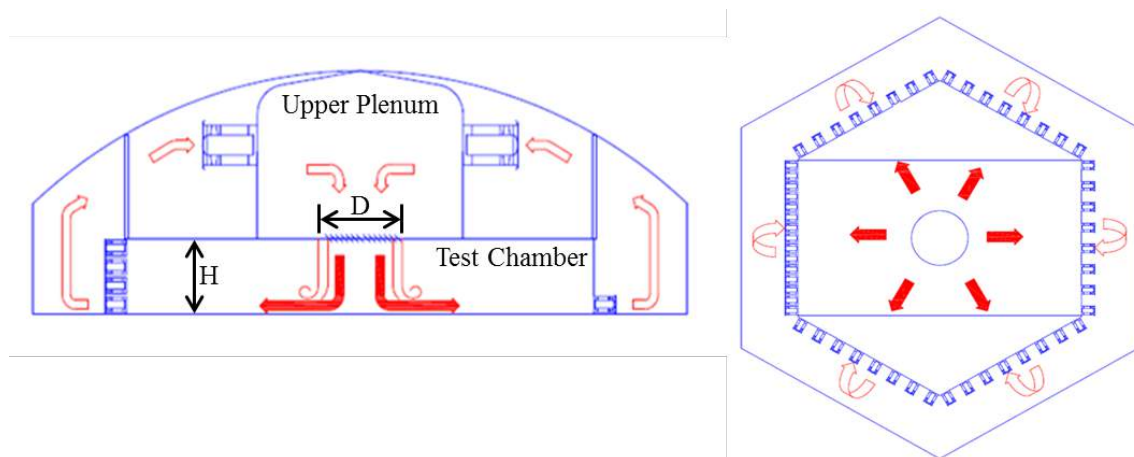


Figure 3: Schematics of downburst production in the WinDEEE Dome. See text for details.

The procedure to generate a dynamic jet flow that impinges on the test chamber floor is as follows:

- The upper plenum which houses six large fans is closed using louvers
- The six fans are turned on and the upper plenum is pressurized
- Once the upper chamber is pressurized, the "guillotine" louvers are opened quickly and the flow is released into the test chamber
- The six upper fans are kept in motion until the end of the sampling time.

The jet flow created impinges on the test chamber floor (Figure 4 and Figure 5) and afterwards the air is evacuated through the peripheral test chamber walls and is then recirculated (Figure 3).



Figure 4: Graphical representation of a downburst created inside of the WindEEE Dome.

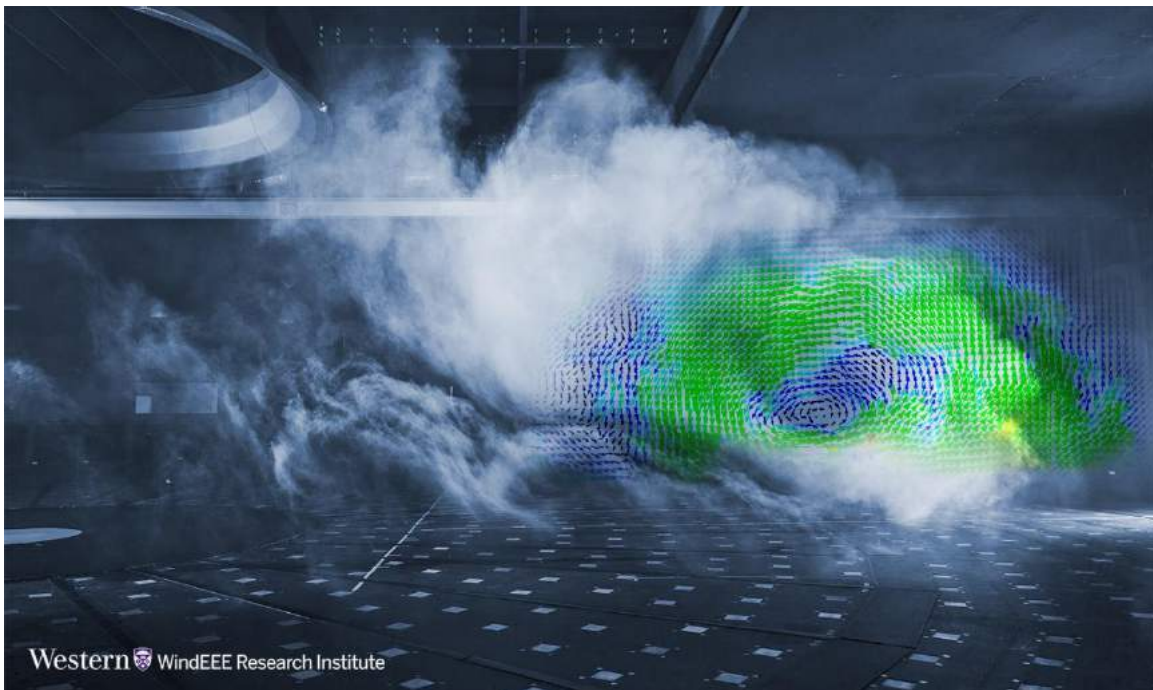


Figure 5: A photograph of a downburst created in WindEEE Dome overlapped with the flow features obtained using the PIV technique. .

3 The analytical model of downbursts

3.1 Mathematical form

The analytical model of downbursts described in this study is a subsequent version of the OBV model originally developed by Oseguera and Bowles (1988) and Vicroy (1991) (therefore the name OBV model). This model is an axisymmetric, stationary model for the non-turbulent downburst winds based on the integration of the continuity equation. The stationary model was afterwards modified by Chay et al. (2006) in order to account for time dependency of storm intensity as well as for the contribution of the background (environmental) winds to the resulting flow field. The radial (U_r) and vertical (U_z) components of the downburst flow with background winds (U_b) present are given as:

$$U_r(x, y, z, t) = \Pi(t) \frac{U_{rm} r}{r_m(t)} \frac{e^{(-c_1 \frac{z}{z_m})} e^{(-c_2 \frac{z}{z_m})}}{C} e^{\left(\frac{1 - \left(\frac{r}{r_m(t)} \right)^{2\alpha}}{2\alpha} \right)} + U_b \quad (1)$$

and

$$U_z(x, y, z, t) = \Pi(t) \frac{r z_m}{r_m(t)} \frac{e^{-(c_1 \frac{z}{z_m} + 1)}}{c_1} - \frac{e^{-(c_2 \frac{z}{z_m} + 1)}}{c_2} e^{\left(\frac{1 - \left(\frac{r}{r_m(t)} \right)^{2\alpha}}{2\alpha} \right)} \left(2 - \left(\frac{r}{r_m(t)} \right)^{2\alpha} \right). \quad (2)$$

Here, r represents the radial distance from the downburst center, z is the elevation above ground, t is time, U_{rm} is the maximum radial velocity which occurs at the height z_m above ground and at the radial distance $r_m(t)$ from the downburst center, where $r_m(t)$ is given as $r_m(t) = r_{m0} + kt$ with k being the rate of change of r_m with time and r_{m0} is the initial value of r_m . The linear trend of $r_m(t)$ is in accordance with the radar observations of downbursts by Hjelmfelt (1988). The model constants have the recommended values (Vicroy 1991) of $c_1 = -0.15$, $c_2 = -3.275$, $\alpha = 2$ and $C = e^{-c_1} - e^{-c_2}$. The time-dependent storm intensity $\Pi(t)$ is modeled as:

$$\Pi(t) = \begin{cases} -\frac{t}{t_{max}}, & 0 \leq t < t_{max} \\ e^{-\frac{t-t_{max}}{t_{total}}}, & t > t_{max} \end{cases}, \quad (3)$$

where t_{max} is the time at which the downburst reached maximum intensity and t_{total} is the total duration of the downburst.

The fluctuating wind component is generated using spectral decomposition method (Shinozuka, 1972; Lizhong and Letchford, 2004)

$$u = a(t) \sqrt{2} \sum_{k=1}^N \sqrt{\Delta \omega_k S(\omega_k)} \cos(\omega_k t + \varphi_k) \quad (4)$$

where $\omega_k = 2\pi f_k$ is the angular frequency, φ_k are the random phase angles in the interval from 0 to 2π , $\Delta \omega = \omega_u/N$, ω_u is the cut-off frequency and $S(\omega_k)$ is the power spectral density function. A von Karman spectra in the form:

$$\frac{nS(n)}{\sigma_u} = \frac{\frac{4nL_u}{\bar{U}}}{\left(1 + 70.7 \left(\frac{nL_u}{\bar{U}}\right)^2\right)^{5/6}} \quad (5)$$

where σ_u is the turbulence intensity, L_u is the integral length scale and $n = \frac{Lf}{\bar{U}}$. Romanic et al. (2016) demonstrated that there is a negligible difference between the fluctuating wind speeds generated using von Karman and Kaimal spectra.

The fluctuations are amplified through the factor $a(t)$ in Eq. (4) utilizing the amplitude modulating the process of the mean wind speed (Lizhong and Letchford, 2004). The modulation function is defined as $a(t) = \eta \bar{U}(t)$, where η is empirically determined to be about 0.1 and $\bar{U}(t)$ is the moving average of the measured wind speed time series.

3.2 The computer model

The modified OBV model is coded in Matlab 2016a[®]. The generated software contains two main interfaces as indicated in Figure 6 and Figure 7. The description of both modules of the model is provided below.

Reconstruction of the mean wind field of a downburst can be performed in two ways: (1) a generic downburst can be created using an arbitrary combination of input parameters or (2) a reconstruction of a measured downburst can be performed setting up the input parameters in order to fit the measured winds. The parameters included in the Observations panel (Figure 6) represent the specifications of measurements. The time- and frequency-related parameters in the panel are needed in Eqs. (1) – (5) to calculate time dependency of the event. The desired height at which the downbursts is reconstructed is also specified. Note that an additional time parameter, named T_{gust} is also present in the panel. The authors of this study are currently working on two major modifications of the existent OBV model.

The first modification is related to the analytical reconstruction of thunderstorm gust front which typically precedes the downburst event and can frequently be seen in full-scale measurements. Reconstruction of the gust will require the T_{gust} time to be specified.

The second improvement of the existing OBV model is to account for both background (environmental) wind speeds as well as the storm motion itself. The current model uses the surface wind velocity as the velocity of the storm translation. This assumption is inaccurate because the translation of the storm is not in the same direction and with the same magnitude as the surface winds.

The Downburst panel in Figure 6 contains the physical parameters of the reconstructed downburst. All these parameters are constituent parts of the analytical equations described in the previous sub-section. An important feature of the developed model is that it enables determination of all physical parameters of a downburst event if the time series of wind speed measurements is provided. Namely, the sliders assigned to each of the physical parameters in the Downburst panel enable the simulations calculations of both radial and vertical velocities [Eqs. (1) and (2)]. Cross-correlation between the reconstructed (calculated) and measured downburst wind speeds is calculated at the same time. The highest cross-correlation coefficient can be used to identify the most likely combination of downburst parameters (e.g. U_{rm} , r_m and z_m) associated with the full-scale event.

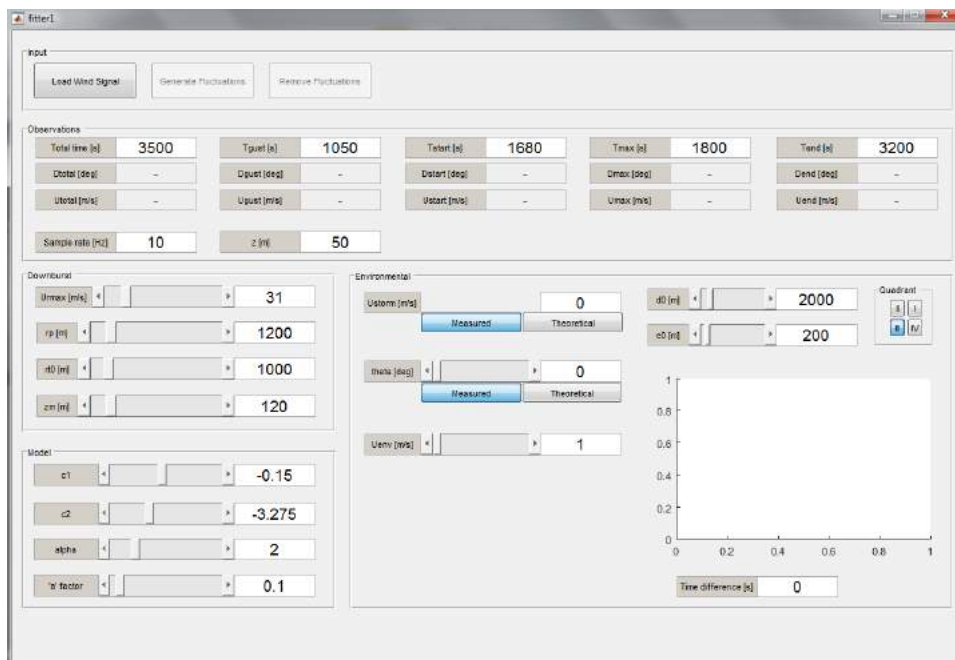


Figure 6: Developed computer code for downburst reconstruction based on the modified OBV model: the mean wind field.

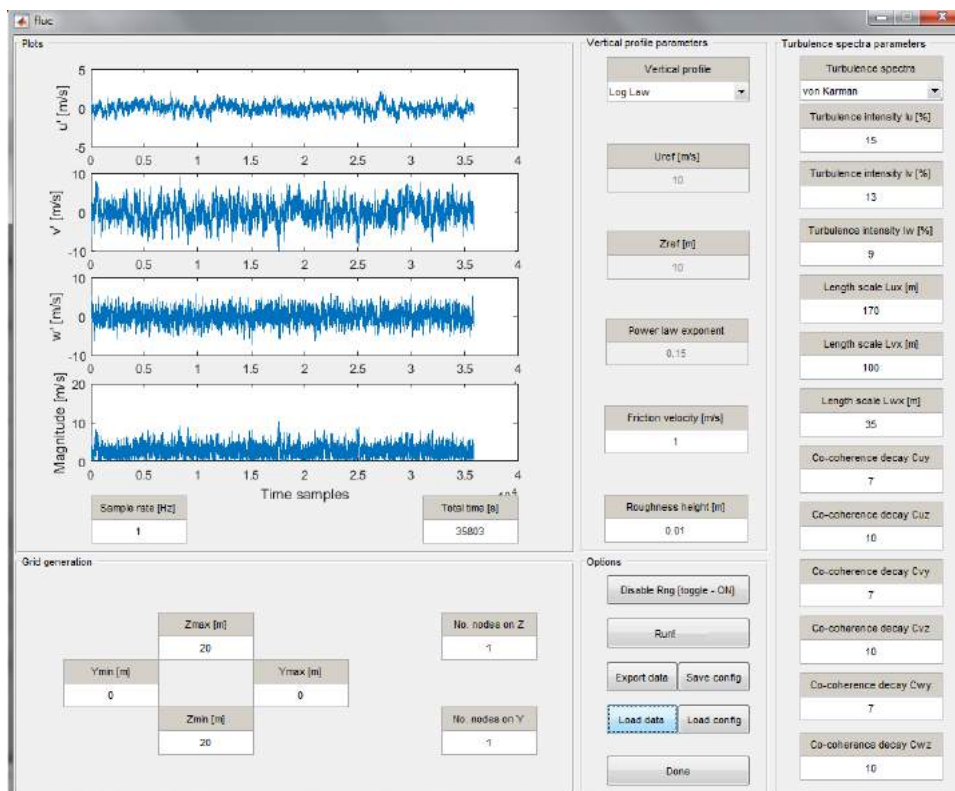


Figure 7: Developed computer code for downburst reconstruction based on the modified OBV model: the fluctuating wind components.

Model constants are provided in the Model panel. These constants should generally not be changed, but their manipulation has nevertheless being made possible for the research purposes.

The environmental parameters such as the storm initial position in respect to the measurement point, surface wind velocity and storm velocity are specified in the Environmental

panel in Figure 6. Note that the software is using the Cartesian coordinates with the origin placed at the measurement mast and not at the downburst center.

The fluctuating wind generator (Figure 7) has the four main panels. Frequency and time parameters have to be specified in the Plots panel. The Grid Generation panel specifies the number of special points for which the fluctuating wind components want to be generated. In a case of a point measurement (e.g. a single anemometer mounted at a meteorological mast), Z_{\max} is equal to Z_{\min} and the number of nodes in both z- and y-directions is 1. If, on the other hand, a user is, for instance, interested in generating a fluctuating wind components for five anemometers positioned along a mast with the lowest anemometer at 5 m and the highest at 25 m above ground then $Z_{\max}=25$ m, $Z_{\min}=5$ m and the number of nodes on z-axis is 5.

The user can choose between two wind speed profiles: (1) logarithmic or (2) power, as well as between two turbulence spectra: (1) von Karman or (2) Kaimal. The necessary input parameters for wind speed profiles and spectra generation are specified in the Vertical Profile Parameters and Turbulence Spectra Parameters panels in Figure 7, respectively.

The random generator of phase angles φ_k in Eq. (4) can be manually switched on or off (Disable Rng button). This feature of the model is implemented for the research purposes.

4 Coupling Methodology

The proposed coupling methodology between the analytically reconstructed downbursts and WindEEE Dome with applications to urban environments can be explained as follows: the downburst model described above (Section 3.2) can be used to fit full scale downburst measurements such as wind speed and wind direction records from a cup or sonic anemometer or even LiDAR measurements. As a result the model produces equivalent impinging jet parameters such as the inflow jet diameter, the maximum radial velocity and its position with respect to the approximated downburst center. These parameters can then be used as starting parameters for the physical simulation of downburst such as the case with the WindEEE Dome (Figures 3, 4 and 5).

Therefore a scaled model of an urban environment can be generated and a downburst-like jet replicated inside the WindEEE Dome based on the parameters identified by the model. The turntable located in the center of the WindEEE Dome enables the rotation of the physical model and thus the simulation of the different translational directions of the storm. Such coupled experiments enable the precise measurements of the peak wind or pressure coefficient values at various locations in an urban environment. The same scenario can be imagined in relation to CFD simulations of urban environment; however, for peak load calculations the current CFD are not yet as reliable as the physical simulations.

Several applications of the proposed coupled method can be envisaged. The methodology can be used to investigate and provide improvements to the resistance of cities, city blocks and individual buildings and structures to severe thunderstorm winds. It could be used to investigate the propagation of surface downburst winds over various roughness of the underlying urban surfaces and therefore help define and improve numerical parametrization of surface thunderstorm wind fields.

References

[Atkins and Wakimoto 1991] Nolan T. Atkins, Roger M. Wakimoto, Wet Microburst Activity over the Southeastern United States: Implications for Forecasting, *Weather and Forecasting*, vol. 6 n° 4, Pages 470-482.

- [Chay et al. 2006] Michael Chay, Faris Albermani, Richard Wilson, Numerical and Analytical Simulation of Downburst Wind Loads, *Engineering Structures*, vol. 28 n° 2, Pages 240-254, January 2006
- [Fujita 1981] Theodore T. Fujita, Tornadoes and Downbursts in the Context of Generalized Planetary Scales, *Journal of Atmospheric Sciences*, vol. 30 n° 8, Pages 1511-1534, August 1981
- [Fujita 1985] Theodore T. Fujita, *The Downburst: Microburst and Macrobust*, University of Chicago, 136 pages, June 1985
- [Hangan 2014] Horia Hangan, The Wind Engineering Energy and Environment (WindEEE) Dome at Western University, Canada, *Wind Engineers, Japan Association for Wind Engineering*, vol. 39 n° 4, Pages 350-351, October 2014
- [Hjermfelt 1988] Mark R. Hjermfelt, Structure and Life Circle of Microburst Outflows Observed in Colorado, *Journal of Atmospheric Sciences*, vol. 27 n° 8, Pages 900-927, August 1988
- [Holmes and Oliver 2000] John D. Holmes, Steve Oliver, An Empirical Model of Downburst, *Engineering Structures*, vol. 22 n° 9, Pages 1167-1172, September 2000
- [Jesson et al. 2015] Michael Jesson, Mark Sterling, Chirs Letchford, Matthew Haines, Aerodynamic Forces on Generic Buildings Subject to Transient, Downburst-Type Winds, *Journal of Wind Engineering and Industrial Aerodynamics*, vol. 137, Pages 58-68, February 2015
- [Kim and Hangan 2007] Jongdae Kim, Horia Hangan, Numerical Simulations of Impinging Jets with Applications to Downbursts, *Journal of Wind Engineering and Industrial Aerodynamics*, vol. 95 n° 4, Pages 279-298, April 2007
- [Kim et al. 2007] Jongdae Kim, Horia Hangan, Ho Eric, Downburst versus Boundary Layer Induced Wind Loads for Tall Buildings, *Wind and Structures*, vol. 10 n° 5, Pages 481-494, 2007
- [Lizhong and Letchford 2004] Lizhong Chen, Chris W Letchford, A Deterministic–Stochastic Hybrid Model of Downbursts and its Impact on a Cantilevered Structure, *Engineering Structures*, vol. 26 n° 5, Pages 619-629, April 2004
- [Mason et al. 2009] Matthew S. Mason, Graeme S. Wood, David F. Fletcher, Numerical Simulation of Downburst Winds, *Journal of Wind Engineering and Industrial Aerodynamics*, vol. 97 n° 11, Pages 523-539, November 2009
- [NCEI 2016] National Centers for Environmental Information, Quality Controlled Local Climatological Data, *National Oceanic and Atmospheric Administration*, Web page: <https://www.ncdc.noaa.gov/data-access>. Accessed: 29 April 2016, March 2016
- [Nicholls et al. 1993] Mel Nicholls, Roger A. Pielke, Robert N. Meroney, Large Eddy Simulation of Microburst Winds Flowing around a Building, *Proceedings of the 1st International on Computational Wind Engineering, Journal of Wind Engineering and Industrial Aerodynamics*, vol. 46-47, Pages 229-237, August 1993
- [Oke 1988] Tim R. Oke, The Urban Energy Balance, *Progress in Physical Geography*, vol. 12 n° 4, Pages 471-508. December 1988
- [Orf et al. 2012] Leigh Orf, Erica Kantor, Eric Savory, Simulation of a Downburst-Producing Thunderstorm using a Very High-Resolution Three-Dimensional Cloud Model, *13th*

International Conference on Wind Engineering, Journal of Wind Engineering and Industrial Aerodynamics, vol. 104-106, Pages 547-557, May-July 2012

[Oseguera and Bowles 1988] Rosa M. Oseguera, Roland L. Bowles, *A simple, Analytical 3-dimensional Downburst Model Based on Boundary Layer Stagnation Flow*, NASA Technical Memorandum n° 100632, 19 pages, July 1998

[Romanic and Hangan 2015] Djordje Romanic, Horia Hangan, Coupling of Numerical Weather Prediction Models and Physical Simulations for Urban Wind Environment, *9th International Conference on Urban Climate (ICUC9)*, July 20-24, 2015, Toulouse, France

[Romanic et al. 2016] Djordje Romanic, Dan Parvu, Horia Hangan, Fluctuating Wind Generator: Theoretical Concept and Model, *1000 Islands Fluid Mechanics Meeting*, April 22-24, 2016, Gananoque, Ontario, Canada

[Rotach 1993] Mathias W. Rotach, Turbulence Close to a Rough Urban Surface Part I: Reynolds Stress, vol. 65 n° 1, Pages 1-28, July 1993

[Shinozuka, 1972] Masanobu Shinozuka, Monte Carlo solution of structural dynamics, *Computers & Structures*, vol. 2 n° 5-6, Pages 855-874, February 1972.

[Straka and Anderson 1993] Jerry M. Straka, John R. Anderson, Numerical Simulations of Microburst-producing Storms: Some Results from Storms Observed during COHMEX, *Journal of the Atmospheric Sciences*, vol. 50 n°10, Pages 1329-1348, April 1993

[SPC 2016] Storm Prediction Center, Storm Prediction Center Severe Weather GIS (SVRGIS), *National Oceanic and Atmospheric Administration's National Weather Service Storm Prediction Center*, Web page: <http://www.spc.noaa.gov/gis/svrgis/>, Accessed: 26 April 2016, March 2016

[Vicroy 1991] Dan D. Vicroy, *A Simple, Analytical, Axisymmetric Microburst Model for Downdrafts Estimation*, NASA Technical Memorandum n° 104053, 13 pages, February 1991

[Wakimoto 1985] Roger M. Wakimoto, Forecasting Dry Microburst Activity over the High Plains, *Monthly Weather Review*, vol. 113 n° 7, Pages 1131-1143, July 1985

[Zhang et al. 2013] Yan Zhang, Partha Sarker, Hui Hu, An Experimental Study of Flow Fields and Wind Loads on Gable-Roof Building Models in Microburst-Like Wind, *Experiments in Fluids*, vol. 54, Pages 1-21, May 2013

To evaluate the sustainability of urban planning projects through an LCA approach: example of application of the NEST tool and requirements for its use in the context of Ecuador and Latin America

Nicolas Salmon^{1,2*}, Grace Yopez-Salmon^{1,2,3}, Marc Lotteau^{4,5}

¹ YES Innovation, Armero Oe7-261 y el Oro, Quito, Ecuador; nsalmon@yes-innovation.com

² Pontificia Universidad Católica del Ecuador, Facultad de Arquitectura, Av. 12 de Octubre 1076 y Roca, Quito, Ecuador

³ Universidad de las Américas, Facultad de Arquitectura, Calle Queri, Quito, Ecuador

⁴ Nobatek, 67 rue de Mirambeau, 64600 Anglet, France

⁵ University of Bordeaux, ISM, UMR 5255, 351 Cours de la Libération, 33400 Talence, France

Keywords: Sustainable neighborhood; life cycle analysis (LCA), sustainable urban planning, decision support tool, adaptation to Latin America

Abstract

Urban planners are facing a growing demand for high performance projects in terms of control and reduction of environmental impacts. However, the complex and multi-dimensional concept of sustainable urban development often loses its core substance when confronted to practice realities of urban projects because of a lack of adapted decision support tools. The question arises as to how the effective consideration of the environment and the limitation of the project impacts can be taken into account as soon as the early design stages? As an answer to this question, we developed NEST (Neighborhood Evaluation for Sustainable Territories), a life cycle assessment (LCA) tool for the built environment at the neighborhood scale. LCA has been increasingly used to assess the environmental impacts of construction products and buildings during the last 25 years. And today, a new trend stems in the application of LCA to larger systems such as urban islets or neighborhoods. NEST addresses early design stages, and uses 3D models of neighborhood projects to quantitatively assess a set of environmental impacts. In this paper we propose a presentation of the tool, and an application through the case study of a new development project for a peri-urban area. Moreover we analyze the opportunity and the requirements for the adaptation of the tool, initially developed in Europe, under the context of Latin America, whether it is for the availability of data and for the coherence with specific challenges and political objectives in the area of South America.

1. Introduction

More than fifty percent of the world population (2011) lives in urban areas [1] and the built environment, referring to the building and transportation sectors, is a major hotspot of resource use and environmental impacts. For instance it accounts for 62% of global final energy consumption (2009) [2] and 55% of greenhouse gas emissions (2004) [3]. In industrialized countries, buildings are responsible for 42% final energy consumption, 35% greenhouse gas emissions and more than 50% of all extracted materials [4].

In this general context, urban planners are facing a clear demand for projects of higher environmental performance from both public and private sectors. This environmental performance and associated environmental impacts are related to numerous interconnected issues such as: resources consumption, waste production, water consumption, greenhouse gases emissions, biodiversity protection, air quality, etc. The neighborhood scale appears to be relevant to address most of these issues [5]. It is a typical operational scale for urban development projects and integrates key levers for urban eco-design. Indeed, this focus on the neighborhood scale is driven by the need to address district scale levers to design buildings and neighborhoods of higher environmental performance and to address key issues such as bioclimatic design, shared equipment (e.g. district heating), urban density or mobility issues. For instance, decisions made at the settlement level (orientation, compactness, urban density) largely affect heating / cooling loads, a major contributor to the energy balance of an urban area. [6] states that it seems more likely that the environmental and energy concerns that nowadays focus mainly on buildings will soon be transferred to neighborhood planning.

As an answer to this growing interest for sustainability investigation and planning at the neighborhood scale, we developed NEST (Neighborhood Evaluation for Sustainable Territories): a tool based on life cycle assessment (LCA) for quantitative assessment of environmental impacts of urban project.

NEST has been designed taking into account the operational practice of urban design and to be used from the sketch stage of a project. Based on the 3D model of a development project, NEST assesses a set of indicators reflecting major environmental issues in sustainable urban design. NEST calculates LCA indicators as well as more classical urban sustainability indicators in order to provide a broad and quantitative assessment of the environmental performance of neighborhood projects. All indicators are expressed per user to facilitate comparison of alternative scenarios (a neighborhood user is either an inhabitant or a non-resident worker).

NEST has already been applied on several urban planning operations in France and has proven its ability to enhance the design process by allowing a continuous analysis of the project environmental performance with a life cycle perspective [7]. In the context of Latin America the use of NEST may also be of great interest, however its application faces two major difficulties:

- Data integrated in the tools are originated from Europe and specific key data has to be adapted. This is a technical issue but it is complicated by the lack of LCA data for South America.
- Regional issues and challenges for cities are different from Europe and these different stakes need to be integrated in the approach if indicators can be produced to evaluate them

3 Case study

NEST was experimented in several urban projects in France, allowing for its validation regarding its ability to start and feed the discussions on sustainability between project stakeholders (urban planner, developer, mayor, technicians, etc.). For instance, it enables a quick and broad comparison of scenarios for urban planners to improve their proposal. This type of analysis has been conducted together with a design team on a new development project for a peri-urban area located in the southern France area “Pyrénées Atlantiques”. The aim of the study was to investigate to which extent environmental impacts of an environmental-friendly scenario (sc.0) differ from those of a business as usual scenario (sc.1) (Fig. 1).



Figure 1: (left) scenario 0, (right) scenario 1

The project aims at creating a new neighborhood (1.73 ha) close to the center of a small community located 10 km away from the main agglomeration. The population carrying capacity of the site was set to 350 users; this information is critical for the impacts calculation and emphasizes the importance of density in an urban project. There is also a target of functional mixity with a majority of housing but also some offices, shops and a school.

Two scenarios were established with the design team: one with a stronger investment on sustainability and higher density (sc.0) and another more representative of “business as usual” planning approaches in this area (sc.1) with more individual houses. Both scenarios respond to the same initial program (regarding equipment, parks, roads, parking and housing) but in different ways, leading to different impacts, quality of life, usage and technical answers.

Sc.0 is more interesting from an environmental point of view. The master plan is based on integrated urban gardens, pedestrian areas, smaller roads for cars, fewer parking spaces per dwelling, vegetated parks, deeper functional mixity (more offices and shops). All buildings are energy efficient (45 kWh/m²/year), most of them include solar energy production (PV and thermal). Regarding soil sealing and storm water management, there are large areas of green spaces and green roofs. All buildings have dedicated spaces for waste “at source recycling”, local bicycles shelters, and are equipped with water consumption reduction systems. Grey water reuse is considered in some buildings. Sc.0 has a capacity of 386 users (75% inhabitants and 25% non-resident workers).

Sc.1 has a lower density with more individual houses. There are more mineralized surfaces and more parking lots per user. Buildings energy performance is lower (corresponding to the French RT2012 standard criteria). There is no renewable energy production and no green roofs. Sc.1 has a lower capacity of 291 users (67% inhabitants and 33% non-resident workers).

Both scenarios have the same population distribution that is representative of a long term trend in the area of the project with 45% active people, 25% children and students and 30% retired people.

Due to the fact that the nearest town is located 10 km away and that public transportation services are insufficient, both mobility scenarios are largely based on individual vehicles. However, sc.0 gives more importance to cycling and walking with dedicated facilities. Mobility scenarios are specified for different types of users; at the level of the whole community of users, scenarios are detailed below (Table 1).

Scenario	Car	Bus	Cycling	Walking
0	71%	5%	6%	19%
1	79%	5%	2%	14%

Table 1: mobility scenarios

Both projects were modeled in NEST, which means 3D modeling (Fig. 1) and input of scenario characteristics, in order to evaluate their impacts. Main results for each indicator are presented in the following section.

4 Results

4.1 Primary energy consumption (Fig. 2)

The total level of primary energy consumption of sc.1 (33 000 MJpe/year/user) is 36% higher than for sc.0 (24 300 MJpe/year/user). In sc.0 buildings operation, building materials and individual transportation respectively account for, 37%, 26% and 33% of primary energy consumption. Even if buildings operation remains the main contributor, the strategy towards density, high performance buildings and renewable energy production leads to 85% less impact (9 100 MJpe/year/user) than sc.1 (16 900 MJpe/year/user). It is also interesting to note the really high contribution of individual transportation due to the fact that the project is located 10 km away from the main employment and services area. We also observe the impact of a neighborhood facilitating walking and cycling with 10% less impact from individual transportation in sc.0.

Scenario 0 - Primary Energy / year / user (MJ)			Scenario 1 - Primary Energy / year / user (MJ)		
Category	Primary Energy	%	Category	Primary Energy	%
Building Materials	6 302	26%	Building Materials	6 068	18%
Building Operation	9 064	37%	Building Operation	16 921	51%
Infrastructure Materials	553	2%	Infrastructure Materials	863	3%
Individual transport	8 092	33%	Individual transport	8 891	27%
Collective Transport	282	1%	Collective Transport	282	1%
TOTAL	24 293	100%	TOTAL	33 025	100%

Figure 2: (left) primary energy consumption (sc.0); (right) primary energy consumption (sc. 1)

4.2. Climate change (Fig. 3)

With 1430 kgeqCO₂/year/user, sc.1 shows a 31% increase compared to sc.0. For both scenarios, individual transport is the most impacting contributor to this indicator with around 43% of the emissions in sc.0 and 36% of emissions in sc.1. This point is well representative of the importance of transport on the environmental performance of a project. If the site is in a rural or peri-urban area, the impact of transport might counterbalance the sustainability efforts realized at the scale of buildings, roads and other project elements. In sc.0, due to highly energy efficient buildings, the second contributor is building materials (30%) whereas in sc.1 it is buildings operation (34%). This distribution and difference between energy and Climate Change indicators is mainly explained by the 10 km distance between the site and the main

economic area, and by the fact that electricity use is a low generator of CO₂ in France (for energy consumption in buildings).

Scenario 0 - CO ₂ / year / user (KgEq)			Scenario 1 - CO ₂ / year / user (KgEq)		
Category	Primary Energy	%	Category	Primary Energy	%
Building Materials	327	30%	Building Materials	317	22%
Building Operation	221	20%	Building Operation	491	34%
Infrastructure Materials	55	5%	Infrastructure Materials	86	6%
Individual transport	470	43%	Individual transport	517	36%
Collective Transport	17	2%	Collective Transport	17	1%
TOTAL	1 090	100%	TOTAL	1 428	100%

Figure 3: (left) climate change indicator (sc.0); (right) climate change indicator (sc. 1)

4.3. Other indicators

In order to assess the impact of land conversion on biodiversity, the initial land occupation is characterized as follow: 50% artificial, 30% agricultural, 10% urban and 10% vacant green land. The score of biodiversity loss related to land use is 33% higher for sc.1 (88 PDF/y/user vs. 67 PDF/y/user for sc.0) because of higher areas of mineralized public spaces and less areas of gardens. For both scenarios, the score of biodiversity loss related to land conversion is negative (-6 PDF/year/user for sc.0, -9 PDF/year/user for sc.1) which means that through land conversion, the development brings biodiversity potential.

Both scenarios have a similar total waste production of about 4.5 t/year/user (87% comes from construction works). In sc.0 all buildings have a dedicated area for recycling and organic waste composters. Furthermore a specific “low waste agreement” for construction works is mandatory for all buildings to be contracted. These measures lead to 42% less non sortable waste for sc.0 than for sc.1.

Air pollution is essentially tied to individual transport (about 95% for both scenarios).

In sc.0 strategies like water saving systems or recovery and treatment of drinking water and rainwater, leads to a quite low level of drinking water consumption (35 m³/y/user) and a significant use of non-potable water (34% of total water consumption). Sc.1. is less engaged in terms of limitation of water consumption with 87 m³/y/user of drinking water only. Regarding storm water management, there is still more to do to manage rain water infiltration through the choice of pavement materials (65% runoff for sc.0 and 73% runoff in sc.1).

Both scenarios show good results in terms of m² of housing and green spaces per user. Sc.1 is better in terms of parking availability but sc.0 is better in terms of transportation offer (with dedicated facilities for cycling and walking). In terms of accessibility to services both scenarios are similarly handicapped by the distance to the agglomeration and the fact that all services cannot be secured within the neighborhood.

5 Discussion

Our analysis allowed visualizing two alternatives based on two different urban principles and demonstrated the interest of such quantitative assessment. Sustainability is a complex matter for urban planning and quantitative assessment of environmental impacts in line with urban planning practice makes it more tangible and realistic to address.

In comparison with sc.1, the neighborhood user (inhabitant or non-resident worker) in sc.0 is clearly less energy consumer (-36%), emits less greenhouse gases (-31%), generates less non sortable waste (-42%), and consumes less drinking water (-65%). It is also important to note that the neighborhood includes more comfortable buildings and hosts more people; 24% more users and 32% more inhabitants than in sc.1 (the “baseline scenario”). Furthermore in

sc.1, the low density model impeded reaching the 350 users target and the number of users is 291 only.

Cost analysis is also a critical part of the assessment and may generate contrast with the environmental assessment. For now, NEST only accounts for an estimate of construction costs and some operation costs and requires further research to shift to an overall view of the project lifecycle economics.

At a more general level, this case study highlighted the relevance of an evaluation process for the early stage of urban project design. The tool enables the quantification of a number of environmental impacts indicators, some of which are LCA indicators. This quantification relies on a simplified LCA methodology (i.e. meta-analysis of LCAs of neighborhood components) which is appropriate for early stage assessment in a project. Indeed this methodology is aligned with the data availability at the master planning stage of an urban development project.

NEST analysis revealed comparable contributions of building materials, building operation and transportation to both life cycle primary energy consumption and life cycle greenhouse gases emissions. These individual contributions in both scenarios and for both indicators range from 20% to 50%. The compared analysis of the two scenarios permitted to highlight major differences between scenarios such as the fact that in the sustainable scenario the predominance of the operation phase is lessened, or the fact that the buildings embodied energy in the sustainable scenario is higher than in the business as usual scenario.

NEST tool allows for a new approach of knowledge-based design for urban planning. This evaluation proved to be really complementary to the planner's design skills and was a powerful mean to emphasize the dialogue about sustainability and particularly environmental performance between the design team, engineers and the local city.

6 Requirements for an application to Ecuador and Latin America

The use of NEST in a new regional environment means that some adaptation has to be realized to consider two important issues:

- LCA data is geographically specific; it means for example that data corresponding to a production in France will not be pertinent for an analysis realized in another country because processes are different. This is the case for example of the energy production processes. Other data are on the contrary not strongly dependent of the region; this is the case for example of global products and processes like the use of cars.
- Indicators have to correspond to both global and local environmental stakes, and need to reflect also local societal challenges that may differ from one world region to another. For example urban security and poverty mitigation are key stakes in Latin America whereas they are not priority considerations in urban projects in France.

6.1 Background data adaptation

Key data has to be reconsidered in order to insure a proper assessment. This is especially the case for energy data that is very sensitive to national energy production infrastructures and that is integrated in many other data sets. This modification will impact directly on the energy (considering energy efficiency of the energy production system) and greenhouse gas emissions indicators. Data about energy consumption and production is not available for specific countries like Ecuador but it is on a regional Latin American scale. This data can be used as a first estimation. However, considering the specificity of a country like Ecuador that develop a particularly high capacity of hydroelectricity production, it will be much more pertinent for a proper analysis of urban projects to develop a specific data set corresponding to

the energy mix of each country. Such development is possible as the background data is available and pertinent at global scale in this case.

Another key data to be adapted is the set corresponding to building construction. In this case NEST calculation is based on a database developed by Nobatek from a statistical approach of numerous LCA of buildings realized in France. This data has to be replaced either by a generic data about building construction available at global scale within the Eco Invent database, or, better, by a specific data to be created through the realization of LCA of representative buildings in Ecuador. This last option is possible as the core data for this exercise (traditional building materials and processes) are available either for Latin America or at global scale.

The other indicators are much less sensitive to geography and could be applied directly.

6.2 Local indicators corresponding to local challenges

Beyond the urban planning theories and sustainability principles that founded the initial choice and development of indicators [8], the adaptation of NEST to Latin America implies to consider local perspective in terms of challenges and threats for the cities in this area. A first approach of this indicators' construction work is based on the following multi scale societal and political inputs:

- Global scale: the UNO adopted in 2016 a set of world objectives, called sustainable development goals for 2030 [13], that are considered as prime importance in Latin America. Goal number 11 is dedicated to cities, looking for “making cities inclusive, safe, resilient and sustainable”. It includes the following considerations
 - access to housing, services and transport
 - participatory, integrated and sustainable human settlement planning
 - heritage protection
 - protection from disasters
 - impact of cities (i.e. air quality and waste management)
 - access to green and public spaces
 - links between urban, peri-urban and rural areas
 - integrated policies towards inclusion, resource efficiency, mitigation and adaptation to climate change, and resilience to disasters
 - building sustainable and resilient buildings utilizing local materials
- Latin America scale: a private initiative from the company Siemens with a great number of large Latin American cities [14] has lead in 2010 to the definition of an index for green cities in Latin America. It takes into account the following issues:
 - Energy and CO2 emissions
 - Buildings and land use
 - Transport efficiency
 - Waste
 - Water
 - Sanitation
 - Air quality
 - Sustainability governance
- Country scale, the example of Ecuador: the Ecuadorian government settled through its “Plan nacional del buen vivir” [15] for the period 2013-2017 a large set of objectives, stakes and policy orientations. For the sustainability in cities, it includes:
 - Access to a safe and inclusive habitat (3.8 and 3.9); it integrates with more details:
 - Heritage conservation and refurbishment
 - Participatory process for decision making in urban planning

- Urban model integrating sustainability and quality of life
- Housing for people suffering handicap
- Safe and sure housing
- Use of natural resources for construction and alternative energy production
- Housing quality
- Housing deterioration prevention
- Access to water and sanitation services (3.10)
- Meeting and public spaces (5)
 - Spaces for physical activity promoting health
 - Public spaces free of pollution
 - Priority to walking and cycling in urban planning
 - Support to urban regeneration
- Deficiency and renewable energy (7.7)
- Mitigation and adaptation to climate change (7.10)
- City scale, the example of Quito: the Quito metropolitan district defined in 2014 a set of indicators [16] to follow the efficiency of its policy in terms of sustainable city. These indicators include the following considerations for the urban environment:
 - Energy and CO₂
 - Land use
 - Transport
 - Waste management
 - Water
 - Sanitation
 - Air quality
 - Urban agriculture
 - Ecological footprint

From this global analysis we see logically that several issues cannot be integrated in the evaluation provided by an LCA approach as it is not directly correlated to the neighborhood project scenario (which is what is evaluated by NEST) but to the process of urban planning: for example governance participatory issues. Beyond these process aspects, we can detect several potential improvements in the NEST indicator set that could help the tool to be more pertinent within the context of Latin America and more especially Ecuador. For example the promotion of alternative transport like walking and bicycling is considered as a mean (for air quality improvement, energy consumption reduction and CO₂ emissions reduction) and not as an objective itself, like it could be for public space occupation quality or for health reasons. Another example is urban agriculture that is considered in the land use calculation but not as an objective itself, it could be easily integrated.

A large improvement potential and adaptation need is in the social aspect, with issues correlated to accessibility and inclusion. Such issues correlated to social science would require integrating works from social LCA approach, which is an interesting perspective for future developments. Lastly, resilience, risk management and safety are today not directly considered in LCA tools and here also the social LCA science may be a new field of sourcing for solutions for NEST to integrate such issues in its evaluation.

7 Conclusion

NEST development was based on two observations: (i) urban planners lack resources to take into account the environmental impacts of their projects early enough and, (ii) urban sustainability cannot be addressed through a monocriteria optimization approach (e.g.

building energy efficiency) and requires a multicriteria approach enabled by a quantitative-based decision support tool.

The scientific and practical interest of such life cycle assessment is twofold. On the one hand it enables the comparison of a neighborhood's main contributors to life cycle environmental impacts. On the other hand, and through scenario comparison, it enables to put in perspective the relative effects of some environmentally friendly design choices compared with the overall impacts in a specific impact category.

NEST current version has already been used on several projects and has proven its effectiveness. However, to help urban planners make the best compromises between various sustainability dimensions, some new developments are in progress. Among others we are working on taking into account urban microclimate (solar radiation, natural light, wind, etc.) as design inputs.

Another development approach is, as discussed in this document, the adaptation of NEST to other geographical areas. First work has been realized to adapt it to other European countries; it is now proposed to develop NEST applicability to the case of Latin America and more especially Ecuador. The assessment presented in this document is a first step to define a new set of indicators that could be compatible with NEST approach (quantitative analysis and short panel of indicators for an efficient communication) and integrator of the most recent environmental and societal stakes in Latin America.

References

- [1] United Nations Department of Economic and Social Affairs, “*Population, Development and the Environment 2013*,” 2013. ISBN: 9789211515091.
- [2] IEA, *World Energy Outlook 2011*. IEA Publications, 9 rue de la Fédération, 75739 Paris Cedex 15, 2011
- [3] B. Metz, O. Davidson, P. Bosch, R. Dave, and L. Meyer, *Contribution of Working Group III to the Fourth Assessment Report of the Intergovernmental Panel on Climate Change*. Cambridge: Cambridge University Press, 2007. ISBN: 978-0-521-88011-4.
- [4] European Commission, “*Roadmap to a Resource Efficient Europe*,” Brussels, 2011.
- [5] C. Charlot-Valdieu and P. Outrequin, *Concevoir et évaluer un projet d'éco-quartier: avec le référentiel INDI.*, Editions du Moniteur, Paris, 2012. ISBN: 2-281-19499-X.
- [6] J. Oliver-Solà, A. Josa, A. P. Arena, X. Gabarrell, and J. Rieradevall, “*The GWP-Chart: An environmental tool for guiding urban planning processes. Application to concrete sidewalks*,” *Cities*, vol. 28, no. 3, pp. 245–250, Jun. 2011
- [7] M. Lotteau, G. Yopez, N. Salmon 2015, “*Environmental assessment of sustainable neighborhood projects through NEST, a decision support tool for early stage urban planning*” *Procedia Engineering*, Volume 115, Pages 69-76, 2015,
- [8] G. Yopez-salmon, “*Construction d'un outil d'évaluation environnementale des écoquartiers : vers une méthode systémique de mise en œuvre de la ville durable*,” Université Bordeaux 1, 2011.
- [9] T. Ramesh, R. Prakash, and K. K. Shukla, “*Life Cycle Energy Analysis of a Multifamily Residential House: A Case Study in Indian Context*,” *Open J. Energy Effic.*, vol. 2, no. March, pp. 34–41, 2013

- [10] J. B. Guinée, M. Gorrée, R. Heijungs, G. Huppes, R. Kleijn, A. de Koning, L. van Oers, A. W. Sleswijk, S. Suh, H. A. U. de Hae, H. de Bruijn, R. van Duin, and M. A. J. Huijbregts, *Handbook on Life Cycle Assessment. Operational Guide to the ISO Standards*. Dordrecht: Kluwer Academic Publishers, 2002.
- [11] M. Goedkoop and R. Spriensma, “*The Eco-indicator99: a damage oriented method for life cycle impact assessment: methodology report*,” Amersfoort, 2000. ISBN: 9072130774.
- [12] AFNOR, Norme NF P01-010, *Qualité environnementale des produits de construction*, AFNOR Editions. La Plaine Saint-Denis, 2004.
- [13] United Nations sustainable development goals, www.un.org/sustainabledevelopment
- [14] Economist intelligence unit, Siemens, “Indice de ciudades verdes de America Latina”, 2010
- [15] Secretaria Nacional de Planificación y Desarrollo del Ecuador, “*Plan nacional del buen vivir 2013-2017*”, 2014
- [16] Distrito Metropolitano de Quito, J.C. Baca, D. Enriquez, N. Narvaez, D. Salvador, “*Indicadores de ciudad sostenible*”, 2014

Object-Oriented Approach to Urban Canyon Analysis

Timofey E. Samsonov¹, Pavel I. Konstantinov², Mikhail I. Varentsov²

¹Department of Cartography and Geoinformatics, Faculty of Geography, Lomonosov MSU, Moscow, Russia, Leninskiye Gory 1, 119234
e-mail: tsamsonov@geogr.msu.ru

²Department of Meteorology and Climatology, Faculty of Geography, Lomonosov MSU, Moscow, Russia, Leninskiye Gory 1, 119234
e-mail: kostadini@mail.ru, mvar91@gmail.com

Keywords: urban canyon; urban climate; spatial analysis, object-oriented analysis, meteorological modeling.

Abstract. *The study applies object-oriented analysis to the extraction of urban canyons and introduces the concept of directed urban canyon which is then being experimentally applied in urban meteorological modelling. Summary of current approaches for describing urban canyon geometry is provided. Then a new theoretical approach to canyon delineation and three-level hierarchical classification is presented. The study discloses an original methodology based on triangular irregular network (TIN) designed to allow extraction of directed and undirected urban canyons from cartographic data and estimation of their geometric characteristics. Obtained geometric properties of canyons are coupled with land use data into the database, which is then applied in micro-to-local scale temperature and wind modelling.*

1 Introduction

A theory of urban canyons has been originally developed by Oke (Nunez & Oke 1977, Oke 1987) in the second part of XX century. According to this theory, an urban canyon is a three-dimensional space between buildings with two boards (building walls) and a bottom (the road). The main canyon parameters are its height H and width W , which together define height/width ratio that is being widely used in urban climate modeling. In some cases, canyon length L of the canyon and its azimuthal direction (orientation) θ are also being used. Figure 1 illustrates these characteristics. Short-term dependencies between the meteorological regime of urban canyons and their characteristics are significantly less investigated than their climatic properties. Almost all the existing models of the urban boundary layer consider canyons as one of the numerous land cover types, like parks or water bodies (Kusaka et al. 2001, Martilli et al. 2002). Dynamic models such as WRF (Shamarock et al. 2008) include urban block that can assimilate one fixed direction of an urban canyon (Kusaka et al. 2001).

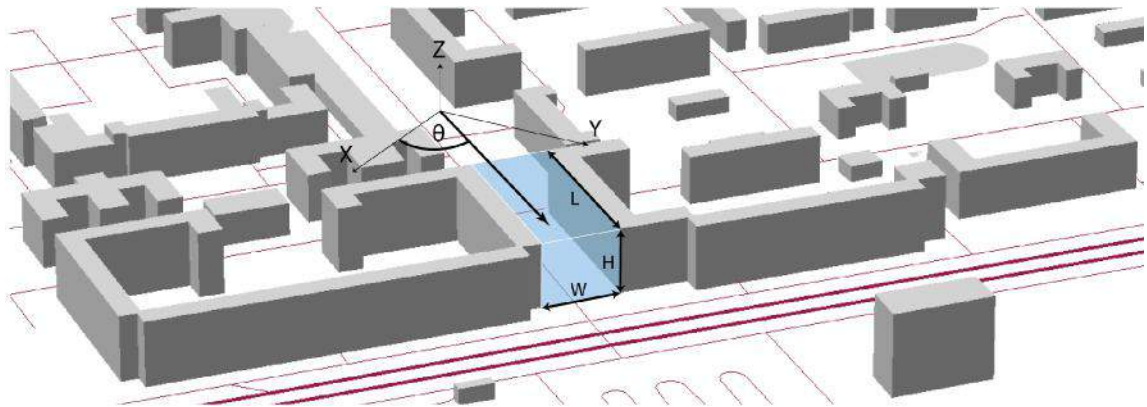


Figure 1: Urban canyon and its parameters. W — width, H — height, L — length, θ — direction

However, this approach is suitable for the cities with regular built-up layout and one prevailing canyon direction only. Masson (2000) developed a reductive scheme of thermal balance calculation for urban areas with more chaotic structure by integrating all possible canyon directions. This scheme was implemented as urban block in COSMO_CLM meteorological model (Trusilova et al. 2013). Inclusion of specialised urban module results in more detailed urban weather and climate forecasts. However, for some large cities like Moscow, Russia with radial-circular street layout prevailing, or Tokyo with its irregular street network, coarse canyon descriptions are correct for modeling average daily characteristics only and, consequently, for climatic predictions (Kislov & Konstantinov 2011).

Short-term prediction of diurnal variation of meteorological parameters needs detailed description of urban environment. This description can be effectively derived from spatial data such as spatial databases (Lindberg 2007, Gal & Unger 2014) and remote sensing imagery (Moran 2010, Peeters & Etzion 2010, Pu et al. 2011). During the last two decades, significant progress has been achieved in development of supporting methods based on Geographical Information Systems (GIS). A wide array of urban geometric characteristics (Burian et al. 2002) can be derived and used in various tasks including meteorological modeling (Gal et al. 2008), architecture planning (Kropf 1996) and even robots' navigation (Hrabar et al. 2005).

The main investigated geometric characteristics of an urban environment include canyon height/width ratio, sky view factor (percentage of visible sky from the point, abbreviated as SVF, see (Johnson & Watson 1984)) and frontal area index (the ratio between area of the walls visible from a particular direction, to the area of the cell on which these buildings are located, see (Raupach 1992)). Various algorithms are designed for calculation of these parameters, and results are used for urban climate investigations. Ratti et al. (2006) proposed a raster algorithm to estimate canyon height/width

ratio. Unger (2009) revealed the connection between urban heat island and sky view factor using 3D Urban Database. Wong et al. (2011) calculated a frontal index and estimated urban ventilation from cartographic databases in various azimuthal directions. Chen & Ng (2011) used cartographic databases for SVF and frontal area density calculation, classified them to derive thermal load map and wind dynamic map respectively, and finally produced climatic map classes.

Urban geometry characteristics are usually calculated for *one point*, thus characterising particular location in urban space. Raster-based approach often helps to solve such tasks. If urban *digital elevation model* (DEM) is used for calculation, then height/width ratio or sky view factor are calculated for each raster cell using focal analysis (Ratti et al. 2006, G'al & Unger 2014). The frontal area index, which is an integral value over some area, is also calculated by regular grid tessellation of the city (Wong et al. 2011).

At the same time, a large demand in characterization of an urban environment coming from architects, planners and meteorologists has lead to the emergence of such an interdisciplinary field as *urban morphology* (Moudon 1997), which suggests the city to be described in terms of its physical form. In urban morphology approach the city is decomposed into three major elements: buildings, plots and streets, while four levels of detail are possible in investigation: building/plot, street level, city and regional levels. Various classifications are developed to decompose city structure (Kropf 1996, Osmond 2010, Oliveira 2013). Kropf (1996) developed the concepts of specificity level, resolution level and outline/external form in urban morphology analysis. Bohm (1998) introduced the urban structural unit idea, which was lately evolved by Osmond (2010), who, in turn, introduced the hierarchy of inbuilt spaces such as parks. Recently Oliveira (2013) proposed the *morpho* approach to assess the urban form. His methodology considers only physical properties of an urban form and includes a limited number of characteristics that are used to estimate the degree of *urbanity*. It included estimation of accessibility, density and divergence of urban elements. One of the major parts of this study was related to the calculation of parameters of street networks and centerlines based on works of Hillier et al. (2010) and Turner (2007).

From this summary we can differentiate between two alternative approaches to investigation of urban environment. Urban climate researchers are interested in local or continuously distributed characteristics. Urban morphologists study the city as a structure of discrete geometric objects, each having its functional properties. The intersection of both approaches leads us naturally to the definition of urban canyon. It also gives raise to the urban canyon investigation from a new point of view, which is in between local point-wise calculations, and those averaged over some abstract area, representing the level of analysis of the canyon itself. Such investigations require a methodological framework to the definition, extraction and description of canyons as geometric elements of urban environment with the focus on meteorological applications. By using this integrated approach we will be able to make assumptions like "this particular canyon has high h/w ratio and this one has low value". Or "this chain of canyons is long and stable in direction and is subject to wind acceleration". Because each canyon is analysed as a separate object, we should call this approach *object-oriented*.

In this paper we present main theoretical principles and some methods that can be applied for object-oriented urban canyon analysis in terms of meteorological applications. We offer a classification of canyons in two types: directed and undirected, and also the following classification scheme for buildings in terms of canyon type they form based on topological relationships. A three-level hierarchy of the canyons based on their spatial extent and relationship with road network is introduced. Canyons are geometrically delineated using vector database whereas their geometric properties are calculated using triangulation. These properties can then be averaged across individual canyons or over some area (i.e. model cell). Results obtained for Moscow city are then statistically assessed and analysed. Using this methodology a multi-scale database containing combined information on general urban canyon characteristics and land cover distribution has been developed.

2 Methodology

Object-oriented analysis of canyons is based on the assumption that canyons are physical spaces that can be extracted as geometric volumes with particular shape. Local geometry of an urban canyon is mainly defined by the distance between buildings and their height. Canyon azimuthal orientation (direction) also plays an important role. It influences diffusion, advection and wind velocity. In classic theory, a canyon describes the relationship between each pair of buildings. Every new pair composes a new canyon. However, when neighboring canyons have common longitudinal axis, it can result in the wind acceleration or blocking effects.

This leads us to the natural conjecture that such canyons can be chained into one lengthy volume called directed canyon. We can say that the length L of a directed canyon is much larger than its width W : $L \gg W$. It also should have constant or gradually changing direction. In most cases directed canyons are formed by street network, thus the edges of a street network can be considered as the axes of directed canyons. All other spaces between buildings, which are not crossed by street network are formally considered to be undirected canyons in our theory.

We offer the following classification of canyon levels that can be used for modeling of land-atmosphere interactions at different scales. It has strong connections with standard scales of urban climatology:

1. *Micro-canyons*. The basic level, at which limits of each canyon are defined by each pair of buildings (a "pure" classic canyon). Micro canyon extraction does not differentiate between directed and undirected canyons. This level of canyon is atomic and should be used for *microclimate* tasks such as investigation of canyon energy balance, building energy use or estimation of thermal comfort conditions. Information about micro-canyons will be useful (as usual) in detailed TEB-models. Architects can find micro-level useful for finding an optimal placement and geometric parameters of individual buildings in the surrounding context. The typical linear scale of micro-canyons is tens of meters.
2. *Meso-canyons*. Intermediate level which is defined as the chain of micro-canyons between two crossroads. Long meso-canyons can be subdivided into sections having homogeneous built-up (the same construction materials, number of floors etc.). This level is atomic to the city's directed canyons network and should be used for modeling *local and meso-scale* atmospheric processes. Possible applications include urban weather forecasts and estimation of the urban energy balance (UEB). In general, now it is clear that urban meteorological modelling is developing in direction of scale enlargement and information about directed canyons is essential for validation and usage of these models as boundary conditions for horizontal advection equation. The typical linear scale of meso-canyons is hundreds of meters.
3. *Macro-canyons*. Global level, at which canyons are identified by road network strokes. The concept of strokes has been developed by Thomson & Richardson (1999) for street network generalization and is based on the "good continuation" principle. This principle means that network edges that join at one point with small deviation angle, can be merged into one lengthy stroke. This is the chain of meso-canyons. Macro canyon level can be used for some specific tasks such as analysis of main city ventilation corridors. Obtaining detailed information about macro-canyons can be useful also for extreme wind events prediction in city. Because this type of meteorological forecasts is quite important for urban infrastructure, specialised meso-scale wind models can be developed in the future. The same holds for meso-canyons. Typical size of macro-canyons in large cities varies from hundreds of meters to kilometres.

The list of spatial data needed for canyon extraction includes:

1. Geometry of individual building footprints
2. Heights of buildings
3. Linear street network (for derivation of directed canyons)
4. Land cover polygons (for exclusion of spaces that cannot be attributed to canyons, e.g. forest areas).

In case when canyons should be extracted with true bottom surface city DEM is also required. In turn, a true 3D description would also demand for full 3D geometry of buildings. We will describe 2D case where the bottom of every canyon is considered flat and every building is virtually extruded to its height and is considered to be a prism. All calculations are based on these assumptions.

The resulting methodology of object-oriented canyon analysis consists of the following stages (Samsonov et al., 2015):

1. Extract canyons and classify them into directed and undirected. Classify buildings according to their topological relationships with the two types of canyons stated above.
2. Extract canyons' hierarchy for canyon-based analysis.
3. Estimate canyon local and average height, width and their ratio.
4. Estimate modal directions of directed canyons.

The canyon is a space between buildings (Oke 1987). Our approach follows this statement straightforwardly. To cover the space between neighboring buildings we need to connect their corners and walls by some space tessellation. In 2D case, where each building is represented by its polygonal footprint, this task can be simply solved by constructing a TIN (de Berg et al. 2008) which includes the vertices and polygon edges as its elements. Only triangles outside of the buildings should be considered. We also assume that canyon can be formed not only by a pair of buildings, but by a pair of one building and tall vegetation polygon too.

Based on this approach, the following GIS-based methodology for extraction and classification of urban canyons has been developed:

1. Triangulate the vertices and edges of building polygons and polygons of tall vegetation (forests), which can also form canyons with buildings. Constrained Delaunay triangulation allows preserving existing edges.
2. Use spatial query to reject the triangles inside the buildings and forested areas.
3. Select triangles that have at least one vertex belonging to the building (two others can belong to the forest). Attribute them as being canyons.
4. Select canyon triangles intersected by street network. Attribute them as elements of directed canyons.
5. Invert canyon triangles selection and attribute resulting triangles as elements of undirected canyons.

If needed, forested areas can be simply excluded from canyon extraction by excluding triangles that connect buildings and forest polygons.

As canyons are produced by the building environment, all buildings can be classified in terms of the type of the canyon they form. Four cases are possible based on topological relationship *touches* (Egenhofer & Franzosa 1991).

- directed (*touches* directed canyons & *not touches* undirected canyons);
- undirected (*touches* undirected canyons & *not touches* directed canyons)
- directed and undirected (*touches* both types of canyons);
- no canyon (*not touched* by any canyon).

An example of canyon areas extraction and building classification is presented in Figure 2. Note that this classification does not include the "classic" individual canyons which are defined by 1:1 relationship between each pair of buildings, but rather *the spaces occupied by canyons*. Next, the hierarchy of canyon objects can be extracted.

Object-oriented analysis of canyon characteristics may deserve averaging them *per each canyon* and not per each modeling cell. This can be important not only for micro-scale meteorological modeling but also for urban morphology studies and their social and economic applications, such as thermal comfort conditions estimation (Konstantinov et al. 2014).

Extraction of canyon objects hierarchy introduced in the previous Theory section is illustrated in (Figure 3). At *micro* level every canyon is defined by the union of the triangles between each pair of the buildings. If we want to extract the *directed* canyon formed by current building, an algorithm should look for a building pair across the street network edge.

Spatial join operation should be applied to extract meso- and macro-canyons. First, every triangle is attributed with the identifier of network edge or stroke it belongs to (here we consider that every street is represented by one edge). Generally each triangle receives several identifiers, which would be true for triangles covering crossroads point. Crossroads triangles are excluded from meso-canyons. First and last crossroads triangles are also excluded from the macro-canyon. Finally the triangles with the common street identifiers are merged in order to get the area occupied by each particular canyon. Looking at Figure 3 one would infer that meso-canyon is limited by one street between crossroads, and macro canyon is formed by the chain of meso-canyons connected at crossroads.

The length L of directed canyon is then simply derived as the total length of the street network elements it covers. For micro level the corresponding part of the network edge should be used instead.

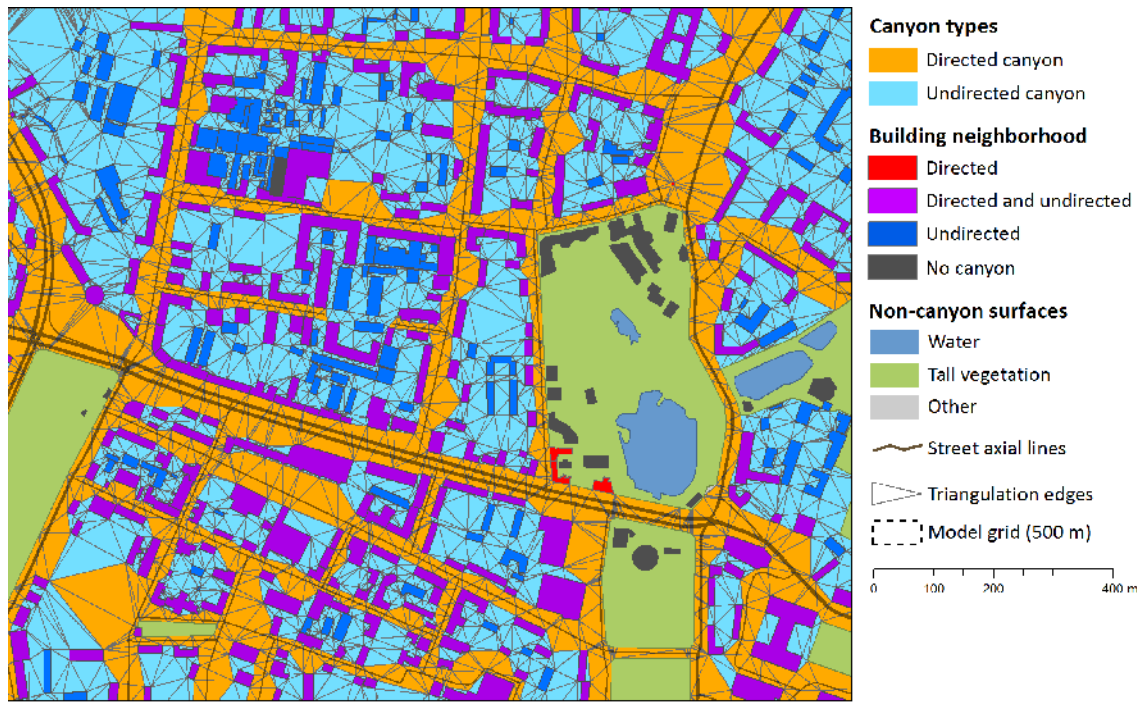


Figure 2: Types of canyons and canyon-producing buildings

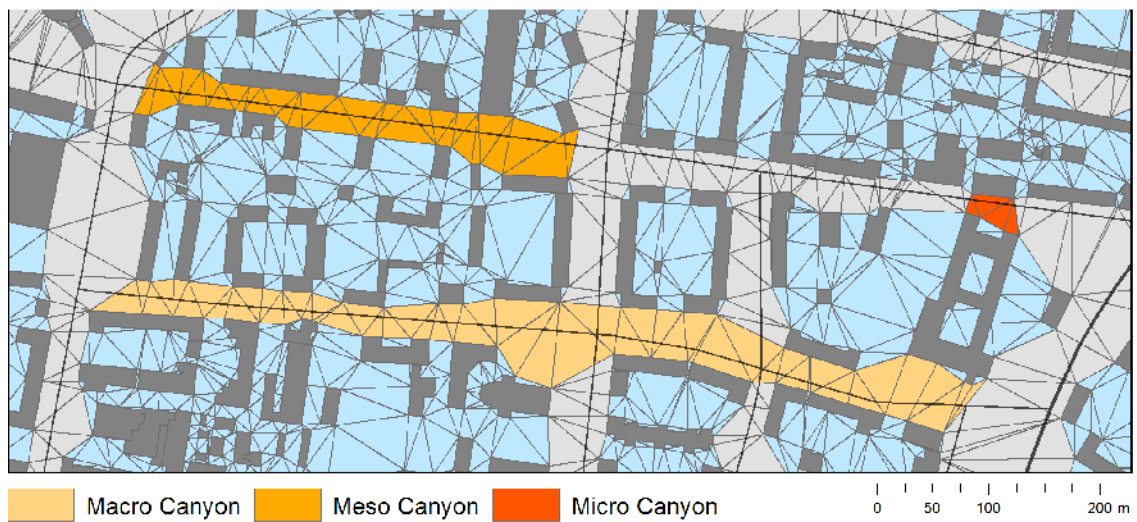


Figure 3: Hierarchy of directed canyons

4. Results

Various characteristics of canyons and land cover were calculated and included into the database that describes urban environment in Moscow, Russia for meteorological modeling purposes. The list of characteristics depends on the requirements of the input data for model. In our case data was prepared for URB_MOS model (Konstantinov et al. 2014). Derived database includes the information about land cover types ratios, urban canyon geometric characteristics discussed in this paper, average SVF and frontal area index for each cell, which were derived using well-known algorithms (G'al et al. 2008, Chen & Ng 2011).

Simple land cover classification used in the database includes the categories that can be easily extracted from the vector cartographic data: a) buildings, b) roads, c) green spaces, d) water, e) industrial, f) other. This classification scheme differs from traditional schemes like those used in (Grimmond & Souch 1994) and (Lemonsu et al. 2008) in a way that it does not include pervious/impervious surfaces and tall vegetation as types of land cover. It is more topographically than physically oriented. This is because cartographic data does not always include information about building and road materials, ground type in open spaces, and also is not sufficiently detailed in description of green spaces that could be mixture of forest, bushes and open grass. Better differentiation can be achieved by using remote sensing imagery. However, the scope of the current research is strictly limited to capabilities of cartographic data.

Data sources supporting this work include GIS Region Prof topographic Moscow database by Geocentre Consulting Ltd. SRTM90 and ASTER GDEM digital elevation models were also used at modeling stage. Land cover classification was performed in Esri ArcGIS for Desktop 10.1 software. Customised software for canyon extraction and description has been developed using Java programming language. Statistical assessment of geometric parameters was performed in R software. We derived three tables for $R = 1000, 500$ and 200 meters to allow sequential downscaling of the modeling process. The database is maintained in ArcGIS for Desktop 10.1 software.

For this section we focused on the most significant characteristics and their statistical assessment. This analysis include:

- (1) land cover distribution in "average" cell;
- (2) plan and frontal area index;
- (3) canyon height, width and h/w ratio;

OpenStreetMap data was used as the raw material for calculations. Geocentre Consulting building levels database was used to enrich building data for canyon height and h/w ratio calculation. Statistical analysis of the results was performed in R software and reflects only cells inside the Moscow Ring Automobile Road (known as MKAD in Russian), which borders the main body of the Moscow city.

Land cover types distribution reflects proportions in which various surfaces are mixed inside an average cell. Our observation revealed that land cover distribution does not depend on the cell size. An average modeling cell consists of water (3.4%), buildings (6.2%), industrial areas (10%), roads (12.8%), tall vegetation (18.9%), and other (nonclassified) surfaces (48.7%) which we conventionally attribute to natural (pervious) surfaces (Figure 11).

Considering results that are obtained from cartographic data we should mention the loss of information induced by generalization process. In urban environment the most intensive generalization concerns green spaces. Many areas of tall vegetation inside city plots and between buildings are missed from the data when compared to space images. Individual trees are omitted. Despite the fact that this error can be negligible in the scale of the big city, it can become significant in detailed micro-climate analysis. In such cases we recommend using satellite data for most precise estimation of vegetation area throughout the territory.

Plan area index map and its histogram are presented on Figures 5 and 6. We used 500 m grid resolution for map as it allows best compromise between readability and detail. Statistics on this and following geometric parameters were calculated only inside the cells that include at least one building. This was made to exclude the territories in which canyon effects are insignificant.

As can be seen, plan area index distribution has bimodal shape irrespective of grid resolution with one mode near zero value and another slightly larger than mean value. These modes have relatively equal frequencies with small values dominating more while grid resolution increases.

Frontal area index map is shown on Figure 7. Here we show the distributions inside

500 m cells for different azimuthal directions. The shape of the histogram (Figure 8) is also bimodal, however it is more wide and flattened. The scale dependence showed behavior similar to plan area index: small values become more dominating.

The main transversal characteristics of canyon are its width, height and h/w ratio. As proposed TIN-based methodology allows precise local estimation of these parameters, we firstly derived them "as is" and then compared results to the values averaged by grids of different resolutions. As in the case of plan and frontal area index, we excluded from our analysis the triangles that have zero building height (these can be triangles touching not attributed objects). Then the whole selection of triangles was used for estimation of mean values. The mean width of directed and undirected canyons equals to 45 and 38 meters accordingly. At the same time mean building height equals to 19.5 and 13 meters for buildings that comprise directed canyons and those that located inside city blocks and comprise only undirected canyons. The smaller height of the latter is mostly influenced by prevailing of infrastructural buildings such as kindergartens, transformer vaults and local stores.

The picture of canyon h/w ratio for 500 m resolution is presented on Figure 9. Statistical distribution of the values for 200, 500 and 1000 m resolutions is shown on Figure 10. In these figures we cut long tails containing outliers for better representation and set maximum value to 1.5. It can be seen that smaller grid sizes produce values that are statistically closer to the reference values obtained by averaging TIN triangles. Comparing to plan and frontal area indexes derived histograms have two distinct differences. At first, they have unimodal distribution with single mode close to the mean value. At second, it is clear that h/w ratio is much more sensitive to grid resolution than plan and frontal area indexes. As grid resolution increases, the excess becomes more significant. This fact shows that if the h/w ratio is included as one of the model parameters, it is more reliable in fine grid resolutions.

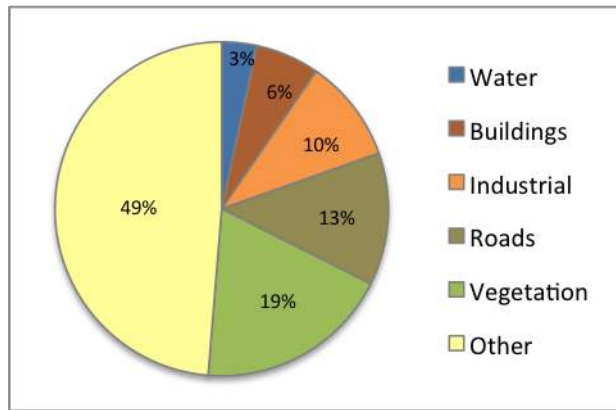


Figure 4. Ratio between various surface types in Moscow

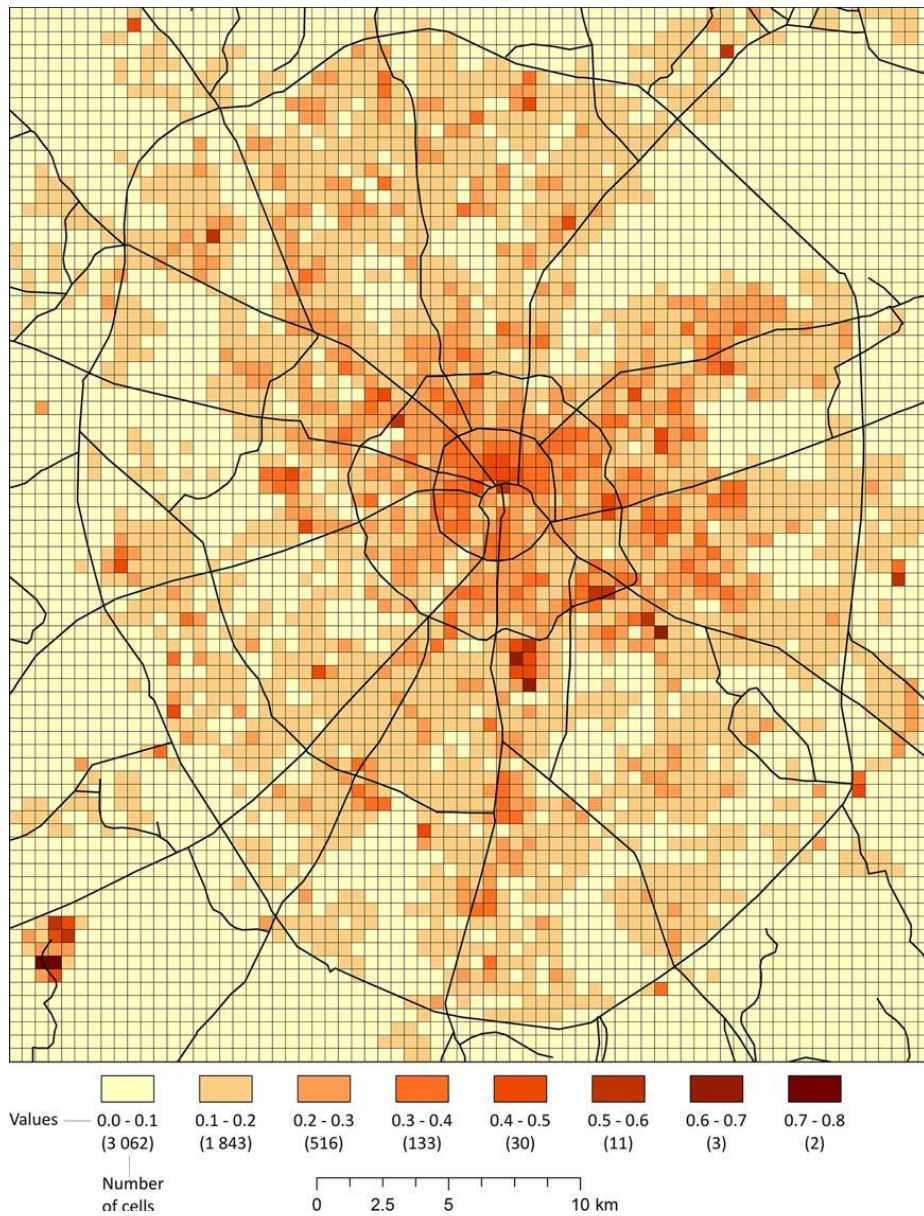


Figure 5. Plan area index (building density). Cell size = 500 m

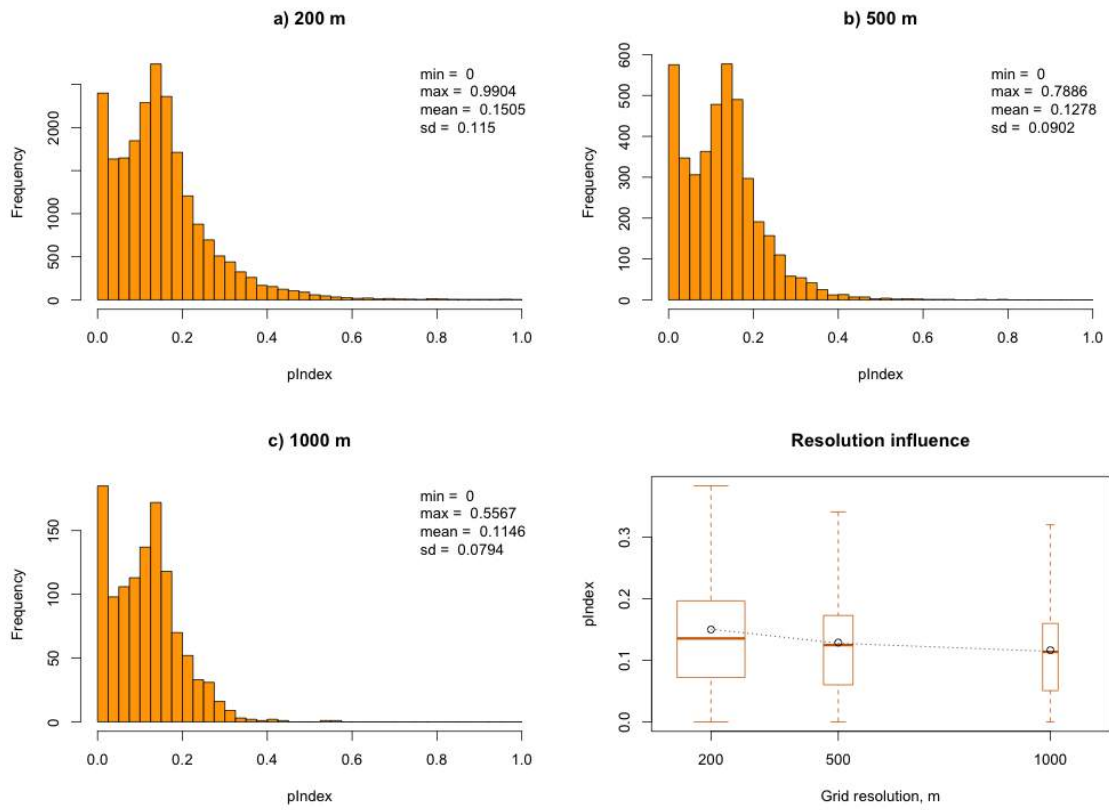


Figure 6. Histograms of plan area index values for different grid resolutions

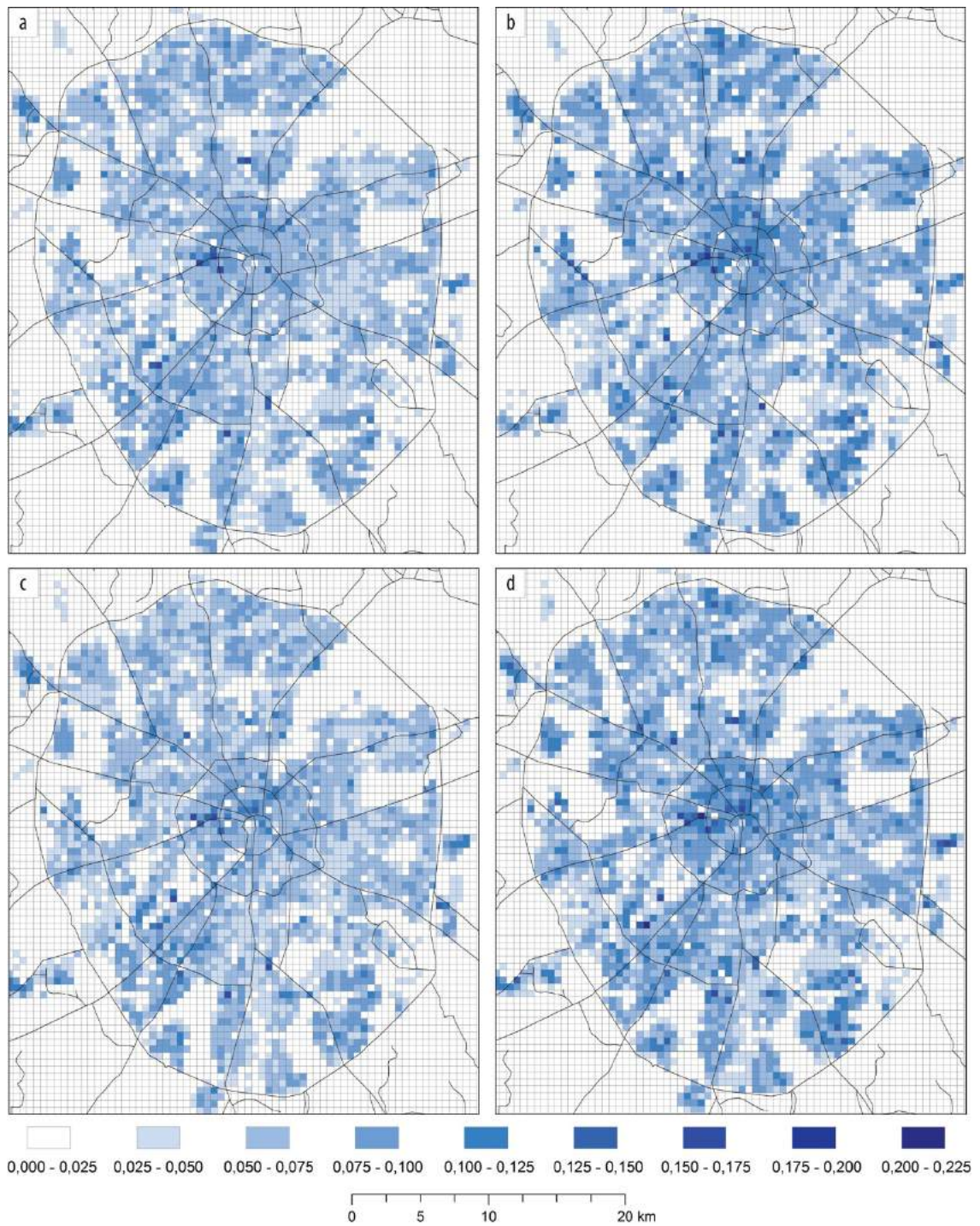


Figure 7. Frontal area index for different wind directions. Cell size = 500 m. Azimuth: a) 0° ; b) 45° ; c) 90° ; d) 135° ;

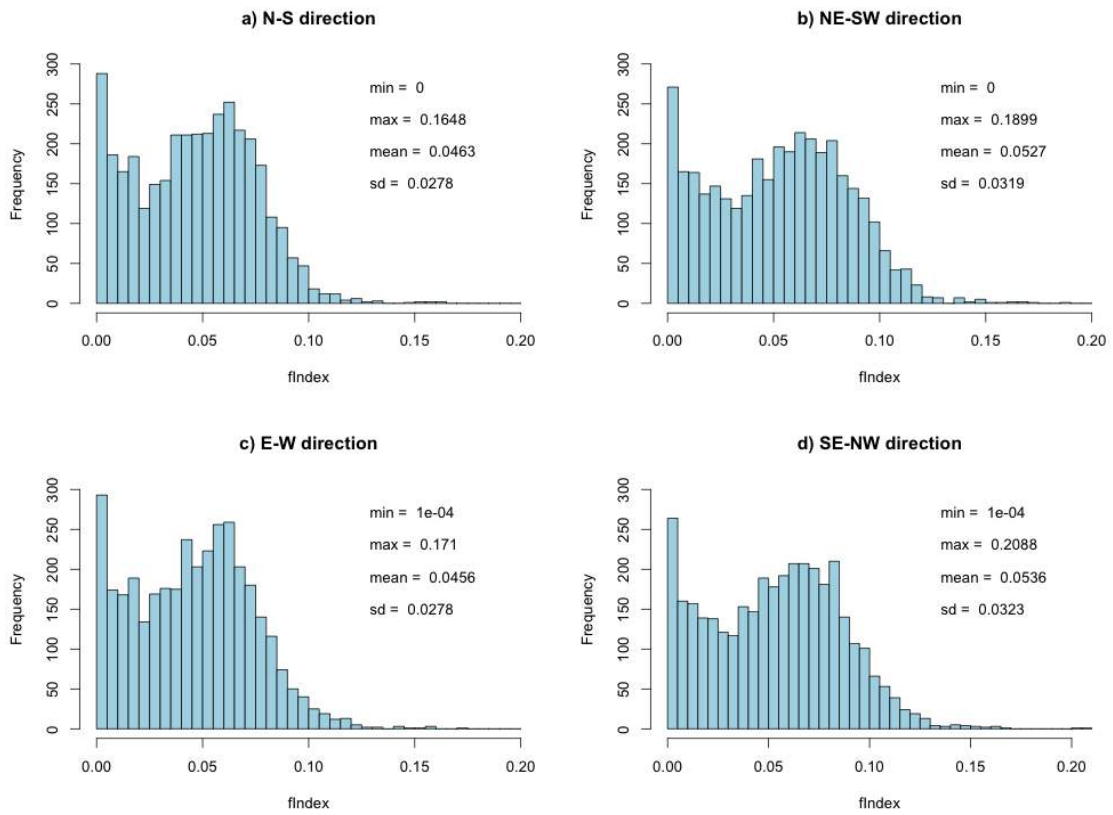


Figure 8. Histograms of frontal area index values for different orientations. Azimuth: a) 0° ; b) 45° ; c) 90° ; d) 135° . Cell size = 500 m.

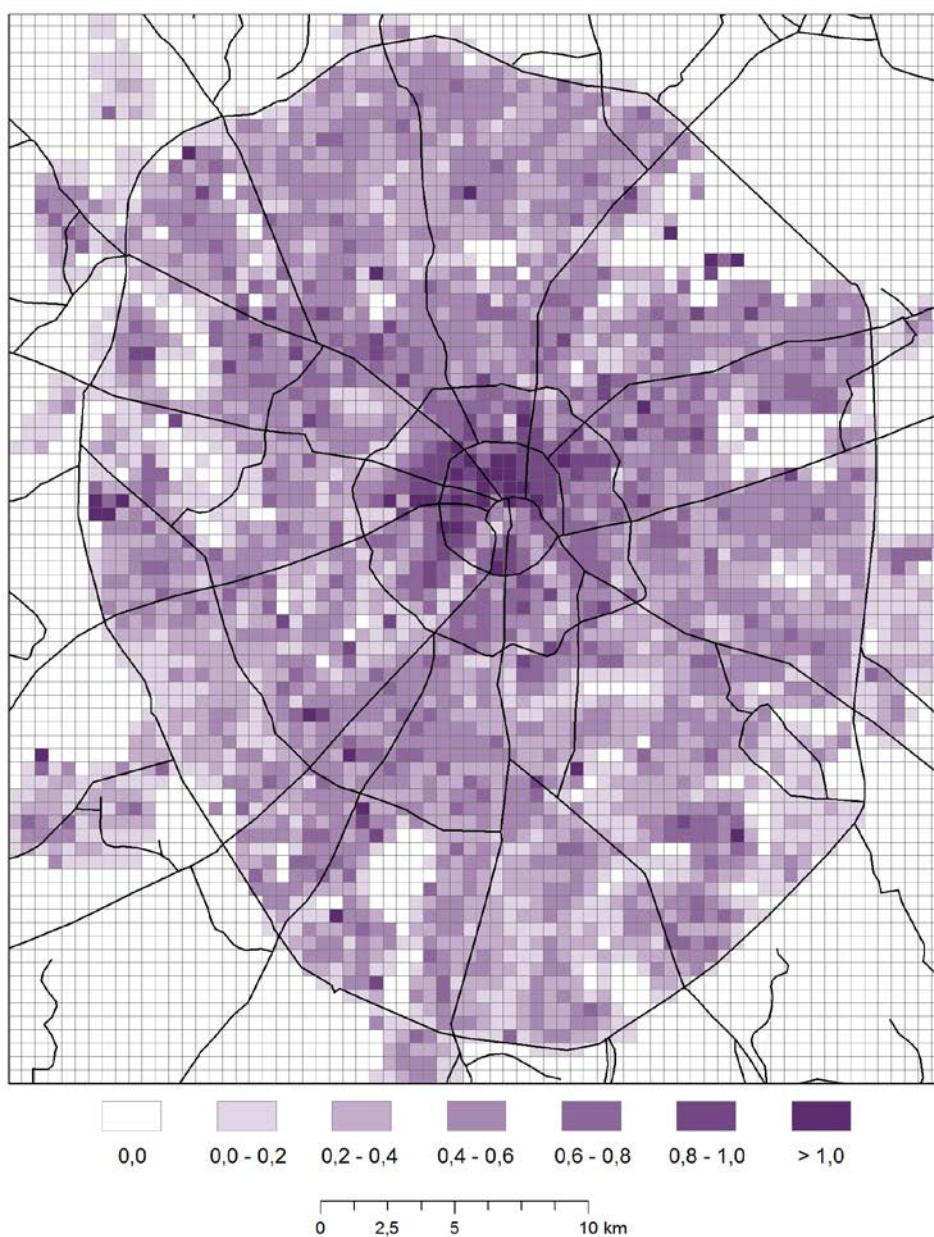


Figure 9. Height/width ratio. Cell size = 500 m

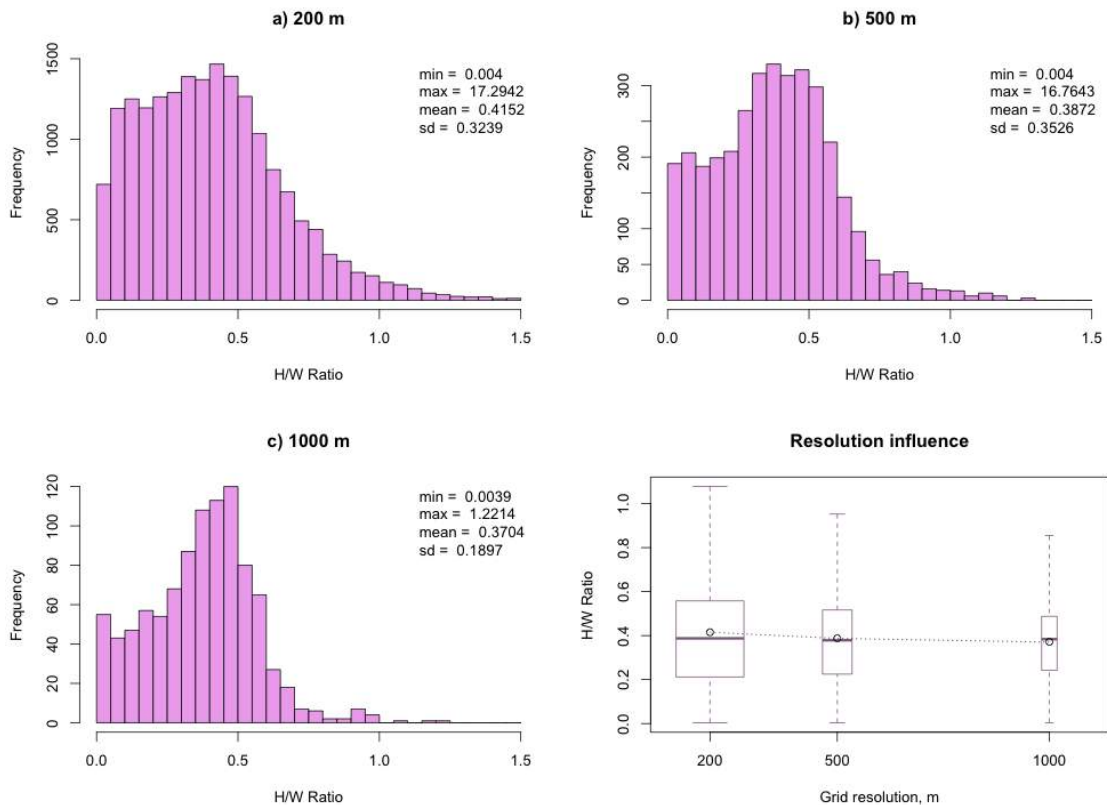


Figure 10. Histograms of H/W ratio for different grid resolutions

5. Discussion

In many investigations of urban canopy layer remote sensing data is used. At the same time most of the parameters related to urban canyon geometry are much simply derived from cartographic data. This work is oriented in the latter direction. The described approach is not tied to specific GIS software and allows derivation of analogous databases for any city.

The main results presented in this paper can be summarized in following points:

- (1) The concept of the directed canyon and method of directed canyons extraction from TIN; building classification in relation to directed canyons.
- (2) TIN-based method for canyons delineation and estimation of their geometric parameters;
- (3) The multiresolution database of urban canyon and land cover characteristics in- side Moscow city with resolutions of 200, 500 and 1000 m.
- (4) Cartographic and statistical assessment of the database content. Plan area and frontal area indexes showed bimodal distribution not highly sensitive to the grid resolution. H/W ratio showed unimodal distribution highly sensitive to grid resolution. Average land cover distribution is also estimated for Moscow and showed little changes between different grid sizes.

Our calculations are based on several assumptions. The first is ratio of the pervious and impervious surfaces for industrial areas, which was set to 1/1. The second is criteria of selection of territories with tall vegetation which are rather conditional and can be significantly improved using remote sensing data. The third is assumption that the directed canyons delineation depends on the presence of linear street network.

Acknowledgements

This study was supported by Russian Foundation for Basic Research grants RFBR 13-05-41306-RGO_a, RFBR 15-35-21129-mol_a_ved and RFBR 15-35-70006. The work of Dr. Samsonov is partially supported by President of Russia grant for Leading scientific schools NSh-2248.2014.5. The work of Dr. Konstantinov is partially supported by President of Russia grant for young PhD scientists MK-6037.2015.5. Authors would like to thank Geocentre Consulting Ltd for providing Moscow city vector database.

References

1. Bohm, P. (1998), Urban structural units as a key indicator for monitoring and optimising the urban environment, in 'Urban ecology', Berlin, pp. 442–445.
2. Burian, S. J., Brown, M. J. & Linger, S. P. (2002), 'Morphological analyses using 3D building databases: Los Angeles, California', *National Laboratory Rep LA-UR-02-0781*. Los Alamos National Laboratory p. 66.
3. Chen, L. & Ng, E. (2011), 'Quantitative urban climate mapping based on a geographical database: A simulation approach using Hong Kong as a case study', *International Journal of Applied Earth Observations and Geoinformation* 13(4), 586–594.
4. de Berg, M., Cheong, O., van Kreveld, M. & Overmars, M. (2008), *Computational Geometry: Algorithms and Applications*, 3rd edition edn, Springer Berlin Heidelberg, Springer Berlin, Heidelberg.
5. Egenhofer, M. J. & Franzosa, R. D. (1991), 'Point-set topological spatial relations', *International Journal of Geographical Information Systems* 5(2), 161–174.
6. Gal, T., Lindberg, F. & Unger, J. (2008), 'Computing continuous sky view factors using 3D urban raster and vector databases: comparison and application to urban climate', *Theoretical and applied climatology* 95(1-2), 111–123.
7. Gal, T. & Unger, J. (2014), 'A new software tool for SVF calculations using building and tree-crown databases', *Urban Climate (in press)* p. 13.
8. Grimmond, C. & Souch, C. (1994), 'Surface description for urban climate studies: a GIS based methodology', *Geocarto International* 9(1), 47–59.
9. Hillier, B., Turner, A., Yang, T. & Park, H.-T. (2010), 'Metric And Topo-Geometric Properties Of Urban Street Networks: Some convergences, divergences and new results', *The Journal of Space Syntax* 1(2), 279.
10. Hrabar, S., Sukhatme, G., Corke, P., Usher, K. & Roberts, J. (2005), Combined optic-flow and stereo-based navigation of urban canyons for a UAV, in '2005 IEEE/RSJ International Conference on Intelligent Robots and Systems', IEEE, pp. 3309–3316.
11. Johnson, G. T. & Watson, I. D. (1984), 'The determination of view-factors in urban canyons.', *Journal of Applied Meteorology* 23(2), 329–335.
12. Kislov, A. V. & Konstantinov, P. I. (2011), 'Detailed spatial modeling of temperature in Moscow', *Russian Meteorology and Hydrology* 36(5), 300–306.

13. Konstantinov, P. I., Varentsov, M. I. & Malinina, E. P. (2014), 'Modeling of thermal comfort conditions inside the urban boundary layer during Moscow's 2010 summer heat wave (case-study)', *Urban Climate (in press)* p. 10.
14. Kropf, K. (1996), 'Urban tissue and the character of towns', *URBAN DESIGN International* 1(3), 247–263.
15. Kusaka, H., Kondo, H., Kikegawa, Y. & Kimura, F. (2001), 'A simple single-layer urban canopy model for atmospheric models: Comparison with multi-layer and slab models', *Boundary-Layer Meteorology* 101, 329–358.
16. Lemonsu, A., Leroux, A. & Belair, S. (2008), A general methodology of urban land cover type classification for atmospheric modelling, Technical report, Meteo France, Centre National de Recherches Meteorologiques.
17. Lindberg, F. (2007), 'Modelling the urban climate using a local governmental geo-database', *Meteorological Applications* 14(3), 263–273.
18. Martilli, A., Clappier, A. & Rotach, M. W. (2002), 'An urban surface exchange parameterisation for mesoscale models', *Boundary-Layer Meteorology* (104), 261–304.
19. Masson, V. (2000), 'A physically-based scheme for the urban energy budget in atmospheric models', *Boundary-Layer Meteorology* 94(3), 357–397.
20. Moran, E. F. (2010), 'Land cover classification in a complex urban-rural landscape with Quickbird imagery', *Photogrammetric engineering and remote sensing* 76(10), 1159–1168.
21. Moudon, A. V. (1997), 'Urban morphology as an emerging interdisciplinary field', *Urban morphology* 1(1), 3–10.
22. Nunez, M. & Oke, T. R. (1977), 'The energy balance of an urban canyon', *Journal of Applied Meteorology* 16, 11–19.
23. Oke, T. R. (1987), *Boundary Layer Climates*, 2nd edition edn, Routledge.
24. Oliveira, V. (2013), 'Morpho: a Methodology for Assessing Urban Form', *Urban morphology* 17, 21–33.
25. Osmond, P. (2010), 'The urban structural unit: towards a descriptive framework to support urban analysis and planning', *Urban morphology* 14, 5–20.
26. Peeters, A. & Etzion, Y. (2010), Automated recognition of urban objects for morphological urban analysis, in 'Core Spatial Databases -Updating, Maintenance and Services -from Theory to Practice', Haifa, Israel, pp. 58–63.
27. Pu, R., Landry, S. & Yu, Q. (2011), 'Object-based urban detailed land cover classification with high spatial resolution IKONOS imagery', *Int. J. Remote Sensing* 32(12), 3285–3308.
28. Ratti, C., Di Sabatino, S. & Britter, R. (2006), 'Urban texture analysis with image processing techniques: winds and dispersion', *Theoretical and applied climatology* 84(1-3), 77–90.
29. Raupach, M. R. (1992), 'Drag and drag partition on rough surfaces', *Boundary-Layer Meteorology* 60(4), 375–395.
30. Samsonov, T. & Konstantinov, P. (2014), Openstreetmap data assessment for extraction of urban land cover and geometry parameters required by urban climate modeling, in 'Extended Abstract Proceedings of the GIScience 2014, September 23-26, Vienna, Austria', Vol. 40 of *GeoInfo Series*, Hochschulerschaft, TU Vienna Vienna, Austria, pp. 395–399.
31. Samsonov T. E., Konstantinov P. I., Varentsov M. I. Object-oriented approach to urban canyon analysis and its applications in meteorological modeling // *Urban Climate*. — 2015. — Vol. 13. — P. 122–139. DOI: 10.1016/j.uclim.2015.07.007
32. Shamarock, W., Klemp, J. B., Dudhia, J., Gill, D. O., Barker, D. M., Duda, M. G., Huang, X., Wang, W. & Powers, J. G. (2008), *A description of the advanced research WRF version 3: NCAR technical note TN-475+STR*, National Center for Atmospheric Research Boulder, Colorado, USA.

33. Thomson, R. C. & Richardson, D. E. (1999), The 'good continuation' principle of perceptual organization applied to the generalization of road networks, *in* 'Proceedings of the ICA 19th International Cartographic Conference', pp. 1215–1223.
34. Trusilova, K., Fruh, B., Brienen, S., Walter, A., Masson, V., Pigeon, G. & Becker, P. (2013), 'Implementation of an Urban Parameterization Scheme into the Regional Climate Model COSMO-CLM', *Journal of Applied Meteorology and Climatology* 52(10), 2296–2311.
35. Turner, A. (2007), 'From axial to road-centre lines: a new representation for space syntax and a new model of route choice for transport network analysis', *Environment and Planning B: Planning and Design* 34(3), 539–555.
36. Unger, J. (2009), 'Connection between urban heat island and sky view factor approximated by a software tool on a 3D urban database', *International Journal of Environment and Pollution* 36, 59–80.
37. Wong, M. S., Nichol, J., Ng, E., Guilbert, E., Hei, K. & Kwok, P. (2011), 'GIS techniques for mapping urban wind ventilation, using frontal area index and least cost path analysis', *The International Archives of the Photogrammetry, Remote Sensing and Spatial Information Sciences* 38, 586–591.

Solar Cooling in the Ecuadorian Contexts

María A. Sanchez del Hierro^{1,2}, Jairo Acuña², Tannya K. Pico², Jorge D. Czajkowski³

¹ Facultad de Arquitectura y Urbanismo Universidad Nacional de La Plata, Calle 124 & Avenida 51 E,
La Plata, Argentina
e-mail: masanchezd@puce.edu.ec

² Pontificia Universidad Católica del Ecuador, Facultad de Arquitectura, Av. 12 de Octubre 1076 y
Roca, Quito, Ecuador
e-mail: jairo.acuna.p@gmail.com, tkpico@puce.edu.ec

³ Laboratorio de Arquitectura y Hábitat Sustentable. Facultad de Arquitectura y Urbanismo.
Universidad Nacional de La Plata, Calle 124 & Avenida 51 E, La Plata, Argentina / CONICET
e-mail: czajko@ing.unlp.edu.ar

Keywords: Solar Cooling, Sustainable Buildings, Climate Control, Performance, Ecuador, Andes.

Abstract. *Ecuador presents four specific climates: Coast, Andes, Amazonia and Galapagos. This paper discusses the interest of solar cooling systems implementation in each case. The hot and humid climate of the Coast and Amazonia is similar to other tropical and equatorial climates where these techniques have been tested and described widely. Besides, the Andean climate of Quito (2800 meters above the sea level) and the very constrained conditions of Galapagos Islands are not yet well documented. This paper sets some guidelines for furthest research in the Ecuadorian contexts.*

1. Introduction

Since the middle of the last century we depend on the use of conditioning equipment to reach comfort levels within our buildings, ignoring the pressure on nonrenewable energy resources and the consequent environmental degradation caused by their use. An alternative to change this view is aimed by trying to achieve comfortable buildings that function as efficient thermodynamic systems that interact with their environment and try to reach minimum energy consumption.

Research in the use of energy is generally focused in heating energy, which is the predominant concern in cold or moderate climates. In contrast we can see that the energy consumption of electrical appliances for cooling in summer (or in warm areas) has been less analyzed and regulated, although demand has risen sharply as the installation of equipment for cooling due to high thermal loads in buildings. We know that these charges have their roots in the attractive glass façade that poses several challenges when protecting from radiation, as well as the increased internal loads due to computer equipment, lighting and electrical appliances that define the current lifestyle. Depending on how extreme climate and the type of construction, energy demand for cooling often remains constant and can be covered by passive systems or active cooling systems.

Passive cooling systems can reduce the consumption of both cooling and heating, to a limited minimum. Considering this limit and potential, non-conventional technologies are being studied more intensively. This paper aims to synthetically describe the technologies being investigated or under experimentation. An assessment in the Ecuadorian context is presented.

2. Cooling Demand

The annual sale of electric refrigeration units reaches approximately 43 million, with China as the largest consumer (12 million), followed by the US (11.8 million). In Europe the number is less (about 2.8 million in 2002) but with growing demand. It is estimated that growth is $3\text{m}^2 / \text{hab.}$ in 2000 to $6\text{m}^2 / \text{hab.}$ in 2020.¹ This increase in sales of air conditioners is due, on the one hand, to the increased thermal loads in buildings that basically consists of two components: sensible load (external and internal), which has an effect on the ambient temperature; and latent load, that affects indoor air moisture. The internal loads are provided by heat sources in the building, mainly by the electronic devices we use today. On the other hand, the increased demand for comfort by the user during summer. To meet the cooling requirements there are a need to find new methods that are less energy intensive and less costly.

According to studies by Eicker (2009) on the normative present in the European Union for efficient buildings, they should achieve the following characteristics for winter:

Excellent thermal insulation skin, high quality glass with U-values of at least $1.5 \text{ Wm}^{-2}\text{K}^{-1}$, with a reasonable overall energy transmittance g of 60% and heat recovery from the air conditioning. But the performance of these buildings in the summer depends on some additional features: Excellent sunscreen façade (preferably outside the building), schemes of

¹ Data from the European Commission, 2006 (Action Plan for Energy Efficiency: Realising the potential, 2006)

night ventilation to partially remove the daytime loads, geothermal heat exchangers to pre cool the air conditioning or use directly in parts of the building, in addition to the internal load that should be the lowest possible².

3. Solar Cooling

If a building cannot be cooled by passive means as stated above, there are some active technologies that can be used. At present, the dominant method is compression refrigeration, which has 90% of the world market despite its coefficient of performance (COP) systems is 3.0 on average (the best equipments reach only a COP of 5.0). Under this premise it has been allowed a combined method that provides the same comfort conditions but allowing a supply of air conditioning that does not require the production of big quantities of cold water and a reduction of primary energy consumption.

Solar thermal conversion systems are a group of very varied and numerous technological solutions. It is not intended to deepen on each one, but to provide an overview of this type of energy exploitation systems. The basic conceptual diagram can be seen in Figure 1.

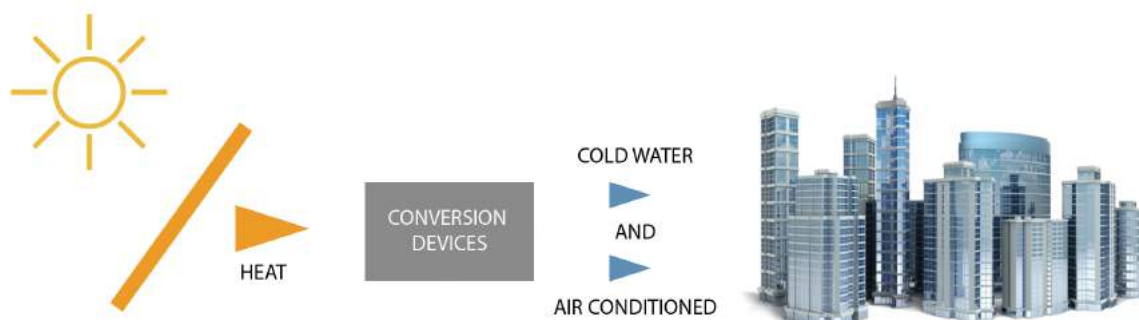


Figure 1. Basic conceptual diagram solar cooling

Source: based on König et al. (2012)

The solar cooling is based on harnessing the sun's heat to achieve cooling. As for solar radiation gain will depend on the location of the building in the earth's crust. There is a primary energy supply (sun) that has a temporal coincidence between the demand for air conditioning and maximum sunlight. The maximum radiation load is usually found within hours of delay in relation to the maximum exposure of the device, so you can easily offset this with a short term accumulator. That is why they have the great advantage to be used when matching the highest levels of demand and production, as the conditioning needs of a building occur at the time of greatest solar radiation (Henning et.al.2012).

² In Argentina the normative in force on thermal conditioning in buildings are IRAM 11549, IRAM 11601, IRAM 11603, IRAM 11605, IRAM 11659-1, IRAM 11659-2.

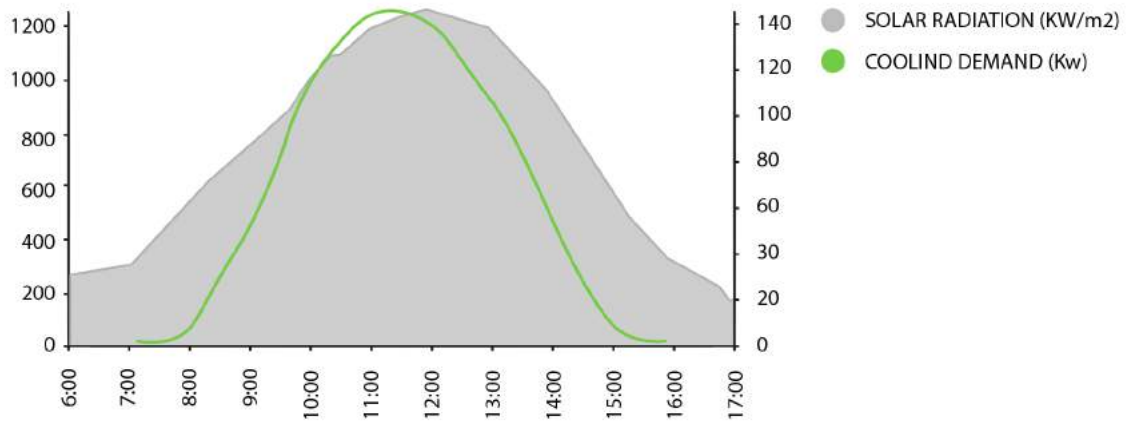


Figure 2. Graph of cooling demand and solar radiation

Source: Based on Martínez Sánchez, 2007

López Villada (2010) summarizes the wide variety of combinations between solar collection and cooling technologies. Following, there is a review of them.

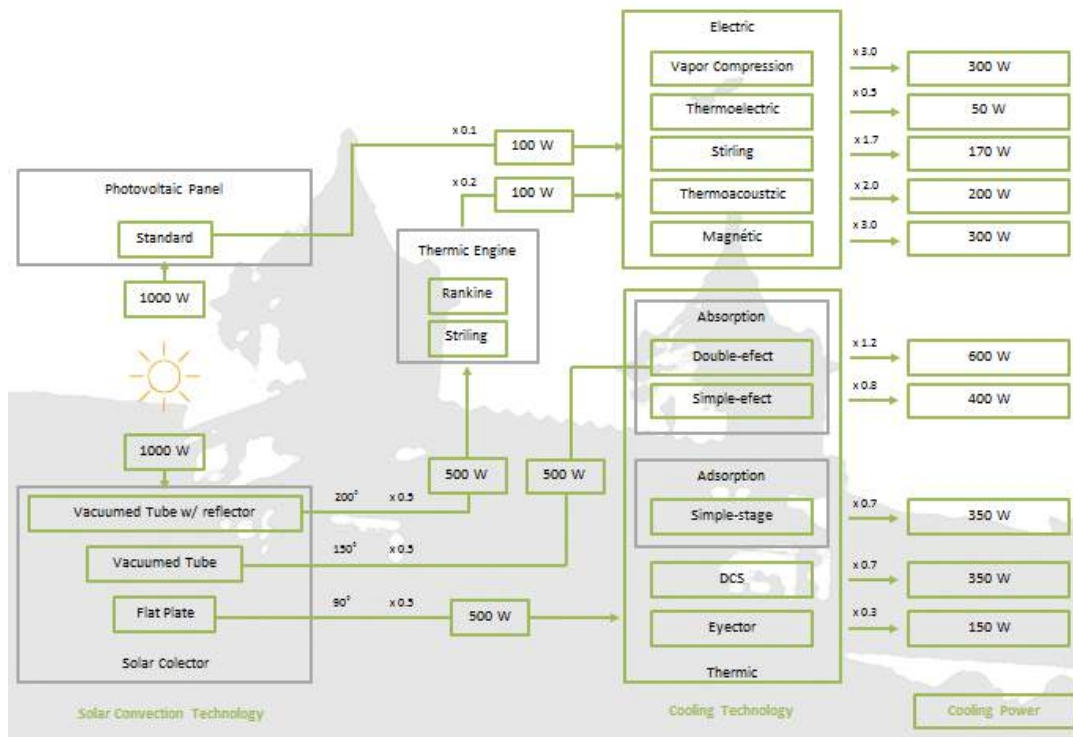


Figure 3. Performance of different technological options for solar cooling systems

Source: based on López Villada, 2010

3.1. Components

Collection system.- Solar cooling facilities feed hot liquid at varying temperatures based on different equipment. The collectors are selected according to the characteristics of the machine to be used.

Buffer tank accumulator.- These deposits are placed to stabilize the flow and temperature of liquid supplied to the machine. Dimensioning the flow rate and power depend on the installation.

Backup boiler.- Depending on the characteristics of the machine and the chosen type of solar collector sometimes is desirable to use a backup boiler to overheat the water from the solar collection system. Typically it uses the same boiler that provides hot water for heating in winter.

Backup cooler.- It is used for situations where solar hot water production is not enough.

Energy dissipation system.- It is necessary to count on this system, which may be a cooling tower or a wind turbine for cooling, or even geothermal dissipation.

Distribution system.- The energy produced can be distributed by a coolant floor or by fan coil systems.

Regulatory system.- Is important to have a team of regulatory probes, valves and other devices. These can be electronic.

3.2. Solar collection technologies

Thermal cooling systems can be connected with different solar thermal systems depending on the operating temperature. The main components of these systems are the collection system, plumbing system, hydraulic system, accumulation system and exchange system. We should note that careful selection of the type of collector in the planning stage is crucial to achieve energy saving goals. We will describe 3 types of collectors: flat plate collectors, vacuum tubes and parabolic dish concentrators.

Flat plate collectors .- They consist of an insulated metal box with a glass or plastic cover and a dark absorber plate. Solar radiation is absorbed by the plate and this quickly transfers heat to a fluid flowing through tubes in the manifold. The carrier fluid may be water or water-glycol, since the installation is at risk of low night temperatures and prevent freezing in the collector. By having a toxic element is necessary to install a secondary circuit. In the case of solar heating they are of great interest, collectors of high quality with selective coating of the absorber, which often have other features to reduce heat losses, hence expect an acceptable use in the temperature range of refrigerating machines for stationary use. (Cadena et.al. 2009)

Vacuum tube collectors.-They consist of a set of vacuum tubes (or evacuated) containing an absorber with selective treatment that collects solar energy and transfers it to a heat-bearer fluid. Due to the insulating properties of the vacuum, heat losses are reduced and temperatures of between 77 ° C and 117 ° C can be reached. Generally these collectors are used in high temperature applications. These collectors advantage is that they capture radiation more effectively than flat collectors due to its cylindrical shape, which allows rays impinge on the pipes during most of the day. They are well suited for industrial heating applications and can also be an effective alternative for domestic heating in regions where there is little or poor radiation. There are two types of vacuum tube collectors according to the method for the heat exchange between the plate and the carrier fluid: direct flow and heat pipe.

Compound parabolic concentrators (CPC) .- The stationary CPC concentration have a radiation system for higher temperatures , achieving minimization of losses and a yield close to 50%. Collectors are high performance and high quality.

CPCs large magnitude is made of a highly reflective material. These need a tracking system to keep the paraboloid axis pointing towards the sun, which can be achieved in two ways: tracking azimuth / elevation: where the hub rotates about an axis perpendicular to the plane tangent of the place varying its azimuth and also another perpendicular to vary its inclination. The polar tracking where the hub swivels parallel to the axis of rotation of the earth has a constant rate of 15° / hour.

3.3. Cooling technologies

Absorption.- The absorption chiller is a device that allows transferring energy from one source to another, from low temperature to high temperature with a small additional energy consumption. Its operation is based on the ability of certain substances to absorb a refrigerant that may be lithium bromide (acts as absorbent) and water or ammonia (as the cooler) and water. One distinguishes between single acting machines and double effect by the temperature at which water is: the double acting need superheated water ($120-190^\circ\text{C}$) or steam (3-10 bar) while single effect can operate with hot water ($80-95^\circ\text{C}$).

You can also use a triple-phase technology without refrigerant. The process alternating three states of aggregation (solid, liquid and gas) allowing continuous cooling or heating. These teams can operate in three different modes: loading, heating and cooling. Charging mode stores energy drying a salt (lithium chloride) can then be used when necessary. You can also receive thermal energy while supplying heat or cold and hot water production simultaneously. These machines differ in three aspects of lithium bromide type: have an internal storage reservoir in each of the storage where you can store chemical energy intensive; they work intermittently with two parallel accumulators; they have been designed to use relatively low and stable inside the storage temperature, which is optimized for use with solar thermal collectors (Sitio Solar, 2013).

Adsorption.- Unlike absorption machines instead of a liquid absorbent a solid adsorbent, silica-gel, and water is used as coolant. These teams consist of: an evaporator, two adsorbent chambers and a condenser. In the evaporator, the low pressure water evaporates; cooling water at 6°C or at the temperatures required (can cool water of up to 6°C to 3°C). Evaporation of water produced, is adsorbed in an adsorption chamber by dehydrating, which is saturated. While, in the other chamber the hot water passes through the heat exchanger, regenerating the desiccant that had previously adsorbed water vapor. The evaporated water is condensed dehydrating by cooling water in the condenser to be returned back to the evaporator. The cooling water passes through the exchanger equipment of the adsorption chamber, absorbing power delivered by the condensation of water vapor and then passed through the condenser. By a cooling tower is cooled to the temperature required to be introduced again in the equipment (Sitio Solar, 2013).

The operating cycle is not continuous (has a loading phase and another discharge). The COP of these machines is between 0.55 to 0.65. The temperature of the hot source may be from 55°C , ie lower than absorption machines .

Steam jet.- It is a compression technology that has a steam jet compressor that allows the use of solar energy or waste heat from processes as its source of energy. The compressor

contains two refrigerant circuits: one for the generation of cold and the other for steam generation. The compressor compresses the refrigerant vapor and transports it into the condenser.

In the refrigeration cycle part of the condensed refrigerant flows into the evaporator which is connected to the jet compressor suction side. The refrigerant absorbs ambient heat or heat of the heater and evaporated. Refrigerant vapor is sucked by the jet compressor and recompressed vapor.

The steam cycle pumps the other part of the condensate into a steam generator. A deposit evaporates the refrigerant electrically heated; steam generated drives the steam jet compressor.

Heat engines.- The application of Stirling engines that we want to mention is the small-scale cogeneration and micro- cogeneration , ie the simultaneous production of electricity and thermal energy . The use of Stirling engines in solar applications is not a new issue, as work done by John Ericsson in 1864 invented a hot air engine running on solar energy are cited(Garcia Menendez,2013). It is an external combustion engine, allowing it to adapt to solar energy and are machines that develop a regenerative cycle; does not require the generation of thermal energy within, it only needs to add heat at one end while at the other is removed. That heat can come from any source, in this case: solar.

Within the energy conversion systems based on Stirling engines, the Dish-Stirling systems are the most developed. Solar concentrators are usually paraboloids of revolution with point source. The receiver is the link between the hub and the engine, ie is where the electro-mechanical energy is converted into thermal energy as efficiently as possible. Most receptors are cavity with an opening through which enters the radiation from the concentrator and stored in the absorber, which is situated behind the opening and reaches high temperatures. Receptors can be classified into direct and indirect, depending on the manner in which heat is transferred from the absorber to the working gas of the Stirling engine. In the direct recipients as heater tubes are those which absorb radiation, while in the indirect recipients fluids are used in phase change between the absorber and the heater tubes.

Research in such systems is a hot topic in the northern hemisphere, in Europe and North America³. We investigated the possibility of developing systems operating at low temperatures (typically reaches temperatures of 400-450 ° C) that would be in the order of 180 ° C, given that you can achieve a technological simplification and cheapening of the installation. One possibility is to use vacuum tubes as capture system, then convert the thermal energy in a turbine cycle organic fluid Rankine (ORC). This system still has high costs but expected to fall in the future.

One advantage of Stirling engines is that they are able to operate with very low temperature differences, making them potentially suitable machines used in combination with flat plate collectors or other low temperature devices. Stirling engines promise advantages with a particular focus on small-scale microgeneration, raising less than 1 kW units. (Garcia Menendez,2013)

³ The company Stirling Energy Systems marketed the system based on a 26kW U4-95 engine that had a solar conversion efficiency of more than 31% reached on March 31, 2008 in New Mexico USA. At present there are 3 systems emphasizing marketing Ripasso Energy 30kW, measured in South Africa; Cleanenergy 22kW with V161 engine, Swedish company; And Infinia 3kW developed by Sunpower and incorporates a free piston Stirling engine (Garcia Menendez, 2013)

We can name some mechanisms that use different fuels, have different yields or sizes, and produce heat at different temperature levels: steam turbines, turbines, organic Rankine cycle turbines process Kalina, Stirling engines, steam engines, engines gas, liquid fuel engines, a standard gas, micro turbines and fuel cells. That is why this waste heat and cooling are linked.

Peltier effect.- It was discovered in the early nineteenth century by J. Peltier and involves passing an electric current through the junction of two dissimilar metals being capable of cooling the board if you drive in the right direction.

Elements currently used in solid form, rather than two metals. These thermoelectric coolers are performing well when it comes to produce cold in a small volume. The main advantages lean in their small size, they are silent because they have no moving parts, also contain liquid or gas which makes them harmless to the environment. One of the drawbacks of these units is that when the passage of electric current is interrupted, the temperature inside rises rapidly to the one of the environment.

Magneto - Caloric effect.- Magnetic refrigeration is based on magneto caloric effect , it is an intrinsic property of some magnetic materials . It is defined as the response of some magnetic materials to a varying magnetic field which manifests as changing the isothermal entropy and adiabatic temperature change. Modern magnetic refrigeration jumped when Zimm et al. developed machines operating successfully for applications for domestic and industrial use. One of the first tests operated with a magnetic field of a superconducting magnet 5Tesla . With 10K temperature range reached a cooling power of 600W , a COP of 10 and a maximum of 60 % of Carnot efficiency (Forofrío , 2008). The main material used in prototypes is gadolinium (Gd) and their compounds, getting cool below ambient temperature.

Cooling is achieved in the stage where suddenly suppresses magnetic field , the material is placed in thermal contact with the object to be cooled . The object is cooled and the material is heated until both reach an equilibrium temperature. The process can be repeated reaching a stable value in which the cooling capacity of the material equals heat leakage from the outside to the object. (Aragon Investiga, 2010) Several commercial houses and technological laboratories are testing prototypes for cooling systems based on magnetic materials including Astronautics Laboratory - Arnes , Chubu Electric- Toshiba , Sichuan Institute - University of Nanking.

Thermo-acoustic methods.- The thermal noise machines are devices that convert thermal energy into acoustic power and vice versa. There are two main branches of study in this discipline: cooling and pressure machines. It is based on two important thermodynamic principles: raising the temperature of a gas when compressed and temperature drop when expanded; and when two substances are placed in direct contact, heat will flow from the hotter to the colder substance. Higgins, in 1777, Rijke in 1859, Sondhaus in 1850 investigated the acoustic oscillations in tubes with heat at one end. In the 1980s Wheatley, Swift and Hofles Los Alamos National Laboratory are, among others, responsible for several advances in practice with thermos acoustic engines and refrigerators.

This system must have basically a resonant tube, a speaker attached to one end, a stack thermos acoustics is simply a solid with small channels or pores, two heat exchangers and a working gas. When the speaker is excited by an acoustic signal, a wave causes the working fluid to move through the stack, where the pressure, temperature and speed vary with time is generated. This process is intended to heat transfer from the coldest to the hottest part side thereby promoting the cooling cycle. (Peinado Rodriguez, et al, 2011)

4. Assessment

4.1. Ecuadorian climatic conditions

Ecuador has a very diverse climatic condition, that also varies over the years, due to the influence of el Niño and Humboldt ocean currents. The topography plays an important role in the distribution of climatic conditions, since altitude varies from sea level to 6,000 meters; and the location right on the Equator. The study of the climate in Ecuador started in 1890 with the Astronomical Observatory of Quito, with the first meteorological station. Then in 1944 the meteorological Service of Ecuador was created, and the first meteorological network was put into place. After a few years the National Institute of Meteorology and Hydrology (INAMHI) started the publication of its Meteorological Yearbook up to date. Nowadays the network has around 383 stations, differentiated by the installed equipment and the data collected.

Ecuador is divided into four regions: Amazonia, Andes, Coastal and Galapagos Islands.

Cities in the Coast .- This region contains the most populated cities of the country. The coastal region covers a coastal strip of about 100 km. Wide, with extreme values of 180 km in the latitude of Guayaquil and 40 km in the southern part. It can be divided into two distinct units:

The coastal mountain range extends on the Western and North - Western areas (Canguillo and mountains of Jama, Cuaque hills, mountains of Chindul and Mache) which maximum height does not exceed 800 m. At Puerto Lopez the mountain range slouches eastward at Guayaquil where it disappears (Colonche hills and Chongén).

At the South, the peninsula of Santa Elena and the Puna Island are characterized by small mountain ranges between 100m and 200m height, isolated hills (Yoma Animas: 420 m) and lowlands near the sea.

At the foot of the Andes, the Guayas River Plain is a pit collapse with fluvio-marine, filling about 80 km wide; bordered to the east by alluvial fans is bounded on the north by reliefs raised. This plain slopes gently to the south where it is replaced by an alluvial Plain, in floodable part, which is extended by a narrow strip to Peru (INAMHI, 1983).

With the elaboration of the new building code NEC 2011, it opens up the opportunity to include the use of renewable energy in buildings. There was a lack of onsite information regarding the solar resource, the stations network only measures the sunshine duration. Therefore in 2008, the National Council of Electrification CONELEC, developed the Solar Map of Ecuador based on satellite information of the US NREL between 1985 and 1991 using interpolation of 1Km² cells. One must take into consideration that this method has its limits, several studies show this differences (Suehrcke, et.al. 2013; Grossi Gallegos, Raichijk, 2010)

The following table summarizes the characteristics of major cities in the coast of Ecuador.

City	Population 2016	Latitude	Longitude	[K] 22- Year Averaged Insolation Clearness Index (0 to 1.0)	Altitude (M.A.S.L.)	Mean solar radiation Wh/m ² (day)
GUAYAQUIL	2,617,349	-2.2038160	-79.8974530	0.46	35.19	4370
SANTO DOMINGO DE LOS TSACHILAS	426,910	-0.2205563	-79.2902133	0.39	520.48	3440
MACHALA	276,669	-3.2664990	-79.9538270	0.49	8.45	4200
ESMERALDAS	210,833	0.9500000	-79.6666667	0.41	12.66	4350
QUEVEDO	200,217	-1.0225124	-79.4604035	0.42	55.86	3780

Note: Population figures from INEC (2016), Latitude, Longitude and Altitude from IGM (2016), [K] Insolation Clearness Index, Temperature and Humidity from NASA (2016), Mean Solar Radiation from NEC (2011)

Table 1: CHARACTERISTICS OF THE MAIN CITIES IN THE Coast

Considering the solar input of 4KWh/m² day, the cooling power production can be between 200W up to 2400W depending the technology that can be used. The electric technologies can produce between 200W and 1200W. The thermic technologies can produce from 450W up to 2400W. Research has shown that in similar climates like Malasya (Assilzadeh et. al. 2005), Burkina Faso (Buchter et al., 2005), or in Shangai and Hong Kong (La et.al., 2011) in China, these technologies have a wide range of operationg conditions and therefore a good opportunity for application. In Guayaquil, research has been done with adsoption cooling in a single story office building (Boera, A, 2012).

Cities in the Amazonia.- This region is the less populated area of Ecuador, thus is the most biological diverse and where petroleum is exploited.

It is characterized by a strong average temperature, around 25 ° C and by significant total rainfall, almost always greater than 3000 mm, up to more than 6,000 mm. The rainfall distribution is very regular throughout the year except for a weak recession between December and February. The relative humidity is high, in the order of 90% and the sky is often cloudy (approximately 1,000 hours annually insolation). In addition to the Amazonia plain, this kind of weather affects the North end of the country. There are few data on the Amazon region but it is likely that, in general, the annual sunshine duration does not exceed 1,200 hours, with some exceptions in less rainy sites (INAMHI, 1983).

As there is no break in the growing season, vegetation is evergreen forest.

The following table summarizes the characteristics of major cities in the amazonia of Ecuador.

City	Population 2016	Latitude	Longitude	[K] 22- Year Averaged Insolation Clearness Index (0 to 1.0)	Altitude (M.A.S.L.)	Mean solar radiation Wh/m ² (day)
TENA	72,499	-0.9962970	-77.8136040	0.38	507.29	43350
PUYO	33,557	-1.4923930	-78.0024130	0.44	929.25	3800
ZAMORA	30,355	-4.0620940	-78.9486230	0.42	910.14	4350
MACAS	18,984	-2.3062240	-78.1153710	0.42	1032.83	4090

Note: Population figures from INEC (2016), Latitude, Longitude and Altitude from IGM (2016), [K] Insolation Clearness Index, Temperature and Humidity from NASA (2016), Mean Solar Radiation from NEC (2011)

Table 2: CHARACTERISTICS OF THE MAIN CITIES IN THE Amazonia

The solar input varies among the cities, but in average the solar input is the same as in the coastal cities. The cooling power production can be between 200W up to 2400W depending

on the technology. In these areas is not common to find conventional AC units, offering an advantage for insertion of solar cooling technologies

Cities in the Andes.- This region is the most active in the country. Quito, the capital city, is located in the Andean region, as well as many medium size cities.

In the Sierra and the inter-zone, the insolation is almost always greater than 1,000 hours per year, except for the very rainy places. It is possible to say that varies from 600 to 1400 h between 500 and 1,500 meters high; and between 1,000 and 2,000 h in 1500-3000 meters high. One can reach even higher values at higher places. (INAMHI, 1983).

The following table summarizes the characteristics of major cities in the Sierra of Ecuador.

City	Population 2016	Latitude	Longitude	[K] 22- Year Averaged Insolation Clearness Index (0 to 1.0)	Altitude (M.A.S.L.)	Mean solar radiation Wh/m ² (day)
QUITO	2,597,989	-0.1806530	-78.4678340	0.42	2930.11	4990
CUENCA	591,996	-2.8966170	-79.0076210	0.45	2547.56	4350
AMBATO	369,578	-1.2402100	-78.6200790	0.44	2675.05	4550
LOJA	253,625	-3.9901380	-79.2044600	0.49	2081.68	4350
RIOBAMBA	252,865	-1.6734850	-78.6479920	0.44	2772.45	4490
IBARRA	207,907	0.3626778	-78.1306667	0.39	2218.29	4560

Note: Population figures from INEC (2016), Latitude, Longitude and Altitude from IGM (2016), [K] Insolation Clearness Index, Temperature and Humidity from NASA (2016), Mean Solar Radiation from NEC (2011)

Table 3: CHARACTERISTICS OF THE MAIN CITIES IN THE Sierra

The solar input is higher than in the coast or Amazonia areas. Considering that the solar input can be 4.5KWh/m²d, the cooling production could be in ranges from 225W up to 2700W depending on the technology. But there has to be one special consideration, since the temperature and humidity in this areas is not high. Uses of this technology could be for high rise buildings or special cooling needs.

Cities in Galapagos.- In the archipelago only 5% of the territory can be urbanized. The major city is Puerto Ayora in Santa Cruz Island. "The island province of Colon (Galapagos Archipelago) has a variety of thermal and rainfall climates. The coastal areas are generally dry and arid and rain increases with altitude up to a certain limit and then drops again the frequency and intensity of rain". This statement defines quite well the general conditions of the insular climate that, ultimately, is comprised of a series of microclimates at very short distances. The truth is that dominated the influences of the Humboldt current, height and exposure to the winds; the climatological information available in this region is still scarce.

In the lower parts the average temperatures fluctuate around 23°C and annual rains could vary between 150 and 500 mm. In the highlands temperatures drop a few degrees and the precipitations reach 2,000 mm near annual values, spread over two seasons, from January to May and August to September. (INAMHI, 1983).

In the Archipelago of Colon, the annual number of hours of sunshine should be equal to or greater than 2,000 hours in the coastal strip.

City	Population 2016	Latitude	Longitude	[K] 22- Year Averaged Insolation Clearness Index (0 to 1.0)	Altitude (M.A.S.L.)	Mean solar radiation Wh/m ² (day)
GALAPAGOS	25,124	-0.8292780	-90.9820670	0.59	151.47	5835

Note: Population figures from INEC (2016), Latitude, Longitude and Altitude from IGM (2016), [K] Insolation Clearness Index, Temperature and Humidity from NASA (2016), Mean Solar Radiation from NEC (2011)

Table 4: CHARACTERISTICS OF THE MAIN CITIES IN THE GALAPAGOS ARCHIPIELAGO

The solar input is the highest among the country. The cooling power production can be between 290W up to 3480W depending the technology that can be used. The electric technologies can produce between 290W and 1740W. The thermic technologies can produce from 870W up to 3480W. Since it is a special environment that is away from the continent, the potential of use for this cooling option is seen as an opportunity.

5. Remarks and future research

Taking into consideration that the solar input in Ecuador ranges from 3000 Wh/m²d to 5000 Wh/m²d, the opportunities to harvest the resource are great. There has to be a consideration on the solar collection technology then there is a low clearness sky coefficient (kt) for the majority of cities in the country.

The technologies that can be applied for solar cooling need to continue research. For the main coastal cities there is a need for further applied research to get on site results. It is important to find the optimal solution for each environment, besides considering the climate also the final use.

There is a need for future assessment of barriers of implementation. With regard to the economic investment, a study in Europe showed that the initial investment is higher for these technologies and the savings range from 16% to 55% (Allouhi, A. et. al., 2015). The social appropriation of the technological solutions has to be discussed; the habit to own an AC device versus a new technology depends on the awareness of the end user.

References

- [Allouhi et. al. 2015] Allouhi, A., T., Kousksou, A. Jamil, P. Bruel, Y. mourad, Y. Zeraouli. 2015. Solar driven cooling systems: An updated review. *Renewable and Sustainable energy Reviews*. 44 (2015) 159-181
- [Aragón investiga 2010] Aragón Investiga, Gobierno de Aragón. 2010. aragoninvestiga.org <http://www.aragoninvestiga.org/Hacia-los-sistemas-de-refrigeracion-magnetica/>.
- [Assilzadeh F, et.al. 2005] Assilzadeh F, Kalogirou SA, Ali Y, Sopian K. Simulation and optimization of a LiBr solar absorption cooling system with evacuated tube collectors. *Renew Energy* 2005;30:1143–59.
- [Boera, A. 2012] Boera Vera, Andrés. 2012. Modelling and Simulation of a Solar Powered Absorption Cooling System in a Tropical Climate City for Small-Scale Application. Dissertation. Department of Architecture of Built Environment. University of Nottingham, Nottingham, UK.
- [Buchter F, et.al. 2003] Buchter F, Dind P, Pons M. An experimental solar - powered adsorptive refrigerator tested in Burkina-Faso. *Int J Refrig* 2003;26:79–86.
- [Cadena, et. al. 2009] Colectores solares para agua caliente. Cadena, Carlos, Placco, Cora y Saravia, Luis. 2009. Salta : INENCO, UNSa - CONICET, 2009.
- [Grossi Gallegos, Raichijk 2010] Correlaciones empíricas de la irradiación solar normal directa con la heliofanía efectiva. Grossi Gallegos, H, Raichijk, C. 2010. [ed.] ASADES. Buenos Aires : s.n., 2010, AVERMA, Vol. 14.
- [European Commission 2006] European Commission . 2006. Bruselas. *Action Plan for Energy Efficiency: Realising the potential*. : s.n., 2006. COM(2006)545 final.
- [Eicker 2009] Eicker, Ursula. 2009. Low Energy cooling for sustainable buildings. John Wiley and Sons. Witshire. Great Britain
- [Foro frío. 2008] Foro frío. 2008. Forofrio.com. [En línea] 2008. <http://www.forofrio.com/>.
- [Garcia Menendez 2013] Garcia Menendez, David. 2013. *Tesis Desarrollo de motores Stirling para aplicaciones solares*. Universidad de Oviedo. Departamento de Física. Oviedo, España
- [Henning et al. 2012] Henning, Hans-Martin, A. Morgenstern, T. Nunez, E. Thümmeler, T. Urbaneck, U. Uhlig, E. Wiemken. 2012. *Kühlen und Klimatisieren mit Wärme*. Karlsruhe : FIZ; BINE Informationsdienst, Bonn, 2012.

- [IGM 2016] IGM. Instituto Geográfico Militar. [On line] 2016. <http://www.geoportaligm.gob.ec/portal/>
- [INAMHI 1983] INAMHI. Instituto Nacional de Meteorología e Hidrología. 1983. ORSTOM PRONAREG Project: Climas del Ecuador - Fundamentos explicativos. Pierre Pourrut.
- [INEC 2016] INEC. Instituto Nacional de Estadísticas y Censos. 2016. Censo de población y vivienda 2010.
- [König et.al. 2012] *Wärme und Kälte. Effiziente Kältetechnik und solare Kühlung.* König, Holger; Henning, Hans-Martin, Kalz, Doreen; Krause, Michael und Schweigler, Christian. 2012. 2012, FVEE Themen.
- [La D, et. Al. 2011] La D, Dai Y, LiY ,Ge T, Wang R. Case study and theoretical analysis of a solar driven two - stage rotary desiccant cooling system assisted by vapor compression air conditioning .SolEnergy2011;85:2997–3009.
- [Lopez Villada 2010] Lopez Villada, Julio. 2010. *TESIS: Integración de sistemas de refrigeración solar en redes de distrito de frío y de calor.* [ed.] Escola Tecnica Superior d Enginyeria Química (ETSEQ). Tarragona : Universitat Rovira I Virgili, 2010.
- [Martínez Sánchez 2007] Martínez Sánchez, Rafael. 2007. *Proyecto de dimensionamiento, montaje y análisis de una instalación de climatización basado en un sistema solar térmico y una máquina de absorción de pequeña potencia.* [ed.] Ingeniería Industrial. Cartagena : Universidad Politécnica de Cartagena, 2007.
- [NASA 2016] NASA. National Aeronautics and Space Administration: Atmospheric Science Data Center. [On line] 2016. <https://eosweb.larc.nasa.gov/cgi-bin/sse/grid.cgi?email=na>
- [NEC 2011] NEC. Normativa Ecuatoriana de la Construcción. 2011 Draft law. Chapter 14: Renewable energy.
- [Peinado Rodriguez 2011] Peinado Rodriguez, Andres. 2011. Diseño y construcción de un sistema de refrigeración termoacústico. *Tesis. Universidad Industrial de Santander.* Bucaramanga, Colombia : Facultad de ingenierías fisicomecanicas. escuela de Ingeniería mecánica, 2011.
- [Suehrke et.al. 2013] Relationship between sunshine duration and solar radiation. Suehrke, H., Bowden, R., Hollands, K.G.T. 2013. 92, s.l. : Elsevier, 2013, Solar Energy, págs. 160-171.

[Sitio Solar 2013] Sitio Solar, S.L. 2013. Sitiosolar.com. *portal de energias renovables*. [En línea] 2013. <http://www.sitiosolar.com/>.

Real-time material computation in architectural design: Experiments on the development of interactive form finding tools.

Seiichi Suzuki Erazo¹

¹ Institute of Building Structures and Structural Design – University of Stuttgart
Stuttgart-Germany
e-mail: s.suzuki@itke.uni-stuttgart.de

Keywords: particle system, form finding, material computation, computational design.

***Abstract.** A variegated set of problems start appearing when evaluating structural performances and materialization capabilities of freeform shapes generated through traditional geometrical constraint modelling. The main problematic to face is the continuous adaptation of complex geometries into standard structural typologies leading towards the inefficient use of materials and energy. A rather different approach is the exploration of novel structural systems through numerical form finding methods in which materials can be considered as active agents driving the entire design process. A condition that is only possible through fastest developments in composite materials and simulation technology. Compared to other methods, special attention is devoted to the use of dynamic methods enabling easiest implementations and fast computations which means an increased interactivity between designers and digital models. A more desirable condition for the interactive exploration of shape.*

In this context, this paper investigates the potential of particle spring systems for the integration of material's behaviors in the design process of different innovative structural systems. In doing so, the development of highly flexible and interactive computational frameworks is presented by using a basic numerical scheme built upon the Velocity Verlet integration. Three different implementations are then described for the numerical form finding of bending-, surface- and tensile form-active structures respectively.

1 Introduction

Described by DeLanda (DeLanda 2001) as a pure cerebral design philosophy, the superimposition of physical forms over obedient and standard materials remain a common practice in architectural design. Commercial CAD packages have been developed as digital tools for geometrical modelling without considering the physical behavior of materials. Although geometrically constraint modelling allow larger design spaces for form-exploration deriving into complex freeform geometries, a variegated set of problems start appearing when evaluating structural performances and materialization capabilities of such geometries.

Because geometries need to be adjusted into traditional “form-passive” structural systems, shape cannot actively adapt to loading conditions. Designs are then solved by thickening cross-sections or stiffening materials, and not by inexpensive re-computations of initial geometries. An approach that radically differ to form generation in natural systems where material is expensive and shape is cheap (Vincent 2009). Consequently, efforts for sustainable architectures need to be readdressed for achieving maximal performances with minimum material and energy.

With fastest developments in information technologies, new computational design paradigms based on the integration of material behaviors are emerging. On this basis, novel “active” structural typologies (e.g. form-active, bending-active) can be explored by considering material not as a merely inanimate matter but rather as an active agent driving the entire design process. The key characteristic of these structures is the development of optimal forms by means of analog and numerical form-finding processes driven by the reciprocal dependency of finding the correct geometry, minimizing masses and redirecting forces. For that reason, form finding defines the process of generating an optimal static equilibrium shape for an explicitly defined loading condition (Adriaenssens et al. 2014). Its definition can be equally extended to the process of finding a geometrical solution satisfying not only structural but also architectural and fabrication constraints.

Numerical form finding based on the Finite Element Method (FEM) can generate a complete mechanical description of physical structures including those based on large deformations. Nevertheless, they are time-consuming and lack a key element necessary for every design practice, real-time interactivity. In early design stages, fast approximations of material’s behaviors are rather more desirable than expensive computations of complex mechanics. Compared with other methods, dynamic methods like Particle Spring Systems (PSS) allows easiest implementations and fast computations enabling real-time interactions between designers and models.

With the aim of exploring alternative design approaches leading towards more sustainable architectures, this paper presents contributions of different experiments for form finding novel structural typologies by using PSS.

2 Previous work

With the introduction of numerical methods for shape exploration, computational workflows are gaining in complexity. In the past two decades, PSS method has become an important research area in computational graphics and, recently, have gained adepts in the architectural community. PSS is built upon Hooke’s law of elasticity and Newton’s three law of motion where different forces applied to a system of interconnected particles can approximate the mechanical behavior of rigid and non-rigid objects. The use of particle-spring systems has been introduced in architectural design by Killian and Ochsendorf (Killian, Ochsendorf 2005) and then explored by several research using force-based formulations

(Ahlquist, Menges; Bertin 2013; Clifford 2013; Fleischmann, Menges 2012; Harding, J., and P. Shepherd 2011) including the renowned development of Rhinoceros-Grasshopper plugin Kangaroo I (Piker 2013; Senatore, Piker 2015). Special attention also demands contributions on constraint-based formulations like the development of the ShapeOp library (Bouaziz et al. 2014; Deuss et al. 2015) being at the basis for the new solver of Kangaroo II. A wide range of open-source physics library used for scientific and game programming are available that includes the Bullet-Physics-Library (Bullet Physics Library) and the Nvidia PhysX library (Nvidia).

3 Numerical Scheme

In this section we will present the numerical scheme adopted for all implementations. PSS relay on the process of discretizing a continuum body into a set of particles connected by springs where internal and external forces are applied in order to realistically simulate a physical phenomenon. The principal purpose of PSS is to trace step by step the motion of particles under applied forces by iteratively computing velocities and updating positions.

In general terms, a particle i is defined as a virtual object described through a data structure that store scalar information regarding a fictitious mass M_i and a set of three-dimensional vectors storing position \vec{x}_i , velocity \vec{v}_i and acceleration \vec{a}_i . Particle's motion is then governed by Newton's second law rearranged for solving accelerations as in eq. (1), where F_i denotes force accumulation.

$$\vec{a}_i = M_i^{-1} F_i \quad (1)$$

Because force accumulation relates to the summation of all internal and external forces apply to each particle as in eq. (2), particle's acceleration can be rewritten as in eq. (3) by substituting eq. (1) into eq. (2).

$$F_i = \sum_{j=1}^n f_{i,j} \quad (2)$$

$$\vec{a}_i = M_i^{-1} \sum_{j=1}^n f_{i,j} \quad (3)$$

Moreover, the variegated set of forces available for simulating physical behaviors can be categorized as unary, binary and n-ary which basically relate to the number of particles required for computing the force. Unary forces are normally considered as external like gravity, wind or drag forces. On the other hand, binary and n-ary forces are considered as internal since they describe the relation between two or more particles being the common case of springs. Axial forces originated from the connection of two particles i and j by a Hooke spring are defined in eq. (4) where k_s is the stiffness coefficient of the spring, k_d is its damping coefficient and r is the natural length of the spring, or the rest length.

$$\vec{t}_i = - \left[k_s (|\vec{x}_i - \vec{x}_j| - r) + k_d \frac{(\vec{v}_i - \vec{v}_j)(\vec{x}_i - \vec{x}_j)}{|\vec{x}_i - \vec{x}_j|} \right] \frac{\vec{x}_i - \vec{x}_j}{|\vec{x}_i - \vec{x}_j|} \quad \text{and} \quad \vec{t}_j = -\vec{t}_i \quad (4)$$

Finally, the numerical integration schema for updating particle's position and velocity is based on the Verlet-Velocity Method by using the following system of equations.

$$x_{t+\Delta t} = x_t + v_t \Delta t + \frac{a_t \Delta t^2}{2} \quad (5)$$

$$v_{t+\Delta t} = v_t + \frac{a_t + a_{t+\Delta t}}{2} \Delta t$$

4 Experiments

4.1 Form-finding of form-active tension structures

Common types of form-active tensile structures are membranes and cable-nets. According to Engel's categorization of structural actions (Engel 2007), such structures carry external loads by pure tension without shear or bending moments. In doing so, the geometry needs to match the flow of forces affecting the structure. That is when varying loads or support conditions, the geometry must be able to adapt and change.

An interactive form finding tool was developed using the Processing programming language in which the designer has the capacity to dynamically alter stiffness coefficients, support conditions, metric parameters and force configurations. Such degree of flexibility is allowed by treating the initial assembly of particles in the context of a general network formulation. To be precise, particles' connectivity is stored through branch-node matrices. Initial numerical experiments have been formulated on the basis of quadrangular meshes with regular polygonal boundaries, whereas scaled analog models for validation have been made from a synthetic elastic textile (e.g. Lycra). In this case, geometrical complexity is introduced by altering support conditions as show in Figure 1.

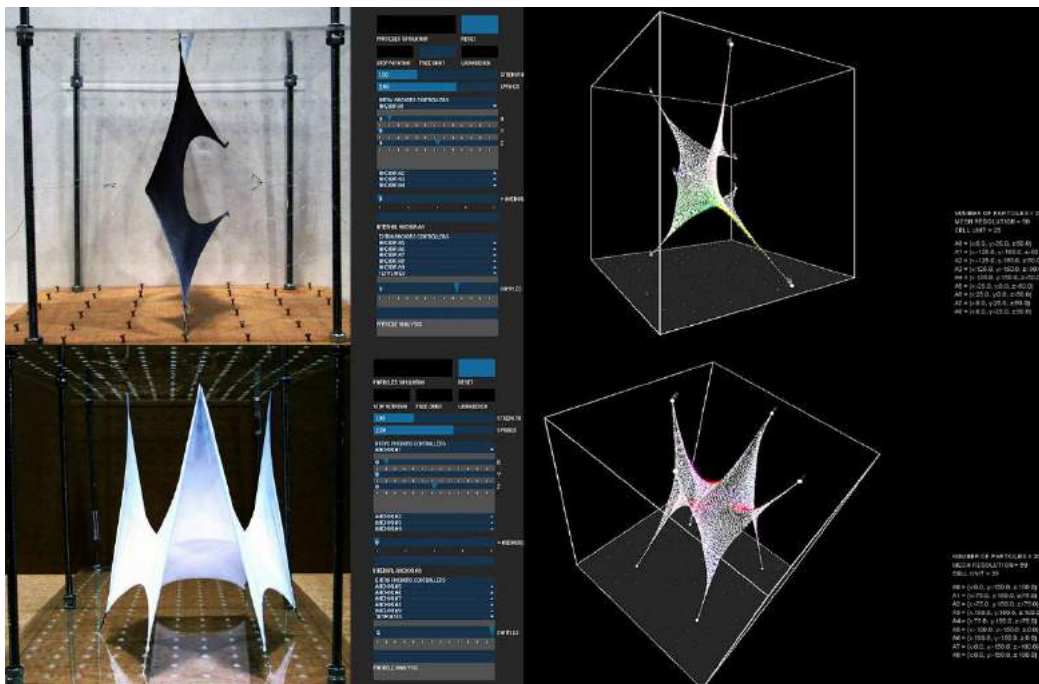


Figure 1: Comparison between analog and digital models with different support conditions

Initial experiments were focused on extracting correct stiffness coefficients for PSS in order to match real material properties. From here, the topology of the mesh is modified by

introducing inner holes with the purpose of studying complex membranes 'aggregations. Anchored particles were uniquely located at the outer boundary of the mesh while common connected particles were located on internal boundaries. Figure 2 shows a type of aggregation between two components where the mean curvature on each vertex of the mesh is displayed. On this basis, a multi-dimensional membrane can be generated where each component shaping the system is transferring stresses to its closest neighbors.

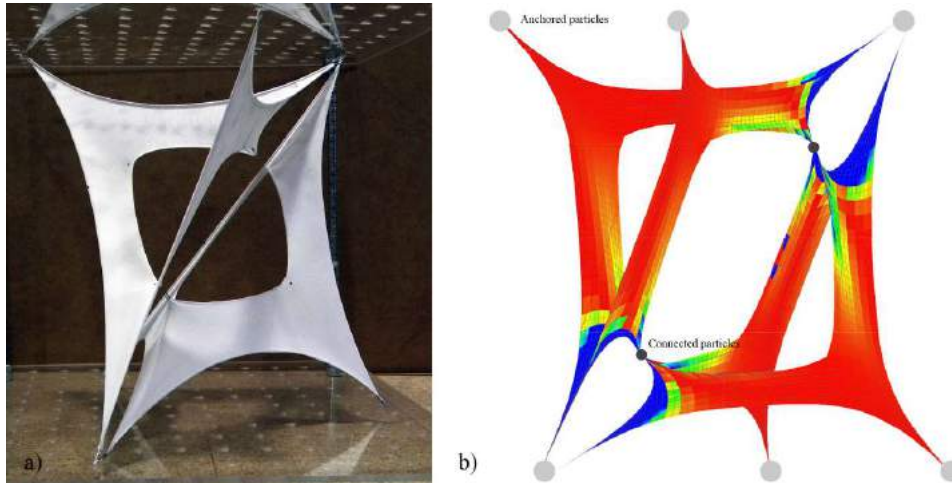


Figure 2: a) Aggregation of two membranes with complex topology, b) digital model displaying mean curvature.

A complex aggregation of multiple components was finally designed by using results of previous experiments. The aggregation start and end with a “solid” membrane while the internal distribution is composed of multiple membranes with inner holes. Internal membranes are then defined with four anchored particles on external boundaries and an equal number of connected particles on internal boundaries. As a result, a complex morphological space emerges from the progressive aggregation of rather simple topological components (Figure 3).



Figure 3: Final prototype showing the complex morphology emerging from simple components 'aggregation.

4.2 Form-finding of surface-active structures

Common types of surface-active structure are shells and folded structures. Surface-active structures are systems of rigid planes where external loads are carried through tension, compression and shear resistance (Engel 2007). Because we are dealing with non-flexible structures, an interactive form-finding tool for folded structures using the Processing programming language has been developed on the basis of rigid body dynamics. That is, a very high stiffness coefficient is assigned to springs interconnecting sets of particles so that they can be considered as rigid connections. Rigid connections are then allowed to rotate in relation to a specific axis under applied forces.

At this point, the design process of a shell-like folded structure is briefly presented. The aim of the study is to understand how freeform geometries can be generated by means of folding mechanism controlling local curvatures. Analog models made of paper and cardboard were produced for deriving form finding parameters. Initial studies were focused on analyzing a polygonal geometry from where the basic motion of rigid parts can be derived as show in Figure 4a. Aggregation of further components provides a mechanism for controlling local curvatures on the new system. It has been observed that higher degrees of curvature can be incorporated into the system by altering the length of common edges (Figure 4b).

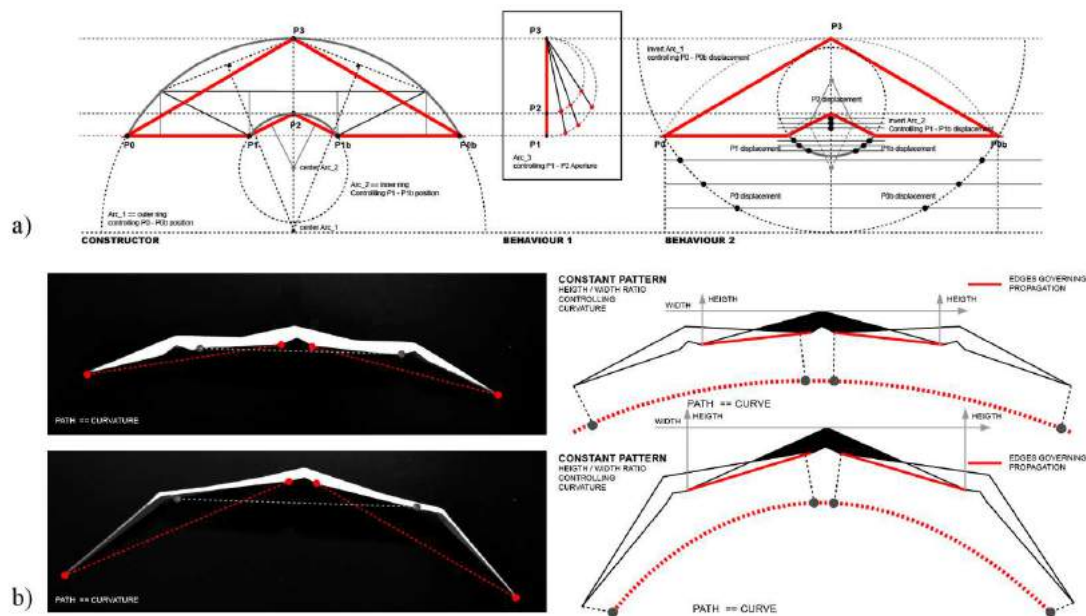


Figure 4: a) Rotation of rigid connections through axis constrains. c) Curvature control through aggregation.

The final design of the shell structure was then carried through a custom-built planar grid constructed by tessellating a surface with the initial polygonal element previously analyzed. In this case, tessellation rules were defined on the basis of aggregation experiments. Such grid was used as the initial input for starting form finding. During form finding, the designer has the capability to dynamically specify axes of rotation, force configuration and metric parameters (Figure 5a). The resultant freeform geometry is presented in Figure 5b.

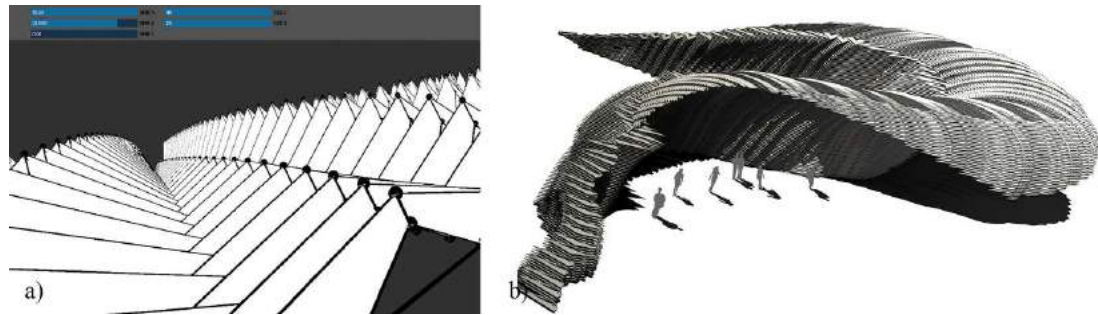


Figure 5: a) Interactive form finding tool based on rigid body dynamics, b) Design of the shell-like folded structure.

4.3 Form-finding of bending-active structures

Bending-active structures are structural systems constantly exposed to bending stresses where geometry is the result of large elastic deformation. Major advantages of these structures rely on the capacity to produce complex geometries from linear or planar components (Lienhard 2014.). Because of its design complexity, bending-active structures require a parallel understanding of geometric behavior and structural performance only possible through a multistep modelling workflow. The case study presented in the following corresponds to the design and fabrication of a bending-active chair.

The computational workflow has been divided in three main processes associated with shape exploration (i.e. form finding), structural analysis and fabrication. The numerical PSS scheme was implemented in the Rhinoceros/Grasshopper modelling environment using the Python scripting language. A triangular mesh with a rectangular boundary was used for starting form finding. For computing bending stiffness, vector forces were calculated through the weighted sum of particle positions (Volino, Magnenat-Thalmann 2006). Additionally clamped support conditions were defined by anchoring regions of particles. Figure 6a shows the equilibrium shape resulting from the form finding process. A finite element analysis (FEA) was then carried on the form found geometry by using the Millipede (Sawapan) plugin for Grasshopper. The structural capacity of the bending-active chair was analyzed by applying a vertical load in its central area (figure 6b). For fabrication, the initial unstrained geometry was laser cut by employing a thin laminated MDF board. A pair of elastic cables were used to activate bending by pulling opposite points on the component (Figure 6c).

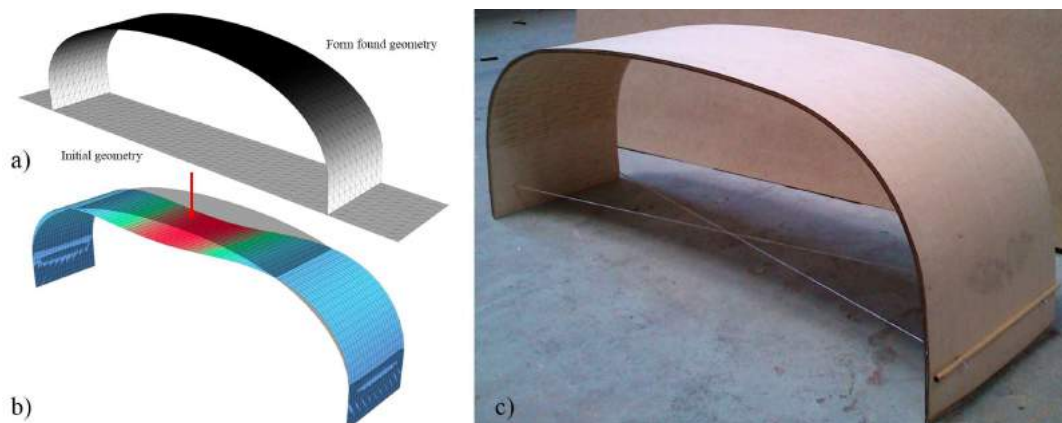


Figure 6: a) Form finding process from an unstrained mesh, b) FEM analysis of structure deformation under applied loads, c) 1:1 prototype of the bending-active chair

5 Conclusion

Traditional geometric modelling in architectural design is focused on the generation of complex freeform geometries without real consideration of structural and materialization capabilities. A condition that is continuously deriving into the production of highly inefficient structures. With fastest developments on information technologies, new structural systems with increased performances are emerging. Such systems are characterized by the development of optimal forms by means of numerical form-finding processes in which material behavior needs to be integrated in the design process.

In this context, we have shown that PSS is the most suitable method for interactive form-finding applications. A numerical PSS scheme was presented which has been implemented within a varied set of computational environments for simulating bending-, surface and tensile form-active structures. In the special case of bending-active structures an extra formulation for computing bending forces was implemented, while for surface-active structures a very high stiffness coefficient was assigned to springs.

Even if all computation frameworks presented before have been developed for an interactive exploration of material and geometric properties during form finding, efforts are still required when addressing dynamic alterations of topology without completely resetting the simulation. The main problem to face is the data structure design when information is dynamized. In other words, dynamic resizing of topological data without losing consistency of connectivity.

BIBLIOGRAPHY

Adriaenssens, Sigrid; Block, Philippe; Veenendaal, Diederik; Williams, Chris (2014): Form finding and optimization of shell structures. Abingdon, Oxon: Routledge.

Ahlquist, Sean; Menges, Achim: Behavioral-based Computational Design Methodologies: Integrative processes for force defined material structures. In Joshua M. Taron (Ed.): Integration through computation: proceedings of the 31st annual conference of the Association for Computer Aided Design in Architecture. With assistance of 2011. US.

Bertin, Trevor (2013): Evaluating the use of particle-spring systems in the conceptual design of grid shell structures. Master Thesis. Massachusetts Institute of Technology, Massachusetts, US.

Bouaziz, Sofien; Martin, Sebastian; Liu, Tiantian; Kavan, Ladislav; Pauly, Mark (2014): Projective dynamics. In ACM Trans. Graph. 33 (4), pp. 1–11. DOI: 10.1145/2601097.2601116.

Bullet Physics Library: Bullet Physics Library. Available online at <http://bulletphysics.org/wordpress/>, checked on 4/29/2016.

Clifford, Brandon (2013): Thicker Funicular: Particle-Spring Systems for Variable-Depth Form-Responding Compression-Only structures. In: International Conference on Structures and Architecture.

DeLanda, Manuel (2001): Philosophies of design. The case of modelling software. In Jaime Salazar (Ed.): Verb Processing: Actar.

Deuss, Mario; Deleuran, Anders; Bouaziz, Sofien; Deng, Bailin; Piker, Daniel; Pauly, Mark (2015): ShapeOp: A Robust and Extensible Geometric Modelling Paradigm. In

Ramsgaard, Thomsen, Tamke, Gengnagel, Faicloth, Scheurer (Eds.): *Modelling Behaviour*.

Engel, Heino (2007): *Structure systems*. 3rd ed. Hatje Cantz.

Fleischmann, Moritz; Menges, Achim (2012): Physics-Based Modelling as an alternative approach to geometrical constraint-modeling for the design of elastically-deformable material systems. In: *Proceedings of the 30th International Conference on Education and research in Computer Aided Architectural Design in Europe*.

Harding, J., and P. Shepherd (2011): Structural form-finding using zero-length springs with dynamic mass. In: *International Association for shell and spatial structures*.

Kilian, Axel; Ochsendorf, John (2005): Particle-spring systems for structural form-finding. In: *Journal of the International Association for Shell and spatial Structures*.

Lienhard, Julian (2014.): *Bending-active structures: Form-finding strategies using elastic deformation in static and kinetic systems and the structural potentials therein*. Doctoral Thesis. Institut für Tragkonstruktionen und Konstruktives Entwerfen.

Nvidia: PhysX. Available online at <http://www.geforce.com/hardware/technology/physx>, checked on 4/29/2016.

Piker, Daniel (2013): Kangaroo. Form Finding with Computational Physics. In *Archit Design* 83 (2), pp. 136–137. DOI: 10.1002/ad.1569.

Sawapan: Millipede. Available online at <http://www.sawapan.eu/>, checked on 4/30/2016.

Senatore, Gennaro; Piker, Daniel (2015): Interactive real-time physics. In *Computer-Aided Design* 61, pp. 32–41. DOI: 10.1016/j.cad.2014.02.007.

Vincent, Julian (2009): Biomimetic Patterns in Architectural Design. In *Archit Design* 79 (6), pp. 74–81. DOI: 10.1002/ad.982.

Volino, Pascal; Magnenat-Thalmann, Nadia (2006): Simple linear bending stiffness in particle systems. In Carol O'Sullivan (Ed.): *Proceedings of the 2006 ACM SIGGRAPH Eurographics symposium on Computer animation*.

Computational analysis of an urban park's impact on the Antwerp microclimate

Yasin Toparlar^{1,2}, Bert Blocken^{1,3}, Bino Maiheu², GertJan van Heijst⁴

¹ Department of Built Environment, Eindhoven University of Technology
Eindhoven, the Netherlands
e-mail: y.toparlar@tue.nl

² Environmental Modeling Unit, Flemish Institute for Technological Research
Mol, Belgium

³ Department of Civil Engineering, KU Leuven
Leuven, Belgium

⁴ Department of Applied Physics, Eindhoven University of Technology
Eindhoven, the Netherlands

Keywords: Urban microclimate, Computational Fluid Dynamics (CFD), vegetation, scenario analysis, adaptation measures.

Abstract. *Urban areas are formed by replacing natural surroundings with man-made environments and they create their own microclimates, which can be different from that of their rural counterparts, potentially affecting energy use and human morbidity and mortality. Since the 19th century, research on urban microclimate has progressed, mainly based on observational techniques. With the advances in computational resources since the 1980s, simulation approaches such as Computational Fluid Dynamics (CFD) have been frequently used to test, optimize and even regulate urban design alternatives. In this study, CFD simulations are performed to predict air temperatures in the central area of Antwerp and to analyze the effect of an urban park on the urban microclimate. Using the municipal database, a high-resolution computational domain and grid of the region are generated. The 3D Unsteady Reynolds-Averaged Navier-Stokes (URANS) equations are solved in combination with the realizable k -epsilon turbulence model to determine the wind flow and heat transfer. In the first part of this study, resulting air temperatures inside the city center are compared with the measurements recorded during 29-30 June 2013. Compared with the measurements, the CFD simulations reproduce the air temperatures fairly well, with a correlation coefficient (R) of 0.97. CFD simulations are then performed considering three design scenarios: the scenario with the urban park (base case); a scenario with an open space instead of the park (case-1); and a scenario with buildings instead of the park (case-2). The results show that, compared with the base case, case-1 shows increased air temperatures in the wake region of the park over a distance of 205 m, with a maximum temperature increase of 2.8 °C. For case-2, air temperatures are found to be increasing over a distance of 244 m with a maximum increase of 4.4 °C*

1 Introduction

The World Urbanization Prospects report published by the United Nations (UN) (United Nations, 2014) documents the rapid trend towards urbanization. The urbanization conveys a challenge from a climatic point of view. As urban settlements are formed by replacing natural environments, they create their own, unique climates, which may affect the energy consumption of buildings and human morbidity and mortality.

Research on urban microclimates started in the 19th century (Mills, 2014) and ever since, has progressed mostly with observational techniques, such as field measurements and experiments (Mirzaei and Haghighat, 2010). Later, computational methods such as Computational Fluid Dynamics (CFD) and Energy Balance Models (EBM) have started to emerge as new tools of urban climate studies. With the advances in computational resources, urban climatology is increasingly becoming a design and engineering field, with which urban design alternatives can be tested, optimized, and regulated (Moonen et al., 2012).

Urban microclimate can be affected by various measures. In recent history, the effects of parks, water bodies, and materials on urban microclimate have been documented in various measurement studies (Lindley et al., 2006; Müller et al., 2014; Yow, 2007). However, CFD analysis on the effect of such measures on urban microclimate is still scarce. CFD enables researchers to conduct scenario analyses for the implementation of adaptation measures (Blocken, 2014). For instance, the effect of an urban park on the surrounding microclimate can be quantitatively assessed with CFD by comparing cases with and without the park whereas a similar comparison would not be feasible with field measurements. In addition, the control of boundary conditions allows a controlled investigation where different scenarios can be assessed under the same meteorological conditions.

One of the urban formations which can reduce air temperatures during a hot day is an urban park. According to the measurements reported in some early studies (Ca et al., 1998; Jauregui, 1991), an urban park can reduce the air temperature inside its wake region, improving thermal comfort and reducing air conditioning costs. Some studies referred to this phenomenon as the urban park cooling island (Chow et al., 2011; Declet-Barreto et al., 2013).

To the best of our knowledge, the first CFD study to numerically model the park cooling island was conducted by Honjo and Takakura (1990), focusing on a 2D computational domain. The study conceptualized the park's cooling effect (Figure 1) by modeling the park as a heat sink. In CFD studies, use of source/sink terms instead of explicit modeling of urban forms (buildings, trees etc.) has been a common methodology since the 1970s (e.g., Meroney and Yamada, 1972). The study by Honjo and Takakura (1990) analyzed the park cooling effect based on two parameters: 1) Range of the cooling effect, referring to the horizontal distance where the park cooling effect is present and 2) intensity of the effect, referring to the maximum decrease in air temperature (Figure 1). Honjo and Takakura (1990) showed that a park formation with an edge length of 400 m can reduce air temperatures for a distance of 700 m away from the park (range of the cooling effect) with a maximum change around 2°C (intensity of the effect).

A similar analysis on the range and the intensity of the cooling effect would be more difficult to assess for studies on 3D domains. Due to the differences in the distribution of the vegetation sources and buildings, the effect would be different in every vertical plane. However, some CFD studies assessed the cooling effect based on these parameters, either by focusing on the plane which would exhibit the maximum effect or by focusing on the center plane of the park with respect to the prevailing wind direction.

Dimoudi and Nikolopoulou (2003) considered a 3D generic urban domain to evaluate the effect of park size on the cooling. According to the results, the size of the park could

significantly change the cooling potential and with the park size of $18 \times 18 \text{ m}^2$, the cooling was noticeable over a range of 50 m, with an intensity of 6°C (Dimoudi and Nikolopoulou, 2003), compared to the case without the park.

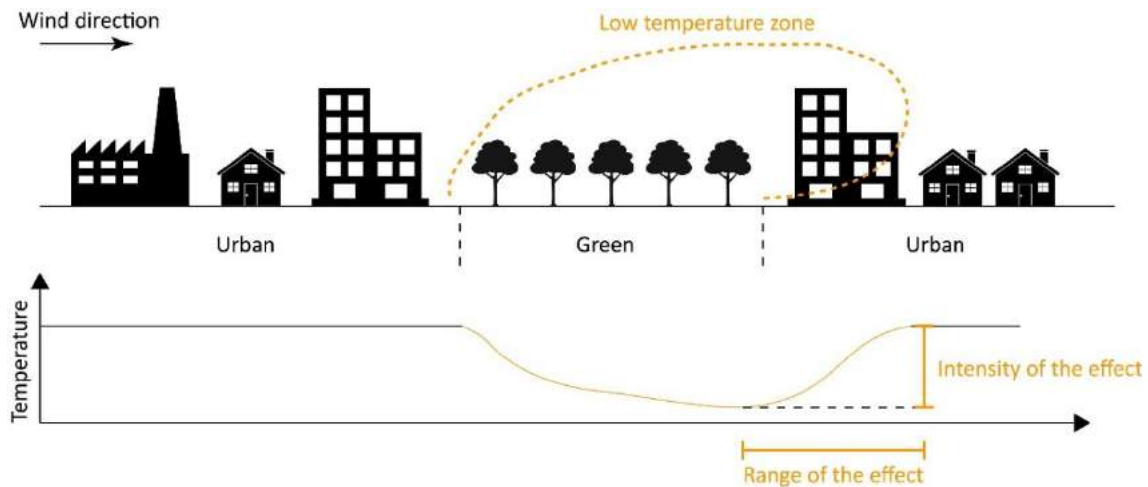


Figure 1: Schematic representation of the cooling effect of a park. The figure demonstrates the two parameters: range of the cooling effect and the intensity of the cooling effect. (Modified from Honjo and Takakura (1990))

Yu and Hien (2006) considered the effect of an urban park in a 3D domain with building blocks of different heights. The study showed that with the introduction of a park with a size of $25 \times 20 \text{ m}^2$, the cooling effect was noticeable for around 45 m, with a maximum temperature decrease of approximately 2°C (Yu and Hien, 2006).

Vidrih and Medved (2013) focused on parks with different Leaf Area Indices (LAI). The parks were modeled on an area of $140 \times 140 \text{ m}^2$. The simulations showed that with a LAI of $2.0 \text{ m}^2/\text{m}^2$, the cooling effect was noticeable for 140 m on the leeward side of the park with a maximum temperature change of 3.6°C (Vidrih and Medved, 2013). There are some CFD studies investigating park cooling islands but focusing on thermal comfort and average temperature differences rather than the range and intensity of the cooling effect (Müller et al., 2014; Taleghani et al., 2014).

Among the previous CFD studies on this topic, there is a lack of CFD studies for real urban areas with validation. This study aims to investigate the effect of a typical urban park in Antwerp, Belgium in two phases: 1) Comparison of air temperatures from CFD simulations with field measurement data and 2) Comparison of the cases with and without the urban park and demonstrating the range and intensity of the park cooling island. Section 2 of this paper describes the study area. Section 3 presents the CFD settings and parameters and section 4 summarizes the results. The paper is finalized with conclusions (section 5).

2 Description of the study area

Antwerp is a city located in the north of Belgium. As a densely populated, growing port city, Antwerp has already been the subject of urban heat island studies in the recent past (De Ridder et al., 2014). Inside the Antwerp city center, an urban park named Stadspark, which has a triangular shape with approximately 410 m edge length, is located. The park is mainly composed of trees, walking paths and a pond.

Field measurements of meteorological parameters in and around Antwerp were conducted by the Flemish Institute for Technological Research (VITO) at two locations, one in a rural measurement site approximately 10 km away from the city center and the other inside the city, approximately 400 m south of the Stadspark (Figure 2). VITO has collected 15-minute averaged

data for air temperature, relative humidity, solar radiation, wind direction and wind velocity from June 2012 till September 2013. This study focuses on two specific days, 29-30 June 2013.

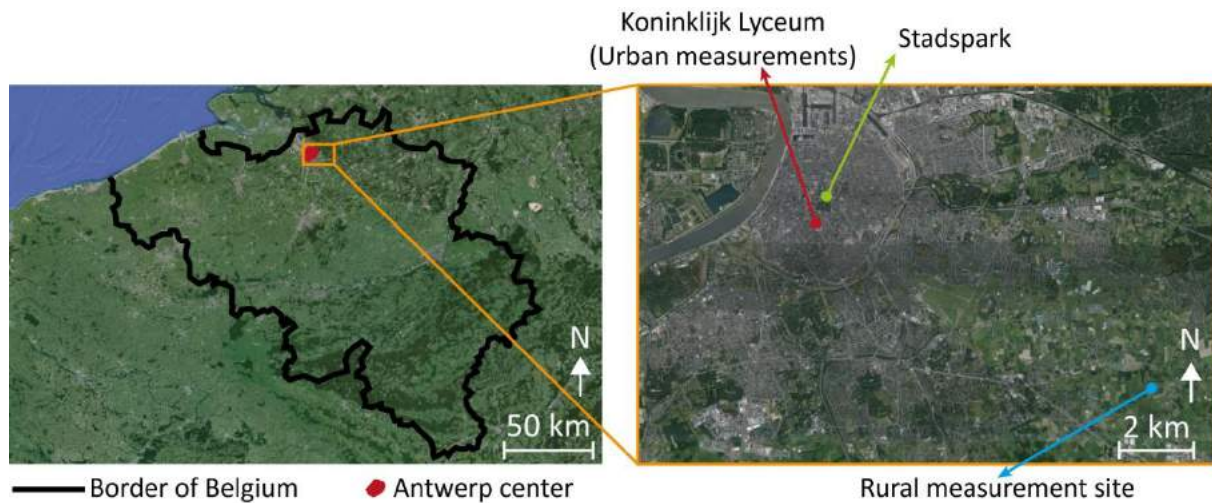


Figure 2: Figure on the left shows the location of Antwerp in Belgium. Figure on the right shows the location of the measurement sites and the investigated park.

The study is conducted in two parts. In the first part, the focus is to validate resulting air temperatures from CFD simulations with the field measurements recorded at the city center. In the second part, the existing Stadspark is replaced first by an open space and then with representative buildings. The aim of the second part is to assess the range and intensity of the park cooling effect caused by the Stadspark.

3 CFD simulations: computational settings and parameters

A 3D computational domain is generated based on the municipal drawings acquired from the Antwerp city authorities. The area of interest for this study is the Stadspark and the surroundings up to a distance of 850 m from the Stadspark (Figure 3). The outside of the area of interest is implicitly modeled with an appropriate aerodynamic roughness length (z_0), estimated using the updated Davenport Roughness Classification (Wieringa, 1992) (Figure 3). All buildings within the area of interest are modeled explicitly and trees are modeled as porous volumetric zones (Figure 4). The highest building inside the domain has a height of 60 m (H). To determine the extent of the domain and for generating a high-quality grid, several CFD best practice guidelines are used (Blocken, 2015; Franke et al., 2007; Tominaga et al., 2008). According to these settings, a square shaped computational domain is generated. The domain size is $6.5 \times 6.5 \times 0.42 \text{ km}^3$ ($L \times W \times H$) and it contains 9,078,916 hexahedral cells. For the remainder of the paper, the letter H will be used for the height of the highest building (60 m) and H_{domain} will be used for the height of the domain (420 m).

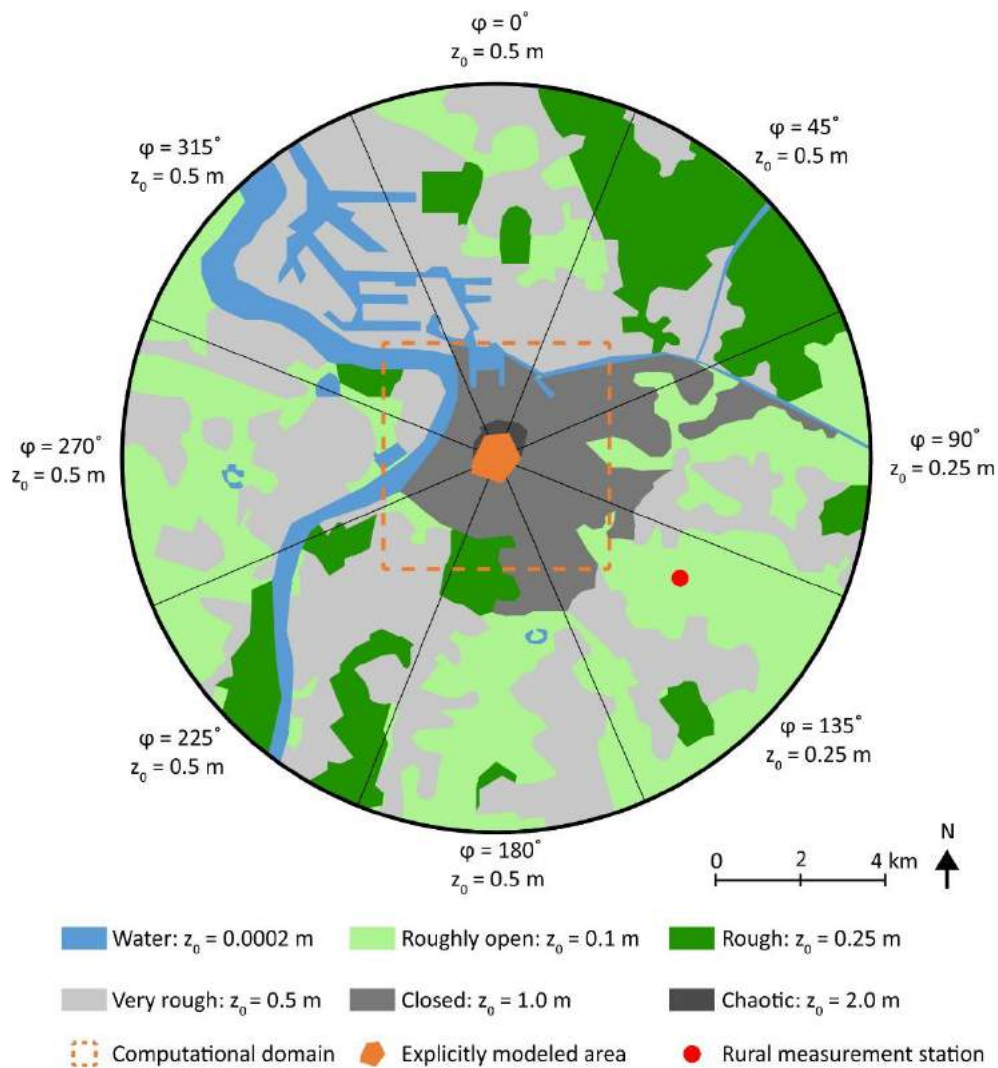


Figure 3: Terrain surrounding the modeled urban area with a radius of 10 km. The estimated aerodynamic roughness length (z_0) is shown for different angles. The computational domain used in this study is represented by the orange dotted square.

Two of the vertical boundaries are defined as velocity inlets and the remaining two are defined as pressure outlets with zero static gauge pressure, depending on the wind direction (denoted as flow boundary in Figure 4). The top part of the domain is modeled as a free-slip wall, assuming zero normal gradients for all the variables. The ground level and the building surfaces are modeled as wall type boundaries with standard wall functions modified for roughness.

At the inlets, a logarithmic mean wind speed profile ($U(z)$) (m/s) is used. The reference wind speed is time dependent and is based on the meteorological data provided. For turbulent kinetic energy ($k(z)$) (m^2/s^2) and turbulence dissipation rate ($\varepsilon(z)$) (m^2/s^3), the profiles are defined as (Richards and Hoxey, 1993):

$$k(z) = \frac{u^{*2}}{\sqrt{C_\mu}} \quad (1)$$

$$\varepsilon(z) = \frac{u^{*3}}{\kappa(z+z_0)} \quad (2)$$

where κ is the von Karman constant ($=0.41$), u^* (m/s) is the boundary layer friction velocity and C_μ is the model constant ($=0.09$). The air temperature at the inlet is imposed based on the meteorological data obtained from the rural location. The profiles are shown in Figure 5.

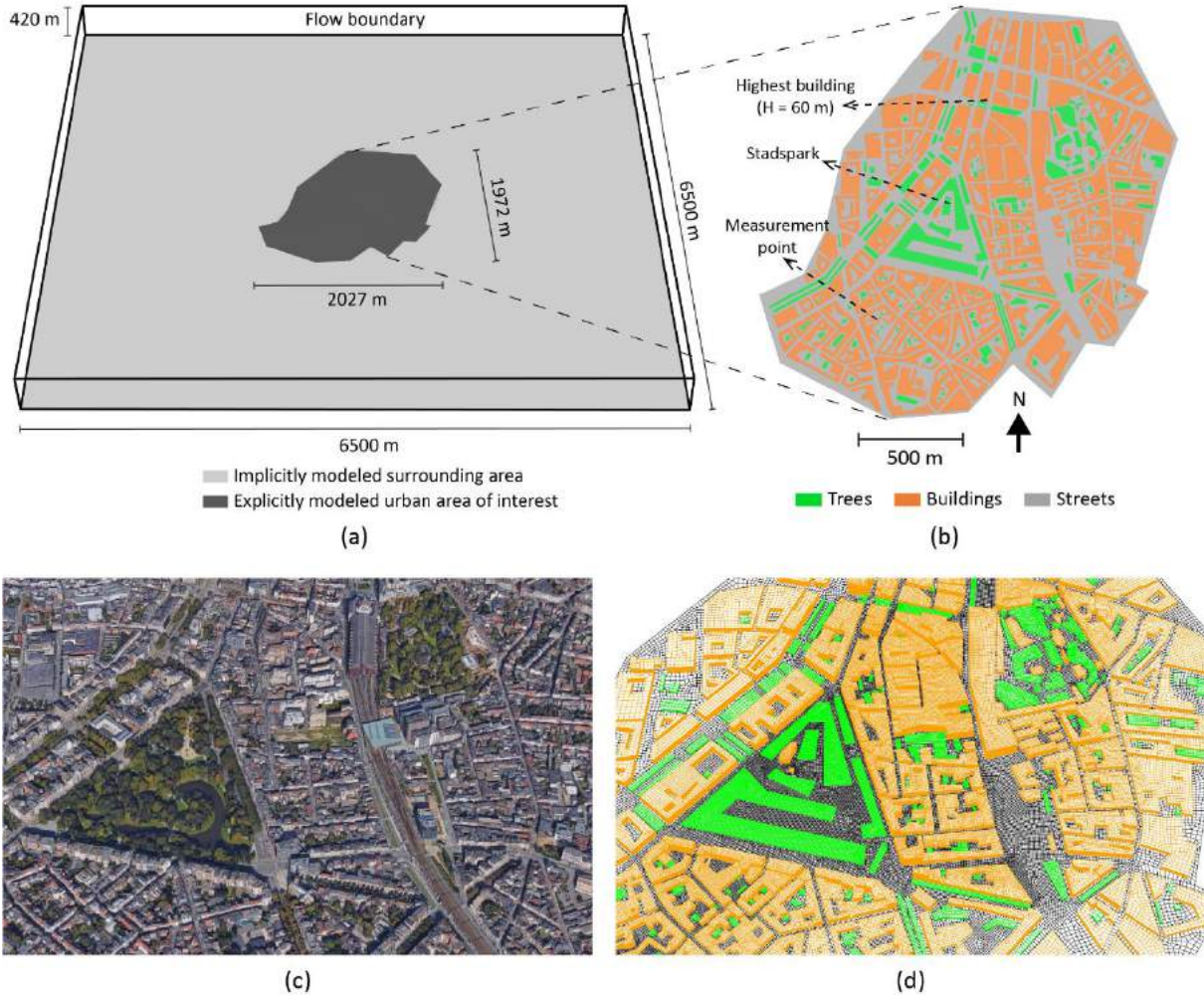


Figure 4: Computational domain. a) View of the complete domain; b) View of the explicitly modeled part of the domain with buildings, trees and streets. c) Aerial view of the area of interest from south (source: Google Maps) d) Corresponding computational grid on building, street and tree surfaces (total cell count: 9,078,916 cells)

At the walls, the standard wall functions (Launder and Spalding, 1974) are used in combination with the sand-grain based roughness modification (Cebeci and Bradshaw, 1977) and the parameters k_S (roughness height)(m) and C_S (roughness constant) are determined from their appropriate relationship with the z_0 . CFD simulations were performed using the commercial software ANSYS Fluent (ANSYS Inc., 2009) and thus the roughness relationship is given by (Blocken et al., 2007):

$$k_S = \frac{9.793 z_0}{C_S} \quad (3)$$

In line with equation 3, in the region where the buildings are implicitly modeled, the parameters are defined as: if $z_0 = 0.5$, then $k_S = 0.7$ and $C_S = 7$, and if $z_0 = 0.25$, then $k_S = 0.7$ and $C_S = 3.5$. For the explicitly modeled area of interest, the $z_0 = 0.03$, with $k_S = 0.1$ and $C_S = 2.9$.

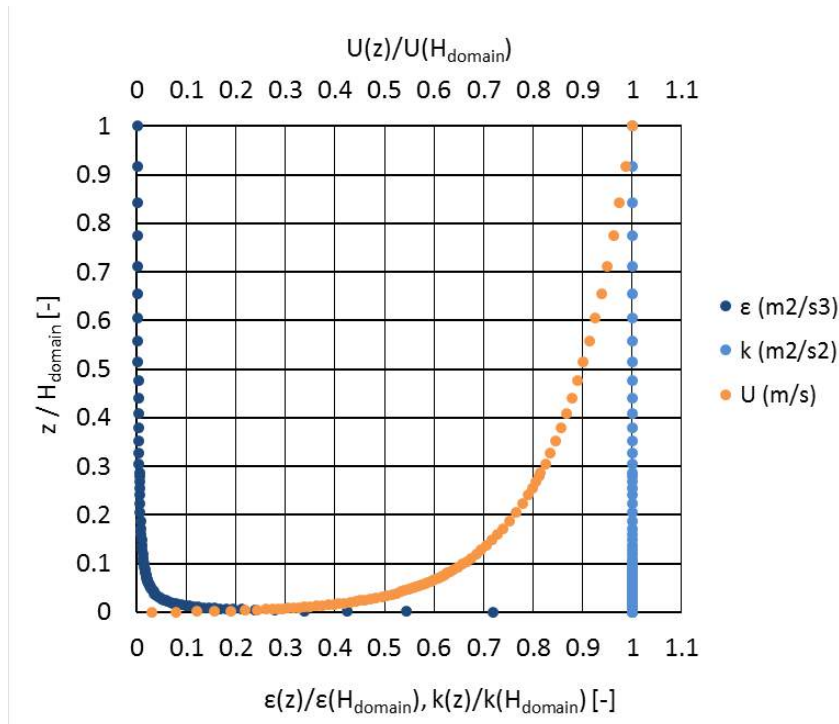


Figure 5: Normalized profiles of mean wind velocity $U(z)$, turbulent kinetic energy $k(z)$ and turbulence dissipation rate $\epsilon(z)$. The profiles are normalized with respect to $H_{\text{domain}} = 420$ m.

The ground plane of the domain is modeled implicitly as a 10 m thick earth layer with zero heat flux at the bottom. Different than one of the recent CFD microclimate studies with a similar methodology (Toparlar et al., 2015), in this study, the ground is modeled with three dimensional conduction equations, where the effect of thermal diffusivity is more pronounced

The trees inside the domain are modeled as porous volumetric zones with source and sink terms used in previous studies (Balczó et al., 2009; Gromke et al., 2015). For the tree crown to resemble a typical tree in Antwerp, the volumetric zone is defined from 3 m to 9 meter high. The corresponding volumetric zones affect the momentum of the flow, turbulent kinetic energy and turbulence dissipation rate. In addition, a sink term based on the study by Gromke et al. (2015) representative of the cooling effect and a shading coefficient are imposed. A shading coefficient is applied to reduce the absorptivity of the ground wall below the trees based on an earlier study (Armson et al., 2012).

The 3D unsteady Reynolds-averaged Navier-Stokes (URANS) equations are solved with the realizable k - ϵ turbulence model (Shih et al., 1995) for closure. The radiation equations are solved with the P1 radiation model (ANSYS Inc., 2009) and natural convection is modelled with the Boussinesq approximation. Second order discretization schemes are used for pressure, convection and viscous terms. Unsteady simulations are performed with a time step size of 15-minutes and each time step is calculated with 100 iterations, yielding scaled residuals of 10^{-4} to 10^{-5} for velocity components, 10^{-4} for k , ϵ and continuity and 10^{-7} for energy and radiation.

4 Results

The results are presented in two parts. In part 1, meteorological conditions measured at the rural area are imposed as the boundary conditions and the air temperatures from the CFD simulations are compared with the measurements obtained inside the urban area. In part 2, three cases are compared, the first being the base case with the park, the second with an open space instead of the park and the third with buildings instead of the park. The results of part 2 are

evaluated based on the range and the intensity of the cooling effect as mentioned in the introduction.

4.1 Part 1: Comparison of air temperatures

With the settings described in section 3, unsteady simulations are performed based on the meteorological conditions reported for 29-30 June 2013. The simulations on 29 June were performed to initiate the cyclic behavior of the ground thermal storage. Therefore the results are compared only for the 30th of June. The urban measurement station of VITO is located on the roof of the Koninklijk Lyceum high school building and the simulation results are obtained from the same location, which is 2 meter above the building rooftop, standing at 18 m from the ground level.

Two comparative charts are provided in Figure 6. In Figure 6a, the diurnal variation of air temperatures are provided as reported in measurements and calculated by CFD simulations. Overall, a fairly good agreement can be observed between the simulations and measurements, especially in repeating the diurnal variation. CFD simulation results seem to slightly underestimate the air temperatures, which might be related to the average absorptivity value imposed on the roof surfaces. In Figure 6b, the normalized temperatures are compared and a correlation coefficient (R) of 0.97 is found from the comparison. With the fairly good agreement, the CFD approach followed can be considered reliable in predicting air temperatures for this case study.

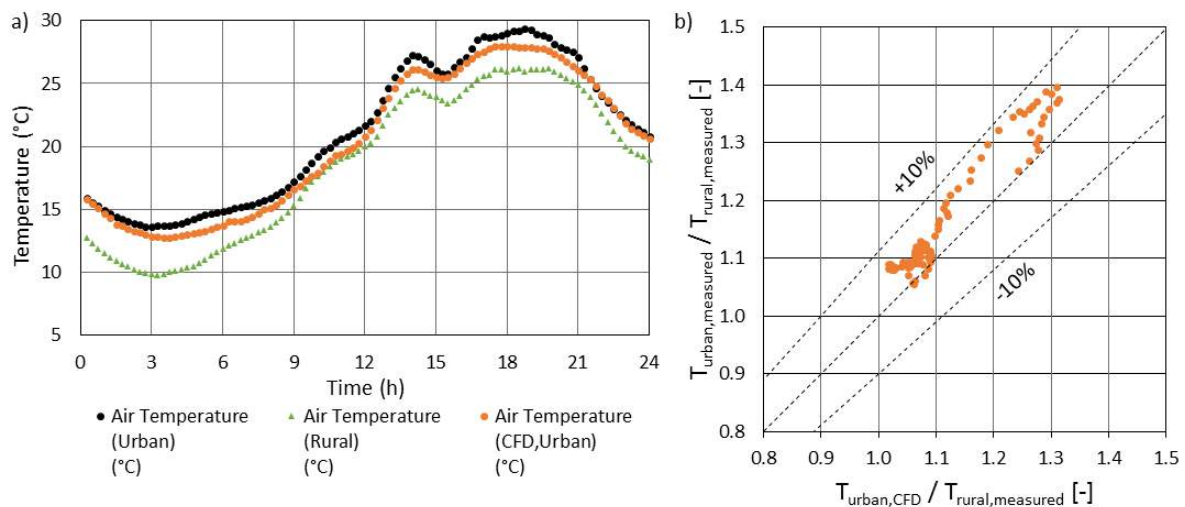


Figure 6: Comparison of air temperatures from CFD simulations and urban measurements. a) Comparison of the diurnal variation in air temperature for 30 June 2013; b) Comparison of CFD and measurements for urban air temperatures normalized with respect to the rural air temperature.

4.2 Part 2: The effect of urban park on the microclimate

Three different grids are used to assess the cooling effect of the park. The first grid, used for the base case simulations, contains the original Stadsspark. The second grid contains an open space instead of the park, similar to a public square but without the trees of Stadsspark. The third grid contains buildings with 13 m height, which is the average building height in the area of interest. The buildings in the third grid are placed where the trees of the Stadsspark are originally positioned.

The results are evaluated for 15:00 in the afternoon, where the cooling effect is more profound. The cooling effect is demonstrated using horizontal contour plots in the wake region of the park. To determine the cooling effect, results are presented by subtracting the base case

simulation results from the results of the other cases (case with open space and case with buildings). The horizontal distribution of the temperature variance is depicted in Figure 7.

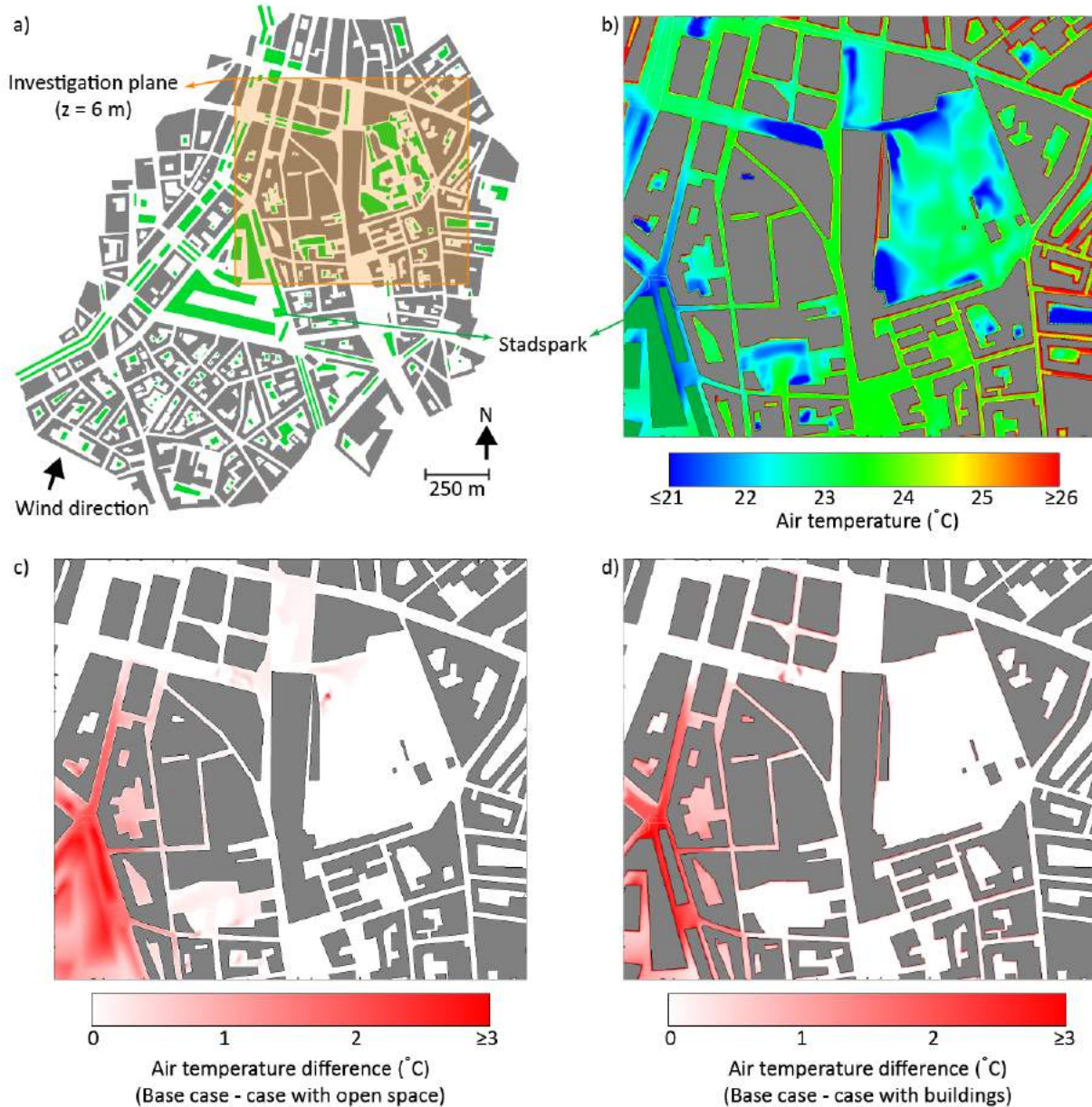


Figure 7: a) The distribution of buildings and trees at $z = 6$ m height. The investigation plane is determined based on the wake region of the park; b) Contours of air temperature on the investigation plane for the base case scenario; c) Contours of air temperature difference between the case with open space and the base case; d) Contours of air temperature difference between the case with buildings and the base case.

According to the results, both of the modifications to the existing park scenario increases air temperatures inside the wake region. Based on the comparative analysis, the maximum park cooling effect can be summarized as:

- Case 1 - Compared with the case with open space:
 - o Range of the cooling effect: 205 m
 - o Intensity of the cooling effect: 2.8°C
- Case 2 - Compared with the case with buildings
 - o Range of the cooling effect: 244 m
 - o Intensity of the cooling effect: 4.4°C

The investigated park, which has a triangular shape with approximately 410 m edge length on all sides is not a very dense one. There are several gaps for walking paths and a pond in the middle of the park, reducing the vegetated area. In comparison with previous CFD studies, the results of the cooling effect seem to be reasonable.

The study also evaluates the cooling effect on the vertical planes and the climate around individual buildings. However, due to space limitations, these parts are omitted from this paper. Future studies on the park cooling effect can investigate different heights of the buildings surrounding the park.

5 Conclusions

- CFD simulations are performed to analyze the effect of an urban park on the microclimate of Antwerp city center. The study was conducted in two parts.
- In part 1, CFD simulations results of air temperatures are compared with field measurements from 29-30 June 2013. It was found that the CFD approach followed predicted the measured air temperature with fairly good accuracy, leading to a correlation coefficient (R) of 0.97 between simulations and measurements.
- Later, the cooling effect of the park was investigated with three different scenarios: 1) base case with the park; 2) case with an open space instead of the park and 3) case with buildings instead of the park.
- With the implementation of buildings, air temperatures in the wake region can increase over a distance of 244 m, with a maximum temperature increase of 4.4°C. With the implementation of an open space instead of the urban park, air temperatures in the wake region can increase over a distance of 205 m, with a maximum temperature increase of 2.8 °C.

References

- ANSYS Inc., 2009. ANSYS FLUENT 12.0 Theory Guide.
- Armson, D., Stringer, P., Ennos, A.R., 2012. The effect of tree shade and grass on surface and globe temperatures in an urban area. *Urban For. Urban Green.* 11, 245–255.
- Balczó, M., Gromke, C., Ruck, B., 2009. Numerical modeling of flow and pollutant dispersion in street canyons with tree planting. *Meteorol. Zeitschrift* 18, 197–206. doi:10.1127/0941-2948/2009/0361
- Blocken, B., 2015. Computational Fluid Dynamics for urban physics: Importance, scales, possibilities, limitations and ten tips and tricks towards accurate and reliable simulations. *Build. Environ.* 91, 219–245. doi:10.1016/j.buildenv.2015.02.015
- Blocken, B., 2014. 50 years of Computational Wind Engineering: Past, present and future. *J. Wind Eng. Ind. Aerodyn.* 129, 69–102. doi:10.1016/j.jweia.2014.03.008
- Blocken, B., Stathopoulos, T., Carmeliet, J., 2007. CFD simulation of the atmospheric boundary layer: wall function problems. *Atmos. Environ.* 41, 238–252. doi:10.1016/j.atmosenv.2006.08.019
- Ca, V.T., Asaeda, T., Abu, E., 1998. Reductions in air conditioning energy caused by a nearby park. *Energy Build.* 29, 83–92. doi:10.1016/S0378-7788(98)00032-2
- Cebeci, T., Bradshaw, P., 1977. *Momentum Transfer in Boundary Layers.* Hemisphere

Publishing Corporation, New York.

- Chow, W.T.L., Pope, R.L., Martin, C.A., Brazel, A.J., 2011. Observing and modeling the nocturnal park cool island of an arid city: Horizontal and vertical impacts. *Theor. Appl. Climatol.* 103, 197–211. doi:10.1007/s00704-010-0293-8
- De Ridder, K., Lauwaet, D., Maiheu, B., 2014. UrbClim - a fast urban boundary layer climate model. *Urban Clim.* 12, 21–48. doi:10.1016/j.uclim.2015.01.001
- Declet-Barreto, J., Brazel, A.J., Martin, C.A., Chow, W.T.L., Harlan, S.L., 2013. Creating the park cool island in an inner-city neighborhood: Heat mitigation strategy for Phoenix, AZ. *Urban Ecosyst.* 16, 617–635. doi:10.1007/s11252-012-0278-8
- Dimoudi, A., Nikolopoulou, M., 2003. Vegetation in the urban environment: microclimatic analysis and benefits. *Energy Build.* 35, 69–76. doi:10.1016/S0378-7788(02)00081-6
- Franke, J., Hellsten, A., Schlünzen, H., Carissimo, B., 2007. Best practice guideline for the CFD simulation of flows in the urban environment, COST Guidelines. COST Office, Hamburg.
- Gromke, C., Blocken, B., Janssen, W.D., Merema, B., van Hooff, T., Timmermans, H.J.P., 2015. CFD analysis of transpirational cooling by vegetation: Case study for specific meteorological conditions during a heat wave in Arnhem, Netherlands. *Build. Environ.* 83, 11–26. doi:10.1016/j.buildenv.2014.04.022
- Jauregui, E., 1991. Influence of a large urban park on temperature and convective precipitation in a tropical city. *Energy Build.* 16, 457–463.
- Lauder, B.E., Spalding, D.B., 1974. The numerical computation of turbulent flows. *Comput. Methods Appl. Mech. Eng.* 3, 269–289. doi:10.1016/0045-7825(74)90029-2
- Lindley, S., Handley, J., Theuray, N., Peet, E., McEvoy, D., 2006. Adaptation Strategies for Climate Change in the Urban Environment: Assessing Climate Change Related Risk in UK Urban Areas. *J. Risk Res.* 9, 543–568. doi:10.1080/13669870600798020
- Meroney, R.N., Yamada, T., 1972. Numerical and physical simulation of a stratified airflow over a series of heated islands, in: *Proceedings of Summer Simulation Conference*. San Diego, California.
- Mills, G., 2014. Urban climatology: History, status and prospects. *Urban Clim.* 10, 479–489. doi:10.1016/j.uclim.2014.06.004
- Mirzaei, P.A., Haghghat, F., 2010. Approaches to study Urban Heat Island – Abilities and limitations. *Build. Environ.* 45, 2192–2201. doi:10.1016/j.buildenv.2010.04.001
- Moonen, P., Defraeye, T., Dorer, V., Blocken, B., Carmeliet, J., 2012. Urban Physics: Effect of the micro-climate on comfort, health and energy demand. *Front. Archit. Res.* 1, 197–228. doi:10.1016/j.foar.2012.05.002
- Müller, N., Kuttler, W., Barlag, A.-B., 2014. Counteracting urban climate change: adaptation measures and their effect on thermal comfort. *Theor. Appl. Climatol.* 115, 243–257. doi:10.1007/s00704-013-0890-4
- Richards, P., Hoxey, R., 1993. Appropriate boundary conditions for computational wind engineering models using the k-epsilon turbulence model. *J. Wind Eng. Ind. Aerodyn.* 46 & 47, 145–153.
- Shih, T.-H., Liou, W.W., Shabbir, A., Yang, Z., Zhu, J., 1995. A new k- ϵ eddy viscosity model for high reynolds number turbulent flows. *Comput. Fluids* 24, 227–238.

doi:10.1016/0045-7930(94)00032-T

- Taleghani, M., Sailor, D.J., Tenpierik, M., van den Dobbelsteen, A., 2014. Thermal assessment of heat mitigation strategies: The case of Portland State University, Oregon, USA. *Build. Environ.* 73, 138–150. doi:10.1016/j.buildenv.2013.12.006
- Tominaga, Y., Mochida, A., Yoshie, R., Kataoka, H., Nozu, T., Yoshikawa, M., Shirasawa, T., 2008. AIJ guidelines for practical applications of CFD to pedestrian wind environment around buildings. *J. Wind Eng. Ind. Aerodyn.* 96, 1749–1761. doi:10.1016/j.jweia.2008.02.058
- Toparlar, Y., Blocken, B., Vos, P., van Heijst, G.J.F., Janssen, W.D., van Hooff, T., Montazeri, H., Timmermans, H.J.P., 2015. CFD simulation and validation of urban microclimate: A case study for Bergpolder Zuid, Rotterdam. *Build. Environ.* 83, 79–90. doi:10.1016/j.buildenv.2014.08.004
- United Nations, 2014. *World urbanization prospects: The 2014 revision*, United Nations. New York.
- Vidrih, B., Medved, S., 2013. Multiparametric model of urban park cooling island. *Urban For. Urban Green.* 12, 220–229. doi:10.1016/j.ufug.2013.01.002
- Wieringa, J., 1992. Updating the Davenport roughness classification. *J. Wind Eng. Ind. Aerodyn.* 44, 357–368.
- Yow, D.M., 2007. Urban Heat Islands: Observations, Impacts, and Adaptation. *Geogr. Compass* 1, 1227–1251. doi:10.1111/j.1749-8198.2007.00063.x
- Yu, C., Hien, W.N., 2006. Thermal benefits of city parks. *Energy Build.* 38, 105–120. doi:10.1016/j.enbuild.2005.04.003

RADIATIVE PERFORMANCE ASSESSMENT OF TWO ROOFS IN MEDITERRANEAN AND EQUATORIAL CLIMATES.

J. Torres-Quezada¹, A. Pages-Ramon², H. Coch³ and A. Isalgué⁴

¹ Architecture & Energy. School of Architecture of Barcelona UPC.
Av. Diagonal, 649, 7th floor. 08028 Barcelona. Spain
e-mail: jefferson.torres@estudiant.upc.edu

² anna.pages, ³ helena.coch@upc.edu

⁴ aisalgué@fnb.upc.edu

Keywords: Radiative cooling, roof surface temperature, sky temperature.

Abstract. *In regions where the roof surface is the most exposed to solar radiation, the reduction of the heat flux transmitted through this element has a great impact on the cooling demand of buildings. Studying the possibilities of reducing cooling loads can highly influence the environmental and carbon footprint of the building stock worldwide.*

Although the main strategy to prevent solar access would be implementing shading systems, another approach could be taking advantage of the radiative cooling effect of the roof itself. Its efficiency depends on the roof properties (color, mass, thermal transmittance, etc) and on climate conditions (radiation, wind, humidity, etc).

This paper deals with a comparative assessment of the radiative performance of two roofs exposed to different amounts of solar radiation depending on their percentage of cloudiness, and the repercussions over its surface temperature. Its aims is to evaluate the effect of radiative cooling depending on the local climates.

Temperatures of two similar roofs, in Terrassa 41°33'LN (Spain) and in Santa Rosa 3°27'LS (Ecuador), were measured. Their transmittance, optical and thermal mass properties were considered in the-calculations.

The results obtained indicate that the effect of using the sky as a heat sink has a higher impact on the roof located in Terrassa (Spain) than the one in Santa Rosa (Ecuador).

The results support that this behavior responds to the influence of the high presence of cloudiness on equatorial climates, which reduces significantly the heat losses in long wave radiation. The heat mass storage capacity of the roof could hinder even more the radiative cooling effect of the roof.

1 Introduction

High levels of solar radiation, temperature and humidity lead to uncomfortable conditions. In pursuit to offset these conditions within the building, the use of cooling systems has increased in the last few decades, which have a great impact on the building energy consumption. Several studies have concluded that in warm humid climates, more than 50% of their electricity demand is destined to these systems [Koch-Nielsen, 2002]. Therefore passive strategies to mitigate indoor overheating in regions with these climates, like Mediterranean and Equatorial, contribute considerably in reducing their cooling demands [Butera, 1994].

There are different passive cooling strategies to improve the thermal comfort in hot-climate buildings [Kamal, 2012]. One of them consists in preventing the overheating inside the building through the opaque elements of the envelope. Conforming to Tong, the major part of the air-conditioning load comes from the heat gains of these elements [Tong, 2014]. On the Mediterranean and Equatorial regions, due to their high sun altitude on summer and during the whole year respectively, the roof is the element that receives the highest amount of solar radiation. Hence, it is the opaque component of the envelope mainly involved in the building heat gains, according to some studies it can represent 70% of these gains [Vijaykumar, 2007]. Thus the roof also determines energy consumption patterns.

Various authors have developed an ensemble of strategies, which generally fall into three categories: protection, control and reduction from solar radiation [Al-Obaidi, 2014][Geetha, 2012]. The first two approaches deal with prevention and thermal storage capacity of the building structure respectively, and the third approach is about reducing heat gains through dissipation techniques that take off excess heat from the building using an environmental sink of lower temperature and natural heat transfer. These techniques are divided into four types [Santamouris, 2013][Givoni, 1994]: Ground, which consists in transferring heat by conduction; water, which transfers the heat by evaporation; ambient air, which transfers the heat by convection, and sky, which transfers the heat by long wave radiation.

The present investigation focuses on the roof heat losses by radiative cooling, specifically presents a comparative assessment of the radiative performance on two roofs exposed to different amounts of solar radiation depending on their different sky conditions, and their repercussions on its surface temperature. It targets to evaluate the effect of radiative cooling in different climates.

2 METHODOLOGY

The methodology implemented in this study is based on an experimental and calculation work carried out on two similar roofs located in different cities with Mediterranean and Equatorial climates. The parameters considered to make the analysis are solar and long wave radiation, outdoor air and roof surface temperature.

2.1 The study areas weather

One of the roofs considered in this study, referred as R1, belongs to the Museo de la Ciencia y la Técnica de Catalunya (Catalunya Science and Technic Museum) building located in Terrassa, a city in the province of Barcelona Spain, at longitude 2°00'E, latitude 41°33'N and altitude 286 masl, which lies in the Mediterranean climatic zone. The annual weather conditions are generally characterized by hot summers and moderate cool winters. The mean daily temperature in the summer is 25.7°C and the mean relative humidity is 58%, Fig 1a, with scant rainfalls during the whole year.

The highest intensity of solar radiation in Terrassa is in July, with 7.33 kWh/m²/day, and the lowest is in December with 1.91 kWh/m²/day. Most of the annual average radiation comes from its direct component, which represents the 68% [Sancho, 2012]. This is due to the low percentage of cloud cover in this region, where the yearly average is 34.3% [Wilson, 2016].

The other roof analyzed, referred as R2, belongs to a residential building located in Santa Rosa, a city in the south coast of Ecuador, at longitude 79°58'W, latitude 03°27'S and altitude 14 masl, which lies in the tropical climatic zone. This region is characterized for its warm-humid climate throughout the whole year. The mean daily temperature is 26.8°C and the mean relative humidity is 85%, Fig 1b. Additionally heavy rainfalls occur in the wet season running from January to April, which accounts for most of the yearly 1600 mm precipitation.

The main characteristic in this climate is its high and constant intensity of solar radiation between 4.05 kWh/m²/day and 4.9 kWh/m²/day throughout the entire year on the horizontal plane. From this range, 63% belongs to the diffuse radiation [CONELEC, 2008]. The prevalence of this type of radiation is due to the high cloudiness condition typical in this climate, where the yearly average is 78%, with a maximum average of 87% in October and minimum average in April of 65% [Wilson AM, 2016].

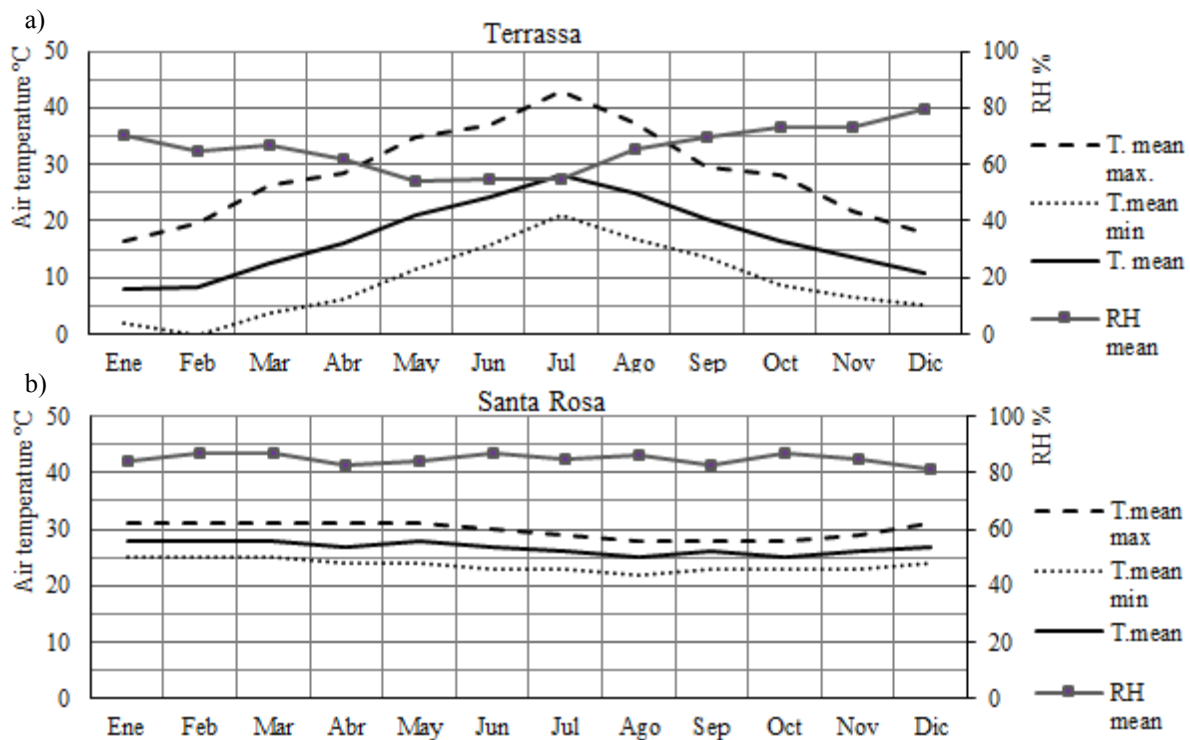


Fig. 1. Air temperature and relative humid a) Terrassa and b) Santa Rosa.

2.2 Roof characteristics

R1 is a shed roof, which covers an area of 11000 m² by 161 Catalonian vaults arranged in a grid of 7 modules in the east-west way and by 23 modules in the north-south way. Every semi-vault is defined by a double bent built in brick, the same as its surface finish. It has a 0.33m thickness composed by various layers with an air gap in the middle as shown in Fig. 2a.

R2 is a horizontal ribbed slab divided in two ways, which covers an area of 117 m². It is made of reinforced concrete with a 0.20m thickness and filled with hollow light concrete blocks as shown in Fig.2b. Its surface finish is the same concrete.

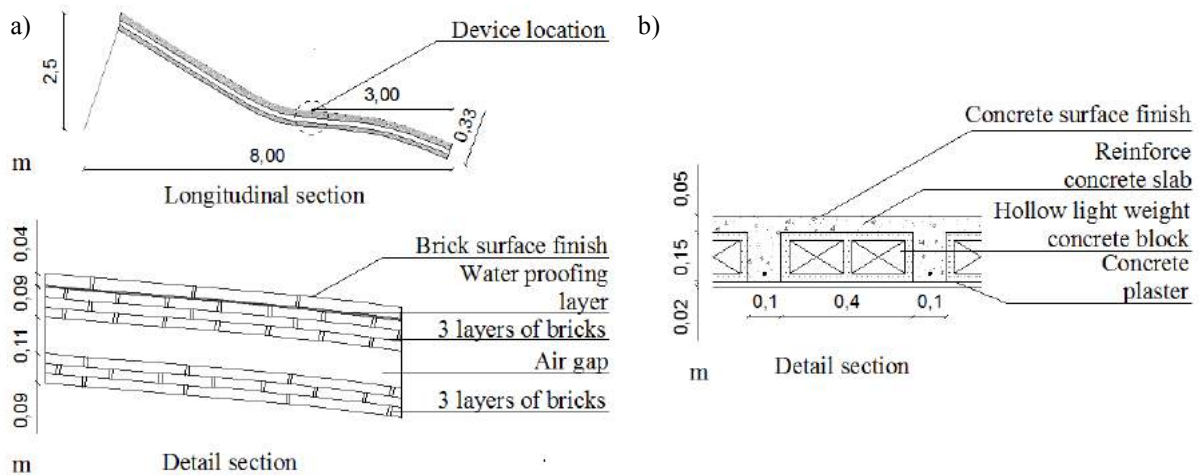


Fig. 2. Construction specifications a) longitudinal section and detail of R1 and b) detail of R2.

As previously mentioned these two roofs have similar thermal and optical properties. They have similar thermal transmittance and thermal storage capacity, though they do not have the same thickness. With respect to their optical surface properties, they both have high emittance and they also have high solar absorptance values. Concrete in optimal conditions usually has a lower solar absorptance value than brick, however due to the aging and the lack of maintenance of the R2 surface, this factor increases considerably. All specific values are shown in Table 1.

Code	Surface material	Solar absorptance α (%)	Emittance ϵ (%)	Thermal Transmittance U (W/m ² .K)	Thermal mass ω (W.h/m ² .K)
R1	Red brick	75*	90*	2,13**	88**
R2	Old Concrete	80*	90*	2,77**	100**

Table. 1. Material Properties for R1 and R2. *[ASHRAE, 2001], **Calculations

2.3 Parameters and periods

It is necessary to clarify that all the parameters considered and named in this paper are for the outside environment, while all hours are referred to solar time.

As it stated before, the parameters considered for both cases are the solar radiation, long wave radiation, air temperature and roof surface temperature.

In the experimental work on R1, the information of all these parameters was collected from July 1 to July 8, 2015. The data measured on site were: the short wave radiation, the long wave radiation and the surface temperature. The equipment used to monitor was: for short wave irradiance, a pyranometer MS-020VM with a spectral range from 350nm to 1100nm, for long wave irradiance, the pyrgeometer IR02 with a spectral range from 4.5 μ m to 40 μ m, a field view angle of 150°. These two instruments were set to collect data in 5 min intervals and were stored in a data logger. A multifunctional meter T435 was used to monitor the surface temperature. This instrument is a portable 4 digit thermometer which uses a three external K-type thermocouples wire as temperature sensors. The measures were captured at 20-min interval and stored in a memory data included in the thermometer. These devices were placed on the symmetry axis of the same vault, at a distance of 3m from the window, as shown in Fig. 2a. We have checked, with a thermo-graphic camera FLIR-I7, that this place is the

representative point of the thermal condition of the vault. The module selected in the grid was the tenth from north, and the third from west. While the air temperature data was gathered from the database of the Terrassa weather station, ID: ITERRASS3, located 300m from this building, at longitude 2°00'48''E, latitude 41°33'59''N and altitude 307 masl, and the information was collected in 20-min intervals.

All data for experimental work on R2 was collected from December 19 to December 26, 2015. The short wave radiation and air temperature parameters were taken from the database of the airport weather station of this city, located 3 km from this house, at longitude 79.98°W, latitude 3.44°S and altitude 50 masl, with data gathered at 1 hour interval. The roof surface temperature parameter was measured on site using an infrared thermometer with accuracy ranging from +/- 1.5% or +/- 1.5°C, spectral range 8-14 μm , and emissivity range from 0.1 to 1 calibrated at 0.90 according to its surface roughness [ASHRAE, 2001]. The measures were captured at 30-min interval. Additionally, since it was not possible to take measurements of long wave radiation, the sky temperature was measured in different points on the sky vault. In order to make an approximation of this heat flux equation (1) was applied, which involves the sky and the surface temperature, and it is given as:

$$q_r = \sigma \varepsilon (T_s^4 - T_{sky}^4) \quad (1)$$

Where, σ = constant of Stefan, ε = emittance of surface for long wave radiation, T_s = surface temperature and T_{sky} = sky temperature.

3 RESULTS AND DISCUSSIONS

3.1 Results for R1

From the measurements collected during an eight day period on R1, we have analyzed two days, July 6 and July 8. These days were chosen due to their different air temperature, solar radiation and percentage of cloud cover. The mean daily temperature on July 6 was 31.5°C, the average of solar radiation was 304 W/m² with a clear sky; while on July 8 was 28.8°C and 250 W/m² with overcast sky conditions. The results for both days are shown in Fig. 3. The heat flux of solar and long wave radiation, Fig. 3a and c, and the surface and air temperature, Fig. 3b and d.

The results on July 6, Fig. 3a, shows a solar radiation curve with no interruptions, which reflected the completely clear sky conditions throughout the whole day. This radiation appears at 04h30, it rises until its peak 1000 W/m² at 12h00 approximately, and then it starts to fall down until disappearing at 19h30. In regards to the long wave radiation, during the periods from 00h00 to 04h30 and 19h30 to 24h00, the roof is emitting an average of -87 W/m², then at 04h30 when the solar radiation appears the heat losses start to rise up until reaching its peak at 13h20 approximately with a value of -192 W/m². This maximum has a 01h20 lag time compare with the solar radiation peak. After this, it decreases its heat losses until the solar radiation disappears and comes back to its constant behavior at night.

According to the results from July 6, it is clear the direct relationship between the performance of the solar and long wave radiation. However this behavior varies with the presence of cloudiness; such is the case of July 8, Fig.3b. The performance of solar radiation in this day is erratic, especially in the afternoon. The flux in the morning period shows a curve quite similar to the one on July 6, but with few interruptions and irregularities. However after this, it falls drastically and displays a very inconstant line throughout the entire afternoon until disappearing at approximately 19h00. A similar performance is observed in the long wave radiation curve. The heat flux of the two analyzed days has a similar behavior in the morning

although the values of its heat losses are not the same. For instance, the peak value on July 8 is 25 W/m² lower than the one on July 6. After midday this radiation become totally erratic reducing its heat losses until -26 W/m² at 21h00, which reflected the high temperature of the sky, then it raises again to an average value of -75 W/m² until midnight.

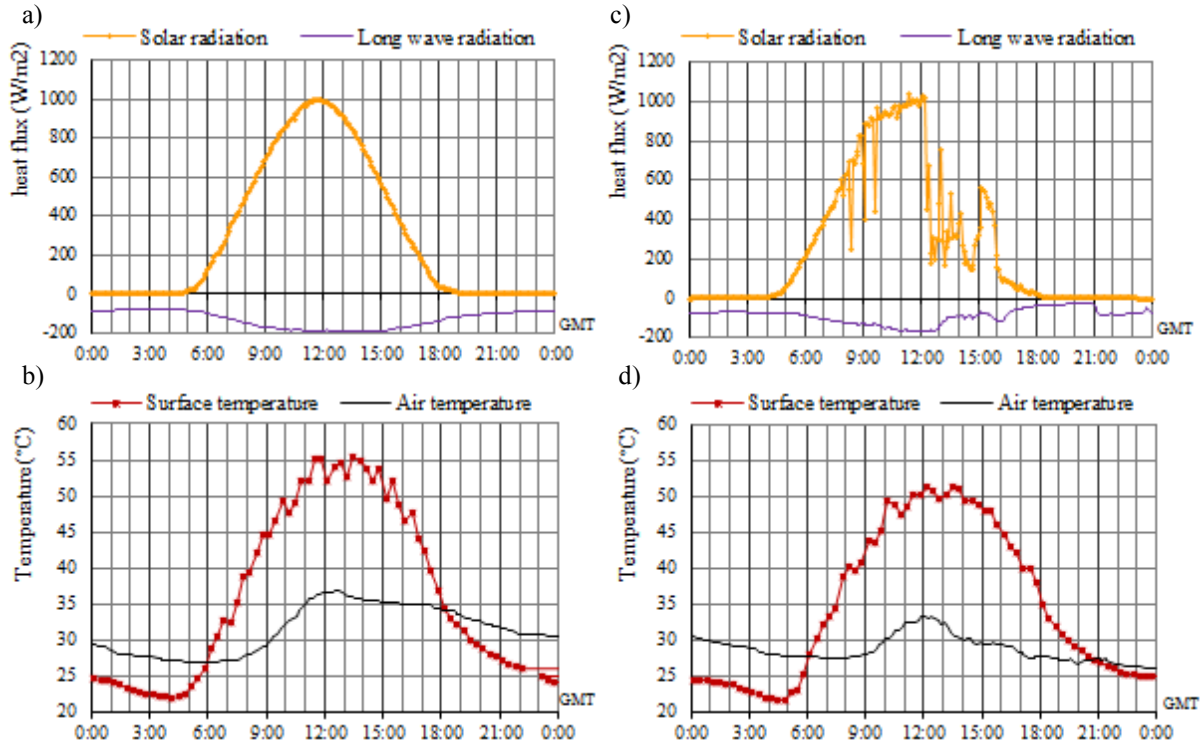


Fig. 3. Results for R1 on July 6, left, and July 8, right, a) and c) Heat flux for solar and long wave radiation, and b) and d) Surface and air temperature.

In order to analyze these behaviors, a comparison took place between the average of solar and long wave radiation of these two days, as is shown in Fig.4. In the case of the solar radiation an additional comparison was made with the theoretical value for these specific days. This was obtained from a computational simulation using the Heliodon software [Benoit Beckers, 2006].

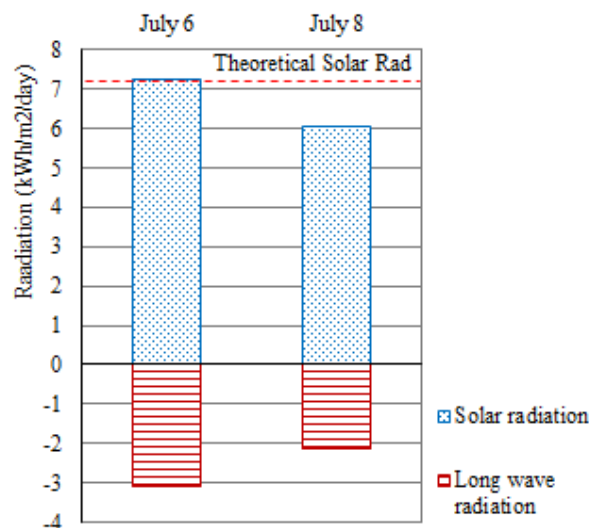


Fig. 4. Comparison of the R1, average of solar and long wave radiation, on July 6 and July 8.

The results of the total solar radiation on July 6 shows the same value that theoretically must receive this surface, 7.3 kWh/m^2 , unlike to the July 8 which is 6 kWh/m^2 . This decrease of 1.3 kWh/m^2 represents a reduction of the 17%. Whereas the long wave radiation in the same days, July 6 and July 8, goes from 3.1 kWh/m^2 to 2.1 kWh/m^2 respectively. This decrease of 1 kWh/m^2 represents a reduction of the 32%. Hence we can infer from this that the reduction of solar radiation in an overcast day is in a lower proportion than the one in the long wave radiation, which can have repercussions on its surface temperature.

In regards of the influences of these radiative performances on the roof surface temperature in these two days, shown in Fig 3b and d, it did not reflect a large difference, despite of their different amount of solar radiation. The higher difference is observed on their peak values at 12h00. This difference is around of 3°C , from 55°C to 52°C , corresponding to July 6 and July 8 respectively. This performance implies that the non-proportional reduction between solar radiation and long wave radiation in these two days, as previously mentioned, in fact has repercussions on the surface temperature.

3.2 Results for R2

From the data collect for R2, two days were chosen for analysis, December 23 and December 26. These days presented similar climatic conditions. The mean daily temperature during both days was around 27°C . The difference of solar radiation average is 27 W/m^2 and both have high cloudiness conditions. However their differences depends on the different percentage and period of cloud cover during the daytime. The results for both days are shown in Fig. 5, the radiation heat flux data, Fig. 5a and c, and the surface and air temperature, Fig.5b and d.

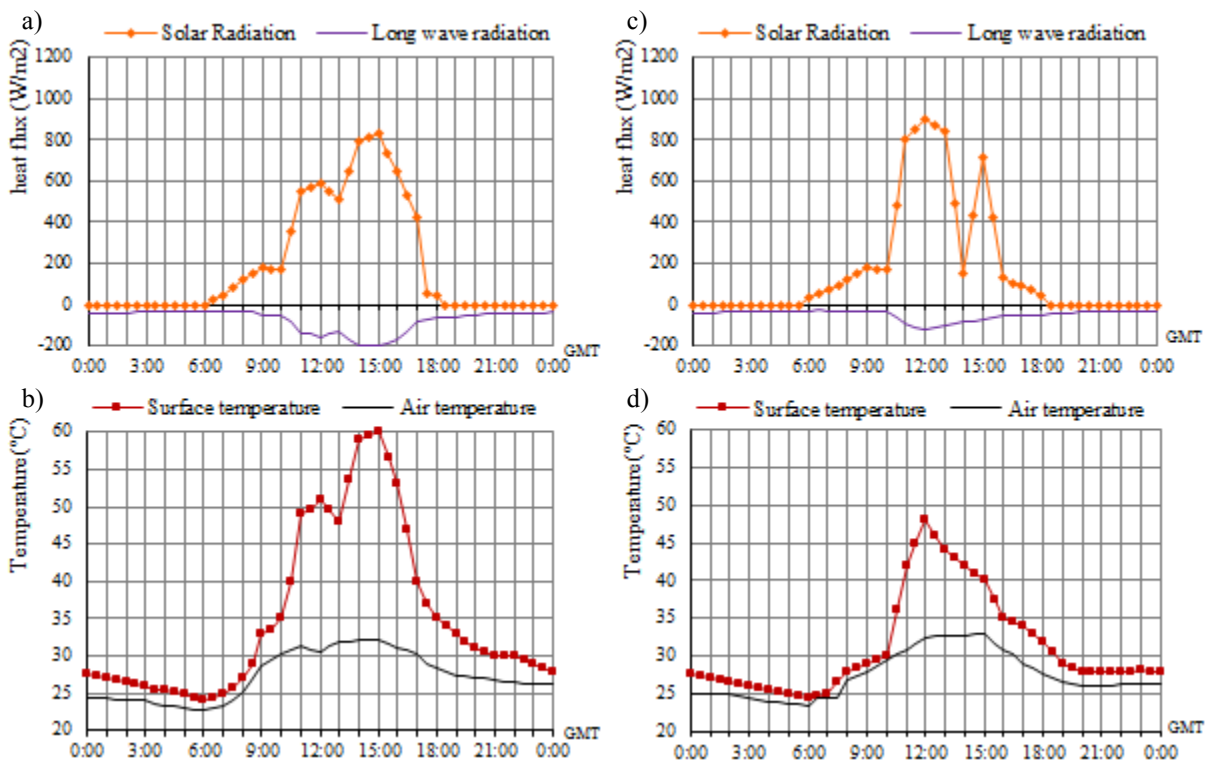


Fig. 5. Results for R2 on December 23, left, and December 26, right, a) and c) Heat flux for solar and long wave radiation, and b) and d) Surface and air temperature.

With respect to the radiation results on December 23, Fig 5a, it is observed in the period from 06h00, when the sun rises, until 13h00, the solar radiation does not exceed the 600 W/m², even until 10h00 is under 200 W/m². After this, it reaches its peak 830 W/m² at 15h00, and then it falls with a constant curve until disappear at 18h30. This behavior reflected a high cloud cover condition in the morning and a lower percentage in the afternoon period. Whereas on December 26, Fig. 5c, its peaks appears around at midday even higher than the previous case but only happened during short and specific periods, from 11h00 to 13h00 and another peak at 15h00. The rest of the day the amount of this radiation does not exceed the 200 W/m².

The results of the long wave radiation, obtained from Eq. (1), shows a direct relationship with the solar radiation, as the same in the R1 analysis. This is reflected in the coincidence in their peak time for both days. However the peak values are not the same. The long wave radiation peak on December 26 is lower than the one on December 23 whereas in the solar radiation peaks occurs the opposite. The principal observation from these results is the low amount of the heat losses all through the day. The period when the heat losses in long wave radiation exceed the -100 W/m² on December 23 was during 5 hours, from 11h00 to 16h00, while on December 26 it was from 11h30 to 13h00, just 1.5 hour.

The same analysis used on R1 is used for R2 comparing the average of solar and long wave radiation of these two days, as is shown in Fig.6, and the additional comparison between the solar radiation results with the theoretical value. This additional evaluation was used to show the influence of the high percentage of cloudiness, typical in these regions, on the reduction of the solar radiation. The total of this radiation from December 23 to December 26 goes from 4.7 kWh/m² to 4.15 kWh/m². This decrease of 0.55 kWh/m² represents a reduction of the 12%. However if we compare with the theoretical value, this decrease become to 1.3 kWh/m² and 1.85 kWh/m². This represents a reduction from the theoretical radiation of 22% and 31% for December 23 and December 26 respectively. Whereas for the long wave radiation, the total heat losses from December 23 to December 26 goes from -1.8 kWh/m² to -1.2 kWh/m², this decrease of 0.6 kWh/m² represents a reduction of the 33%. Hence we can imply from this, the same as in R1 analysis, the solar heat gains reduce its amount depending of the cloudiness percentage, however the heat losses in long wave radiation on the roof also reduce but in a higher proportion.

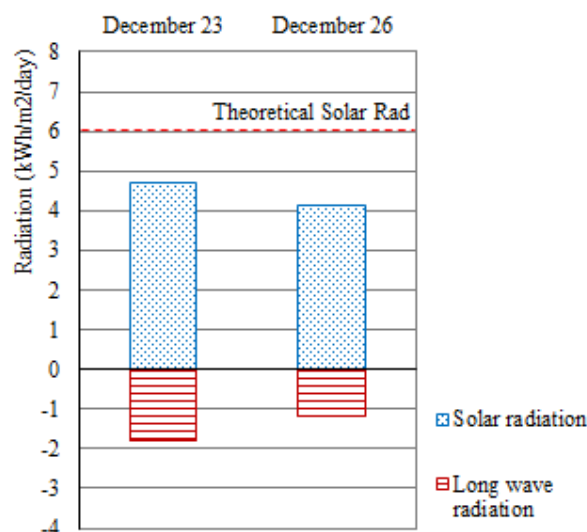


Fig. 6. Comparison of the R2, average of solar and long wave radiation, on December 23 and December 26.

In regards of the influences of these results on the roof surface temperature. When we compare the data of this two days, shown in Fig 5b and d, it is observed a total different behavior. These differences are reflected in the mean daily surface temperature, which on December 23 is 35°C while on December 26 is 31°C. The higher difference is observed on their peak values around of 12°C, from 60°C to 48°C, in different hours. These peaks are corresponding to the peaks of solar radiation which do not have great difference. These different behaviors depend on another factor involve in the surface temperature response, which is the high thermal mass of this roof. This factor retards the heating velocity of the surface, and hinder its heat release. On December 26 the low amount of solar radiation during the morning and the short peak periods at midday does not achieve to increase the surface temperature. Whereas on December 23 the solar radiation is constantly rising up during the entire morning, the roof is storing this heat and reached its maximum higher and later than the one on December 26. After this, they both reduce their temperatures with a slower behavior

3.3 Comparisons

This section studies in detail the thermal heat flux behavior of the two analyzed roofs. In order to compare their different surface temperature responses through the day in the 4 examples explained so far and to match these results with the properties of the roofs.

Keeping in mind the different amount of heat fluxes throughout the day depending on the sky conditions, the day was divided into four periods: the first from midnight until the sun rise, the second from the sunrise to midday, the third from the midday to the sunset and the last one from the sunset to midnight. The sunrise and sunset are corresponding to each city. To support the analysis of the repercussions of the radiative heat fluxes on the surface temperature, the concept of the thermal balance of a surface under the sun is used [Bretz, 1998], shown in the Eq. (2). This concept describes the action of solar radiation heat flux on a surface temperature and the net radiation exchange with its environment.

$$(1 - a).I = \sigma\varepsilon(T_s^4 - T_{sky}^4) + h_c(T_s - T_o) \quad (2)$$

Where I , is the total solar radiation incident on the surface, W/m^2 , a is the albedo of the surface; h_c , the coefficient convection, $W/m^2.K$; T_s , the surface temperature, °C, and T_o , the outdoor air temperature, °C. Where it can infer that the difference between the surface and the air temperature shows the influence of the total net radiation on the roof. Eq. (3).

$$(T_s - T_o) = [(1 - a).I - \sigma\varepsilon(T_s^4 - T_{sky}^4)]/h_c \quad (3)$$

Fig. 8 shows the comparison of the average difference (ΔT), between the roof surface and air temperature, with the partitioned heat fluxes, for R1 and R2, on July 6 and 8, December 23 and 26, in the 4 periods mentioned. These results obtain from Eq.3 consider the solar absorptance and the emittance, but not the coefficient of the convective conductance due to the similarity of the surfaces and the scant of high air velocity is assumed to have same value.

About the repercussions on the surface temperature at daytime, it is observed the higher influence of the total net radiation is in all afternoon periods, even when the major amount of solar radiation is in the morning. This support the influence of the heat storage capacity on the roof surface temperature. The highest influence is shown on December 23, +18°C, despite the solar radiation in this day is lower than R1 days. This surface response is due to the solar radiation is constantly increasing during the morning and reaches its peak in the afternoon.

With respect to the repercussions at nighttime, it is observed the R1 reduce its surface temperature under the air temperature, for both analyzed days, whereas R2 keeps higher than air an average of 3°C and 2°C on December 23 and December 26 respectively. This behavior

response to the low amount of heat losses in R2, an average of 0.24 kWh/m², due to the overcast conditions of its location. Similar value is shown on July 8 on R1, in the period from 18h00 to 24h00. These results reflect the influence of these sky conditions and the thermal mass over the radiative cooling effect.

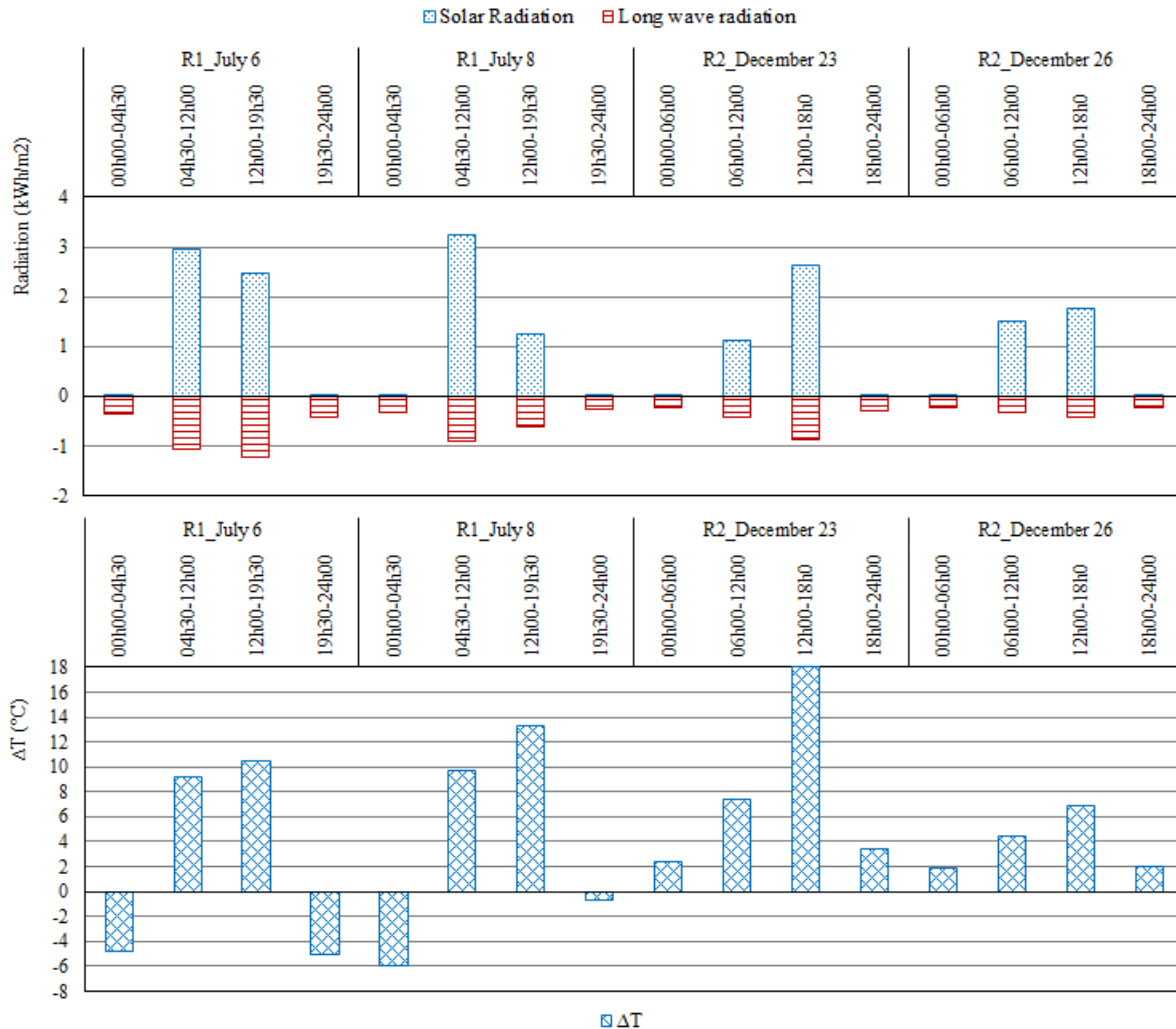


Fig. 8. Comparison between the total heat flux of solar and long wave radiation, and ΔT , partitioned into four periods, on July 6 and July 8 for R1, and December 23 and December 26 for R2.

4 CONCLUSIONS

This study arises from the aim to analyze the performance of radiative cooling as a heat dissipation technique. In order to accomplish this goal, the thermal behavior of two similar roofs, located in Terrassa and Santa Rosa, exposed to different amounts of solar radiation depending on their sky conditions were monitored. From these monitored results we conclude that:

The radiative cooling effect has a higher impact on the roof located in Terrassa, R1, than the one in Santa Rosa, R2. The surface temperature reduction for R1 was in an average of -4°C and for R2 was +2.4°C compare to the air temperature at nighttime. Additionally, the comparison of the two analyzed days for R1 shows a higher impact of this strategy in the day with clear sky conditions than in the overcast day.

Since roof heat losses, in long wave radiation, are conditioned by the atmosphere temperature, the high cloudiness percentage in equatorial climates reduces significantly this

heat flux. The results of this study support that in these regions the lowest average, -50 W/m^2 , of this radiation represents the 40% of the highest average in Mediterranean climates, -129 W/m^2 .

Finally this investigation sustain that in equatorial climates, where the overcast conditions predominate throughout the whole year, the use of high thermal mass hinders even more the radiative cooling effect on the roof surface temperature.

Acknowledgements:

This work has been partially supported by the Spanish Ministry of Economy under project code: BIA2013-45597-R, JTQ acknowledges to the scholarship of the Superior Education, Science, Technology and Innovation Secretary (SENESCYT) (ref. no. AR6C 9307) from the Government of Ecuador.

References

- [AEMET 2012] Agencia Estatal de Meteorología, *Atlas de Radiación Solar en España utilizando datos del SAF de Clima de EUMETSAT*, AEMET, 158 pages, 2012. Available at: http://www.aemet.es/documentos/es/serviciosclimaticos/datosclimatologicos/atlas_radiacion_solar/atlas_de_radiacion_24042012.pdf [Accessed May 11, 2016].
- [Al-Obaidi 2014] Karam M. Al-Obaidi, Mazran Ismail, Abdul Malek Abdul Rahman, Passive cooling techniques through reflective and radiative roofs in tropical houses in Southeast Asia: A literature review, *Frontiers of Architectural Research*, vol. 3, n°. 3, Pages 283–297, 2014.
- [ASHRAE 2001] ASHRAE, *ASHRAE Handbook-Fundamentals*, ASHRAE, 892 pages, 2001.
- [Beckers 2006] Benoit Beckers, Luc Masset, 2006. Heliodon 2 software, available at: www.heliodon.net.
- [Bretz 1998] Sarah Bretz, Hashem Akbari, Arthur Rosenfeld, Practical issues for using solar-reflective materials to mitigate urban heat islands. *Atmospheric Environment*, vol. 32, n°. 1, Pages 95–101, 1998.
- [Butera 1994] Federico M. Butera, Energy and buildings in Mediterranean countries: Present and future, *Renewable Energy*, vol. 5, Pages 942–949, 1994.
- [CONELEC 2008] Consejo Nacional de Electricidad, *Atlas solar del Ecuador con fines de generación eléctrica*, Corporación para la investigación energética, 50 pages, 2008. Available at: http://www.conelec.gob.ec/archivos_articulo/Atlas.pdf [Accessed May 1, 2016].
- [Geetha 2012] N.B. Geetha, R. Velraj, Passive cooling methods for energy efficient buildings with and without thermal energy storage—A review, *Energy Education Science and Technology Part A: Energy Science and Research*, vol. 29, n°. 2, Pages 913–946, 2012.
- [Givoni 1994] Baruch Givoni, *Passive and low energy cooling of buildings*, John Wiley and Sons, Inc., 120 pages, 1994.
- [Kamal 2012] Mohammad Arif Kamal, An overview of passive cooling techniques in buildings: design concepts and architectural interventions, *Acta Technica Napocensis: Civil Engineering & Architecture*, vol. 55, n°. 1, Pages 84–97, 2012.

[Koch-Nielsen 2002] Holger Koch-Nielsen, *Stay cool: a design guide for the built environment in hot climates*, Earthscan, 160 pages, 2002.

[Santamouris 2013] Mattheos Santamouris, Dionysia Kolokotsa, Passive cooling dissipation techniques for buildings and other structures: The state of the art, *Energy and Buildings*, vol. 57, Pages 74–94, 2013.

[Tong 2014] Shanshan Tong, Hua Li, Kishor T. Zingre, Man Pun Wan, Victor W.-C. Chang, Swee Khian Wong, Winston Boo Thian Toh, Irene Yen Leng Lee, Thermal performance of concrete-based roofs in tropical climate, *Energy and Buildings*, vol. 76, Pages 392–401, 2014.

[Vijaykumar 2007] K.C.K. Vijaykumar, P.S.S. Srinivasan, S. Dhandapani, A performance of hollow clay tile (HCT) laid reinforced cement concrete (RCC) roof for tropical summer climates, *Energy and Buildings*, vol. 39, n°. 8, Pages 886–892, 2007.

[Wilson 2016] Adam M. Wilson, Walter Jetz, 2016. Remotely Sensed High-Resolution Global Cloud Dynamics for Predicting Ecosystem and Biodiversity Distributions, *PLoS Biol* 14(3): e1002415.doi:10.371/journal.pbio.1002415, available at: <http://www.earthenv.org/>, [Accessed May 10, 2016].

Periodic 3D model to optimize urban shapes for solar radiation

T. Vermeulen¹, C. Knopf-Lenoir², L. Merino¹, P. Villon², and B. Beckers²

¹ Facultad de ingeniería civil,
Universidad de Concepción, Edmundo Larenas 219, Concepción, Chile
e-mail: thibaut.vermeulen@gmail.com, lumerino@udec.cl

² Laboratoire Roberval, UMR 7337
Compiègne University of Technology – Sorbonne University,
Rue Roger Couffolenc, CS 60319
60203 Compiègne – France
catherine.vayssade@utc.fr, pierre.villon@utc.fr, benoit.beckers@utc.fr

Keywords: Urban geometry, urban cell, solar radiation, optimization

Abstract. *Solar radiation is a significant input for energy and light in buildings, and its access depends highly on the shape of the city. Theoretical test cases – blocks, canyons, courtyards – are common in the study of the solar exposure of an urban fabric. This paper presents a geometric formalization of a district as a periodic fabric composed of a repeated urban cell. This definition allows us to evaluate solar radiation considering replica of the studied district as solar masks. An example of optimization using an evolutionary algorithm to find an optimal set of block heights for direct solar access at different dates is then presented. The results show patterns that clearly illustrate the relation between sun path and optimal urban design for solar energy potential.*

1 Introduction

In order to respect itself and the engagement it recently took in Paris at the occasion of the conference of the parties of 2015 (among others), the world community will have to double its efforts to reduce greenhouse gases emissions and, for its high contribution to the latter, energy consumption.

The building sector is known to represent a significant energy consumer [Pérez-Lombard, 2008]. Furthermore, this sector has a high improvement potential, for it is possible to reduce drastically the use phase energy consumption of a building through efficient construction methods (thermal insulation, mechanical ventilation), and a right adaptation to the climatic and geologic properties of the land.

In this context, solar radiation should be constantly taken care of in architecture for its various aspects: thermal passive energy, daylighting, solar and thermal panels, for the useful part, but, on the other side, risks of overheating discomfort, and intensification of the urban heat island.

In the literature, the relation between solar radiation and the urban shape is studied on one hand by simulating and comparing realistic or existent district [Compagnon, 2004; Sarralde, 2014]. On the other hand, various studies simplify the city by canyons [Kanters, 2012; Strømman-Andersen, 2011; Krüger, 2010; Van Esch, 2012], blocks [Ratti, 2003], courtyards [Muhaisen, 2006] or typologies of houses [Hachem, 2011; Hachem, 2013] in order to link solar access to general morphological parameters of the city: aspect ratio, height, density, granularity. Furthermore, the use of optimization have recently increased in the field, exploring wider sets of geometric configurations of buildings [Kämpf, 2010; Vermeulen, 2015; Vermeulen, 2013].

When evaluating the solar potential of a district, the urban context (surrounding buildings) plays a role as masks, and reflectors if the reflections are taken into account. It seems logical to consider this border as part of an optimization or design problem: a “good” configuration of the district must avoid casting shadows on pre-existing buildings when solar energy and daylight is needed.

In the case of a study of new buildings in a real district, the border can be logically defined by the surrounding buildings and masks. Nevertheless, in order to study the sun capture of theoretical shapes, several situations exist:

- the district is located in an open environment, and the masks are neglected;
- an arbitrary urban context is considered: for example, all the surrounding buildings are set at an average height;
- urban context is randomly generated on the basis of the typology of the same district [Cheng, 2006].

In the second case, the choice can prevent generalizing the results: why would the buildings to be optimized have varying heights and not the context?

In the third case, the influence of a context consisting in buildings of random heights should also be evaluated. But again: the random context, even if it represents a diversity more in line with the variability of the optimized buildings, is not a general case.

These remarks motivate the use of a new geometric description of the district as a regular urban fabric whose basic element, called “cell” is subjected to optimization. Therefore, the urban context is homogeneous with the sub-area of interest: these are copies of it.

A description of the urban cell for solar radiation simulation is described in the next section. An optimization test case for maximizing direct solar radiation on a set of blocks is then presented and some results are shown.

2 Definition of the Urban Cell

We call urban cell a delimited urban area with buildings that can have parameterized heights or properties. From this definition, a periodic urban fabric can be defined as the infinite repetition in each direction of the urban cell. This repetition generates solar masks which will vary in the optimization process in a similar manner as the cell itself.

In the present work, we illustrate the urban cell with a representation of the city as blocks of varying height centered on parcels. However, its definition could be successfully derived in a variety of urban shapes that observe translation symmetries (canyons, courtyards).

The cell is associated with the representation of a block area on a rectangular grid. It is composed by $n_x \times n_y$ locations. The cell is then repeated on the sides as masks. An example of cell dimensions of 3x3 is shown in fig.1.

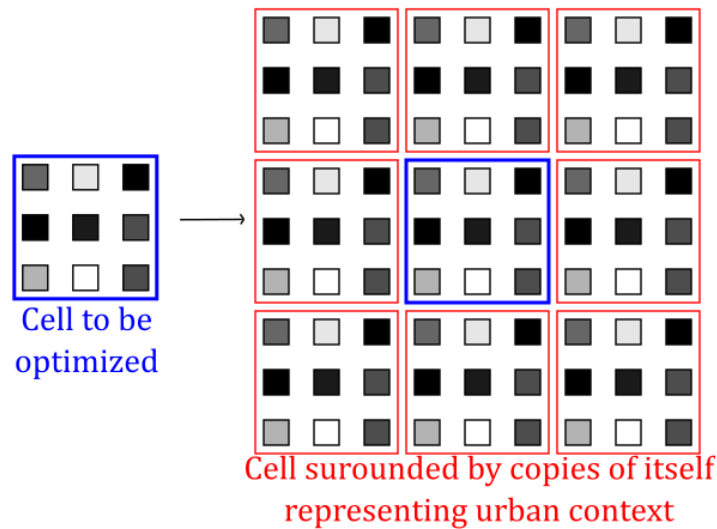


Figure 1. Example of urban cell. Grey level represent building height

When using a periodic definition of a district, a building whose height increases also generates masks around it whose proximity depends on the size of the cell. The influence of the masks regarding the sun exposure of a building decreases with the distance. Thus, the dimensions of the cell is *a priori* likely to influence solar energy that can capture a building, and can be an interesting parameter with which to play. To give an example of generated periodic fabrics, urban cells of dimensions 2x2, 3x3, and 4x4, reproduced to form 7x7 buildings districts, are shown in Fig.2.

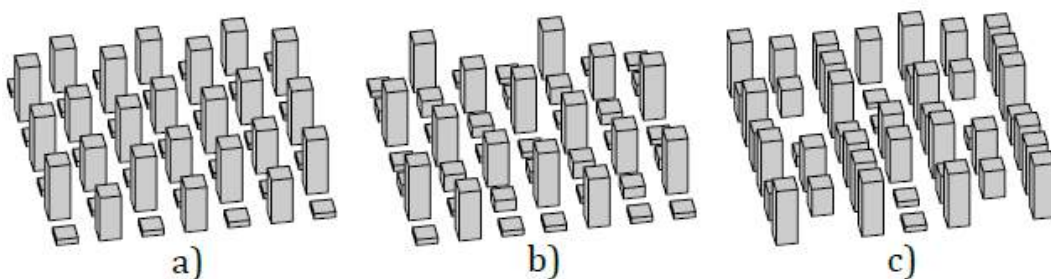


Figure 2: Examples of cells of dimensions 2x2 (a), 3x3 (b) and 4x4 (c)

3 Optimization Methodology

3.1. Geometry and parameters of the optimization test case

We consider a cell that takes the form of a square grid of parcels of 20 x 20 m in the center of which are arranged square base buildings of base 10 x 10 m. Each building may consist of 0-to-10 floors of 3 meters height. The vector of variables to be optimized is constituted of the integer number of floors x_i of building i .

$$\vec{x} = \{x_1, \dots, x_{N_{building}}\}$$

The cell representation presupposes regularity of the urban fabric. Also, to consider whether some urban cells are better than others, different optimization tests are performed by varying three parameters:

- Three periods of interest are considered: 21 December (winter solstice), March 21, which is equivalent to September 21 (equinox) and June 21 (summer solstice). Solar radiation at the summer solstice is actually undesirable, and the radiation at the equinoxes, which brings a lot of energy to buildings because of a low sun in the sky, is also associated with risk of overheating. However, these dates are included to illustrate the reaction of the shape of the district to different geometries of solar radiation. The resulting optimal shape for direct energy maximization in summer should be considered as layouts to avoid.
- The volume of built area, which ranges from 33%, 50% and 66% of the maximum volume, where the maximum volume represents the overall built volume when all buildings are 10 floors high.
- The cell size may vary from a grid of 2 x 2 to 6 x 6.

In order to compare districts with comparable total building envelope, a constraint is imposed on the total volume to be built.

3.2. Solar radiation simulation and objective function

The objective function to be maximized consists in the overall direct irradiation on the urban cell on a one-day period by clear sky conditions, at the latitude of 50° N. The simulation uses a sky model developed by [Liu, 1960], and later adapted by [Campbell, 1998]. The shadows are computed at each time step by projections methods. This solar energy simulator has been formerly used for related optimization problems [Vermeulen, 2015].

The time step for solar radiation integration is set to 30 minutes.

In the present definition of the urban cell, the urban context is assumed repeated infinitely while, in practice, it needs to be limited in a balance between computation time and accuracy. For this purpose, a calculation radius is determined in which the context will be generated independently for each building. For example, for a cell of 3x3 blocks, treated with a radius of representation of six, nine urban geometries will be created, each having at its center a building of the cell and six rows of buildings repeating the cell in each direction.

3.3. Optimization method

An evolutionary algorithm is used for the optimization of the urban cell. It is based on a population of individuals (here: districts) which is evolved along generations to improve the value taken by the objective function [Eiben, 2003]. The structure of the optimization algorithm is presented in Figure 3.

The algorithm is fully described in [Vermeulen, 2015]. It showed a good ability to converge for similar parameterizations of districts. The main features of the algorithm are summarized below.

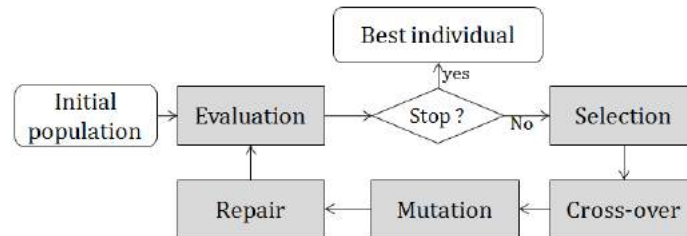


Figure 3. Structure of the evolutionary algorithm

As a selection operator, we use a $(\mu + \lambda)$ -*Evolution Strategy* [Beyer, 2002], which means that the μ best individuals regarding the objective function are selected to be “parents” and to generate λ offsprings. The selected individuals are kept in the population for the next generation.

The crossover operator has to combine two admissible configurations to provide two offsprings satisfying the volume constraint and showing better performance. With the μ selected parents, $\lambda = 2\mu$ offsprings are created. A classical one-point crossover is performed: the vector of heights of the two parents are cut and exchanged. The cutting point is chosen randomly.

The mutation function consists in moving a building to an empty parcel. If there is no empty parcel, the building either exchange location with another building, or is destroyed and its volume distributed on existing buildings. The mutation over the parameters is performed over the district with a probability of occurrence set to 0.7 on the population of offsprings, which means 70 % of the newly created districts through cross-over are mutated.

The crossover cut point is selected randomly, so the resulting configurations have no reason to satisfy the volume constraint. To correct this, a repair operator has been implemented. This operator modifies the values of height, and thus increases the diversity in the population. Two types of corrections are used: the distributed correction evenly distributes or removes the difference between created district and desired built volume uniformly on all buildings; the localized correction adds or removes volume to a single building until one of its bounds is reached, then the latter is achieved to other random positions until the volume constraint is respected. As low populations are used, it is important to maintain the diversity. Therefore, the reparation operator applies randomly one of these two rules.

4 Results

Three optimization tests were run for each density, cell size and calculation date. A radius of calculation of 7 is used in all cases (seven rows of buildings generated in each direction around the evaluated building), which may require various replications of cells in each direction. The population of districts for the optimization process is set to $3(4+6c)$, where c is the cell size. Finally, it should be noted that the surface energy shown in buildings is the average over each facade. The figures of the next sections include the representation on one cell without its context, and a plan view with the cell repeated once in each direction. These representations are therefore different from the geometries generated for the calculation.

In the following, comments on results are given separately for the effect of calculation date, density and cell dimensions on the features of the best patterns found.

4.1. Effect of the date

A sample of results for the three considered dates (winter and summer solstice, and the equinox) is presented on Figure 4. One can notice that, for winter solstice and the equinox, the presented optimal configurations show east-west rows of maximum height buildings, while the presented optimal configuration for summer solstice has high buildings on every north-south row of buildings. It has to be noticed that various configurations are nearly equivalent, and the features of the best cells are better observed studying results for diverse cell size and volume. From this study, the results show:

- For the winter solstice, where the sun stays close to the horizon, with solar energy mainly coming from the south, the most efficient urban layouts all have at least one building of maximum height in each north-south strip. It can be observed that rows of high buildings or checkerboard patterns are equally efficient.
- At the equinox, the solar radiation is strong from direction south-east and south-west. The best urban layouts are constituted by east-west rows of maximum height buildings. The checkerboard pattern is not efficient for this date.
- At the summer solstice, the solar rays have low incidence on the facades in the middle of the day and are more potent when the sun is east or west, emphasizing the corresponding facades. All the best layouts have buildings of maximum height in every east-west strip. The checkerboard pattern is also efficient in this case.

From these observations, it appears that east-west rows of buildings are the most efficient for winter period, while being very inefficient at the summer solstice.

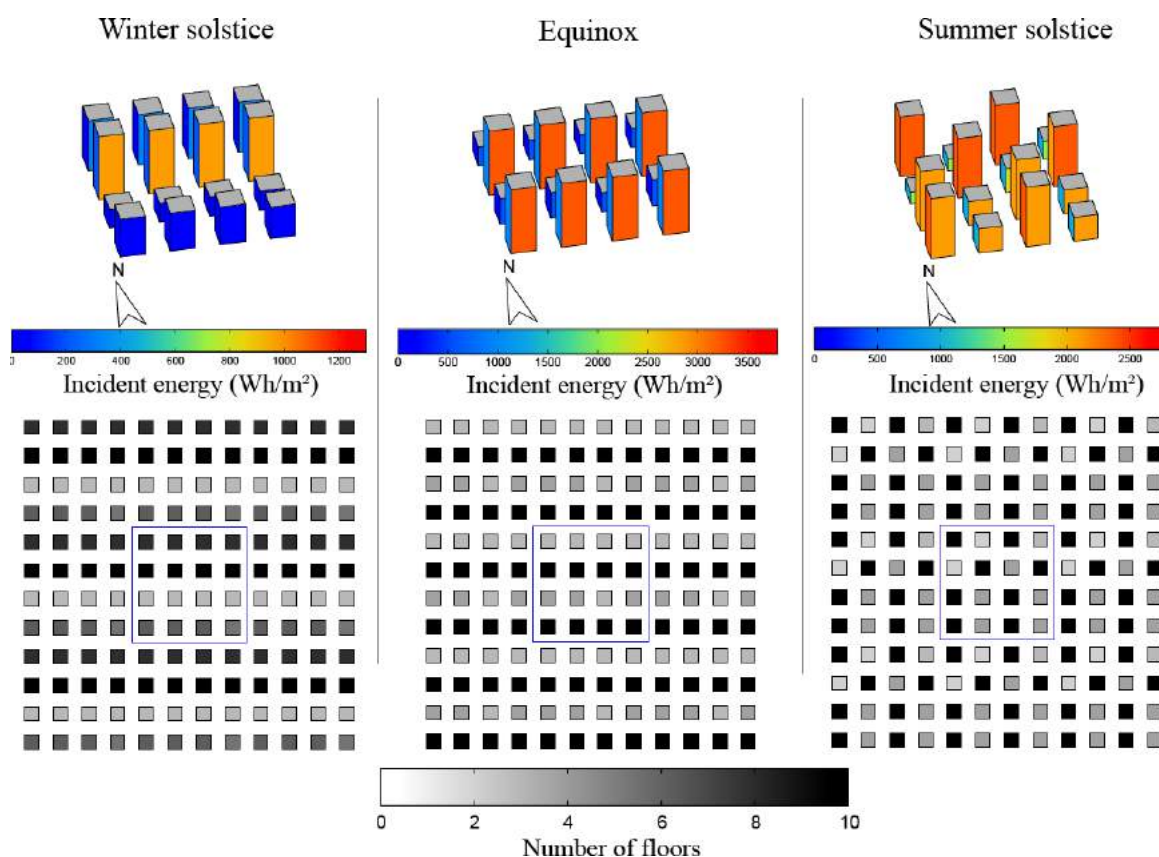


Figure 4. Best urban cells found for solstices and equinox (50° N, cell 4x4, volume=66%Vmax)

4.2. Effect of the density

When raising the desired density of the district, each added block will be able to collect less solar energy than the previous one. The effect of the raising density is twofold. Primarily, it raises the maximum overall direct solar energy potential to a certain point where it is capped, as showed in [Vermeulen, 2015]. Secondly, the features of an optimal cell appear sequentially: the features of high density cells are usually composed of patterns already noticeable in the low density districts. Eventually, in the high density cases, some of the remaining volume is located where it is not well exposed, as it can be noticed on the Figure 5.

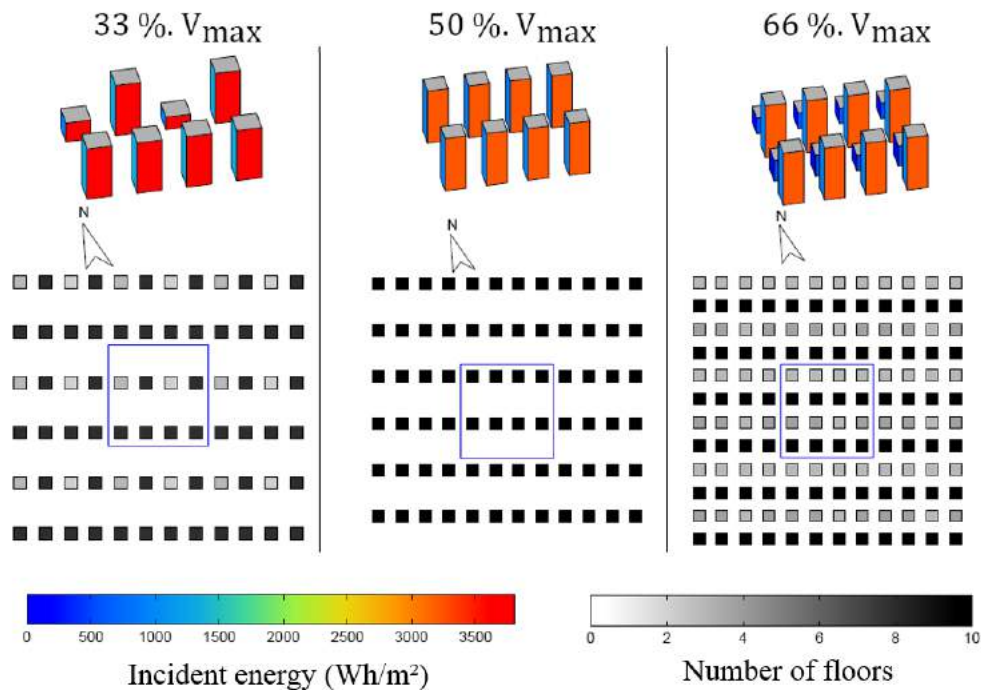


Figure 5. Best urban cells found for built densities of 33 %, 50 % and 66 % V_{max} (50° N, cell 4x4, equinox)

4.3. Effect of the urban cell dimensions

The dimensions of the urban cell add more diversity to the possible patterns of district: a 6x6 cell could have all its volume in a limited perimeter of the cell whereas a 2x2 cell will necessarily generate a district with some homogeneity as no 2x2 empty spaces could exist in the resulting urban fabric. Illustrations of optimal results for the winter solstice, for a built volume of 66 % of the maximum volume, for various cell dimensions are presented on Figure 6. The presented configurations have similar objective function value per parcel (respectively 133 kWh, 134 kWh, 136 kWh, 134 kWh and 134 kWh per parcel). The higher diversity granted by the larger cells can be observed.

Further optimization case show that the cell dimensions does not improve the highest radiation per building that can be captured by the district for given conditions of solar radiation and density, However, the largest cells tend to have a lower worst value of objective function per building, for the reason evocated earlier.

Finally, the optimal shapes for winter solstice treated in section 4.1 can be analysed on Figure 6, where the cells show diverse geometries but always have maximum height buildings on each north-south strip, sometimes aligned in the form of east-west rows. Furthermore, stair-like shapes descending toward North can be observed, hiding the roofs which are not taken into

account in the objective function behind the higher buildings. The plan view helps seeing these: maximum height buildings (black squares) are in most cases followed by one to three buildings of decreasing heights.

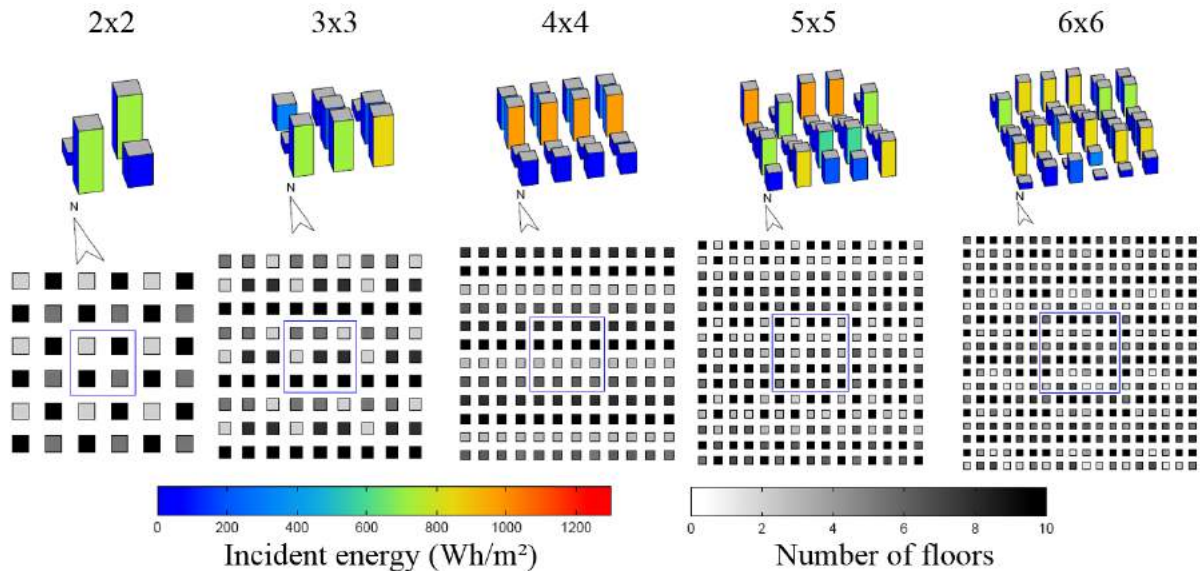


Figure 6. Best urban cells found of dimensions 2x2 to 6x6 (50° N, winter solstice, volume=66%Vmax)

5 Conclusion

The access to solar radiation in dense cities has been the subject of many studies in the last years, due to growing concerns about energy use in buildings and improvement of the simulation tools. Among these works, the study of simplified urban geometries is a common way of searching the general features of a good city regarding some criteria.

The paper presents a geometric description of a simplified district laying on a definition of the district as a periodic fabric composed of infinitely reproduced urban cell. The urban cell definition is then used in a study of optimization of urban shapes for direct solar radiation maximization, where the context of the parameterized district is constituted by reproduction of itself. This way, the boundary effects of having a predetermined fixed context are avoided.

Three optimization conditions are then presented: varying date for solar direct radiation, varying density of the district to be built and varying cell size. The results show that:

- Good urban shapes for winter solstice direct radiation (latitude 50° N) all have high buildings in each north-south strip; for the equinox, the good shapes have east-west rows of high buildings; for summer solstice radiation, the good shapes have high buildings on each east-west strip and small buildings in between to capture solar radiation when the sun is higher in the sky.
- The density has an impact on the overall radiation that can be captured, and optimal low-density patterns can usually be recognized in dense optimal configurations.
- The size of the cell does not influence the maximum direct energy that can be captured with a given built density but grants higher diversity in the set of nearly optimal configurations.

In the study of urban radiation, it is not rare to formulate the hypothesis of a regular district, and the urban cell could therefore be used for further studies of urban shape optimization, with

variation on the type of buildings and their parameters, in order to understand better the best features of a good urban shape regarding solar access for local needs and climate specificities.

Acknowledgments

The authors would like to thank the CONICYT for the financial support to the present work through the research project FONDEF ID14i10208.

References

- [Beyer 2012] H Beyer, H Schwefel: Evolution strategies—A comprehensive introduction. *Nat. Comput.*:3–52 (2002).
- [Campbell 1998] GS Campbell, JM Norman: *An Introduction to Environmental Biophysics*. ed 2 (1998).
- [Cheng 2006] V Cheng, K Steemers: Urban form, density and solar potential, in : 23rd Conference on Passive and Low Energy Architecture (2006), pp 6–8.
- [Compagnon 2004] R Compagnon, 2004, Solar and daylight availability in the urban fabric, *Energy and Buildings*, vol. 36, no 4.
- [Eiben 2013] A Eiben, J Smith: *Introduction to evolutionary computing*. (Springer, 2003, Available from:
- [Hachem 2011] C Hachem, A Athienitis, P Fazio: Investigation of solar potential of housing units in different neighborhood designs. *Energy Build* 43:2262–2273 (2011).
- [Hachem 2013] C Hachem, P Fazio, A Athienitis: Solar optimized residential neighborhoods: Evaluation and design methodology. *Sol Energy* 95:42–64 (2013).
- [Kämpf 2010] JH Kämpf, D Robinson: Optimisation of building form for solar energy utilisation using constrained evolutionary algorithms. *Energy Build* 42:807–814 (2010).
- [Kanters 2012] J Kanters, M Horvat: Solar Energy as a Design Parameter in Urban Planning. *Energy Procedia* 30:1143–1152 (2012).
- [Krüger 2010] E Krüger, D Pearlmutter, F Rasia: Evaluating the impact of canyon geometry and orientation on cooling loads in a high-mass building in a hot dry environment. *Appl Energy* 87:2068–2078 (2010).
- [Liu 1960] B Liu, R Jordan: The interrelationship and characteristic distribution of direct, diffuse and total solar radiation. *Sol Energy* 4:1–19 (1960).
- [Muhaisen 2006] AS Muhaisen: Shading simulation of the courtyard form in different climatic regions. *Build Environ* 41:1731–1741 (2006).
- [Pérez-Lombard 2008] L Pérez-Lombard, J Ortiz, C Pout: A review on buildings energy consumption information. *Energy Build* 40:394–398 (2008).
- [Ratti 2003] C Ratti, D Raydan, K Steemers: *Building Form and Environmental Performance : Archetypes, Analysis and an Arid Climate*. *Energy Build* 35:49–59 (2003).
- [Sarralde 2014] JJ Sarralde, DJ Quinn, D Wiesmann, K Steemers: Solar energy and urban morphology: Scenarios for increasing the renewable energy potential of neighbourhoods in London. *Renew Energy*: 1–8 (2014).
- [Strømman-Andersen 2011] J Strømman-Andersen, P Sattrup: The urban canyon and building energy use: Urban density versus daylight and passive solar gains. *Energy Build* 43:2011–2020 (2011).
- [Vermeulen 2013] T Vermeulen, JH Kämpf, B Beckers, *Urban form optimization for the energy performance of buildings using Citysim*, Proceedings of CISBAT 2013 cleantech for smart cities and buildings, 2013
- [Vermeulen 2015] T Vermeulen, C Knopf-Lenoir, P Villon, B Beckers: Urban layout optimization framework to maximize direct solar irradiation. *Comput Environ Urban Syst* 51:1–12 (2015).
- [Van Esch 2012] MME Van Esch, RHJ Looman, GJ De Bruin-Hordijk: The effects of urban and building design parameters on solar access to the urban canyon and the potential for direct passive solar heating strategies. *Energy Build* 47:189–200 (2012).

Pertinence of social inclusion design methods in communities

Enrique V. Villacís¹, María L. Rodríguez², Cynthia C. Ayarza², and Klaus Rueckert³

¹ Pontificia Universidad Católica del Ecuador-Arquitectura Diseño y Artes
Ave. 12 de octubre 1076 y Roca, Quito, Ecuador
evvillacis@puce.edu.ec

² ENSUSITIO Arq.
Rafael León Larrea N24-20, Quito, 170517, Ecuador
lora_rv@ensusitioarq.com
contact@ensusitioarq.com

³ Technische Universität Berlin-Faculty VI-Institute of Architecture-Department Design and Structure
Strasse des 17. Juni 152, Berlin, 10623, Germany
Klaus.Rueckert@tu-berlin.de

Keywords: Socialization, Participation, Opinion Leader, Sustainable Urban Planning.

Abstract. *A specific approach to social inclusion method for the design process in a community, even if tested, does not assure the effectiveness within time and different future projects. This paper is based on a case study of three different design processes taken place on the rural community of San Jose de Olaes - Ecuador, dealing with the importance of participation. After having a successful process with the participatory design of one specific need, we were not able to apply this participatory design process in other projects to come, because of different circumstances based on time, product and especially common interest. We will illustrate this process and how there is no recipes in the inclusive design process not even within the same community and almost the same period of time.*

1 INTRODUCTION

Social inclusion has become a must for the development of the design process within community projects. Sometimes as a technical team we tend to categorize and standardize processes but we have to be aware of the specific needs and processes during the life time of a community leading to the best understanding of social inclusive tools rather than standard recipes, as in the other hand “social exclusion may cause harm but also bring psychological benefits, though not usually for both parties. Social inclusion and exclusion is a dialectic in which the parties may vary their complicity or dispute. Some excluded parties may ultimately find ways to create a positive outcome for themselves, for instance, by redefining what is important or by exposing and challenging the legitimacy of the bases of exclusion”. (Abrams, Hogg, & Marques, 2005)

This investigation is the result of a process of over a year’s work in the community of San José de Olaes developing design-built projects on the basis of participatory design and construction. Based on three different projects we will illustrate the dissimilar ways of appropriation of this inclusive design process and how this affects communities both in a positive and negative way. Our aim is not to categorize the effectiveness of participatory and inclusive methods but to raise awareness on how particular communities and processes need particular approaches; no recipes apply on this kind of projects. Although we found the results of the participatory design process for the community church, this was not the rule for projects to come, because of the specific time and interest the community had.

We will first introduce some concepts about inclusion and different levels of participation in community design processes, as a foundation, in order to analyze and compare three different design-build processes taken place by the *Con lo que Hay* workshop¹ chronologically in San Jose de Olaes, the community kitchen, the church and the shadow. We think it is important to compare these three different cases in order to illustrate how, during this period of time, the participatory involvement evolved, leaving us with the question on how pertinent inclusion may be in these type of projects.

2 SOCIAL INCLUSION: General concepts

First we should understand a general debate within social inclusion and exclusion, “Social inclusion/exclusion is more interesting and dynamic than either social cohesion or social capital, for it is poised on the very contradiction evinced by all of these terms: how does one go about including individuals and groups in a set of structured social relationships responsible for excluding them in the first place? Or, put another way, to what extent do efforts at social inclusion accommodate people to relative powerlessness rather than challenge the hierarchies that create it? To what degree might we consider willful social exclusion by groups an important moment of conflict, an empowered act of resistance to socio-economic systems that, by their logic and rules, continue to replicate and heighten the material hierarchies of inequality? I pose these questions because many who embrace the concept of social inclusion emphasize how it goes beyond simple matters of income or material inequalities and their state enforced redistribution (Barata, 2000), or even of securing basic human rights (Bach, 2002). Rights and redistribution, it is argued, are necessary but not

¹ “Con lo que hay” with what is available an academic architecture studio within FADA-PUCE Quito, for levels seven and eight as a pre-professional opportunity where students ultimately apply their academic knowledge along with social work within a specific community¹. The workshop embraces diagnosis, analysis, conceptualization, design and participatory architectural construction themes, through to design and publication of manuals for future use by the population where they intervene. It works with resources and problematic specific to every location and social environment. The results depend on the surroundings of the project, space, time, and specially the community. The involvement may go from helping a community understand their real necessities or the community showing us our necessities and with the possibility of building an infrastructure. www.ensustioarq.com.

sufficient conditions for people ‘to be accepted and to participate fully within our families, our communities, and our society’, as one definition of social inclusion stakes the territory [(Guildford, 2000), p. 1].” (Labonte, 2004)

It has become fashionable, on every level of the decision making process, from state to local government, to talk about social inclusion, especially in communities when developing processes for their infrastructure. In order to understand social inclusion we must understand social exclusion, “For some it is synonymous with poverty. Others emphasize inadequate social participation, lack of social integration and lack of power. While related to poverty, social exclusion is a quite distinct concept that is also linked to the important notion of social capital. Social capital can be defined as the networks of social relations that are characterized by norms of trust and reciprocity that facilitate cooperative behavior (Stone, 2001) and build a cohesive society (Winter, 2000). Social disadvantage has been linked in a recent Australian study to lower levels of social trust and higher levels of crime (Cameron, 2005)” (Alan, Gray, & Edwards, 2008)

It is said that it is important to have participatory processes so every voice in the community will be heard and everyone will see their work reflected on the infrastructure, “citizens, individually and collectively, shall participate as leading players in decision making, planning and management of public affairs and in the people’s monitoring of State institutions and society and their representatives in an ongoing process of building citizen power. Participation shall be governed by the principles of equality autonomy, public deliberation, respect for differences, monitoring by the public, solidarity and interculturalism. The participation of citizens in all matters of public interest is a right, which shall be exercised by means of mechanisms of representative, direct and community democracy. (Asamblea Constituyente, 2008). By inclusion, we refer to take account of every member of a community or its representative, minority or majority.

Being socially included means that people have the resources, opportunities and capabilities they need to: *See Fig.1.*

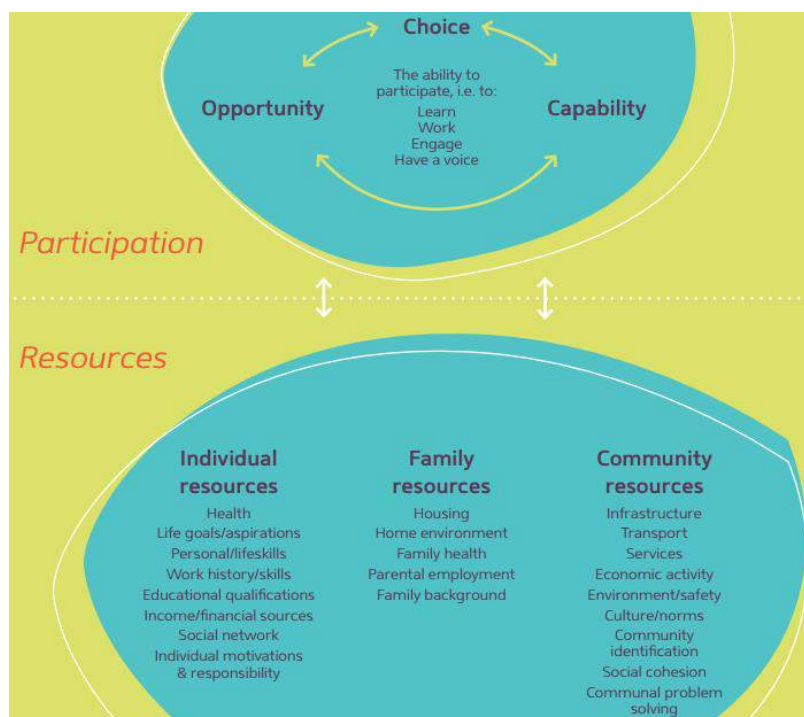


Fig.1. Social inclusion conceptual framework-Participation and resources (Board, 2010)

- Learn (participate in education and training).
- Work (participate in employment, unpaid or voluntary work including family and career responsibilities).
- Engage (connect with people, use local services and participate in local, cultural, civic and recreational activities).
- Have a voice (influence decisions that affect them).

“Design processes that involve user participation concern issues of representation in the early stages of design, when users’ needs and expectations are being expressed. A participatory approach is used to investigate the nature of design discussion during the early stages of design. It is shown that the ideology of inclusive design is similar to the ideology of participatory design. The ability of language-use to reveal user preference is explored through the analysis of architect–user conversations. Investigating architect and user interaction revealed that tacit knowledge can be made explicit and the difficulty of generalizing user-needs from user statements.” (Luck, 2003)

Socialization, participation and personal leadership are concepts that exists in order to validate inclusion within the decision making process in communities. *See Fig.2.*



Fig.2. Types of decision making processes

Opinion leader, “- those who’s opinion they value. Opinion leaders are found in all strata of society. A specific person can be an opinion leader in certain areas and an opinion follower in others. The more highly a person esteems the opinion leader, the more influential the opinion leader will be in shaping the person’s product and brand choices.” (Kotler & Scheff, 1997) When a community is ruled by one person that, although not being the elected leader, effectively takes decisions based on his knowledge or his personal believes. “Elsewhere in the world, and even in smaller social units within the democracies, social decisions are sometimes made by single individuals or small groups and sometimes (more and more rarely in this modern world) by a widely encompassing set of traditional rules for making the social choice in any given situation, e.g., a religious code.” (Arrow, 1978) Historically, matriarchy and patriarchy have been two models of leading cultures, in which the leader takes action, based on his/her wisdom or their counselors. This has not changed for several communities and countries. And in the name of democracy we have "majorities" which paradoxically are minorities leading processes for the majorities and minorities. In Latin America, and the Andes specifically, usually a community is led by the older males that take decisions, frequently they are not majority by number in the community but are the ones that take the economic resources to their families, and because of this fact then they know, or think they know, what their families and communities need in terms of infrastructure. In the other hand, women in communities are mainly meant to take care of children, their homes and community activities.

Participation, to have every member of the community involved in the design and or construction process of an infrastructure, “The ability to participate: i.e. to learn, work, engage, have a voice” (Board, 2010), although this seems to be the ideal process it can be

conflictive for communities taking on account its historic development within inclusive process.

Socialization, to have a design solution already developed and make it accessible for evaluation by all the community in order to validate it. “A natural way of arriving at the collective preference scale would be to say that one alternative is preferred to another if a majority of the community prefer the first alternative to the second.” (Arrow, 1978)

In the Andean contexts and specifically in the community of San Jose de Olaes located 25 minutes east of the city of Quito, a farmers community that has been self-isolated from the city, their way of life relies on the economic sustenance from the older men, and the women in the maintenance of the house and raising children. In this context all the community decisions are made by the men, and basically by the opinion leader, that usually is not the president of the community. Everyone in the community relies and trusts on the point of view of this person for its relevance even if he may be wrong or if his decisions are made based on prejudices. The participatory construction process in this community is based on the "minga"² in which after taking the decision of having a infrastructure build, all the community, including the minorities, work based on the guidance of the construction workers form the community, usually men 30 to 50 years old. The design of a particular infrastructure is not a concern, how it will be done is said by the men and usually minorities, woman and youngsters are just workforce. In this environment, their projects were designed and built during the same year and these examples will illustrate the way participation and inclusion of minorities was held within the community.

3 CASE STUDY: “CON LO QUE HAY” WORKSHOP IN SAN JOSE DE OLAES

The president of the community of San Jose de Olaes approach the Con lo que Hay workshop in order to design and build the community church. We as a workshop, with professional support³, started a one year process beginning with a diagnosis based on the analysis of the process held by the design-build of the community kitchen followed by the participatory design-build of the church and finishing with the design-build of the shadow under the umbrella of the socialization.

3.1 The community kitchen: opinion leader process. See Fig.3

This process was taken place while we, the Con lo que Hay workshop, arrived to the community and served us a diagnosis about how the community handles their infrastructure design and build processes.

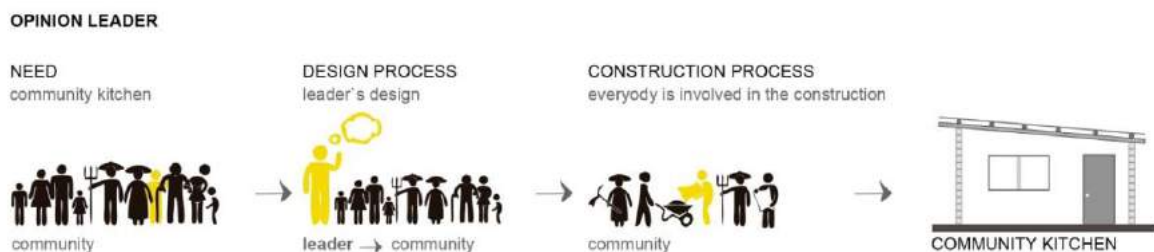


Fig.3. Personal leadership design process

² Voluntary communal labor, cooperative work; crew of cooperative workers.-Kichwa word. (HarperCollins Publisher Limited, 2016)

³ ENSUSITIO ARQ: **IN ITS PLACE** Architecture a studio/workshop based in Quito-Ecuador, working **with what is available in its place**. The studio collaborates with Con Lo Que Hay workshop in order to assure professional results for academic processes.

The community on its own faced this project.

- The design process was on site and took one meeting in which the men of the community show their design based on their construction skills, knowledge and resources.
- The design was focused on the constructions skills rather than in the women's requirement for cooking, this is a room with one window that has no ventilation or any facility for its main purpose. *See Fig.4.*

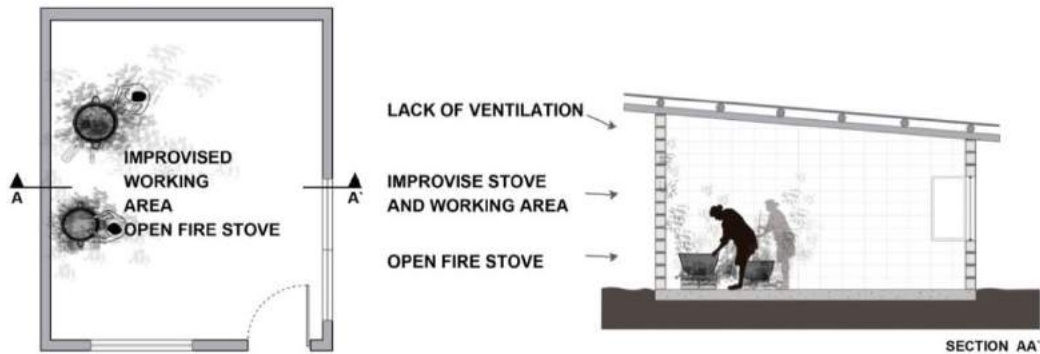


Fig.4. Kitchen floor plan and section

- The construction was fast and did not require any technological improvement or transfer of technology for the community. *See Fig.5.*
- During the construction the men lead the process and the women were mere workforce.
- The infrastructure was built in three months.



Fig.5. Kitchen external view, Kitchen internal view

3.2 The church: participation process. *See Fig.6.*

Our aim as Con lo que hay workshop based on the not inclusive design process of the communal kitchen was to include ideally every member of the community on the thinking and development of the design process of the San Jose de Olaes Church, it has come to conclusion that a participation process was an effective tool for this matters for this specific time and project.



Fig.6. Participation design process

- We as a participatory design workshop with Con lo que hay, an academic workshop and Ensusitio Arq., a professional studio, were involved in this process.
- The design took approximately two months of participation from the portion of the community that was interested in this process, mainly women and few men. *See Fig.7*

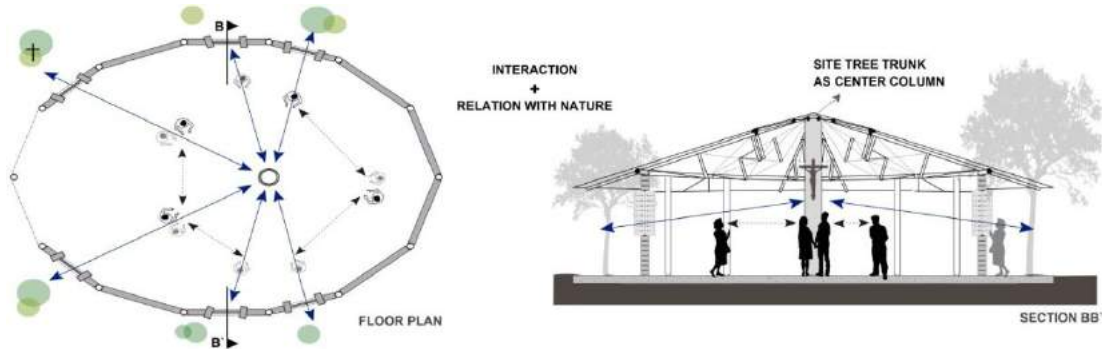


Fig.7. Chapel floor plan and section

- During the construction process the women of the community took active action in order to make their decision heard, sometimes strongly against the construction men.
- The church still is under construction. *See Fig.8.*



Fig.8. Chapel exterior view, Chapel interior view

3.3 The shadow: socialization process. *See Fig. 9.*

After these two experiences a new infrastructure necessity emerges for the community it is decided to make a cover, as grandstand to the soccer field, and a playground for the kids. Since the community was worn out because of the long design and built process from the Church leading to some lack of interest the workshop took this project, with a smaller group of participants, a few ladies and almost no men. Leading us to rethink of the ideal of the participatory design and switching to a socializations design, in order to expedite the design and building process.



Fig.9. Socialization design process

- A group of the minority from the community and the technical team faced this project.

- The design was focused on the requirements of the people who will actually use this infrastructure; lady's and kids rather in the construction system. *See Fig.10.*

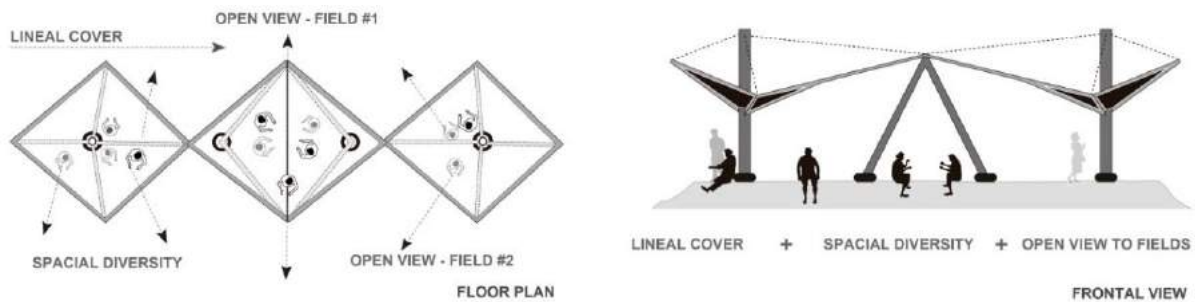


Fig.10. Cover floor plan and elevation

- The design process was made by the technical team based on these minority requirements and validated by the community via socialization.
- The construction was mainly a responsibility of the technical team with the support of a small part from the community including not only the small group of lady's that took part of the design process but most of the lady's form the community.
- During the construction the technical team led the process and the women shared the responsibility.
- The infrastructure was design and built in four months. *See Fig.11.*



Fig.11. Built cover and Cover used by community

4 CONCLUSION:

Effectiveness in this kind of projects is very difficult to measure since qualitative variables are very subjective. For example the Community Kitchen is a completed project but its non-inclusive design process affects directly the health to the users of the building. In the other hand a participatory design process for the Church created friction within the community, and this power conflict lead to the infrastructure to take long time to design and build, although the design is a high success as an architectural functional and symbolic piece. The socialization process during the design a building process for the shadow was a result of observation of previous work, it would have been a mistake for us to push for a participatory design process based on the apparently success of the Church, we choose to use the socialization tool specially based on the time specific circumstance of the community and the scale and interest for the project.

No recipes allowed within specific contexts, force processes can lead to auto exclusion and conflicts within the same communities. Sometimes, architects, sociologists, cultural producers, tend to think that inclusion should be a must, forgetting that for some environments inclusion might be a conflict producer and sometimes we tend to create systems and ideal process based

on previous success forgetting to analyze the time life of communities and their specific processes.

References

- [Abrams, Hogg & Marques 2005] Domini Abrams, Michael D. Hogg, M. A., & Jose M Marques. *The social psychology of inclusion and exclusion*. Psychology Press, New York, Hove, 2005
- [Alan, Gray & Edwards 2008] Hays Alan, Matthew Gray, & Ben Edwards.. *Social inclusion: origins, concepts and key themes*. Australian Capital Territory: Social Inclusion Unit, Canberra, 2008
- [Arrow 1978] Kenneth Arrow . *Social choise and individual values*, Wiley, New York, 1978
- [Asamblea Constituyente 2008] Asamblea Constituyente, *Constitución de la República del Ecuador* , page 69. Registro Oficial No. 449, Montecristi, 2008
- [Board 2010] Australian Social inclusion Board, Inclusion in Australia, *Inclusion in Australia: How Australia is faring* . Pages 13-15, Commonwealth of Australia, Canberra, 2010
- [Encyclopedia Britanica 2016] Encyclopeda Britanica, Inc., <http://www.britannica.com>. Retrieved 01 05, 2016, from <http://www.britannica.com/topic/minority>, 2016
- [Harper 2016] Harper Collins Publisher Limited. (2016). [collinsdictionary.com](http://www.collinsdictionary.com). Recuperado el 05 de 01 de 2016, de <http://www.collinsdictionary.com/dictionary/spanish-english/minga>
- [Kotler & Scheff 1997] Philip Kotler & Joanna Scheff, *Standing Room Only: Strategies for Marketing and Performing Arts*. Boston, United States of America: HBS Press. Boston, 1997
- [Labonte 2004] Ronald Labonte, HEALTH PROMOTION INTERNATIONAL, *Social inclusion/exclusion: dancing the dialectic, Vol. 19. No. 1*, Page 117, 2004
- [Luck 2003] Rachael Luck, *Design Studies*. Elsevier, 24(6), Pages523-553. November, 2003

Application of Large-Eddy Simulations in Evaluating Ventilation over 3D Building Data Retrieved from Satellite Images

Weiwen Wang¹, Yong Xu², and Edward Ng³

¹ School of Architecture, The Chinese University of Hong Kong
Shatin, N.T., Hong Kong SAR, China
e-mail: w.wang@cuhk.edu.hk

² Institute of Future Cities, The Chinese University of Hong Kong
Shatin, N.T., Hong Kong SAR, China
e-mail: xuyong@cuhk.edu.hk

³ School of Architecture, Institute of Environment, Energy, and Sustainability, and Institute of Future Cities, The Chinese University of Hong Kong
Shatin, N.T., Hong Kong SAR, China
e-mail: edwardng@cuhk.edu.hk

Keywords: Large-Eddy Simulation, Urban Ventilation, Building Height Extraction.

Abstract. *Computational fluid dynamics (CFD) techniques, such as the Reynolds-averaged Navier-Stokes (RANS) model and large-eddy simulations (LES), are widely used in urban ventilation studies. Unfortunately, realistic digital elevations of urban areas required in CFD studies are not always available. Therefore, there is a need to extract urban information from satellite images that can be used for, but not limited to, studies of the urban wind environment. This study evaluates 3D building geometries extracted from different satellite images by LES of pedestrian-level ventilation. As a case study, three sets of digital elevation data extracted from satellite images in an urban area of Mong Kok, Hong Kong, are assessed. The LES model, entitled the Parallelized LES Model (PALM), is first validated by a CFD guideline of simulating flows around single building. Wind characteristics in urban elevations extracted from two single satellite images and the fused result are then compared with those from realistic data in the same area, using identical LES settings. The result shows that building heights extracted from the TerraSAR-X synthetic aperture radar (SAR) image and the fused results of SAR and the WorldView-2 optical (Stereo) images are reasonable for air ventilation assessment (AVA). Better performance in representing tall buildings, rather than low buildings, is found to be more important in building height extraction for AVA purposes.*

1. Introduction

According to the World Health Organization (WHO), the urban population in 2014 accounted for 54% of the total global population, up from 34% in 1960, and it continues to grow. Rapid urbanization causes a number of problems such as urban heat islands (UHIs) and air pollution, which threaten the health of city inhabitants. Urban ventilation is found to be a way of mitigating these problems [Arnfield, 2003; Ng, 2009; Shi, 2015; Wong, 2011]. Good air ventilation is very important for high-quality and healthy living, particularly for high-density cities in tropical and subtropical regions with a hot and humid climate. Thermal comfort can be achieved by capturing natural wind. To achieve neutral thermal sensation in an urban environment, a wind speed of 0.9–1.3 m/s is needed for a person wearing light clothing under shaded conditions [Ng, 2012].

In the literature of urban air ventilation studies, various research methods have been used to describe the complex flows over urban environments. Computational fluid dynamics (CFD) techniques such as the Reynolds-averaged Navier-Stokes (RANS) model, large-eddy simulation (LES), and direct numerical simulation (DNS) are among the commonly used tools [Brunner, 2003; Ng, 2011]. Urban ventilation is strongly influenced by wind speed and direction, which in turn are affected by three-dimensional urban morphology [Ramponi, 2015; Skote, 2005; Yang, 2013]. Unfortunately, realistic digital elevations of urban areas required in CFD studies are not always available for open access, especially in the less developed regions of the world where urban population growth is concentrated. Furthermore, surface geometries and urban morphologies are found to have a significant influence on UHI [Unger, 2004], especially for regions with a hot and humid microclimate [Emmanuel, 2006]. High-resolution digital elevations have been extensively used in studies of urban climate and outdoor thermal comfort [Lindberg, 2010]. Therefore, there is a need to develop methodologies of extracting building heights in urban areas from satellite images that can be used for, but not limited to, studies of urban ventilation.

There are three kinds of building height extraction from available remote sensing data: Stereo photogrammetry technology with pairs of optical images (hereafter referred to as Stereo images), synthetic aperture radar (SAR) technology, and light detection and ranging data (LiDAR) technology. However, there are limitations to these methods: (1) Stereo images tend to underestimate the height of tall buildings, and taller buildings predict larger errors [Eckert, 2010]; (2) the interferometry of SAR provides noisy and incomplete data, particularly for high-density urban areas where mutual interference of surrounding buildings are significant [Colin-Koeniguer, 2014; Sportouche, 2011]; and (3) LiDAR data is expensive and is limited by flight restrictions for applications in large urban areas [Zhou, 2014]. Therefore, recent studies have also been devoted to the integrated use of different kinds of data for building height retrieval [Sportouche, 2011; Xu, 2015; Zhou, 2014].

The objective of the present study is to assess the performance of building height extractions from different kinds of satellite images for potential use in urban ventilation studies with CFD techniques. Evaluation of building height extraction from satellite images from the perspective of a particular application, i.e., urban ventilation, has rarely been attempted to date as far as we know. What affects pedestrian comfort directly is the wind flow

within cities, in particular, the local turbulence level [Britter, 2003]. We therefore use an LES model to produce CFD simulations in this study. LES overcomes the deficiencies of RANS by explicitly resolving large, energy-containing turbulent eddies and parameterizing only small (subgrid) scale turbulence [Rodi, 1997; Tamura, 2008]. The dimensionality, spatial resolution, and turbulence intensity that an LES model can handle are superior compared to most of the other methodologies, and sometimes also to other CFD models, i.e., RANS and DNS [Castillo, 2011]. LES provides not only mean flow fields but also instantaneous turbulences, which are especially important for human comfort at the pedestrian level in the urban canopy layer [Keck, 2014].

2 Neighborhood-Scale Urban Geometries

An approach that jointly uses high-resolution WorldView-2 Stereo images and multi-temporal TerraSAR-X SAR images to retrieve building heights in high-density urban areas, which has the advantage of both datasets, was proposed by a recent study in Hong Kong [Xu, 2015]. In the present study, actual (measured) urban elevations (building heights) in a neighborhood on the Kowloon Peninsula provided by the Hong Kong Planning Department are utilized as topography input for the LES model. It is the same domain of Mong Kok used in Xu [2015], given in Figure 1a. Both are $1.2\text{km} \times 1.2\text{ km}$ and have a horizontal resolution of 2m. The methodology proposed by Xu [2015] for retrieving building heights in urban areas using both Stereo and SAR images assumes that the building footprints are known and involves two main stages: First, estimated initial building heights are retrieved from Stereo and SAR images, respectively; second, according to an object-based fusion approach, the initial building heights are then combined. The bias of building heights between actual data and data extracted from Stereo images, SAR images, and the fused result of the two kinds of images is given in Figure 1b, c, and d, respectively.

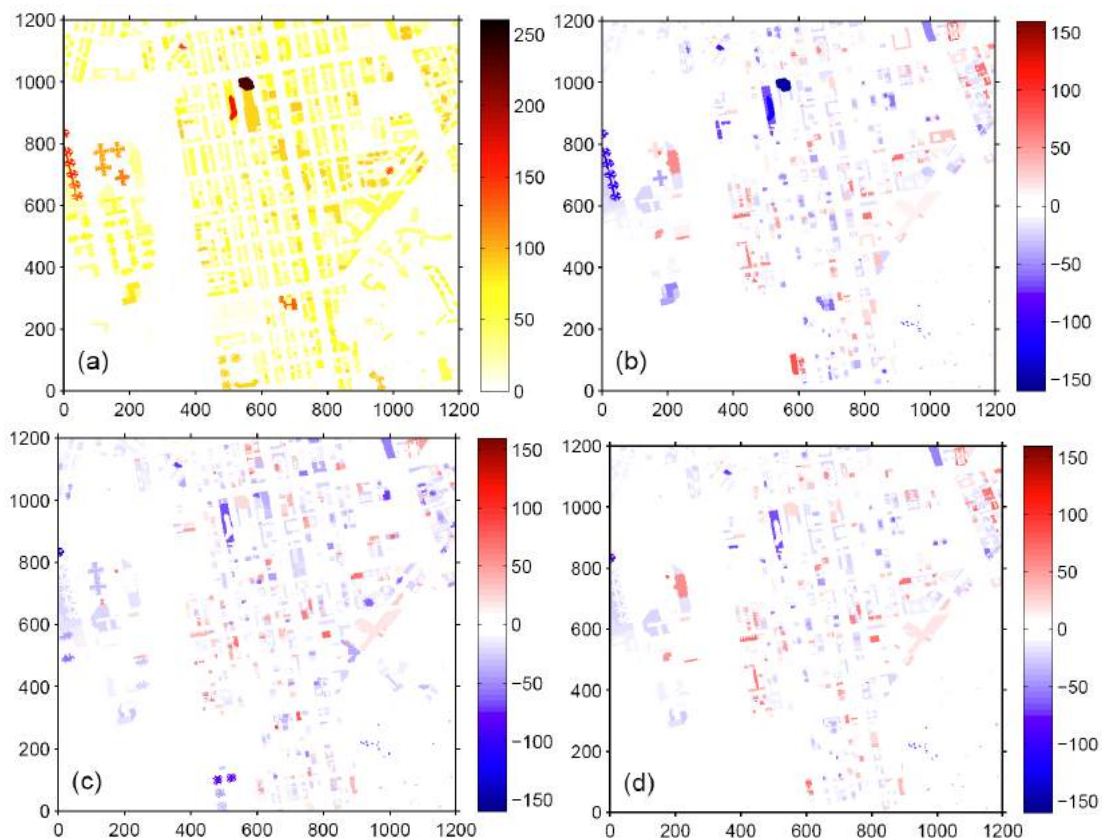


Figure 1: (a) Actual urban elevations (building heights) in a $1.2\text{km} \times 1.2\text{km}$ neighborhood in Mong Kok. Bias between actual data and data extracted from (b) Stereo images, (c) SAR images, and (d) fused result of the two kinds of images

3 The Parallelized Large-Eddy Simulation Model (PALM)

The LES model used in this study is the Parallelized LES Model (PALM) for atmospheric and oceanic flows, which has been developed at the Institute of Meteorology and Climatology of the Leibniz Universität Hannover since 1997 [Raasch, 2001]. PALM has been validated for simulating flows and turbulence characteristics at the street-canyon and neighbourhood scale [Letzel, 2008] and has been widely used in studies of urban street-canyon flows in recent years [Inagaki, 2011; Kanda, 2013; Park, 2014; Park, 2012; Razak, 2013], including high-density urban areas in Hong Kong [Letzel, 2012] and Macau [Keck, 2014]. The code used in this study is the most updated PALM version 4.0 [Maronga, 2015]. More details can be found on the PALM homepage (<https://palm.muk.uni-hannover.de/trac>).

3.1 Indicator and simulation setup

In air ventilation assessment (AVA) studies, we are especially interested in the pedestrian-level wind velocity. The wind velocity ratio (VR) is used as an indicator, which is calculated by

$$VR = V_p / V_\infty \quad (1)$$

where V_p is the wind velocity at the pedestrian level (2m above the ground), and V_∞ is the wind velocity at the top of the wind boundary layer and is not affected by ground roughness [Ng, 2009]. A top boundary layer of 500m is commonly used in Hong Kong AVA studies [Hong Kong Planning Department, 2008].

As we are focusing mainly on VR, the input wind speed is not very important, and if high wind speed is used, more computational time will be needed because the time step has to be shorter. Therefore, a low-velocity geostrophic wind of 1.5 m/s [Keck, 2014] is prescribed to save computational time. The time step sizes are optimized in PALM. Horizontal grid sizes are equidistantly 2m. The vertical grid spacing is 2m below 300m and stretched with a stretch factor of 1.08 above. CFD equations are spatially discretized on an Arakawa-C grid in PALM. Scalar variables are defined at the grid centers, while velocity components are shifted by half of the grid spacing. Therefore, horizontal wind velocity output from the 1m and 3m levels is linearly interpolated (averaged) to obtain V_p at 2m above the ground. V_∞ is derived from 500m. The total simulation time is 6 hours. The first 4 hours are excluded in the analysis of the results, as the turbulences need this time to spin-up. The simulated results from the 5th to the 6th hours are averaged for analysis. East and southwest (225°) winds, the prevailing annual and summer winds in Hong Kong, respectively, are simulated for assessment of building height extraction from satellite images. The no-slip bottom boundary condition with a Prandtl layer and the free-slip top boundary condition are applied to horizontal velocity components. As the targeted area is surrounded by urban areas, a simple cyclic (periodic) boundary condition setup in both the streamwise and spanwise directions is sufficient for the task. The simulations are restricted to neutral atmospheric stratification, i.e., thermal effects are not considered.

By default, PALM has six prognostic quantities. But as neutral stratification assumption is adopted, calculation of temperature equation is switched off. Variables including the velocity components u , v , w and the subgrid-scale turbulent kinetic energy e will be involved in our calculations, while the potential temperature θ , specific humidity q_v or a passive scalar s will not be involved. The separation of resolved scales and subgrid-scales is implicitly achieved by averaging the governing equations over discrete Cartesian grid volumes [Maronga, 2015]. Time step lengths are optimized by PALM codes and varying. For our main runs, the

maximum value of time step is 20 seconds, and the number of time steps for a simulation time of 21,600 seconds are around 20,000~25,000.

3.2 Model validation

We use the CFD guidelines proposed by a working group from the Architectural Institute of Japan (AIJ) to verify the PALM codes. To calibrate CFD simulations of air ventilation, AIJ guidelines conducted a series of cross-comparisons of wind data from RANS, LES, DNS, and wind tunnel tests [Tominaga, 2008]. We conducted a LES experiment of the 2:1:1 shape building model that complies with the AIJ guidelines [Mochida, 2002; Yuan, 2012]. The CFD setups and experimental data for verification can be found in the AIJ webpage (www.aij.or.jp/jpn/publish/cfdguide/index_e.htm). The inlet mean wind profile is the same as that given in the guidelines. The horizontal computational domain size is 172m × 108m. PALM does not allow differential grid spacing horizontally, an equidistant grid size of 1m is used. In the vertical direction, a grid size of 0.5m is adopted in below 24m and a stretch with a stretch factor of 1.05 is applied in above. With vertically 90 levels, the domain height is about 100m.

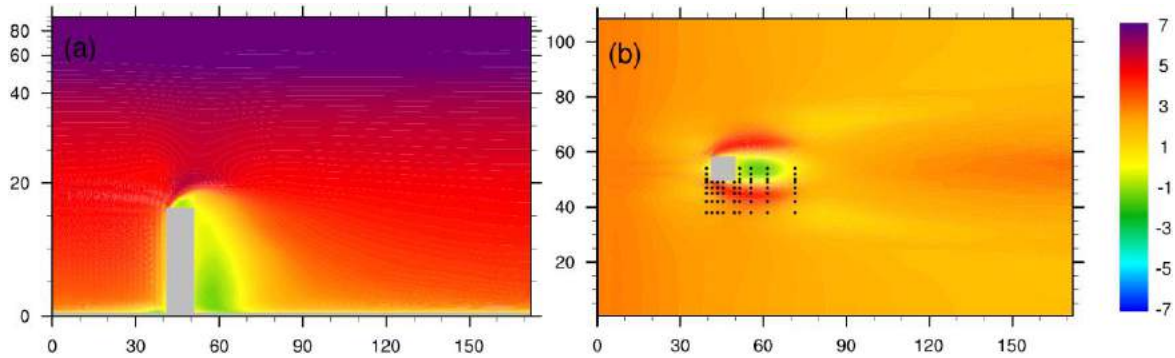


Figure 2: LES results of (a) vertical section of u-wind, and (b) horizontal section of u-wind at 1m height for validation of PALM codes. The grey box denotes the single building and black dots in (b) denote test-points for comparison in Figure 3b

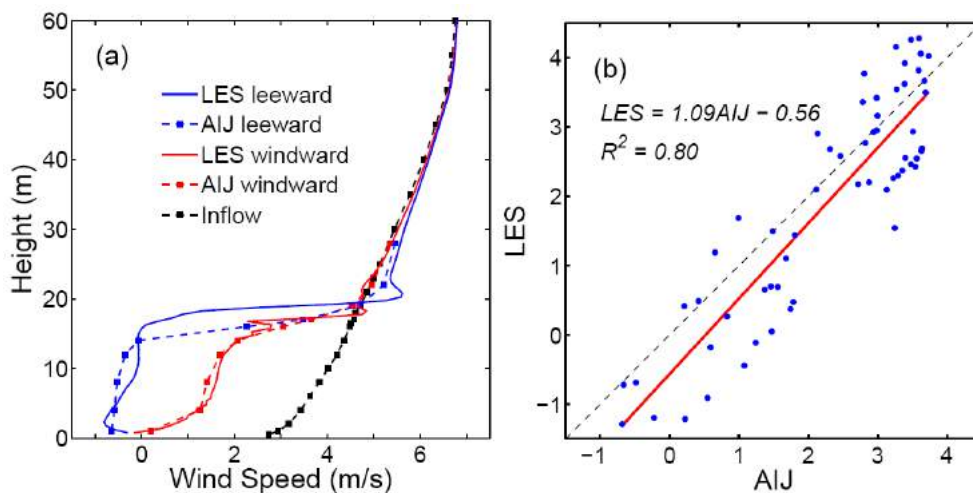


Figure 3: Cross-comparison between Architectural Institute of Japan (AIJ) experimental data and PALM results: (a) Vertical wind profiles in the windward (red lines) and leeward (blue lines) position at 2m from the building, the inlet mean wind is shown by the black profile. (b) Linear regression between AIJ and PALM results in the test points at 1m height shown in Figure 2b

The PALM-computed results for model validation are presented in Figure 2. Figure 2a is streamwise velocity of an x-z section located at the middle of the computational domain, while Figure 2b is streamwise velocity at 1m above ground. Correspondingly, Figure 3a compares velocity profiles at 2m away from the single building at windward (red lines) and leeward (blue lines), while Figure 3b is a scatter plot of PALM-computed and AIJ experimental velocity at 60 test points, which locations are shown in black dots of Figure 2b. Stronger rooftop vortex and velocity fluctuation compare to AIJ data can be observed from Figure 3a, but overall good agreement between the two suggests that PALM can capture the wind profile features around building. As this study focus on pedestrian-level ventilation, computational performance of PALM in reproducing near-surface velocity is more importantly. Cross-comparison of Figure 3b gives substantial confidence of using PALM in the present study.

4 Evaluation of ventilation over 3D building data

4.1 Effects of average size

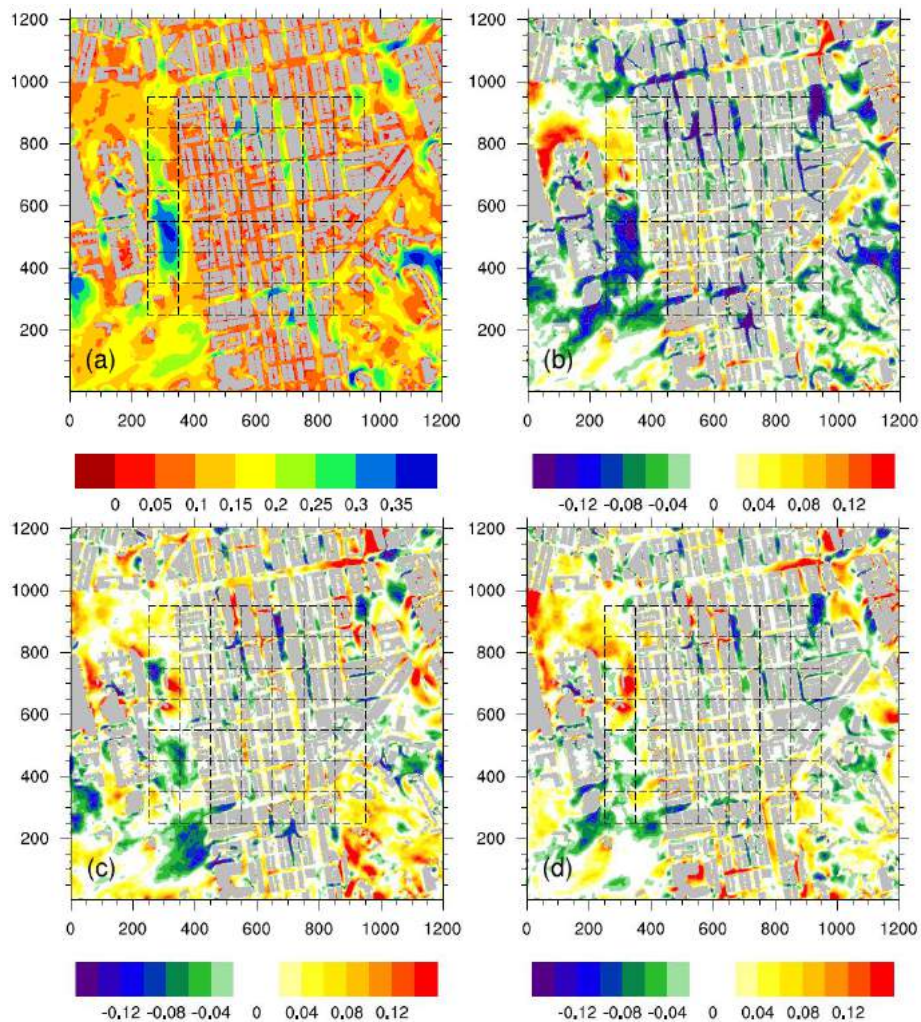


Figure 4: (a) PALM-computed VR in actual topography; deviations of VR from actual topography and topography retrieved from (b) Stereo images, (c) SAR images, and (d) fused result of the two images. The black dashed boxes denote the $100\text{m} \times 100\text{m}$ domains for zonally averaged VR. Wind input is from the east (right)

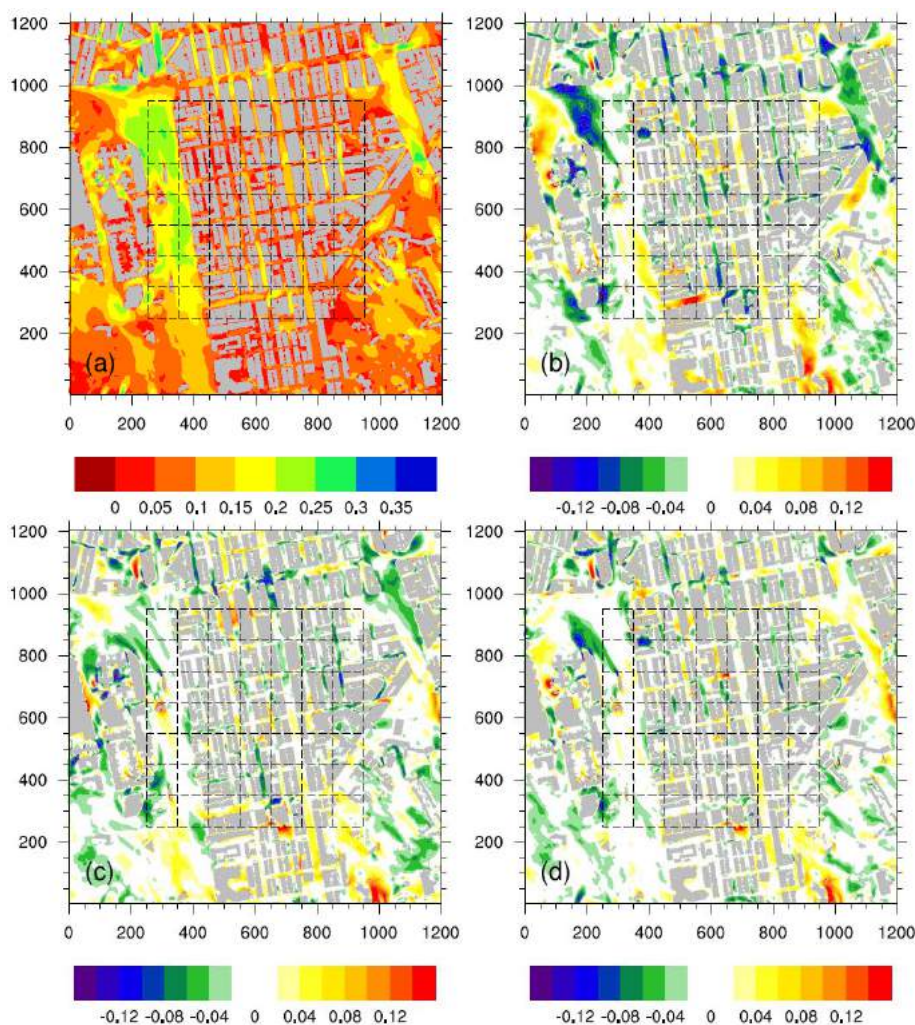


Figure 5: Same as Figure 4 but with wind input from the southwest

Wind direction	Average size	RMSEs Stereo	RMSEs SAR	RMSEs Fused
East	100m × 100m	0.040	<u>0.026</u>	0.028
East	50m × 50m	0.046	0.035	0.035
Southwest	100m × 100m	0.017	0.014	<u>0.009</u>
Southwest	50m × 50m	0.023	0.020	<u>0.016</u>

Table 1: Root mean square errors (RMSEs) of VR between extracted and actual building heights in different LES experiments (wind directions) and average sizes. The largest (smallest) value in each row is bolded (underlined)

Results of PALM-computed VR with wind input from the east (southwest) to actual topography and biases from extracted topography are given in Figure 4 (Figure 5). Urban planners and researchers may care more about the site-averaged VR than the VR at specific points. We select two kinds of grid sizes to check whether the comparative results are sensitive to this parameter. One is 100m × 100m while the other is 50m × 50m, with a unique buffer width of 250m. A buffer width of 250m can match the requirement of AVA [Ng, 2009], as the tallest building in the research area is 255m (Figure 1). Generally, it is suggested that

simulated results in the outer regions near the horizontal boundary are not reliable. The $100\text{m} \times 100\text{m}$ grids are shown in dashed boxes in Figures 4 and 5. For the grid size of $50\text{m} \times 50\text{m}$, the resolution is simply doubled.

Table 1 lists all the root mean square errors (RMSEs) of PALM-calculated VR between extracted and actual topography. The largest and smallest values in each row are highlighted, bolded for the largest value and underlined for the smallest value. Referring to the average size, the results can be compared for wind input from east and southwest respectively. It is found that the average sizes do not change the order of RMSEs from three sets of topography in case of southwest wind. The average size has a slight effect on the RMSE order in case of east wind, as can be seen from Table 2. Generally, the effects of average size on the overall RMSEs are not significant. Therefore, the scatter plots and linear regressions in Figure 6 are conducted with samples from the average size of $50\text{m} \times 50\text{m}$, which obtains more samples than an average size of $100\text{m} \times 100\text{m}$.

4.2 Effects of wind direction

Roughly speaking, VR is lower in the simulation with southwesterly input than in that with easterly input, which may be due to the street orientations in the area. Change in the input wind direction causes modifications in local (subdomains in the neighborhood) urban morphology and geometry parameters in AVA, such as the frontal area density. The local roughness length in the LES model takes effect when the wind sweeps across the ground and walls. The higher the proportion of ground and walls the wind has to sweep across, the larger the friction effects on the wind. Therefore, effects of wind direction on air ventilation are combined with local roughness length.

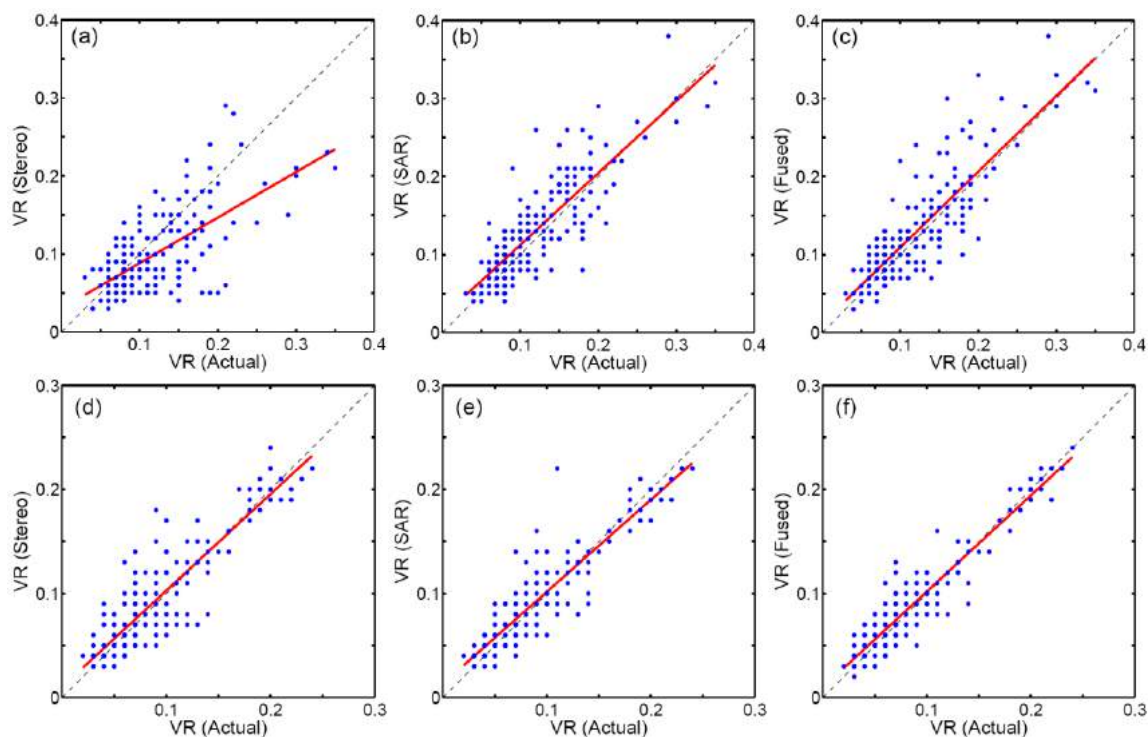


Figure 6: Scatter plots (blue dots) and linear regressions (red solid lines) of PALM-computed VR with actual topography and topography extracted from (a, d) Stereo image, (b, e) SAR image, and (c, f) fused result of the two images. Wind input is from the east (southwest) for a–c (d–f). Average size is $50\text{m} \times 50\text{m}$.

RMSEs in Table 1 suggest that building heights extracted from Stereo images give the worst performance compared with the other two methods. When comparing SAR and fused results, it is found that the fused results have better performance when given a southwest wind, while the SAR result is slightly better in case of east wind. Figure 6 further demonstrate the performance of data retrieved from different methods. It can be seen that the Stereo result has a large bias from the actual topography in the LES experiment with east wind (Figure 6a), while it has a better performance in the LES experiment with southwest wind (Figure 6d). The performances of SAR and the fused results are close to each other and reasonable in the LES experiment with both east and southwest wind (Figures 6b, c, e, and f).

4.3 Effects of building height

Using the average absolute difference from measured data to evaluate the retrieved results, Xu [2015] discovered that Stereo images provide better results for buildings below 100m, particularly for buildings below 50m, while SAR images provide better results for higher buildings (e.g., above 100 m). Tall buildings are underestimated by the Stereo images, which can be seen in Figure 1b. If we check the details of VR bias inside the congested urban spaces (dashed grid boxes in Figures 4 and 5), which are reliable because lateral boundary areas are avoided, it can be seen that a larger bias can be found in the Stereo result than in the SAR result in the simulations, particularly for wind input from the east. This implies that a better representation of higher buildings may contribute more to the quality of pedestrian-level ventilation simulations, as high-rise buildings can experience high wind loads and concentrate pedestrian-level winds [Liu, 2005; Yim, 2009].

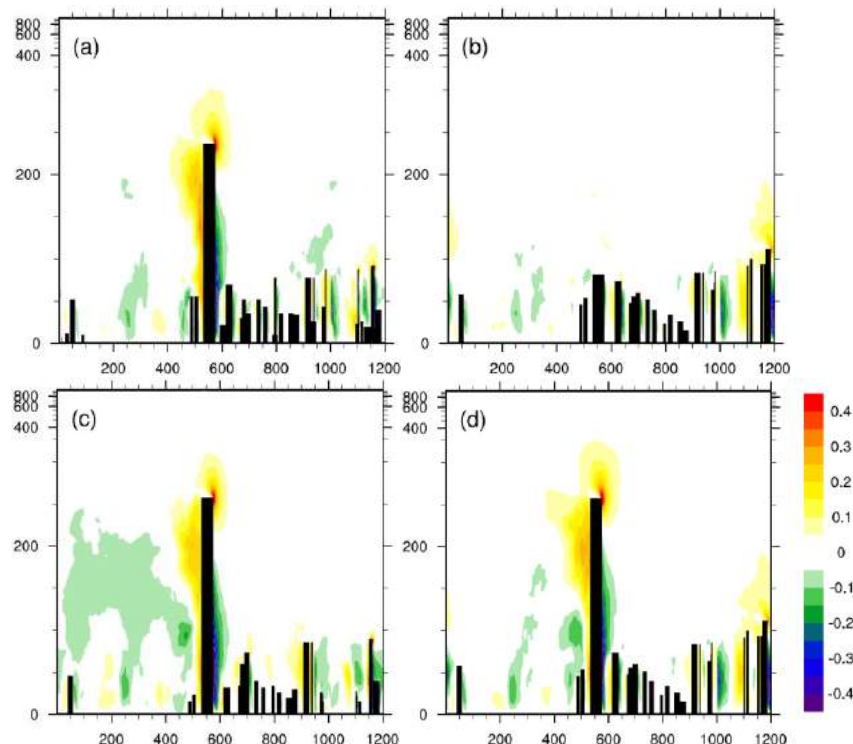


Figure 7: Time-averaged vertical velocity in a specific section with a high-rise building from (a) actual urban elevations, and urban elevations extracted from (b) Stereo image, (c) SAR image, and (d) fused result of the two images. The wind input is from the east (right)

We further demonstrate this dynamically using an extreme case: the tallest building is at a coordinate of approximately $x=550\text{m}$, $y=1000\text{m}$ (Figure 1). Figure 7 shows the vertical

velocity of the x-z cross section at $y=1000\text{m}$, which crosses the tallest building on the site. The results of the LES experiment with east wind input from all four topography datasets are shown. It is obvious that both the SAR and fused results can capture the high-rise building as well as the vertical motion around it, while the Stereo result fails to do so. When the wind comes from the east (right-hand side of Figure 7), the high-rise building blocks the wind and results in strong sinking motion on its windward side and rising motion in front of its steeple and on the leeward side. This vertical motion will further induce horizontal winds and gusts at the pedestrian level, and hence increase ventilation in the subdomain where the high-rise building stands. It is also noteworthy that a similar structure of vertical motion can be found around relatively high buildings in Figure 7, which suggests that better performance in representing higher buildings, rather than lower buildings, is more important in building height extraction for AVA purposes.

5 Discussion

Extraction of urban information from satellite images has become a hot topic in remote sensing studies [Colin-Koeniguer, 2014; Jin, 2005; Sportouche, 2011; Zhou, 2014], as these techniques are important for urban studies [Ren, 2011]. Therefore, assessment of these techniques should be done in combination with urban applications, which is the origin of the present study. As a case study, building information in a high-density urban area in Mong Kok, Hong Kong, including both actual information and that retrieved from satellite images, is adopted from a newly published report [Xu, 2015] and is evaluated by comparing pedestrian-level ventilation in an LES model. This is challenging because urban wind environments are extremely sensitive to urban morphologies and building geometries [Shi, 2015; Yang, 2013]. The accuracy requirement of urban geometries and building heights for AVA studies may be higher than that for other studies, such as thermal analysis without considering wind effects. As one can imagine, the effects of buildings on thermal conditions arise mainly through shading and anthropogenic heat generated by the buildings, and these effects are more localized than effects of building geometries on the wind environment.

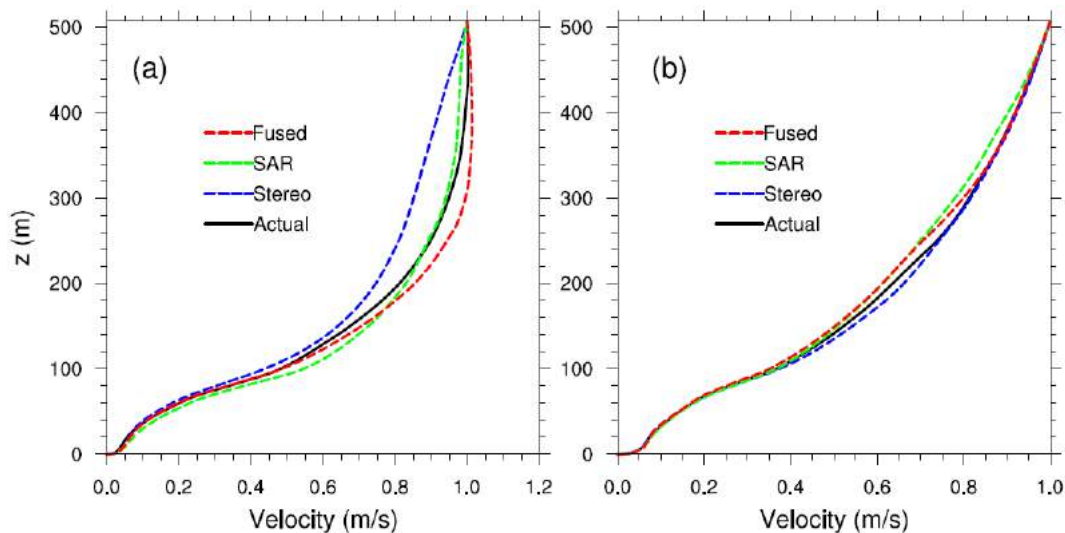


Figure 8: Horizontally averaged wind profile within the canopy normalized by the velocity at the canopy top (500m). (a) Wind input from the east, and (b) Wind input from the southwest

Our results show that simulated pedestrian-level wind speed is sensitive to the given wind directions, which in essence are sensitive to building geometries. The term “roughness length”

discussed in this study is not the city-scale roughness length that is applied in wind tunnel tests, but the so-called “local roughness length” that is imposed in each local grid box adjacent to a horizontal or vertical surface [Letzel, 2012]. The city-scale roughness length in front of the targeted area (a city or a neighbourhood) for generating the input wind profile in wind tunnel tests or CFD is not involved in the LES experiments in this study. The reason is to save simulation domain, and in turn, computational time. As mentioned, a vertically unique wind velocity is imposed. Associated with the cyclic boundary condition setting and adequate time (4 hours) for turbulence spin-up, a sufficient vertical wind profile can be generated in the simulation, as shown in Figure 8. Figure 8 also implies that the performance in reproducing the horizontally averaged velocity profile in the canopy layer is generally consistent with the performance in pedestrian-level VR. The result from Stereo data (dashed blue lines) has a larger discrepancy from the actual (solid black lines) compared to the SAR (dashed green line) and fused data (dashed red line), particularly for the case of wind input from the east (Figure 8a), which agrees with the scatter plot in Figure 6a showing the largest discrepancy when compared to other cases.

Finally, studies on urban wind environments using the LES technique require accurate urban morphologies and building geometries, i.e., precise urban elevation data. For the retrieved data used in this study, building footprints are assumed to be known before the building heights are extracted. Hence the street patterns are basically the same among all four sets of data evaluated in this study, and differences in pedestrian VR are caused mainly by building height and building volume differences. However, building footprints are probably not known, in the case of not knowing the realistic elevation data. Building height retrievals from satellite images without knowing building footprints and corresponding evaluations from the perspective of urban applications should be initiated in further studies.

6 Conclusions

This study performs a set of LES experiments using PALM to evaluate building height extraction from satellite images in an urban area of Mong Kok, Hong Kong. This comparative study is done from the practical perspective of urban ventilation. Major findings can be summarized as follows: First, building heights extracted from the Stereo image have the worst performance compared to those from the SAR image and the fused result of both images. Both the SAR and fused results can be considered acceptable for AVA purposes in this assessment in terms of their low RMSEs compared with the actual results. Second, it is known that high-rise buildings produce strong concentrated wind loads at the pedestrian level, and it is documented that data extracted from Stereo images produce better representations of low buildings, while data extracted from SAR images provide better results with high buildings. This may be the reason why a larger bias is found in the Stereo result than in the SAR result in both east and southwest wind simulations. A further implication for this point is that retrieval methods with better representation of higher buildings, and in turn better reproduction of the overall urban layer wind structure in CFD simulations, can obtain better urban ventilation results for AVA purposes.

Acknowledgments This study was supported by the Research Grants Council of the Hong Kong Special Administrative Region (Project No. 14408214), and Institute of Environment, Energy and Sustainability, CUHK (Project ID: 1907002).

References

- [Arnfield 2003] Arnfield A. J., Two decades urban research: a review of turbulence, exchanges of energy and water, and the urban heat island, *International Journal of Climatology*, vol. 23, Pages 1-26, 2003
- [Britter 2003] Britter R. E., Hanna S. R., Flow and dispersion in urban areas, *Annual Review of Fluid Mechanics*, vol. 35 no. 1, Pages 469-496, 2003
- [Castillo 2011] Castillo M. C., Inagaki A., Kanda M., The effects of inner- and outer-layer turbulence in a convective boundary layer on the near-neutral inertial sublayer over an urban-like surface, *Boundary-Layer Meteorology*, vol. 140 no. 3, Pages 453-469, 2011
- [Colin-Koeniguer 2014] Colin-Koeniguer E., Trouve N., Performance of building height estimation using high-resolution PolInSAR images, *IEEE Transactions on Geoscience and Remote Sensing*, vol. 52 no. 9, Pages 5870-5879, 2014
- [Eckert 2010] Eckert S., Hollands T., Comparison of automatic DSM generation modules by processing IKONOS stereo data of an urban area, *IEEE Journal of Selected Topics in Applied Earth Observation and Remote Sensing*, vol. 3 no.2, Pages 162-167, 2010
- [Emmanuel 2006] Emmanuel R., Johansson E., Influence of urban morphology and sea breeze on hot humid microclimate: the case of Colombo, Sri Lanka, *Climate Research*, vol. 30, Pages 189-200, 2006
- [Hong Kong Planning Department 2008] Hong Kong Planning Department, Working Paper 2B: Wind tunnel benchmarking studies, batch I, in: *Urban climatic map and standards for wind environment - feasibility study*, 587 pages, November 2008
- [Inagaki 2011] Inagaki A., Castillo M. C. L., Yamashita Y., Kanda M., Takimoto H., Large-eddy simulation of coherent flow structures within a cubical canopy, *Boundary-Layer Meteorology*, vol. 142 no.2, Pages 207-222, 2011
- [Jin 2005] Jin X., Davis C. H., Automated building extraction from high-resolution satellite imagery in urban areas using structural, contextural, and spectral information, *EURASIP Journal on Applied Signal Processing*, vol. 14, Pages 2196-2206, 2005
- [Kanda 2013] Kanda M., Inagaki A., Miyamoto T., Gryschka M., Raasch S., A new aerodynamic parameterization for real urban surfaces, *Boundary-Layer Meteorology*, vol. 148 no. 2, Pages 357-377, 2013
- [Keck] Keck M., Raasch S., Letzel M. O., Ng E., First results of high resolution large-eddy simulations of the atmospheric boundary layer, *Journal of Heat Island Institute International*, vol. 9 no. 2, Pages 39-43, 2014
- [Letzel 2008] Letzel M. O., Krane M., Raasch S., High resolution urban large-eddy simulation studies from street canyon to neighbourhood scale, *Atmospheric Environment*, vol. 42 no. 38, Pages 8770-8784, 2008
- [Letzel 2012] Letzel M. O., Helmke C., Ng E., An X., Lai A., Raasch S., LES case study on pedestrian level ventilation in two neighbourhoods in Hong Kong, *Meteorologische Zeitschrift*, vol. 21 no. 6, Pages 575-589, 2012
- [Lindberg 2010] Lindberg F., Grimmond C. S. B., Continuous sky view factor maps from high resolution urban digital elevation models, *Climate Research*, vol. 42 no. 3 Pages, 177-183, 2010

- [Liu 2005] Liu H., Jiang Y., Liang B., Zhu F., Zhang B., Sang J., Studies on wind environment around high buildings in urban areas, *Science in China Ser. D Earth Sciences*, vol. 48 Supp. 2 Pages, 102-115, 2005
- [Maronga 2015] Maronga B., Gryschka M., Heinze R., Hoffmann F., Kanani-Sühring F., Keck M., Ketelsen K., Letzel M. O., Sühring M., Raasch S., The Parallelized Large-Eddy Simulation Model (PALM) version 4.0 for atmospheric and oceanic flows: model formulation, recent developments, and future perspectives, *Geoscientific Model Development Discussions*, vol. 8 no. 2, Pages 1539-1637, 2015
- [Mochida 2002] Mochida A., Tominaga Y., Murakami S., Yoshie R., Ishihara T., Ooka R., Comparison of various κ - ϵ models and DSM applied to flow around a high-rise building — Report on AIJ cooperative project for CFD prediction of wind environment, *Wind Structure*, vol. 5, Pages 227-44, 2002
- [Ng 2009] Ng E., Policies and technical guidelines for urban planning of high-density cities – air ventilation assessment (AVA) of Hong Kong, *Building and Environment*, vol. 44 no. 7, Pages 1478-1488, 2009
- [Ng 2011] Ng E., Yuan C., Chen L., Ren C., Fung J. C. H., Improving the wind environment in high-density cities by understanding urban morphology and surface roughness: A study in Hong Kong, *Landscape and Urban Planning*, vol. 101 no. 1, Pages 59-74, 2011
- [Ng 2012] Ng E., Cheng V., Urban human thermal comfort in hot and humid Hong Kong, *Energy and Buildings*, vol. 55, Pages 51-65, 2012
- [Park 2012] Park S. B., Baik J. J., Raasch S., Letzel M. O., A large-eddy simulation study of thermal effects on turbulent flow and dispersion in and above a street canyon, *Journal of Applied Meteorology and Climatology*, vol. 51 no. 5, Pages 829-841, 2012
- [Park 2014] Park S. B., Baik J. J., Large-eddy simulations of convective boundary layers over flat and urbanlike surfaces, *Journal of the Atmospheric Sciences* 71(5):1880-1892, 2014
- [Raasch 2001] Raasch S., Schröter M., PALM - A large-eddy simulation model performing on massively parallel computers, *Meteorologische Zeitschrift*, vol. 10, Pages 363-372, 2001
- [Ramponi 2015] Ramponi R., Blocken B., de Coen L. B., Janssen W. D., CFD simulation of outdoor ventilation of generic urban configurations with different urban densities and equal and unequal street widths, *Building and Environment*, vol. 92, Pages 152-166, 2015
- [Razak 2013] Razak A. A., Hagishima A., Ikegaya N., Tanimoto J., Analysis of airflow over building arrays for assessment of urban wind environment, *Building and Environment*, vol. 59, Pages 56-65, 2013
- [Ren 2011] Ren C., Ng E., Katzschner L., Urban climatic map studies: a review, *International Journal of Climatology*, vol. 31 no. 15, Pages 2213-2233, 2011
- [Rodi 1997] Rodi W., Ferziger J. H., Breuer M., Pourqui e M., Status of large eddy simulation: results of a workshop, *Journal of Fluids Engineering*, vol. 119 no. 2, Pages 248-262, 1997
- [Schatzmann 2011] Schatzmann M., Leitl B., Issues with validation of urban flow and dispersion CFD models, *Journal of Wind Engineering and Industrial Aerodynamics*, vol. 99 no. 4, Pages 169-189, 2011
- [Shi 2015] Shi X., Zhu Y., Duan J., Shao R., Wang J., Assessment of pedestrian wind

environment in urban planning design, *Landscape and Urban Planning*, vol. 140, Pages 17-28, 2015

[Skote 2005] Skote M., Sandberg M., Westerberg U., Claesson L., Johansson A., Numerical and experimental studies of wind environment in an urban morphology, *Atmospheric Environment*, vol. 39 no. 33, Pages 6147-6158, 2005

[Sportouche 2011] Sportouche H., Tupin F., Denise L., Extraction and three-dimensional reconstruction of isolated buildings in urban scenes from high-resolution optical and SAR spaceborne images, *IEEE Transactions on Geoscience and Remote Sensing*, vol. 49 no.10, Pages 3932-3946, 2011

[Tamura 2008] Tamura T., Towards practical use of LES in wind engineering, *Journal of Wind Engineering and Industrial Aerodynamics*, vol. 96 no.10-11, Pages 1451-1471, 2008

[Tominaga 2008] Tominaga Y., Mochida A., Yoshie R., Kataoka H., Nozu T., Yoshikawa M., et al., AIJ guidelines for practical applications of CFD to pedestrian wind environment around buildings, *Journal of Wind Engineering and Industrial Aerodynamics*, vol. 96, Pages 1749-61, 2008

[Unger 2004] Unger J., Intra-urban relationship between surface geometry and urban heat island: review and new approach, *Climate Research*, vol. 27, Pages 253-264, 2004

[Wong 2011] Wong M. S., Nichol J., Ng E., A study of the “wall effect” caused by proliferation of high-rise buildings using GIS techniques, *Landscape and Urban Planning*, vol. 102 no. 4, Pages 245-253, 2011

[Xu 2015] Xu Y., Ma P., Ng E., Lin H., Fusion of WorldView-2 stereo and Multitemporal TerraSAR-X images for building height extraction in urban areas, *IEEE Geoscience and Remote Sensing Letters*, vol. 12, Pages 1795-1799, 2015

[Yang 2013] Yang F., Qian F., Lau S. S. Y., Urban form and density as indicators for summertime outdoor ventilation potential: A case study on high-rise housing in Shanghai, *Building and Environment*, vol. 70, Pages 122-137, 2013

[Yim 2009] Yim S. H. L., Fung J. C. H., Lau A. K. H., Kot S. C., Air ventilation impacts of the “wall effect” resulting from the alignment of high-rise buildings, *Atmospheric Environment*, vol. 43 no. 32, Pages 4982-4994, 2009

[Yuan 2012] Yuan C., Ng E., Building porosity for better urban ventilation in high-density cities – A computational parametric study, *Building and Environment*, vol. 50, Pages 176-89, 2012

[Zhou 2014] Zhou G. Q., Zhou X., Seamless fusion of LiDAR and aerial imagery for building extraction, *IEEE Transactions on Geoscience and Remote Sensing*, vol. 52 no. 11, Pages 7393-7407, 2014



*Empowered lives.
Resilient nations.*



Pontificia Universidad
Católica del Ecuador



Facultad
arquitectura, diseño y artes
PUCE



MAS
Maestría en Arquitectura
y Sostenibilidad



utc
SORBONNE UNIVERSITES



UNIVERSITÉ
DE PAU ET DES
PAYS DE L'ADOUR

ISBN 978-9942-951-53-3



9 789942 951533